Study of New Functional Molecular Materials Based on π-Conjugated Oligomers, Dithiafulvene, and Tetrathiafulvalene Vinylogues

by

© Karimulla Mulla

A Thesis submitted to the

School of Graduate Studies

in partial fulfillment of the requirements

for the degree of Doctor of Philosophy

Department of Chemistry

Memorial University

May 2014

St. John's Newfoundland

Abstract

This thesis is primarily aimed at the development of new functional organic materials based on two classes of important π-conjugated molecular building blocks, namely conjugated oligomers and tetrathiafulvalene analogues (TTFVs). While rational molecular design has been the overarching theme of my synthetic and characterization work, the ultimate objective of this research is locked on exploring applications in nanoscale molecular and supramolecular materials and devices. The detailed thesis work consists of three major projects as summarized below.

The first project investigates a series of boronic acid functionalized π-conjugated oligomers as efficient fluorescence chemosensors for some biologically important analytes (e.g., monosaccharides and fluoride ion). The novelty of this project lies in the design of diverse shapes and π-conjugation patterns of the oligomer fluorophores. In particular, structurally-defined co-oligomers made of phenylene ethynylene and phenylene vinylene repeat units (simply referred to as OPE/OPV hybrids), which were constructed in linear, cruciform, and H-shapes. Synthetic access to these unprecedented π-oligomers has allowed systematic characterizations and comparative studies to be conducted, leading to in-depth understanding of the fundamental structure-property relationships. The second project deals with the synthesis of dithiafulvalene (DTF) endcapped OPE/OPV co-oligomers and the characterization of their supramolecular interactions with carbon nanomaterials (fullerenes and carbon nanotubes). These studies indicate that the DTF functionality plays a key role in enhancing the non-covalent binding

of the DTF-derived oligomers with fullerenes and carbon nanotubes, owing to the excellent electron-donating properties of DTF. The third project embarked on the design of a group of novel TTFV-arene hybrids as synthetic receptors for fullerenes and transition metal ions. The chemical synthesis of these functional materials has been implemented on the basis of various classical and modern organic synthetic methodologies, such as the Arbuzov reaction, the Horner-Wittig reaction, the Sonogashira coupling and the Cu-catalyzed alkyne azide coupling (one of the flagship click reactions). The use of such high-yielding reactions paved the way for modular preparation of TTFV-based chemosensors and other functional molecular systems.

While a major portion of this thesis work is dedicated to advanced organic synthesis, material characterizations using state-of-the-art instrumental techniques constitutes an indispensible part as well. It is worth highlighting that the characterization work done in this thesis encompasses a broad range of analytical methods, including UV-Vis absorption and fluorescence spectroscopy, electrochemical (cyclic voltammetry and differential pulse voltammetry) analyses, atomic force microscopy (AFM), and single-crystal X-ray structure analysis. Moreover, the acquired UV-Vis and fluorescence data in the studies of chemosensors and receptors were subjected to a comprehensive global spectral fitting analysis to elicit equilibrium constants and binding stoichiometry in an accurate and reliable manner.

Acknowledgements

It is a pleasure for me to express my sincere gratitude and respect to my supervisor, Prof. Yuming Zhao, for his genuine guidance and support during my research at Memorial University. Dr. Zhao is a brilliant supervisor, and his passion and enthusiasm for chemistry inspired me so much. Dr. Zhao, you are a great mentor and you have been very generous in sharing your rich and valuable knowledge with me. I am truly grateful to you from the bottom of my heart.

I would like to acknowledge my supervisory committee members, Prof. David Thompson and Prof. Ray Poirier, for their encouragement and helpful suggestions during my research work.

I would like to thank Prof. David Thompson again, as well as his Ph.D student Mr. Prateek Dongare, who provided excellent collaborations on the spectral studies of some compounds. I am so grateful to Prof. Alex Adronov, at McMaster University, and his Ph.D student, Mr. Shuai Liang (who obtained his Master's in our group), who have also been much appreciated collaborators with our group. Sincere thanks to Prof. Louise Dawe for analyzing and solving single crystal structures, and to Mrs. Lidan Tao for mass spectrometric analyses.

I would also like to thank Dr. Guang Chen for his training and invaluable suggestions during my study. I also would like to extend my thanks to all my lab mates, especially to Master's student Ms. Kathleen Woolridge, for her kind help and discussions

over the years. Special thanks to all other members of the organic chemistry division for their enthusiasm and team spirit in this program.

I would like to expand my thanks to include all the professors of the organic chemistry department at Memorial, including Prof. Paris Georghiou, Prof. Graham Bodwell, and Prof. Sunil Pansare, for their advice and well-considered suggestions during my study.

Finally, I would like to thank my wonderful family, my parents, my wife, and my daughter for their unconditional love and support throughout the course of my Ph. D.

Contents

List of Figures

List of Schemes

List of Tables

List of Abbreviations and Symbols

1D	one-dimension
2D	two-dimension
A	acceptor
ADMET	acyclic diene metathesis
AFM	atomic force microscopy
AIE	aggregation-induced emission
Bu	butyl
cm	centimeter
CM	cross metathesis
COT	1,3,5,7-cyclooctatetraene
CoMoCAT	cobalt-molybdenum catalyzed nanotubes
CNTs	carbon nanotubes
CuAAC	Cu-catalyzed alkyne azide coupling
CV	cyclic voltammetry
CVD	chemical vaporization deposition
D	donor
d	doublet
dd	doublet of doublet
DBU	1,8-diazabicyclo[5.4.0]undec-7-ene
dec	decomposed

DFT	density functional theory
DIBAL	diisobutylaluminium hydride
DMF	dimethyl formamide
DMSO	dimethyl sulfoxide
DNA	deoxyribonucleic acid
DPA	di-2-picolylamine groups
E_g	bandgap energy
EL	electroluminescence
Et	ethyl
FET	Field effect transistor
FMO	frontier molecular orbital
FRET	fluorescence resonance energy transfer
FTIR	Fourier transform Infrared
g	gram(s)
GO	graphene oxide
h	hour(s)
HRTEM	high-resolution transmission electron microscopy
HOMO	highest occupied molecular orbital
HiPCO	high pressure CO disproportionation
ICT	intramolecular charge transfer
IL	ionic liquid
IR	infrared
ITO	indium tin oxide

kV	kilovolts
LCD	liquid crystal display
LCMS	liquid chromatography-mass spectrometry
LDA	lithium diisopropylamide
LED	light emitting diode
LHMDS	lithium hexamethyldisilazide
LUMO	lowest unoccupied molecular orbital
m	multiplet
m/z	mass to charge ratio
mA	milliampere
MALDI-TOF	matrix assisted laser desorption/ionization-time of light
Me	methyl
MEH-PPV	poly-2-methoxy-5-(2-ethylhexoxy)-*p*-phenylenevinylene
mg	milligram(s)
MHz	megahertz
min	minute(s)
mL	milliliter
mmol	millimole
mol	mole
mp	melting point
MPA	3-mercaptopropionic acid
MS	mass spectrometry
MWNTs	multi walled carbon nanotubes

NBS	N-bromosuccinimide
NLO	nonlinear optics
nm	nanometer
NMR	nuclear magnetic resonance
OFET	organic field effect transistor
OLED	organic light emitting diode
OTFT	organic thin-film transistors
OPE	oligo(*p*-phenyleneethynylene)
OP	oligo(*p*-phenylene)
OPV	oligo(*p*-phenylene vinylene)
OT	oligo(*p*-thiophene)
P	para
PA	poly(acetylene)
PAHs	polyacyclic hydrocarbons
PAM	phenylacetylene macrocycle
PCBM	[6,6]-phenyl C_{61}-butyric acid methyl ester
PCC	pyridinium chlorochromate
PCT	photoinduced charge transfer
PDA	poly(diacetylene)
PDC	pyridinium dichromate
PDT	photodynamic therapies
*p*DTFF-*m*T	poly(dithiafulvalene-fluorene-*co*-*m*-thiophene)s
PEDOTPSS	poly(3,4 ethylenedioxylenethiophene)-polystylene sulfonic acid

PET	photoinduced electron/energy transfer
PFs	polyfluorenes
PFVs	poly(fluorylenevinylene)s
PTs	polythiophenes
Ph	phenyl
P3HT	poly(3- hexylthiophene)
PPE	poly(p-phenyleneethynylene)
ppm	parts per million
PPP	poly(p-phenylene)
PPV	poly(p-phenylenevinylene)
PSCs	polymer based solar cells
PTA	poly(triacetylene)
PVC	polyvinyl chloride
PVP	polyvinylpyrrolidone
QDs	quantum dots
RBM	radial breathing mode
RCM	ring-closing metathesis
ROMP	ring-opening metathesis polymerization
s	second or singlet
satd	saturated
STM	scanning tunneling microscope
SWNTs	single walled carbon nanotubes
t	triplet

tb	triplet of doublet
TBAB	tetra-*n*-butylammonium bromide
TBACl	tetra-*n*-butylammonium chloride
TBAF	tetra-*n*-butylammonium fluoride
TBAI	tetra-*n*-butylammonium iodide
TEAB	tetraethylammonium bromide
TEM	transmission electron microscope
TfOH	trifluoromethanesulfonic acid
THF	tetrahydrofuran
THPC	tetrakis(hydroxymethyl)phosphonium chloride
TIPS	triisopropylsilyl
TIPSA	triisopropylsilylacetylene
TLC	thin-layer chromotography
TMEDA	tetramethylethylenediamine
TMS	trimethylsilyl
TMSA	trimethylsilylacetylene
TMV	tobacco mosaic virus
TTF	tetrathiafulvalene
TTFV	tetrathiafulvalene vinylogue
TTFAQ	N,N,N',N'-tetrathiafulvaleneanthraquinone
UV-Vis	ultraviolet-visible
UV-Vis-NIR	ultraviolet-visible-near Infrared
V	volt

W	watt
XRD	X-ray diffraction
δ	chemical shift
λ_{em}	maximum emission wavelength
λ_{max}	maximum absorption wavelength

Chapter 1

Introduction

1.1 An Overview of Nanomaterials

The word “nano” has captured considerable attention from almost all scientific disciplines in the past few decades, as it shows the way to the nanometer-scale world where the smallest human–made devices can have a communication with the atoms and molecules of the natural world.[1] In general, nanotechnology and nanoscience refer to the study and manipulation of nanosize materials. These nanomaterials are characterized by their spatial dimensions, ranging from about 0.1 nm to 500 nm, and they have demonstrated novel applications in numerous fields. Nanomaterials exhibit significantly different chemical and physical properties compared to the bulk materials with the same chemical composition. The unique and unprecedented structural properties of nanomaterials can lead to new generation of devices and technologies, however, the synthesis of nanomaterials with controlled sizes and shapes is a challenging task. For this reason, great efforts have been made by material chemists to pursue useful synthetic methods to access well-defined nanomaterials as well as to explore their practical applications.

The beginning of nanotechnology can be traced back to a visionary statement by Richard Feynman, a famous physicist who won the Noble prize in physics in 1965. In 1959, Feynman gave a series of lectures on physics at an American Physics Society meeting held at Caltech. In one of the lectures, he started with that, "*there is plenty of room at the bottom, not just room at the bottom, what I demonstrate is that there is plenty of room that you can decrease the size of things in a practical way"*. With that being said, he continued to suggest that ordinary machines could be brought to the molecular level by a step down process. Eventually, this lecture laid the foundation for a new field of science and technology, which is now widely known as nanotechnology. In theory, the production of nanomaterials can be conducted via two major approaches, "top-down" and "bottom-up", as categorized by professor Ozin at the University of Toronto.[2] The top-down approach has been mainly developed by the community of solid-state physicists and it is associated with the break-down of bulk materials using microfabrication methods to nanometer size with a desired shape. However, this method has an important limitation; that is, a large proportion of materials is wasted during the production process. On the other hand, the bottom-up approach, which has been mostly adopted by chemists, utilizes the fundamental principles of self-assembly to make nanomaterials with large superstructures from small molecular building blocks. The field of nanochemistry has thus grown explosively because of an increasing interest in the bottom-up approach by chemists and it provides an alternative to the preparation of nanomaterials that cannot be accessed via the top-down approach.

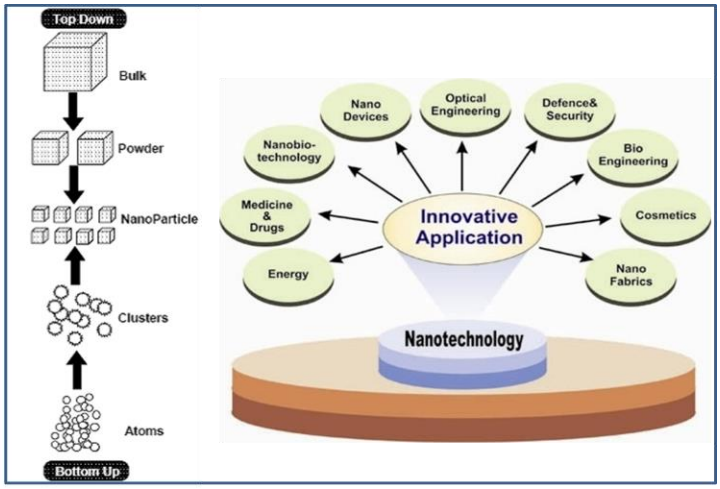

Figure 1.1: Schematic diagram showing the top-down and bottom-up approaches for the synthesis of nanomaterials (left) and applications of nanomaterials (right) (Adopted from reference 2 with permission).

One of the greatest challenges in nano-science and technology is how to synthetically create functional nanomaterials with desired properties, high degrees of structural order, and high performance. In recent years, the bottom-up approach for the synthesis of nanomaterials has become more popular than the top-down approach, as it allows better structure and property control at the molecular level. A thorough understanding of the concepts of supramolecular chemistry has enabled various synthetic protocols to be developed for precise and convenient assembly of molecular components into complex supramolecular structures. Nature has created a vast array of complex nanostructures on the nanometer scale with amazing accuracy and precision. This has been a key inspiration behind the synthetic methodologies developed to create nanostructures through the bottom-up approach. For example, an understanding of the

self assembly of tobacco mosaic virus (TMV) has inspired the construction of some analogous nanodevices (Figure 1.2).[3]

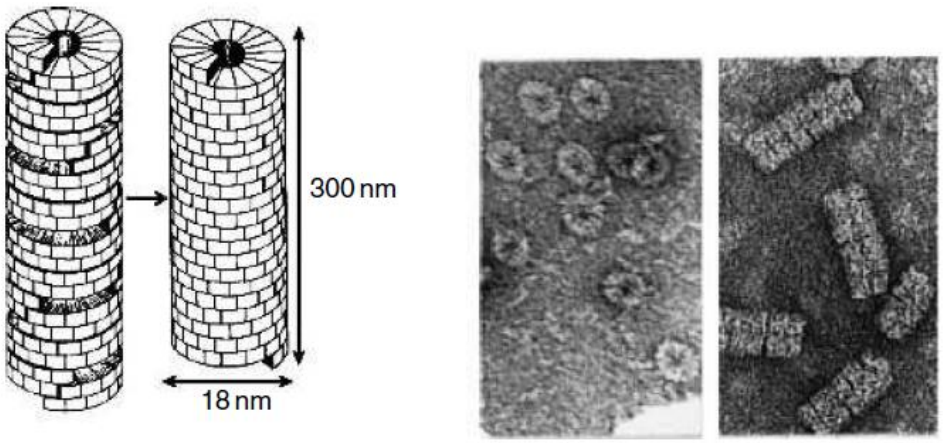

Figure 1.2: Self assembly of TMV virus (Adopted from reference 3 with permission).

It is a known fact that mimicking naturally existing nanostructures based on the current synthetic chemistry is too complicated and always challenging. More efforts are needed to first understand the self-assembling behavior in biological nanostructures. Presently, one of the key goals in the research on nanotechnology is aimed at the creation of ultra-miniaturized nanodevices that show superior properties and unprecedented molecular functions. Initially, the development of new nanomaterials and new fabrication methodologies for molecular devices was mainly based on inorganic materials. However, in the last two decades, there has been an exponential growth of nanotechnology as a result of the development of new synthetic strategies for organic based nanomaterials in conjunction with the availability of advanced research tools for their characterization and manipulation. In this respect, the number of π-conjugated organic nanomaterials for

electronic, optoelectronic and photonic applications has increased significantly and the use of organic nanomaterials has encompassed a wide range of fields; for example, organic light-emitting diodes (OLEDs), organic thin-film transistors (OTFTs), optical lasers, photodynamic therapies (PDT), and organic solar cells.[4] In the following section, some landmarks in recent nanochemistry research will be introduced and discussed.

1.2 Landmarks in Nanochemistry

There are several milestones in the history of nanoscience and nanotechnology. In the mid 1980s, Eric Drexler, one of the founding fathers of modern nanotechnology, introduced the concept of building nanomaterials in an atom-by-atom manner and dreamed of constructing nanomachines.[5] Since then the focuses on nanoscience and nanotechnology have interfaced with other disciplines, such as biology, chemistry, electrical engineering, and many others, to create a completely new area of research. According to Drexler, a nanomachine is a toolbox consisting of many nanorobots. Each of the nanorobots can move molecules so quickly and place them in a systematic manner to produce any kinds of desirable substances. He also envisioned that these tiny machines would interact directly with the molecular components of cells and be capable of repairing the tissue or killing frozen cells. However, with the current technology, this imaginary concept is most unlikely to happen soon. On the other hand, there are on-going investigations into mimicking biologically existing materials that are of great interest to current nanotechnology research.

1.2.1 Supramolecular Chemistry

The most important field of chemistry that has indeed accelerated the development of nanoscience and nanotechnology is supramolecular chemistry. Jean-Marie Lean, a renowned French chemist, is known as the father of supramolecular chemistry. He shared the 1987 Noble Prize in chemistry with Donald Cram and Charle Pedersen for his pioneered work in supramolecular chemistry. Simply defined as "beyond the molecular chemistry", supramolecular chemistry primarily focuses on the studies of the non-covalent interactions between molecules rather than the covalent forces within molecules; for instance, how molecules recognize each other and self-assemble into functional supramolecular systems.[6]

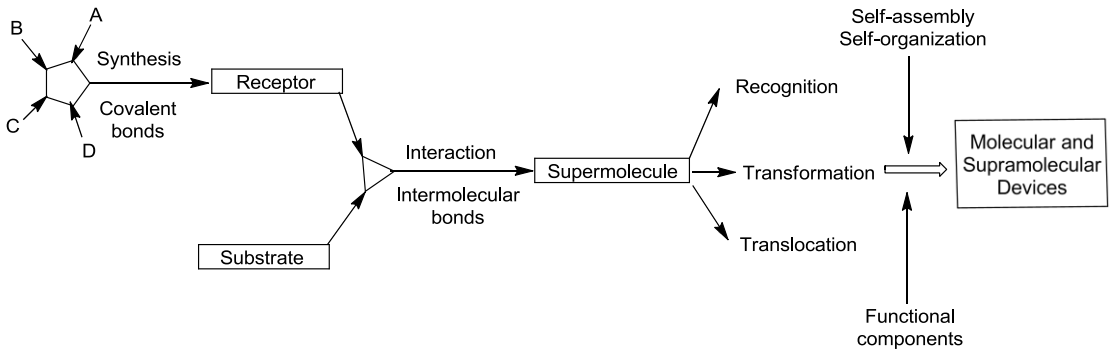

Scheme 1.1: From molecular to supramolecular chemistry: molecules, supermolecules, molecular and supramolecular devices.

The discipline of supramolecular chemistry has expanded substantially accelerated during last two decades, with a thorough understanding of the principles of molecular recognition and self-organization has been well established. The knowledge

offers guidance to the creation of functional molecular nanostructures and devices.[6] For instance, numerous synthetic receptors capable of recognizing specific substrates have been developed based on the fundamental principles of non-covalent interactions taking place in guest-host chemistry. The non-covalent forces are usually weaker than covalent bonding, but if there are numerous such forces acting together between molecules oriented at appropriate distances and geometries, the overall interaction can be strong enough to dictate the molecular and supramolecular properties. Typical non-covalent forces include ion-ion, ion-dipole, and dipole-dipole interactions as well as π-stacking, van der Waals forces, and hydrophobicity.

Self-assembly and self-organization processes in combination with molecular recognition mechanisms offer an alternative to both top-down and bottom-up nanofabrication approaches for creating various advanced supramolecular materials and nanomaterials.[6] Self-assembly is a process of association between two or more molecules by spontaneous non-covalent binding forces to create large nanostructures with desirable shapes. For example, the most complex structure of DNA has been made by the self-organization process, where two individual strands self-assemble via hydrogen bonding and aromatic π-stacking to form a double helical structure. The development of self-assembly as a synthetic approach to create highly ordered functional nanomaterials has been a great challenge. However, synthetic chemists have found ways to control the physical behavior of various molecular materials by altering the functional groups within the molecules. For example, Yagai *et al.* recently demonstrated the hierarchical self-assembly of amide substituted azobenzene dimers into toroidal, tubular, and helical

nanostructures under the control of temperature, concentration, or light (Scheme 1.2).[7] This is one of the finest examples of synthetically derived nanomaterials that mimic biologically existing systems such as the Tobacco Mosaic Virus (TMV).

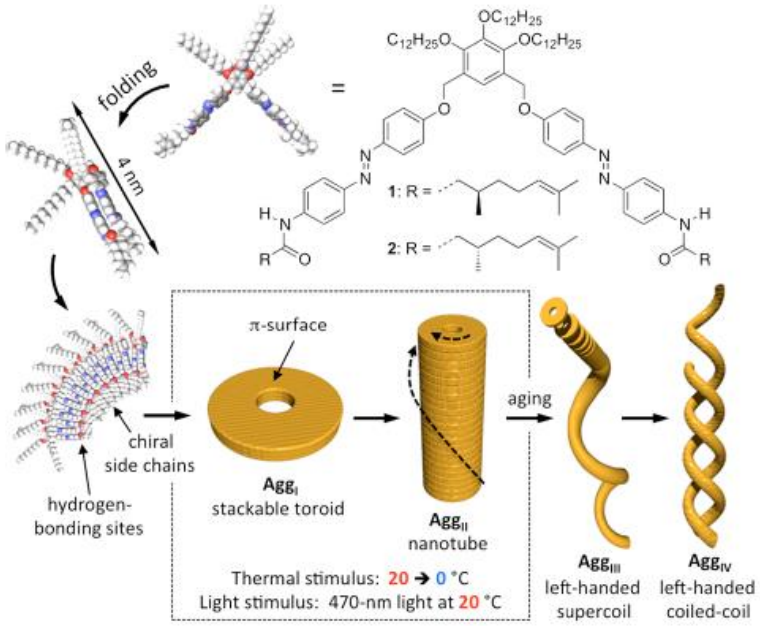

Scheme 1.2: Schematic representation of hierarchical self-assembly of compound **1** (Adopted from reference 7 with permission).

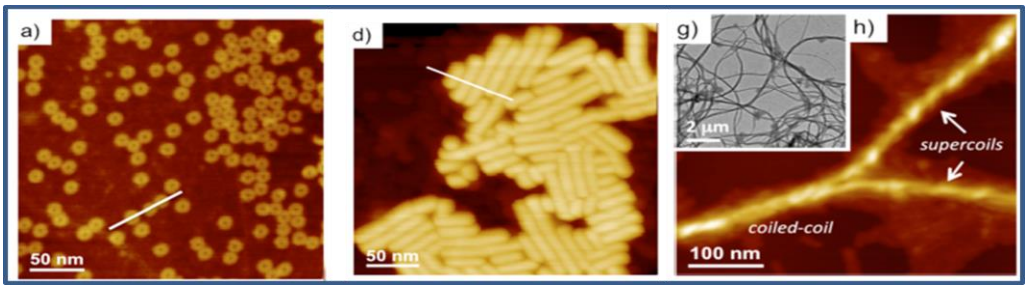

Figure 1.3: AFM images of compound **1** (left and middle), and TEM image of the aggregates of compound **1** (Adopted from reference 7 with permission).

1.2.2 Carbon Nanomaterials

1.2.2.1 Discovery of Fullerenes

Another important milestone in nanotechnology is the discovery of [60]fullerene, which was deemed as the first carbon nanomaterial. Robert Curl, Richard Smalley, and Harold Kroto made the discovery of C_{60} in 1985, which led them to winning the Noble Prize in chemistry in 1996. Their experimental techniques for the production of fullerenes were published in *Nature* in 1985.[8] Among all hollow-carbon materials discovered, C_{60} has been the most thoroughly studied fullerene because it is relatively stable, highly symmetric, and can be abundantly produced.

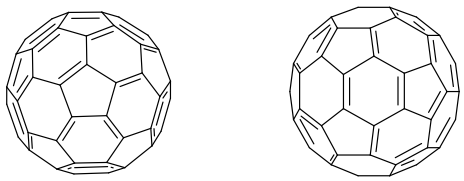

Figure 1.4: Structures of C_{60} (left) and C_{70} fullerenes (right).

C_{60} fullerene appears like a soccer ball in shape and it consists of 12 pentagons and 20 hexagons fused all together. The molecule is spherical and each of the C-C bond angles is deviates from the ideal 120^{o} for an sp^2-hybridized carbon center, which in turn results in a significant bond angle strain. As a result, fullerene exhibits characteristics resembling a polyalkene system. The relief of this strain is primarily responsible for the chemical reactivity of C_{60} fullerene. The electronic properties of C_{60} dictate that it has a

low-lying triply degenerate LUMO level, which makes C_{60} a good electron acceptor. Upon reduction, the surface of C_{60} can hold up to six electrons in total.

Initially, C_{60} could be synthesized only in small quantities due to the low yield of the production method. In 1990, Wolfgang Kratschmer and Donald Huffman came up with a simple method of producing C_{60} fullerene by arc-vaporization of graphite, which opened the avenue for large-quantity production of C_{60}.[9] Indeed, the scientific community immediately benefited from this discovery, while the study of C_{60} based nanomaterials has been substantially developed ever since then. The low solubility of fullerenes in common organic solvents and water restricts their use in various applications. However, covalent and non-covalent functionalizations of C_{60} fullerene have produced a wide variety of C_{60} fullerene derivatives which not only show greatly improved solubility but also retain most of the properties of pristine C_{60}.

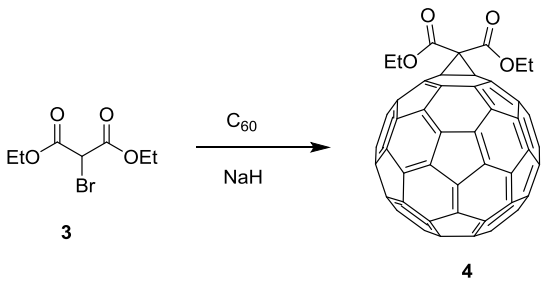

Scheme 1.3: Cyclopropanation reaction on C_{60} fullerene.

In recent years, the scientific community has made tremendous efforts to develop new synthetic methodologies for the functionalization of fullerenes. Among them cycloaddition and nucleophilic addition reactions have been most widely used, since C_{60}

fullerene behaves as an electron-deficient alkene rather than a polyaromatic hydrocarbon. In 1993, Bingel for first time devised a cyclopropanation protocol for C_{60} fullerene (i.e., the Bingel reaction), which later has become the most widely used method for regioselective functionalization of fullerenes.[10] In this method, the nucleophilic addition of an anion to fullerenes takes place first followed by an intramolecular nucleophilic substitution (Scheme 1.3), leading to the formation of methanofullerene derivatives.

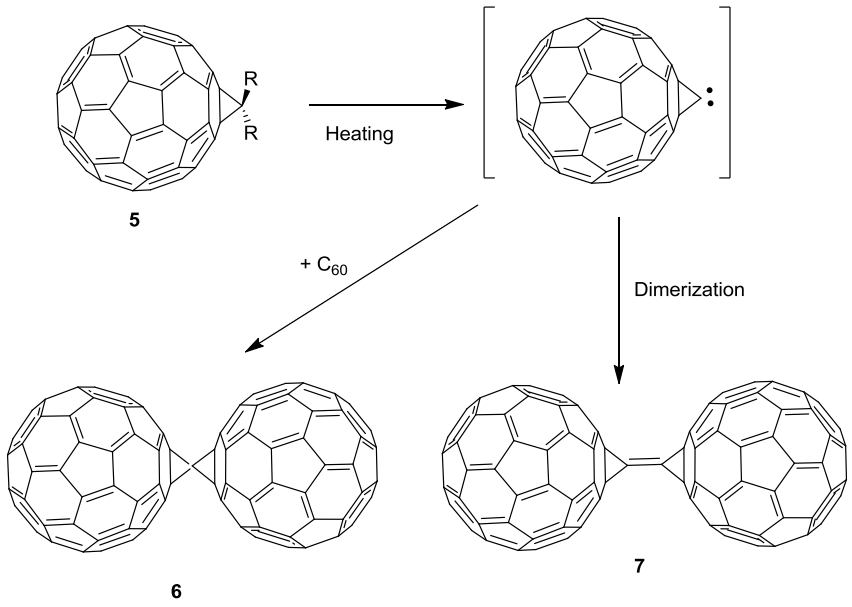

Scheme 1.4: Formation of fullerene dimers via carbene dimerization.

Eventually, the cyclopropanation reaction has been successfully applied to the functionalization of various fullerenes and set a platform for the development of novel fullerene derivatives such as fullerene-dendrimers, fullerene-containing thermo-liquid crystals, and fullerene dimers.[11,12] In 1999, Dragoe and co-workers reported fullerene dimers C_{121} and C_{122} which were prepared through a carbene intermediate of

methanofullerene as outlined in Scheme 1.4.[13] It is worth noting that the researchers performed STM imaging of the C_{121} and C_{122} dimers, and the results clearly showed a dumbbell like molecular shape (Figure 1.4).

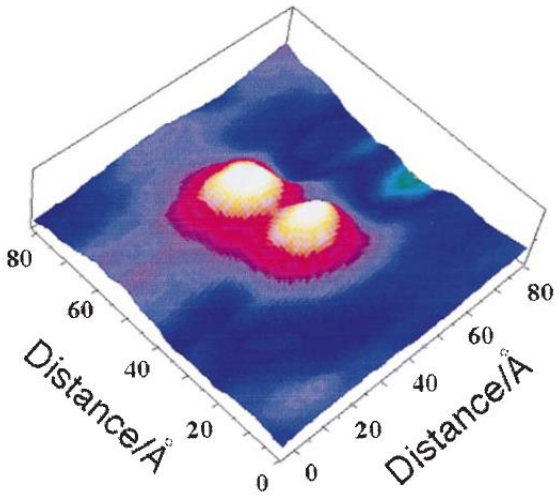

Figure 1.5: STM image of C_{122} deposited on graphite. (Adopted from reference 13 with permission)

Recently, a variety of supramolecular C_{60} and tetrathiafulvalene (TTF) based dyads and polyads have been constructed by [4+2] cycloaddition reactions in which the TTF group acts as an electron donor. In 2002, Guldi and co-workers reported a series of C_{60}-TTF dyads where an anthracene containing π-extended TTF unit was linked to C_{60} by the Diels-Alder reaction (Scheme 1.5).[14]

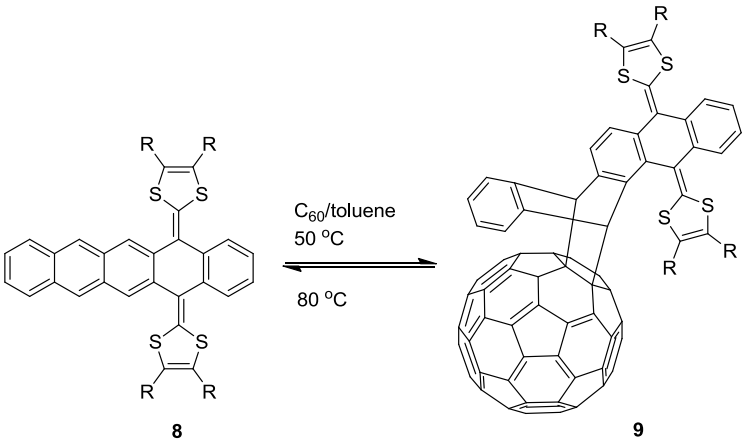

Scheme 1.5: Fluorescence switches based on C_{60}-TTF dyads **9**.

The cycloaddition reaction shown in Scheme 1.5 is thermally reversible, which enables the molecular system to function as a fluorescent switch. Other examples of active dyads bearing TTF functionalities and porphyrin units have been reported where electron transfer reactions were observed. The inherent photonic and electronic properties of fullerenes have played an active role in the development of nanoscale materials and devices. One of the most successful applications of fullerenes is related to the electron transfer process (artificial photosynthesis) in which the electron donors such as TTFs, metallocenes, amines, π-conjugated oligomers and dendrimers are connected to electron accepting fullerenes. The electron transfer process can easily take place between fullerene and a chromophore that absorbs light such as porphyrin and phthalocyanine. In the case where non-photoactive units are involved, such as TTF and ferrocene units, the fullerene gets excited at first by light irradiation to a singlet excited state and then the electron transfer occurs from donor to acceptor.

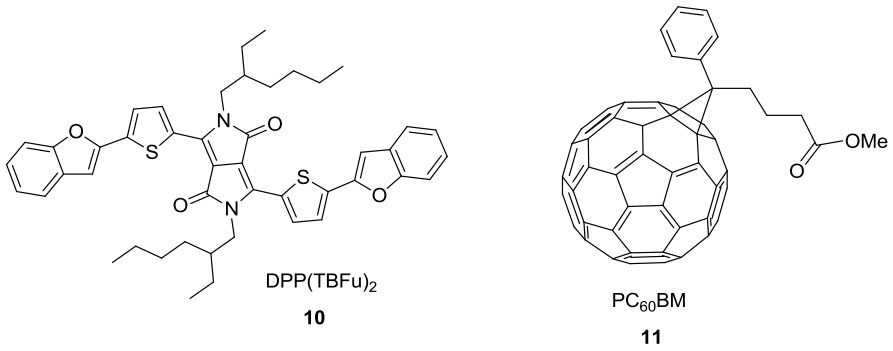

Figure 1.6: Chemical Structures of compounds **10** and **11**.

The design of organic solar cells comprised of fullerenes and organic active materials has become the most promising field in materials science over the past few years. These devices are mostly fabricated based on the so-called "bulk heterojunction" (BHJ) approach in which C_{60} acts as an electron acceptor and organic materials such as organic conjugated polymers and oligomers as donors.[15-17] The use of functionalized fullerenes such as C_{61}-butyric acid methyl ester ($PC_{60}BM$) has greatly increased the interactions of fullerenes with soluble organic materials when compared to the case of using pristine C_{60} fullerene.

In 2009, Nguyen and co-workers designed and synthesised a solution-processable DPP-based thiophene derivative by using a fused benzofuran core blended with $PC_{60}BM$ **11** (Figure 1.6).[18] The obtained LUMO level of $DPP(TBFu)_2$ **10** is much higher than that of PCBM with a difference of 0.5 eV. The bulk heterojunction solar cell using this small molecule as electron donor and $PC_{71}BM$ as electron acceptor yielded the best power conversion efficiency of over 5.2 % at a solar irradiation of 100 mW cm^{-2} with a high fill

factor of 0.48 at low light intensity at 23 mW cm $^{-2}$, when a mixture of 70/30 donor/acceptor (by weight) is used as the active layer.

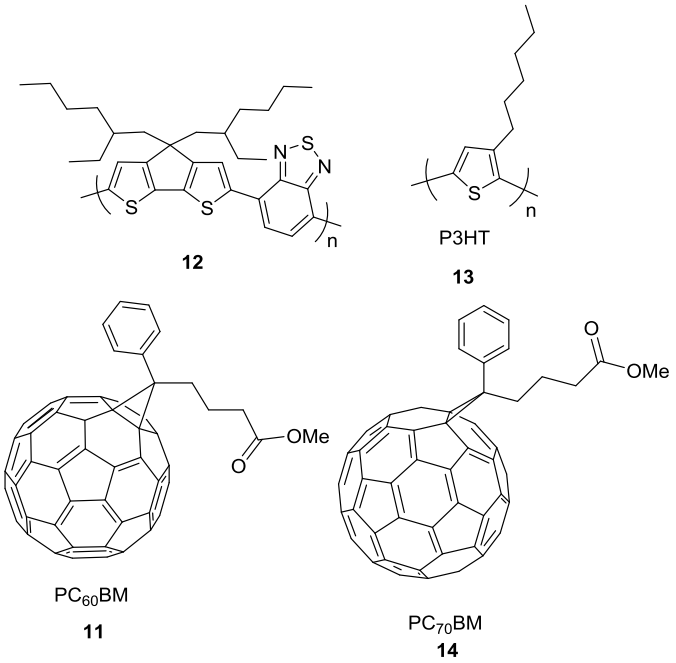

Figure 1.7: Structures of polymers **12**, **13** and fullerene derivatives **11** and **14**.

As another example, in 2007, Heeger and co-workers reported a multi-layer bulk heterojunction tandem cell comprised of polythiophene-based materials **12** and **13** as active layers, and $PC_{60}BM$ **11** and $PC_{70}BM$ **14** as electron acceptors (Figure 1.7).[19] The two polymer-fullerene cells are separated by a TiO_2 layer and a highly conductive hole transport layer made of poly(3,4 ethylenedioxylenethiophene)-polystyrene sulfonic acid (PEDOTPSS). A much higher efficiency has been achieved with this tandem cell, a value of 6.5 % at low light intensity of 7.8 mA/cm^2.

Over the past few years, polymer-based solar cells have been continuously optimized for better performance. The current state-of-the-art of polymer solar cell have reached an efficiency of 8.6% and higher.[20-22] More recently, in 2011, researchers at Mitsubishi Chemicals reported an organic solar cell with 9.2% power conversion efficiency, which may compete with the traditional inorganic solar cells. So far this is the highest value ever claimed in the field of organic solar cells. However, the power conversion efficiency is not the only important factor relevant applications. Other factors such as the lifetime and stability of the organic materials being used must also be taken into consideration. In general, most of the organic semiconducting materials undergo photo-catalyzed reactions with oxygen or water to form non-semiconducting species.[23] There are two main approaches to increase the stability of organic materials. The first is to develop materials with intrinsic stability at ambient conditions. The second strategy is to use encapsulation techniques to limit the exposure of organic semiconducting materials to reactive elements.

With the ever growing research on novel fullerene materials, the supramolecular architectures containing fullerenes have received significant attention due the fact that fullerenes can form relatively stable complexes with aromatic moieties via non-covalent forces, such as hydrogen bonding, metal templates, and π-stacking. An interesting class of supramolecular nanoring structures have been constructed which can incorporate fullerenes in their cavity by means of concave-convex π-staking. In general nanorings are cyclic loops with continuous overlap of π-orbitals along their cyclic backbones.

In 2003, Oda and co-workers synthesized a series of paraphenyleneacetylene carbon nanorings with the average diameters of 13.2 and 17.3 Å. With these nanorings, Oda investigated their host-guest interactions with fullerenes. The experiments showed that [6]paraphenyleneacetylene **15** formed a 1:1 complex with fullerene **4** (Scheme 1.6), whereas [8]paraphenyleneacetylene exhibited very weak binding with fullerene **4**. Furthermore, the complex of [6]paraphenyleneacetylene **15** and a fullerene derivative has been characterized by X-ray analysis to reveal the precise features of the binding (Figure 1.8).[24]

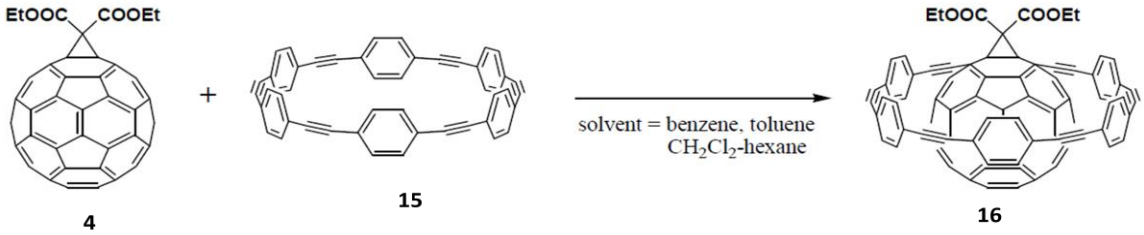

Scheme 1.6: Complexation of fullerene derivative **4** with [6]paraphenyleneacetylene nanoring (Adopted from reference 24 with permission).

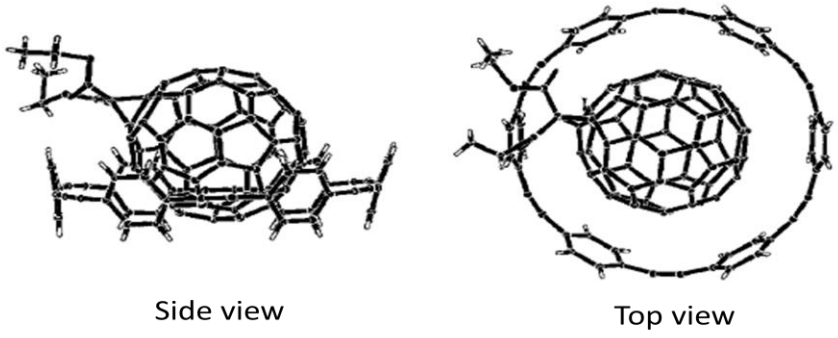

Figure 1.8: X-ray structure of **4@15** (Adopted from reference 24 with permission).

Another type of interesting fullerene-containing supramolecular architecture is the carbon peapod (Figure 1.9) discovered in the late 1990s as side products of carbon nanotube production. In the year 2000, Luzzi and Smith reported the first production method for carbon peapods.[25] The fullerene balls are successfully introduced into the cavity of carbon nanotubes by laser vaporization and subsequent annealing of raw carbon nanotubes in the presence of nitric acid and fullerenes. Recently, advanced methods for production of carbon peapods have been reviewed, and nowadays carbon peapods can be prepared by easy and cost-effective procedures.[26]

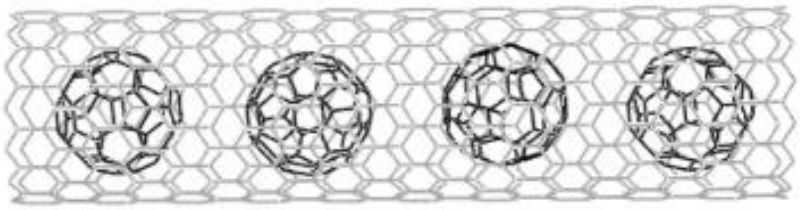

Figure 1.9: Structure of a carbon peapod (Adopted from reference 27 with permission).[27]

1.2.2.2 Discovery of Carbon Nanotubes

Carbon nanotubes (CNTs) were discovered in 1991 as a new class of carbon allotropes.[28] Since then, CNTs have become enormously popular and have triggered an explosive growth of research and development. Unlike fullerenes, the CNTs are tubular-shaped carbon nanomaterials (imagine a sheet of graphite being rolled into a tube), and were initially observed as a minor byproduct of fullerene synthesis. A great deal of effort has been made in last two decades towards their synthesis, purification, and structural

elucidation. CNTs can be single-walled carbon nanotubes (SWNTs) and multi-walled carbon nanotubes (MWNTs) in terms of layer formation (Figure 1.10).

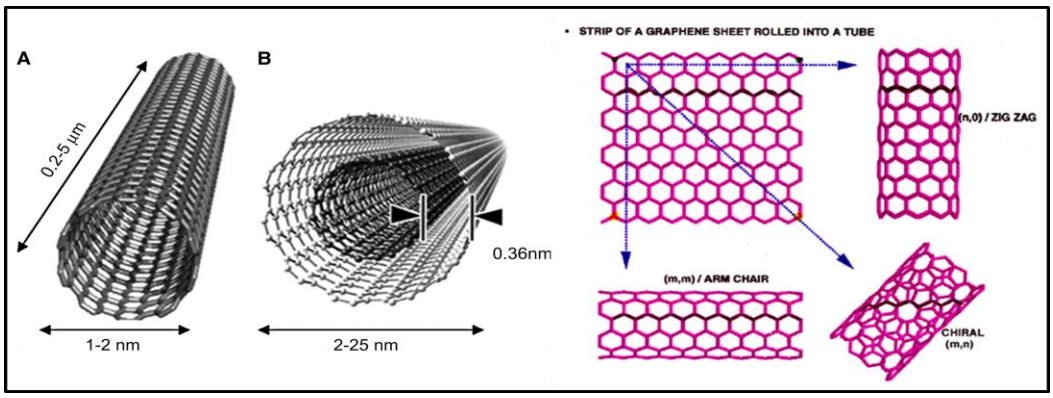

Figure 1.10: Representative structures of SWNTs, MWNTs and three different types of SWNTs according to the angle of chiral vector.

It is almost impossible to name CNTs based on the IUPAC nomenclature rules; however, the structure of CNTs is characterized according to the different angles in which a graphene sheet is rolled up to form various types of SWNTs, such as "zigzag", "armchair", and "chiral" (Figure 1.10). They are defined based on the chiral vector (C_h) of graphene lattice and a pair of descriptors (n,m). If n = m, CNTs are called armchair, when m = 0, they are named zigzag nanotubes, otherwise they are identified as chiral (Figure 1.10). In the case of armchair CNTs, the graphene sheet is turned by 30^o before it starts to roll up, whereas in chiral CNTs the rolling angle is between 0^o and 30^o. These wrapping angles have profound effects on the electronic properties of CNTs, as they dictate the changes in wave functions before and after wrapping of the graphene sheet. In terms of electronic properties, CNTs can be categorized into "metallic" and

"semiconducting" tubes. If n-m=3x (x is an integer), the CNTs are referred as metallic, otherwise they are semiconducting.

In addition to their excellent optical and electrical properties, CNTs also exhibit unique mechanical and thermal properties that make them very useful in current science and technology. The properties of a CNT usually depend on the radius and the helicity (or chirality) of the tube. The C-C bond present in a CNT is considered as one of the strongest bonds in nature, providing high tensile strength and stiffness normally about 220 times that of steel. It has been noted that the Young's modulus for CNTs is several times larger than diamond, which gives a very high elastic strength to the tubes.[29] The sidewall of an ideal SWNT is composed of hexagonal networks of carbon atoms with sp^2 hybridization, whereas the end cap contains hexagonal as well as pentagonal networks of carbon atoms.

In general, the chemical reactivity of CNTs arises from their π-orbital mismatch around the tube. It has been known that, the mechanical deformation on the curved surface of a CNT may directly influence its chemical reactivity. For example, it is predicted by the calculations that the hydrogenation energies of C atoms around the center of the CNT increases as the bending angle increases from 0^o to 40^o (Figure 1.11).[30]

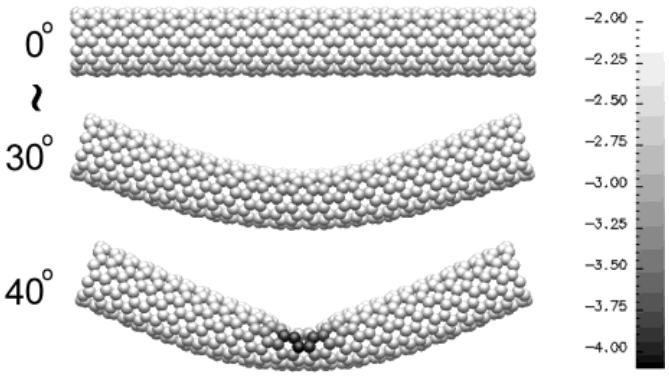

Figure 1.11: Chemical reactivity (hydrogenation energy) change as a function of bending angle (Adopted from reference 30 with permission).

SWNTs can interact strongly with one another to form more or less closely packed bundles of highly complex architectures by supramolecular forces such as π-π interactions and van der Waals forces on their sidewalls.[31] The bundling effect of SWNTs makes it extremely difficult to disperse them in solvents. This restricts the direct use of SWNTs in device fabrication. To overcome this obstacle, various chemical functionalization methods have been developed, among which the so-called covalent and non-covalent functionalization methods have been extensively investigated. Details of these methods will be discussed in Chapter 3.

Many methods have been exploited for producing CNTs, while some commercial "as-prepared" SWNTs are actually named after their production methods; for example, high pressure CO disproportionation (HiPCO), and cobalt-molybdenum catalyzed (CoMoCAT) nanotubes. These nanotubes have been popularly used in research and various applications; however, the preparation of SWNTs with specific diameters and

lengths is very challenging. Several groups have been engaged in synthesizing structurally uniform SWNTs. In 2013, Itami and co-workers reported the total synthesis of SWNTs by using carbon nanorings such as cyclic polypheneylenes as templates (See Figure 1.12).[32]

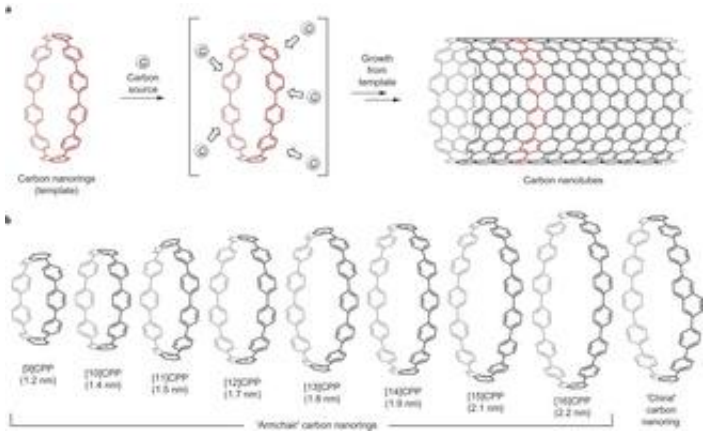

Figure 1.12: A 'growth-from-template' strategy for the bottom-up synthesis of carbon nanotubes (Adopted from reference 32 with permission).

Another promising approach for the synthesis of SWNTs is by "carbon nanotube cloning" which allows the consistent growth of carbon nanotubes with selected chirality and uniform diameter. Although only preliminary progress has been made in this direction, there is a hope that this could solve this important problem in nanotube chemistry. This process involves the preparation of the end cap of a CNT followed by the cloning of this end under chemical vapor deposition (CVD) conditions. In 2010, Liu and co-workers reported the synthesis of SWNTs from an opened C_{60} fullerene by the end cap approach (as shown in Figure 1.13). In this work, CVD growth of nanotubes from a defined half-fullerene end cap was successfully achieved at 900 ^{o}C for 20 min.[33]

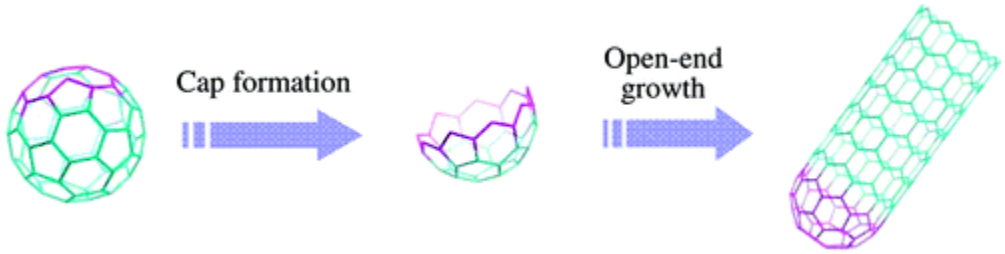

Figure 1.13: CVD growth of an end cap to a carbon nanotube (Adopted from reference 33 with permission).

- **Applications of carbon nanotubes**

CNTs have captured a great deal of interest because of their unique mechanical, electronic, and chemical properties that make them the leading nanomaterials in various applications.[34-36]

One of the most interesting applications associated with CNTs is hydrogen gas storage, which is an ideal source of energy because of its environmental friendliness and capability of regeneration. Because of their specific cylindrical and hollow geometry, SWNTs are excellent candidates for storing gases and liquids within their cavity.[37,38] However, to make this technology commercially viable, large-scale and low-cost preparation methods for CNTs must be well established, while a number of obstacles arising from the effect of other materials on hydrogen storage also need to be overcome. CNTs can be used as templates for making nanowires and nanosheets, taking advantage of the strength, durability, and flexibility of CNTs. A superelastic CNT has been reported (Figure 1.14) as a nanosheet with elongation strength about 220% at 80-1900 kelvin temperatures.[39]

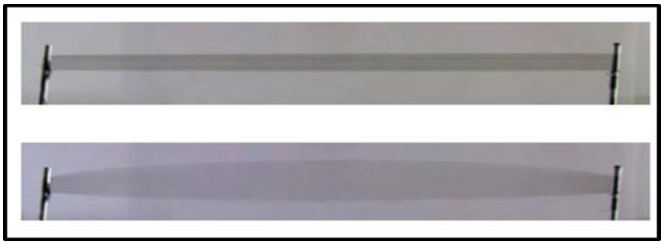

Figure 1.14: Photographic image of a rigidly end-supported 50-mm-long by 2-mm-wide nanotube sheet strip (top), and the same sheet strip expanded in width by applying 5 kV with respect to ground (bottom) (Adopted from reference 39 with permission).

In addition to the applications mentioned above, CNTs have also found uses in many other fields; for example, biosensors,[40] nanomedicine,[41] conductive textiles,[42] and organic solar cells,[43] just to name few.

1.2.2.3 Discovery of Graphene

The most recent milestone in the history of nanochemistry is the discovery of graphene which is a two-dimensional crystalline form of sp^2 hybridized carbon. This nanomaterial was first isolated by Novoselov *et al*. in 2004,[44,45] and since then, it has become a subject of intense research, not only for theoretical curiosity, but also for many application aspects. The graphene sheet has been a theoretical model for understanding the structural properties of CNTs and fullerenes and it is also considered as a basic building block for carbon nanomaterials as shown in Scheme 1.7.

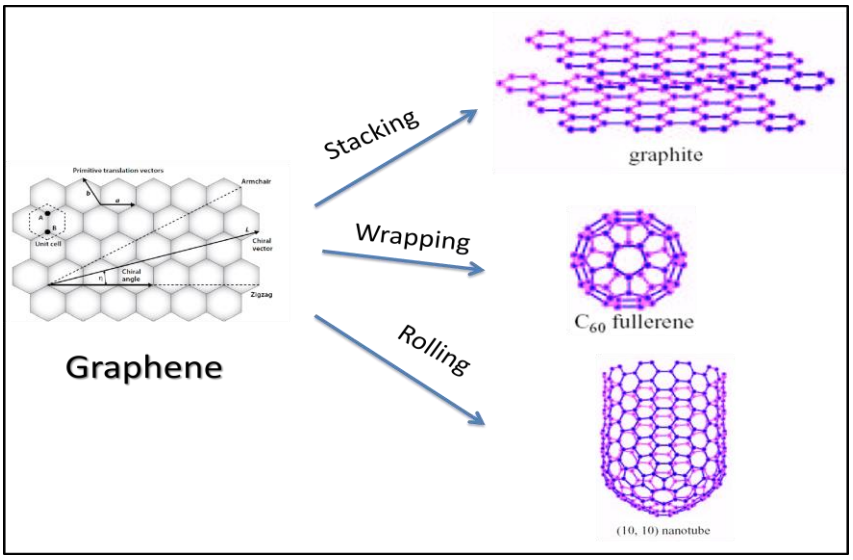

Scheme 1.7: Formation of nanomaterials from graphene.

Due to its high transparency (~ 97.7%),[46] high carrier mobility (200 000 $cm^2 v^{-1} s^{-1}$),[44] large specific surface area (2630 $m^2 g^{-1}$ for single-layer graphene),[47] high Young's modulus (~ 1 Tpa),[48] and excellent thermal conductivity (3000-5000 $W m^{-1} K^{-1}$),[49] graphene has become the most interesting candidate in electrical,[50,51] mechanical,[48,52] and optoelectronic devices.[46] Ever since Novoselov and Geim's first isolation of single-layer graphene, the research on graphene-based materials has grown at a spectacular pace. A simple "pealing" method has been developed by using a tape to extract single layers of graphene from graphite flakes. Although this technique requires a lot of patience and practice, it has indeed produced high quality single layer graphene (Figure 1.15).[44]

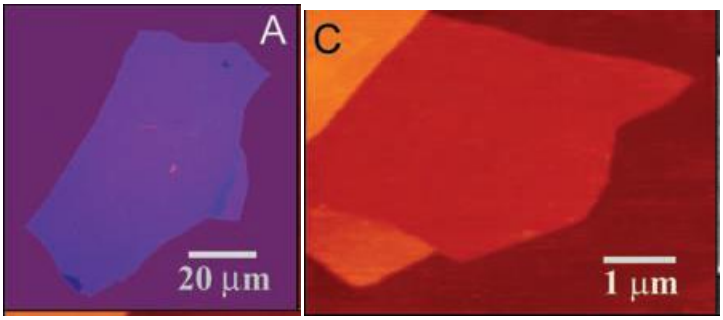

Figure 1.15: Photograph of a multilayer graphene flake with thickness ~3 nm (left), and AFM image of single-layer graphene (Adopted from reference 44 with permission).

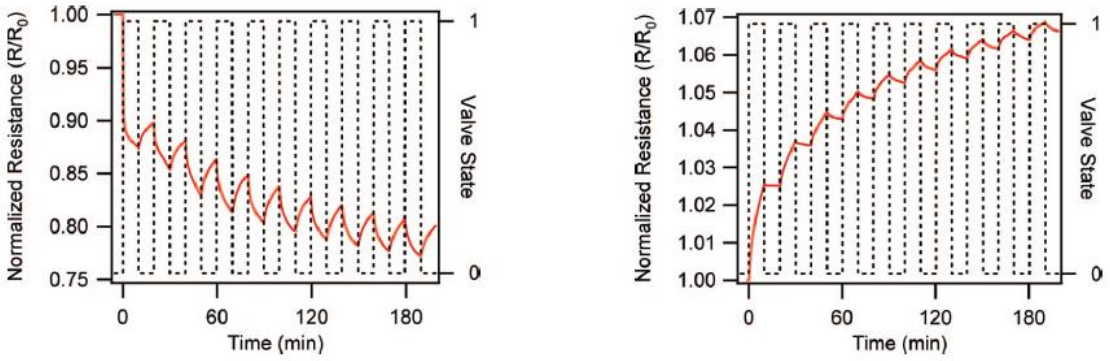

Figure 1.16: The resistance of p-type material decreases upon exposure to electron withdrawers (e.g., NO_2) and increases upon exposure to electron donors (e.g., NH_3) (Adopted from reference 55 with permission).

Recently, a number of groups has been working on graphene-based chemical sensors,[53,54] where the resistance of graphene material was monitored in response to the interactions with various analytes. For instance, Kaner's group demonstrated a moderate sensory function of chemically derived graphene materials for a few small-molecule analytes, such as NO_2, NH_3, and dinitrotoluene at ambient temperatures.[55] In particular,

electron-donating groups were found to increase the hole population in pristine graphene, leading to increased conductivity as illustrated in Figure 1.16.

Because of its high transparency, single layer graphene can replace the current standard indium tin oxide (ITO) as a coating material in optoelectronic devices, including LEDs and dye-sensitized solar cells. The first graphene-based transparent conductor was reported in 2008 by Miller and co-workers.[56] This group used a simple method for the fabrication of graphene layers from dip-coating of graphene oxide (GO) sheets on the substrate followed by thermal annealing. However, the solar cell built on graphene materials gave a PCE of 0.26%, which was much lower than those of ITO-based devices.

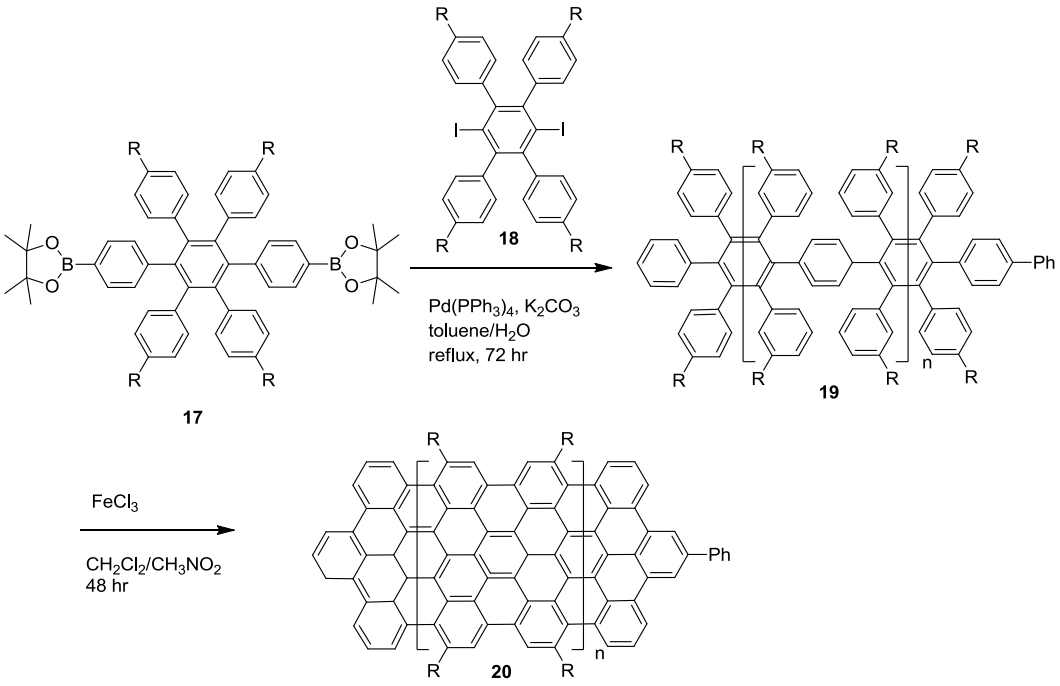

Scheme 1.8: Synthesis of two-dimensional graphene nanoribbon **20.**

Many groups are interested in synthesizing graphene-like polycyclic aromatic hydrocarbons (PAHs) as they can be used as models for understanding the properties of graphene. A major breakthrough in this area emerged in 2008, when the synthesis of nanoribbon-like PAHs **20** up to 12 nm in length was reported by Mullen's group.[57] SEM and TEM characterizations are shown in Figure 1.17, which disclose well-ordered layers of graphene. The Suzuki-Miyaura reaction was used as a key step in the synthesis (Scheme 1.8).

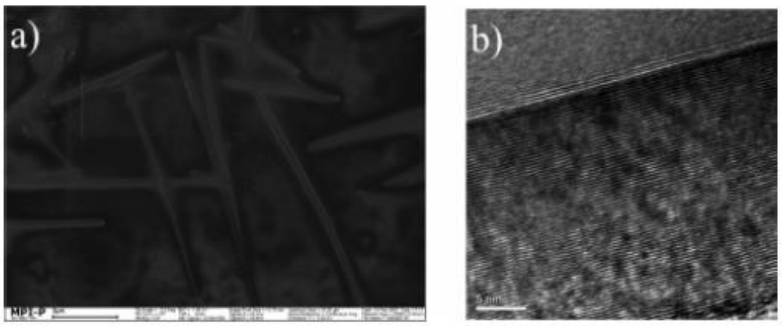

Figure 1.17: SEM and TEM images of polymer **20** (Adopted from reference 57 with permission).

1.2.2.4 Conjugated Polymers (CPs)

Research on conjugated polymers (CPs) has been the most appealing field to both academic and industrial sectors since 1977, when the metallic properties of doped polyacetylenes (PAs) were first discovered. It was demonstrated that the PAs could be oxidized in the presence of iodine vapors and displayed an electric conductivity of 10^{-5} S.[58] This unique property of CPs thus opened a door to a new area in materials science,

many thanks to the seminal work of three pioneering scientists, Heeger, MacDiarmid, and Shirakawa, who were later honored with the 2000 Nobel Prize in Chemistry.

For years, remarkable progress has been made on the synthesis and device applications of functionalized CPs. From the 1990s, research on CPs has received another boost after Holmes and co-workers discovered the electroluminescent property of poly(*p*-pheneylenevinylene)s (PPVs) and demonstrated their use in organic light emitting diodes (OLEDs). In an OLED, the emitting layer material such as PPV is placed between two metallic electrodes as schematically illustrated in Figure 1.18.[59] This discovery has become one of the most important landmarks in the history of polymer science. Due to their small band gap of about 2.5 eV and electroluminescent properties, PPVs have been considered as one of the most useful light emitting conjugated polymers.

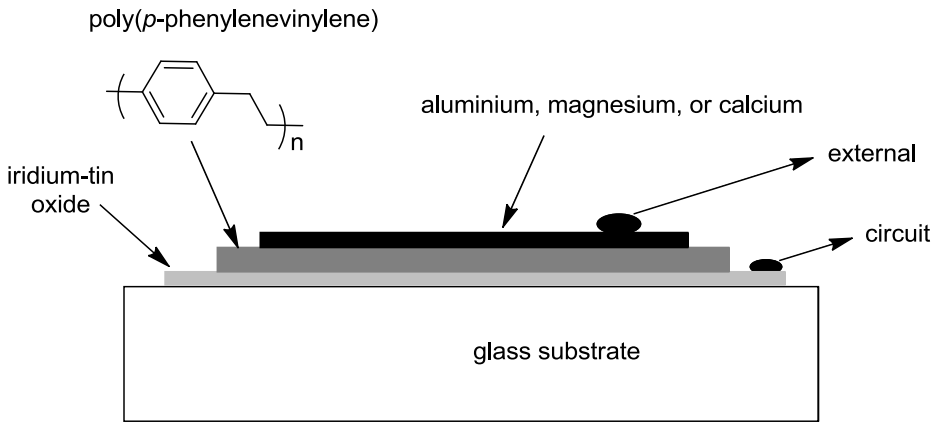

Figure 1.18: Schematics of an electroluminescent device fabricated using PPV as the active material.

The efficiency of an optoelectronic device, such as an OLED, can be altered by inclusion of functional groups into the backbone of the polymer-based active material as well as by changing the length of the alkyl substitutions on the side chain of the polymer. In addition to PPVs, a large number of polymer-based light emitting diodes has been demonstrated in the literature; for example, polycarbozoles, polyfluorenes (PFs), and polythiophenes (PTs). The electronic properties of all these polymers are different, offering controllability over a wide range of emission colors. Due to their relatively large bandgaps, PFs tend to give blue-colored light emission, whereas PPVs are generally green light emitters and PTs are red light emitting.

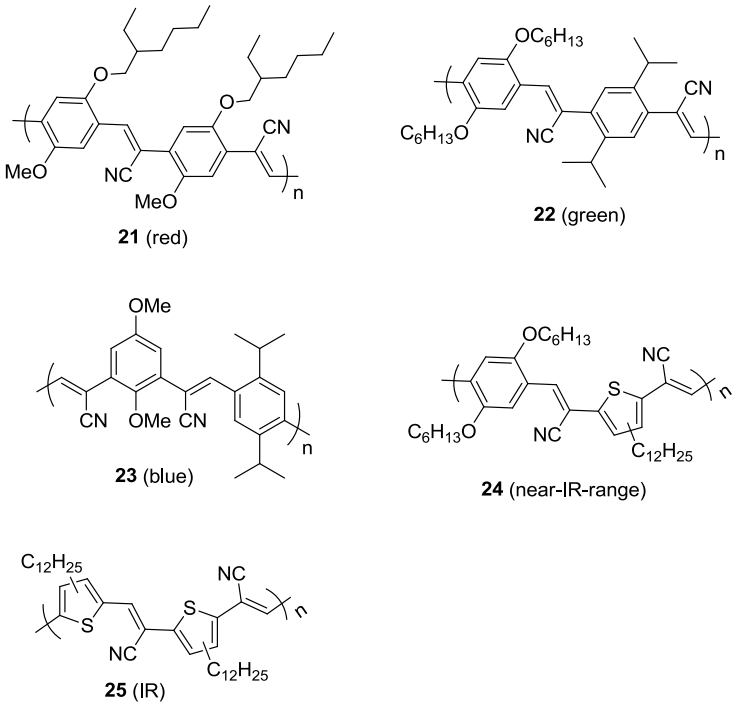

Figure 1.19: Structures of cyano-substituted PPV derivatives for electroluminescence.

Examples developed as polymeric light emitting materials **21**-**25** are shown in Figure 1.19.[60-62] It is worth noting the high power efficiency of 5 cd A^{-1} corresponding to a luminous intensity of 1000 cd M^{-2} measured for MEH-CN-PPV **21** at 6 V. From the viewpoint of commercial viability, the polymer-based LEDs are quite promising, as they offer thinner, lighter and higher-resolution displays than conventional LED materials. Many big companies have already started marketing OLED gadgets, including some popular electronic products such as Google Nexus-one, Samsung Jet, Wave, Galaxy-S, Nokia N8 and E7, and several HTC phones.

Another type of important devices built on conjugated polymers is the solid-state lightning device, which offers new opportunities for electronic and semiconducting industries. The delocalized π-electrons present in conjugated polymers make them capable of absorbing sunlight directly, generating long lived charge separation and enabling proper charge transport to usable electric power.

The first laser application of conjugated polymers was demonstrated in 1992 by Moses and co-workers. In their experiment, a solution of poly-2-methoxy-5-(2-ethylhexoxy)-*p*-phenylenevinylene (MEH-PPV) **26** in xylene was photo-pumped at 534 nm. The laser input and output powers were monitored at different concentrations. Interestingly, when dilute solutions were used, the laser output power increased very rapidly. The researchers also measured the spontaneous emission intensities of MEH-PPV **26** solutions. There was a significant reduction in the spectral line width observed in the laser output occurred, providing evidence for laser action (Figure 1.20).[63]

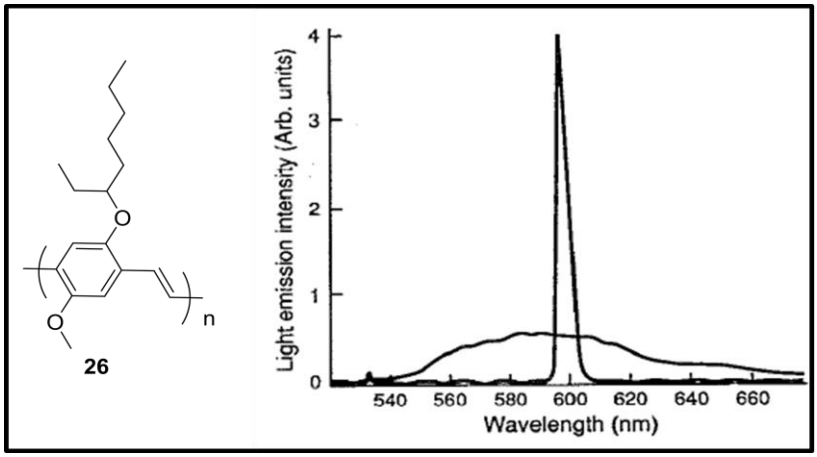

Figure 1.20: Structure of MEH-PPV **26** (left), and comparison of the spontaneous emission spectra of the MEHPPV chromophore (measured without one of the external cavity mirrors in diluted solution) to spectrum of the MEH-PPV laser (measured with the two external cavity mirrors, in a more concentrated solution of 1mg/mL) (right) (Adopted from reference 63 with permission).

After this successful demonstration of laser application of conjugated polymers in the solution phase, many research groups continued to develop solid-state lasers based on conjugated polymers. In 1996, Heeger and co-workers reported the first solid-state laser application using an MEH-PPV/polystyrene film blended with suspended titanium dioxide (TiO_2) nanoparticles.[64]

Without any doubt, conjugated polymers have been the most appealing materials to many future sciences and technologies. In addition to the applications mentioned above, many commercial devices have been fabricated, in which the conjugated polymers are used as the active materials. For example, photoconductors,[65] polymer solar cells

(PSCs),[19] laser dyes, scintillators,[66] switching and signal processes,[67] nonlinear optics (NLO),[68] and optical data storage media.[69]

1.3 The Heart of Nanochemistry

The heart of nanochemistry still lies in the design and synthesis of functional nanomaterials. Nanomaterials can be broadly divided into two categories, inorganic, and organic. Compared to the organic nanomaterials (conjugated polymers, oligomers, macromolecules, dendrimers, and small functional organic molecules), the inorganic materials (nanoparticles, clusters, and quantum dots) have been more extensively studied since the very beginning of the rise of nanoscience. However, progress towards the development of synthetic methodologies for the production of both organic and inorganic nanomaterials has been remarkable in past two decades. In the following section, some of the important synthetic methods for producing nanomaterials will be presented based on the literature.

1.3.1 Inorganic Nanomaterials

Several methods have been employed for the preparation of inorganic nanomaterials (e.g., nanocrystals), and in most cases, the synthesis followed the top-down approach. The most common method used for the preparation of metal nanoparticles is the reduction of metal salts in the presence of suitable capping agents such as polyvinylpyrrolidone (PVP) and tetrakis(hydroxymethyl)phosphonium chloride (THPC). For example, Au nanocrystals can be obtained by the reduction of $HAuCl_4$ with THPC

acting as the capping agent.[70] As described by Liz-Marzan and co-workers, Ag nanocrystals were synthesized by using *N*,*N*-dimethylformamide (DMF) as both the stabilizing agent and capping agent.[71,72]

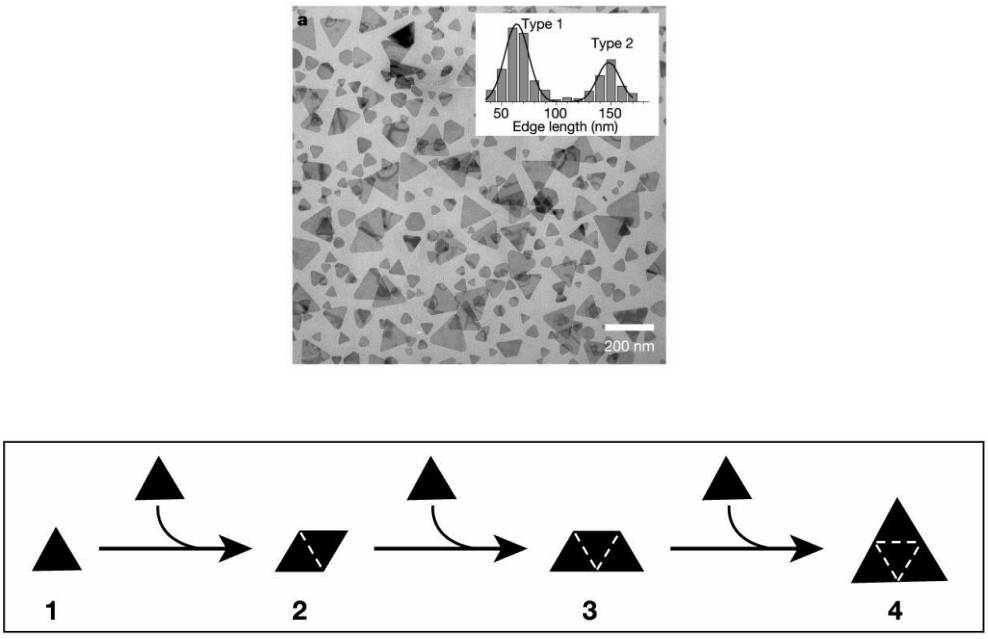

Figure 1.21: TEM image of Ag nanoprisms (top), and schematic diagram of the proposed light-induced fusion growth of Ag nanoprisms (bottom). (Adopted from reference 73 with permission)

In 2003, Mirkin and co-workers came up with a new strategy for preparing Ag nanoprisms which was published on *Nature* in 2003. As shown in Figure 1.21, the Ag nanoprisms were formed by irradiating a mixture of sodium citrate and bis(*p*-sulfonatophenyl)phenylphosphine dihydrate dipotassium capped Ag nanocrystals under irradiation of a 150 W xenon lamp. The TEM image showed that two different size

distributions of nanoprisms were observable.[73] The scope of this light-driven process has later been extended to the synthesis of branched nanocrystals.[74]

In 2006, Sun and co-workers synthesized magnetic FePt nanocubes with an average size of 6.9 nm. In the procedure, FePt nanocubes were synthesized by a reaction of oleic acid and $Fe(CO)_5$ with a benzyl ether/octadecene solution of $Pt(acac)_2$. The resulting nanocubes could self-assemble into textured super lattice arrays (Figure 1.22). This type of nanocrystals can be potentially used as high density information storage materials[75] and high performance permanent magnets.[76]

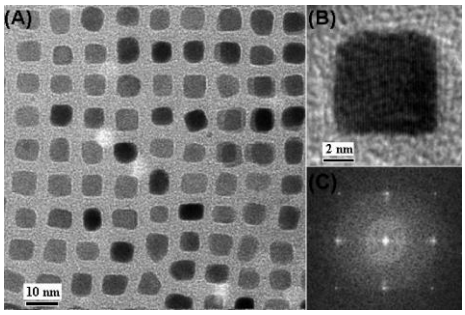

Figure 1.22: (A) TEM images of (A) $Fe_{50}Pt_{50}$ nanocubes, (B) HRTEM image of a single FePt nanocube, (C) FFT of the cube in (B) (Adopted from reference 75 with permission).

Metal oxide nanocrystals can be synthesized by solvothermal decomposition of organometallic precursors. However, this method usually involves reactions carried out at high temperatures in a sealed tube. When low-boiling solvents are used, very high pressures are generated during the process. As described by Steigerwald and co-workers, the TiO_2 nanoparticles can be prepared by reacting low-valent organometallic precursors

such as bis-(cyclooctatetraene)titanium ($Ti(COT)_2$) with dimethylsulfoxide (DMSO) in *o*-dichlorobenzene.[77]

Among all metal oxide nanocrystalline materials, ZnO nanocrystals have been the most intensively studied systems, owing to their unique optoelectronic properties. They are highly semiconducting materials with a large bandgap of 3.37 eV and a large excitation binding energy of 60 meV. The potential applications of these nanocrystals include UV-lasers, light-emitting diodes, solar cells, and sensors. Recently Hyeon and co-workers demonstrated a non-hydrolytic sol-gel method could be used to produce ZnO nanocrystals in hexagonal and rod shapes (Figure 1.23). In this reaction the ZnO nanocrystals are produced by the reaction of zinc acetate with 1, 12-dodecanediol in the presence of surfactants at 250 ^{o}C.[78]

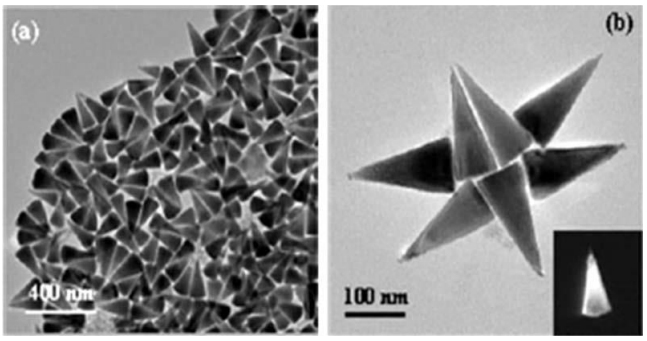

Figure 1.23: TEM images of cone-shaped ZnO nanocrystals (Adopted from reference 78 with permission).

In the past two decades, significant advances have been made in the synthesis of quantum dots (QDs), colloidal nanocrystals of metal chalcogenides. QDs are highly

semiconducting, visible-luminescent nanoparticles composed of an inorganic core surrounded by an organic outer layer of surfactant molecules. Research progress in QDs has found many applications in optoelectronic devices and biological labeling. The emission properties of QDs can be tuned by varying their sizes and shapes as shown in Figure 1.24. The QDs made of CdTe/CdS and CdSe/ZnS can strongly emit luminescence in specific spectral ranges and have been successfully used for the fabrication of fluorescent sensors. For example, the synthesis of CdTe QDs can be performed in the aqueous phase by reacting NaHTe solution with a solution of $CdBr_2$ in 3-mercaptopropionic acid (MPA) at 60 ^{o}C.[79]

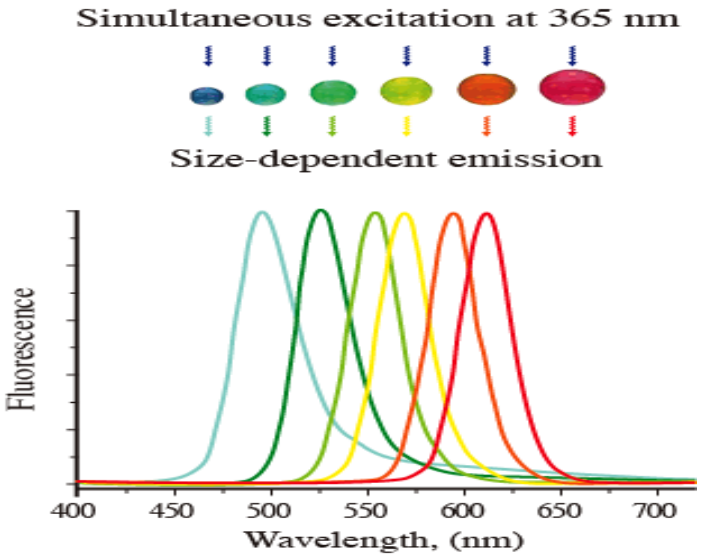

Figure 1.24: Size dependent emission profiles of QDs.

1.3.2 Organic Nanomaterials

As discussed previously, a major challenge in organic material design lies in how to synthesize materials with a high degree of structural order and well-defined properties. This requires the development of more efficient and versatile synthetic methodologies that are task specific, capable of tackling molecules of great complexity, and widely accessible to many synthetic chemists. Fortunately, during the past few decades, the number of important synthetic methodologies being explored for the synthesis of advanced organic based materials has grown significantly. In the following section, three of the most popular synthetic approaches for the synthesis of organic materials, which appear more often in the literature than others, will be reviewed.

1.3.2.1 Olefin Metathesis Reactions

The emergence of olefin metathesis has greatly expanded the scope of organic synthetic chemistry in materials science. The olefin metathesis reaction allows the reorganization of carbon-carbon double bonds between different olefins. In the last decade, the olefin metathesis reaction has been applied to the synthesis of naturally existing compounds as well as functional organic materials.

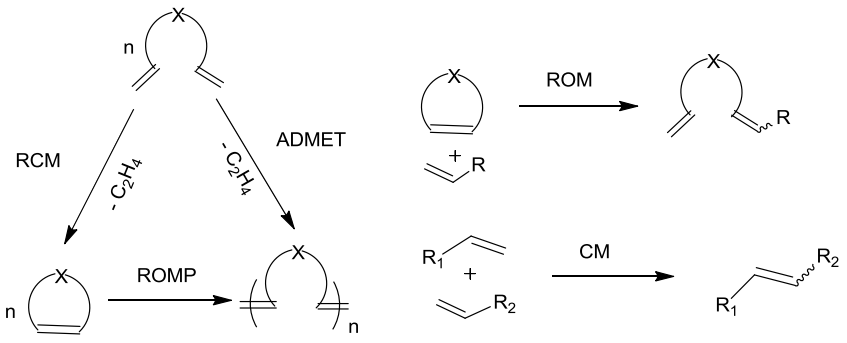

Scheme 1.9: Summary of types of olefin metathesis reactions.

Although the olefin metathesis reaction was reported as early as 1967, the true nature of this reaction was revealed in 1971, when professor Chauvin discovered the mechanism for olefin metathesis reaction by envisioning a metallacyclobutane intermediate (Scheme 1.10).[80] Elucidation of this reaction mechanism has indeed opened the door for the development of more and more efficient catalysts.

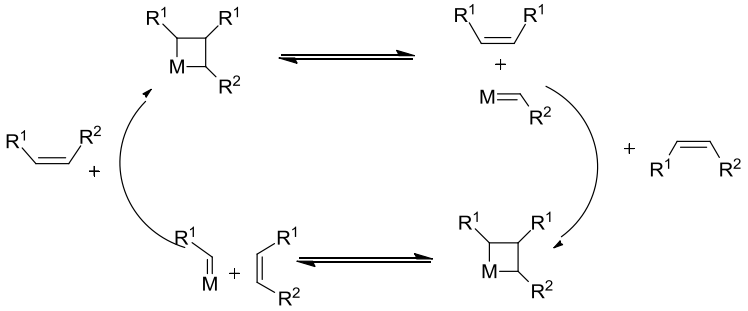

Scheme 1.10: Chauvin's mechanism for the olefin metathesis reaction.

As shown in Scheme 1.9,[81] olefin metathesis is used in different processes such as intermolecular reactions, cross metathesis reactions (CM), ring-opening cross metathesis reactions, diene-based reactions such as acyclic diene metathesis (ADMET), ring-closing

metathesis (RCM), and ring-opening metathesis polymerization (ROMP). Through these reactions, it is possible to have access to novel olefinic materials that would be very difficult to make via other methods.

The scope of the olefin metathesis reaction would have been limited if improvements in catalyst performance had not flourished. In order to achieve high selectivity in olefin metathesis, a wide variety of ruthenium based catalysts as well as other metal catalysts has been investigated to achieve high activity, stability, and functional group tolerance. Figure 1.25 shows the metal catalysts developed for all types of olefin metathesis reactions.[81]

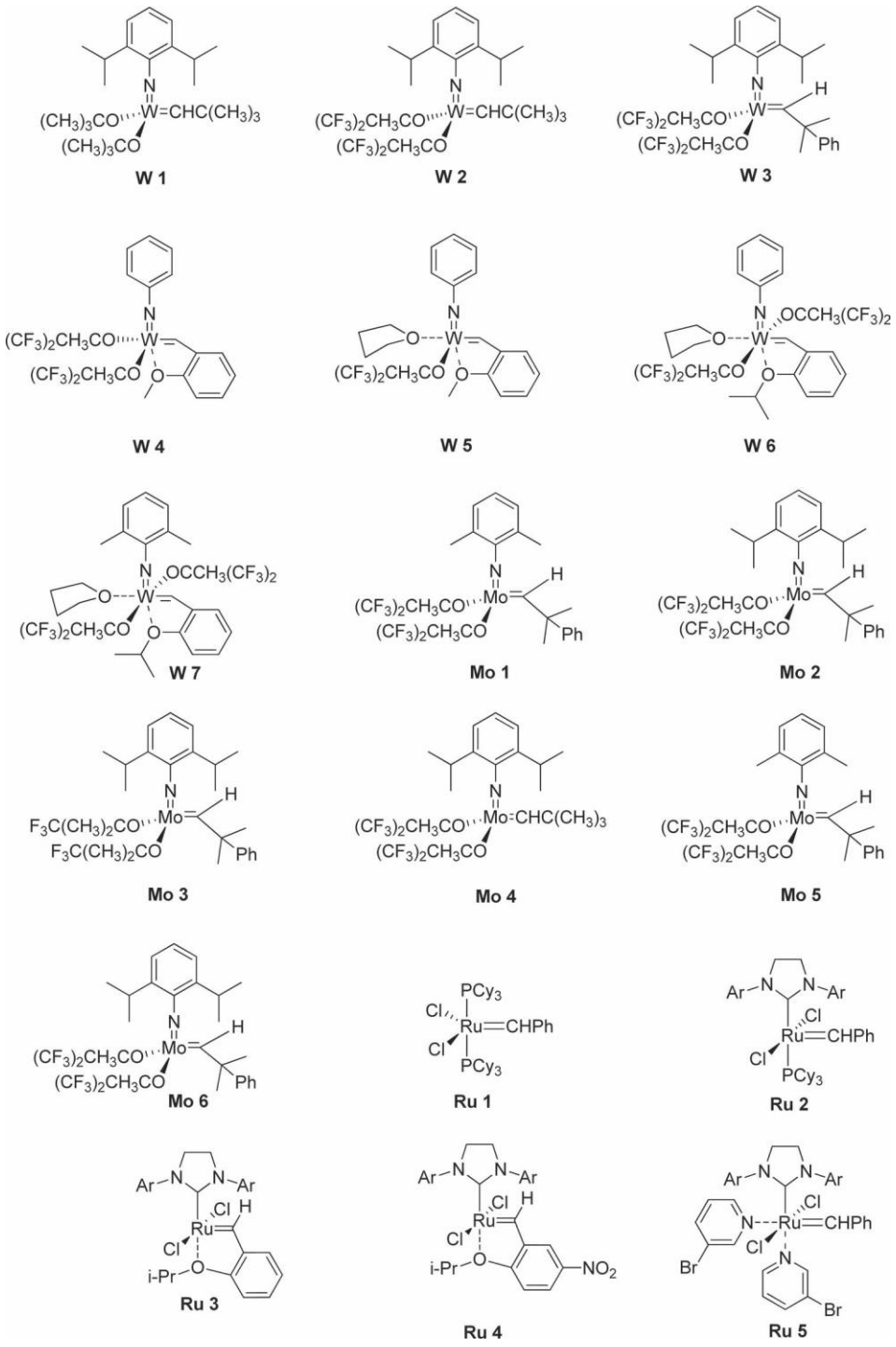

Figure 1.25: Examples of catalysts developed for olefin metathesis reactions (adopted from reference 81 with permission).

- **Applications of Olefin Metathesis Reactions**

Whenever a carbon-carbon double bond exists, the olefin metathesis reaction has played a major role as scissors to rearrange the bond connection. In this respect, many synthetically challenging molecules such as natural products, small and large organic functional materials, higher oligomers and conducting polymers, dendrimers, and macrocycles have been successfully synthesized by using olefin metathesis reactions. Of many applications, only a narrow selection of important examples which emerged in the recent literature will be reviewed in the following section.

- **Synthesis of Natural Products**

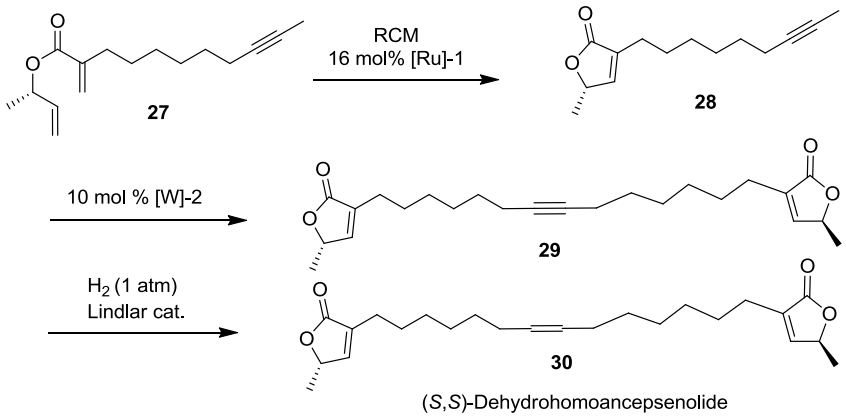

Scheme 1.11: Total synthesis of (*S*,*S*)-(+)-dehydrohomoancepsenolide **30**.

In the year 2000, Furstner and Dierkes reported the total synthesis of a natural product, (*S*,*S*)-(+)-dehydrohomoancepsenolide **30**, which involved sequential ring closing metathesis (RCM) and alkyne metathesis reactions.[82] The cyclic butenolide precursor was first constructed by an RCM reaction catalyzed by Grubb's catalyst. Subsequent alkyne

metathesis with the Schrock catalyst followed by partial catalytic hydrogenation reaction using the Lindlar's catalyst successfully yielded the natural product **30** (Scheme 1.11).

Very recently, a short route (five steps, 60% overall yield) for insect pheromones (pest control agents) with *Z*-selectivity of 88% was reported by Grubbs and co-workers. The synthesis began with a commercially available starting material, 4-pentenol (**32**), which was subjected to cross metathesis reaction (CM) with 1-dodecene to afford precursor **33**. A sequence of tosylation, alkylation, and finally epoxidation reactions led to natural product **36** as shown Scheme 1.12.[83]

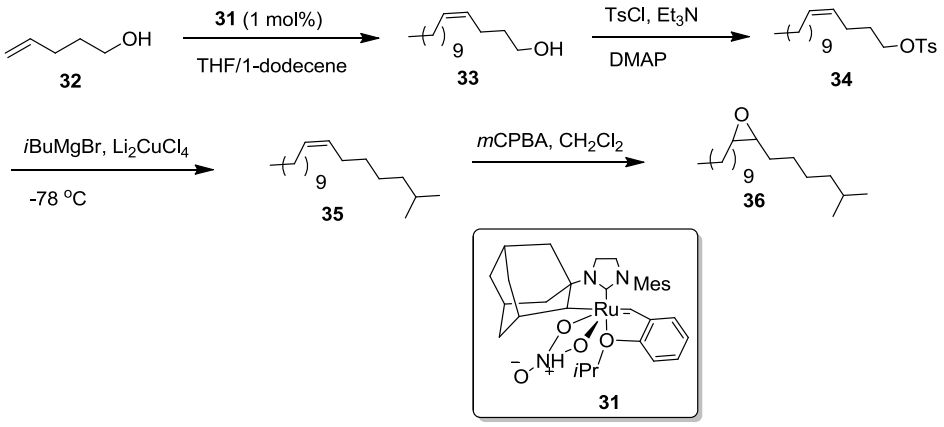

Scheme 1.12: Total synthesis of pheromone **36**.

- **Synthesis of Functional Organic Materials**

The ring opening metathesis polymerization (ROMP) reaction is one of the most important reactions that have been widely used for the preparation of many conducting polymers. This reaction involves the ring opening of a cycloalkene, where the release of ring strain provides the driving force for the reaction. The first industrial application of

ROMP reaction was launched in the year of 2000.[84] The ring opening reaction of cyclopentene produced *trans*- and *cis*-cyclopentamers as the products. This reaction is very attractive for the synthesis of polyacetylenes (PAs).

In 2003, Grubbs and co-workers prepared a series of endcapped polyenes (telechelic polymers) and polyacetylenes by the ring opening metathesis reaction (ROMP) on 1,3,5,7-cyclooctatetraene (COT) in the presence of a wide range of endcapping reagents (Sheme 1.13). The resulting polymers retain high solubility even when the chain length reaches up to 20 double bonds.[85]

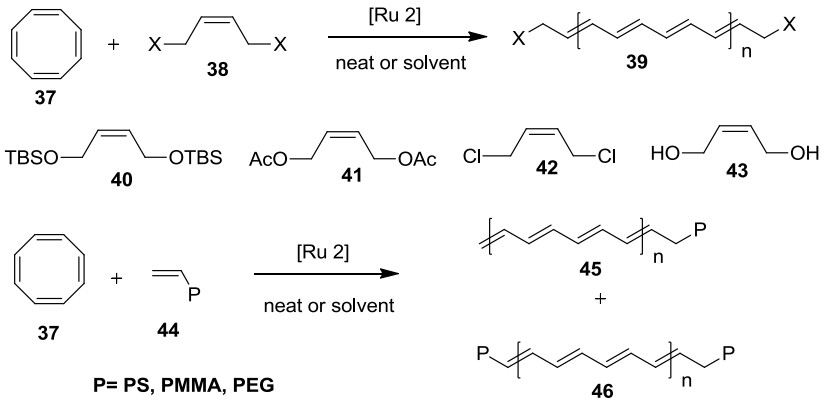

Sheme 1.13: Synthesis of polyacetylene polymers (the structures of the catalyst are shown in Figure 1.25).

Poly(phenylenevinylene)s (PPVs) and poly(fluorylenevinylene)s (PFVs) can be efficiently prepared by acyclic diene metathesis (ADMET) reactions. The first application of the ADMET reaction was attempted by Eichinger in 1992 in the synthesis of PPVs **48** (Scheme 1.14). Due to the lack of solublizing groups, this polymer was

highly insoluble.[86] The problem was later tackled by putting long alkyl chains on polymer backbone, such as polymer **51**.[87]

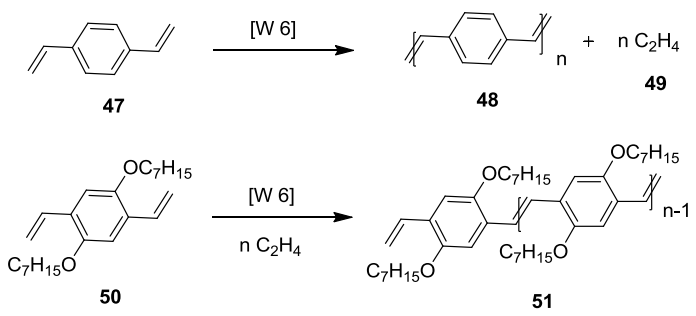

Scheme 1.14: Synthesis of PPVs by olefin metathesis reaction (the structures of the catalyst are shown in Figure 1.25).

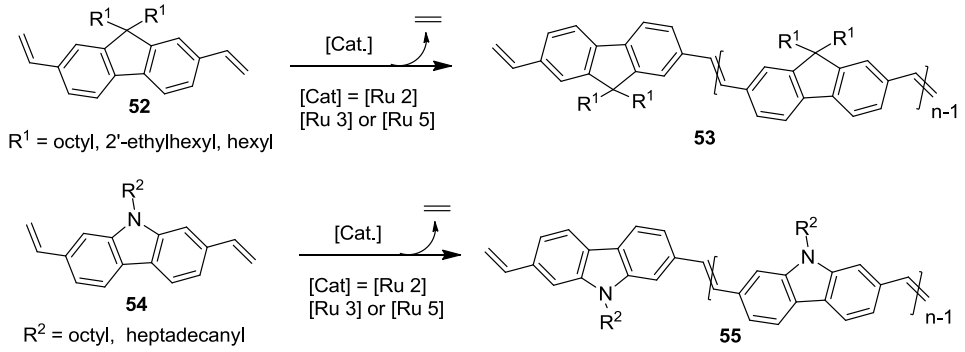

Scheme 1.15: Synthesis of PCVs, and PFVs via the ADMET reaction.

In 2001, Nomura *et al*. synthesized both PFVs and poly (carbobezoylenevinylene)s (PCVs) by employing ruthenium-catalyzed ADMET reactions on monomers **52** and **54** (Scheme 1.15).[88] The polymers were investigated by UV-Vis absorption and emission spectroscopy. Surprisingly, both of the polymers exhibited the same absorption maximum, indicating that the nitro substituent in PCVs has little effect

on the electronic properties in comparison with those of PFVs. This work highlights the importance of the ADMET reaction in preparation of conjugated polymers with tunable functionality.

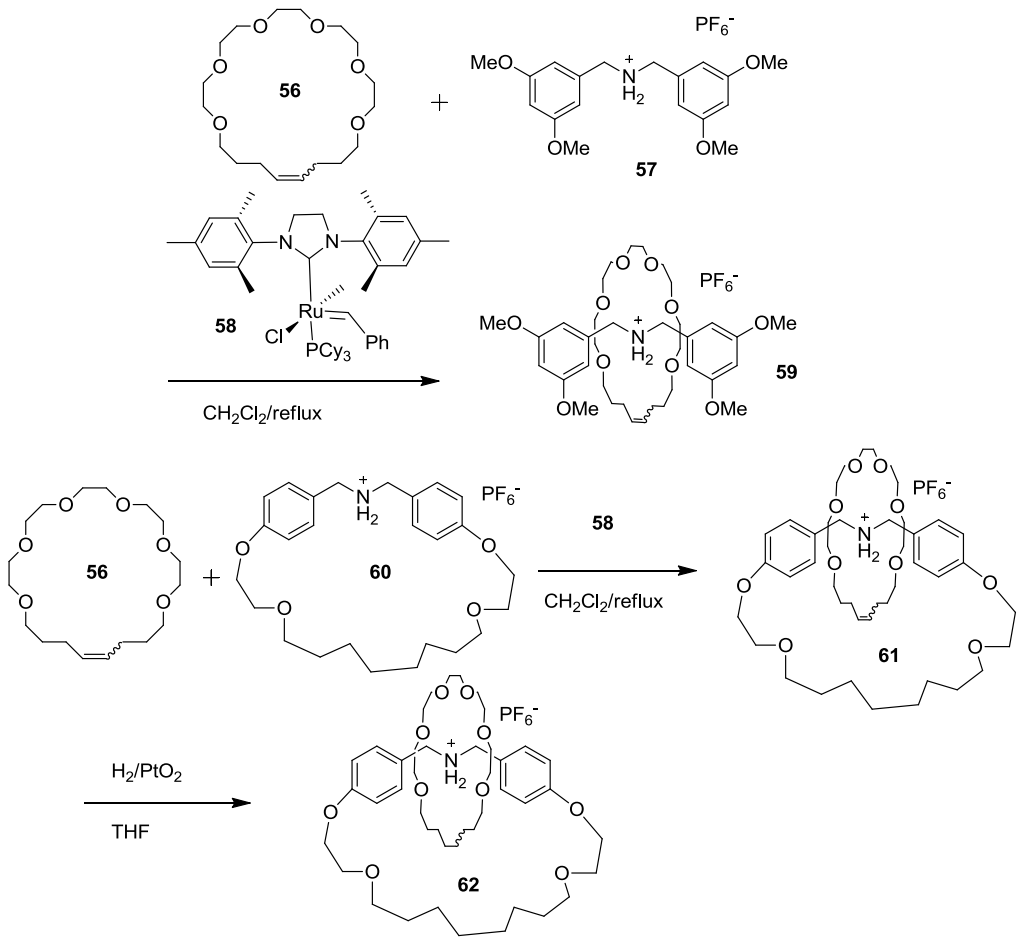

Scheme 1.16: Synthesis of magic rings.

An important approach for synthesis of mechanically interlocked macrocycles such as catenanes and rotaxanes relies on the use of olefin metathesis reactions. These macrocycles have been used as the key components in the active monolayers of some electronic devices, such as volatile bistable switches in both memory and logic

circuits.[89,90] One example of the synthesis of [2]catenane and [2]rotaxanes using the ring closing olefin metathesis reaction (RCM) is the work done by Stoddart and Grubbs in 2005. The RCM reaction between macrocyclic polyether **56** and macrocycle **60** gives [2]catenane **61** in 75% yield. In the same way, dumbbell-shaped component **57** and macrocycle **56** yielded [2]rotaxanes **59** in the presence of the Grubbs' catalyst (Scheme 1.16).[91]

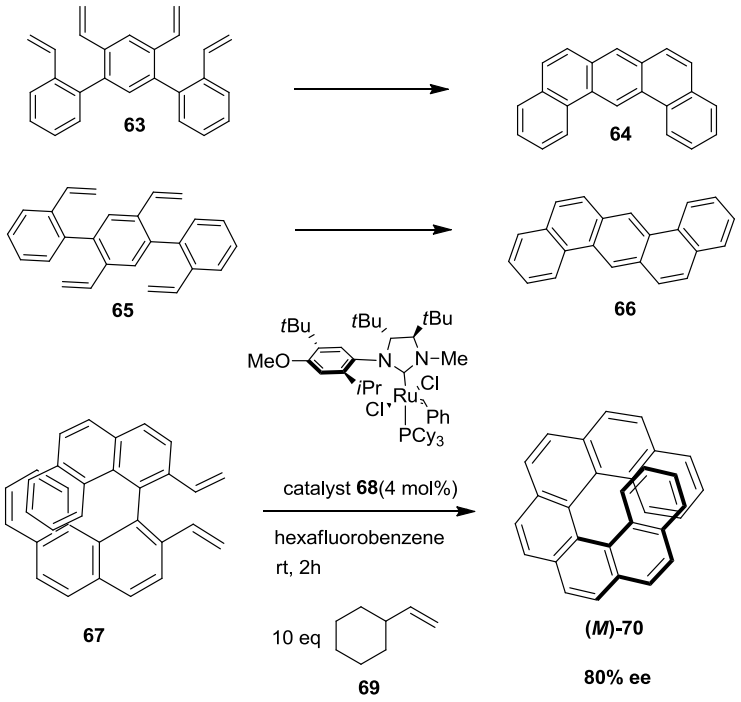

Scheme 1.17: Synthesis of PAHs and helicenes through olefin metathesis.

The RCM approach has been further expanded to the field of polyaromatic hydrocarbon (PAHs) and helicene chemistry. PAHs are interesting molecular materials as they provide models to understand the properties of fullerenes and carbon nanotubes. For example, as shown in Scheme 1.17, a double RCM reaction has been used for the

construction of PAHs **63** and **64**.[92] In 2006, Collins *et al*. described the synthesis of helicenes using the RCM reaction as shown in Scheme 1.17.[93] This methodology can easily produce substituted helicenes and in most cases they are *M*-selective.

1.3.2. 2 Cross-Coupling Reactions

Cross-coupling reactions are the most highly studied reactions in organic synthesis and research on these reactions has indeed revolutionized modern synthetic methodologies for pharmaceuticals, natural products, and organic materials. Metal-catalyzed cross-coupling reactions are considered as an important class of C-C and C-N bond forming reactions. A large number of synthetic methods has been developed and reported in the literature based on metal-catalyzed cross-coupling reactions, while studies dedicated to the development of novel ligands, mostly phosphine ligands, for various organometallic catalysts have constituted one of the major focuses of this research.

So far, a vast array of interesting research articles, reviews and books has been published on the topic of metal-catalyzed cross-coupling reactions. Transition metals such as palladium and nickel have been of particular interest in the development of C-C and C-N bond forming reactions because of their versatility and high functional group tolerance. In recent years, the use of other transition metals, such as iron and cobalt, as catalysts for coupling reactions has also received great attention in order to develop methodologies with good reactivities and relatively low costs.

As shown in Scheme 1.18, cross-coupling reactions can be broadly categorized in to two types. Some cross-coupling transformations have been developed based on the nature of electrophilic and nucleophilic partners, and they are mostly named reactions including Heck, Suzuki, Negishi, Stille, Buchwald, and Sonagashira reactions (Figure 1.26). Because of their pioneered research on the development of Pd-catalyzed cross coupling reactions, three scientists, Richard F. Heck, Ei-ichi Negishi, and Akira Suzuki, shared the 2010 Nobel Prize in chemistry.

Among all cross-coupling reactions, the Sonagashira, Suzuki, and Stille reactions are widely utilized in the synthesis of conjugated materials. The following section will present the synthesis of a few molecular materials reported in the recent literature.

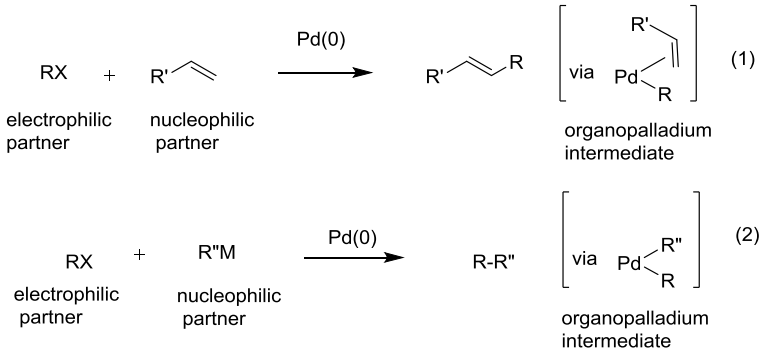

Scheme 1.18: General representation of cross-coupling reactions using Pd(0) catalyst.

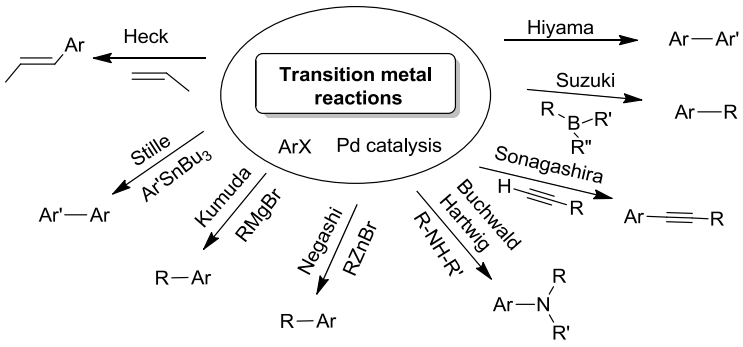

Figure 1.26: Popular transition metal catalyzed coupling reactions.

In 2005, Tykwinski and co-workers demonstrated the synthesis of the longest *iso*-polydiacetylenes (*iso*-PDAs) that showed a unique cross-conjugated π-framework.[94] These type of material exhibit large third-order nonlinear optical properties (NLO), and are potentially useful for the fabrication of signal processing devices. As shown in Scheme 1.19, the *iso*-polydiacetylene **75** was synthesized through Pd-catalyzed cross-coupling reactions (Sonagashira reactions) with a vinyl triflate precursor **72** as a coupling partner. UV-Vis analysis showed a steady redshift of λ_{max} with increasing chain length from dimer to higher oligomers of *iso*-PDAs. Further, the fluorescence spectra of *iso*-PDAs gave enhanced emission intensity as the oligomer chain length increased. Interestingly, the *iso*-PDAs (n > 7) adopt a coiled helical conformation in solution.

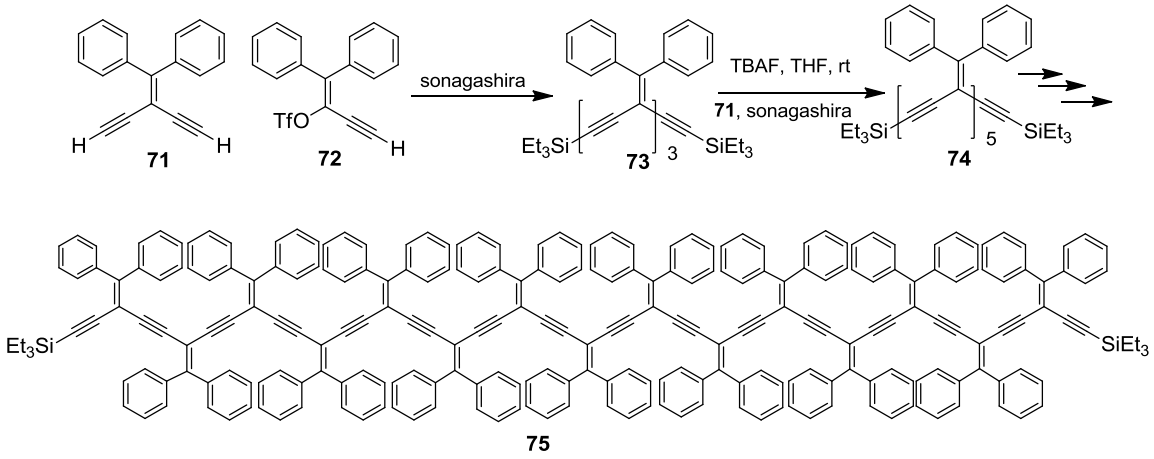

Scheme 1.19: Synthesis of *iso*-PDAs by the Tykwinski group using Sonogashira coupling reactions.

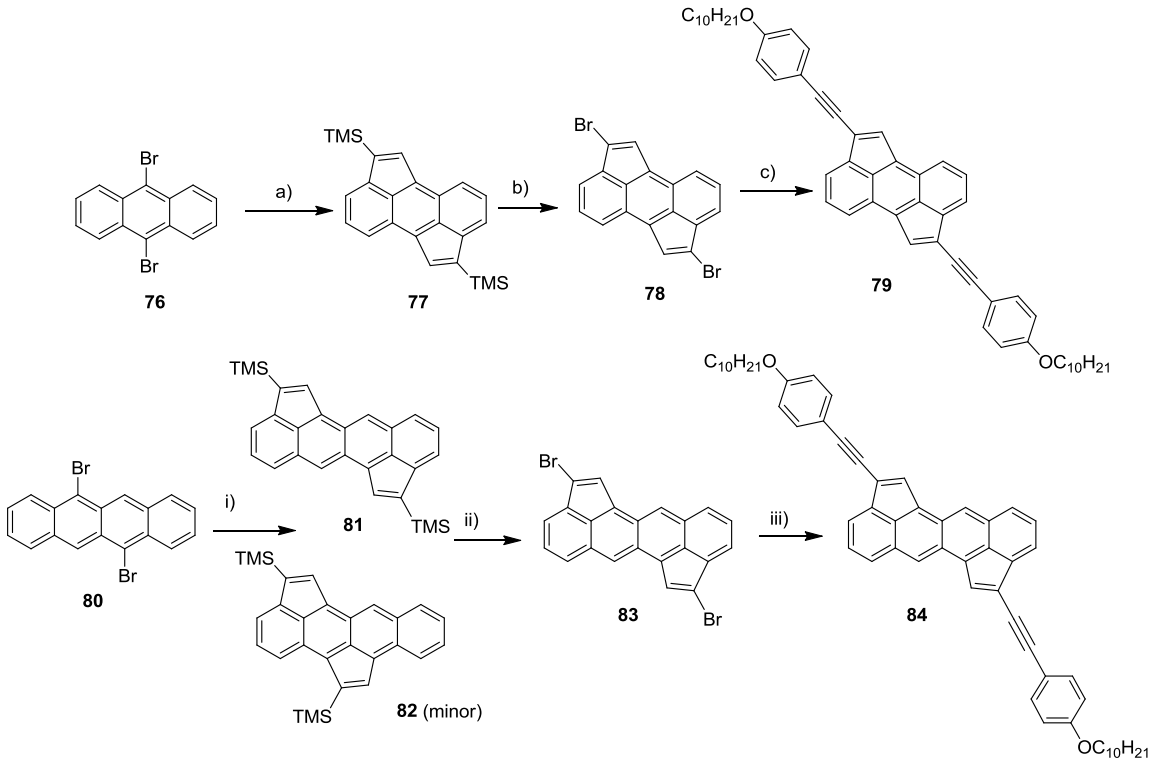

Scheme 1.20: Synthesis of CP-PAHs materials.

Recently in 2012, Plunkett *et al*. reported the synthesis of two cyclopenta-fused polycyclic aromatic hydrocarbons (CP-PAHs) and demonstrated their electron accepting properties (Scheme 1.20).[95] The synthesis was started by using Pd-catalyzed cross-coupling reactions of trimethylsilylacetylene (TMSA) and dibromo compounds **76** and **80**. The TMS groups were successfully converted to bromides with *N*-bromosuccinimide (NBS) to generate corresponding dibomo partners **78** and **83**. Finally, Sonagashira cross-coupling reactions were employed to couple the dibromo partners (**78** and **83)** with the phenylacetylene building block to give the desired CP-PAHs **79** and **84**. The resulting CP-PAHs possess low optical band gaps (1.52 and 1.51 eV respectively) and they display two reversible reductions as displayed by fullerene and its derivatives. Fluorescence

quenching experiments suggested that electron transfer was observed between the poly(3-hexylthiophene) (P3HT) donor and the CP-PAHs acceptor. These materials could be potentially used as electron acceptors in place of fullerenes.

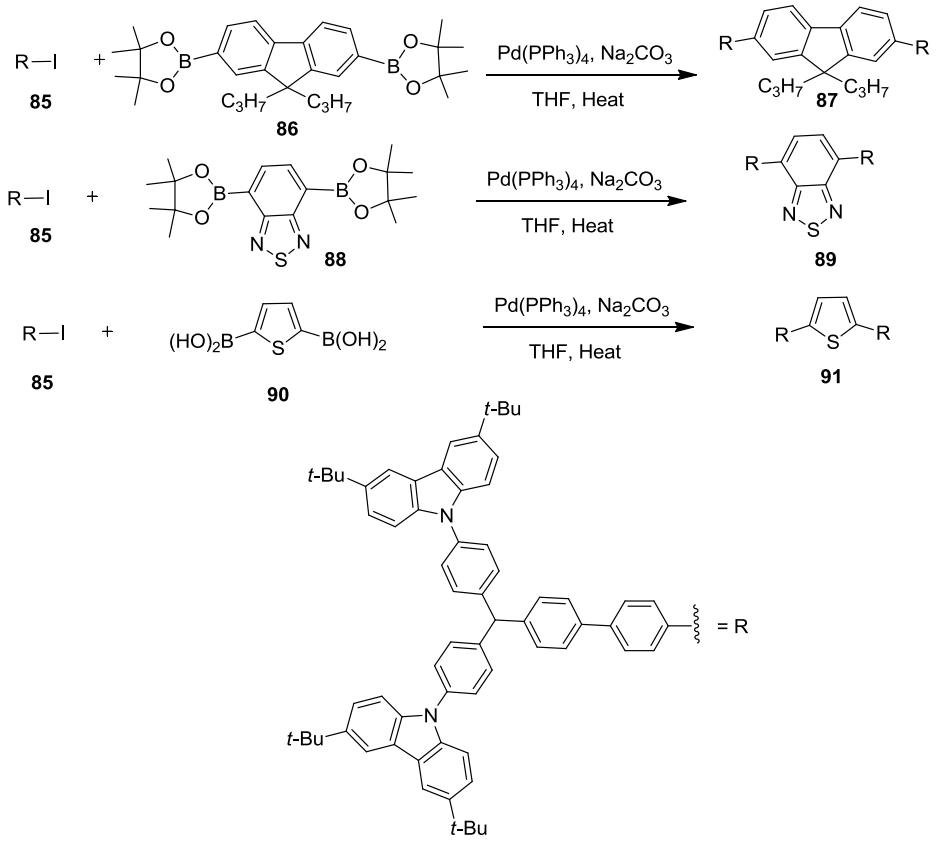

Scheme 1.21: Synthesis bis(carbazol-9-ylphenyl)aniline end-capped oligoarylenes by the Suzuki reactions.

In 2013, Promarak and co-workers synthesized a series of bis(carbazol-9-ylphenyl)aniline end-capped oligoarylenes (BCPA-Ars) by Pd-catalyzed cross-coupling reactions (Suzuki reactions) of a diiodo intermediate **85** with corresponding boronic acids and boronates as shown in Scheme 1.21. It was demonstrated that by varying the π-

conjugation length of respective oligoarylenes, the energy gap between HOMO and LUMO could be easily tuned. Upon illumination the solutions or thin films of these oligoarylenes, different emission colors were observed ranging from blue to red. Further, these oligoarylenes were applied in an OLED device as the active components. The results showed that the single-layer OLED gave a luminance efficiency of 3.85 cd A^{-1} and a low turn-on voltage of 2.4 V.[96]

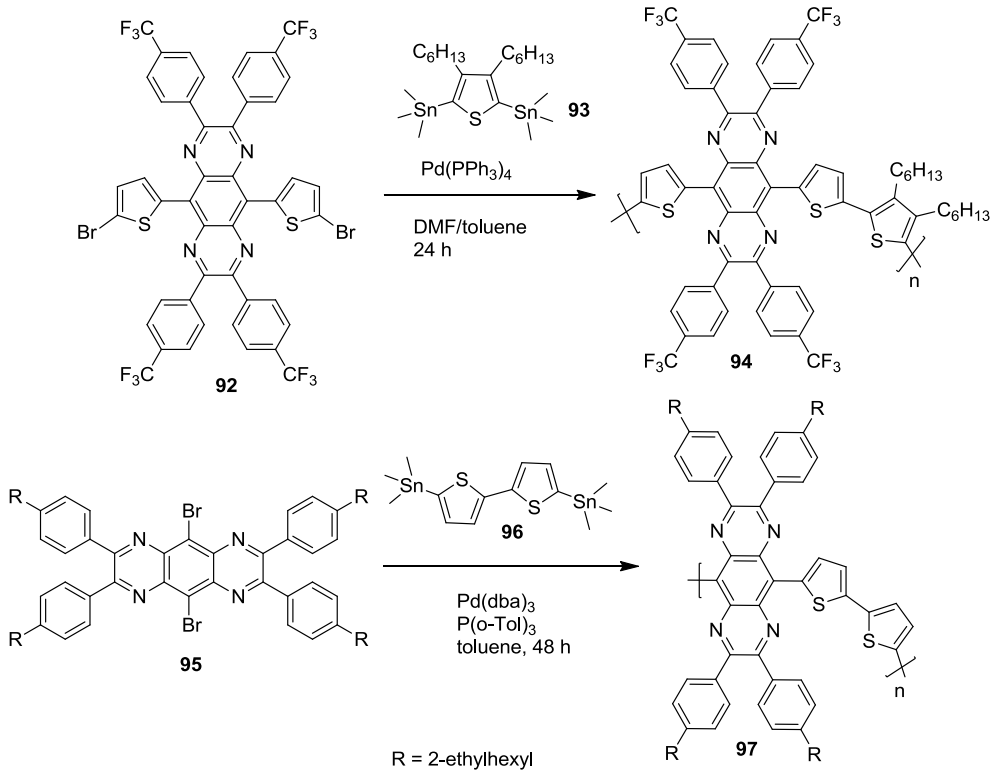

Scheme 1.22: Synthetic route for pyrazinoquinoxaline containing thiophene based conjugated polymers.

In 2013, Janssen and co-workers prepared a series of pyrazinoquinoxaline containing thiophene based conjugated polymers through Stille cross-coupling

polymerization of corresponding pyrazinoquinoxaline dibromo precursors with stanyl derivatives **93** and **96** under Pd catalysis (Scheme 1.22).[97] The LUMO energy level was increased from -4.0 to -3.8 eV when the electron-withdrawing CF_3 groups were replaced with electron-donating ethylhexyl chains in the case of polymer **97**. Efficient electron transfer was observed from polymer **97** to the $PC_{71}BM$ acceptor.

1.3.2. 2 Homo-Coupling Reactions

In parallel to cross-coupling reactions, metal-catalyzed homo-coupling reactions have also received considerable attention in the construction of a wide range of molecular materials such as conjugated oligomers, dendrimers, polymers, and macrocycles. Homo-coupling of various terminal alkynes is one of the most popular reactions utilized to create functional polymer/oligomer materials. Cu(I) salts are extensively used as catalysts in these reactions.

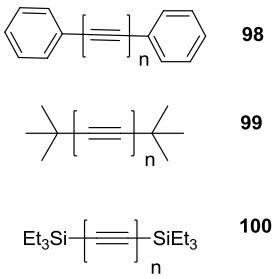

Figure 1.27: Structures of compounds **98**, **99**, and **100**.

Some synthetically challenging alkynyl compounds such as oligoynes and polyynes can be readily constructed by Cu-catalyzed oxidative homocoupling reactions. Due to their unique electronic, optical, and photophysical properties, oligoynes and

polyynes and their derivatives are more often used as molecular wires and one-dimensional molecular rods. A series of oligoynes has been synthesized and some of them are listed below. In 1970, Walton and co-workers prepared a series of bistrimethyl protected oligoynes. The longest oligoyne obtained was composed of 16 C≡C repeating units. However, due to their instability, these oligoynes were not completely characterized as they polymerized quickly when the solvent was removed.[98]

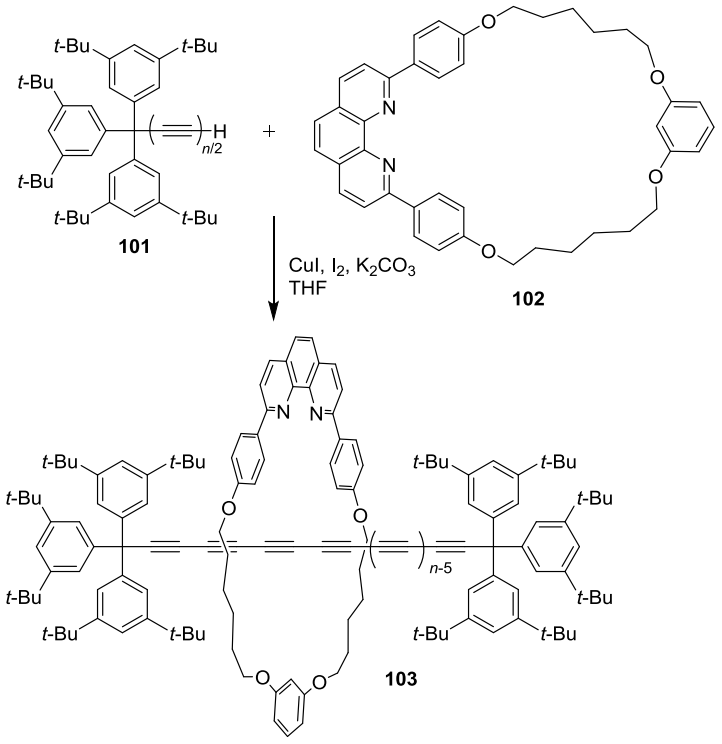

Scheme 1.23: Synthesis of polyynes rotaxanes **103**.

Recently, Tykwinski and co-workers disclosed that the stability of long oligoynes could be improved if they were terminated by bulky endcapping groups such as platinum

phosphine complexes and dendrimers. They have synthesized the longest monodisperse polyyne by using 'super trityl', tris(3,5-di-tert-butylphenyl)methyl (Tr*), as the terminating group. The polyyne is composed of 22 repeating conjugated C≡C units with 44 *sp* carbon atoms and represents the longest oligoynes reported so far.[99] In 2012, the Tykwinski group in collaboration with the Anderson group reported a series of polyyne-based rotaxanes which contain a phenanthroline-based macrocycle.[100] The rotaxanes **103** was successfully synthesized by Cu-catalyzed homo-coupling reactions of alkynes **101** in the presence of the phenanthroline-based macrocycle **102**. The single crystal structure of **103** was elucidated by X-ray analysis, showing a solid-state packing motif of oligoynes into pairs. π-Stacking was observed between phenanthroline units. This type of polyyne rotaxanes are expected to show higher stability than the corresponding polyynes with same length.

In 2013, Morin and co-workers demonstrated the synthesis and self-assembly behavior of the phenylacetylene macrocycle **114**. This compound acted as the precursor to intriguing organic "nanorods". For the synthesis, sequential Cu-mediated homo-coupling and Pd-catalyzed cross-coupling reactions were performed (Scheme 1.24).[101] The gelation properties of macrocycle **114** were studied in common organic solvents. The results suggested that the supramolecular assembly of macrocycle **114** led to nanofibers with diameters of *ca*. 200 nm and lengths on the scale of microns. By irradiating the organogel under a UV lamp at 254 nm, a covalent network of nanorods was formed.

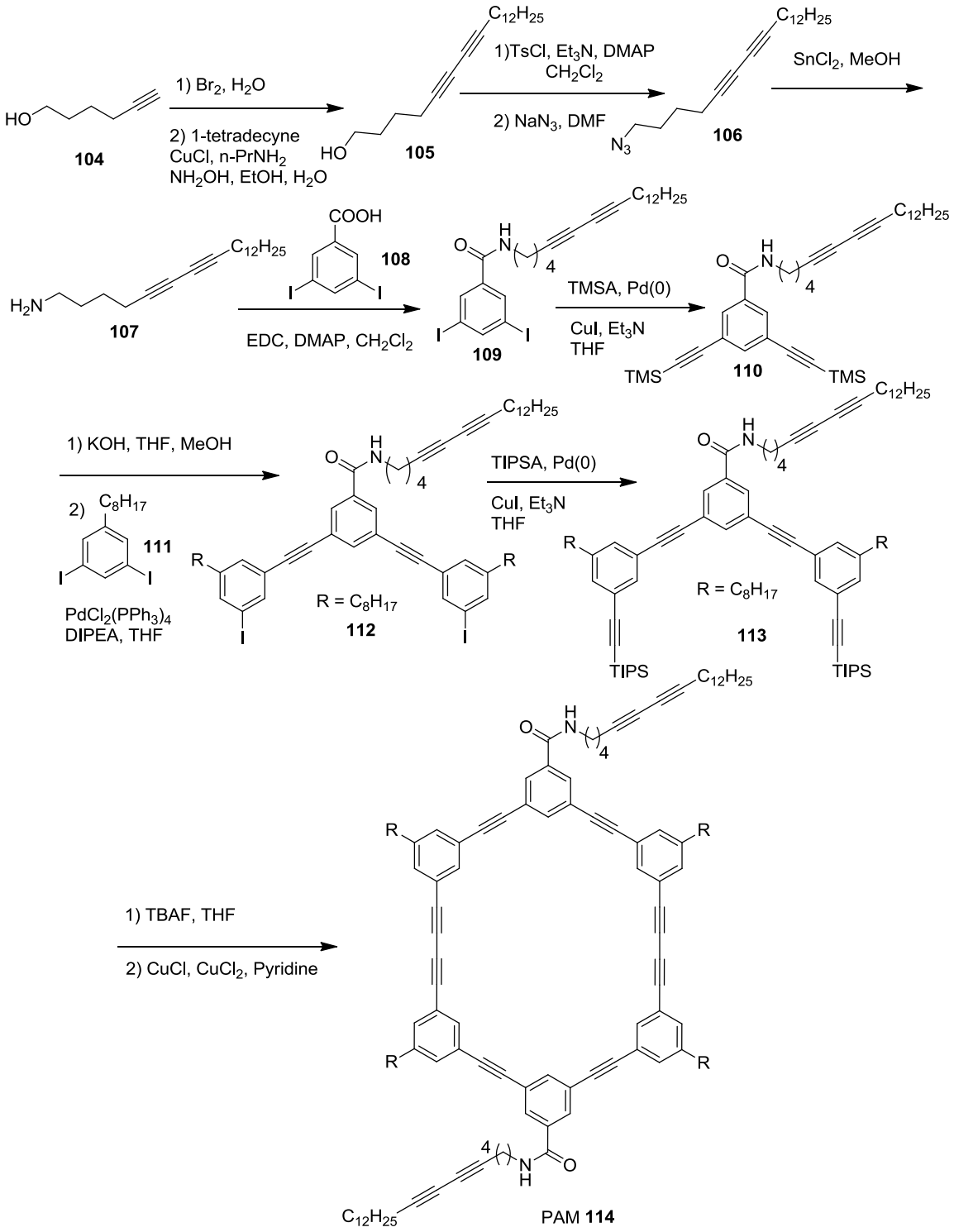

Scheme 1.24: Topochemical polymerization of phenylacetylene macrocycle (PAM **114**).

1.3.2. 3 Click Reactions

Over the past decade, increasing attention has been devoted to novel methodologies for the preparation of synthetically challenging architectures. In this respect, the concept of click chemistry emerged from a landmark review describing a new synthetic strategy for organic chemistry in 2001 by Sharpless and co-workers.[102] As described in this review, an ideal click reaction must meet the following criteria:

- Modularity and of wide application scope
- High yielding
- Generation of inoffensive by-products that can be removed without chromatography
- Stereospecific (but not necessarily enantioselective)
- Simplicity in experimental implementation
- Easy availability of starting materials and reagents

Based on the above criteria, several chemical reactions that have been identified as click reactions (Scheme 1.25) and are classified into four major categories:

1) Cycloaddition reactions (most commonly Huisgen 1,3-dipolar cycloaddition[6–9])
2) Nucleophilic ring-opening reactions of strained heterocyclic electrophiles (epoxides, aziridines and aziridinium ions)
3) Non-aldol carbonyl chemistry (oximes and hydrazones)
4) Additions to carbon–carbon multiple bonds (especially thiol–ene chemistry and Michael additions)

Among all click reactions, the most extensively studied reaction is the copper-catalyzed Huisgen 1,3-dipolar cycloaddition of terminal azides and alkynes to form 1,2,3-triazole rings. Originally, the Huigen reaction was performed at high temperatures yielded 1,4- and 1,5-substituted 1,2,3-triazoles. The use of Cu(I) catalysts results exclusively in the formation of 1,4-substituted 1,2,3-triazole (Scheme 1.26) and this reaction is undoubtedly the premier example of click reactions.

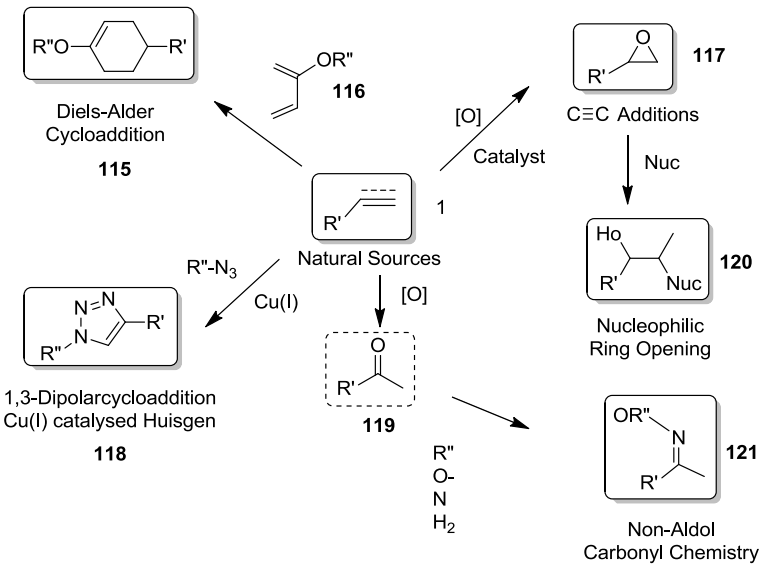

Scheme 1.25: Types of click reactions

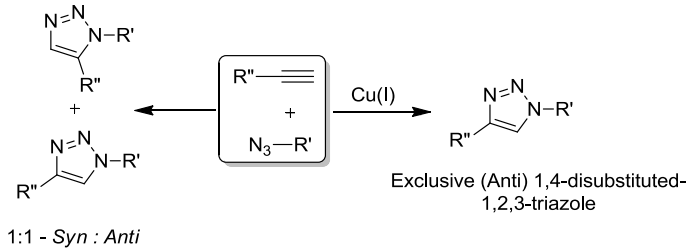

Scheme 1.26: The Huisgen cycloaddition and CuAAC reactions.

Based on independent research by the Sharpless and Meldal groups, the Cu-catalyzed alkyne azide coupling (CuAAC) reaction has been widely adopted for the synthesis of many functional organic materials. A brief review on this topic is given below.

The CuAAC reaction has been used in the synthesis of hyper-branched dendritic macromolecules. In the preparation of dendrimers, the issues of poor solubility and lengthy chromatographic separation are challenges frequently encountered. To circumvent these problems, the synthesis requires the use of reactions with high yield and specificity, such that the demand of processing and separation subsequent to the reaction would be minimized. To this end, Hawker, Fokin, and Sharpless pioneered the field of efficient dendrimer synthesis by devising a highly reliable two-step convergent synthetic method (Scheme 1.27)[103].

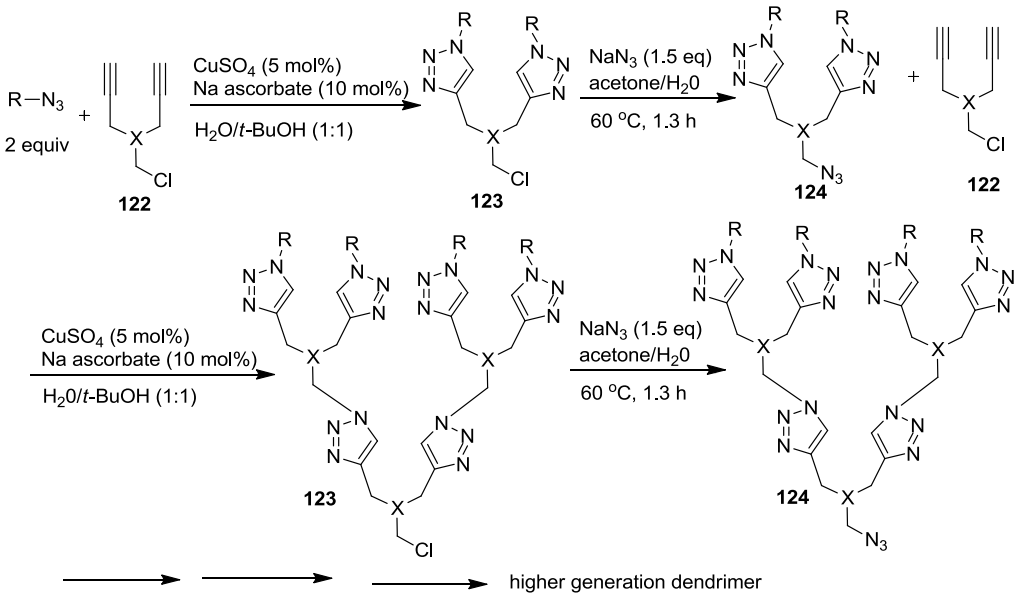

Scheme 1.27: Convergent synthesis of dendrimers using the CuAAC reaction.

In 2005, Hawker and co-workers prepared an unsymmetrical diblock dendrimer **127** in which two dendrons **125** and **126** were connected through a triazole linker by the CuAAC reaction as shown in Scheme 1.28. This type of unsymmetrical dendrimer allows the introduction of a variety of functional groups to dendrimers.[104]

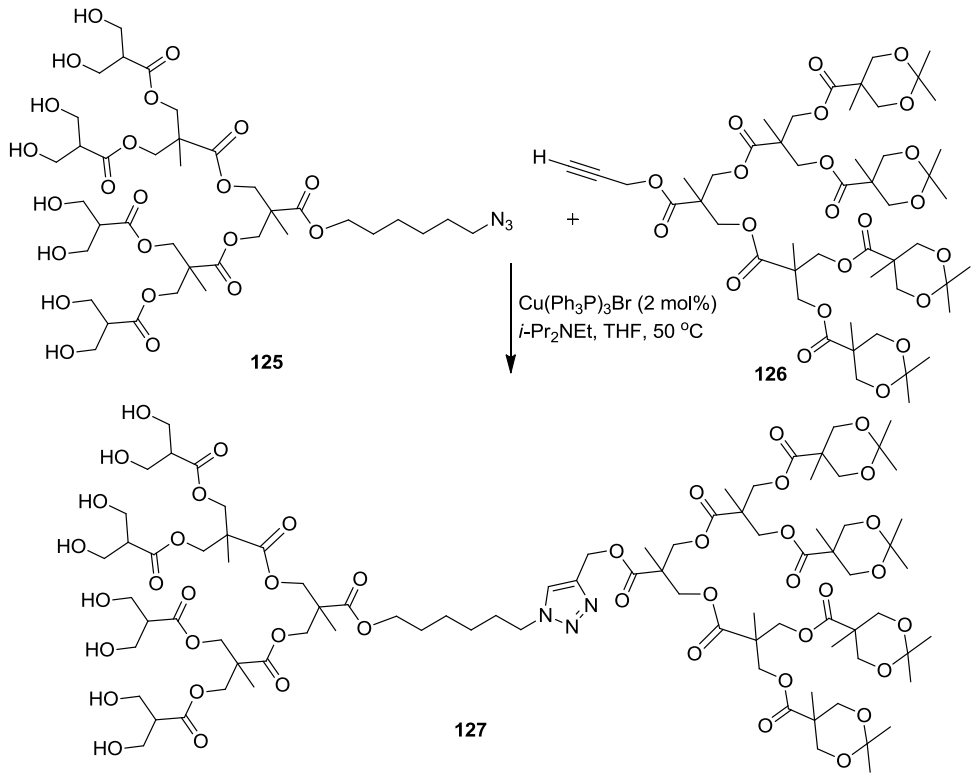

Scheme 1.28: Synthesis of a diblock dendrimer **127**.

Many applications of the CuAAC reaction have been found in polymer science, since the CuAAC reaction provides an efficient synthetic tool for both polymer backbone construction and side-chain functionalization. In 2005, Bunz and co-workers synthesized a class of functionalized poly(phenylene ethylene)s (PPEs) by using the CuAAC reaction. In the synthesis, both pre- and post-functionalization methods were used (Scheme 1.29).[105] The post-functionalization method allows a large variety of functional groups to be introduced after the polymer backbone is constructed. In the case of pre-functionalization, the polymerization reaction is the last step of the synthesis. The pre-functionalization method has some advantages over the post-functionalization method;

for example, it allows the correction of monomers if necessary. Overall, it has been demonstrated that the CuAAC reaction is suitable for both the pre- and post-functionalization methods in making polymers. The CuAAC reaction has been applied to the synthesis of numerous types of polymers, such as linear conjugated polymers, biopolymers, cyclic dendronized polymers, macrocyclic polymers, and triblock-copolymers.

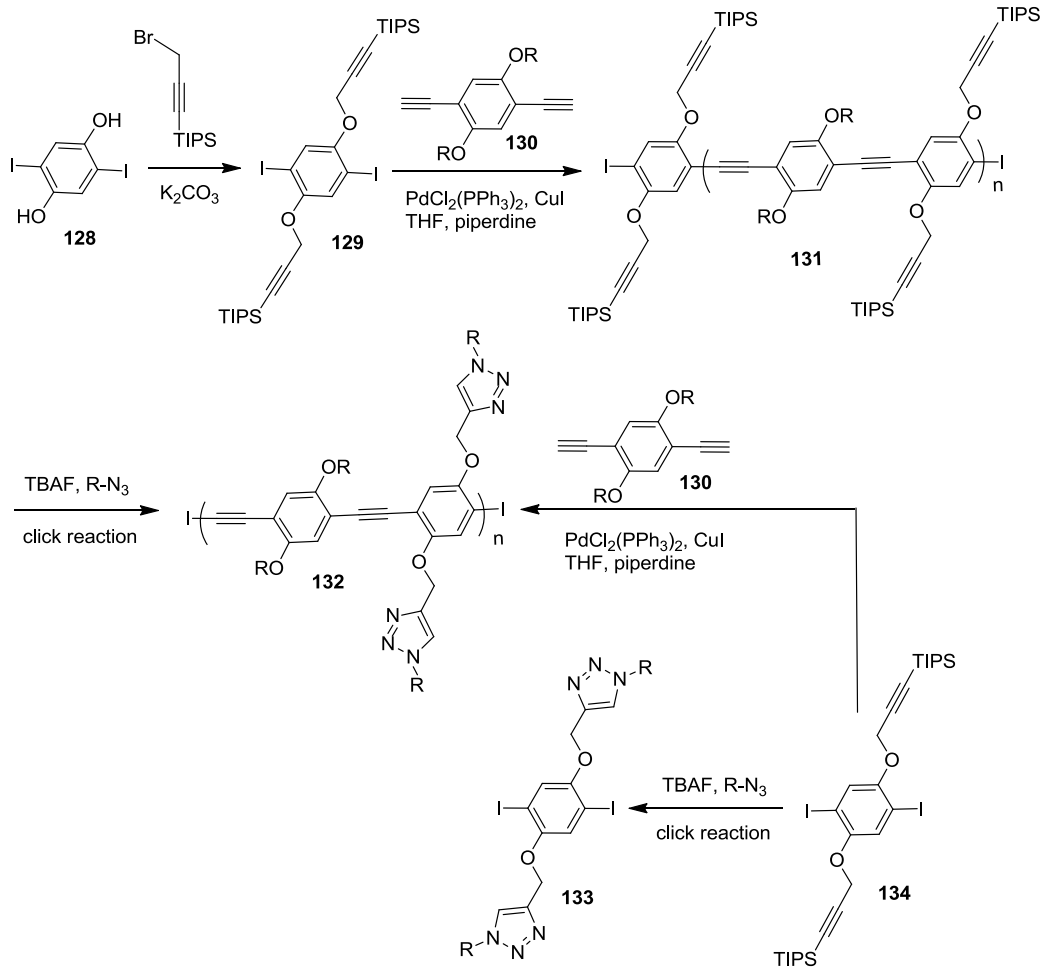

Scheme 1.29: Pre- and post-functionalization of poly(*p*-phenylene ethynylene)s (PPEs).

In 2012, Song and co-workers reported the incorporation of single-walled carbon nanotubes (SWNTs) into the network of a polyvinyl alcohol hydrogel through the CuAAC click reaction (Scheme 1.30). The results showed that SWNTs could be dispersed with the alkyne functionalized polymer in dimethyl sulfoxide (DMSO), and gelation occurred after the resulting SWNT/polymer complexes was subjected to the CuAAC reaction.[106] These hybrid materials acted as electrically conducting hydrogels and could be useful for biomedical applications.

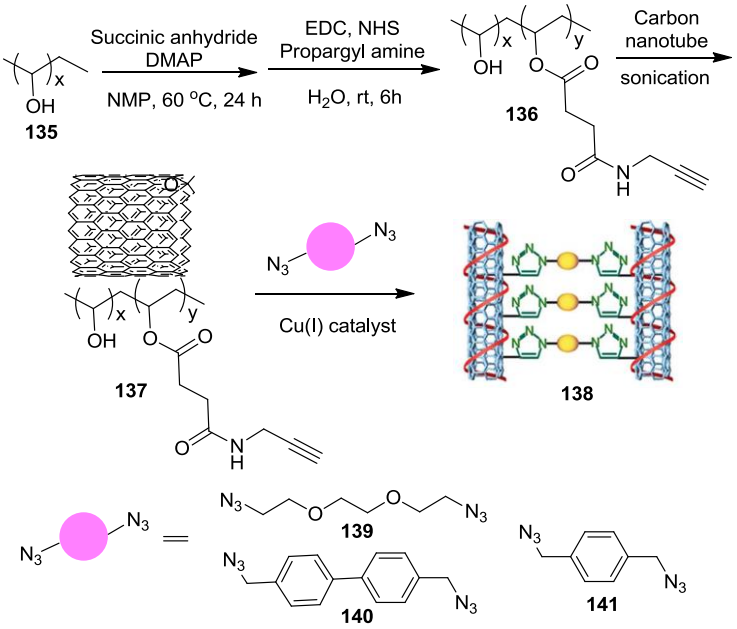

Scheme 1.30: Preparation of carbon nanotube hydrogels via the CuAAC reaction (Adopted from reference 106 with permission)

The 1,4-disubtituted triazole unit resulting from the click reaction has not only been extensively investigated as a robust linker in material synthesis, but is also frequently employed as an integral part in the preparation of many synthetic receptors.

This has greatly promoted the studies of the so-called “click derived” chemical sensors in recent years. The triazole group is well known to bind with both cations and anions. The chemical sensing process in general involves the detection of changes that are signaled by the interaction of a receptor group with an analyte. Many chemosensors have been designed based on the photophysical and/or electrochemical changes that take place when they are bound to certain analytes. The changes can be detected by UV-Vis, fluorescence, and electrochemical methods, depending on the nature of the reporter group attached to the receptor. In this respect, many “click generated” chemosensors have been developed for the detection of biologically and environmentally important species.

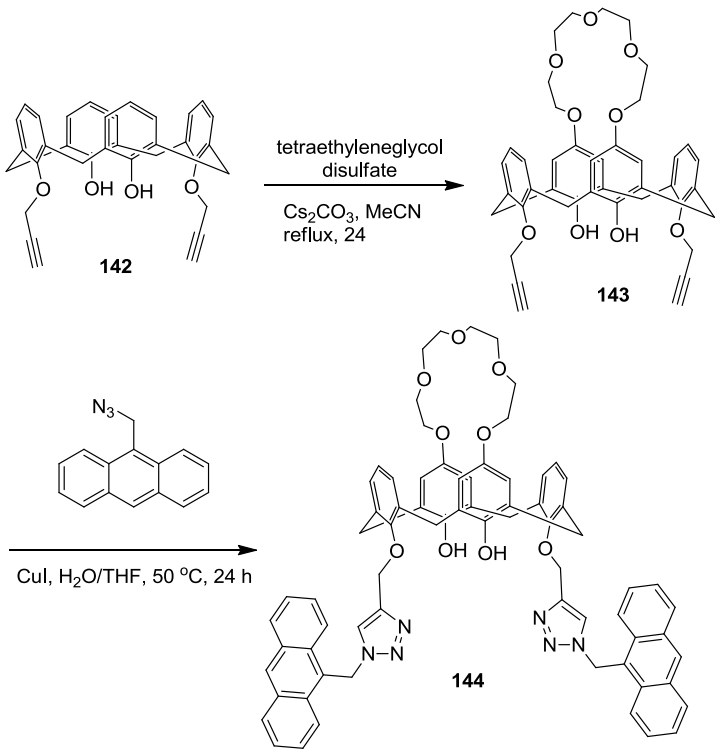

Scheme 1.31: Click synthesis of chemosensor **144**.

In the following section, selected examples of chemosensors recently reported are reviewed, where the "click generated" triazole unit functions as both the structural (linker) and functional (receptor or ligand) component in the chemosensor design.

In 2007, Chung and co-workers designed and synthesized a calixarene-based chemosensor in which an anthracene chromophore was attached to the lower rim of calix[4]arene via the click reaction (Scheme 1.31).[107] A double CuAAC reaction between the calixarene precursor **143** and 9-(azidomethyl)anthracene led to calixarene receptor **144**. Fluorescence titration experiments demonstrated that the emission intensity of receptor **144** could be significantly reduced with increasing addition of Pb^{2+}. Interestingly, when the solution of Pb^{2+}@**144** complex was titrated with K^+, the emission intensity was significantly enhanced resulting in the formation of complex K^+@**144**. As receptor **144** contains two binding sites (triazole and crown ether), it could be potentially used for sensing both Pb^{2+} and K^+ cations.

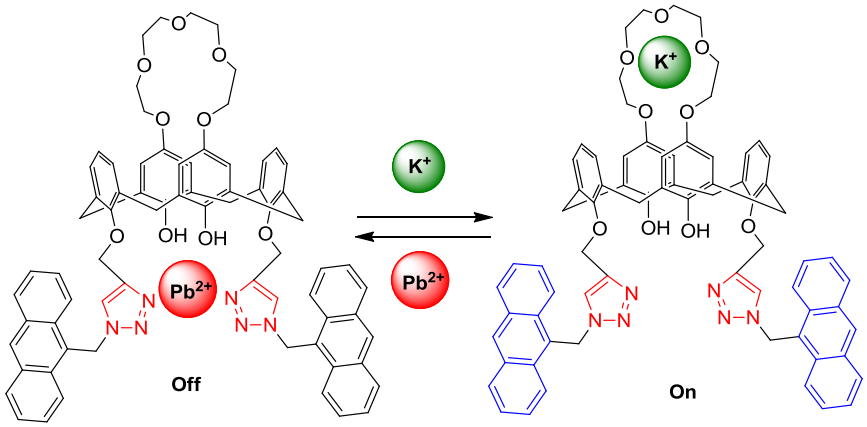

Figure 1.28: Binding models of chemosensor **144** with metal ions.

Bunz and co-workers prepared a water soluble chemical sensor based on benzothiadiazole by performing double click reactions of the intermediate resulting from desilylation of diethynylbenzothiadiazole **145** with azide precursor **146**.[108] The resulting double-click product showed excellent selectivity for Cu^{2+} ions as evidenced by UV-Vis and florescent spectroscopic analyses. The UV-Vis spectral changes showed an isosbestic point at 409 nm upon titration with $CuSO_4$. The fluorescence of **146** was substantially quenched when Cu^{2+} ion was continuously added.

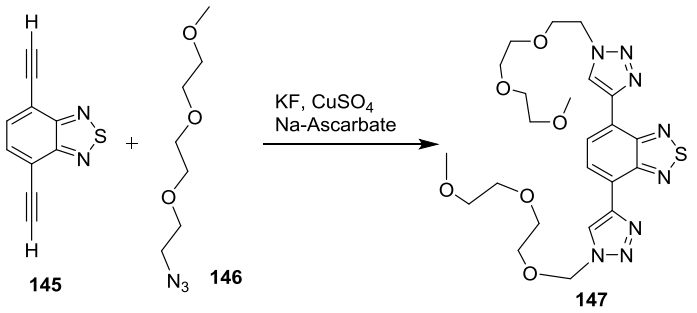

Scheme 1.32: Synthesis of chemosensor **147**.

Recently, in 2010, Flood and co-workers synthesized and demonstrated the switching properties of some light-active foldamers (**153** and **154**) in the presence of chloride ions. The foldamers were synthesized through multiple CuAAC reactions as shown in Scheme 1.33. In the presence of Cl^- ion, under visible light (465 nm), the foldamer **153** adopts a *trans-trans* conformation in the form of a chloride-receptor complex. Upon irradiation of complex under UV light at 365 nm, **153** is switched to a *cis-cis* conformation, resulting in the dissociation of chloride ion as shown in Figure 1.29. The switching events were monitored by UV-Vis and ^{1}H NMR analyses.[109]

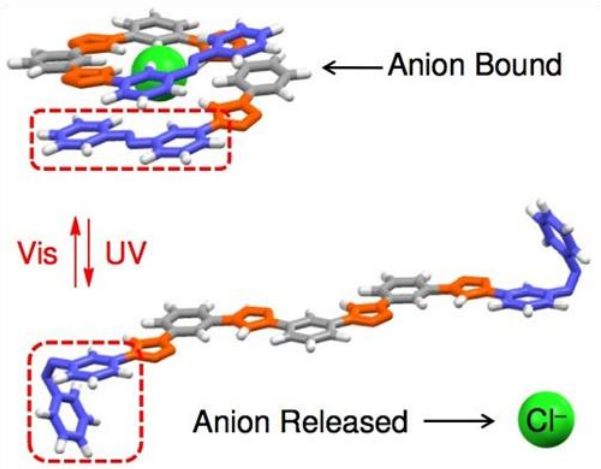

Figure 1.29: Functioning of a molecular photo-switch containing click generated triazole linkers (Adopted from reference 110 with permission).[110]

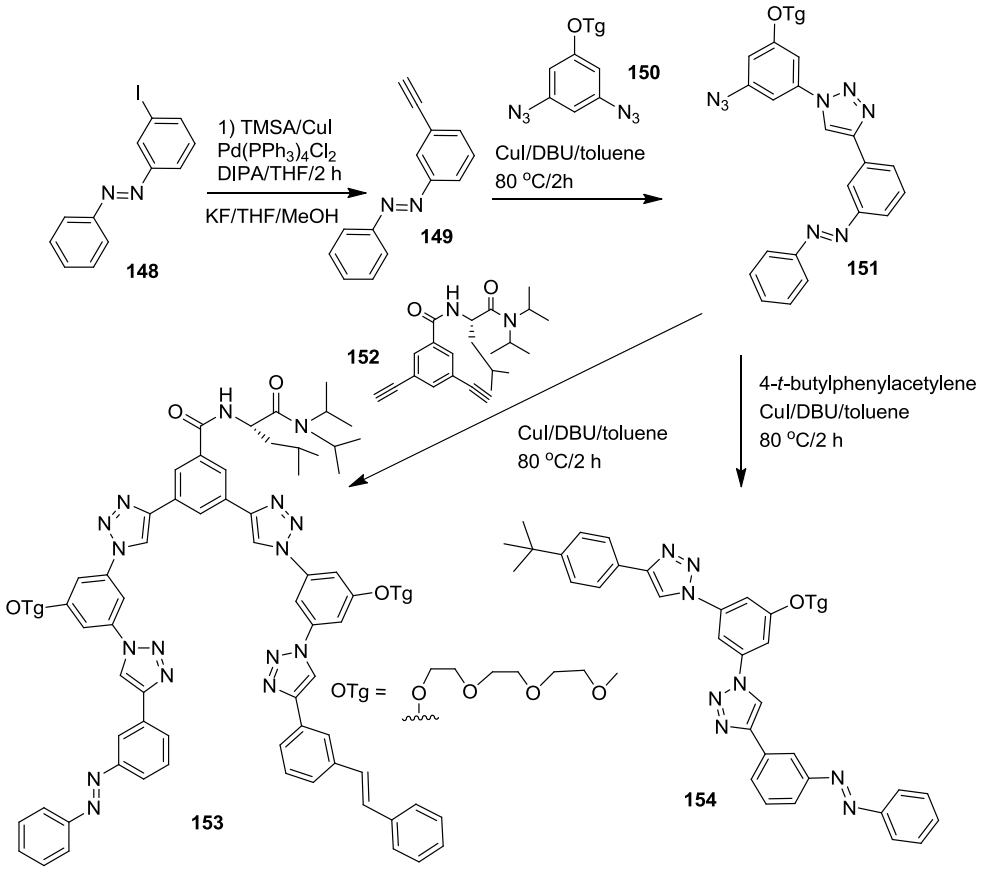

Scheme 1.33: Synthesis of light active foldamers **153** and **154**.

1.4 Molecular Materials and Devices Based On Conjugated Oligomers

π-Conjugated materials have attracted increasing attention in materials chemistry. π-conjugated organic polymers have been extensively investigated and very successfully applied in device fabrications for many years. Small molecules, on the other hand, also show interesting properties and promising application potential. Especially, well-defined monodispersed π-conjugated oligomers are alternatives to their relatively large polymer

cousins, and, in many cases, their use in device fabrication can lead to significant improvement of device performance.

The word “oligomer” is generally used to refer to the compound that carries relatively fewer repeating units than a polymer structure, or in a simple way, an oligomer can considered as the intermediate structure between a small molecule and a polymer. Unlike polymers, oligomers are easy to prepare and purification requires less effort. As such, an oligomer can be readily obtained with monodispersity, meaning that all the oligomer molecules have an identical number of repeat units in the backbone. Monodispersed π-conjugated oligomers feature some advantageous physical properties over polydisperse polymers. These include precise HOMO and LUMO energy levels, no structural defects, and good solubility in common organic solvents. The structural uniformity of monodispersed π-conjugated oligomers make them an effective models for studying structure-property relationships which offer guidance to understanding the complex properties of corresponding polymers.

Significant progress has been made on the study of well-defined conjugated oligomers as novel molecular materials, and there have been many articles and reviews devoted to related topics. The versatility in applications has made conjugated oligomers very promising candidates in materials science. Depending on the π-electron delocalization in their molecular design, the monodisperse π-conjugated oligomers can take several different shapes, ranging from linear (1D) to multi-dimensional (2D, 3D)

structures. Among all of them, the linear π-conjugated oligomers have been the most studied as a result of their relatively easy synthetic access.

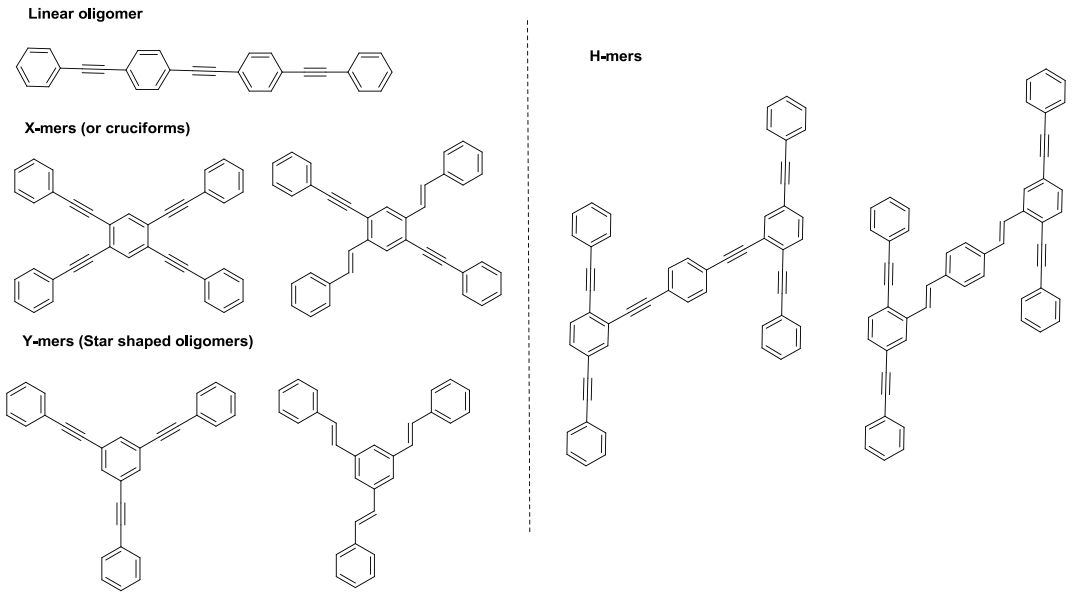

Figure 1.30: Examples of 1D and 2D π-conjugated oligomers.

The emergence of higher-order multi-dimensional oligomers (especially 2D) has captured increasing interest in the community of oligomer chemistry in recent years. These oligomers were synthesized and investigated mainly aiming at exploration of some unprecedented molecular properties that can be used in development of novel molecular sensors,[111,112] switches,[113] nonlinear optical materials (NLO),[114] organic field effect transistors (OFET),[115] photoluminescence,[111] and so on. According to the literature, 2D-conjugated oligomers can be generalized into X-, Y- and Z-shaped assemblages (referred as X-mers, Y-mers, and Z-mers as shown in Figure 1.30).[116] The following sections will

highlight on selected example of 1D and 2D conjugated oligomers that have received much attention in recent research.

1.4.1 Chemical Sensors Based On π-Conjugated Oligomers

A chemosensor is a molecular or supramolecular ensemble that can give detectable responses (e.g., optical or electrochemical changes) upon binding to some analytes. This requires the structure of a chemosensor to possess three essential components: receptor, reporter, and linker. Many synthetic receptors based on small organic molecules have been developed for metal ions, anions, and biologically important molecules. In most cases the chemosensors were designed to give rapid and significant UV-Vis, fluorescent, and electrochemical responses to chemical binding. For instance, after an analyte is bound to a chemosensor, it is possible to observe a change in the spectroscopic or electrochemical properties of the reporter unit attached to the receptor. If a fluorophore or chromophore is used as the reporter, changes in emission properties can render the system a fluorescent sensor, while changes in absorption properties give a colorimetric sensory function. If a redox-active unit is used as the reporter, the system becomes an electrochemical sensor. In order to increase the efficiency and selectivity of any chemical sensor, several parameters, including the molecular architecture, selection of chromophore/fluorophore, binding mechanisms, and solvation effects, must be carefully considered. The molecular architecture is an important factor, since it dictates the binding strength and selectivity. For this reason, many pre-organized molecular

shapes have been explored in chemosensor design; for example, molecular tweezers, macrocycles, molecular cages, and so on.

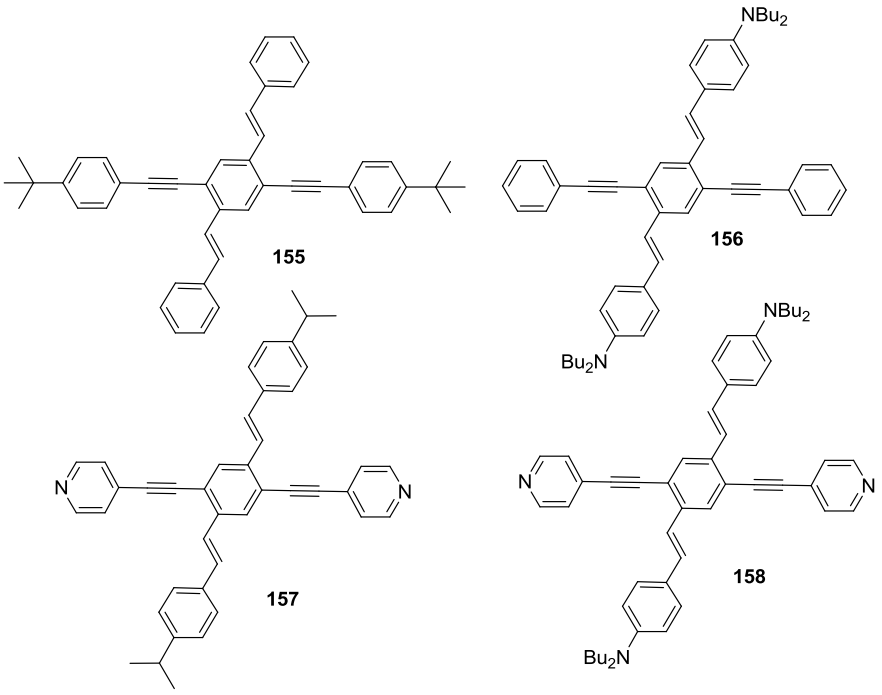

Figure 1.30a: Structures of cruciforms **155-158**.

Despite their remarkable photophysical properties, conjugated oligomers have not been thoroughly studied in chemical sensing applications. However, in recent years, the research towards the development of chemosensors based on conjugated oligomers has been progressing rapidly. The Bunz group synthesized a series of donor-substituted functional cruciform oligomers (X-mers) **155-158** and demonstrated their chemical sensing properties with different metal ions.[117] A combination of Horner-Witting olefination and Sonagashira coupling reactions has been employed in the construction of cruciforms. The fluorescence titration data reveals that the compound **158** is blueshifted

from 570 nm to 420 nm on addition of 0.84 eq of Zn^{2+} ion. On addition of 4 eq of Zn^{2+} ion, the emission of cruciform **158** is redshifted back to 530 nm as shown in Figure 1.31. In the case of cruciform **156**, addition of Zn^{2+} ion leads to a blueshift of the fluorescence band, while the addition of Zn^{2+} ion to cruciform **157** leads to a redshift. The emission spectra of cruciform **156** and **157** do not change with addition of more Zn^{2+} ion. These results indicate that the substituents on the cruciform backbone play a major role in the sensing functions and control the binding preference of the metal ions.

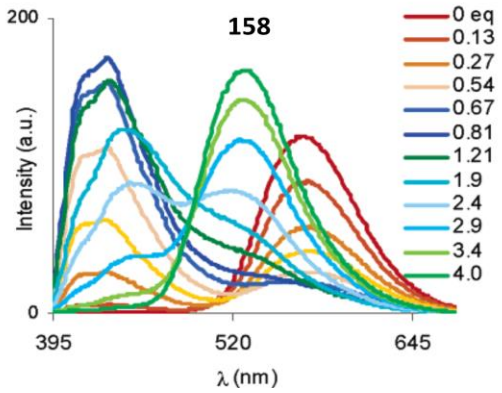

Figure 1.31: Emission spectra of cruciform **158** upon addition of Zn^{2+} ion (Adopted form reference 117 with permission).

By structural modifications of the cruciform skeleton, selectivity for different metal ions can be achieved. As another example, in 2008 Zhao and co-workers prepared a series of H-shaped π-conjugated co-oligomers based on linear oligo(phenyleneethynylene)s (OPEs) and oligo(phenylenevinylene)s (OPVs). They studied the molecular properties of these H-shaped oligomers and performed titrations of

metal ions and trifluoroacetic acid (TFA) with them. The H-shaped oligomers were synthesized mainly through Sonagashira and Horner-witting reactions.

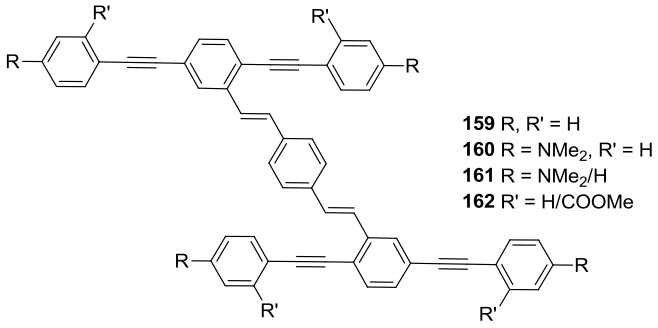

Figure 1.32: Structures of H-shaped OPE/OPV oligomers.

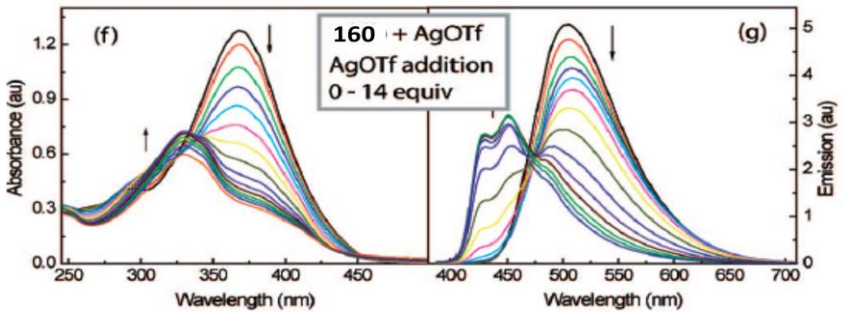

Figure 1.33: Absorption (left) and emission (right) spectral changes of compound **160** in the presence of AgOTf (Adopted from reference 118 with permission).

The fluorescence and UV-Vis titrations of **160** and **161** showed that during the titration with Ag^{+} or TFA, a shift of isosbestic point was observed, suggesting the involvement of multistep processes in the binding (Figure 1.33). Based on the spectral changes, these H-shaped oligomers were found to be useful as sensors for transition metal ions.[118]

1.4.2 Molecular Materials Based on Oligomer-Fullerene Hybrids

During the past decade, the number of C_{60}/π-conjugated oligomer donor-acceptor ensembles being explored as advanced materials for electronic and photonic applications has grown significantly. The driving force behind this research is to find a molecular approach to improve the so-called "bulk heterojunction" (BHJ) organic photovoltaic cells using C_{60} and π-conjugated oligomers as electron acceptor and donor components respectively. This type of device can be made by two different approaches. In the first approach, the active components such as C_{60} and conjugated oligomers can be mixed by some mechanical methods, while the second approach involves the synthesis of hybrid compounds in which the C_{60} fullerene and conjugated oligomers are covalently connected to each other.

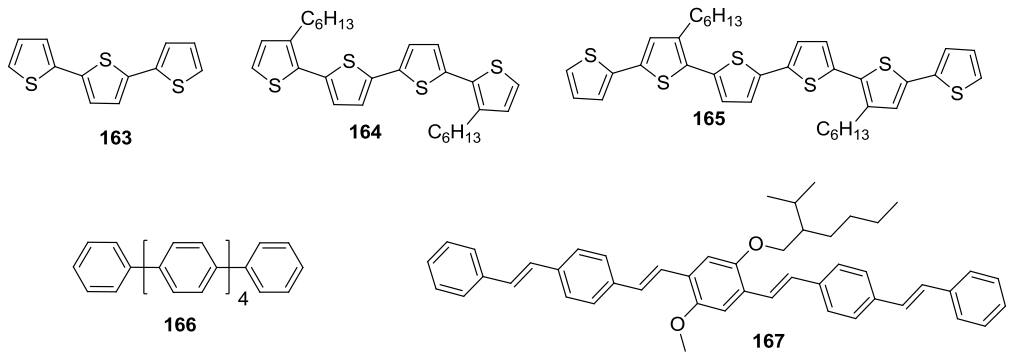

Figure 1.34: Examples of conjugated oligomers used in blends with C_{60}.

The blends of semiconducting conjugated oligomers, such as oligo-(phenylenevinylenes) (OPVs) and oligothiophenes (OTs) with C_{60} have been applied in some new types of plastic solar cells which yielded comparatively moderate power

efficiencies. A major problem associated with this kind of device is the tendency of the active materials, especially of pristine C_{60}, towards severe phase segregation. In addition, clustering frequently occurs in the blends to form strong aggregates. However, this problem has been solved through the second approach where covalently linked C_{60}/oligomers hybrids are used as the active components of devices.

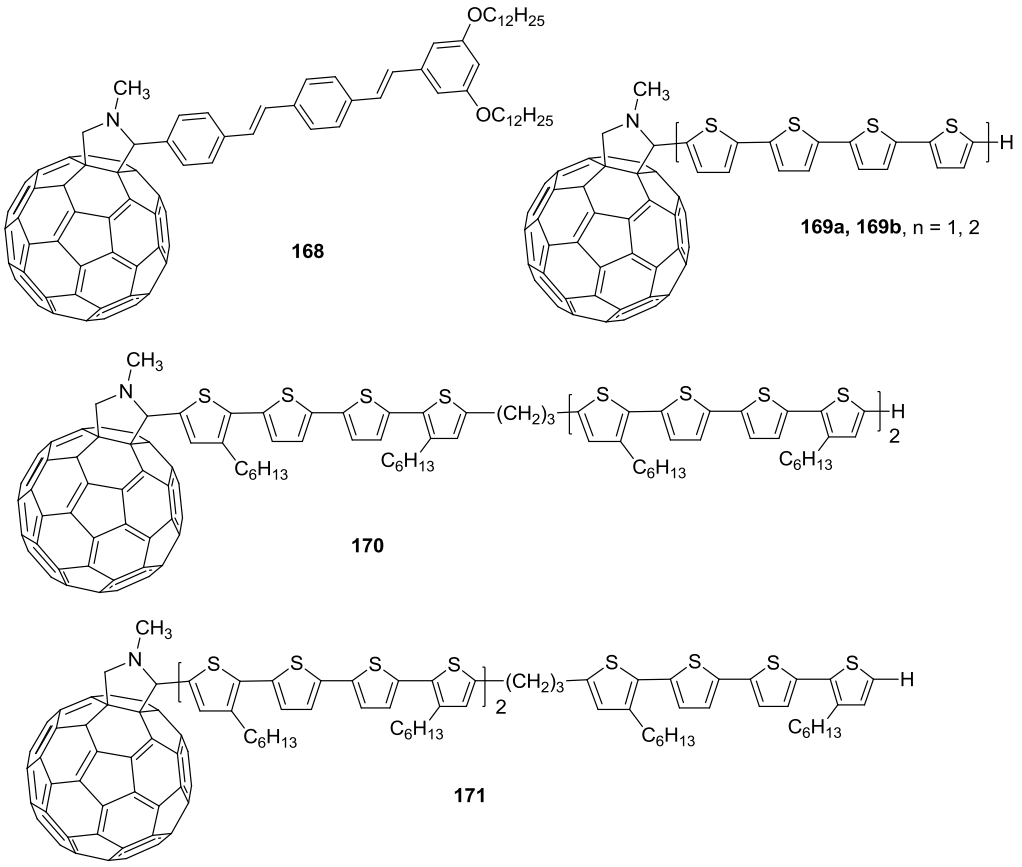

Figure 1.35: Structures of C_{60}-OPV and C_{60}-OT dyads.

A huge number of C_{60}-oligomer hybrid systems (dyads and triads) have been reported in the literature, and their photophysical properties have been investigated. For example, Nierengarten *et al*., in 2000 prepared a fulleropyrrolidine derivative based an

OPV-C_{60} dyad for the first time (Figure 1.35). After a thorough investigation of the photophysical properties of **168**, a simple photovoltaic device was fabricated by spin-coating a thin film of **168** between an indium-tin oxide (ITO) coated glass electrode and a vacuum evaporated aluminum electrode. This device gave a short circuit current density (J_{SC}) of 10 uA . cm^{-2} and an open circuit voltage (V_{OC}) of 0.46 V under monochromatic irradiation (400 nm, 12 mW . cm^{-2}).[119]

In 2005, Otsubo and co-workers synthesized a series of oligothiophene-fullerene dyads **169a-b** and two triads **170-171** (Figure 1.35). In the triads, quaterthiophene (4T) **170** and octithiophene (8T) **171** are connected through a methylene group and these oligomers are attached to a C_{60} fullerene. The cyclic voltammograms and electronic absorption spectra of these triad compounds showed that there was no electronic interaction among the three electroactive components in the ground state. The low emission intensity of **170** and **171** pointed to facile electron transfer and/or energy transfer from the oligothiophene to C_{60}. Comparison between the emission spectra of triads (**170** and **171**) and dyads (**169a-b**) suggested that the additionally attached octithiophene or quaterthiophene units in the triads were in fact involved in the photodeactivation mechanism. The devices made by 4T-8T-C_{60} showed a relatively poorer photovoltaic performance than the 8T-C_{60} device, due to the absence of long distance charge separation via photoinduced electron transfer.[120]

In 2006, Gust and co-workers prepared a hybrid star-shaped dendrimer **172**, comprised of aryleneethynylene units surrounding a hexaphenylbenzene core. The

oligomer was linked to a porphyrin-fullerene (donor-acceptor) segment (Figure 1.36).[121] Photoinduced electron transfer was observed between the porphyrin unit and fullerene which resulted in a long-lived $P^{\cdot+}$-$C_{60}^{\cdot-}$ charge-separated state. The charge recombination rates were measured and are 8.9 ns for **46a** and 15.3 ns for **46b**. The authors suggested that this type of system can be a functional mimic of natural photosynthetic antenna-reaction center complexes.

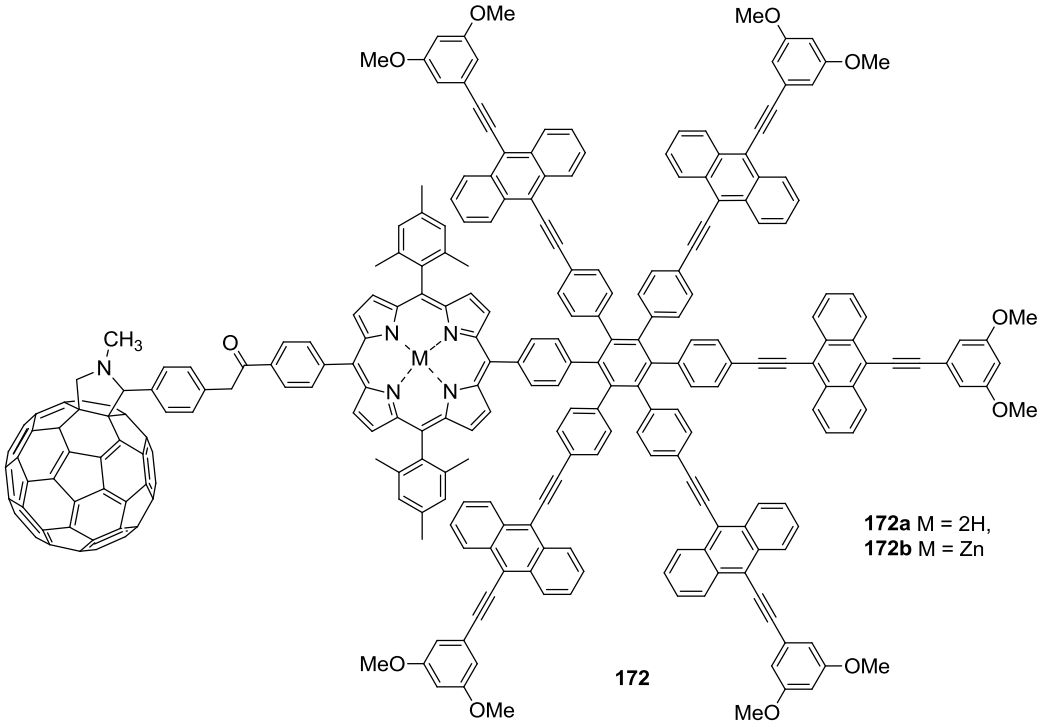

Figure 1.36: Structure of C_{60}/Star shaped dendrimer.

The design of single-molecule sized nanomachines such as molecular motors, switches, and gears has become a topical research area in recent years. The pioneering research in this area was made by Professor James Tour at Rice University who opened a new avenue for the construction of nanoscale machines based on conjugated oligomers.

In 2005, the Tour group prepared a class of surface-rolling molecules known as "nanocars", the "chassis" of which were constructed by rigid, H-shaped OPE units, and the wheels of which were spherical organic groups, such as [60]fullerene and carborane (Figure 1.37).[122] The results disclosed in his publications on the fullerene-wheeled nanocars demonstrated that a nanocar remains stationary on the surface until the surface temperature reaches to 170 ^{o}C due to strong interactions between the fullerene wheels and the gold surface. Above this temperature, the molecule starts rolling on the surface by translation and pivoting motion in two-dimensional paths as evidenced by STM imaging studies.

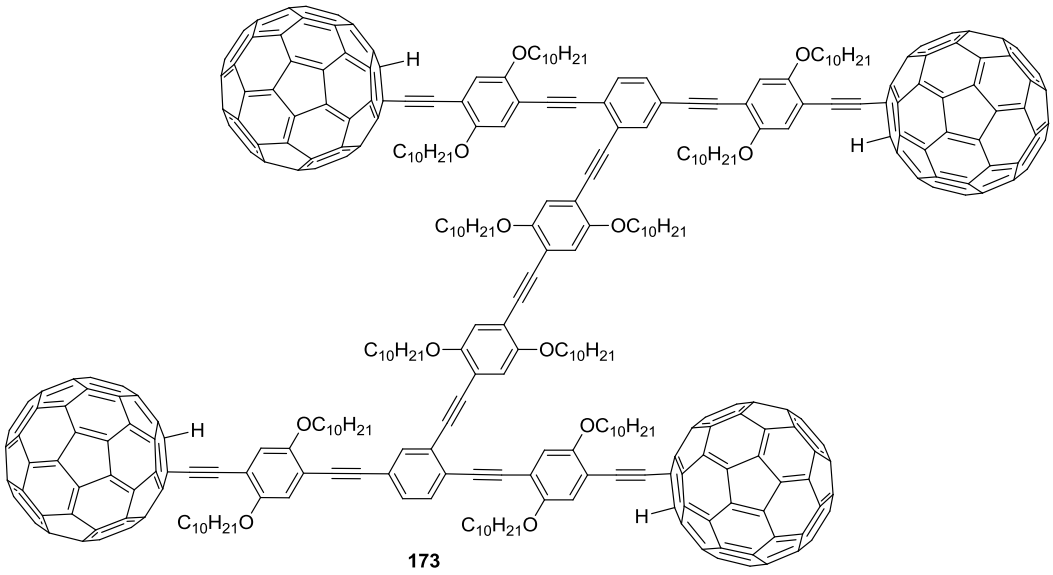

173

Figure 1.37: One example of Tour's Nanocars.

In 2006, the Zhao group constructed a C_{60}-tetraayne-C_{60} molecular dumbbell (Figure 1.38). Solid-state thermal polymerization of this molecular dumbbell at 160 ^{O}C

led to highly extended C_{60}-polyenyne networks, and this type of polymer could be potentially used as an active materials in various optical devices.[123]

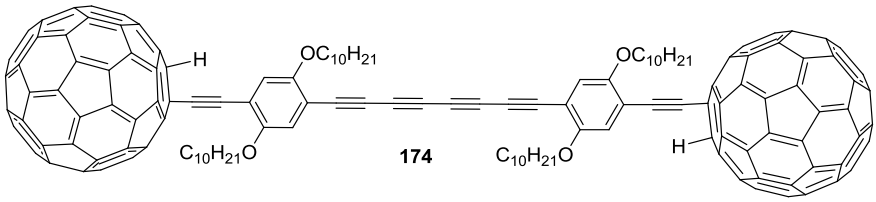

Figure 1.38: Structure of Zhao's molecular dumbbell.

1.4.3 Organic Light Emitting Diodes Based On Conjugated Oligomers

As mentioned earlier, the organic light emitting diodes (OLEDs) are one of the important classes of molecular materials and extensive research has been carried out to promote these materials into commercialization. The development of OLEDs began in the 1980s when the first report on efficient and low-voltage OLEDs from p-n heterostructure devices using thin films of vapor-deposited organic materials was disclosed by Tang's group.[124] A following breakthrough work was done by Holmes and co-workers on electroluminescence of conjugated PPVs.[59] Since then, many different types of OLEDs materials based on π-conjugated oligomers have been synthesized and fabricated, such as oligothiophenes (OTs, oligophenylenes (OPs), and oligo(phenylenevinylene)s (OPVs) and so on.

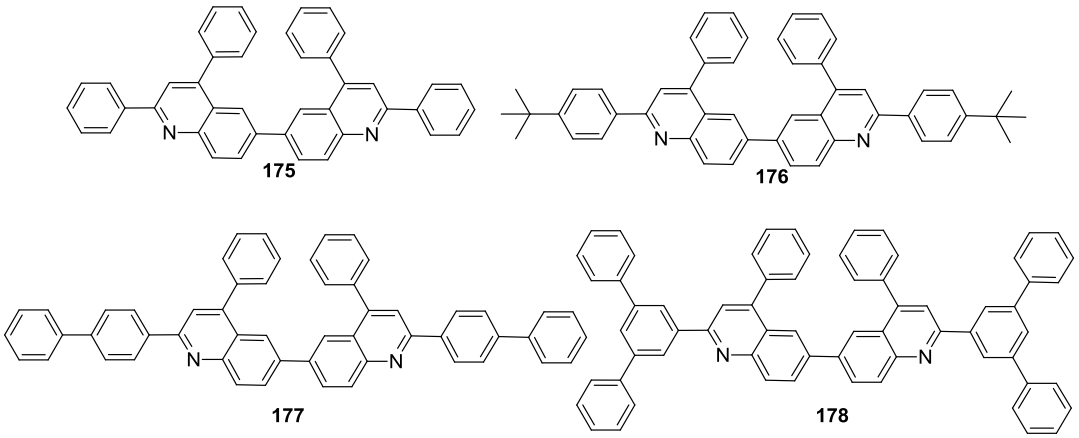

Figure 1.39: Structures of blue-light emitting oligoquinolines **175-178**.

In 2007, Tonzala and co-workers reported several highly emissive n-type conjugated oligoquinolines **175-178** (figure 1.39).[125] Owing to their reversibility during the reduction process and high electron affinities (2.68-2.81 eV), these oligomers acted as good electron transport materials. Furthermore, devices fabricated based on these oligomers as blue emitting materials have shown the best performance with a high brightness (19740 cd m^{-2} at 8.0 V), high efficiency (cd A^{-1}), and external quantum efficiency of 6.56% at 1175 cd m^{-2}.

As shown in Figure 1.40, another important class of OLEDs materials based on fluoro-substituted oligoarylenevinylenes **179-182** has been prepared by Liu and co-workers.[126] These oligomers are highly fluorescent with high quantum yields (ϕ = 0.98-0.68) and the colors of emission (448-579 nm) are significantly affected by the positions of the fluoro substituents. This fluoro-substitution effect on the emissions can be rationalized by means of HOMO-LUMO simulations. Among all oligomers prepared,

oligomer **179a** gave a remarkable high external quantum efficiency (η_{ext}= 4.87%) at *J* = 20 mA cm^{-2}, a high luminescence efficiency of 5.91 cd A^{-1} at *J* = 53 mA cm^{-2}, and a maximum brightness at 10.2 V of 22 506 cd m^{-2}.

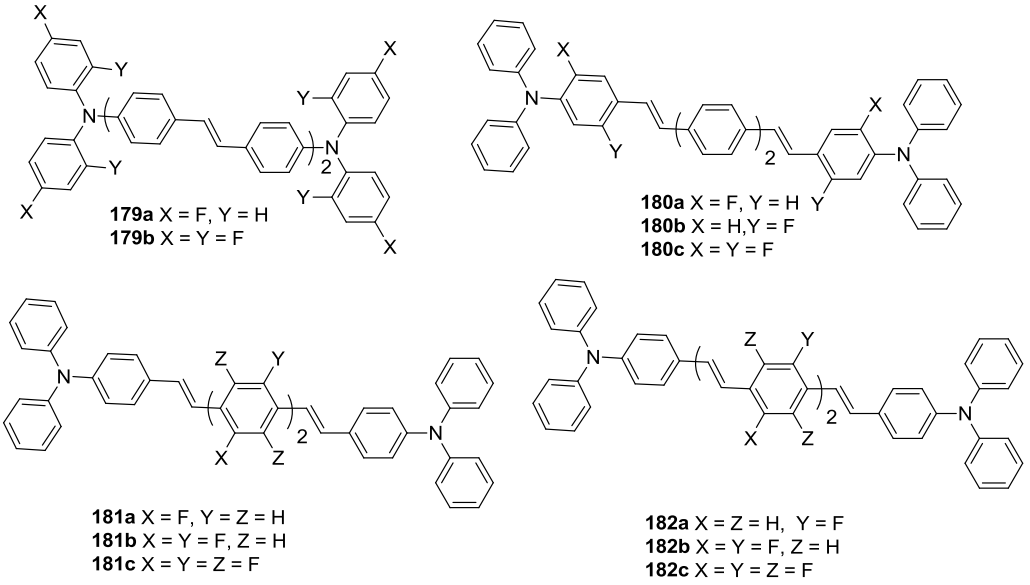

Figure 1.40: Structures of fluoro-substituted oligo(arylenevinylene)s **179-182**.

1.4.4 Molecular Wires Based On π-Conjugated Oligomers

Recently, the development of highly conducting molecular wires has attracted great attention due to their potential applications in the area of nanoelectronics, since their precise lengths and bonding architectures can enhance their molecular charge transport properties. As such, these materials are often used in various electronic devices such as semiconducting molecular wires or rods. For years, single molecular electronic devices have been pursued based on conjugated oligomers such as oligothiophenes, oligo(phenyleneethylene)s, and oligophenylenes. In 2007, Aso and co-workers

synthesized oligothiophenes **183** with a length of 10 nm using a block coupling synthetic protocol based on the Stille coupling reaction (Figure 1.41).[127] The authors suggested that, due to their long effective conjugation lengths and high carrier transport nobilities, these oligothiophenes could be potentially used as molecular wires in single molecular electronic devices.

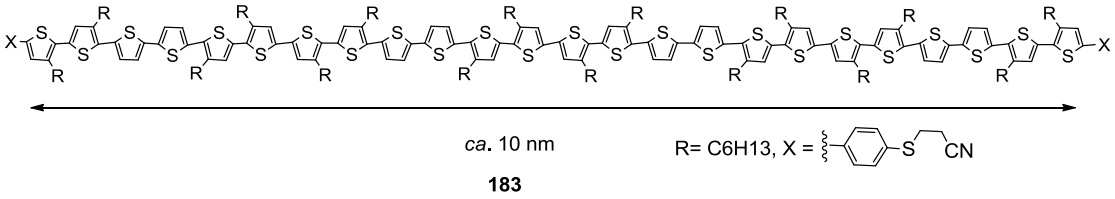

183

Figure 1.41: Structure of oligothiophene molecular wire **183**.

In 2009, the Krebs group prepared an OPV derivative **184** with a chain length of 12 nm. By stepwise Horner-witting reactions, OPVs containing 3-19 phenyl units were synthesized (Figure 1.42). Thioacetate functional groups were introduced to the endgroups for the formation of gold-thiolate bond to silicon-on-insulator (SOI) based vertical nanogap electrical devices (VNDs). The results suggested that the functionalized OPVs gave a nonlinear response with a major onset conductance around 1.4 V bias voltage.[128]

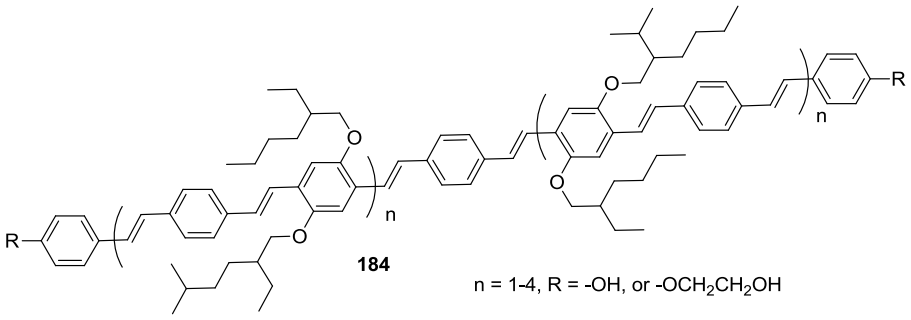

Figure 1.42: Structure of an OPV based molecular wire.

1.5 Outline of the thesis

This PhD thesis has accomplished three major projects focusing on the synthesis and property characterization of functionalized π-conjugated oligomers and TTFV-based molecular materials. A modular click strategy based on the CuAAC reaction has been utilized to a great extent in the synthetic work. Detailed studies on these functional materials are elaborated in Chapters 2 to 4.

Chapter 2 focuses on the synthesis and molecular properties of boronic acid functionalized 1D and 2D conjugated oligomers with linear, cruciform, and H-shaped structures. The synthetic routes have involved the use of Sonagashira coupling, Witting-Horner, and click reactions as the key steps. Electronic and spectroscopic properties of these functionalized oligomers with different saccharides were investigated by UV-Vis absorption and fluorescence spectroscopic analyses. The results indicate that these boronic acid functionalized oligomers have unique environment-sensitive fluorescence properties, which enable them to act as efficient fluorescence sensors to detect and discriminate saccharide molecules under physiological conditions (aqueous, pH 7.41). It

is also demonstrated that the boronate-appended oligomers showed remarkably sensitive fluorescence turn-off sensing of fluoride ions. The results of this project highlight the importance of tuning and manipulation of the fluorophore to improve the performances of π-conjugated oligomer-based fluorescent chemo- and bio-sensors.

Chapter 3 describes the synthesis of a new class of dithiafulvene (DTF) end-capped oligomers, and the supramolecular interactions of these oligomers with fullerenes and SWNTs. The supramolecular properties were studied by UV-Vis-NIR, fluorescence spectroscopy, Raman spectroscopy, atomic force microscopy (AFM), and cyclic voltametry. It has been found that when these oligomers interact with fullerenes, the C=C bond of DTF undergoes a facile oxidative cleavage reaction in air and ambient light to form highly fluorescent aldehyde-endcapped oligomers as the product. Further, the DTF-oligomers not only show the ability to disperse SWNTs in chloroform, but also can release the SWNTs under the control of solvent properties. Overall, the work in this project has demonstrated that DTF is a fascinating substituent group which not only introduces rich redox and electronic properties, but can also bring about novel chemical reactivities, and photophysical and supramolecular properties to organic functional materials.

Chapter 4 introduces the synthetic approaches to the construction of a series of TTFV derivatives including TTFV macrocycles and TTFV tweezers. These compounds were investigated as receptors for fullerenes, saccharides, anions, and certain transition metal ions by UV-Vis and fluorescence spectroscopy, and cyclic voltametry.

Electrochemical sensing of boronic acid functionalized TTFV derivatives with different saccharides has been successfully demonstrated. The results from TTFV-anthracene based tweezers and macrocycles disclose that these receptors give fluorescence turn-on response to fullerenes as well as metal ions. It was also demonstrated that in the presence of TFA these TTFV-based receptors can easily release fullerenes. The results disclosed in this chapter underscore the importance of using TTFV-arene hybrids to design and prepare fluorescent and electrochemical properties with different analytes.

1.6 References

(1) Rao, C. N. R. *Nanomaterials Handbook*, **2006**.

(2) Ozin, G. A. *Adv. Mater.* **1992**, *4*, 612-649.

(3) Butler, P. J. G. *Phil. Trans. R. Soc. Lond. B.* **1999**, 537-550.

(4) Lo, S.-C.; Burn, P. L. *Chern. Rev.* **2007**, *107*, 1097-1116.

(5) Drexler, K. E. *Proc. Natl. Acad. of Sci. USA.* **1981**, *78*, 5275-5278.

(6) Lehn, J. M. *Rep. Prog. Phys.* **2004**, *67*, 249-265.

(7) Yagai, S.; Yamauchi, M.; Kobayashi, A.; Karatsu, T.; Kitamura, A.; Ohba, T.; Kikkawa, Y. *J. Am. Chem. Soc.* **2012**, *134*, 18205-18208.

(8) Kroto, H. W.; Heath, J. R.; O'Brien, S. C. *Nature* **1985**, *318*, 162-163.

(9) Krätscher, W.; Lamb, L.; Fostiropoulos, K.; Huffman, D. R. *Nature* **1990**, *347*, 354-358.

(10) Bingel, C. *Chem. Ber.* **1993**, *126*, 1957-1959.

(11) Even, M.; Heinrich, B.; Guillon, D.; Guldi, D. M.; Prato, M.; Deschenaux, R. *Chem. Eur. J.* **2001**, *7*, 2595-2604.

(12) Dardel, B.; Guillon, D.; Heinrich, B.; Deschenaux, R. *J. Mater. Chem.* **2001**, *11*, 2814-2831.

(13) Dragoe, N.; Tanibayashi, S.; Nakahara, K.; Nakao, S.; Shimotani, H.; Xiao, L.; Kitazawa, K.; Dragoe, N.; Kitazawa, K.; Achiba, Y.; Kikuchi, K.; Nojima, K. *Chem. Commun.* **1999**, 85-86.

(14) Herranz, M. a. A.; Martin, N.; Ramey, J.; Guldi, D. M. *Chem. Commun.* **2002**, 2968-2969.

(15) Yu, G.; Gao, J.; Hummelen, J. C.; Wudl, F.; Heeger, A. J. *Science* **1995**, *270*, 1789-1791.

(16) Granstrom, M.; Petritsch, K.; Arias, A. C.; Lux, A.; Anderson, M. R.; Friend, R. H. *Nature* **1998**, *395*, 257-260.

(17) Tang, C. W. *Appl. Phys. Lett.* **1986**, *48*, 183-185.

(18) Walker, B.; Tamayo, A. B.; Dang, X.-D.; Zalar, P.; Seo, J. H.; Garcia, A.; Tantiwiwat, M.; Nguyen, T.-Q. *Adv. Funct. Mater.* **2009**, *19*, 3063-3069.

(19) Kim, J. Y.; Lee, K.; Coates, N. E.; Moses, D.; Nguyen, T.-Q.; Dante, M.; Heeger, A. J. *Science* **2007**, *317*, 222-225.

(20) Gilot, J.; Wienk, M. M.; Janssen, R. A. J. *Appl. Phys. Lett.* **2007**, *90*, 143512.

(21) Kim, J. Y.; Lee, K.; Coates, N. E.; Moses, D.; Nguyen, T.-Q.; Dante, M.; Heeger, A. J. *Science* **2007**, *317*, 222-225.

(22) Sista, S.; Park, M.-H.; Hong, Z.; Wu, Y.; Hou, J.; Kwan, W. L.; Li, G.; Yang, Y. *Adv. Mater.* **2010**, *22*, 380-383.

(23) Hoppe, H.; Sariciftci, N. S. *J. Mater. Res.* **2004**, *19*, 1924-1945.

(24) Kawase, T.; Tanaka, K.; Fujiwara, N.; Darabi, H. R.; Oda, M. *Angew. Chem. Int. Ed.* **2003**, *42*, 1624-1628.

(25) Luzzi, D. E.; Smith, B. W. *Carbon* **2000**, *38*, 1751-1756.

(26) Yudasaka, M.; Ajima, K.; Suenaga, K.; Ichihashi, T.; Hashimoto, A.; Iijima, S. *Chem. Phys. Lett.* **2003**, *380*, 42-46.

(27) Britz, D. A.; Khlobystov, A. N.; Wang, J.; O'Neil, A. S.; Poliakoff, M.; Ardavan, A.; Briggs, G. A. D. *Chem. Commun.* **2004**, 176-177.

(28) Iijima, S. *Nature* **1991**, *354*, 56-58.

(29) Lu, J. P. *Phys. Rev. Lett.* **1997**, *79*, 1297-1300.

(30) Park, S.; Srivastava, D.; Cho, K. *Nano Lett.* **2003**, *3*, 1273-1277.

(31) Tasis, D.; Tagmatarchis, N.; Bianco, A.; Prato, M. *Chem. Rev.* **2006**, *106*, 1105-1136.

(32) Omachi, H.; Nakayama, T.; Takahashi, E.; Segawa, Y.; Itami, K. *Nature Chem.* **2013**, *5*, 572-576.

(33) Yu, X.; Zhang, J.; Choi, W.; Choi, J.-Y.; Kim, J. M.; Gan, L.; Liu, Z. *Nano Lett.* **2010**, *10*, 3343-3349.

(34) Tans, S. J.; Devoret, M. H.; Dai, H.; Thess, A.; Smalley, R. E.; Geerligs, L. J.; Dekker, C. *Nature* **1997**, *386*, 474-477.

(35) Wong, E. W.; Sheehan, P. E.; Lieber, C. M. *Science* **1997**, *277*, 1971-1975.

(36) Zhang, M.; Fang, S.; Zakhidov, A. A.; Lee, S. B.; Aliev, A. E.; Williams, C. D.; Atkinson, K. R.; Baughman, R. H. *Science* **2005**, *309*, 1215-1219.

(37) Dillon, A. C.; Jones, K. M.; Bekkedahl, T. A.; Kiang, C. H.; Bethune, D. S.; Heben, M. J. *Nature* **1997**, *386*, 377-379.

(38) Zandonella, C. *Nature* **2001**, *410*, 734-735.

(39) Aliev, A. E.; Oh, J.; Kozlov, M. E.; Kuznetsov, A. A.; Fang, S.; Fonseca, A. F.; Ovalle, R.; Lima, M. D.; Haque, M. H.; Gartstein, Y. N.; Zhang, M.; Zakhidov, A. A.; Baughman, R. H. *Science* **2009**, *323*, 1575-1578.

(40) So, H.-M.; Won, K.; Kim, Y. H.; Kim, B.-K.; Ryu, B. H.; Na, P. S.; Kim, H.; Lee, J.-O. *J. Am. Chem. Soc.* **2005**, *127*, 11906-11907.

(41) Chan, V. S. W. *Regul. Toxicol. Pharmacol.* **2006**, *46*, 218-224.

(42) Panhuis, M. i. h.; Wu, J.; Ashraf, S. A.; Wallace, G. G. *Synth. Met.* **2007**, *157*, 358-362.

(43) Miller, A. J.; Hatton, R. A.; Silva, S. R. P. *Appl. Phys. Lett.* **2006**, *89*, 113117.

(44) Novoselov, K. S.; Geim, A. K.; Morozov, S. V.; Jiang, D.; Zhang, Y.; Dubonos, S. V.; Grigorieva, I. V.; Firsov, A. A. *Science* **2004**, *306*, 666-669.

(45) Novoselov, K. S.; Jiang, D.; Schedin, F.; Booth, T. J.; Khotkevich, V. V.; Morozov, S. V.; Geim, A. K. *Proc. Natl. Acad. Sci. USA.* **2005**, *102*, 10451-10453.

(46) Nair, R. R.; Blake, P.; Grigorenko, A. N.; Novoselov, K. S.; Booth, T. J.; Stauber, T.; Peres, N. M. R.; Geim, A. K. *Science* **2008**, *320*, 1308.

(47) Stoller, M. D.; Park, S.; Zhu, Y.; An, J.; Ruoff, R. S. *Nano Lett.* **2008**, *8*, 3498-3502.

(48) Lee, C.; Wei, X.; Kysar, J. W.; Hone, J. *Science* **2008**, *321*, 385-388.

(49) Balandin, A. A.; Ghosh, S.; Bao, W.; Calizo, I.; Teweldebrhan, D.; Miao, F.; Lau, C. N. *Nano Lett.* **2008**, *8*, 902-907.

(50) Zhang, Y.; Tan, Y.-W.; Stormer, H. L.; Kim, P. *Nature* **2005**, *438*, 201-204.

(51) Geim, A. K.; Novoselov, K. S. *Nat. Mater* **2007**, *6*, 183-191.

(52) Gomez De Arco, L.; Zhang, Y.; Schlenker, C. W.; Ryu, K.; Thompson, M. E.; Zhou, C. *ACS Nano* **2010**, *4*, 2865-2873.

(53) Schedin, F.; Geim, A. K.; Morozov, S. V.; Hill, E. W.; Blake, P.; Katsnelson, M. I.; Novoselov, K. S. *Nat. Mater.* **2007**, *6*, 652-655.

(54) Robinson, J. T.; Perkins, F. K.; Snow, E. S.; Wei, Z.; Sheehan, P. E. *Nano Lett.* **2008**, *8*, 3137-3140.

(55) Fowler, J. D.; Allen, M. J.; Tung, V. C.; Yang, Y.; Kaner, R. B.; Weiller, B. H. *ACS Nano* **2009**, *3*, 301-306.

(56) Wang, X.; Zhi, L.; Mullen, K. *Nano Lett.* **2007**, *8*, 323-327.

(57) Yang, X.; Dou, X.; Rouhanipour, A.; Zhi, L.; Räder, H. J.; Müllen, K. *J. Am. Chem. Soc.* **2008**, *130*, 4216-4217.

(58) Shirakawa, H.; Louis, E. J.; MacDiarmid, A. G.; Chiang, C. K.; Heeger, A. J. *J. Chem. Soc., Chem. Commun.* **1977**, 578-580.

(59) Burroughes, J. H.; Bradley, D. D. C.; Brown, A. R.; Marks, R. N.; MacKay, K.; Friend, R. H.; Burn, P. L.; Holmes, A. B. *Nature* **1990**, *347*, 539-541.

(60) Moratti, S. C.; Cervini, R.; Holmes, A. B.; Baigent, D. R.; Friend, R. H.; Greenham, N. C.; Grüner, J.; Hamer, P. J. *Synth. Met.* **1995**, *71*, 2117-2120.

(61) Halls, J. J. M.; Baigent, D. R.; Cacialli, F.; Greenham, N. C.; Friend, R. H.; Moratti, S. C.; Holmes, A. B. *Thin Solid Films* **1996**, *276*, 13-20.

(62) Baigent, D. R.; Hamer, P. J.; Friend, R. H.; Moratti, S. C.; Holmes, A. B. *Synth. Met.* **1995**, *71*, 2175-2176.

(63) Moses, D. *Appl. Phys. Lett.* **1992**, *60*, 3215-3216.

(64) Hide, F.; Schwartz, B.; Diaz-Garcia, M. A.; Heeger, A. J. *Chem. Phys. Lett.* **1996**, *256*, 424-430.

(65) Bleier, H. *Organic Materials for Photonics;* **1993**, 77-101.

(66) Meier, H. *Angew. Chem., Int. Ed. Engl.* **1992**, *31*, 1399-1420.

(67) Martin, P. J. *Introduction to Molecular Electronics; Edward Arnold, London,* **1995**, 112-141.

(68) Heeger, A. J.; Long, J. *Jr. Optics and Photonics News* **1996**, *7*, 24-30.

(69) Feringa, B. L.; Jager, W. F.; de Lange, B. *Tetrahedron* **1993**, *49*, 8267-8310.

(70) Duff, D. G.; Baiker, A.; Edwards, P. P. *Langmuir* **1993**, *9*, 2301-2309.

(71) Pastoriza-Santos, I.; Liz-Marzán, L. M. *Langmuir* **2002**, *18*, 2888-2894.

(72) Pastoriza-Santos, I.; Liz-Mar´zan, L. M. *Pure. Appl. Chem.* **2000**, *72*, 83-90.

(73) Jin, R.; Cao, Y. C.; Hao, E.; Me´traux, G. S.; Schatz, G. C.; Mirkin, C. A. *Nature* **2003**, *425*, 487-490.

(74) Kuo, C. H.; Huang, M. H. *Langmuir* **2005**, *21*, 2012-2016.

(75) Moser, A.; Takano, K.; Margulies, D. T.; Albrecht, M.; Sonobe, Y.; Ikeda, Y.; Sun, S.; Fullerton, E. E. *J. Phys. D: Appl. Phys.* **2002**, *35*, R157-R167.

(76) Zeng, H.; Li, J.; Wang, Z. L.; Liu, J. P.; Sun, S. *Nature* **2002**, *420*, 395-398.

(77) Tang, J.; Redl, F.; Zhu, Y.; Siegrist, T.; Brus, L. E.; Steigerwald, M. L. *Nano Lett.* **2005**, *5*, 543-548.

(78) Joo, J.; Kwon, S. G.; Yu, J. H.; Hyeon, T. *Adv. Mater.* **2005**, *17*, 1873-1877.

(79) Thi Dieu Thuy, U.; Thi Kim Chi, T.; Thu Nga, P.; Duc Nghia, N.; Duy Khang, D.; Quang Liem, N. *Adv. Nat. Sci.: Nanosci. Nanotechnol.* **2012**, *3*, 043001.

(80) Chauvin, Y.; Hérisson, J. L. *Makromol. Chem.* **1971**, *141*, 161–176.

(81) Bunz, U. H. F.; Mäker, D.; Porz, M. *Macromol. Rapid. Commun.* **2012**, *33*, 886-910.

(82) Fürstner, A.; Dierkes, T. *Org. Lett.* **2000**, *2*, 2463-2465.

(83) Herbert, M. B.; Marx, V. M.; Pederson, R. L.; Grubbs, R. H. *Angew. Chem.* **2013**, *125*, 328-332.

(84) Dragutan, V.; Streck, R. *Catalytic Polymerization of Cycloolefins*, *Elsevier*, *Amsterdam*, **2000**.

(85) Scherman, O. A.; Rutenberg, I. M.; Grubbs, R. H. *J. Am. Chem. Soc.* **2003**, *125*, 8515-8522.

(86) Kumar, A.; Eichinger, B. E. *Makromol. Rapid Commun.* **1992**, *13*, 311-314.

(87) Thorn-Csányi, E.; Kraxner, P. *Macromol.Chem. Phys.* **1997**, *198*, 3827-3843.

(88) Nomura, K.; Morimoto, H.; Imanishi, Y.; Ramhani, Z.; Geerts, Y. *J. Polym. Sci, Part A: Polym. Chem.* **2001**, *39*, 2463-2470.

(89) Collier, C. P.; Mattersteig, G.; Wong, E. W.; Luo, Y.; Beverly, K.; Sampaio, J.; Raymo, F. M.; Stoddart, J. F.; Heath, J. R. *Science* **2000**, *289*, 1172-1175.

(90) Flood, A. H.; Stoddart, J. F.; Steuerman, D. W.; Heath, J. R. *Science* **2004**, *306*, 2055-2056.

(91) Guidry, E. N.; Cantrill, S. J.; Stoddart, J. F.; Grubbs, R. H. *Org. Lett.* **2005**, *7*, 2129-2132.

(92) Bonifacio, M. C.; Robertson, C. R.; Jung, J.-Y.; King, B. T. *J. Org. Chem.* **2005**, *70*, 8522-8526.

(93) Collins, S. K.; Grandbois, A.; Vachon, M. P.; Côté, J. *Angew. Chem. Int. Ed.* **2006**, *45*, 2923-2926.

(94) Zhao, Y.; Slepkov, A. D.; Akoto, C. O.; McDonald, R.; Hegmann, F. A.; Tykwinski, R. R. *Chem. Eur. J.* **2005**, *11*, 321-329.

(95) Wood, J. D.; Jellison, J. L.; Finke, A. D.; Wang, L.; Plunkett, K. N. *J. Am. Chem. Soc.* **2012**, *134*, 15783-15789.

(96) Khanasa, T.; Prachumrak, N.; Rattanawan, R.; Jungsuttiwong, S.; Keawin, T.; Sudyoadsuk, T.; Tuntulani, T.; Promarak, V. *J. Org. Chem.* **2013**, *78*, 6702-6713.

(97) Schulz, G. L.; Mastalerz, M.; Ma, C.-Q.; Wienk, M.; Janssen, R.; Bäuerle, P. *Macromolecules* **2013**, *46*, 2141-2151.

(98) Johnson, T. R.; Walton, D. R. M. *Tetrahedron* **1972**, *28*, 5221-5236.

(99) Chalifoux, W. A.; Tykwinski, R. R. *Nat. Chem.* **2010**, *2*, 967–971.

(100) Movsisyan, L. D.; Kondratuk, D. V.; Franz, M.; Thompson, A. L.; Tykwinski, R. R.; Anderson, H. L. *Org. Lett.* **2012**, *14*, 3424-3426.

(101) Rondeau-Gagné, S.; Néabo, J. R.; Desroches, M.; Larouche, J.; Brisson, J.; Morin, J.-F. *J. Am. Chem. Soc.* **2012**, *135*, 110-113.

(102) Kolb, H. C.; Finn, M. G.; Sharpless, K. B. *Angew. Chem. Int. Ed.* **2001**, *40*, 2004-2021.

(103) Chan, T. R.; Hilgraf, R.; Sharpless, K. B.; Fokin, V. V. *Org. Lett.* **2004**, *6*, 2853-2855.

(104) Wu, P.; Malkoch, M.; Hunt, J. N.; Vestberg, R.; Kaltgrad, E.; Finn, M. G.; Fokin, V. V.; Sharpless, K. B.; Hawker, C. J. *Chem. Commun.* **2005**, 5775-5777.

(105) Englert, B. C.; Bakbak, S.; Bunz, U. H. F. *Macromolecules* **2005**, *38*, 5868-5877.

(106) Lee, E.; Park, J.; Im, S. G.; Song, C. *Polym. Chem.* **2012**, *3*, 2451-2455.

(107) Chang, K.-C.; Su, I.-H.; Senthilvelan, A.; Chung, W.-S. *Org. Lett.* **2007**, *9*, 3363-3366.

(108) Brombosz, S. M.; Appleton, A. L.; Zappas Ii, A. J.; Bunz, U. H. F. *Chem. Commun.* **2010**, *46*, 1419-1421.

(109) Hua, Y.; Flood, A. H. *J. Am. Chem. Soc.* **2010**, *132*, 12838-12840.

(110) Lee, S.; Flood, A. H. *J. Phys. Org. Chem.* **2013**, *26*, 79-86.

(111) Spitler, E. L.; Shirtcliff, L. D.; Haley, M. M. *J. Org. Chem.* **2006**, *72*, 86-96.

(112) Zucchero, A. J.; Wilson, J. N.; Bunz, U. H. F. *J. Am. Chem. Soc.* **2006**, *128*, 11872-11881.

(113) Grunder, S.; Huber, R.; Horhoiu, V.; González, M. T.; Schönenberger, C.; Calame, M.; Mayor, M. *J. Org. Chem.* **2007**, *72*, 8337-8344.

(114) Yi, Y.; Zhu, L.; Shuai, Z. *Macromol. Theory Simul.* **2008**, *17*, 12-22.

(115) Sun, X. B.; Liu, Y. Q.; Chen, S. Y.; Qiu, W. F.; Yu, G.; Ma, Y. Q.; Qi, T.; Zhang, H. J.; Xu, X. J.; Zhu, D. B. *Adv. Funct. Mater.* **2006**, *16*, 917-925.

(116) Zhou, N.; Wang, L.; Thompson, D. W.; Zhao, Y. *Tetrahedron* **2011**, *67*, 125-143.

(117) Wilson, J. N.; Bunz, U. H. F. *J. Am. Chem. Soc.* **2005**, *127*, 4124-4125.

(118) Zhou, N.; Wang, L.; Thompson, D. W.; Zhao, Y. *Org. Lett.* **2008**, *10*, 3001-3004.

(119) Eckert, J.-F.; Nicoud, J.-F.; Nierengarten, J.-F.; Liu, S.-G.; Echegoyen, L.; Barigelletti, F.; Armaroli, N.; Ouali, L.; Krasnikov, V.; Hadziioannou, G. *J. Am. Chem. Soc.* **2000**, *122*, 7467-7479.

(120) Narutaki, M.; Takimiya, K.; Otsubo, T.; Harima, Y.; Zhang, H.; Araki, Y.; Ito, O. *J. Org. Chem.* **2006**, *71*, 1761-1768.

(121) Kodis, G.; Terazono, Y.; Liddell, P. A.; Andréasson, J.; Garg, V.; Hambourger, M.; Moore, T. A.; Moore, A. L.; Gust, D. *J. Am. Chem. Soc.* **2006**, *128*, 1818-1827.

(122) Shirai, Y.; Osgood, A. J.; Zhao, Y.; Kelly, K. F.; Tour, J. M. *Nano Lett.* **2005**, *5*, 2330-2334.

(123) Zhou, N.; Merschrod S, E. F.; Zhao, Y. *J. Am. Chem. Soc.* **2005**, *127*, 14154-14155.

(124) Tang, C. W.; VanSlyke, S. A. *Appl. Phys. Lett.* **1987**, *57*, 913-915.

(125) Tonzola, C. J.; Kulkarni, A. P.; Gifford, A. P.; Kaminsky, W.; Jenekhe, S. A. *Adv. Funct. Mater.* **2007**, *17*, 863-874.

(126) Li, H. C.; Lin, Y. P.; Chou, P. T.; Cheng, Y. M.; Liu, R. S. *Adv. Funct. Mater.* **2007**, *17*, 520-530.

(127) Endou, M.; Ie, Y.; Kaneda, T.; Aso, Y. *J. Org. Chem.* **2007**, *72*, 2659-2661.

(128) Sondergaard, R.; Strobel, S.; Bundgaard, E.; Norrman, K.; Hansen, A. G.; Albert, E.; Csaba, G.; Lugli, P.; Tornow, M.; Krebs, F. C. *J. Mater. Chem.* **2009**, *19*, 3899-3908.

Chapter 2

Cruciform, Linear, and H-shaped π-Conjugated Oligomers: New Fluorescent Receptors for Detection of Saccharides and Fluoride Ions

2.1 The importance of saccharides

It has been well recognized that carbohydrates such as saccharides, phosphosugars, and nucleotides play an important role in a wide range of biological and pathological processes,[1] including cancer metastasis, cell adhesion, cell signaling, embryo development, egg fertilization, protein function regulation, cellular communications, and so forth.[2-6] The changes occurring in pathological processes such as development of malignancy are often associated with the changes in cell surface carbohydrates. Monitoring the levels of these carbohydrates has become a useful approach for researchers to study various biological systems.

For biomedical applications, monitoring D-glucose is a main research focus, as it provides the metabolic energy for most of higher organisms. The most common condition that results from the ineffective transport of D-glucose in the blood stream is diabetes mellitus.[7] From a medicinal perspective, it is important to monitor blood sugar levels as a means of controlling diabetes. Other conditions resulting from the breakdown in the

transport pathways of D-glucose include cancer,[8] cystic fibrosis,[9] and renal glycosuria.[10] Most clinical methods currently available for glucose monitoring are enzyme-based and usually require invasive amounts of blood to be taken from a pricked finger.[11] The detection principles of these kinds of method are based on immobilized glycoenzyme-catalyzed reactions of saccharide substrates.[12]

It is an undisputed fact that the availability of methods to monitor glucose levels has revolutionised the quantity of life; however, the enzymatic approach has some limitations such as high cost, difficult storage, poor stability, and low specificity. Therefore, there is a need for development of other methods to attain specific and high affinity carbohydrate recognition. In addition to glucose and other monosaccharides (Figure 2.1), and oligosaccharides are also of great importance in biomedical research as they control cell recognition events for infection, inflammation, and immunity.[13]

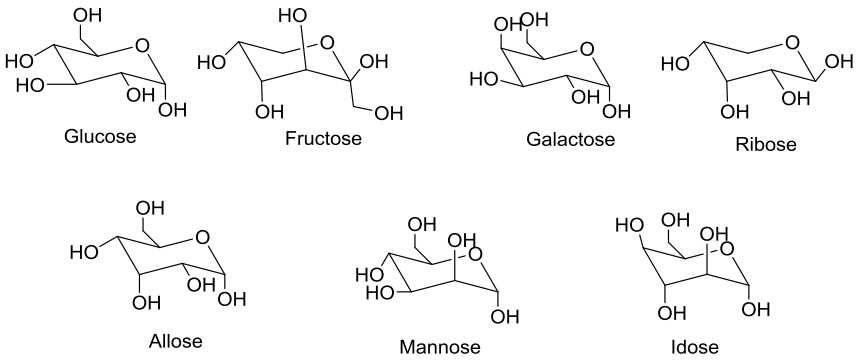

Figure 2.1: Examples of saccharides of biomedical interest.

2.2 Chemosensors and biosensors for saccharide detection

Molecular recognition is a process that involves intermolecular interactions between two or more molecules such as a host and a guest, a lock and a key, a receptor and a substrate. This process is essential for the design of specific selective receptors. Further, for the receptor to be of a practical use, a systematic communication has to be established between the receptor and the outside world. This additional property would convert a receptor into a sensor. In general, chemical sensors can be broadly categorized into either biosensors or synthetic chemosensors. A biosensor makes use of biological analytes such as a protein or enzyme for recognition. A great number of biosensors as receptors for saccharides have been documented in the literature.[14] Expensive analytical techniques are often required to study the binding events taking place in biosensors. Biosensors based on proteins have some limitations due to degradation or environmental factors. To address this issue, alternative approaches have been pursued. A synthetic receptor achieves recognition of the analyte by using synthetically prepared compounds. In this research area, a great amount of attention has been given to the development of molecular receptors and modular sensors for the detection of saccharides in the last two decades. A few examples are highlighted in the following sections which are based on non-boronic acid and boronic acid based saccharide receptors.

2.2.1 Non-boronic acid based synthetic receptors for saccharide detection

Many systems based on non-boronic acid appended synthetic sensors have been reported in the literature which rely mainly on non-covalent interactions such as hydrogen bonding interactions for molecular recognition of saccharides.[15] The

complexation behavior of resorcinarenes, a calixarene based synthetic receptor **185** (Figure 2.2), was studied by Aoyama and co-workers in 1989,[16] which showed non-covalent hydrogen bonding interactions with the hydroxyl groups of saccharides. It was observed that 1,4-*cis* selectivity was dominant in the case of complexation with saccharides through face-to-face recognition.

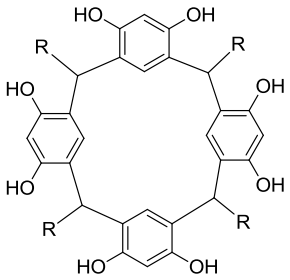

$R = (CH_2)_{10}CH_3$

185

Figure 2.2: Calixarene based synthetic saccharide sensor.

In the reported experimental details, very high concentrations of saccharides were used for complexation and the binding events which were monitored by ^{1}H NMR. D-ribose and 2-deoxyribose were found to be readily extracted into CCl_4 by receptor **185**. ^{1}H NMR studies have confirmed that D-ribose is bound to the hydroxyl groups at C-1 and C-4 of receptor **185**.

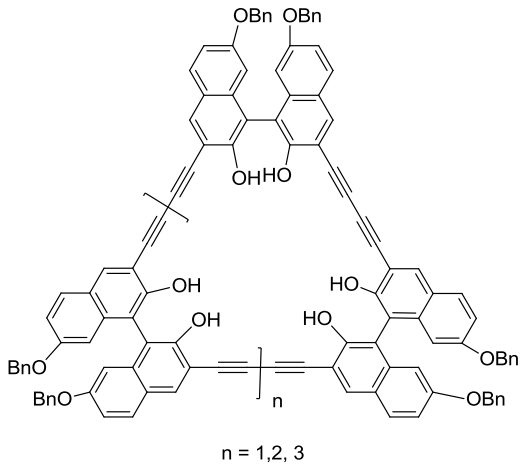

186

Figure 2.3: Structure of binaphthalene derived synthetic receptor **186** for saccharide detection

In 1995, Diederich and co-workers studied the sensing properties of binaphthalene derived macromolecules **186** with different glucopyranosides.[17] The sensor **186** (where n = 1) was shown to have good selectivity for glucopyranosides and the stability constants were measured based on ^{1}H NMR data in $CDCl_3$ at 300K. The change in chemical shift of the OH protons of the receptor **186** was monitored as a function of concentration of guest, through which the formation of stable 1:1 complexes was confirmed.

The majority of non-boronic acid receptors[15] rely on non-covalent interactions and binding with sugar moieties is possible only in aprotic solvents such as chloroform. In aqueous media, a serious drawback is aroused from competitive hydrogen bonding interactions with the solvent. For practical uses or biological applications, the sensors

need to be tuned in such a way that they can perform the sensory functions in aqueous media and under physiological pH. This has been made possible by taking advantage of the selective covalent interactions between boronic acid receptors and saccharides. A wide range of stable boronic acid receptors has been developed and shown to be very useful.

2.2.2 Boronic acid based synthetic receptors for the saccharide detection

Boronic acids have been known for over a century since Michaelis and Becker carried out the first synthesis of phenylboronic acid.[18] They have played a significant role in organic synthesis for many years.[19] In 1954, Kuivila and co-workers reported the binding properties of boronic acids to the diols of mannitol by using a simple phenylboronic acid as receptor, where they observed the formation of a cyclic ester product,[20] indeed this discovery has set up a platform for the development of boronic acid based synthetic receptors.

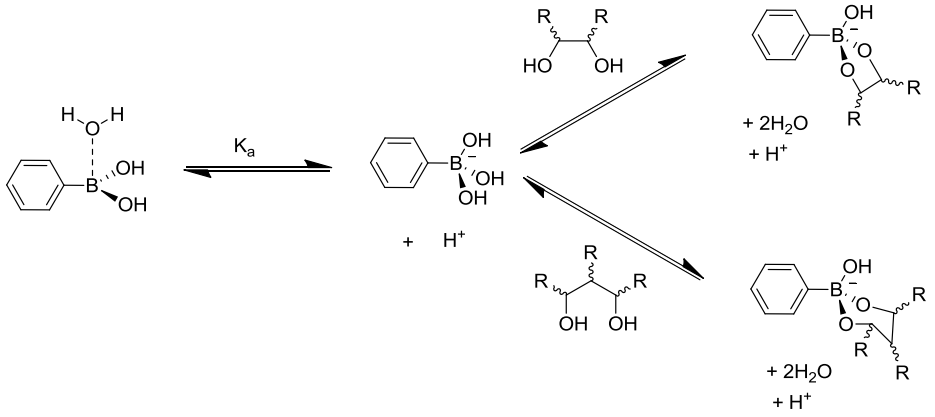

Scheme 2.1: Formation of phenyl boronate complexes with diols.

As the boronic acids interact with diols of the sugars, a covalent bond is formed with 1,2- or 1,3-diols for the formation of a five or six membered rings respectively (Scheme 2.1). This interconversion is very fast in basic aqueous media. In 1959, Lorand and Edwards disclosed the quantitative interactions between phenylboronic acid and polyols, and extracted the binding constants based on pH measurements.[21] They also found that the phenylboronic acid had the following selectivity towards several mono saccharides: D-fructose > D-galactose > D-mannose > D > glucose.

As shown in Scheme 2.2, in the binding between the diols of saccharides and the boronic acid, a few important changes are noticeable.[22] As the binding occurs, the Lewis acidity of the boronic acid is increased, resulting in lowering the pKa of the boronic acid. If the system is buffered at an appropriate pH level, these changes cause a shift in equilibrium from the boronic acid form to the boronate form. The trigonal planar geometry of the boronic acid becomes tetrahedral in the boronate ion. The differences in the rate of 10^4 are observed between these two forms in the equilibrium state. All these changes are carefully considered to generate a signal in the presence of diol.

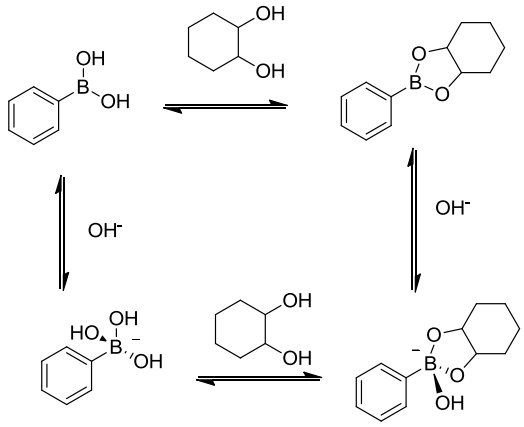

Scheme 2.2: Equilibria of boronic acid-diol interaction in aqueous media.

Over the last two decades, a large array of synthetic saccharide sensors has been developed based upon phenylboronic acid receptors[23,24] and research along this direction is still actively ongoing aiming at further improving sensor performances, for example, sensitivity, selectivity, and stability. Basically, the most common design architecture for a saccharide sensor contains three essential units: receptor, reporter (i.e., read-out unit), and linkage group, wherein the reporter group acts to signal the binding event(s) happening at the receptor through optical or electrical outputs (Figure 2.4).

Organic chromophores, fluorophores, and electrophores are commonly incorporated as reporter units in the design of saccharide sensors, which lead to a variety of colorimetric,[25,26] fluorimetric,[27-29] and electrochemical[30,31] saccharide sensors. Choice of the type of linkage groups is often made to meet the requirements if both sensor performance and synthetic accessibility. The following section will introduce some of examples of fluorescence sensors as it is pertinent to the work of this chapter, although

many systems have been developed based on colorimetric and electrochemical sensing mechanisms.

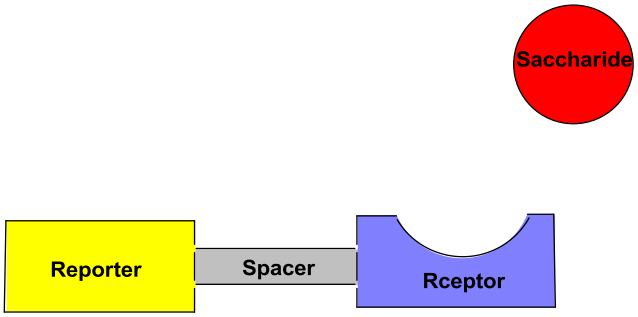

Figure 2.4: Schematic representation of the reporter-spacer-receptor design assembly for sensory systems.

2.2.2.1 Fluorescent sensors for saccharides detection

Different fluorescent receptor systems have been developed to achieve effective sensing functions based on various signaling mechanisms such as photoinduced electron/energy transfer (PET), photoinduced charge transfer (PCT), intramolecular charge transfer (ICT), fluorescence resonance energy transfer (FRET), and aggregation-induced emission (AIE). The evolution of fluorescent saccharide sensors, as well as the mechanisms that are predicted to generate a signal, are discussed below together with some representative examples taken from the literature.

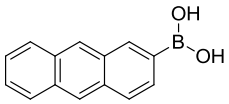

187

Figure 2.5: The first fluorescent sensor for saccharides: 2-anthranylboronic acid.

In 1992, Yoon and Czarnik reported the first fluorescent saccharide sensor, in which they used anthranylboronic acid **187** as a receptor (Figure 2.5).[32] It was noted that, upon addition of fructose, the emission intensity of sensor **187** was decreased by ~ 30%. The typical pK_a of the system was dropped from 8.8 to 5.9, when the boronic acid was converted to boronate anion. The decrease of the emission intensity can be explained by a PET mechanism. When the bound system is in the anionic state, it can be predicted that there is a photoinduced electron transfer between the negatively charged boronate and the vacant ground-state S_o. Although the sensor **187** displayed a modest modulation of fluorescence of 30% in the presence of saccharides, it opened the door to many fluorescent sensors with improvements in selectivity, solubility, sensitivity, and photophysical properties.

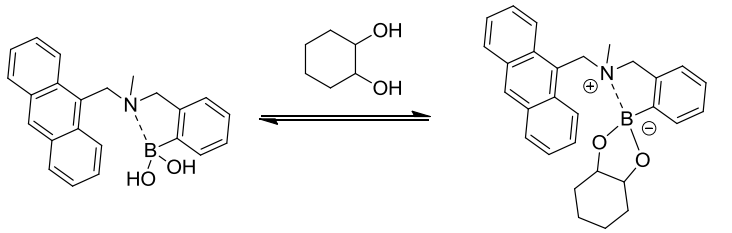

188

188-saccharide complex

Scheme 2.3: Benzylic amine spacer with an anthracene boronic acid receptor.

A plethora of fluorescent saccharide sensors was contributed by Shinkai and James, using a benzylic amine spacer to link a phenylboronic acid receptor to a fluorophore.[24,33] This system is similar to the so-called Wulff-type receptors,[34,35] in which the interaction of boronic acid and an adjacent amine lowers the pK_a of the boronic acid and resulting in effective binding at neutral conditions. In this type of system, the fluorescence of neutral boronic acid is quenched by the PET from the amine to the fluorophore. In the presence of saccharides, however, the fluorescence enhancement is observed when the amine is quaternized and thus unable to donate electrons at both neutral pH and low pH. In this line, the first PET sensor **188** was reported by James *et al*. in 1994, which showed a turn-on response towards different saccharides (Scheme 2.3).[36,37] The sensor showed higher selectivity to fructose than other monosaccharides tested. The order of the selectivity was the same as that documented by Lorand and Edwards for phenylboronic acid receptor.[21]

Shown in Figure 2.6 is an improved sensor system developed by Zhang and Zhu, in which the electron rich tetrathiafulvalene (TTF) unit was introduced as an electron donor and a linker instead of nitrogen.[38] As predicted, the fluorescence of sensor **189** was quenched by PET from the TTF unit. Upon addition of saccharides, the PET from TTF shut down and the fluorescence of the sensor **189** is recovered. The sensor **189** displayed the same selectivity order for different saccharides as others mentioned above.

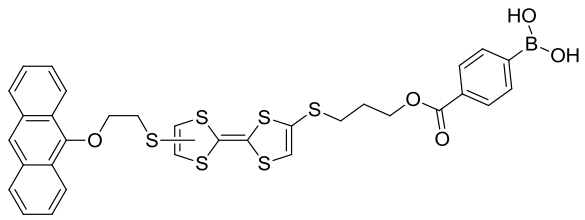

189

Figure 2.6: TTF based sensor **189**

It has been demonstrated in the literature that most monoboronic acid fluorescent sensors show high selectivity and sensitivity to fructose. For biological applications, the receptor design was tuned to achieve selectivity for glucose or other biologically important saccharides by incorporating multiple boronic acids in the design. For this purpose, the so-called "modular approach" has been successfully established as a productive and effective method for the design and preparation of functional saccharide sensors.[39,40] A basic modular sensor is made of a receptor, reporter and a linkage which are connected to the molecular scaffold in such a way as to permit these sub-units to be varied independently.

In 1994, Shinkai *et al* prepared the first glucose-selective boronic acid-based fluorescence sensor **190** (Figure 2.7).[41] The bis-boronic acid sensor **190** showed an excellent selectivity for glucose with a 1: 1 binding ratio. The binding constant was measured to be 3981 M^{-1} for glucose, 316 M^{-1} for fructose and 158 M^{-1} for galactose. The sensor **190** showed similar fluorescence turn-on response for other saccharides to that of sensor **188**. It was noticed that the high glucose affinity shown by sensor **190** allows glucose sensing at sub-mM levels. It was suggested that the C–H…π interactions that

exist between the hydrocarbon skeleton of glucose and the aromatic π surface of the anthracene unit in **190** might contribute to the high affinity for glucose.

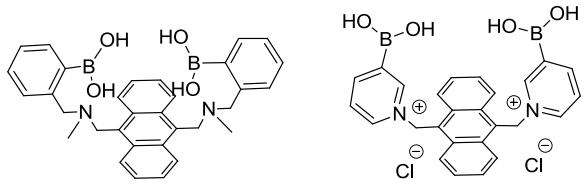

190 **191**

Figure 2.7: Bis boronic acid based modular sensors of glucose detection

A few years later, Norrild and co-workers designed and synthesized a pyridinium derivative of **190**, sensor **191** as shown in Figure 2.7.[42] The ionic nature of sensor **191** improves the water solubility and increases the acidity of the boron centre. These structural modifications allow glucose sensing in completely aqueous solution at physiological pH. The high binding constant of 2521 M^{-1} was calculated from fluorescence spectral titration of sensor **191** with glucose. NMR spectroscopic studies indicated that sensor **191** binds to α-glucofuranose at its 1,2,3,5-hydroxyl groups.

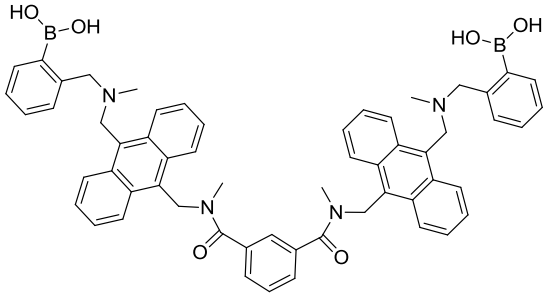

192

Figure 2.8: Wang's saccharide sensor **192**.

Wang and co-workers investigated the sensing properties of a variety of diboronic acid sensors and documented the results in the literature to display the selectivity for glucose.[43-45] For example, the sensor **192** (Figure 2.8) showed fluorescence turn-on response to the all saccharides tested but with different binding affinities.[44] It was noticed that the sensor **192** show high selectivity for glucose. The stability constants go as follows: 34 M^{-1} with D-fructose, 1470 M^{-1} with D-glucose, and 30 M^{-1} with D-galactose. The central benzene ring was replaced with several other fluorophores and the resulting sensors were examined in terms of selectivity for different saccharides.

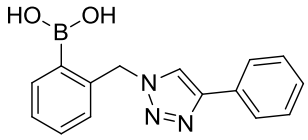

Click fluor 193

Figure 2.9: Molecular structure of click fluor **193**

As seen in the previous sections, most of the florescent saccharide sensors contain an amine group as linker and electron donor (e.g., the Wulff-type receptors). The "click reaction-generated" 1,2,3-triazole moiety was introduced in structural design of saccharide sensors for the first time by James *et al.* in the year 2008.[46] As shown in Figure 2.9, the structure of click-fluor **193** comprised of a phenyl group and an *o*-methylphenylboronic acid moiety connected through a 1,2,3-triazolyl linker through click chemistry. The click-fluor **193** displayed reasonable fluorescent sensing functions towards saccharides in an alkaline aqueous medium (pH 8.21) requiring the presence of

an organic co-solvent (52% wt MeOH in H_2O), while the concentrations of saccharides detected were in the range of *ca.* 10^{-2} to 1 M.

2.3 Objectives of the research reported in this chapter

Detection and recognition of saccharides under physiological conditions and monitoring the concentration of saccharides *in vivo* are challenging tasks that require a sustained effort to be dedicated to the development and refinement of new sensor systems. At present, boronic acid receptors have been extensively used in conjunction with various fluorogenic groups to form functional fluorescent sensors for saccharides. In this context, sensor design has been recently focused on tuning the receptor, donor/ligand, and linkage groups in order to strengthen boronic acid-saccharide binding at neutral pH, to enhance photoinduced electron/energy transfer for effective signaling, and to introduce cooperativity for binding with specific saccharides. On the other hand, the fluorophore component acting primarily as the "read-out" unit of the sensor can significantly influence solvation, steric hindrance of the binding site, and polarity matching with saccharides. Hence, the fluorophore effect also has a key impact on the efficiency and selectivity of fluorescent sensors.

In the current literature, the fluorophores utilized for constructing saccharide sensors are mostly polyaromatic-based fluorogenic groups such as naphthalene, anthracene, and diazobenzene. Conjugated oligomers, owing to the excellent controllability and tunability of their optoelectronic properties, have found wide-ranging applications in fluorescent sensory devices. However, fluorescent saccharide sensors

based on π-conjugated oligomer fluorophores have not been investigated, despite their excellent photophysical properties. To address this issue, we have designed bis- and tetra-boronic acid appended oligomers **194-198** (Scheme 1) as models for a qualitative understanding of the basic structure-property relationships for oligomer-based fluorescent saccharide sensors as a primary goal. Note that the π-frameworks of the oligomer fluorophores are designed in three distinct motifs, cruciform, linear, and H-shapes, in this thesis work. As such, the effect of oligomer fluorophore on sensor properties can be readily probed by way of comparative studies. Since the phenylboronate and phenylboronic acid derivatives are also known as good receptors for fluoride ions, I have herein investigated the fluoride ion sensing properties of boronate precursors of oligomers **194-198**. The following sections outline the detailed synthesis and photophysical investigations of these target oligomers. Some of the data in this chapter have been published in *Org. Biomol. Chem.* **2011**, *9*, 1332-1336 as a communication, in which I am the first author of the paper. Our previous group member Dr. Guang Chen conducted, the AFM studies in this paper and, as part of a collaboration with Professor David W. Thompson, Chemistry Department, Memorial University, his PhD student Mr. Prateek Dongare conducted spectroscopic characterizations of all oligomers with saccharides and anions.

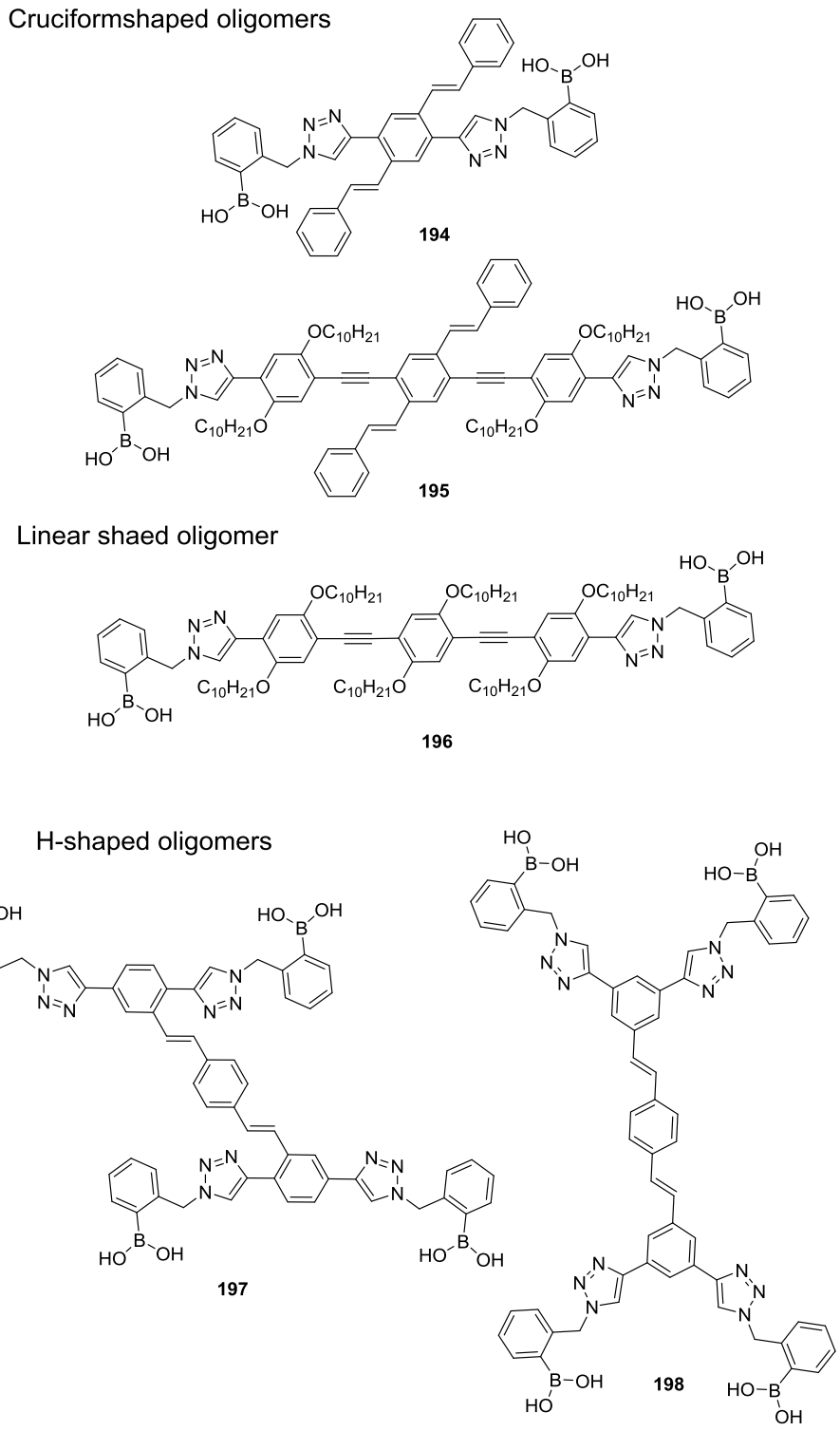

Figure 2.10: Molecular structures of oligomers **193-198** for saccharides detection.

2.4 Results and Discussion

2.4.1 Short and long cruciform-shaped OPV/OPE oligomers

To construct the short cruciform OPV oligomer **194**, two essential precursors **205** and **210** were first synthesized as shown in Schemes 2.4 and 2.5. The synthesis of precursor **205** began with *p*-xylene as the starting material. As shown in Scheme 2.4, iodination of *p*-xylene afforded 2,5-diiodo-1,4-dimethylbenzene **200**. Treating compound **200** with *N*-bromosuccinimide (NBS) gave **201** which was purified by recrystallization from $CHCl_3$ and hexanes.

The dibromide **201** was then subjected to an Arbuzov reaction with $P(OEt)_3$, giving 2,5-diiodo-1,4-bis(diethylphosphonatomethyl)benzene **202** in a yield of 83%. A Horner-Wittig reaction between **202** and benzaldehyde in the presence of NaH afforded phenylenevinylene trimer **203** as a yellow crystalline solid. Treating **203** with trimethylsilylacetylene (TMSA) under the catalysis of Pd/Cu in a mixed solvent of Et_3N and THF gave **204** in a yield of 87%. Removal of the trimethylsilyl (TMS) groups in **204** with K_2CO_3 finally led to the formation of the key precursor **205**.

The synthesis of another key intermediate **210** was started by treating commercially available *o*-bromotoluene with trimethyl borate in presence of *n*-BuLi to provide *o*-tolylboronic acid **207**. A simple esterification reaction was performed between **206** and pinacol to afford compound **208**, which was then subjected to a radical

bromination reaction with NBS followed by azidation in presence of NaN_3 to afford precursor **210** as thick syrup.

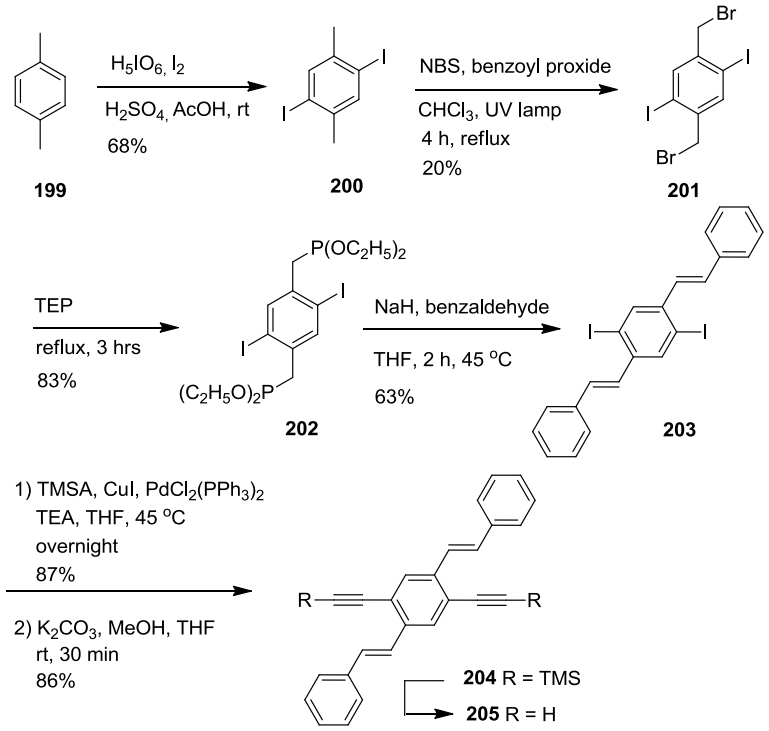

Scheme 2.4: Synthetic route for OPV building block **205**

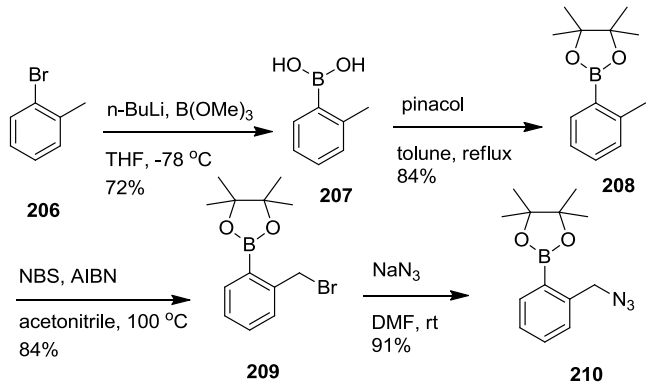

Scheme 2.5: Synthesis of azido-pendant phenylboronate **210**.

With **205** and **210** in hand, the synthesis continued as outlined in Scheme 2.6. A Cu-catalyzed alkyne azide coupling (CuAAC) reaction between the azido-pendant in **210** and the acetylene unit in **205** in the presence of CuI and *i*-Pr_2EtN in DMF at 65 ^oC to provide **211**. Compared with numerous high-yielding CuAAC reactions reported in the literature, the yield of this click reaction was only at a moderate level (69%). The reduced efficiency of this reaction is likely due to some side reactions involving the insertion of Cu into the C–B bonds.[47] The boronate groups of intermediate **211** were then hydrolyzed *via* a transesterification reaction between boronate **211** and excess *o*-tolylboronic acid **207** in dioxane/H_2O to give the short cruciform-shaped OPV oligomer **194** along with the tolylboronate byproduct **208**. It should be noted that compound **208** serves as a useful precursor for the preparation of azido-phenylboronate **210**.

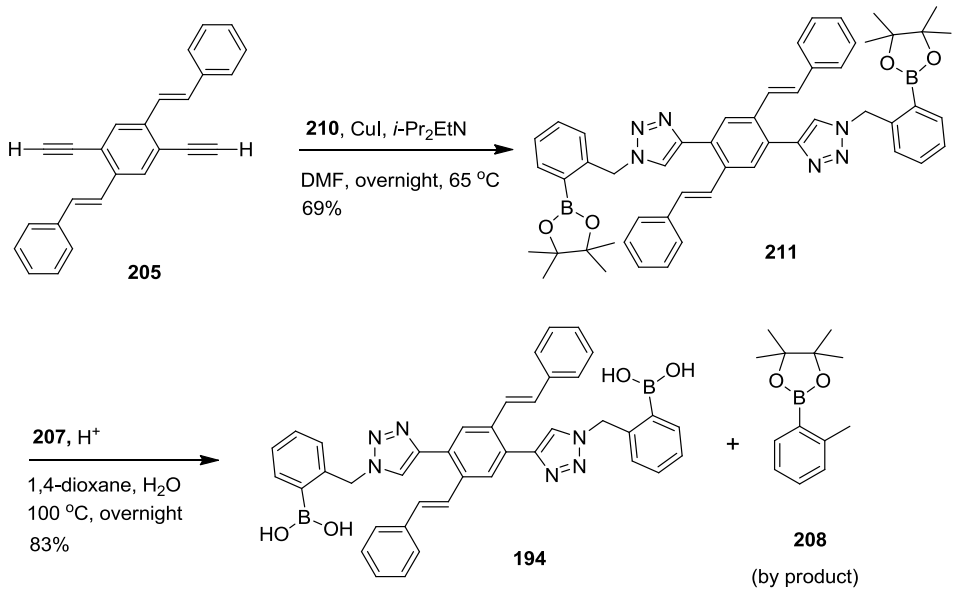

Scheme 2.6: Synthetic route for the preparation of short cruciform OPV oligomer **194**.

Subsequent to the synthesis of short cruciform OPV oligomer **194**, a longer cruciform OPV/OPE oligomer **195** was prepared by using similar synthetic strategy. Outlined in Schemes 2.7 and 2.8 is the designed route to compound **195**. 1,4-Dihydroxybenzene **212** was alkylated with 1-bromodecane in the presence of KOH in refluxing EtOH to give 1,4-bis(decyloxy)benzene **213**, which was then iodinated to afford compound **214** in a yield of 80%. Cross-coupling of **214** with only 0.6 equiv of trimethylsilylacetylene (TMSA) afforded monoiodide **215** as the major product, which was then silylated using triisopropylsilylacetylene (TIPSA), giving compound **216** in a yield of 88%. Compound **216** was treated with K_2CO_3 to selectively remove the TMS group, yielding compound **217** in 91% yield.

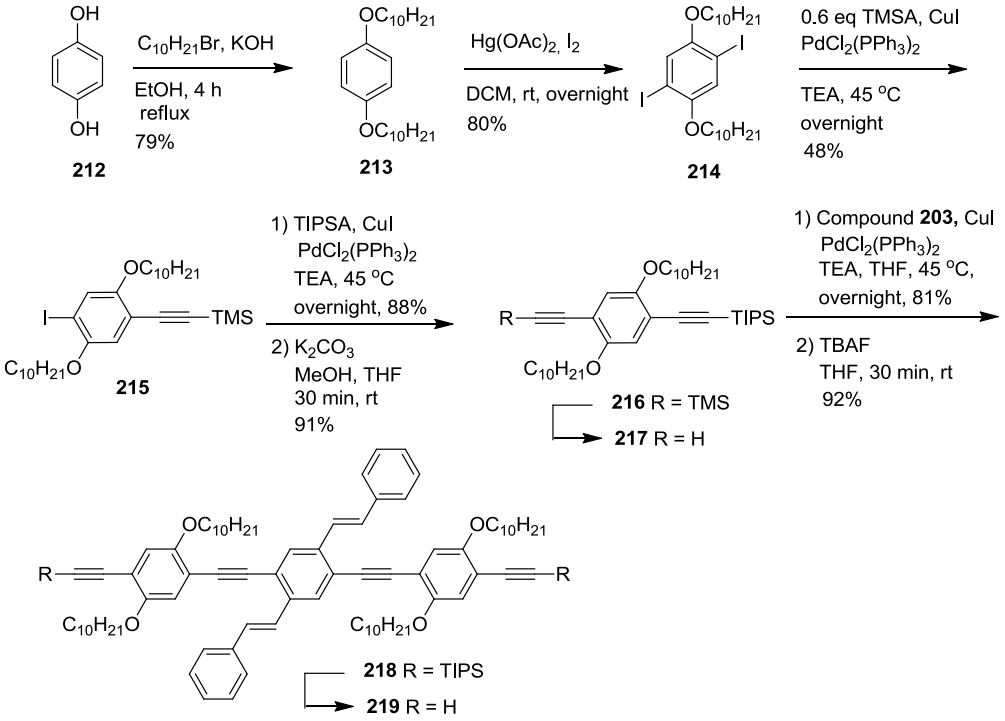

Scheme 2.7: Synthesis of OPV/OPE building block **219**.

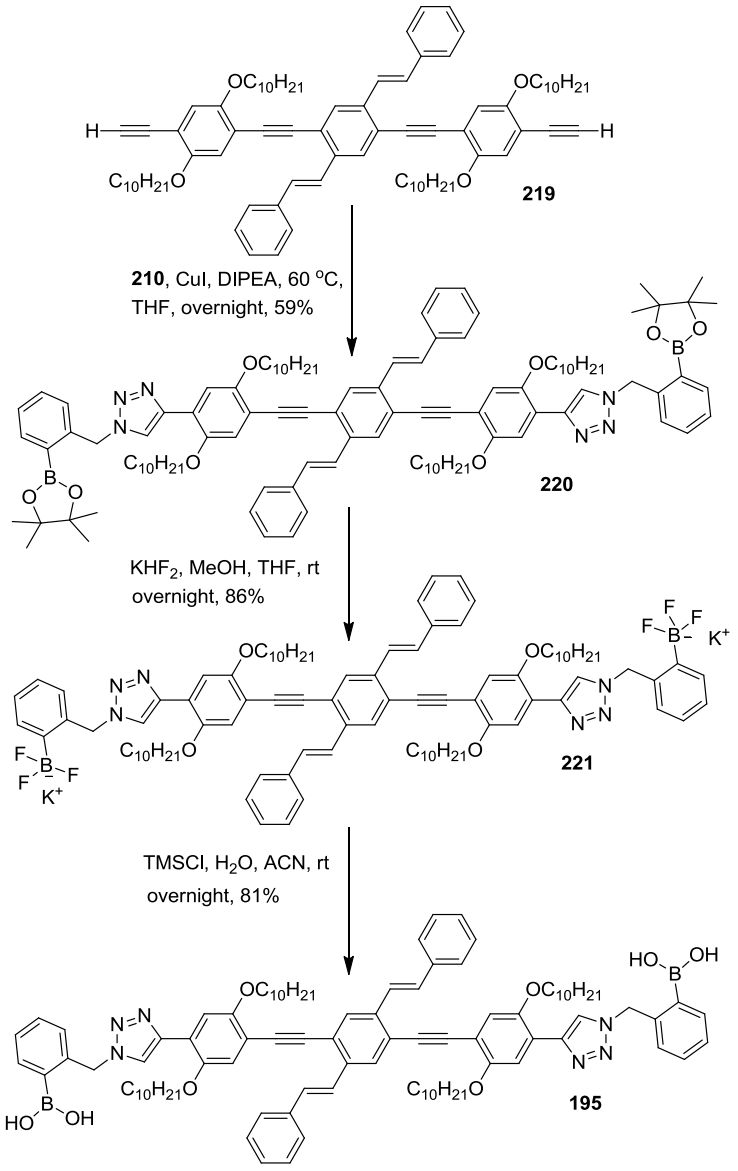

Scheme 2.8: Synthetic route for longer version cruciform OPE/OPV oligomer **195**.

Sonogashira coupling between compound **203** and **217** first produced long cruciform OPV/OPE precursor **218** in 81% yield. After deprotection of **218** with TBAF, the resulting terminal alkyne **219** (Scheme 2.8) was subjected to a CuAAC reaction with compound **210** in presence of CuI, yielding the boronate of long cruciform OPV/OPE

oligomer **220** in 59% yield (Scheme 2.8). For the hydrolysis of **220**, however, the transesterification method was problematic due to the formation of some intractable impurities. A stepwise hydrolysis route was then used, in which the boronate **220** was first converted into trifluoroborate **221** with KHF_2 and then hydrolyzed into boronic acid in the presence of trimethylsilyl chloride (TMSCl). This synthetic route led to the desired long cruciform OPV/OPE oligomer **195** in a very good yield and satisfactory purity (Scheme 2.8).

With the successful synthesis of the previous two cruciforms **194** and **195**, the linear-shaped OPE **196** was prepared according to Scheme 2.9. First compound **214** was cross-coupled with TMSA under Sonagashira conditions and followed by the desilylation reaction with K_2CO_3 to afford phenylacetylene building block **223**. Compound **223** was further elongated by cross-coupling reaction with **214**, yielding OPE trimer **224**, which was desilylated with K_2CO_3 to obtain active phenylacetylene precursor **225** in 88% yield. In a similar manner, linear OPE precursor **225** was reacted with compound **210** under CuAAC reaction conditions, yielding boronate intermediate **226** in 55% yield. A two-step hydrolysis procedure was applied as illustrated in Scheme 2.9 to convert boronate intermediate **226** into corresponding boronic acid-attached linear OPE **196**.

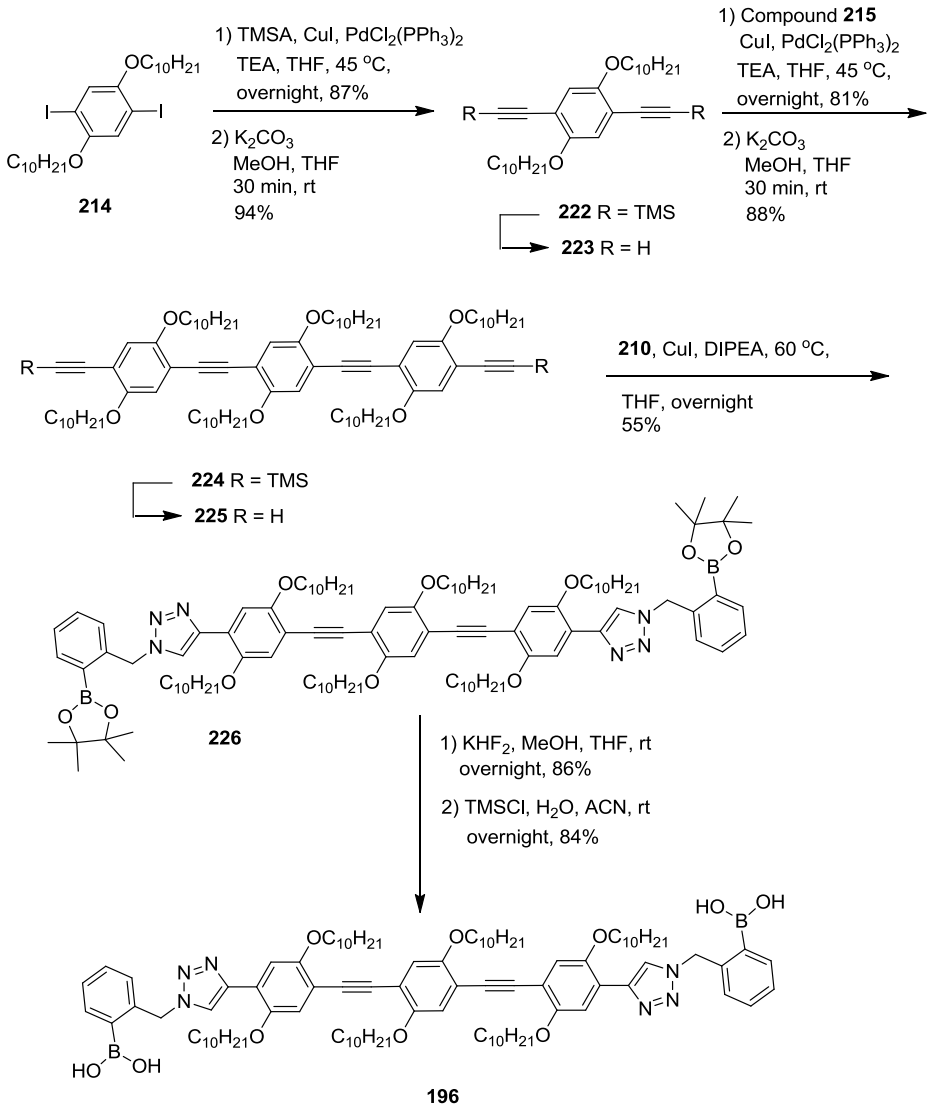

Scheme 2.9: Preparation of OPE trimer oligomer **196**.

2.4.2 Synthesis of H-shaped OPV oligomers

To construct the two isomers H-mer **197** and **198**, two tetraethynyl substituted OPV precursors **237** were first synthesized. The synthesis of these OPV precursors began with the preparation of two key building blocks **232** and **234** as outlined in Scheme 2.10. First, 2-aminobenzoic acid **227** was brominated with Br_2 to give 2-amino-5-

bromobenzoic acid **228**. Compound **228** underwent a diazotization reaction followed by treatment with KI to yield 5-bromo-2-iodobenzoic acid **229**, which was then subjected to an esterification with MeOH in the presence of H_2SO_4 to yield methyl ester **230**. Compound **230** was reduced into benzyl alcohol **231** by diisobutylaluminum hydride (DIBAL). Oxidation of **231** with pyridinium chlorochromate (PCC) resulted in the formation of 5-bromo-2-iodobenzaldehyde **232** in 85% yield. The synthesis of compound **234** began with a radical bromination of *p*-xylene using NBS, which afforded compound **233** in 21% yield. An Arbuzov reaction between **233** and $P(OEt)_3$ then yielded **234** in 56% yield.

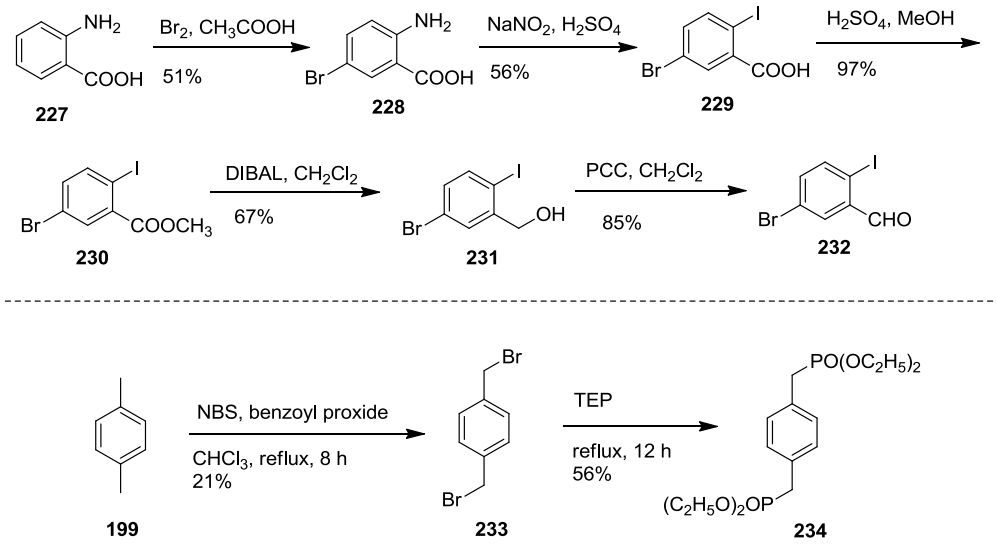

Scheme 2.10: Synthetic route for the precursors **232**, and **234**.

Once the two building blocks **232** and **234** were prepared, a Horner-Wittig reaction was performed between them in the presence of NaH in DMF solvent at room temperature, affording the tetrahalo substituted OPV precursor **235** in 88% yield as a

yellow solid. Cross coupling of **235** with TMSA followed by desilylation reaction resulted in the formation of tetraethynyl OPV precursor **237** as a bright yellow solid (Scheme 2.11).

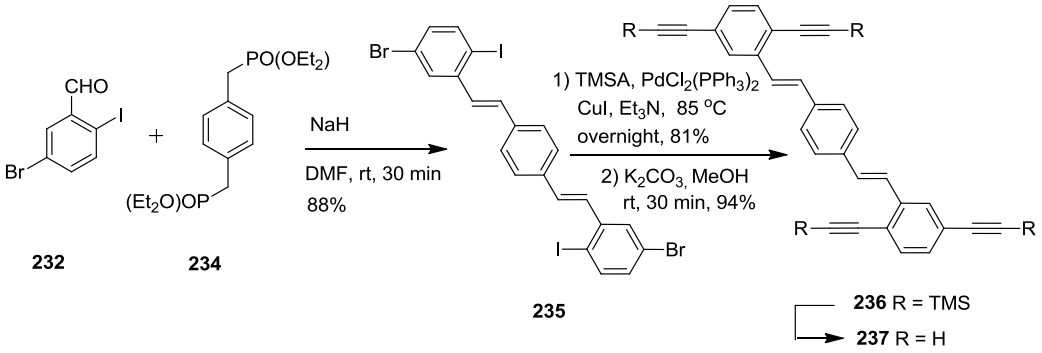

Scheme 2.11: Synthesis of tetraethynyl OPV precursor **237**.

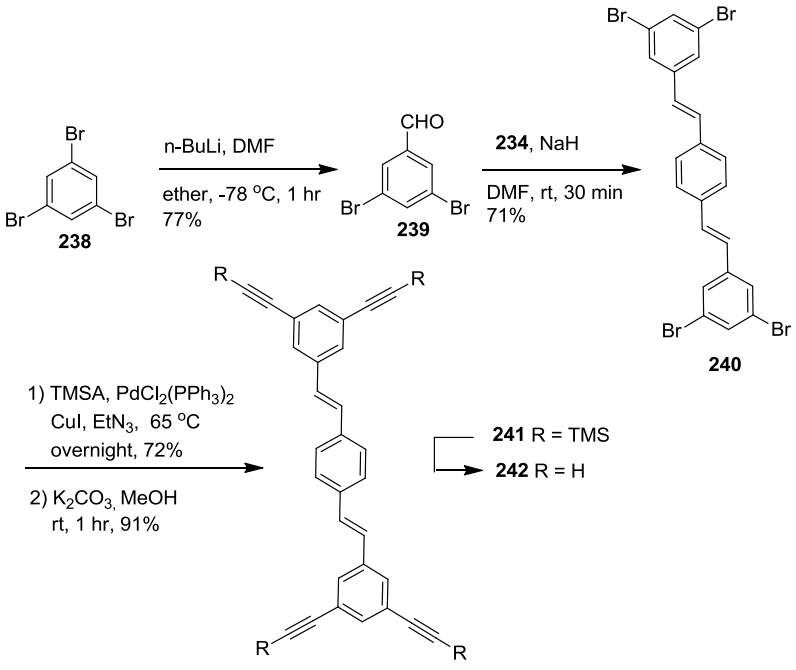

Scheme 2.12: Synthesis of tetraethynyl OPV precursor **242**.

A similar synthetic strategy was applied for the preparation of tetraethynyl OPV precursor **242** as outlined in Scheme 2.12. In the detailed work, a selective formylation was done on 1,3,5-tribromobenzene by using *n*-BuLi and DMF to yield compound **239** in a very high yield. A Horner-Witting reaction between **234** and **239** using NaH as base gave tetrabromo OPV precursor **240** in 71% yield. Finally, cross-coupling reaction on **240** in the presence of excess TMSA under Sonagashira conditions, followed by deprotection reaction with K_2CO_3, yielded the desired precursor **242**.

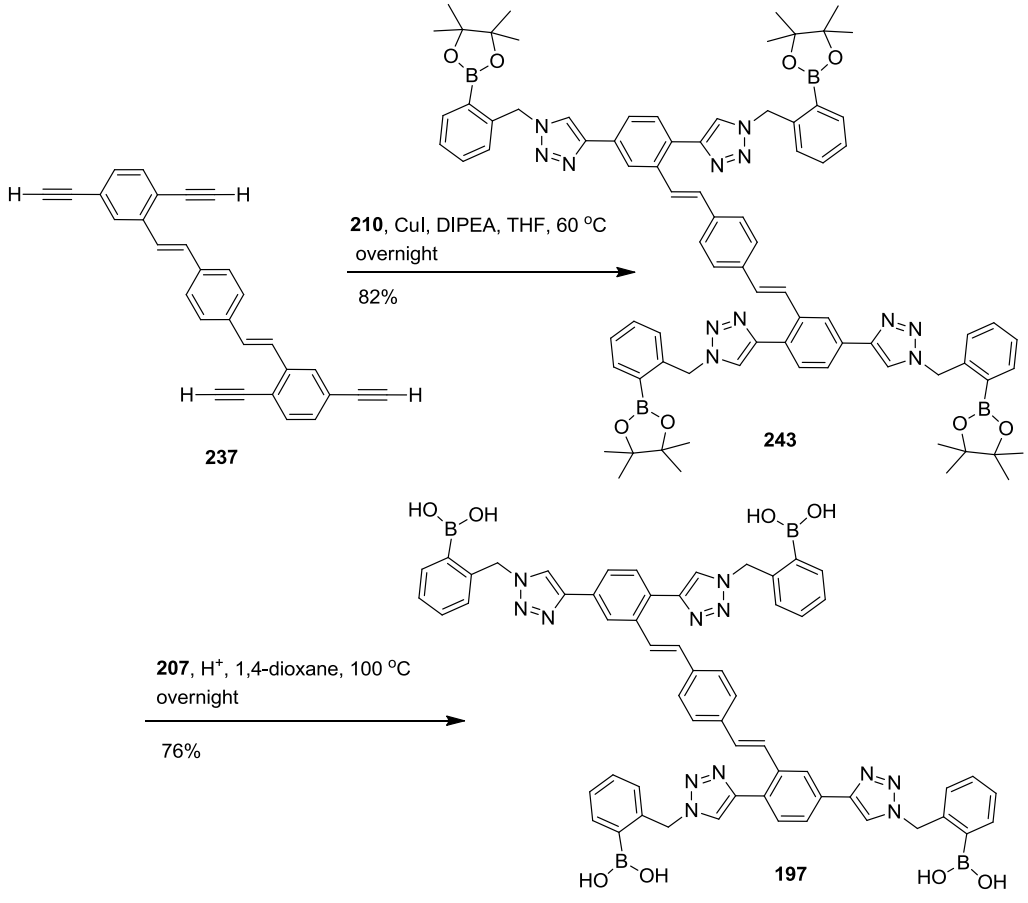

Scheme 2.13: Synthetic route for H-shaped OPV oligomer **197**.

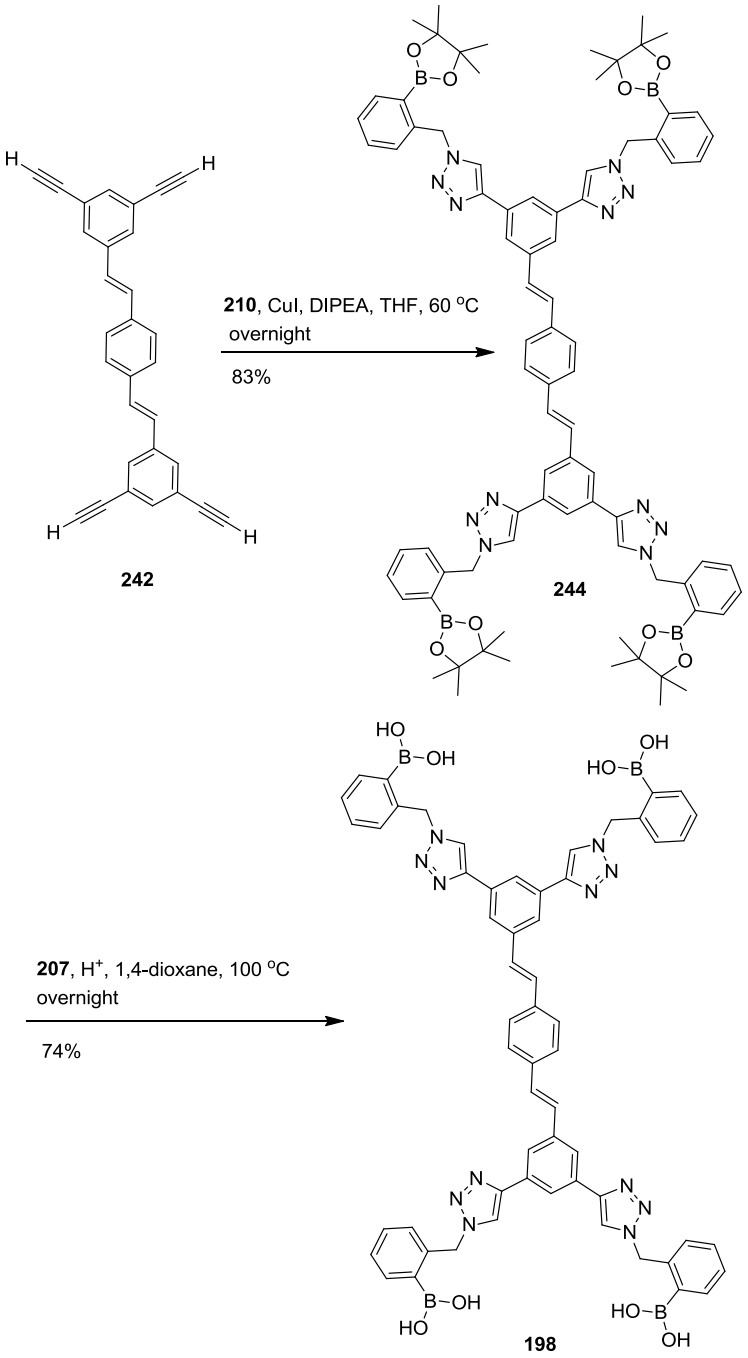

Scheme 2.14: Synthetic route for H-shaped OPV oligomer **198**.

Once the tetraethynyl OPV precursors **237** and **242** were obtained, two functionalized H-shaped OPV oligomers, **197** and **198**, were readily synthesized as outlined in Schemes 2.13 and 2.14. Tetraethynyl OPV **237** was reacted with an azido-phenylboronate ester **210** via the Cu(I)-catalyzed alkyne-azide coupling (CuAAC) reaction to afford tetraboronate-appended H-mer **243** in a very good. OPV H-mer **243** was then deprotected through a transesterification reaction with an excess of *o*-tolylboronic acid **207** to yield the desired H-shaped OPV oligomer **197** in 76% yield (Scheme 2.13). In the same manner, tetraethynyl OPV **242** was "clicked" with tetraboronate groups to give H-mer **244**, which was deprotected to yield the tetraboronic acid appended H-shaped OPV **198** (Scheme 2.14).

2.4.3 Single Crystal Structure of boronate oligomer 211

Single crystals of boronate oligomer **211** were grown by slow evaporation of its solutions in CH_2Cl_2/methanol (1:1) at low temperature (4 ^oC), and their detailed molecular and solid-state structures were characterized by single crystal X-ray crystallography. As can be seen from Figure 2.11, the X-ray structure of **211** shows crystallographic features as follows: (1) the cruciform π-framework takes a non-planar, highly twisted orientation, and (2) the *N* atoms of the triazole rings do not directly interact with the boronate groups.

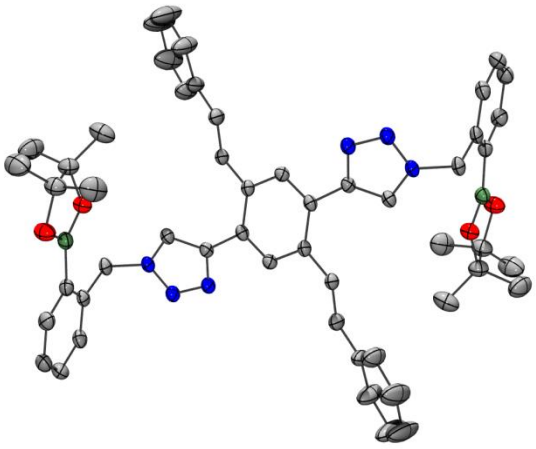

Figure 2.11: ORTEP drawing of boronate cruciform **211** (at 50% probability). Color scheme: grey = carbon, blue = nitrogen, red = oxygen, green = boron.

2.4.4 Electronic spectroscopic properties of cruciform and linear OPE/OPV oligomers

The UV-Vis absorption and fluorescence properties of the prepared boronic acid appended linear and cruciform OPE/OPV oligomers **194**, **195**, and **196** as well as related boronate esters **211**, **220**, and **226** were studied and the results are shown in Figure 2.12. From Figure 2.12A and C, it can be seen that all the oligomers measured show two distinctive $\pi \rightarrow \pi^*$ transition bands in the absorption spectra, while changing the chromophores between two boronic acids or esters resulted in altered energies of absorption bands which are mainly redshifted.

As shown Figure 2.12B, the emission spectral profile of short cruciform oligomer **194** can be assigned to the $S_1 \rightarrow S_0$ transition featuring two distinctive vibronic modes. The spectrum of oligomer **195** exhibits a broad structureless band which is blueshifted relative to that of oligomer **194**. Similar to oligomer **194**, the linear oligomer **196** shows two characteristic bands. However, changing the boronic acid groups in the oligomers to boronate esters results in small changes in the energies of the emission bands, and the spectral features are almost the same as those of boronic acid appended oligomers (Figure 2.12D). All the oligomers are highly emissive as evidenced by their measured quantum yields (Table 2.1).

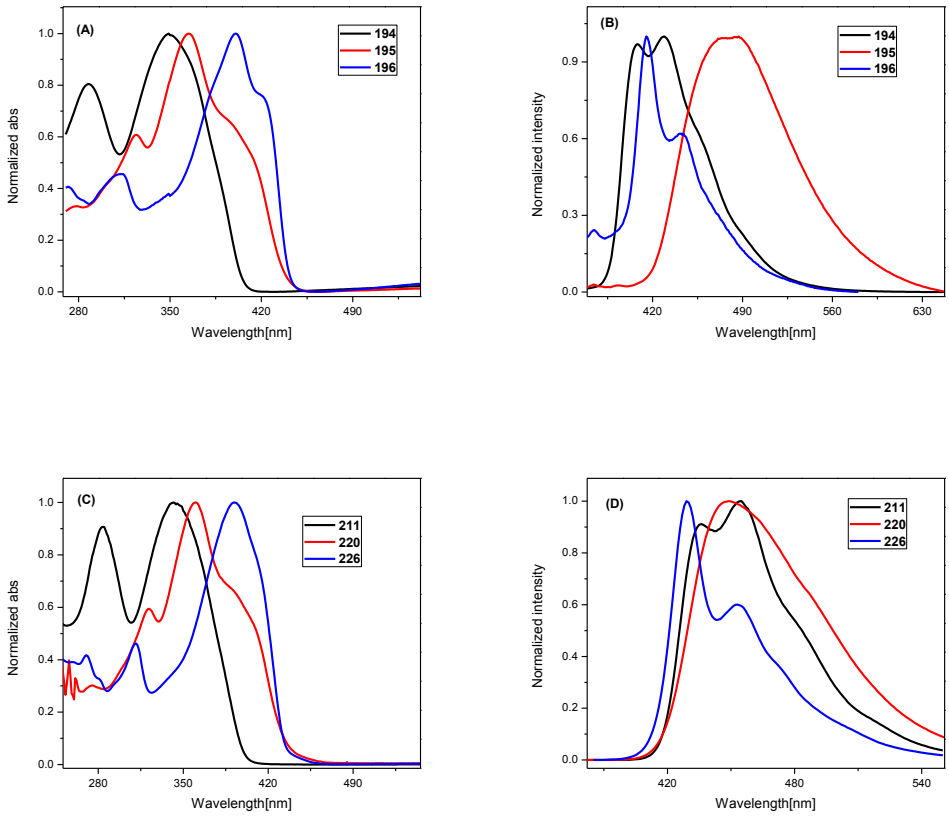

Figure 2.12: Normalized UV-Vis spectra (A) and fluorescence spectra (B) of oligomers **194**, **195**, and **196** measured in DMSO. Normalized UV-Vis spectra (C) and fluorescence spectra (D) of oligomers **211**, **220**, and **226** measured in THF.

Table 2.1: Quantum yield for linear and cruciform oligomers

Oligomer	Φ_{yield}		
	PBS	THF	DMSO
211		0.16	
194	0.075		0.18
220		0.29	
195	0.099		0.28
226		0.23	
196	0.063		0.21

2.4.5 Saccharides sensing of cruciform and linear OPV/OPE oligomers

2.4.5.1 Fluorescence titrations

To evaluate their sugar sensing functions, the OPE/OPV oligomers **194**, **195**, and **196** were subjected to a series of fluorescence titration experiments with four selected sugars, D-fructose, D-ribose, D-galactose, and D-glucose, under physiological conditions. Despite the limited solubility of fluorophores **194**, **195** and **196** in water, their dissolution in a neutral (pH 7.41) aqueous potassium phosphate buffer solution with concentration 10^{-5} M (suited for fluorescence spectroscopic measurements) was readily attained with the aid of a minimal amount of DMSO as the co-solvent (H_2O/DMSO > 99 : 1, v/v).

For the cruciform sensor **194**, significant fluorescence enhancement (turn-on sensing) was observed in the titrations with all the saccharides investigated. Figure 2.13A–D illustrates the fluorescence changes upon titration of **194** with different saccharides. Titrations of the four saccharides resulted in similar trends of spectral changes with increasing addition of saccharide titrants. The emission spectrum of cruciform **194** is composed of a peak at 430 nm and a shoulder at 403 nm. Note that with increasing titration, distinctive vibronic bands emerged, resembling the emission features of boronate ester **211**, which is an indicative of complexation of boronic acid receptors with saccharides to form boronates. The affinities of **194** for saccharides vary to a large extent as manifested by the plots in Figure 2.14, which shows the correlation between fluorescence enhancement (F/F_0) at 430 nm and saccharide concentration.

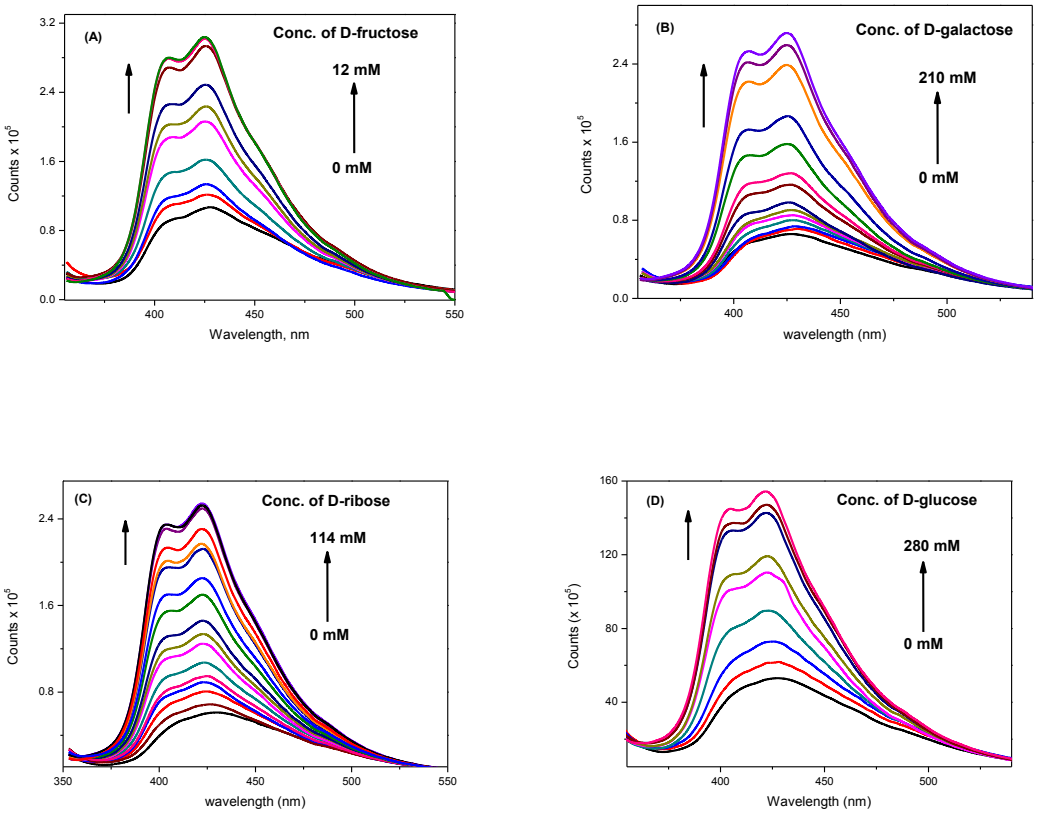

Figure 2.13: Fluorescence titration of **194** (11.8 µM) with D-fructose in an aqueous buffer solution (pH 7.41) at 298 ± 3 K (λ_{ex} = 340 nm). (B) Fluorescence titration of **194** (13.8 µM) with D-galactose in an aqueous buffer solution (pH 7.41) at 298 ± 3 K (λ_{ex} = 340 nm). (C) Fluorescence titration of **194** (13.8 µM) with D-ribose in an aqueous buffer solution (pH 7.41) at 298 ± 3 K (λ_{ex} = 340 nm). (D) Fluorescence titration of **194** (12.0 µM) with D-glucose in an aqueous buffer solution (pH 7.41) at 298 ± 3 K (λ_{ex} = 340 nm).

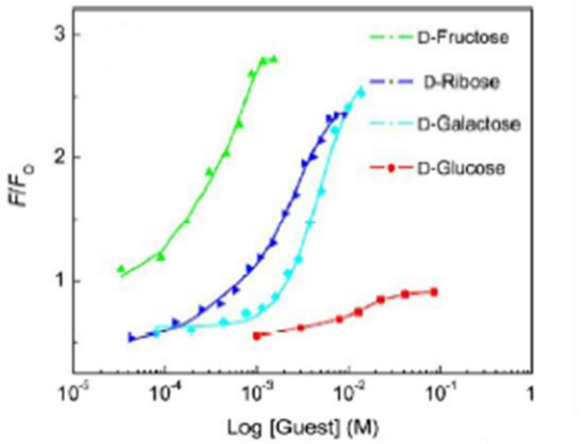

Figure 2.14: Plots of fluorescence enhancement (F/F_o, λ = 430 nm) against saccharide concentrations with fittings extracted from *SPECFIT*.

It can be clearly seen that the sensitivity of cruciform **194** for different saccharides is in the order of: D-fructose > D-ribose ~ D-galactose > D-glucose. Also of remark in Figure 2.14 is the high sensitivity of **194** for D-fructose and D-ribose in the range of 10^{-3} to 10^{-4} M. Such a performance renders cruciform **194** at least comparable if not superior to those water soluble fluorescent sensor systems reported in the recent literature with high saccharide sensitivity under physiological conditions,[28,29,48,49] which are highly desirable features for practical sensing applications (*e.g.* detection or monitoring of saccharides in whole blood).

Table 2.2: Stability constants (*K*) for complexation of cruciform **194** with various saccharides determined by global spectral fitting

Saccharide	**log K_1 (M^{-1})**	**log K_1K_2 (M^{-2})**
D-fructose	4.02 ± 0.5	7.27 ± 0.5
D-ribose	3.24 ± 0.2	6.09 ± 0.1
D-galactose	3.87 ± 0.2	6.26 ± 0.1
D-glucose	2.53 ± 0.3	4.21 ± 0.4

To gain a quantitative understanding of the mechanisms for complexation between sensor **194** and various saccharides, global spectral fitting analysis was undertaken using the modified Marquardt-Levenberg algorithm implemented in the *SPECFIT* software package.[50] Table 1 lists the stability constants (*K*) determined by global spectral fitting.

From Table 2.2, it can be seen that all the four saccharides bind to cruciform **194** in a two-step mechanism. The spatial arrangement of the two boronic acid receptors in

194 does not facilitate any "pincer-like" binding mode with saccharides. D-Fructose shows the strongest binding strength with **194** which is about two orders of magnitude greater than that of D-glucose. The binding constants for D-ribose and D-galactose are similar and stay in the middle range among the four saccharides. The quantitative measurements are in agreement with the trend of saccharide sensitivity as revealed in Figure 2.14.

2.4.5.2 ^{1}H NMR studies on cruciform oligomer 194

As mentioned, the complexation of phenylboronic acid with saccharides (polyols) is reversible and pH dependent,[24] while the formation of stable phenylboronic acid and saccharide complex at neutral pH usually requires a stabilizing effect by some ligand groups, such as in the case of the widely known "Wulff-type" receptor (*o*dialkylaminomethylphenylboronic acid).[34,35] From the fluorescence titration experiments, it is evident that the boronic acid groups in cruciform **194** are effectively bound to saccharides under physiological conditions. This result suggests that the 1,2,3-triazolyl moiety resulting from the click reaction not only acts as a linker group, but plays an important role in saccharide binding.

To gain a deeper insight into this aspect, ^{1}H NMR titration of **194** with D-fructose was then performed. For solubility reasons, the experiments were conducted by adding aliquots of D-fructose dissolved in a phosphate/D_2O buffer solution at pD 7.41 to a DMSO-d_6 solution of **194**. Detailed NMR titration results are presented in Figure 2.15. Although the change of solvent system from water to DMSO may lead to a considerable

degree of variation on binding constants, the binding motif however should not be significantly different. As shown in Figure 2.15, the signal of boronic acid protons (Hb) vanishes gradually with the addition of D-fructose, while the signals of the methylene and aromatic protons (Hc and Hd) show a slight upfield shift by less than 0.1 ppm. These observations also corroborate the transformation of boronic acid to boronate ester in binding to saccharides. Of particular note is that the triazolyl proton (Ha) dramatically shifts downfield by more than 0.2 ppm. This result indicates that the triazolyl group experiences a pronounced change of chemical environment in binding with saccharides, likely induced by either a very strong solvation or a hydrogen bonding effect. Given that solvation interactions are usually affected by dipole-dipole forces without significant selectivity and specificity, hydrogen bonding appears to be a more likely reason for the unique downfield shift of the triazolyl signal.

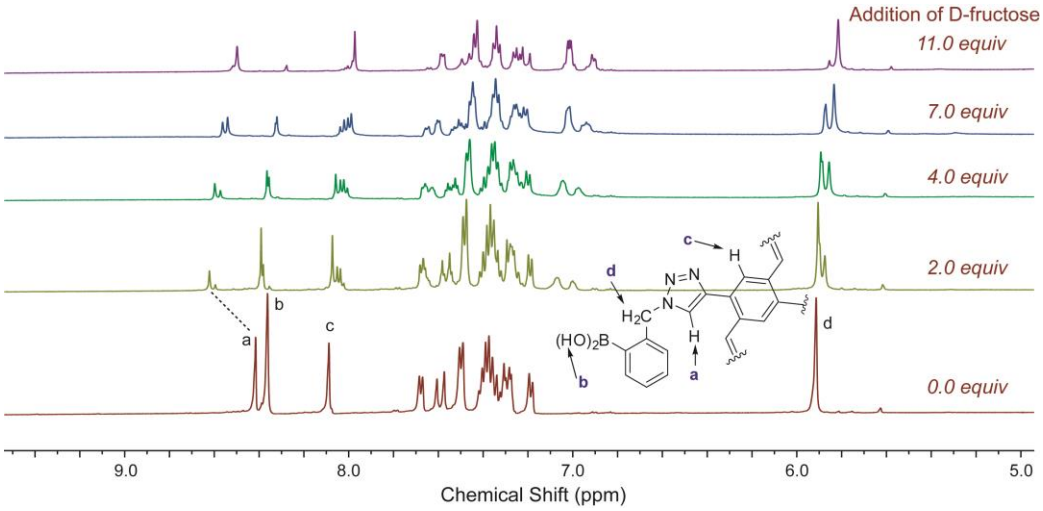

Figure 2.15: ^{1}H NMR titration of **194** with D-fructose in DMSO-d_6 and phosphate buffer solution (pD 7.4) at 298K (showing aromatic region).

2.4.5.3 Molecular modeling studies

According to the model system illustrated in Figure 2.16, in binding with a 1,2-diol, the triazolyl unit adjacent to the phenylboronic acid group acts as a ligand (hydrogen bond acceptor) to coordinate with a molecule of water. This "water insertion" model is analogous to the binding motif of the "Wulff-type" boronic acid receptor in aqueous media. Energetically, it provides stabilization of the boron-diol complex by ΔH = -11.2 kcal mol^{-1}, which well accounts for the significant binding of cruciform **194** with various saccharide in neutral aqueous solutions.

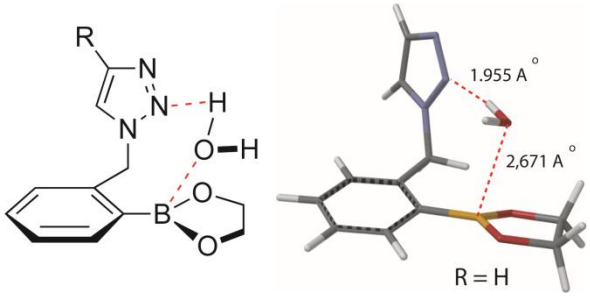

Figure 2.16: DFT (B3LYP/6-31G (d)) optimized structure for the complex of *o*-triazolylmethylphenylboronic acid with ethylene glycol in the presence of water.

2.4.5.4 AFM studies on cruciform oligomer 194

For the remarkable fluorescence transduction properties exhibited by cruciform **194**, neither photoinduced electron transfer (PET) nor intramolecular charge transfer (ICT) mechanism offers meaningful interpretation. Instead, the sensing mechanism can be rationalized from a standpoint of aggregation-modulated emission. Recent studies have disclosed that the aggregation state of OPVs in solution can exert a very significant

impact on their excited-state dynamics and emission yields.[51,52] To shed light on this point, we further analyzed the aggregation behavior of cruciform **194** with and without binding to saccharides. Aliquots taken from the solution prepared for fluorescence titration of **194** with D-fructose were spin-cast on freshly cleaved mica surfaces for atomic force microscopic (AFM) imaging.

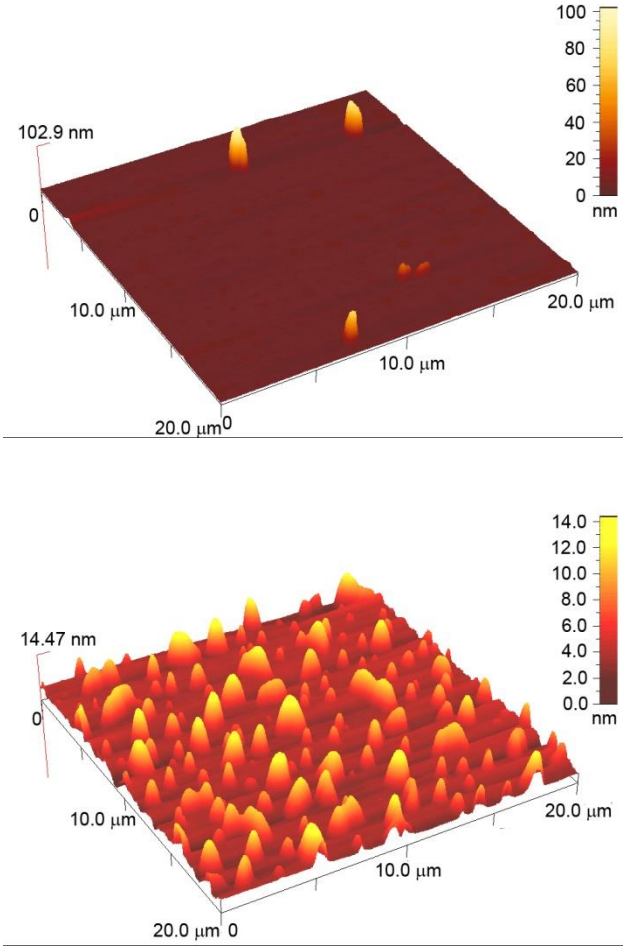

Figure 2.17: AFM image (tapping mode) of aggregates of **194** on mica (top), AFM image (tapping mode) of aggregates of **194** and D-fructose on mica (bottom).

The aggregates of cruciform **194** prior to complexation with D-fructose are in a size range of 60 to 100 nm (Figure 2.17 top). After complexation with D-fructose, much smaller (6–14 nm) aggregates are formed (Figure 2.17 bottom). Clearly, the binding of cruciform **194** with saccharides results in considerably reduced size of aggregates in solution, and it is reasonable to believe that the aggregation effect plays a crucial role in the fluorescence enhancement observed in the titrations of cruciform **194** with various saccharides. Two types of rationalization can be conceived at this juncture. First, the complexation with saccharides leads to increased de-aggregation/solvation of cruciform **194** to suppress fluorescence self-quenching.[53] On the other hand, the possibility that saccharide binding induces more planar OPV orientation in the aggregates of **194** may also offer a sound explanation for the observed fluorescence enhancement. The latter argument is in line with the aggregation-induced emission (AIE) for some π-conjugated systems.[54] The UV-Vis titration data of oligomers **194-196** with saccharides are presented in the appendix.

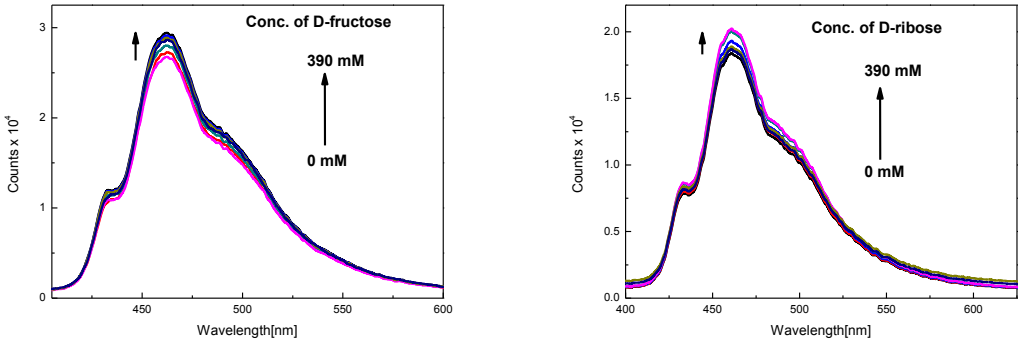

Figure 2.18: (Left) Fluorescence titration of **195** (7.23 µM) with D-fructose in an aqueous buffer solution (pH 8.21) at 298 ± 3 K (λ_{ex} = 350 nm). (Right) Fluorescence titration of **195** (6.83 µM) with D-ribose in an aqueous buffer solution (pH 8.21) at 298 ± 3 K (λ_{ex} = 350 nm).

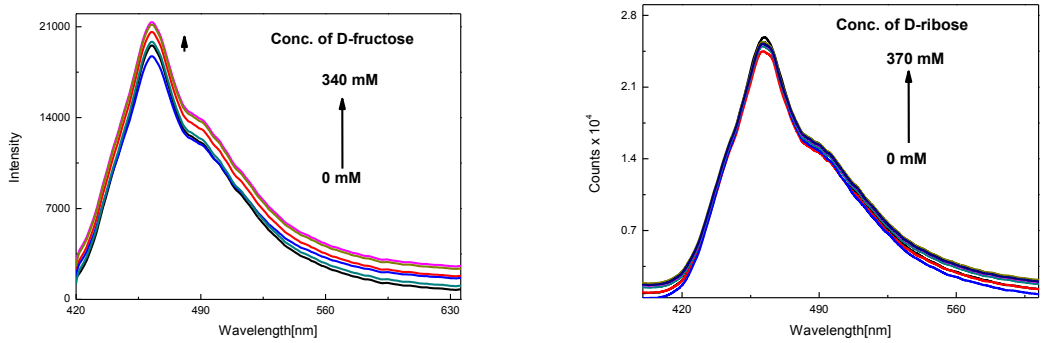

Figure 2.19: (Left) Fluorescence titration of **196** (5.80 µM) with D-fructose in an aqueous buffer solution (pH 8.21) at 298 ± 3 K (λ_{ex} = 350 nm). (Right) Fluorescence titration of **196** (5.80 µM) with D-ribose in an aqueous buffer solution (pH 8.21) at 298 ± 3 K (λ_{ex} = 350 nm).

2.4.5.5 Fluorescence titrations of cruciform oligomer 195 and linear oligomer 196

Finally, fluorescence titrations of cruciform oligomer **195** and linear oligomer **196** with various saccharides in neutral aqueous solutions were also carried out using the same protocol as that for cruciform **194**. To our surprise, the emission spectrum of **195** and **196** did not show any major changes during the titrations with saccharides (Figures 2.18 and 2.19). Increasing the basicity of solution did not improve the sensing function significantly. For instance, addition of D-fructose to **196** in a basic buffer solution at pH 8.21 resulted in only a slight drifting of spectral baseline (Figure 2.19). However, the cruciform oligomer **195** showed minor spectral changes during the titrations at neutral pH (Figure 2.18). Given that boronic acid tends to strongly complex with saccharides under basic conditions, the poor saccharide sensing function displayed by oligomers **195** and **196** can be reasonably ascribed to an inert response to saccharide binding events.

2.4.6 Electronic spectroscopic properties of H-shaped oligomers

The steady-state UV-Vis absorption and emission spectra of H-mers **197** and **198** as well as their boronate ester precursors **243** and **244** were determined and detailed spectral data are shown Figure 2.20. From the absorption spectra (Figure 2.20 left), it is evident that changing the boronic acid groups in the H-mers to boronate esters results in small changes in the energies of the absorption bands, and the band envelopes are almost superimposable. This is consistent with weak electronic coupling between the OPV choromophore and the pendant substituents in the ground state. The spectra of H-mers

197 and **243**, however, have distinctly different intensity patterns with **243** possessing a much greater extinction coefficient for the lowest-energy transition than that of **197**.

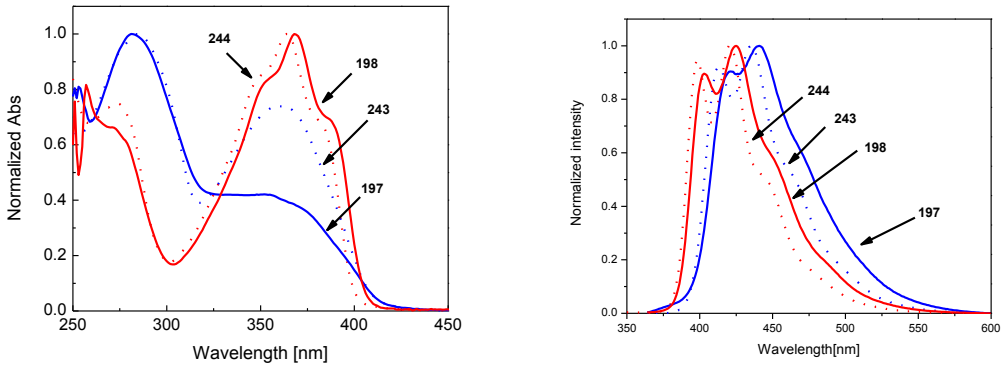

Figure 2.20: UV-Vis (left), and fluorescence spectra (right) of H-mers **197**, **198**, **243**, and **244**; the spectra of **197** and **198** were measured in DMSO, while **243** and **244** in THF.

All the H-mers are highly emissive upon electronic excitation and the emission spectral band shapes isomers are very similar (Figure 2.20 right). The fluorescence quantum yields (Φ) of boronic acid H-mers **197** and **198** measured in DMSO are 0.26 and 0.29 respectively, which are similar to the Φ values of boronate H-mers **243** (0.32) and **244** (0.34) determined in THF. In aqueous solutions, however, the fluorescence properties of the H-mers are considerably altered. From Figure 2.21, it can be seen that the fluorescence intensity of H-mers **197** and **198** shows a gradual depression with an increasing ratio of water as a co-solvent with DMSO. At a certain threshold, the fluorescence spectra of **197** and **198** are changed dramatically into a weak broad band with a notably red-shifted maximum emission wavelength.

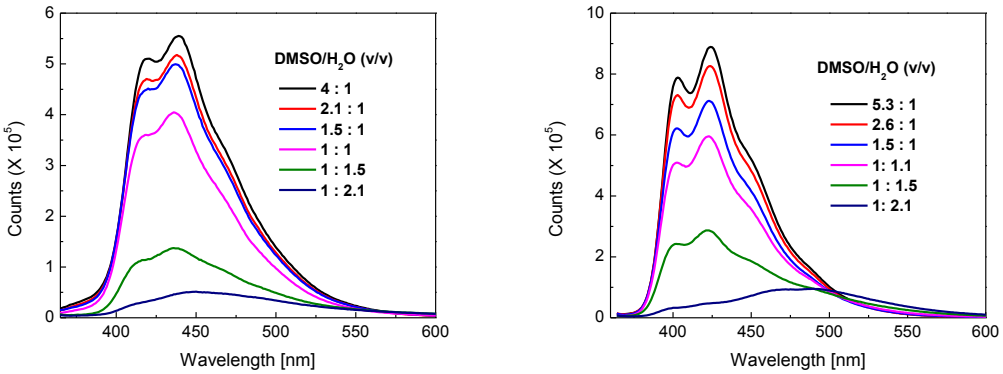

Figure 2.21: Fluorescence spectra of **197** (3.68 µM) left and **198** (3.68 µM) right, measured in a co-solvent system of DMSO/H_2O at varied volumetric ratios.

The emergence of this low-energy band is associated with the triazole group, since OPV precursor **242** when subjected to similar water-dependent measurements showed only fluorescence quenching but no shift of emission peaks was noticed (Figure 2.22).

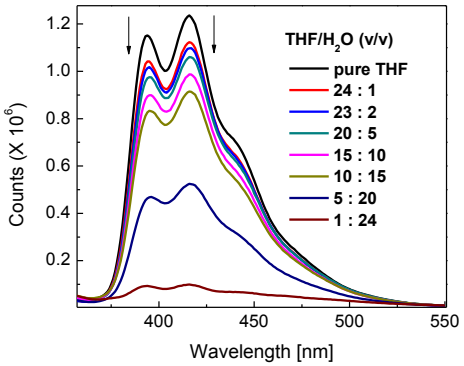

Figure 2.22: Fluorescence spectra of OPV **242** (21.1 μM) measured in a co-solvent system of THF and water at varied volumetric ratios (λ_{ex} = 335 nm).

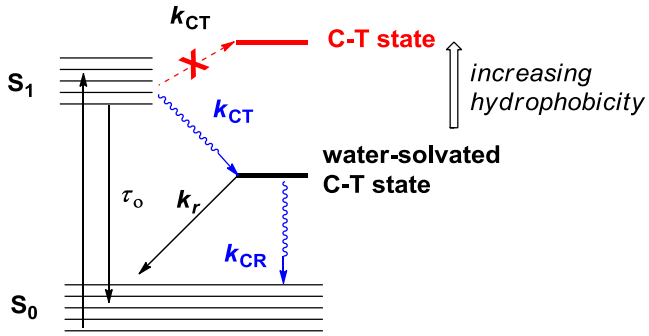

Figure 2.23: Jablonski diagram depicting the mechanism of environment-sensitive fluorescence for H-mers **197** and **198**.

The water-dependent emission behavior is indicative of H-mers **197** and **198** being environment-sensitive,[55-57] and it can be rationalized by the mechanism depicted in Figure 2.23. In the aqueous medium, water solvation stabilizes a charge-transfer (likely from OPV to triazole[58,59]) state to result in the attenuation of $S_1 \rightarrow S_0$ emission and the

emergence of a longer-wavelength C-T emission band. Increasing the hydrophobicity of the solvation environment destabilizes the C-T state and hence restores the $S_1 \rightarrow S_0$ emission.

2.4.7 Saccharides sensing of H-shaped OPV oligomers

The fluorescence sensing properties of H-mers **197** and **198** towards saccharides were investigated by fluorescence titration experiments. H-mers **197** and **198** due to the presence of tetrakis(phenylboronic acid) groups were readily dissolved in an aqueous phosphate buffer (pH 7.41) with the aid of a tiny amount of organic co-solvent DMSO (0.4% v/v). To these H-mer solutions, four selected saccharides, D-fructose, D-galactose, D-ribose, and D-glucose, were titrated respectively. The titration processes were monitored by fluorescence spectroscopy and detailed spectral data are given in Figure 2.24.

In the buffer solution, H-mer **197** gave a weak C-T emission at *ca*. 482 nm. Upon titration of D-fructose, the emission of **197** at 482 nm increased steadily, while a high-energy band at 432 nm assigned to the $S_1 \rightarrow S_0$ emission grew pronouncedly (Figure 2.24A). This trend is in line with the observation in Figure 2.21 (left) indicating that the binding of D-fructose with **197** caused a considerable perturbation to the solvation environment. The same trend of fluorescence changes was observed in the titration of **197** with D-galactose (Figure 2.24B). For the titration of D-ribose, the emission at 482 nm decreased slightly, while the emission at 432 nm grew moderately. The titration of D-glucose led to a moderate increase of emission at both 482 nm and 432 nm. Clearly, the

binding of **197** with D-ribose showed a very different fluorescence behavior than other saccharides, alluding to significant differences in the binding mode.

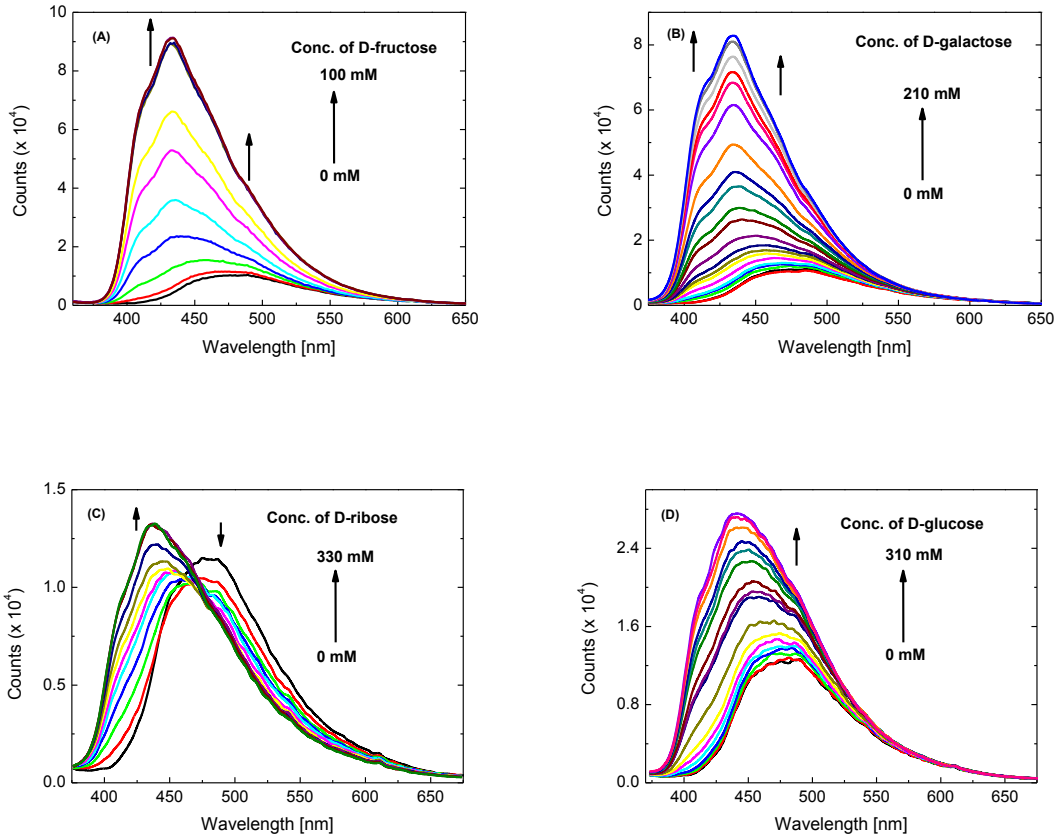

Figure 2.24: Fluorescence titration of H-mer **197** (7.67 µM) with (A) D-fructose, (B) D-galactose, (C) D-ribose, and (D) D-glucose in an aqueous phosphate buffer solution (pH 7.41) at 298 ± 3 K (λ_{ex} = 350 nm).

The fluorescence responses of H-mer **198** to D-fructose and D-galactose (Figure 2.25A and B) are similar to those of H-mer **197**. For the titration of D-ribose with **198**, the C-T emission band at *ca.* 474 nm was significantly quenched, while the $S_1 \rightarrow S_0$

emission band was not observed throughout the titration. Instead, an isosbestic point could be seen at 420 nm. For the titration of **198** with D-glucose, the fluorescence spectra were only slightly changed with a small degree of increase in intensity.

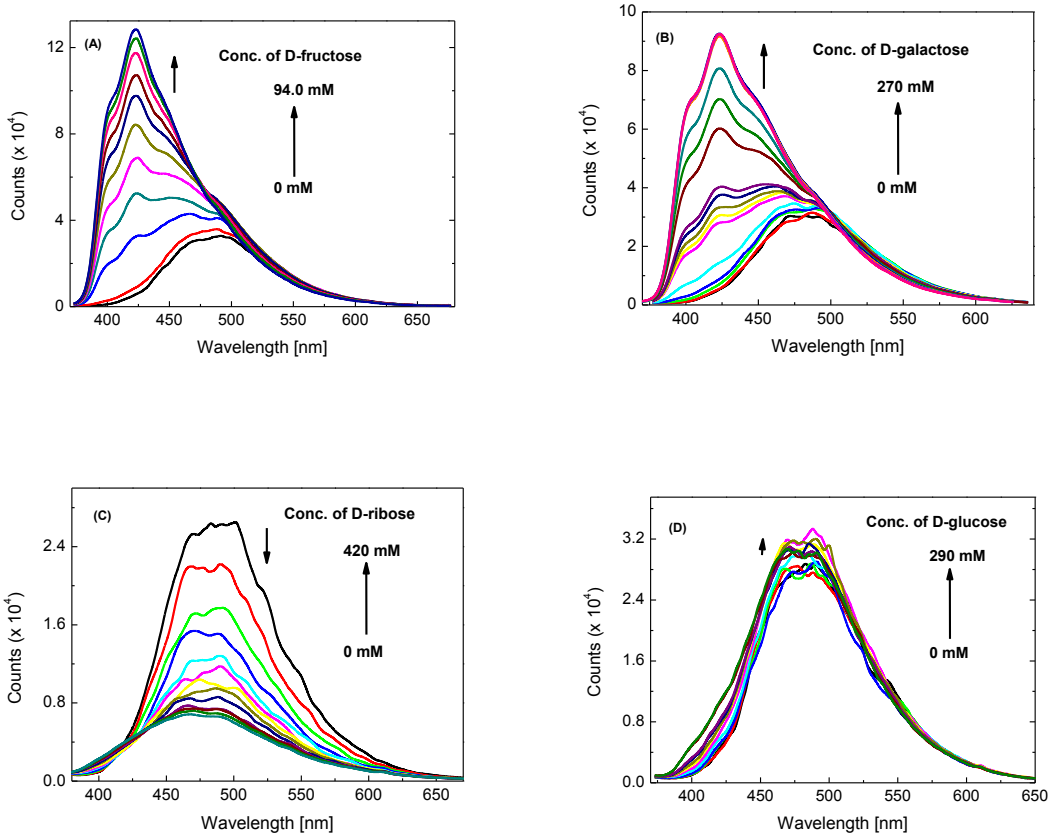

Figure 2.25: Fluorescence titration of H-mer **198** (7.36 μM) with (E) D-fructose, (F) D-galactose, (G) D-ribose, and (H) D-glucose in an aqueous phosphate buffer solution (pH 7.41) at 298 ± 3 K (λ_{ex} = 350 nm).

The fluorescence responses of H-mers **197** and **198** to various saccharides were further assessed in the form of a heat map (Figure 2.26), where the ratios of fluorescence

enhancement (I_s/I_o) for the C-T emission and $S_1 \rightarrow S_0$ bands at the saturation point of titration are depicted. The statistical patterns shown in Figure 2.26 clearly indicate the function of saccharide discrimination by using the two H-mers as fluorescent probes. Such a performance was not present with the short cruciform sensor **194** we previously devised. These results here manifest that proper tuning of the fluorophore unit can lead to improved and/or new sensor functions.

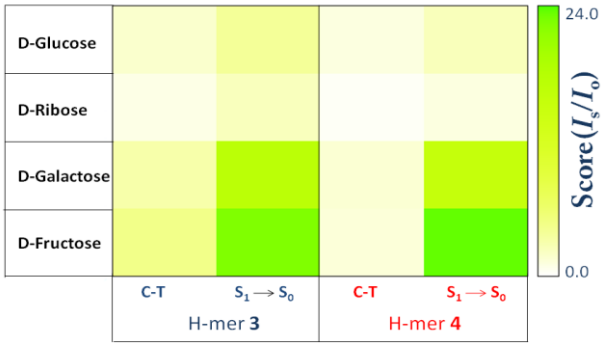

Figure 2.26: Heat map depicting the fluorescence enhancement (I_s/I_o) of the C-T emission and $S_1 \rightarrow S_0$ bands for H-mers **197** and **198** in interacting with four saccharides. I_o and I_s denote the fluorescence intensity measured at the initial and saturation points of titration respectively.

Finally, the fluorescence titration data were subjected to *SPECFIT* analysis to determine the binding stoichiometry and binding constants (Table 2.3). The obtained data shows that H-mer **197** has much greater affinity for saccharides than H-mer **198** does, which testifies to the significant influence of molecular shape on binding properties. The

UV-Vis titrations of H-shaped oligomers **197** and **198** with saccharides are presented in the appendix.

Table 2.3: Stability constants (*K*) for complexation of H-shaped oligomers **197**, and **198** with various saccharides determined by global spectral fitting

Oligomer	Saccharide	log K_1 (M^{-2})	log K_1K_2 (M^{-4})
197	D-fructose	4.78 ± 0.27	9.62 ± 0.14
	D- glucose	2.30 ± 0.091	4.90 ± 0.13
	D- ribose	weak response	weak response
	D- galactose	4.13 ± 0.44	7.33 ± 0.32
198	D-fructose	4.25 ± 0.18	7.72 ± 0.31
	D- glucose	weak response	weak response
	D- ribose	2.65 ± 0.071	4.89 ± 0.11
	D-galactose	4.04 ± 0.29	7.89 ± 0.31

2.4.8 Fluoride ion sensing of cruciform and linear-shaped oligomers

As mentioned earlier, the phenylboronate and phenylboronic acid derivatives, aside from their broad applications in synthetic chemistry, have also been extensively investigated as effective receptor units for anion sensors.[60] The boronate groups in

fluorophores **211**, **220**, and **226**, owing to their large Lewis acidity, are capable of interacting with hard bases, for example, fluoride anion [F^-], to form stable complexes.[61,62] If the complexation causes significantly altered photophysical properties, the fluorophores should give rise to sensing function to [F^-], the detection of which has been of great importance in biological applications.[60]

The interactions of [F^-] with the boronate ester groups in fluorophores **211**, **220**, and **226** were probed by titration of the fluorophores in THF (ca. 10^{-4} to 10^{-5} M) with *n*-Bu_4NF. The titrations were monitored by fluorescence spectroscopy, and the results are shown in Figure 2.27. The emission spectrum of short cruciform fluorophore **211** (Figure 2.27A) shows two vibronic bands at 437 and 455 nm. Upon titration with 4.5 molar equiv of *n*-BuN_4F, the fluorescence intensity of **211** was substantially quenched by ca. 98%, indicating a strong binding with [F^-]. In addition, the two emission bands were redshifted to 443 and 465 nm respectively. For the long cruciform fluorophore **220**, the fluorescence spectrum shows a broad single emission band at 448 nm. Upon [F^-] titration, the emission was attenuated and a notable redshift of the maximum emission peak (λ_{em}) from 448 to 460 nm was observed. After addition of 88 molar equiv of *n*-Bu_4NF, the fluorescence intensity was suppressed by ca. 87%.

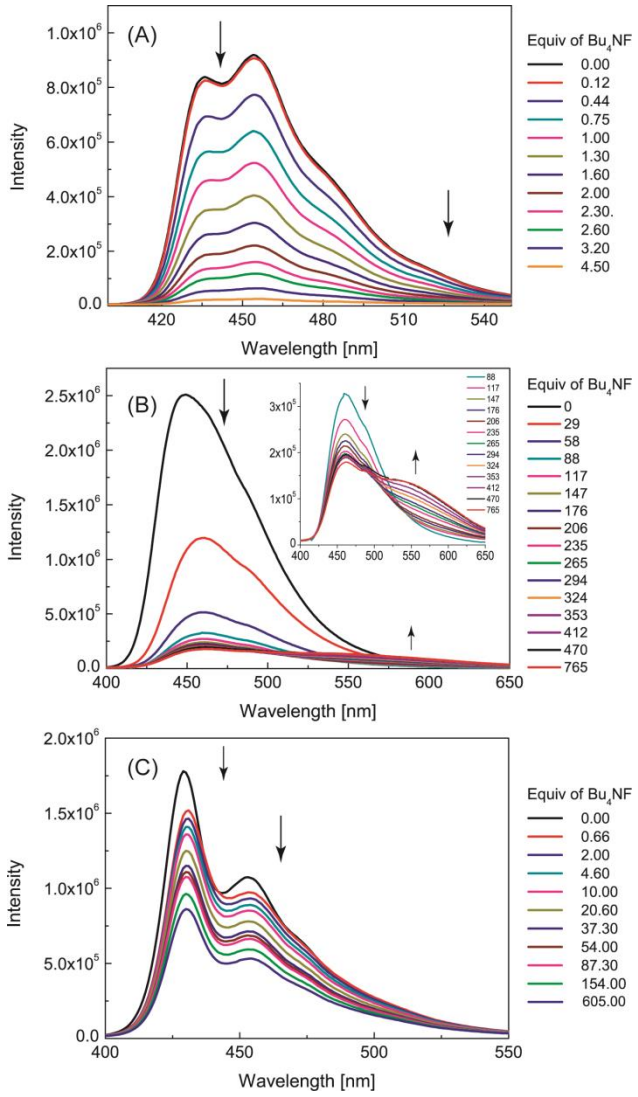

Figure 2.27: Fluorescence titration of boronate-oligomer fluorophores (10^{-4} – 10^{-5} M) with *n*-Bu_4NF in THF at 298 K. (A) Short cruciform **211** (λ_{ex} = 344 nm); (B) long cruciform **220** (λ_{ex} = 360 nm, the inset shows the spectra upon titration of Bu_4NF from 88 to 765 equiv); (C) linear fluorophore **226** (λ_{ex} = 365 nm).

Continued titration of **220** with *n*-Bu_4NF from 88 to 765 molar equiv resulted in only slightly reduced fluorescence intensity at 460 nm and a significant rise of a low-

energy band at 562 nm (Figure 2.27B). Like short cruciform **211**, the fluorescence of linear fluorophore **226** shows two distinctive vibronic bands at 429 and 453 nm. Addition of aliquots of *n*-Bu_4NF up to 605 molar equiv, however, only led to a moderate reduction of the fluorescence intensity (ca. 48% at λ_{em} = 429 nm), without causing any significant shifts of the emission bands (Figure 2.27C). From the fluorescence titration results, it is clear that the cruciform-shaped fluorophores **211** and **220** exhibit much better [F^-] sensing performances than the linear fluorophore **226** does. In particular, the short cruciform **211** shows the sensitivity that is far superior to the others.

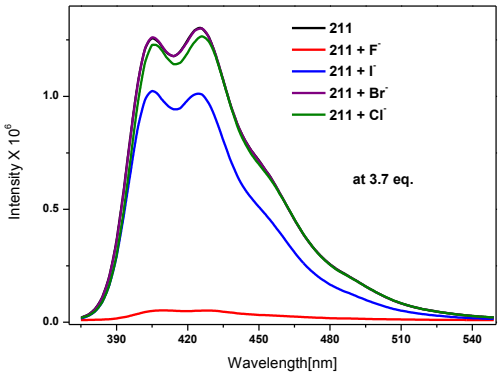

Figure 2.28: Comparision spectra of oligomer **211** with all halides (F^-, Cl^-, Br^-, and I^-) at 3.7 eq.

The fluorescence sensing properties of boronates **211**, **220** and **226** towards other halide anions such as Cl^-, Br^-, and I^- were tested in THF. As shown in Figures 2.29, 2.30, and 2.31, these halides caused very poor to medium fluorescence suppression during the titrations. For example in case of boronate **211**, at the saturation point, only F^- titration

(ca. 3.7 molar equiv) led to substantial fluorescence quenching (> 96%, Figure 2.28) with very large binding constants (Table 2.4), whereas other halide anions caused insignificant fluorescence suppression (*ca*. 0% for Cl^-, 3% for Br^-, and 22% for I^-). Similar trend was noticed with other two boronate oligomers **220** and **226** as well.

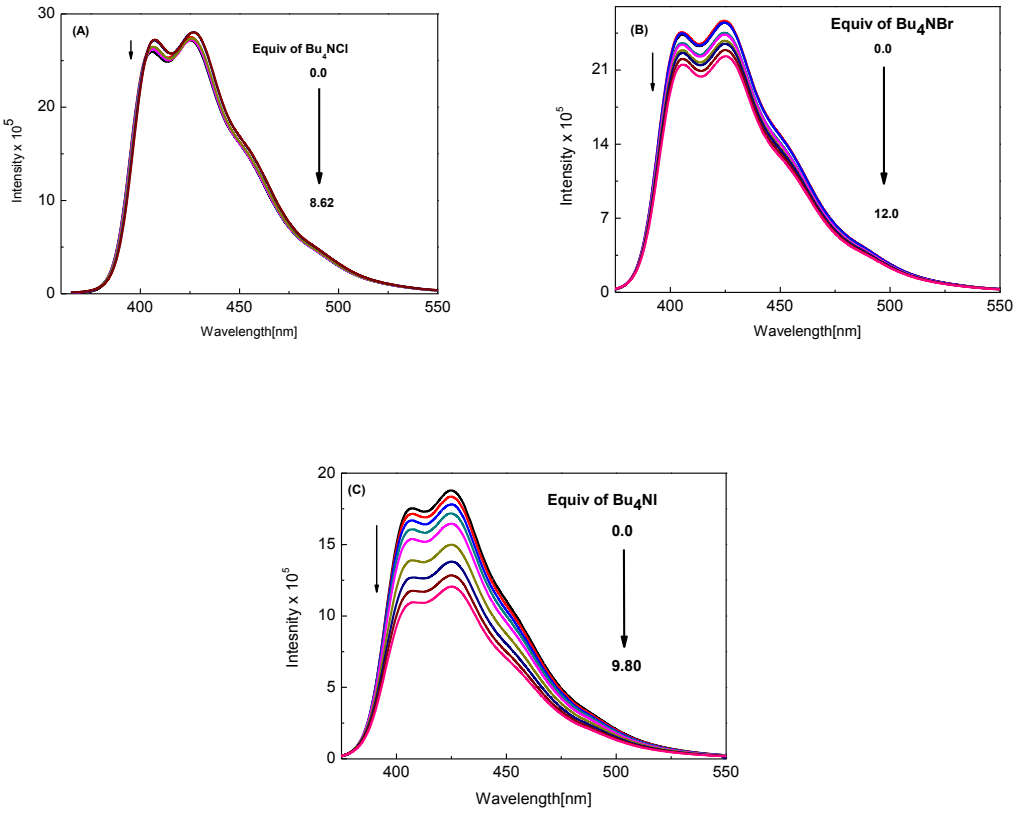

Figure 2.29: (A) Fluorescence titration of boronate-oligomer fluorophore **211** (36.0 µM) with *n*-Bu_4NCl (B) Fluorescence titration of boronate-oligomer fluorophore **211** (42.2 µM) with *n*-Bu_4NBr, and (C) Fluorescence titration of boronate-oligomer fluorophore **211** (38.6 µM) with *n*-Bu_4NI in THF at 298 K (λ_{ex} = 344 nm).

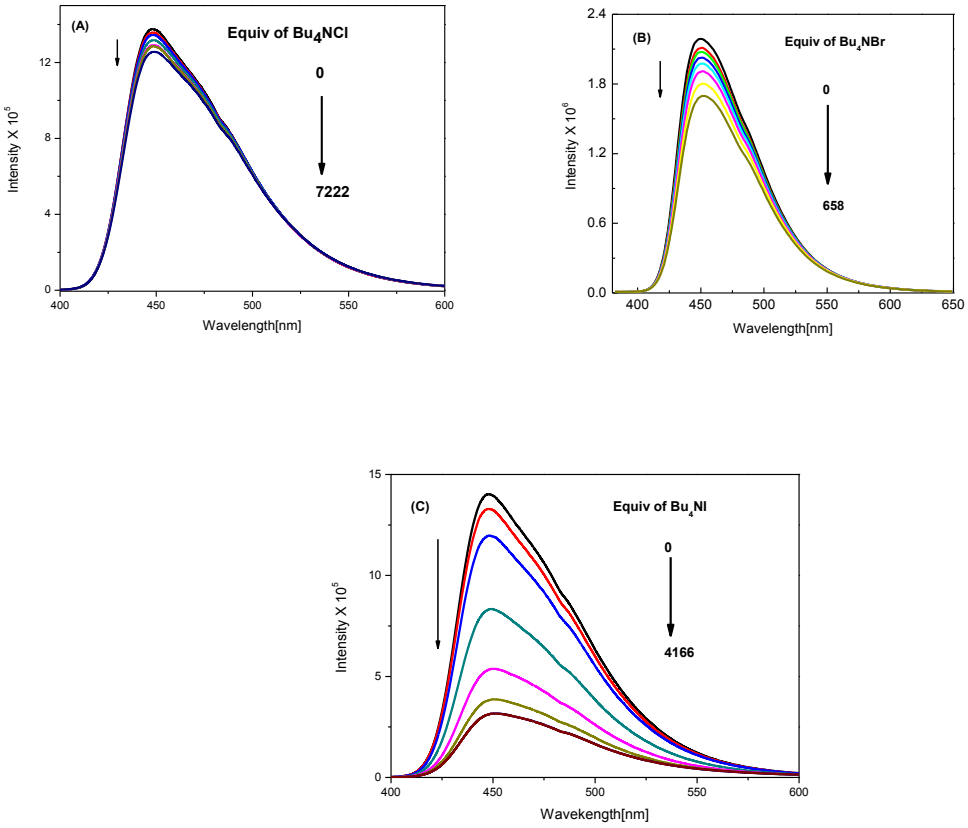

Figure 2.30: Fluorescence titration of boronate-oligomer fluorophore **220** (10.0 µM) with (A) *n*-Bu_4NCl (B) *n*-Bu_4NBr, and (C) *n*-Bu_4NI in THF at 298 K (λ_{ex} = 360 nm).

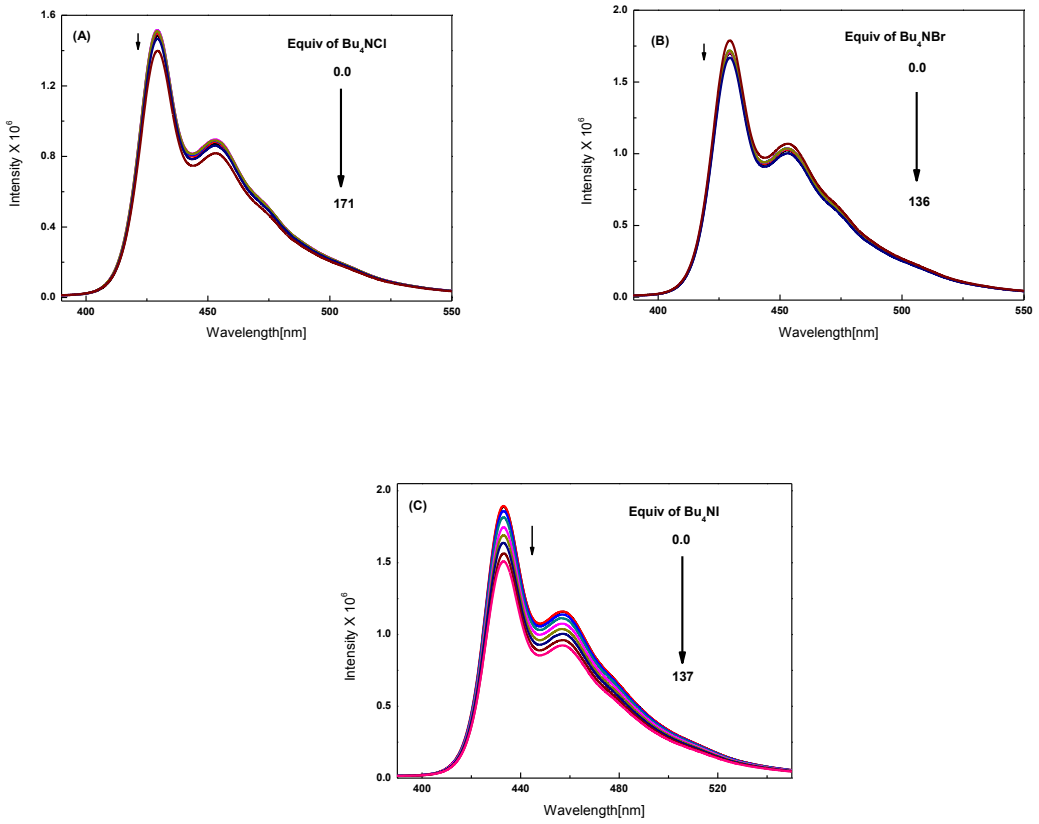

Figure 2.31: Fluorescence titration of boronate-oligomer fluorophore **226** (1.5 μM) with (A) *n*-Bu_4NCl (B) *n*-Bu_4NBr, and (C) *n*-Bu_4NI in THF at 298 K (λ_{ex} = 365 nm).

The fluorescence titration data of oligomers **211**, **220**, and **226** with fluoride ions was subjected to *SPECFIT* analysis to determine stability constants (Table 2.4). The data in Table 2.4 shows that the fluoride ions bind to all oligomers in a one-step mechanism with 1:2 binding stoichiometry.

Table 2.4: Stability constants (*K*) for complexation of cruciform **211, 220, and 226** with fluoride ions determined by global spectral fitting

Oligomer	Binding stoichiometry	log K_1 (M^{-2})
211	1:2	5.66 ± 0.62
220	1:2	4.32 ± 0.31
226	1:2	3.20 ± 0.14

2.4.8.1 NMR studies on cruciform 211

The binding of [F^-] with the boronate ester groups in short cruciform fluorophore **211** was further examined by ^1H and ^{19}F NMR titrations, the results of which indicated that the formation of a tetrahedral fluoro-boronate complex (Scheme 2.15) was the dominant product. Of particular note from the NMR data is that the triazole proton of **3** was considerably shifted from 8.08 to 8.81 ppm after binding with [F^-]. This observation agrees with molecular modeling studies, which suggest a strong fluorine-triazole interaction through a hydrogen-bond as proposed in Scheme 2.15 (the H-F distance is calculated as 2.39 Å). Theoretical calculations have also revealed that such an interaction not only modulated the electron density of the π-oligomer moiety to a significant extent (electrostatic potential maps in Scheme 2.15), but greatly altered its structural and frontier

molecular orbital (FMO) properties (Figure 2.34). These effects thus account for the fluorescence sensing behavior of short cruciform fluorophore **211** to fluoride ions. The UV-Vis titrations of oligomers **211**, **220**, and **226** with all halides are presented in appendix.

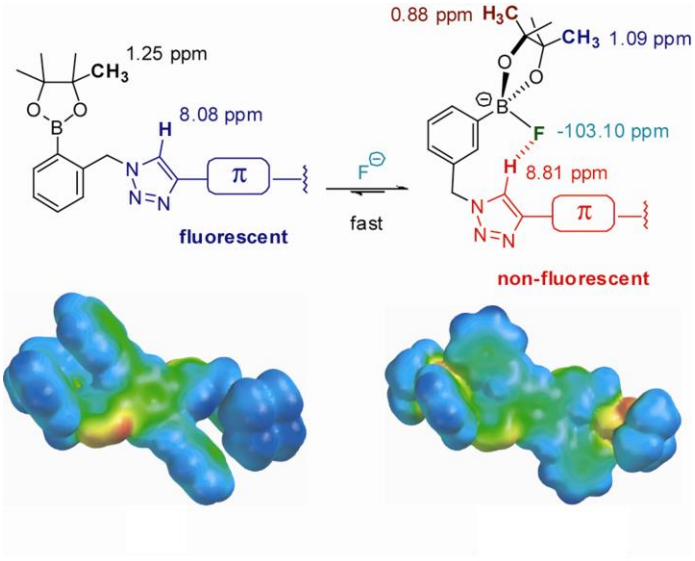

Scheme 2.15: Binding of fluoride ions with phenylboronate **211**.

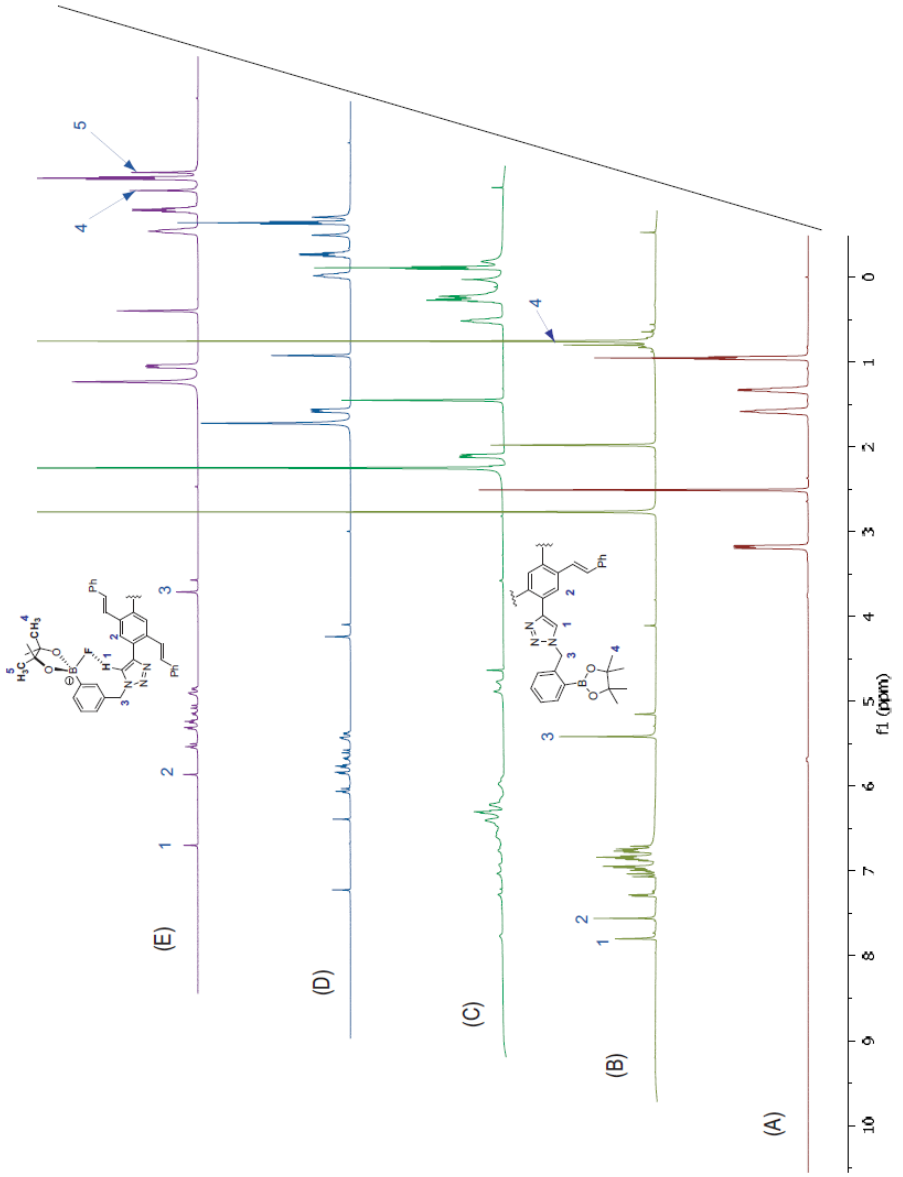

Figure 2.32: ^{1}H NMR (500 MHz, 1:4 CD_2Cl_2/DMSO-d_6) spectra of (A) Bu_4NF and compound **211** (10^{-2} M) in (B) the absence and in the presence of (C) 1.2, (D) 2.4, and (E) 3.6 molar equiv of Bu_4NF.

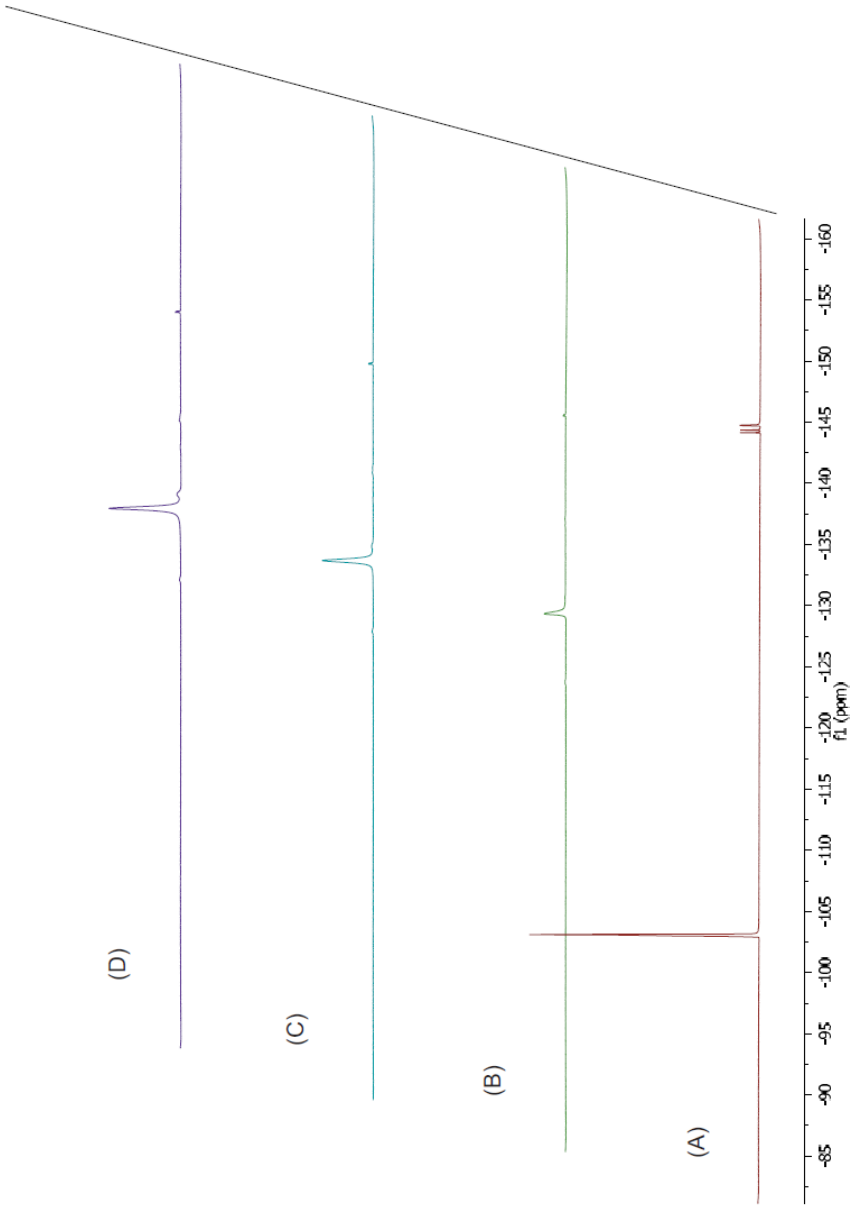

Figure 2.33: ^{19}F NMR (564 MHz) spectra of (A) Bu_4NF in DMSO-d_6 and compound **211** (10^{-2} M) in CD_2Cl_2/DMSO-d_6 (1:4, v/v) in the presence of (B) 1.0, (C) 2.0, and (D) 3.0 molar equiv of Bu_4NF.

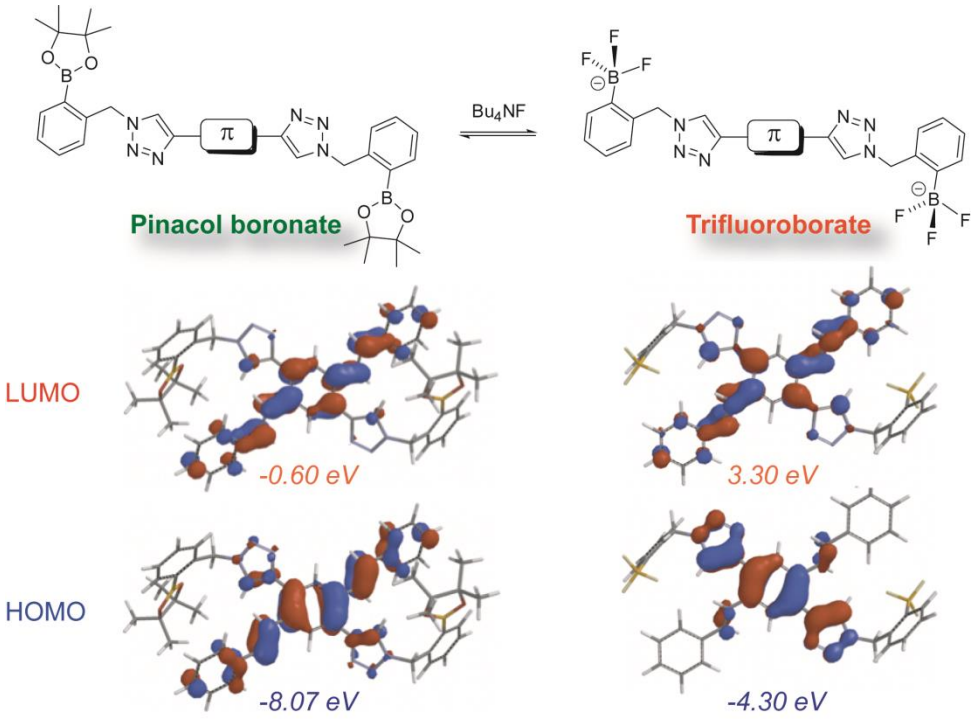

Figure 2.34: FMO plots of (left) cruciform oligomer **211** and (right) [**211** + 2F]$^{2-}$ complex calculated at the AM1 level of theory

2.4.9 Halide ion sensing of H-shaped oligomers

The fluorescence sensing properties of boronate oligomers **243** and **244** towards halide anions (F^-, Cl^-, Br^-, I^-) were tested in THF as similar to the cruciform oligomer **211**. The results from Figures 2.35 and 2.36 indicated that the oligomers **243** and **244** show similar response (fluorescence quenching) to the halides F^-, Cl^-, and Br^- as cruciform oligomer **211** does but with different concentrations of halide ions. We noticed that these oligomers **243** and **244** are more sensitive to fluoride ions than the cruciform

oligomer **211**. Unlike the cruciform **211**, the two H-shaped oligomers **243** and **244** are also sensitive to iodide ions.

The fluorescence titration data of oligomers **243** and **244** with fluoride ions and iodide ions was subjected to *SPECFIT* analysis to determine stability constants (Table 2.5). The data in Table 2.5 shows that the both fluoride ions as well as iodide ions bind to all oligomers in a two-step mechanism with 1:2 and 1:4 binding stoichiometry. The UV-Vis titrations of H-shaped oligomers **243** and **244** with halides are presented in the appendix.

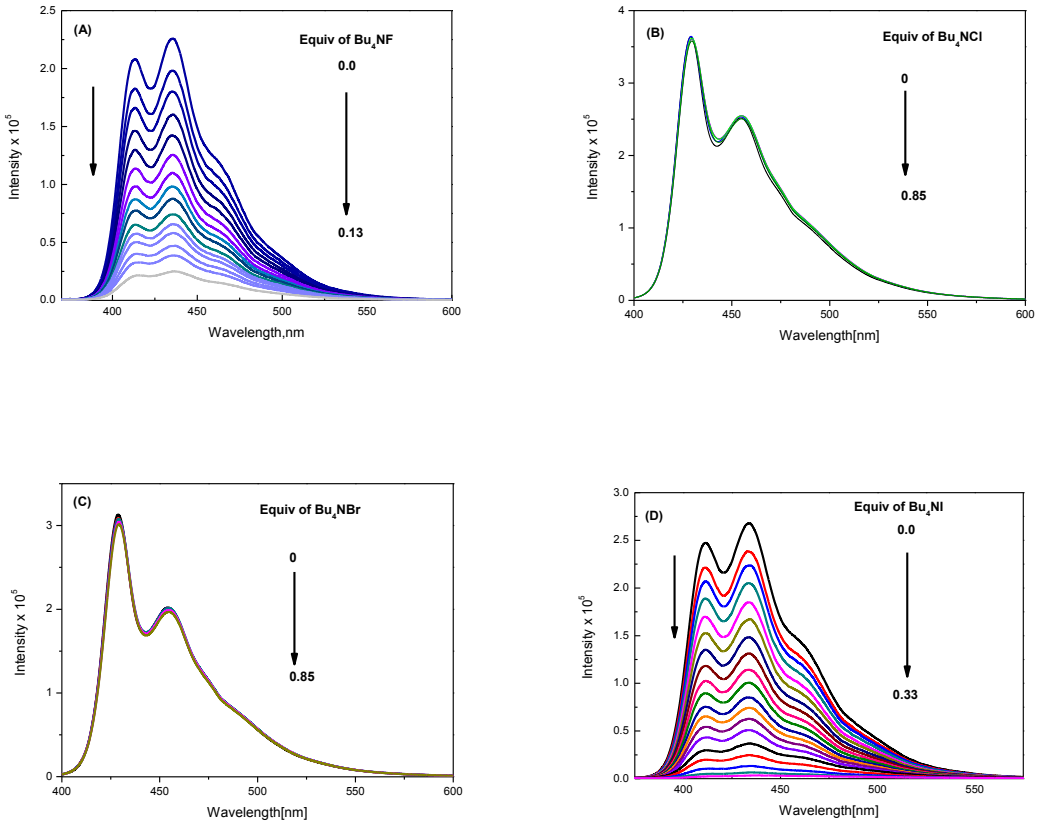

Figure 2.35: Fluorescence titration of boronate-oligomer fluorophore **243** (8.86 µM) with (A) *n*-Bu_4NF, (B) *n*-Bu_4NCl, (C) *n*-Bu_4NBr, and (D) *n*-Bu_4NI in THF at 298 K (λ_{ex} = 360 nm).

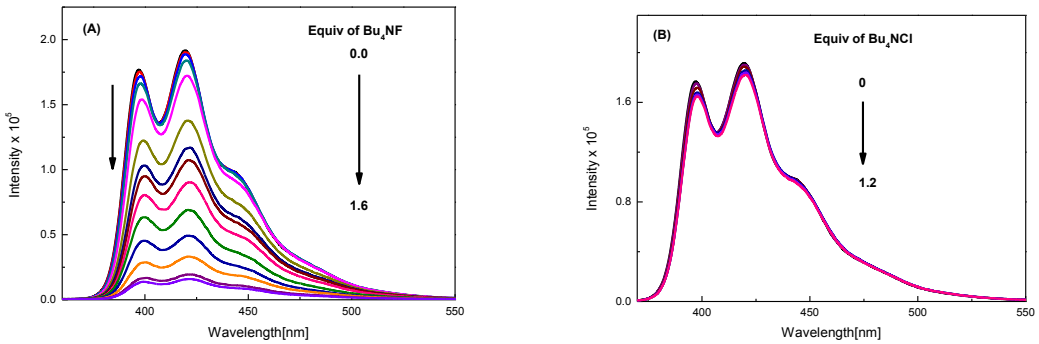

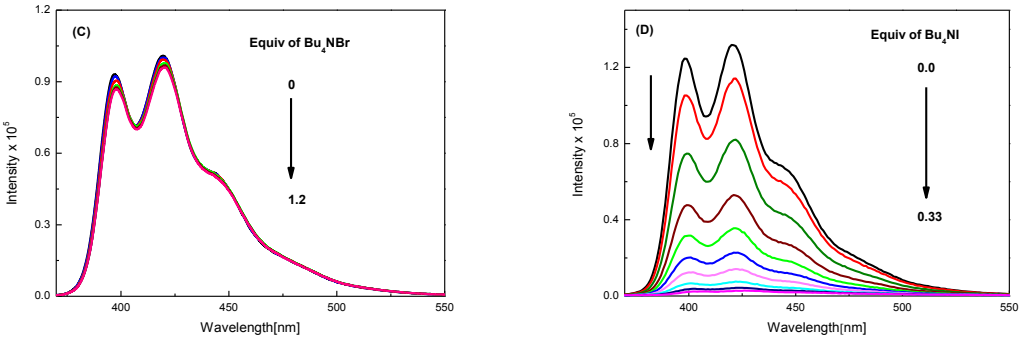

Figure 2.36: Fluorescence titration of boronate-oligomer fluorophore **244** (4.51 μM) with (A) *n*-Bu_4NF, (B) *n*-Bu_4NCl, (C) *n*-Bu_4NBr, and (D) *n*-Bu_4NI in THF at 298 K (λ_{ex} = 365 nm).

Table 2.5: Stability constants (*K*) for complexation of oligomers **243**, and **244** with fluoride and iodide ions

Oligomer	Halide	log K_1 (M^{-2})	log K_1K_2 (M^{-4})
	Fluoride	5.11 ± 0.27	9.11 ± 0.31
197	Iodide	4.07 ± 0.48	7.11 ± 0.30
	Fluoride	4.92 ± 0.47	9.53 ± 0.25
198	Iodide	4.30 ± 0.20	8.09± 0.18

2.4.10 The role of triazole

As a recap from the previous sections, being a linker, the triazole unit plays a significant role in saccharide, as well as fluoride ion, sensing properties. According to the modeling studies, for saccharide sensing, in binding with a 1,2-diol, the triazolyl unit adjacent to the phenylboronic acid group acts as a ligand (hydrogen bond acceptor) to coordinate with a molecule of water. This water insertion model is proposed as analogous to the binding motif of the "Wulff-type" boronic acid receptor in aqueous media. To provide another piece of evidence, we have resynthesized a model compound **245**, according to the literature procedure reported by James and co-workers (Figure 2.37), and performed ^{1}H NMR studies in different solvents.

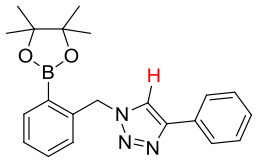

245

Figure 2.37: Molecular structure of model compound **245**.

As seen from Figure 2.39, by changing the solvent from $CDCl_3$ to DMSO-d_6, the triazole proton shifted downfield from 7.74 ppm to 8.49 ppm (difference of about 0.75 ppm). This result indicates that there is strong deshielding on the triazole moiety. This deshielding can't be induced by simply changing solvent from $CDCl_3$ to DMSO-d_6, as the solvent interactions are purely non-specific in nature and attributable to dipole-dipole interactions, resulting in a less than 0.1 ppm shift. As shown in Figure 2.40, it can be predicted that the water present in DMSO-d_6 can co-ordinate with the triazole and cause a significant shift of the triazole proton only. Methylene protons (from 5.91 to 5.87 ppm) and other aromatic protons are less affected by the effect caused by water coordination with boron and triazole. Experimentally, the methylene protons are observed to give less than 0.1 ppm shift when changing the solvent from $CDCl_3$ to DMSO-d_6.

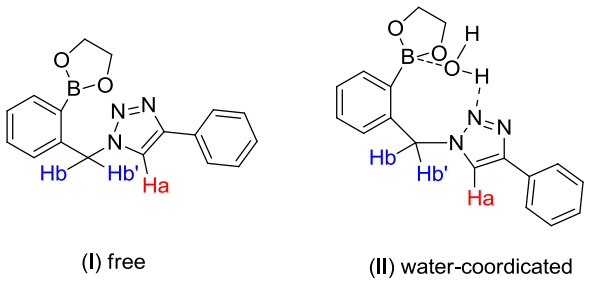

(**I**) free (**II**) water-coordicated

Figure 2.38: Model compound **245** in its free and water-coordinated state.

To shed more light on the solvation and water coordination effects on ^{1}H NMR shifts in the model compound **245**, DFT calculations were conducted. As indicated in Table 2.6, the experimentally observed shift of the methylene protons (-0.04 ppm) in $CDCl_3$ and DMSO-d_6 is consistent with the theoretically calculated value (-0.12 ppm) in the case that the model compound is in the "free" form (I) (Figure 2.38). However, the experimental observed shift of the triazolyl proton (0.75 ppm) from $CDCl_3$ to DMSO-d_6 is considerably greater than the theoretical prediction on the free form (which is 1.92 ppm). Obviously, another stronger effect than solvent polarity is at work. In modeling the water-coordinated form (II) (Figure 2.38), the solvent-dependent shift of the methyl protons (-0.33 pm) appears to be in a reasonable agreement with the experimental value (-0.04 ppm). In the meantime, a significant downfield shift of the triazolyl proton (1.92 ppm) is predicted by the DFT calculations. Although this theoretical value calculated from the water-coordinated model is more than double that of the experimental value, the trend of shift is indeed consistent from one to the other. Moreover, the DMSO-d_6 solvent used contains only a small amount of water, therefore the observed 0.75 ppm shift is mostly likely resulting from an average of "water-bound" and "free" forms in the solution. So far, the solvent-dependent NMR studies concur with the water-insertion modeling proposed in Figure 2.16.

Table 2.6: Theoretical and experimental values of triazolyl and methylene protons.

Solvent	δ (ppm) in $CDCl_3$	δ (ppm) in DMSO-d_6	Δδ (ppm)
Triazolyl proton (exp)	7.74	8.49	0.75
Methylene protons (exp)	5.91	5.87	-0.04
Triazolyl proton (theor)	8.31*	8.42	0.11
Methylene protons (theor) (average of two protons)	5.89*	6.01	-0.12
Triazolyl proton (theor, water-coordinated)	--	10.23	--
Methylene protons (theor, average of two protons, water-coordinated)	--	6.22	--
Triazolyl proton (theor, Fluoride-coordinated)	8.42*	8.55	
Methylene protons (theor, average of two protons, water-coordinated)	4.78*	5.36	

* CH_2Cl_2 was chosen as the solvent in lieu of $CDCl_3$ for the NMR theoretical calculations.

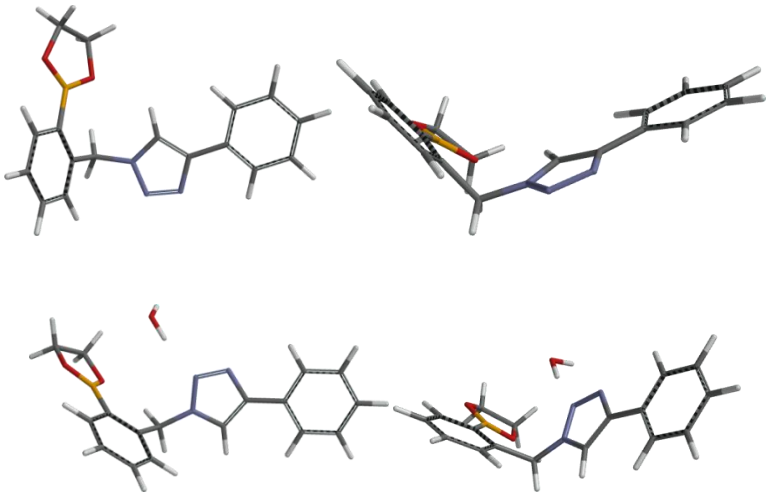

Figure 2.39: (Top) Optimized structure (B3LYP/6-31G*) for [**245**] in DMSO. (E = -996.100106 au, dipole moment = 8.29 Debye), (bottom) Optimized structure (B3LYP/6-31G*) for [**245** + $\mathbf{H_2O}$] in gas phase. (E = -1073.52637 au, dipole moment = 6.14 Debye).

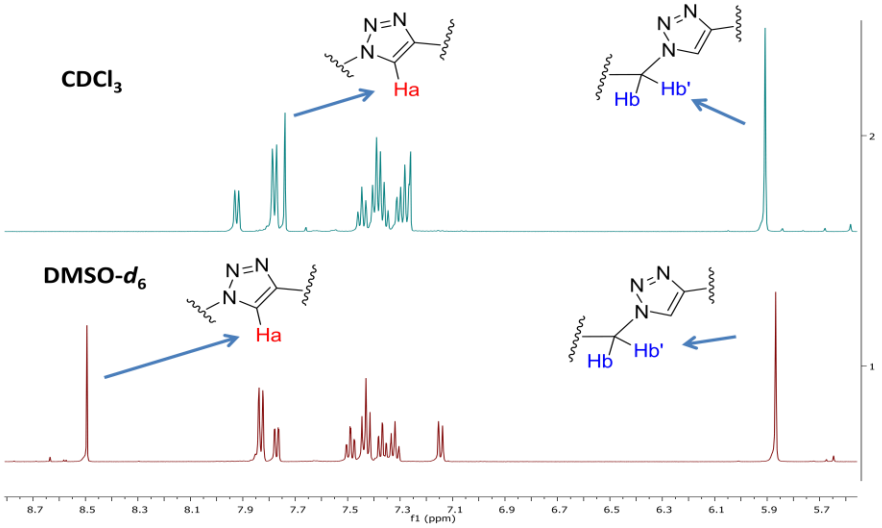

Figure 2.40: Partial ^{1}H NMR spectra of model compound **245** in both DMSO-d_6 and $CDCl_3$.

In another experiment, we performed ^{1}H NMR titrations on model compound **245** with TBAF, in both $CDCl_3$ and DMSO-d_6, to study the binding effect on the triazole proton in the presence of fluoride ions. In $CDCl_3$, as the titration progressed, the triazole proton gradually shifted from 7.74 to 8.64 ppm, a 0.9 ppm shift (Figure 2.41). There is strong hydrogen bonding between the fluoride attached to the boron atom and the triazole proton. This is consistent with the modeling studies proposed in Scheme 2.15. However, in DMSO-d_6, the difference in the shift of triazole proton before and after the fluoride

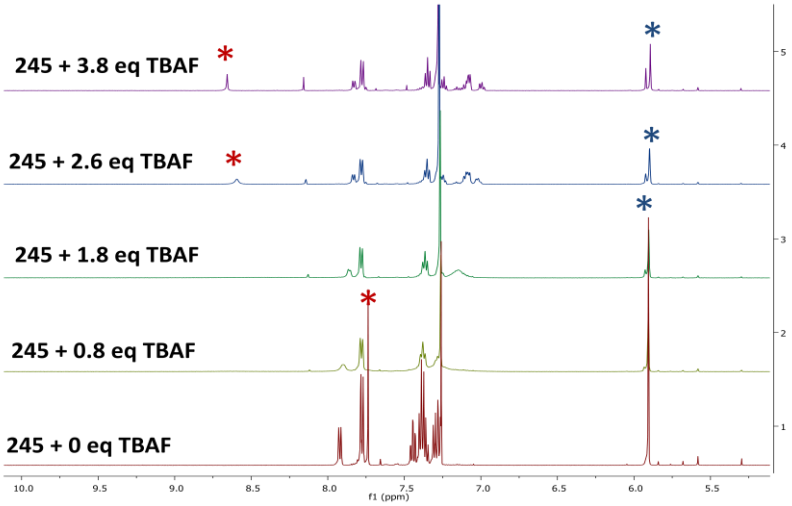

Figure 2.41: Partial ^{1}H NMR spectra of compound **245** in titration with TBAF in $CDCl_3$ showing the aromatic region. Signals labeled by * refers to the triazolyl proton and methylene protons.

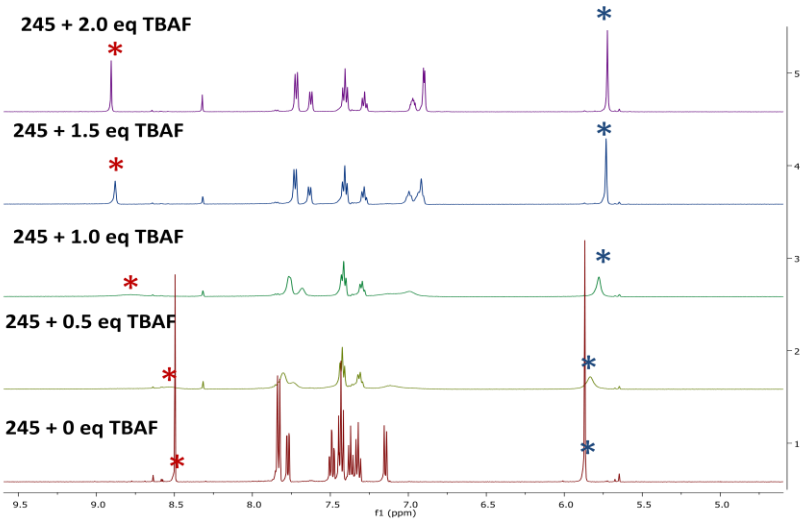

Figure 2.42: Partial ^{1}H NMR spectra of compound **245** in titration with TBAF in DMSO-d_6 showing the aromatic region. Signals labeled by * refers to the triazolyl proton and methylene protons.

addition is considerably reduced, from 8.49 to 8.91 ppm, a 0.4 ppm shift (Figure 2.42). Once again, the different magnitudes of triazolyl proton shifts upon addition of fluoride ion in $CDCl_3$ and DMSO-d_6 support the previous conclusion that the model compound exists in a free form in $CDCl_3$ and a water-bound form in DMSO-d_6. If otherwise (i.e., the model compound stays mainly in free form in DMSO-d_6), the coordination of the boron center with fluoride ion should give a similar degree of downfield shift of triazolyl proton in the two solvents.

2.5 Conclusions

In this chapter, we have prepared a series of fluorescent saccharide sensors **194-198** made up of π-conjugated oligomers click functionalized with phenylboronic acids, in

order to take advantage of the synthetic modularity and efficiency of click chemistry as well as the unique ligand effect of the 1,2,3-triazolyl linker resulting from the click reaction. Electronic and spectroscopic properties of the all oligomers were investigated by UV-Vis absorption and fluorescence spectroscopic characterizations. Cruciform **194** was found to show fluorescence turn-on sensing function for saccharides in an aqueous buffer solution at physiological pH (7.41) with high sensitivity. Of particular interest is that when the oligomer fluorophore was switched to a linear-shaped oligo(phenylene ethylene) (OPE) unit, the saccharide sensing function was diminished completely. The marked difference between cruciform **194** and other two oligomers **195** and **196** in fluorescent sensing for saccharides thus underscores that the *nature of fluorophore with a proper structural design is a determinative factor in controlling the sensory performance*.

As mentioned in the previous sections, a plethora of boronic acid-based sensor systems was reported to operate via mechanisms involving photoinduced electron transfer (PET) and internal charge transfer (ICT). However, these mechanisms appear to be inadequate in accounting for the sensing behavior of cruciform **194**. Previously, we speculated that the sensing mechanism of **194** was tied to de-aggregation processes, but the parameters governing the de-aggregation process remains unclear. To address these issues, we investigated the fluorescent sensing properties of two structurally isomeric H-shaped tetrakis(phenylboronic acid)-OPV hybrids (H-mers **197** and **198**) as model systems with different saccharides. The results from the titrations evidenced that these H-shaped oligomers **197** and **198** can not only detect saccharides at neutral pH, but also they discriminate between various saccharides. The environment-sensitive fluorescence

behavior exhibited by the two H-mers enabled effective sensing and discrimination of various saccharides in neutral water media.

In addition, we have also investigated molecular properties of boronate-appended oligomers **211**, **220**, **226**, **243**, and **244** with halide ions. The titration results have clearly proved that cruciform-shaped boronate-oligomer fluorophores and H-shaped oligomers show better fluoride ion sensing performances than the linear one. In summary, the facile synthesis and remarkable sensor performance of these π-conjugated oligomers for saccharides and fluoride anion respectively attest to a wide-ranging applicability of the "click" functionalization method in the development of new boron-based chemosensors.

2.6 Experimental

Chemicals were purchased from commercial suppliers and used directly without purification. All reactions were conducted in standard, dry glassware and under an inert atmosphere of nitrogen unless otherwise noted. Evaporation and concentration were carried out with a water-aspirator. Flash column chromatography was performed using 240-400 mesh silica gel, and thin-layer chromatography (TLC) was carried out with silica gel F254 covered on plastic sheets and visualized by UV light. Melting points (m.p.) were measured with Fisher-Jones melting point apparatus and are uncorrected. ^{1}H and ^{13}C NMR, and ^{19}F NMR spectra were measured on a BrukerAvance 500 MHz spectrometer and BrukerAvance III 300 MHz multinuclear spectrometer. Chemical shifts are reported in ppm downfield from the signal of the internal reference $SiMe_4$ for ^{1}H and ^{13}C NMR spectra. Coupling constants (*J*) are given in Hz. Infrared spectra (IR) were

recorded on a Bruker tensor 27 spectrometer. UV-Vis-NIR absorption spectra were measured on a Cary 6000i spectrophotometer. Atomic force microscopy (AFM) images were taken with a Q-Scope AFM operated in tapping mode. MALDI-TOF MS analyses were performed on an Applied Biosystems Voyager instrument using dithranol as the matrix.

2,5-Diiodo-*p*-xylene (200)

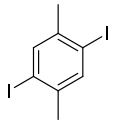

200

To a solution of *p*-xylene **199** (10.0 g, 94.2 mmol), and H_5IO_6 (8.95 g, 39.3 mmol) in water (37.5 mL), H_2SO_4 (5.50 mL), and acetic acid (185 mL) was added iodine (19.1 g, 75.1 mmol). The resulted dark mixture was heated at 100 ^oC under stirring for 4 h. Water (250 mL) was then added and the flask was cooled in ice bath to promote crystallization of the product. The crude product was filtered, washed with water, and recrystallized from acetone to give pure compound **200** as a white solid (22.9 g, 61.9 mmol, 68%). ^1H NMR ($CDCl_3$, 500 MHz): δ 7.65 (s, 2H), 2.34 (s, 6H); The data are consistent with those reported in the literature.[63]

1,4-Bis(bromomethyl)-2,5-diiodobenzene (201)

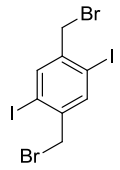

201

To a solution of Compound **200** (10.0 g, 0.0280 mol) in chloroform was added NBS (22.0 g, 0.124 mol), and benzoylperoxide (0.500 g, 2.06 mmol) and then refluxed under a bright light irradiation for 4h. The solution was then allowed to stand overnight at rt for a complete crystallization of the product. The product was filtered together with the succinimide byproduct. Removal of the succinimide by water rinsing afforded the crude product **201**, which was further purified by recrystallization from chloroform and hexane to yield compound **201** as a white solid (2.92 g, 5.66 mmol, 20%). ^{1}H NMR ($CDCl_3$, 500 MHz): δ 7.90 (s, 2H), 4.48 (s, 4H); The data are consistent with those reported in the literature.[63,64]

1,4-Bis(diethylphosphoromethyl)-2,5-diiodobenzene (202)

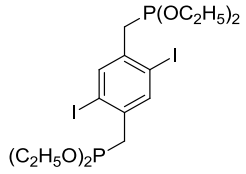

202

Compound **201** (1.83 g, 3.55 mmol) and triethylphosphite (7.40 mL, 46.2 mmol) were taken into a round bottomed flask and refluxed for 3 h. Colorless crystals were formed while cooling the mixture to rt. The excess triethylphosphite was decanted, and the remaining white solid was washed by hexanes multiple times at rt to completely

remove the unreacted triethylphosphite and then dried under vaccum to afford pure compound **202** as a white solid (1.87 g, 2.96 mmol, 83%). ^{1}H NMR ($CDCl_3$, 500 MHz): δ 7.88 (s, 2H), 4.11-4.06 (m, 8H), 3.33 (d, $J_{H,P}$ =20.5 Hz, 4H), 1.29 (t, J = 7.0 Hz, 12H); The data are consistent with those reported in the literature.[63,64]

1,4-Bis((*E*)-2-styryl))-2,5-diiodobenzene (203)

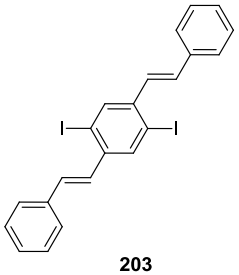

203

To a solution of compound **202** (1.20 g, 1.89 mmol) in dry THF (20 mL) was added NaH (0.114 g, 4.80 mmol) in small portions at 45 ^{o}C under N_2 atmosphere. The solution gradually turned into a vivid purple-red color. Benzaldehyde (0.45 mL, 4.16 mmol) dissolved in THF (10 mL) was added in small portions over a period of 30 min through a syringe. The reaction was kept under stirring and heating for another 2 h before work-up. The reaction mixture was carefully quenched with water and extracted three times with chloroform. The chloroform layer was washed by brine, dried over $MgSO_4$, and concentrated to precipitation. The residual was crystallized from hexanes to yield compound **203** as yellow crystals (0.64 g, 1.20 mmol, 63%). ^{1}H NMR ($CDCl_3$, 500 MHz): δ 8.09 (s, 2H), 7.57 (d, J = 7.5 Hz, 4H), 7.40 (t, J = 7.3 Hz, 4H), 7.31 (t, J = 7.15 Hz, 2H), 7.22 (d, J = 16.0 Hz, 2H), 7.00 (d, J = 16.1 Hz, 2H); The data are consistent with those reported in the literature.[64,65]

1,4-Bis(E-styryl)-2,5-bis(trimethylsilylethynyl)benzene (204)

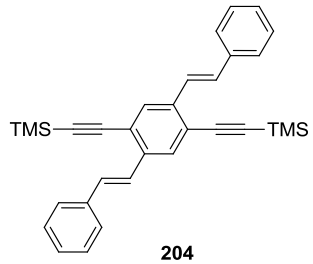

204

Compound **203** (0.40 g, 0.74 mmol), trimethylsilylacetylene (0.42 mL, 3.0 mmol), $PdCl_2(PPh_3)_2$ (26 mg, 0.036 mmol), and CuI (14 mg, 0.073 mmol), were added to THF (10 mL), and Et_3N (10 mL) mixture. The solution was bubbled by N_2 at rt for 5 min, and then stirred at 45 ^oC under N_2 protection overnight. After the reaction was complete as checked by TLC analysis, the solvent was removed in vaccum. The resulting residue was diluted with ethyl acetate, and then was filtered through a $MgSO_4$ pad. The solution obtained was sequentially washed by aq HCl (10%) and brine. The organic layer was dried over $MgSO_4$ and concentrated under vacuum to give a crude product of **204**. The crude product was then purified by silica flash column chromatography (hexanes/CH_2Cl_2, 95:5) to give compound **204** (0.31 g, 0.65 mmol, 87%) as a yellow solid. ^1H NMR ($CDCl_3$, 500 MHz): δ 7.81 (s, 2H), 7.61 (d, *J* = 16.0 Hz, 2H), 7.54 (d, *J* = 7.5 Hz, 4H), 7.38 (t, *J* = 6.5 Hz, 4H), 7.29 (t, *J* = 7.5 Hz, 2H), 7.23 (d, *J* = 16.0 Hz, 2H), 0.33 (s, 18H); The data are consistent with those reported in the literature.[66]

1,4-Diethynyl-2,5-di-(*E*)-styrylbenzene (205)

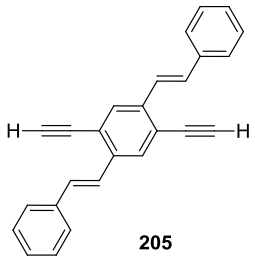

205

To a solution of compound **204** (0.380 g, 0.800 mmol) in 1:1 MeOH/THF (15 mL) was added K_2CO_3 (0.633 g, 4.57 mmol). After being stirred at rt for 30 min, the reaction mixture was diluted with excess water and extracted in $CHCl_3$ two times. The organic layer was washed with water, dried over $MgSO_4$, and concentrated under vacuum to give a crude product of **205**. The crude was purified by silica flash column chromatography (hexanes/CH_2Cl_2, 90:10) to yield compound **205** as a yellow solid (0.227 g, 0.688 mmol, 86%). ^{1}H NMR ($CDCl_3$, 500 MHz): δ 7.87 (s, 2H), 7.59-7.55 (m, 6H), 7.38 (t, *J* = 6.5 Hz, 4H), 7.30 (t, *J* = 6.5 Hz, 2H), 7.19 (d, *J* = 16.0 Hz, 2H), 3.48 (s, 2H); The data are consistent with those reported in the literature.[66]

***o*-tolylboronic acid (207)**

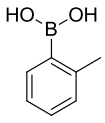

207

To a solution of 2-bromotoluene **206** (5.00 g, 29.2 mmol) in dry THF (100 mL) was added *n*-BuLi (13 mL, 1.2 M, 2.17 g, 33.9 mmol) slowly over a period of 30 min at -78 ^{o}C. Then the reaction mixture was stirred for 1 h at same temperature. This was then added trimethylborate (6.4 mL, 5.96 g, 57.8 mmol) and allow the reaction stirred at rt for

2 hrs before it was quenched with aqueous 1M HCl. The obtained cloudy solution was extracted into ethyl acetate and washed with water two times. The organic layer was separated and dried over $MgSO_4$, and concentrated under vaccum to give crude product **207**. This was further purified by washing with hexanes to afford pure compound **207** as white solid (2.86 g, 21.0 mmol, 72%). ^{1}H NMR ($CDCl_3$, 500 MHz): δ 8.23 (d, *J* = 7.4 Hz, 1H), 7.46 (td, *J* = 7.4, 1.4 Hz, 1H), 7.33-7.27 (m, 2H), 2.82 (s, 3H). The data are consistent with those reported in the literature.[67]

4,4,5,5-tetramethyl-2-o-tolyl-1,3,2-dioxaborolane (208)

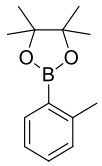

208

Compound **207** (1.20 g, 8.82 mmol), and pinacol (1.25, 10.6 mmol) were added in toluene (100 mL), and refluxed for 2 h by using dean and stark condenser. The reaction was then allowed to cool to rt and washed with water three times. The solvent was dried over $MgSO_4$ and concentrated under vaccum to afford pure product **208** as colorless liquid (1.61 g, 7.38 mmol, 84%). TLC matched with authentic sample,[67] and proceeded to the next step.

4,4,5,5-tetramethyl-2-o-tolyl-1,3,2-dioxaborolane (209)

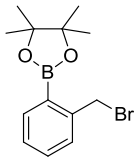

209

To a solution of compound **208** (1.30 g, 5.96 mmol) in acetonitrile (50 mL) was added NBS (1.51 g, 8.88 mmol), and AIBN (15 mg, 0.091 mmol). The reaction mixture was stirred and heated to 100 ^{o}C for 4 h. The solvent was removed under reduced vaccum to give crude product **209**, which was dissolved in ethylacetate and washed several times with water. The organic layer was separated and dried over $MgSO_4$ and concentrated under vaccum to afford pure product **209** as low melting solid (1.51 g, 5.08 mmol, 84%). ^{1}H NMR ($CDCl_3$, 500 MHz): δ 7.82 (d, *J* = 7.2 Hz, 1H), 7.42-7.38 (m, 2H), 7.30-7.28 (m, 1H), 4.98 (s, 2H), 1.38 (s, 12H). The data are consistent with those reported in the literature.[46,67]

azido-pendant phenylboronate (210)

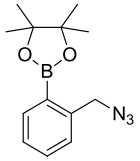

210

To a solution of compound **209** (2.0 g, 6.73 mmol) in dry DMF (15 ml) was added NaN_3 (0.870 g, 13.4 mmol) and stirred at rt for 3 h. After the reaction was monitored by TLC, water was added and the compound was extracted into ether (100 mL). The organic layer was washed with cold water to remove traces of DMF and dried

over $MgSO_4$ and removed under vaccum to afford pure compound **210** as colorless liquid (1.58 g, 6.09 mmol, 91%). ^{1}H NMR ($CDCl_3$, 500 MHz): δ 7.89 (d, *J* = 7.2 Hz, 1H), 7.46 (t, *J* = 7.2 Hz, 1H), 7.35-7.22 (m, 2H), 4.66 (s, 2H), 1.36 (s, 12H). The data are consistent with those reported in the literature.[67]

Pinacolyl boronate-attached cruciform OPV (211)

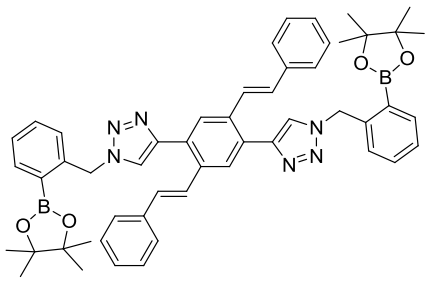

Compound **205** (100 mg, 0.302 mmol), azidophenylboronate **210** (180 mg, 0.695 mmol), and diisopropylethylamine (0.026 mL, 0.151 mmol) were dissolved in DMF (2 mL). The solution was deoxygenated by bubbling N_2 at rt for 5 min, and then CuI (5.76 mg, 0.030 mmol) was added. The reaction mixture was heated at 60 ^{o}C overnight. After the reaction was complete as checked by TLC analysis, the solvent was removed under reduced pressure. The obtained residue was diluted with EtOAc and was subsequently filtered through a $MgSO_4$ pad to remove the inorganic salts. The filtrate was sequentially washed with brine and water. The organic layer was dried with $MgSO_4$ and concentrated under vacuum to give crude product **211**, which was further purified by silica flash column chromatography (EtOAC/hexanes, 3:7) to yield pure compound **211** (177 mg, 0.208 mmol, 69%) as a pale yellow solid. m.p. 191-192 ^{o}C; IR (neat): 2979, 1652, 1598, 1491, 1382, 1348, 1167 cm−1; ^{1}H NMR (500 MHz, CD_2Cl_2): δ 8.08 (s, 2H), 7.89 (d, *J* =

7.3 Hz, 2H), 7.79 (s, 2H), 7.48 (td, *J* = 7.6, 1.2 Hz, 2H) 7.40-7.31 (m, 14H) 7.26 (t, *J* = 7.1 Hz, 2H) 7.14 (d, *J* = 16.2 Hz, 2H), 5.94 (s, 4H), 1.25 (s, 24H); ^{13}C NMR (125 MHz, $CDCl_3$): δ 145.8, 140.8, 137.3, 136.7, 134.9, 131.9, 130.9, 129.4, 128.7, 127.9, 127.6, 127.1, 126.6, 126.3, 123.3, 84.1, 53.4, 24.7 (two peaks fewer than expected due to coincidental peak overlap); HRMS (MALDI-TOF) m/z Calcd for $C_{52}H_{54}B_2N_6O_4$, 848.4393; Found, 849.4525 $[M + H]^+$.

Boronic acid-attached cruciform OPV oligomer (194)

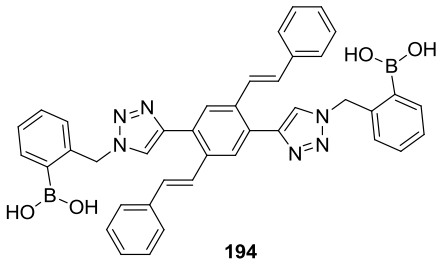

194

To a solution of compound **211** (100 mg, 0.117 mmol) and *o*-tolylboronic acid **207** (96.1 mg, 0.707 mmol) in dioxane (10 mL) was added aqueous HCl (5M, 3 mL). The mixture was stirred and heated at 100 ^{o}C overnight. After the reaction was complete as checked by TLC analysis, the dioxane was removed under reduced pressure. The resulting solid was washed with water and air-dried to afford crude product **194**, which was further purified by recrystallization from MeOH to give pure compound **194** (66.9 mg, 0.097 mmol, 83%) as an off white solid. m.p. 254 - 255 ^{o}C; IR (neat): 3573, 1690, 1658, 1598, 1493, 1442, 1357, 1267 cm−1; ^{1}H NMR (500 MHz, DMSO-d_6): δ 8.42 (s, 2H), 8.36 (s, 4H), 8.09 (s, 2H), 7.68 (d, *J* = 7.3 Hz, 2H), 7.59 (d, *J* = 16.3 Hz, 2H), 7.50 (d, *J* = 7.5 Hz, 4H), 7.42-7.28 (m, 12H), 7.19 (d, *J* = 7.6 Hz, 2H), 5.91 (s, 4H); ^{13}C NMR

(125 MHz, DSMO-d_6): δ 144.9, 139.7, 137.0, 136.0, 134.4, 134.1, 130.4, 130.3, 129.6, 129.1, 128.8, 128.7, 128.3, 128.0, 127.9, 127.7, 127.0, 126.5, 125.8, 124.4, 66.2, 53.0; HRMS (MALDI-TOF) m/z Calcd for $C_{40}H_{34}B_2N_6O_4$, 684.2828; Found, 685.2951 $[M + H]^+$.

1,4-Bis(decyloxy)benzene (213)

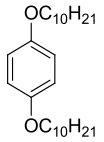

213

1-Bromodecane (13.7g, 61.9 mmol), 1,4-dihydroquinone **212** (3.40 g, 30.9 mmol) and KOH (4.35 g, 77.4 mmol) were added into EtOH (90 mL) and refluxed for 4 h. The reaction was cooled down. Water and CH_2Cl_2 were added. The organic layer was isolated, washed by brine, and dried over $MgSO_4$. After the solvent was removed in vaccum, a pale brown solid was obtained. The solid was recrystallized from methanol to give **213** as white solid (9.59 g, 24.4 mmol, 79%). ^{1}H NMR ($CDCl_3$, 500 MHz): δ 6.82 (s, 4H), 3.90 (t, *J* = 7.0 Hz, 4H), 1.78-1.72 (m, 4H), 1.46-1.41 (m, 4H), 1.38-1.29 (m, 24H), 0.88 (t, *J* = 6.0 Hz, 6H); The data are consistent with those reported in the literature.[63]

1,4-Bis(decyloxy)-2,5-diiodobenzene (214)

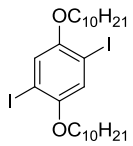

214

To a solution of compound **213** (8.60 g, 22.0 mmol) in CH_2Cl_2 (150 ml) were added $Hg(OAc)_2$ (19.5 g, 61.3 mmol), and I_2 (15.5 g, 61.0 mmol). The dark reaction mixture was stirred overnight at rt, then the formed slurry was filtered through a $MgSO_4$ pad, and rinsed with CH_2Cl_2. The filtrate was washed with $Na_2S_2O_3$ (10% aq), satd. $NaHCO_3$, water, brine, and dried over $MgSO_4$. The solvent was removed in vaccum and the crude product was recrystallized from ethanol to afford product **214** as colorless flakes (11.3 g, 17.6 mmol, 80%). ^{1}H NMR ($CDCl_3$, 500 MHz): δ 7.17 (s, 2H), 3.92 (t, *J* = 6.5 Hz, 4H), 1.82-1.77 (m, 4H), 1.53-1.46 (m, 4H), 1.35-1.28 (m, 24H), 0.88 (t, *J* = 7.0 Hz, 6H); The data are consistent with those reported in the literature.[68]

1,4-Bis(decyloxy)-2-iodo-5-(trimethylsilylethynyl)benzene (215)

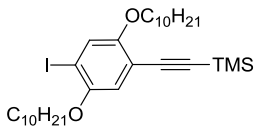

215

Compound **214** (6.50 g, 10.6 mol), trimethylsilylacetyelene (0.850 mL, 6.36 mmol), $PdCl_2(PPh3)_2$ (160 mg, 0.228 mmol), CuI (95.0 mg, 0.500 mmol), Et_3N (20 mL) were added to THF (60 mL). The solution was bubbled by N_2 at rt for 5 min and then stirred at 45 ^oC under N_2 protection overnight. After the reaction was complete as checked by TLC analysis, the solvent was removed under vaccum. To the obtained residue was added EtOAc, and the mixture was filtered through a $MgSO_4$ pad. The filtrate was sequentially washed with aq HCl (10%) and brine. The organic layer was dried with $MgSO_4$ and concentrated under vacuum to afford the crude product, which

was then purified by silica flash column chromatography (hexanes/CH_2Cl_2, 90:10) to yield compound **215** (2.97 g, 4.79 mmol, 48%) as light yellowish solid. ^{1}H NMR ($CDCl_3$, 500 MHz): δ 7.25 (s, 1H), 6.83 (s, 1H), 3.93 (t, *J* = 6.5 Hz, 4H), 1.82-1.75 (m, 4H), 1.53-1.48 (m, 4H), 1.34-1.28 (m, 24H), 0.88 (t, *J* = 6.5 Hz, 6H), 0.25 (s, 9H); The data are consistent with those reported in the literature.[68]

((2,5-Bis(decyloxy)-4-((triisopropylsilyl)ethynyl)phenyl)ethynyl)trimethylsilane (216)

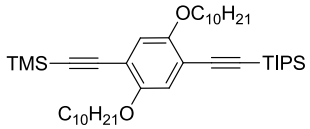

216

Compound **215** (2.20 g, 3.59 mmol), triisopropylsilylacetylene (1.68 mL, 3.93 mmol), $PdCl_2(PPh3)_2$ (0.107 g, 0.152 mmol), and CuI (53.6 mg, 0.286 mmol), and were added to Et_3N (40 mL). The solution was bubbled by N_2 at rt for 5 min and then stirred at 45 ^oC under N_2 protection for overnight. After the reaction was complete as checked by TLC analysis, the solvent was removed by rotary evaporation. To the obtained residue was added chloroform. The mixture was filtered over a $MgSO_4$ pad. Then it was sequentially washed by aq HCl (10%) and brine. The organic layer was dried over $MgSO_4$ and concentrated under vacuum. The crude product was then purified with silica flash column chromatography (hexanes/CH_2Cl_2, 90:10) to yield compound **216** (2.12 g, 3.30 mmol, 88%) as a light yellow solid. The TLC matched with an authentic sample,[63] and the material was used in the next step.

((2,5-Bis(decyloxy)-4-ethynylphenyl)ethynyl)triisopropylsilane (217)

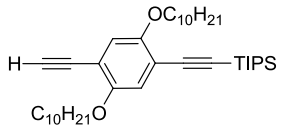

217

To a solution of compound **216** (1.0 g, 1.5 mmol) in 1:1 MeOH/THF (20 mL) was added K_2CO_3 (0.11 mg, 0.82 mmol) and stirred at rt for 30 min. After the reaction was monitored by TLC, the reaction mixture was diluted in chloroform and sequentially washed by aq HCl (10%) and brine. The organic layer was dried over $MgSO_4$. Filtration to remove $MgSO_4$ followed by evaporation under vacuum afforded the crude product which was purified with silica flash column chromatography (hexanes/EtOAc 98:2) to yield compound **217** as pale yellow solid (0.81 g, 1.4 mmol, 91%). TLC matched with authentic sample,[63] and proceeded to the next step.

1,4-Di(E-styryl)-2,5-bis(2,5-bis(decyloxy)-4-triisopropylsilylethynylphenylethynyl) benzene (218)

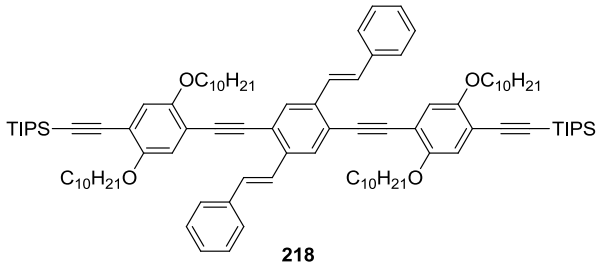

218

Compound **203** (0.50 g, 0.93 mmol), **217** (1.4 g, 2.3 mmol), $PdCl_2(PPh_3)_2$ (19.0 mg, 0.027 mmol), CuI (8.0 mg, 0.042 mmol) were added to THF (30 mL), and Et_3N (60 mL) mixture. The solution was bubbled by N_2 at rt for 5 min, and then stirred at 45 ^oC under N_2 protection for overnight. The reaction mixture was diluted with ethylacetate and

then filtered through a $MgSO_4$ pad. The solution obtained was sequentially washed by aq HCl (10%) and brine. The organic layer was dried over $MgSO_4$ and concentrated under vacuum. The crude product was washed with acetone and dried under vaccum to yield compound **218** (1.1 g, 0.75 mmol, 81%) as a yellowish solid. ^{1}H NMR ($CDCl_3$, 500 MHz): δ 7.91 (s, 2H), 7.76 (d, *J* = 16.5 Hz, 2H), 7.58 (d, *J* = 6.5 Hz, 4H), 7.35 (t, *J* = 7.5 Hz, 4H), 7.29-7.24 (m, 4H), 7.01 (s, 2H), 6.99 (s, 2H), 3.98 (t, *J* = 7.0 Hz, 4H), 3.92 (t, *J* = 6.5 Hz, 4H), 1.82-1,73 (m, 8H), 1.53-1.14 (m, 98H), 0.88-0.84 (m, 12H). The data are consistent with those reported in the literature.[66]

1,4-Bis(E-styryl)-2,5-bis(2,5-bis(decyloxy)-4-ethynylphenylethynyl)benzene (219)

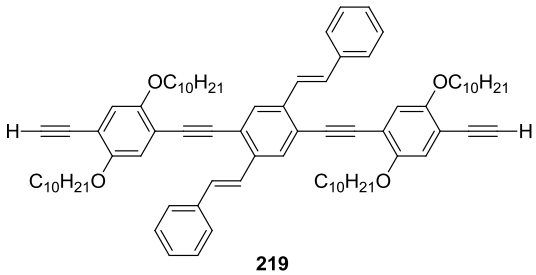

219

To a solution of compound **218** (0.41 g, 0.28 mmol) in THF (40 mL) was added TBAF (0.17 g, 0.55 mmol) and stirred at rt for 30 min. After the reaction was monitored by TLC, the reaction solvent was removed by rotary evaporation. The residue was dissolved in chloroform and sequentially washed by aq HCl (10%) and brine. The organic layer was dried over $MgSO_4$. Filtration to remove $MgSO_4$ followed by evaporation under vacuum afforded the crude product which was washed acetone and dried under vaccum to afford compound **219** as yellow solid (0.29 g, 0.25 mmol, 92%). ^{1}H NMR ($CDCl_3$, 500

MHz): δ 7.92 (s, 2H), 7.75 (d, *J* = 16.5 Hz, 2H), 7.58 (d, *J* = 7.5 Hz, 4H), 7.36 (t, *J* = 7.5 Hz, 4H), 7.29-7.24 (m, 4H), 7.05 (s, 2H), 7.03 (s, 2H), 4.04-4.01 (m, 8H), 3.37 (s, 2H), 1.86-1.71 (m, 8H), 1.53-1.16 (m, 56H), 0.88-0.84 (m, 12H); The data are consistent with those reported in the literature.[66]

Pinacolyl boronate-attached OPV/OPE oligomer (220)

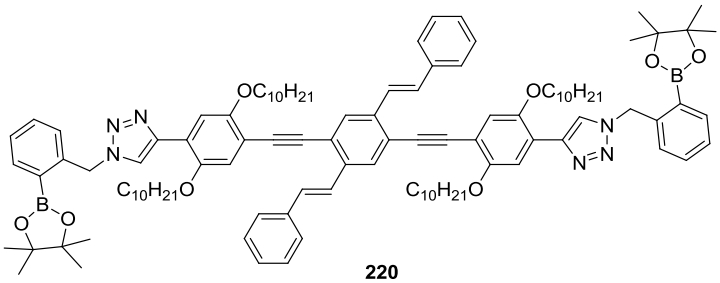

220

Compound **219** (250 mg, 0.216 mmol), compound **210** (185 mg, 0.713 mmol) and DIPEA (0.018 ml, 0.108 mmol) were dissolved in dry THF (10 ml). The solution was degassed by bubbling N_2 at rt for 5 min. Then CuI (8.23 mg, 0.043 mmol) was added, and the reaction mixture was heated at 60 ^oC for overnight. On completion as checked by the TLC analysis, the solvent was removed under reduced pressure. The obtained residue was diluted with CH_2Cl_2 and filtered through a $MgSO_4$ pad. Then the filtrate was sequentially washed with brine and water. The organic layer was dried with $MgSO_4$ and concentrated under vaccum to give crude **220**, which was further purified by silica flash column chromatography (ethyl acetate/ hexane, 2:8) to yield pure compound **220** (214 mg, 0.208 mmol, 59%) as a pale yellow solid. m.p 175 – 176 ^oC; IR (Neat) 2921, 2113, 1601, 1553, 1467, 1443, 1387, 1357, 1271, 1144; ^1H NMR (500 MHz, CD_2Cl_2): δ 8.02 (s, 2H), 7.98

(s, 2H), 7.95 (s, 2H), 7.91 (dd, *J* = 7.4, 1.1 Hz, 2H), 7.79 (d, *J* = 16.4 Hz, 2H, alkenyl H), 7.62 (d, *J* = 7.4 Hz, 4H), 7.44 (dt, *J* = 7.6, 1.4 Hz, 2H), 7.39-7.27 (m, 10H), 7.16 (d, *J* = 7.8 Hz, 2H), 7.14 (s, 2H), 5.93 (s, 4H), 4.18 (t, *J* = 6.7 Hz, 4H), 4.02 (t, *J* = 6.7 Hz, 4H), 1.83-1.71 (m, 8H), 1.49-1.43 (m, 4H), 1.34 (s, 24H), 1.31-1.18 (m, 52H), 0.88 (t, *J* = 7.1 Hz, 6H), 0.83 (t, *J* = 7.2 Hz, 6H); ^{13}C NMR (125 MHz, $CDCl_3$): δ 154.3, 148.7, 142.6, 140.9, 137.4, 137.3, 136.6, 131.7, 130.45, 128.7, 128.66, 128.63, 127.8, 127.7, 126.9, 126.1, 123.8, 122.6, 121.3, 116.2, 112.2, 111.5, 92.6, 92.3, 84.1, 69.7, 68.9, 31.9, 31.8, 29.59, 29.55, 29.36, 29.33, 29.31, 29.30, 29.2, 26.0, 25.9, 24.8, 22.69, 22.67, 14.2; MALDI-TOF MS m/z calcd. for $C_{108}H_{142}B_2N_6O_8$ 1673.108, found 1674.126 $[M + H]^+$.

Trifluoroborate-attached cruciform OPV/OPE oligomer (221)

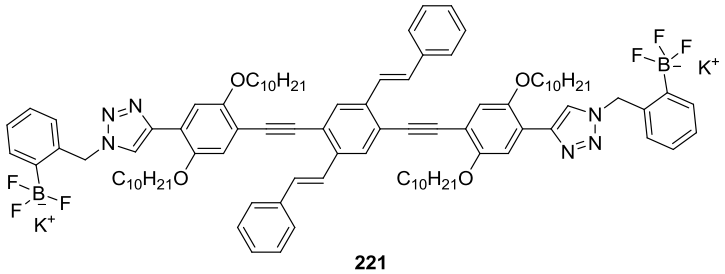

221

Compound **220** (100 mg, 0.059 mmol) in MeOH (5 ml) and THF (5 ml) was added to aqueous potassium hydrogen difluoride (0.8 ml, 3M, 2.36 mmol) within a plastic beaker. The resulting pale yellow color slurry was stirred at rt for overnight. After the reaction was complete as checked by the TLC analysis, the solvent was removed under reduced pressure gave residue. This was then dissolved in hot acetone and filtered, the filtrate was concentrated under vaccum. The obtained crude was crystallized in ether and hexane (1:1) mixture to afford compound **221** (84.0 mg, 0.051 mmol, 86%) as yellow

color solid. m.p. 268 – 270 ^{o}C; IR (Neat) 3407, 2040, 1597, 1466, 1385, 1339, 1059; ^{1}H NMR (500 MHz, DMSO-d_6): δ 8.30 (s, 2H), 8.06 (s, 2H), 7.87 (s, 2H), 7.74 (d, *J* = 16.4 Hz, 2H), 7.65 (d, *J* = 7.1 Hz, 4H), 7.54 (d, *J* = 16.3 Hz, 2H), 7.49 (d, *J* = 6.7 Hz, 2H), 7.41 (t, *J* = 7.4 Hz, 4H), 7.31 (t, *J* = 7.1 Hz, 2H), 7.24 (s, 2H), 7.09-7.02 (m, 4H), 6.89 (d, J = 7.2 Hz, 2H), 5.71 (s, 4H), 4.15 (t, *J* = 6.3 Hz, 4H), 4.03 (t, *J* = 6.4 Hz, 4H), 1.73-1.65 (m, 8H), 1.43-1.36 (m, 4H), 1.28-1.05 (m, 52H), 0.85 (t, *J* = 7.0 Hz, 6H), 0.75 (t, *J* = 7.3 Hz, 6H); ^{13}C NMR (125 MHz, $CDCl_3$): δ 154.4, 149.2, 141.9, 138.8, 137.67, 137.61, 133.0, 131.8, 129.5, 129.1, 129.0, 127.7, 127.6, 126.9, 126.62, 126.61, 125.5, 122.8, 122.3, 117.1, 112.0, 111.6, 93.8, 92.6, 74.3, 70.0, 69.4, 53.8, 32.19, 32.13, 29.91, 29.87, 29.84, 29.7, 29.6, 29.5, 29.4, 29.2, 26.44, 26.42, 25.8, 22.97, 22.95, 14.8, 14.7.

Boronic acid-attached cruciform OPV/OPE oligomer (195)

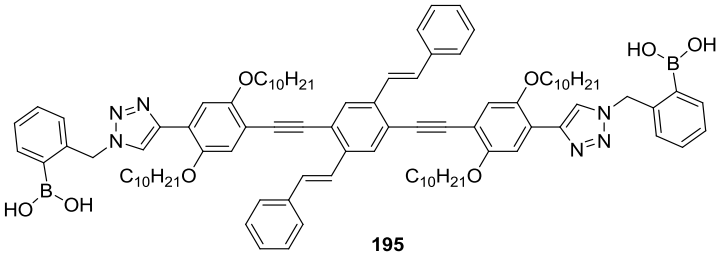

195

To a solution of Compound **221** (65.0 mg, 0.039 mmol) in acetonitrile (5 ml), THF (5 ml) and water (0.05 ml, 2.73 mmol), was added trimethylsilyl chloride (0.1 ml, 0.795 mmol). The resulting clear yellow solution was stirred at rt for overnight. After the reaction was complete as checked by the TLC analysis, the reaction mixture was poured in to water and the obtained solid was filtered and dried. The crude was crystallized in ether and hexane mixture (1:1) to yield pure compound **195** (48.6 mg, 0.032, 81%) as

pale yellow solid. m.p. 205 – 206 ^{o}C; IR (Neat) 3539, 2205, 1598, 1468, 1386, 1272, 1051; ^{1}H NMR (500 MHz, 4:1 acetone-d_6/DMSO-d_6): δ 8.41 (s, 2H), 8.07 (s, 2H), 8.01 (d, J = 8.98, 6H), 7.89-7.85 (m, 4H), 7.72 (d, J = 7.5 Hz, 4H), 7.54 (d, J = 16.4 Hz, 2H), 7.46-7.39 (m, 6H), 7.36-7.32 (m, 4H), 7.28 (s, 2H), 7.24 (d, J = 7.7 Hz, 2H), 5.97 (s, 4H), 4.22 (t, J = 6.3 Hz, 4H), 4.13 (t, 6.5 Hz, 4H), 1.87-1.77 (m, 8H), 1.54-1.48 (m, 4H), 1.45-1.40 (m, 4H), 1.29-1.15 (m, 48H), 0.88 (t, J = 7.0 Hz, 6H), 0.81 (t, J = 7.2 Hz, 6H); MALDI-TOF MS m/z calcd. for $C_{96}H_{122}B_2N_6O_8$ 1508.951 found 1509.967 $[M + H]^+$. No meaningful ^{13}C NMR was obtained due poor solubility.

1,4-Bis(decyloxy)-2,5-bis(trimethylsilylethynyl)benzene (222)

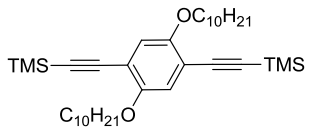

222

Compound **214** (1.30 g, 2.01 mmol), trimethylsilylacetylene (1.40 mL, 10.1 mmol), $PdCl_2(PPh_3)_2$ (28.3 mg, 0.040 mmol), and CuI (15.3 mg, 0.080 mmol), were added to THF (10 mL), and Et_3N (10 mL) mixture . The solution was bubbled by N_2 at rt for 5 min, and then stirred at 45 ^{o}C under N_2 protection overnight. After the reaction was complete as checked by TLC analysis, the solvent was removed in vaccum. The resulting residue was diluted with ethyl acetate, and then was filtered through a $MgSO_4$ pad. The solution obtained was sequentially washed by aq HCl (10%) and brine. The organic layer was dried over $MgSO_4$ and concentrated under vacuum to give a crude product of **222**. The crude product was then purified by silica flash column chromatography

(hexanes/CH_2Cl_2, 95:5) to give compound **222** (1.02 g, 1.76 mmol, 87%) as a yellow solid. ^{1}H NMR ($CDCl_3$, 300 MHz): δ 6.88 (s, 2H), 3.94 (t, *J* = 6.5 Hz, 4H), 1.83-1.73 (m, 4H), 1.51-1.26 (m, 28), 0.88 (t, *J* = 6.5 Hz, 6H), 0.25 (s, 18H); The data are consistent with those reported in the literature.[68]

1,4-Bis(decyloxy)-2,5-diethynylbenzene (223)

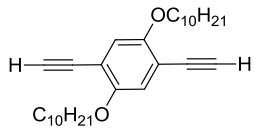

223

To a solution of compound **222** (0.42 g, 0.72 mmol) in 1:1 MeOH/THF (20 mL) was added K_2CO_3 (0.29 g, 2.1 mmol). After being stirred at rt for 30 min, the reaction mixture was diluted with excess water and extracted in $CHCl_3$ two times. The organic layer was washed with water, dried over $MgSO_4$, and concentrated under vacuum to give a crude product of **223**. The crude was purified by silica flash column chromatography (hexanes/CH_2Cl_2, 90:10) to yield compound **223** as a yellow solid (0.29 g, 0.67 mmol, 94%). ^{1}H NMR (500 MHz, $CDCl_3$): δ 6.95 (s, 2H), 3.97 (t, *J* = 6.5 Hz, 4H), 3.32 (s, 2H) 1.82-1.77 (m, 4H), 1.53-1.43 (m, 4H), 1.34-1.27 (m, 24H), 0.88 (t, *J* = 6.5 Hz, 6H). The data are consistent with those reported in the literature.[68]

Synthesis of linear OPE (224)

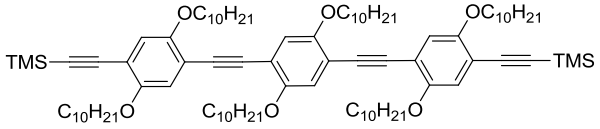

224

Compound **223** (0.22 g, 0.50 mmol), compound **215** (0.79 g, 1.3 mmol), $PdCl_2(PPh_3)_2$ (7.1 mg, 0.010 mmol), and CuI (3.8 mg, 0.020 mmol), were added to THF (10 mL), and Et_3N (10 mL) mixture . The solution was bubbled by N_2 at rt for 5 min, and then stirred at 45 ^oC under N_2 protection overnight. After the reaction was complete as checked by TLC analysis, the solvent was removed in vaccum. The resulting residue was diluted with ethyl acetate, and then was filtered through a $MgSO_4$ pad. The solution obtained was sequentially washed by aq HCl (10%) and brine. The organic layer was dried over $MgSO_4$ and concentrated under vacuum to give a crude product of **224**. The crude product was then purified by silica flash column chromatography (hexanes/CH_2Cl_2, 95:5) to give compound **224** (0.57 g, 0.41 mmol, 81%) as a yellow solid. ^1H NMR (500 MHz, $CDCl_3$): δ 6.99 (s, 2H), 6.95 (d, *J* = 7.8 Hz, 4H), 4.02-3.95 (m, 12H), 1.84-1.78 (m, 12H), 1.51-1.24 (m, 102H), 0.87 (t, *J* = 6.5 Hz, 18H). The data are consistent with those reported in the literature.[69]

Synthesis of acetylenic linear OPE (225)

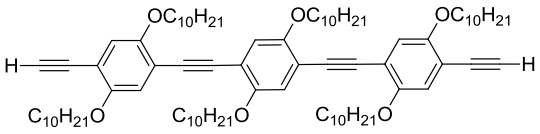

225

To a solution of compound **224** (0.41 g, 0.29 mmol) in 1:1 MeOH/THF (20 mL) was added K_2CO_3 (0.16 g, 1.2 mmol). After being stirred at rt for 30 min, the reaction mixture was diluted with excess water and extracted in $CHCl_3$ two times. The organic layer was washed with water, dried over $MgSO_4$, and concentrated under vacuum to give

a crude product of **225**. The crude was purified by silica flash column chromatography (hexanes/CH_2Cl_2, 90:10) to yield compound **225** as a yellow solid (0.32 g, 0.25 mmol, 88%). ^{1}H NMR (500 MHz, $CDCl_3$): δ 7.00-6.97 (m, 6H), 4.01(t, *J* = 5.7 Hz, 12H), 3.33 (s, 2H), 1.83-1.79 (m, 12H), 1.49-1.25 (m, 84H), 0.87 (t, *J* = 6.5 Hz, 18H). The data are consistent with those reported in the literature.[69]

Pinacolyl boronate-attached linear OPE (226)

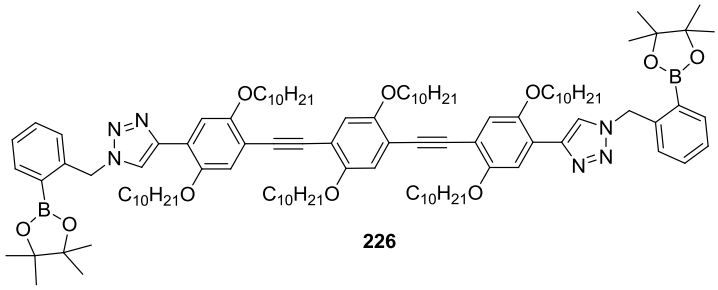

226

Oligomer linear OPE **225** (220 mg, 0.174 mmol), azidophenylboronate **210** (149 mg, 0.574 mmol), and DIPEA (0.015 mL, 0.087 mmol) were dissolved in dry THF (10 mL). The solution was degassed by bubbling N_2 at rt for 5 min, then CuI (6.62 mg, 0.043 mmol) was added. The reaction mixture was heated at 60 ◦C overnight. The progress of the reaction was monitored by TLC. On completion, the solvent was removed under reduced pressure. The resulting residue was diluted with CH_2Cl_2 and filtered through a $MgSO_4$ pad. The filtrate was sequentially washed with brine and water. The organic layer was dried with $MgSO_4$ and concentrated under vacuum to give crude product **226**, which was purified by silica flash column chromatography (EtOAc/hexanes, 15:85) to yield pure compound **226** (171 mg, 0.095 mmol, 55%) as a pale yellow solid. m.p. 84-85 ^{o}C;

IR (neat): 2919, 2100, 1601, 1552, 1466, 1388, 1356, 1271, 1168 cm^{-1}; ^1H NMR (500 MHz, $CDCl_3$): δ 7.96-7.91 (m, 6H), 7.42 (td, *J* = 7.6, 1.4 Hz, 2H), 7.34 (td, *J* = 7.4, 0.9 Hz, 2H), 7.15 (d, *J* = 7.7 Hz, 2H) 7.02 (d, *J* = 4.4 Hz, 4H), 5.94 (s, 4H), 4.15 (t, *J* = 6.7 Hz, 4H), 4.03 (t, *J* = 6.6 Hz, 4H), 3.94 (t, *J* = 6.7 Hz, 4H), 1.90-1.81 (m, 8H), 1.70-1.65 (m, 4H), 1.53- 1.46 (m, 8H), 1.33 (s, 24H), 1.25 (m, 76H), 0.90-0.83 (m, 18H); ^{13}C NMR (125 MHz, $CDCl_3$): δ 154.1, 153.4, 148.7, 142.7, 140.9, 136.6, 131.7, 128.6, 127.7, 123.7, 120.9, 117.4, 116.4, 114.4, 112.6, 111.4, 91.7, 90.5, 84.0, 69.7, 69.6, 68.8, 53.3, 31.93, 31.91, 29.71, 29.70, 29.65, 29.64, 29.60, 29.56, 29.50, 29.43, 29.40, 29.38, 29.37, 29.33, 29.31, 26.06, 26.04, 26.03, 24.8, 22.7, 22.67, 14.1, 14.0; HRMS (MALDI-TOF) m/z Calcd for $C_{112}H_{170}B_2N_6O_{10}$, 1781.3165; Found, 1781.3358 $[M]^+$.

Trifluoroborate-attached linear OPE 226a

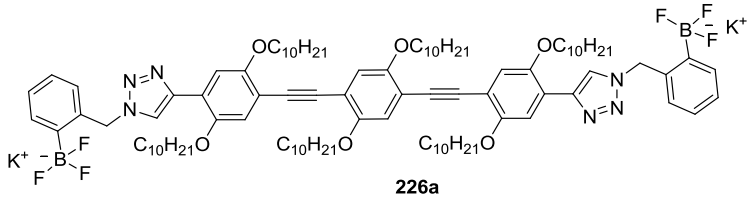

226a

To a solution of compound **226** (100 mg, 0.056 mmol) in MeOH (5 mL) and THF (5 mL) placed in a plastic beaker was added to aqueous KHF_2 (0.75 mL, 3 M, 2.24 mmol). The resulting pale yellow color slurry was stirred at rt overnight. After the reaction was complete as checked by TLC analysis, the solvent was removed under reduced pressure. The residue was dissolved in hot acetone and filtered. The filtrate was concentrated under vacuum, affording crude product **226a**, which was crystallized from Et_2O/hexanes (1:1) to afford compound **226a** (80.2 mg, 0.051 mmol, 86%) as yellow

color solid. m.p. 228-229 ◦C; IR (neat): 3387, 2358, 2101, 1599, 1466, 1389, 1348, 1270, 1058 cm−1; ^{1}H NMR (500 MHz, DMSO-d_6): δ 8.26 (s, 2H), 7.80 (s, 2H), 7.48 (d, J = 7.4 Hz, 2H), 7.08-7.00 (m, 8H), 6.86 (d, J = 7.4 Hz, 2H), 5.70 (s, 4H), 4.08 (t, J = 6.1 Hz, 4H), 4.01 (t, J = 6.2 Hz, 4H), 3.96 (t, J = 6.8 Hz, 4H) 1.78-1.68 (m, 8H), 1.51-1.44 (m, 4H), 1.33- 1.07 (m, 84H), 0.86-0.75 (m, 18H); ^{13}C NMR (125 MHz, DMSO-d_6): δ 154.1, 153.7, 149.2, 142.0, 138.9, 133.0, 127.4, 126.8, 126.5, 125.3, 121.9, 117.5, 116.9, 114.5, 112.6, 111.6, 92.7, 91.2, 74.3, 69.7, 69.3, 69.2, 53.7, 32.23, 32.20, 30.0, 29.97, 29.96, 29.90, 29.87, 29.81, 29.70, 29.69, 29.61, 29.5, 26.46, 26.43, 26.3, 25.8, 22.98, 22.95, 14.7, 14.68, 14.64; MS (ESI, negative) m/z Calcd for $[C_{100}H_{146}B_2F_6N_6O_6]^{2-}$, 831.6; Found, 832.1.

Boronic acid-attached linear OPE (196)

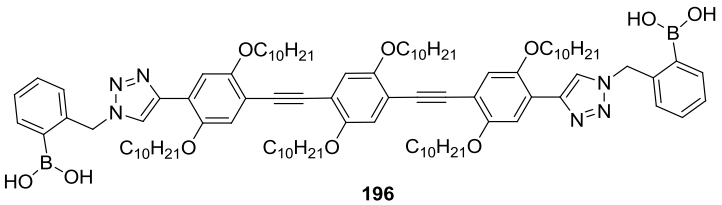

196

To a solution of compound **226a** (58 mg, 0.033 mmol) in acetonitrile (5 mL), THF (5 mL), and water (0.04 mL, 2.33 mmol), was added trimethylsilyl chloride (0.08 mL, 0.665 mmol). The resulting clear yellow solution was stirred at rt overnight. After the reaction was complete as checked by TLC analysis, the reaction mixture was poured in to water and the resulting solid was filtered and air-dried, affording crude product 196, which was crystallized from Et_2O/hexanes (1:1) to yield pure compound 196 (45 mg, 0.027 mmol, 84%) as pale yellow solid. m.p. 161-163 ^{o}C; IR (neat): 3417, 1600, 1457,

1375, 1273, 1046 cm−1; ^{1}H NMR (500 MHz, 4:1 acetone-d_6/DMSO-d_6): δ 8.37 (s, 2H), 8.03 (s, 2H), 7.93 (s, 2H), 7.84 (d, *J* = 7.1 Hz, 2H), 7.42-7.38 (m, 4H), 7.34 (t, *J* = 7.5 Hz, 2H), 7.21 (d, *J* = 7.5 Hz, 2H), 7.11 (s, 2H), 7.09 (s, 2H), 5.96 (s, 4H), 4.16 (t, *J* = 6.2 Hz, 4H), 4.11-4.06 (m, 8H), 1.89-1.81 (m, 8H), 1.63-1.55 (m, 8H), 1.43-1.22 (m, 80H), 0.89-0.81 (m, 18H); No meaningful ^{13}C NMR spectrum was obtained due to its poor solubility. HRMS (MALDI-TOF) m/z Calcd for $C_{100}H_{150}B_2N_6O_{10}$, 1617.1600; Found, 1617.1881 $[M]^+$.

2-Amino-5-bromobenzoic acid (228)

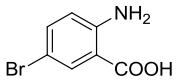

228

To a solution of anthranilic acid **227** (10.0 g, 72.9 mmol) in 160 mL of glacial acetic acid was added 4.7 mL of bromine (14.7 g, 92.1 mmol) was added dropwise at 16 ^{o}C. The product was filtered and then boiled up with 350 mL of water containing 20 mL of conc. HCl. The content was filtered and the insoluble residue was extracted twice with 400 mL of boiling water. The filtrates upon cooling yielded compound **228** (8.01 g, 36.5 mmol, 51%) as a white solid. ^{1}H NMR (500 MHz, $CDCl_3$): δ 8.03 (s, 1H), 7.39 (d, *J* = 8.7 Hz, 1H), 6.59 (d, *J* = 8.7 Hz, 1H) (protons of NH_2 and COOH were not observed due to rapid proton exchange). The data are consistent with those reported in the literature.[70]

5-Bromo-2-iodobenzoic acid (229)

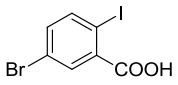

229

To a solution of **228** (3.9 g, 18 mmol), $NaNO_2$ (1.5 g, 22 mmol) and NaOH (0.90 g, 23 mmol) in 55 mL of water was added dropwise to a stirred and cooled solution of 6.4 mL of HCl in 9 mL of water at 0 ^oC over a period of 1.5 h. The stirring was continued for 30 min at same temperature and the formed suspension of diazonium salt was added to a stirred solution of KI (4.5 g, 27 mmol) and 1.1 mL of H_2SO_4 in 7.5 mL of water at 40 ^oC over 20 min. The mixture was then heated to 90 ^oC and stirred for 30 min. The mixture was stirred and cooled. The crude product was filtered and washed with water, and then dissolved in 40% NaOH. The undissolved components were separated by decantation and the clear solution was acidified with concentrated HCl. The product was extracted by diethyl ether. The extract was dried with $MgSO_4$ and concentrated under vacuum. The residue was crystallized from 50% aqueous ethanol to give compound **229** (3.2 g, 10 mol, 56%) as a pale yellow solid. ^1H NMR (500 MHz, $CDCl_3$): δ 8.14 (s, 1H), 7.91 (d, J = 8.3 Hz, 1H), 7.34 (d, J = 7.8 Hz, 1H) (proton on COOH was not observed due to rapid proton exchange). The data are consistent with those reported in the literature.[70]

Methyl 5-bromo-2-iodobenzoate (230)

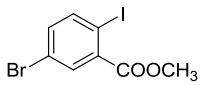

230

To a solution of compound **229** (15.3 g, 48.0 mmol) in methanol (150 mL) was added H_2SO_4 (6 mL) dropwise and then refluxed overnight. The reaction was cooled to rt. The solvent was removed by rotary evaporation. The obtained residue was dissolved in ethylacetate. The solution was washed by brine, and dried over $MgSO_4$. After removal of EtOAc under vacuum, the resulted crude product was purified by silica column chromatography (hexanes/EtOAc, 9:1) to yield compound **230** (15.2 g, 45.0 mmol, 97%) as a pale yellow solid. ^{1}H NMR (500 MHz, $CDCl_3$,): δ 7.94 (s, 1H), 7.84 (d, *J* = 8.0 Hz, 1H), 7.29 (d, *J* = 8.0, 1H), 3.94 (s, 3H). The data are consistent with those reported in the literature.[70]

(5-Bromo-2-iodophenyl)methanol (231)

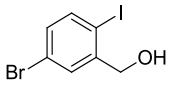

231

To a solution of compound **230** (2.92 g, 8.56 mmol) in dry CH_2Cl_2 (20 mL) was added DIBAL (17.1 mL, 1 M in THF, 17.1 mmol) at 0 ^{o}C. The reaction was slowly warmed up to rt and stirred overnight. The mixture was cooled to 0 ^{o}C, added 15% aqueous citric acid dropwise, and extracted with CH_2Cl_2. The organic layer was washed with brine, and dried with $MgSO_4$. After removal of CH_2Cl_2 under vacuum, the resulting crude product was purified by silica column flash chromatography (hexanes: EtOAc, 8.5:1.5) to give compound **231** as a white solid (1.75 g, 5.59 mmol, 67%). ^{1}H NMR (500 MHz, $CDCl_3$): δ 7.66 (d, *J* = 8.5 Hz, 1H), 7.63 (d, *J* = 2.5 Hz, 1H), 7.14 (dd, *J* = 9.0, 2.0 Hz, 1H), 4.63 (s, 2H). The data are consistent with those reported in the literature.[70]

5-Bromo-2-iodobenzaldehyde (232)

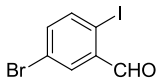

232

To a solution of compound **231** (4.00 g, 12.7 mmol) in 100 mL of CH_2Cl_2 was added PCC (3.81 g, 17.6 mol) portions wise, and celite. The reaction was stirred for another 4 h. The reaction mixture was filtered through celite to remove undissolved materials and the filtrate was concentrated under vacuum to give the crude product of **232**. The crude product was purified by silica flash column chromatography (hexanes/CH_2Cl_2, 70:30) to give compound **232** (3.37 g, 10.8 mmol, 85%) as a white solid. ^{1}H NMR (500 MHz, $CDCl_3$): δ 9.99 (s, 1H), 7.99 (s, 1H), 7.82 (d, *J* = 8.3 Hz, 1H), 7.42 (d, J = 6.1 Hz, 1H). The data are consistent with those reported in the literature.[70]

***α, α'*-Dibromo-*p*-xylene (233)**

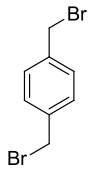

233

To a solution of *p*-Xylene (6.00 g, 56.5 mmol), and benzoylperoxide (20 mg) in 200 mL of $CHCl_3$ was added NBS (20.1 g, 113 mmol) and refluxed under a bright light. After the being refluxed for 8 h, the solution was cooled to rt. The generated succinimide was filtered. The yellow solution was concentrated to give the crude product which was purified by silica flash column chromatography (hexanes) to yield compound **233** (3.20 g,

12.1 mmol, 21%) as a white solid. ^{1}H NMR (500 MHz, $CDCl_3$,): δ 7.37 (s, 4H), 4.48 (s, 4H). The data are consistent with those reported in the literature.[70]

Tetraethyl 1,4-phenylenebis(methylene)diphosphonate (234)

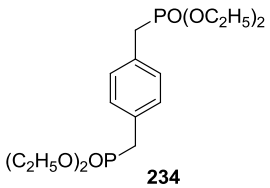

234

1,4-Bis(bromomethyl)benzene **233** (1.00 g, 3.80 mmol) and triethylphosphite (6 mL) were refluxed for 12 h. The mixture was cooled to rt, yielding colorless crystals. The excess unreacted triethylphosphite was decanted. The remaining white solid was washed three times with hexanes and dried under vaccum to afford compound **234** as a white solid (0.81 g, 2.14 mmol, 56%). ^{1}H NMR (500 MHz, $CDCl_3$): δ 7.29 (s, 4H), 4.04-4.00 (m, 8H), 3.14 (d, *J P;H* = 20.6 Hz), 1.25 (t, *J* = 7.5 Hz, 12H). The data are consistent with those reported in the literature.[70]

1,4-Bis(5-bromo-2-iodostyryl)benzene (235)

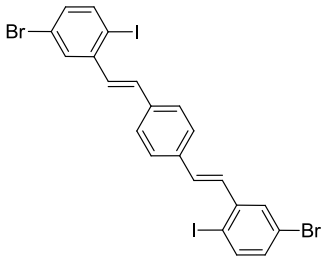

235

To an oven-dried flask protected under N_2 were charged tetraethyl 1,4-phenylene bis(methylene)diphosphonate **234** (0.50 g, 1.32 mmol), 60% NaH (0.15 g, 3.91 mmol), and dry DMF (8 mL). The solution gradually turned into dark orange color. A solution of compound **232** (0.82 g, 2.62 mmol) in DMF (5 mL) was added in small portions over a period of 10 min via a syringe. The reaction was kept under stirring for another 30 min before workup. On completion as checked by TLC analysis, the reaction mixture was poured in to ice, and the obtained solid was filtered, washed with water several times and finally with methanol to give pure product **235** (0.82 g, 1.18 mmol, 88%) as a yellow solid. ^{1}H NMR (300 MHz, $CDCl_3$): δ 7.76 (d, *J* = 2.3 Hz, 2H), 7.72 (d, *J* = 8.4 Hz, 2H), 7.57 (s, 4H), 7.26 (d, *J* = 16.0 Hz, 2H), 7.11 (d, *J* = 2.3 Hz, 1H), 7.08 (d, *J* = 2.3 Hz, 1H), 6.97 (d, *J* = 16.0 Hz, 2H). The data are consistent with those reported in the literature.[70]

1,4-Bis(2,5-bis(trimethylsilylethynyl)styryl)benzene (236)

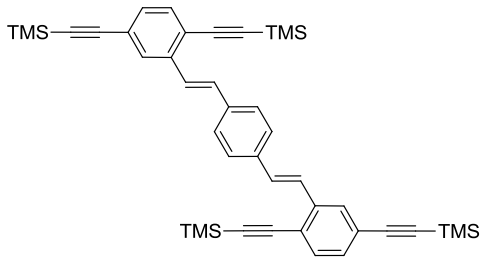

236

To an oven-dried round-bottom flask protected under N_2 were charged compound **235** (0.586 g, 0.848 mmol), trimethylsilylacetylene (0.71 mL, 0.489 g, 4.98 mmol), $PdCl_2(PPh_3)_2$ (87.3 mg, 0.124 mmol)), CuI (47.2 mg, 0.248 mmol), and Et_3N (50 mL). The solution was degassed by N_2 bubbling at rt for 5 min, and then was heated to 85 ^oC under stirring and N_2 protection overnight. After the reaction was complete as checked by

TLC analysis, the solvent was removed by rotary evaporation. The residue was diluted with EtOAc and was filtered through a $MgSO_4$ pad. The solution obtained was sequentially washed with aq HCl (10%) and brine. The organic layer was dried over $MgSO_4$ and concentrated under vacuum to give crude product **236**, which was further washed with methanol and dried to yield pure compound **236** (0.450 g, 0.674 mmol, 81%) as a yellow solid. ^{1}H NMR (300 MHz, $CDCl_3$): δ 7.79 (s, 2H), 7.65 (d, *J* = 16.4 Hz, 2H), 7.54 (s, 4H), 7.42 (d, *J* = 8.0 Hz, 2H), 7.29 (d, *J* = 1.5 Hz, 2H), 7.19 (d, *J* = 16.4 Hz, 2H), 0.31 (s, 18H), 0.27 (s, 18H). The data are consistent with those reported in the literature.[70]

1,4-Bis(2,5-diethynylstyryl)benzene (237)

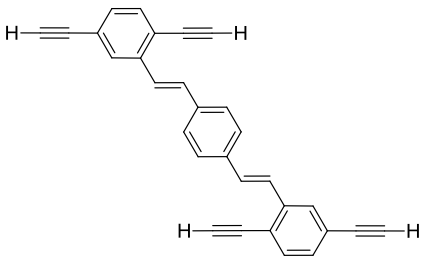

237

To a solution of compound **236** (0.38 g, 0.64 mmol) in MeOH/THF (1:1, 20 mL) was added K_2CO_3 (0.31 g, 2.25 mmol). The mixture was stirred at rt for 30 min, and then the reaction solvent was removed by rotary evaporation. The residue was diluted in CH_2Cl_2 and sequentially washed with aq HCl (10%) and brine. The organic layer was dried with $MgSO_4$ and concentrated under vacuum to afford the crude product of **237**, which was further washed with methanol and dried to yield pure compound **237** (0.23 g, 0.60 mmol, 94%) as a yellow solid. ^{1}H NMR (500 MHz, $CDCl_3$): δ 7.84 (s, 2H), 7.61 (d,

J = 16.3 Hz, 2H), 7.56 (s, 4H), 7.48 (d, *J* = 7.9 Hz, 2H), 7.33 (d, *J* = 7.9 Hz, 2H), 7.18 (d, *J* = 16.3 Hz, 2H), 3.48 (s, 2H), 3.19 (s, 2H). The data are consistent with those reported in the literature [70]

3,5-dibromobenzaldehyde (239)

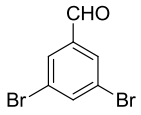

239

To a solution of 1,3,5-tribromobenzene **238** (2.01 g, 6.35 mmol) in ether (63 mL) was added *n*-BuLi (6.25 mL, 1.2 M, 0.481 g, 7.62 mmol) slowly over a period of 30 min at -78 ^{o}C. Then the reaction mixture was stirred for 30 min at same temperature. This was then added dry DMF (4.7 mL, 4.40 g, 20.9 mmol) and allow the reaction stirred at rt for 1 h before it was quenched with aqueous 1M HCl. The obtained cloudy solution was added ether (50 mL) and washed with water two times. The organic layer was separated and dried over MgSO4, and concentrated under vaccum to give crude product **239**. This was further purified by silica flash column chromatography (hexanes/EtOAc, 9.5:0.5) to yield pure compound **239** as off-white solid (1.30 g, 4.92 mmol, 77%). ^{1}H NMR (500 MHz, $CDCl_3$): δ 9.90 (s, 1H), 7.94-7.72 (m, 3H). The data are consistent with those reported in the literature.[71]

1,4-Bis(3,5 dibromostyryl) benzene (240)

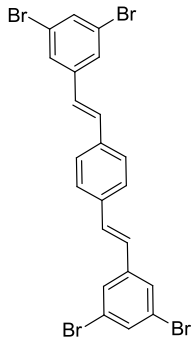

240

To an oven-dried flask protected under N_2 were charged tetraethyl 1,4-phenylene bis(methylene)diphosphonate **234** (0.50 g, 1.44 mmol), NaH (0.13 g, 5.76 mmol), and dry DMF (8 mL). The solution gradually turned into dark orange color. A solution of 3,5 dibromobenzaldehyde **239** (0.76 g, 2.88 mmol) in DMF (5 mL) was added in small portions over a period of 10 min via a syringe. The reaction was kept under stirring for another 30 min before workup. On completion as checked by TLC analysis, the reaction mixture was poured in to ice, and the obtained solid was filtered, washed with water several times and finally with methanol to give pure product **240** (0.61 g, 1.02 mmol, 71%) as a yellow solid. m.p. 256-259.3 ^{o}C; IR (neat): 3021, 1672, 1630, 1575, 1539, 1419, 1100, 948, 838, 736 cm^{-1}; ^{1}H NMR (500 MHz, DMSO-d_6): δ 7.87 (d, J = 1.5 Hz, 4H), 7.71 (t, J = 1.5 Hz, 2H), 7.64 (s, 4H), 7.48 (d, J = 16.4 Hz, 2H), 7.29 (d, J = 16.4 Hz, 2H); ^{13}C NMR (75 MHz, DMSO-d_6): δ 141.5, 136.4, 131.9, 131.2, 128.1, 127.3, 125.7, 122.9; HRMS (MALDI-TOF, +eV) *m/z* calcd for $C_{22}H_{14}Br_4$, 593.7829; found 593.7795 $[M]^+$.

1,4-Bis(3,5-bis(trimethylsilylethynyl)styryl)benzene (241)

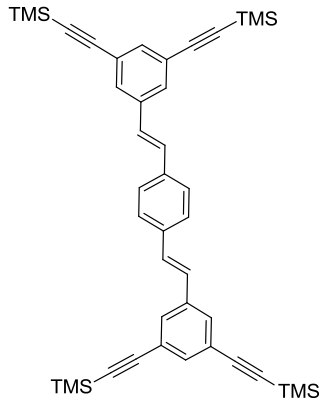

241

To an oven-dried round-bottom flask protected under N_2 were charged compound **240** (0.47 g, 0.78 mmol), trimethylsilylacetylene (1.78 mL, 1.23 g, 12.4 mmol), $PdCl_2(PPh_3)_2$ (0.05 g, 0.07 mmol)), CuI (0.03 g, 0.16 mmol), and Et_3N (30 mL). The solution was degassed by N_2 bubbling at rt for 5 min, and then was heated to 65 ^oC under stirring and N_2 protection overnight. After the reaction was complete as checked by TLC analysis, the solvent was removed by rotary evaporation. The residue was diluted with EtOAc and was filtered through a $MgSO_4$ pad. The solution obtained was sequentially washed with aq HCl (10%) and brine. The organic layer was dried over $MgSO_4$ and concentrated under vacuum to give crude product **241**, which was further washed with methanol and dried to yield pure compound **241** (0.38 g, 0.56 mmol, 72%) as a yellow solid. m.p. 251-253 ^oC; IR (neat): 2955, 2155, 1579, 1423, 1249, 1161, 949, 843 cm^{-1}; ^1H NMR (500 MHz, $CDCl_3$): δ 7.55 (d, J = 1.3 Hz, 4H), 7.49-7.47 (m, 6H), 7.13 (d, J = 16.3 Hz, 2H), 7.02 (d, J = 16.3 Hz, 2H), 0.26 (s, 36H); ^{13}C NMR (75 MHz, $CDCl_3$): δ 137.6, 136.7, 134.4, 129.84, 129.79, 127.11, 127.05, 123.8, 104.0, 95.1, 0.0; HRMS (MALDI-TOF, +eV) *m/z* calcd for $C_{42}H_{50}Si_4$, 666.2990; found 666.2988 $[M]^+$.

1,4-Bis(3,5-diethynylstyryl)benzene (242)

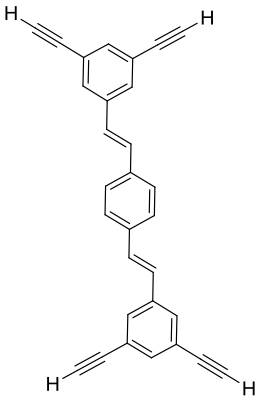

242

To a solution of compound **241** (0.37 g, 0.55 mmol) in MeOH/THF (1:1, 20 mL) was added K_2CO_3 (0.92 g, 6.66 mmol). The mixture was stirred at rt for 1 h, and then the reaction solvent was removed by rotary evaporation. The residue was diluted in CH_2Cl_2 and sequentially washed with aq HCl (10%) and brine. The organic layer was dried with $MgSO_4$ and concentrated under vacuum to afford the crude product of **242**, which was further washed with methanol and dried under vaccum to yield pure compound **242** (0.19 g, 0.51 mmol, 91%) as a yellow solid. m.p. 219-222 ^oC; IR (neat): 3277, 1579, 1426, 1249, 955, 863 cm^{-1}; ^1H NMR (500 MHz, $CDCl_3$): δ 7.61 (d, *J* = 1.6 Hz, 4H), 7.50 (s, 6H), 7.14 (d, *J* = 16.3 Hz, 2H), 7.04 (d, *J* = 16.3 Hz, 2H), 3.11(s, 4H); ^{13}C NMR (75 MHz, $CDCl_3$): δ 137.8, 136.6, 134.4, 130.4, 130.1, 127.1, 126.8, 122.9, 82.5, 78.0; HRMS (MALDI-TOF, +eV) *m/z* calcd for $C_{30}H_{18}$, 378.1409, found 378.1391 $[M]^+$.

Pinacolyl boronate-attached H-shaped OPV oligomer (243)

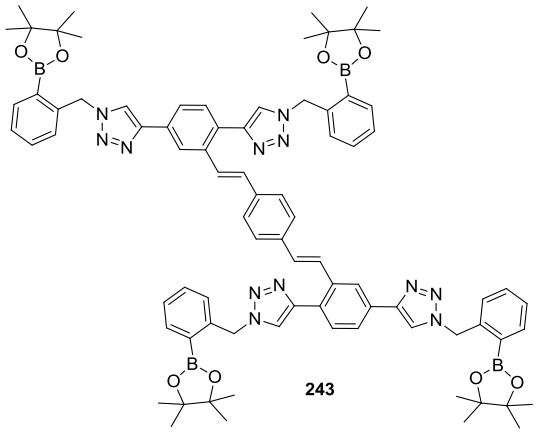

243

Compound **237** (120 mg, 0.32 mmol), azido phenylboronate **210** (822 mg, 3.20 mmol) and $^{i}Pr_2EtN$ (27.6 μL, 0.16 mmol) were dissolved in dry THF (5 mL). The solution was degassed by bubbling N_2 at rt for 5 min. Then CuI (24.6 mg, 0.13 mmol) was added, and the reaction mixture was heated at 60 ^{o}C overnight. After the reaction mixture was complete as checked by TLC analysis, the solvent was removed under reduced pressure. The residue was diluted with CH_2Cl_2. The mixture was filtered through a $MgSO_4$ pad and the filtrate was sequentially washed with brine and water. The organic layer was dried over $MgSO_4$ and then concentrated under vacuum to give crude **243**, which was further purified by silica flash column chromatography (EtOAc/hexanes, 2:8) to yield pure compound **243** (368 mg, 0.26 mmol, 82%) as a pale yellow solid. m.p. 225-227 ^{o}C; IR (neat): 2978, 1602, 1448, 1347, 1266, 1213, 1146, 1053, 962, 859 cm^{-1}; ^{1}H NMR (500 MHz, CD_2Cl_2): δ 8.22 (d, *J* = 1.0 Hz, 2H), 7.95 (s, 2H), 7.92-7.89 (m, 4H), 7.77-7.70 (m, 6H), 7.49-7.46 (m, 6H), 7.40-7.30 (m, 12H), 7.17 (d, *J* = 16.2 Hz, 2H), 5.93 (d, *J* = 2.6 Hz, 8H), 1.38 (s, 24H), 1.24 (s, 24H); ^{13}C NMR (75 MHz, CD_2Cl_2): δ 147.4, 146.6, 141.68, 141.66, 137.4, 137.2, 136.6, 132.3, 132.3, 132.3, 131.6, 131.1,

130.9, 130.3, 129.8, 129.7, 128.4, 128.3, 127.6, 127.5, 125.3, 123.7, 123.6, 121.0 84.8, 84.7, 25.3, 25.2 (two peaks fewer than expected due to coincidental peak overlap); HRMS (MALDI-TOF, +eV) *m/z* calcd for $C_{82}H_{90}B_4N_2O_8$ 1414.7377, found 1414.7374 $[M]^+$.

Boronic acid-attached H-shaped OPV oligomer (197)

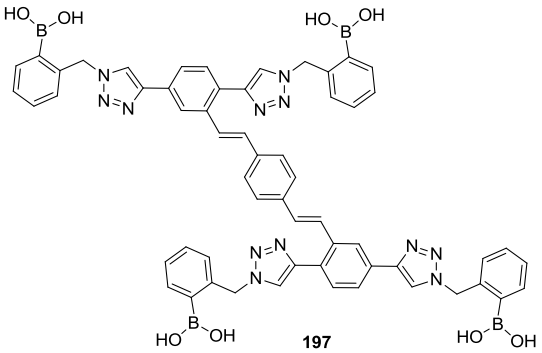

To a solution of compound **243** (70 mg, 0.05 mmol) and *o*-tolylboronic acid **207** (59.6 mg, 0.44 mmol) in dioxane (10 ml) was added HCl (5 M, 2.5 ml). The reaction mixture was stirred and heated at 100 °C overnight. On completion as checked by the TLC analysis, the solvent was removed under reduced pressure. The resulting solid was washed with water, dried and further recrystallized from dioxane to give pure compound **197** (41 mg, 0.038 mmol, 76%) as an off-white solid. m.p. 273-279 ^oC; IR (neat): 3361, 1602, 1448, 1361, 1323, 1268, 961, 826 cm^{-1}; ^1H NMR (500 MHz, DMSO-d_6): δ 8.65 (s, 2H), 8.34 (s, 8H), 8.30-8.29 (m, 4H), 7.87-7.85 (m, 2H), 7.73 (d, *J* = 8.2 Hz, 2H), 7.68-7.62 (m, 4H), 7.51 (s, 4H), 7.40-7.37 (m, 4H), 7.35-7.30 (m, 8H), 7.18 (d, *J* = 7.3 Hz, 2H), 7.13 (d, *J* = 7.9 Hz, 2H), 5.89 (d, *J* = 3.3 Hz, 8H); ^{13}C NMR (75 MHz, DMSO-d_6): δ 145.9, 145.2, 139.72, 139.70, 136.6, 135.3, 134.5, 130.6, 130.1, 129.8, 129.7, 128.64,

128.60, 127.99, 127.88, 127.2, 127.1, 127.0, 126.6, 124.5, 124.2, 122.6, 122.1, 53.1(three peaks fewer than expected due to coincidental peak overlap); HRMS (MALDI-TOF, +eV) *m/z* calcd for $C_{58}H_{50}B_4N_{12}O_{8,}$ 1086.4247, found 1086.3743 $[M]^+$.

Pinacolyl boronate-attached H-shaped OPV oligomer (244)

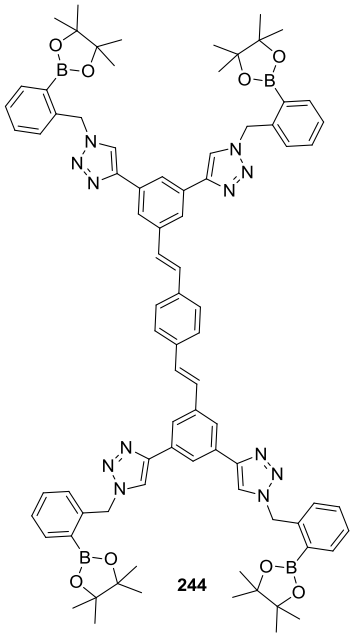

Compound **242** (0.15 g, 0.39 mmol), azido phenylboronate **210** (1.02 g, 3.96 mmol) and $^{i}Pr_2EtN$ (34.5 µL, 0.19 mmol) were dissolved in dry THF (5 mL). The solution was degassed by bubbling N_2 at rt for 5 min. Then CuI (0.03 g, 0.16 mmol) was added, and the reaction mixture was heated at 60 ^{o}C overnight. After the reaction mixture was complete as checked by TLC analysis, the solvent was removed under reduced pressure. The residue was diluted with CH_2Cl_2, and then filtered through a $MgSO_4$ pad. The filtrate was sequentially washed with brine and water. The organic layer was dried over $MgSO_4$ and concentrated under vacuum to give crude **244**, which was further purified by silica

flash column chromatography (EtOAc/hexanes, 3:7) to yield pure compound **244** (0.45 g, 0.32 mmol, 83%) as a pale yellow solid. m.p. 260-262 ^{o}C; IR (neat): 2975, 1602, 1447, 1343, 1268, 1220, 1142, 1051, 956, 853 cm^{-1}; ^{1}H NMR (500 MHz, CD_2Cl_2): δ 8.04 (s, 2H), 7.95-7.90 (m, 12H), 7.56 (s, 4H), 7.47 (t, *J* = 6.8 Hz, 4H), 7.38 (t, *J* = 7.3 Hz, 4H), 7.30-7.20 (m, 8H), 5.92 (s, 8H), 1.37 (s, 48H); ^{13}C NMR (75 MHz, CD_2Cl_2): δ 147.4, 141.6, 139.0, 137.3, 137.2, 132.6, 132.3, 129.7, 129.6, 128.5, 128.4, 127.7, 127.5, 123.5, 122.3, 121.0, 84.8, 25.3; HRMS (MALDI-TOF, +eV) *m/z* calcd for $C_{82}H_{90}B_4N_2O_8$ 1414.7377, found 1414.7423 $[M]^+$.

Boronic acid-attached H-shaped OPV oligomer (198)

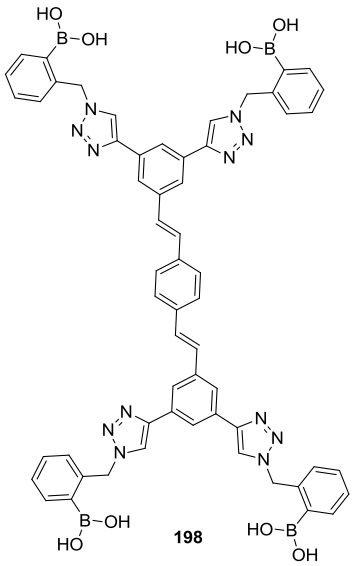

198

To a solution of compound **244**(103 mg, 0.073 mmol) and *o*-tolylboronic acid **207** (87.8 mg, 0.656 mmol) in dioxane (10 mL) was added HCl (5M, 3 mL). The reaction mixture was stirred and heated at 100 ^{o}C overnight. On completion as checked by the TLC analysis, the solvent was removed under reduced pressure. The resulting solid was

washed with water, dried and was further recrystallized from dioxane to give pure compound **198** (58.6 mg, 0.054 mmol, 74%) as an off-white solid. m.p. 267-271 ^{o}C; IR (neat): 3359, 1602, 1449, 1377, 1334, 1256, 1055, 960, 812, 761 cm^{-1}; ^{1}H NMR (500 MHz, DMSO-d_6): δ 8.58 (s, 4H), 8.21 (s, 4H), 8.05 (s, 2H), 7.69-7.67 (m, 8H), 7.41-7.38 (m, 8H), 7.33 (t, *J* = 6.6 Hz, 4H), 7.15 (d, *J* = 7.5 Hz, 4H), 5.88 (s, 8H); ^{13}C NMR (75 MHz, DMSO-d_6): δ 146.0, 139.7, 138.3, 136.5, 134.5, 131.8, 129.7, 128.9, 128.0, 127.1, 127.0, 124.4, 122.6, 122.0, 53.1(two peaks fewer than expected due to coincidental peak overlap); HRMS (MALDI-TOF, +eV) *m/z* calcd for $C_{58}H_{50}B_4N_{12}O_8$, 1086.4247, found 1086.4592 $[M]^+$.

2.7 References

(1) Alvarez-Manilla, G.; Warren, N. L.; Abney, T.; Atwood, J.; Azadi, P.; York, W. S.; Pierce, M.; Orlando, R. *Glycobiology* **2007**, *17*, 677-687.

(2) Varki, A. *Nature* **2007**, *446*, 1023-1029.

(3) Catterall, J. B.; Jones, L. M. H.; Turner, G. A. *Clin. Exp. Metastasis* **1999**, *17*, 583-591.

(4) Casey, R. C.; Oegema, T. R.; Skubitz, K. M.; Pambuccian, S. E.; Grindle, S. M.; Skubitz, A. P. *Clin. Exp. Metastasis* **2003**, *20*, 143-152.

(5) Taylor, M. E.; Drickamer, K. *Introduction to Glycobiology*, Oxford University Press, USA: New York, **2006**.

(6) Catterall, J. B.; Jones, L. M. H.; Turner, G. A. *Clin. Exp. Metastasis* **1999**, *17*, 583-591.

(7) Wild, S.; Roglic, G.; Green, A.; Sicree, R.; King, H. *Diabetes Care* **2004**, *27*, 1047-1053.

(8) Yamamoto, T.; Seino, Y.; Fukumoto, H.; Koh, G.; Yano, H.; Inagaki, N.; Yamada, Y.; Inoue, K.; Manabe, T.; Imura, H. *Biochem. Biophys. Res. Commun.* **1990**, *170*, 223-230.

(9) Baxter. P; Goldhill, J.; Hardcastle, P. T.; Taylor, C. J. *Gut* **1990**, *31*, 817-820.

(10) Elsas, L. J.; Rosenberg, L. E. *J. Clinic. Invest.* **1969**, *48*, 1845-1854.

(11) Newman, J. D.; Turner, A. P. F. *Biosens. Bioelectron.* **2005**, *20*, 2435-2453.

(12) Electricwala, A. *Biochim. Biophys. Acta* **1989**, *990*, 53-57.

(13) Dwek, R. A.; Butters, T. D. *Chem. Rev.* **2002**, *102*, 283-284.

(14) Jelinek, R.; Kolusheva, S. *Chem. Rev.* **2004**, *104*, 5987-6016.

(15) Davis, A. P.; Wareham, R. S. *Angew. Chem. Int. Ed.* **1999**, *38*, 2978-2996.

(16) Aoyama, Y.; Tanaka, Y.; Sugahara, S. *J. Am. Chem. Soc.* **1989**, *111*, 5397-5404.

(17) Anderson, S.; Neidlein, U.; Gramlich, V.; Diederich, F. *Angew. Chem. Int. Ed.* **1995**, *34*, 1596-1600.

(18) Michaelis, A.; Becker, P. *Ber, Dtsch. Chem. Ges.* **1880**, *13*, 58.

(19) Miyaura, N.; Suzuki, A. *Chem. Rev.* **1995**, *95*, 2457-2483.

(20) Kuivila, H. G.; Keough, A. H.; Soboczenski, E. J. *J. Org. Chem.* **1954**, *19*, 780-783.

(21) Lorand, J. P.; Edwards, J. O. *J. Org. Chem.* **1959**, *24*, 769-774.

(22) Spingsteen, G.; Wang, B. *Tetrahedron* **2002**, *58*, 5291-5300.

(23) James, T. D.; Sandanayake, K. R. A. S.; Shinkai, S. *Angew. Chem. Int. Ed.* **1996**, *35*, 1910-1922.

(24) T. D. James; M. D. Phillips; Shinkai, S.; *Boronic Acids in Saccharide Recgnition*, Royal Society of Chemistry: Cambridge, UK, 2006.

(25) Koumoto, K.; Shinkai, S. *Chem. Lett.* **2000**, 856–857.

(26) Edwards, N. Y.; Sager, T. W.; McDevitt, J. T.; Anslyn, E. V. *J. Am. Chem. Soc.* **2007**, *129*, 13575-13583.

(27) Arimori, S.; Bosch, L. I.; Ward, C. J.; James, T. D. *Tetrahedron Lett.* **2001**, *42*, 4553-4555.

(28) Cao, H.; Diaz, D. I.; DiCesare, N.; Lakowicz, J. R.; Heagy, M. D. *Org. Lett.* **2002**, *4*, 1503-1505.

(29) Tan, W.; Zhang, D.; Wang, Z.; Liu, C.; Zhu, D. *J. Mater. Chem.* **2007**, *17*, 1964-1968.

(30) Arimori, S.; Ushiroda, S.; Peter, L. M.; Jenkins, A. T. A.; James, T. D. *Chem. Commun.* **2002**, 2368-2369.

(31) Shoji, E.; Freund, M. S. *J. Am. Chem. Soc.* **2002**, *124*, 12486-12493.

(32) Yoon, J.; Czarnik, A. W. *J. Am. Chem. Soc.* **1992**, *114*, 5874-5875.

(33) Cao, H.; Heagy, M. *J. Fluoresc.* **2004**, *14*, 569-584.

(34) Wulff, G. *Pure Appl. Chem.* **1982**, *54*, 2093-2097.

(35) M. Lauer; Wulff, G. *J. Organomet. Chem.* **1983**, *256*, 1.

(36) James, T. D.; Sandanayake, K. R. A. S.; Shinkai, S. *J. Chem. Soc., Chem. Commun.* **1994**, 477-478.

(37) James, T. D.; Sandanayake, K. R. A. S.; Iguchi, R.; Shinkai, S. *J. Am. Chem. Soc.* **1995**, *117*, 8982-8987.

(38) Wang, Z.; Zhang, D.; Zhu, D. *J. Org. Chem.* **2005**, *70*, 5729-5732.

(39) Arimori, S.; Bell, M. L.; Oh, C. S.; Frimat, K. A.; James, T. D. *Chemical Communications* **2001**, 1836-1837.

(40) Arimori, S.; Bell, M. L.; Oh, C. S.; Frimat, K. A.; James, T. D. *J. Chem. Soc., Perkin Trans. 1* **2002**, 803-808.

(41) James, T. D.; Sandanayake, K. R. A. S.; Shinkai, S. *Angew. Chem. Int. Ed.* **1994**, *33*, 2207-2209.

(42) Eggert, H.; Frederiksen, J.; Morin, C.; Norrild, J. C. *J. Org. Chem.* **1999**, *64*, 3846-3852.

(43) Yang, W.; Gao, S.; Gao, X.; Karnati, V. V. R.; Ni, W.; Wang, B.; Hooks, W. B.; Carson, J.; Weston, B. *Bio. Org. Med. Chem. Lett.* **2002**, *12*, 2175-2177.

(44) Karnati, V. V.; Gao, X.; Gao, S.; Yang, W.; Ni, W.; Sankar, S.; Wang, B. *Bioorg. Med. Chem. Lett.* **2002**, *12*, 3373-3377.

(45) Yang, W.; Fan, H.; Gao, X.; Gao, S.; Karnati, V. V. R.; Ni, W.; Hooks, W. B.; Carson, J.; Weston, B.; Wang, B. *Chem. Biol.* **2004**, *11*, 439-448.

(46) Scrafton, D. K.; Taylor, J. E.; Mahon, M. F.; Fossey, J. S.; James, T. D. *J. Org. Chem.* **2008**, *73*, 2871-2874.

(47) Jin, S.; Choudhary, G.; Cheng, Y.; Dai, C.; Li, M.; Wang, B. *Chem. Commun.* **2009**, 5251-5253.

(48) Trupp, S.; Schweitzer, A.; Mohr, G. J. *Org. Biomol. Chem.* **2006**, *4*, 2965-2968.

(49) Cao, Z.; Nandhikonda, P.; Heagy, M. D. *J. Org. Chem.* **2009**, *74*, 3544-3546.

(50) H. Gampp; M. Maeder; C. J. Meyer; A. D. Zuberbuhler *Talanta* **1985**, *32*, 251.

(51) Gaylord, B. S.; Wang, S.; Heeger, A. J.; Bazan, G. C. *J. Am. Chem. Soc.* **2001**, *123*, 6417-6418.

52) Sherwood, G. A.; Cheng, R.; Chacon-Madrid, K.; Smith, T. M.; Peteanu, L. A.; Wildeman, J. *J. Phy. Chem. C* **2010**, *114*, 12078-12089.

(53) Satrijo, A.; Swager, T. M. *J. Am. Chem. Soc.* **2007**, *129*, 16020-16028.

(54) Lu, H.; Xu, B.; Dong, Y.; Chen, F.; Li, Y.; Li, Z.; He, J.; Li, H.; Tian, W. *Langmuir* **2010**, *26*, 6838-6844.

(55) Signore, G.; Nifosì, R.; Albertazzi, L.; Storti, B.; Bizzarri, R. *J. Am. Chem. Soc.* **2010**, *132*, 1276-1288.

(56) Granzhan, A.; Ihmels, H.; Viola, G. *J. Am. Chem. Soc.* **2007**, *129*, 1254-1267.

(57) Uchiyama, S.; Takehira, K.; Yoshihara, T.; Tobita, S.; Ohwada, T. *Org. Lett.* **2006**, *8*, 5869-5872.

(58) Pourghaz, Y.; Dongare, P.; Thompson, D. W.; Zhao, Y. *Chem. Commun.* **2011**, *47*, 11014-11016.

(59) Grabowski, Z. R.; Rotkiewicz, K.; Rettig, W. *Chem. Rev.* **2003**, *103*, 3899-4032.

(60) Martínez-Máñez, R.; Sancenón, F. *Chem. Rev.* **2003**, *103*, 4419-4476.

(61) Oehlke, A.; Auer, A. A.; Jahre, I.; Walfort, B.; Rüffer, T.; Zoufalá, P.; Lang, H.; Spange, S. *J. Org. Chem.* **2007**, *72*, 4328-4339.

(62) Koskela, S. J. M.; Fyles, T. M.; James, T. D. *Chem. Commun.* **2005**, 945-947.

(63) Zhou, N. Ph.D. thesis, Memorial University, **2008**.

(64) Wilson, J. N.; Windscheif, P. M.; Evans, U.; Myrick, M. L.; Bunz, U. H. F. *Macromolecules* **2002**, *35*, 8681-8683.

(65) Wilson, J. N.; Josowicz, M.; Wang, Y.; Bunz, U. H. F. *Chem. Commun.* **2003**, 2962-2963.

(66) Zhou, N.; Wang, L.; Thompson, D. W.; Zhao, Y. *Tetrahedron Lett.* **2007**, *48*, 3563-3567.

(67) Shao, M. Ph.D. thesis, Memorial University. **2010**.

(68) Shirai, Y.; Zhao, Y.; Cheng, L.; Tour, J. M. *Org. Lett.* **2004**, *6*, 2129-2132.

(69) Mahmud, I. Ph.D. thesis, Memorial University. **2009**.

(70) Zhou, N.; Wang, L.; Thompson, D. W.; Zhao, Y. *Tetrahedron* **2011**, *67*, 125-143.

(71) Chen, L. S.; Chen, G. J.; Tamborski, C. *J. Organomet. Chem.* **1981**, *215*, 281-291.

Chapter 3

Interactions of DTF-endcapped Oligomers with SWNTs and Fullerenes

3.1 Introduction

3.1.1 Importance of functionalized SWNTs

As briefly introduced in Chapter 1, carbon nanotubes (CNTs) are carbon allotropes in tiny cylindrical structures. They can be single-walled carbon nanotubes (SWNTs) and multi-walled carbon nanotubes (MWNTs) in terms of their layers formation. Conceptually, SWNTs can be viewed as a rolled-up sheet of graphene with hemispherical fullerene caps at both ends, while MWNTs are a number of SWNTs concentrically assembled together (Figure 3.1).[1] The diameter of a typical SWNT is usually between 0.7 and 3.0 nm, while those for MWNTs range from 2 and 30 nm.

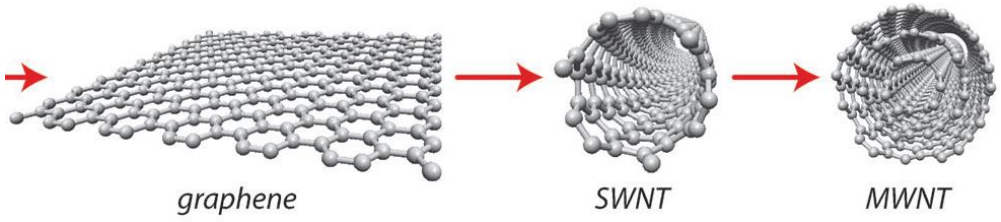

Figure 3.1: Schematic representation showing the rolling of a graphene sheet into a SWNT and MWNT (adopted from reference 1 with permission).

Due to their unique optical, electrical, and mechanical properties such as high aspect ratio, high strength, and excellent current carrying capability, SWNTs have been extensively investigated for many potential applications, including molecular electronics,[2,3] sensors,[4-6] field-emission devices,[7] and components in high-performance composites.[8] However, because of the high cost, lack of solubility, and difficulty of manipulation in all solvents, the applications of SWNTs are still restricted to the preliminary stage. One major obstacle is that SWNTs can interact strongly with another to form more or less closely packed bundles of highly complex architectures by noncovalent forces, such as π-π interactions and van der Waals attractions between their sidewalls. The bundling nature of SWNTs makes them extremely difficult to be dissolved/dispersed in solvents. This limits their direct use in device fabrications where solution-phase processing is involved. To overcome this barrier, various chemical functionalization methods have been developed as shown in Figure 3.2.[9] By these methods, it is possible to solubilize and disperse SWNTs in various solvents, organic and/or aqueous media.

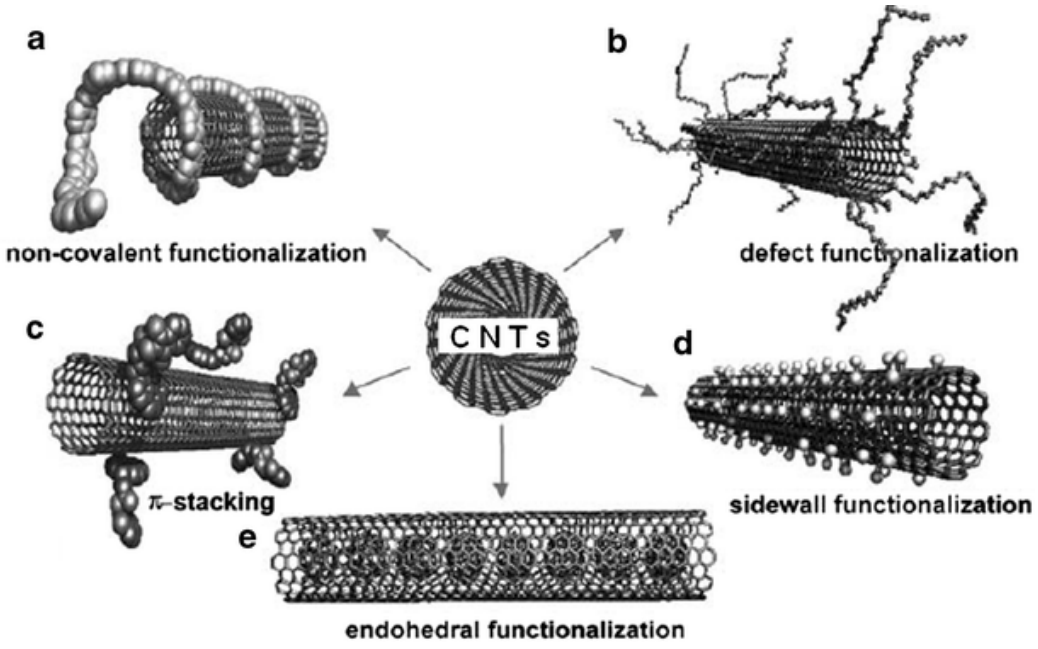

Figure 3.2: Functionalization methods for SWNTs: A) noncovalent exohedral functionalization with polymers, B) defect-group functionalization, C) noncovalent exohedral functionalization with surfactants, D) covalent sidewall functionalization, and E) endohedral functionalization with, for example, C_{60} (adopted from reference 9 with permission).

As summarized in Figure 3.2, the methods used for the functionalization of SWNTs including defect functionalization, covalent functionalization of the sidewalls, noncovalent exohedral functionalization, and endohedral functionalization, have been developed to overcome the solubility limitations. Among these methods, the covalent and noncovalent sidewall functionalization methods have been widely exploited during recent years as they can offer effective ways not only to remove impurities, such as remaining catalysts employed in the nanotube synthesis, from as-produced SWNT samples, but also

to break aggregates to form individualized and well dispersed SWNTs. The following sections will briefly discuss two types of SWNT functionalization methods, namely covalent and noncovalent functionalization.

3.1.2 Covalent functionalization of SWNTs

In this method, SWNTs are covalently modified by introducing a variety of functional groups on their surface of SWNTs. The covalent method, however, invariably causes changes in the hybridization state of the carbon atoms functionalized from sp^2 to sp^3. Among various reactions, oxidation is the most widely studied one for SWNT functionalization, which normally can be induced at the tips or at defects in the nanotube side walls to generate carboxylic acid functional groups. In a typical oxidation process, SWNTs are treated with HNO_3 which oxidizes the surface and introduces carboxylic acid groups. These carboxylic acid groups can be used as chemical anchors for further attachment of other organic molecules. As such, the solubility of functionalized SWNTs can be greatly improved, for example in common organic solvents[10] or even in water.[11] Moreover, by varying the functional groups, the properties of covalently functionalized SWNTs can be greatly altered in comparison with the intrinsic properties of pristine SWNTs.

Gromov and co-workers[12] reported the synthesis of a class of soluble functionalized SWNTs by attaching amino groups to carboxylated SWNTs. As shown in the Scheme 3.1, two synthetic approaches have been devised. The first method involves the formation of amide-SWNTs followed by the Hofmann rearrangement (path A), while

the second uses a Curtis rearrangement of acid chloride groups attached to SWNTs to form amino-SWNTs.

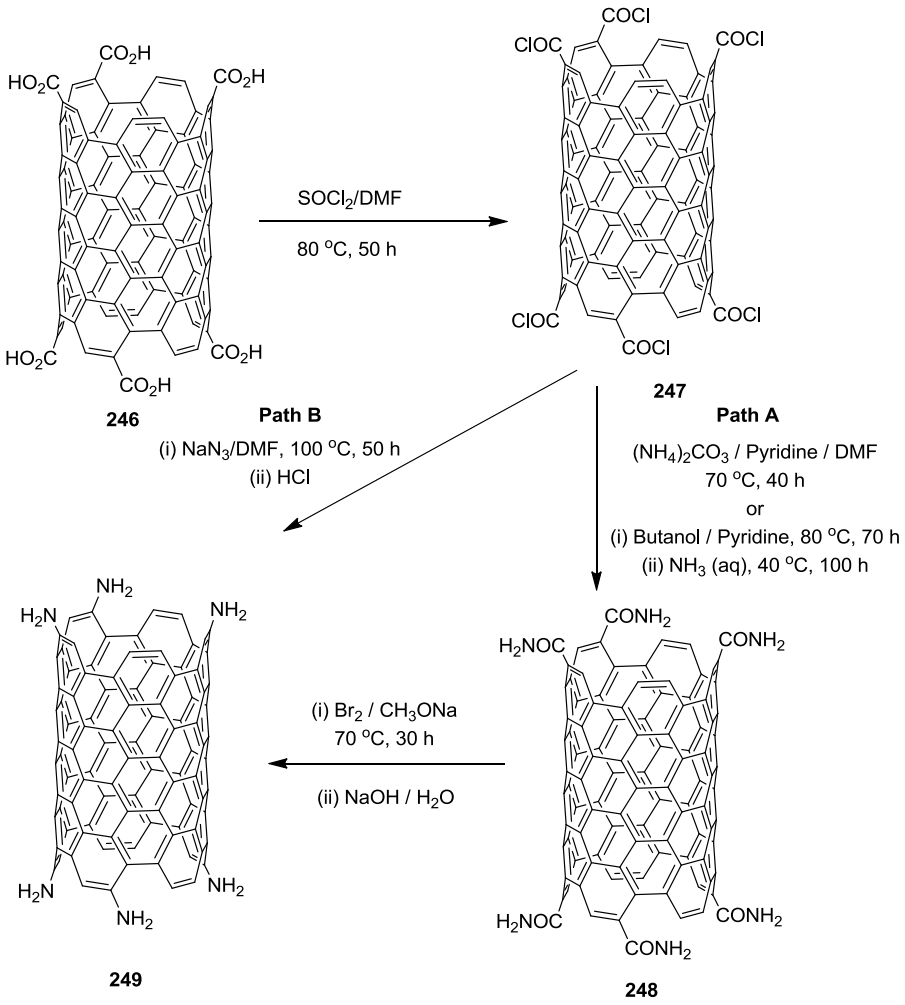

Scheme 3.1: Synthesis of amino-functionalized SWCNTs via the Hofmann rearrangement of carboxylic acid amide (path A) and the Curtius reaction of acyl azide (path B)

In 2005, Adronov and co-workers reported the covalent functionalization of SWNTs by using the CuAAC reaction (click reaction) between alkyne-functionalized

SWNTs and azido-polystyrenes (Scheme 3.2).[13] The resulting polystyrene functionalized SWNTs achieved very high solubility in organic solvents, such as THF, $CHCl_3$, and CH_2Cl_2.

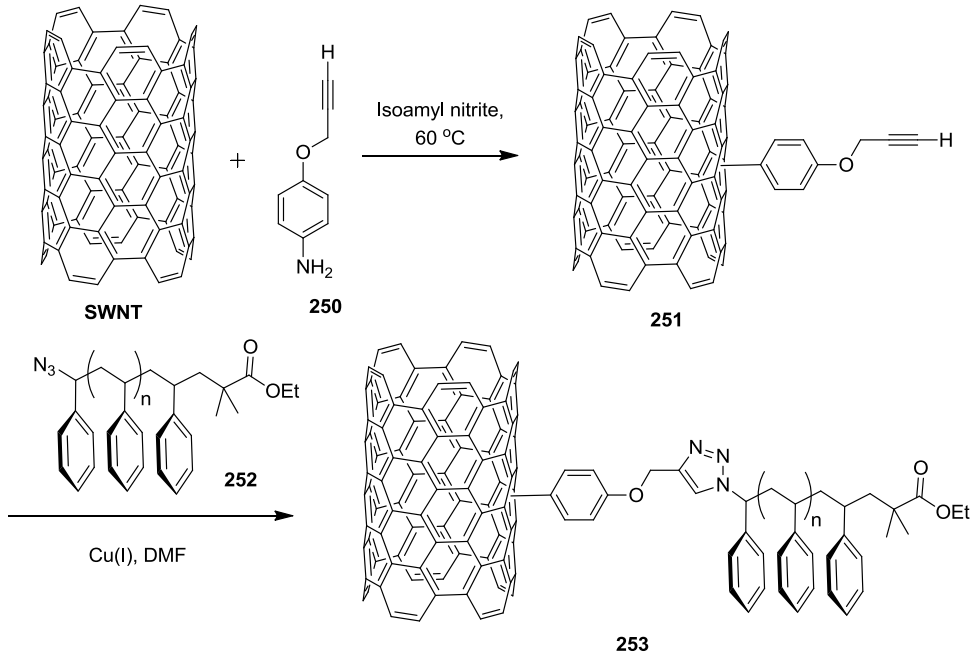

Scheme 3.2: Adronov's preparation of polystyrene functionalized SWNTs via the CuAAC reaction.

In another example, Guldi and co-workers functionalized SWNTs with zinc porphyrins and studied the donor-acceptor properties of the resulting SWNTs-ZnP conjugates. As described in Scheme 3.3,[14] a simple click reaction approach was applied between alkyne-functionalized SWNTs and the zinc porphyrin azide counterparts. The click derived SWNTs-ZnP conjugates were found to have good solubility in organic solvents. Furthermore, characterizations based on steady-state and time-resolved

spectroscopic measurements indicated the formation of reduced SWNT and oxidized ZnP species after photoexcitation.

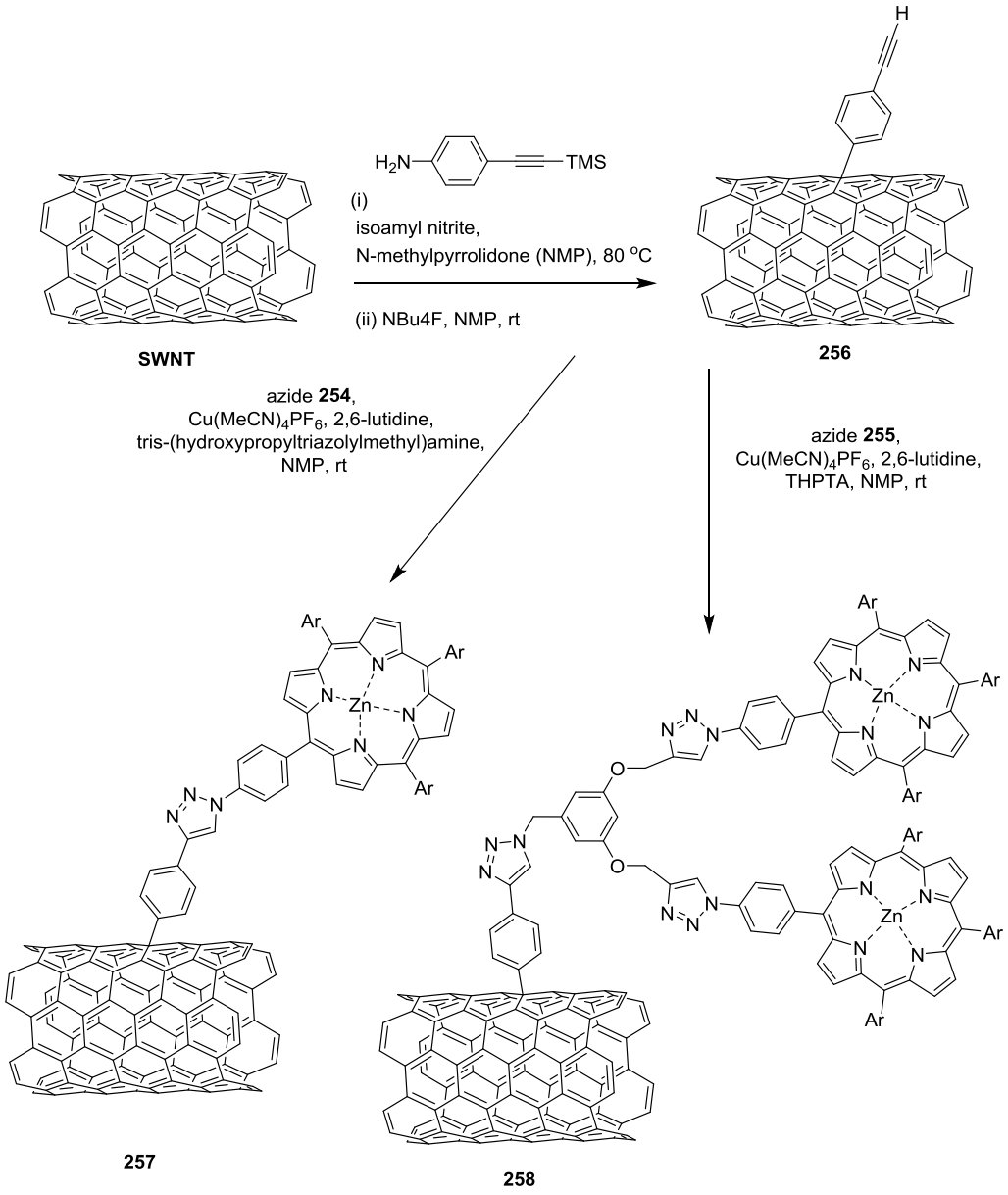

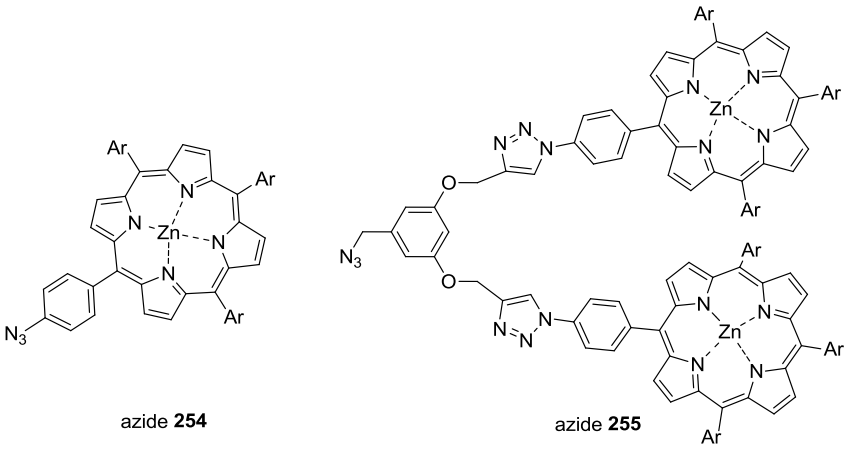

Scheme 3.3: Functionalization of SWNTs with zinc porphyrin azides by click strategy

In 2007, Langa and co-workers for the first time reported the synthesis of a conjugated hybrid of C_{60}-fullerene and SWNTs by the amidation reaction of carboxylic acid functionalized SWNTs and amine derived C_{60} fullerene (Scheme 3.4).[15] An esterification reaction with *n*-pentanol on the remaining acid chloride groups brought good solubility to the complex. It was suggested that this type of nanoscale hybrid material could be potentially useful in optoelectronic devices.

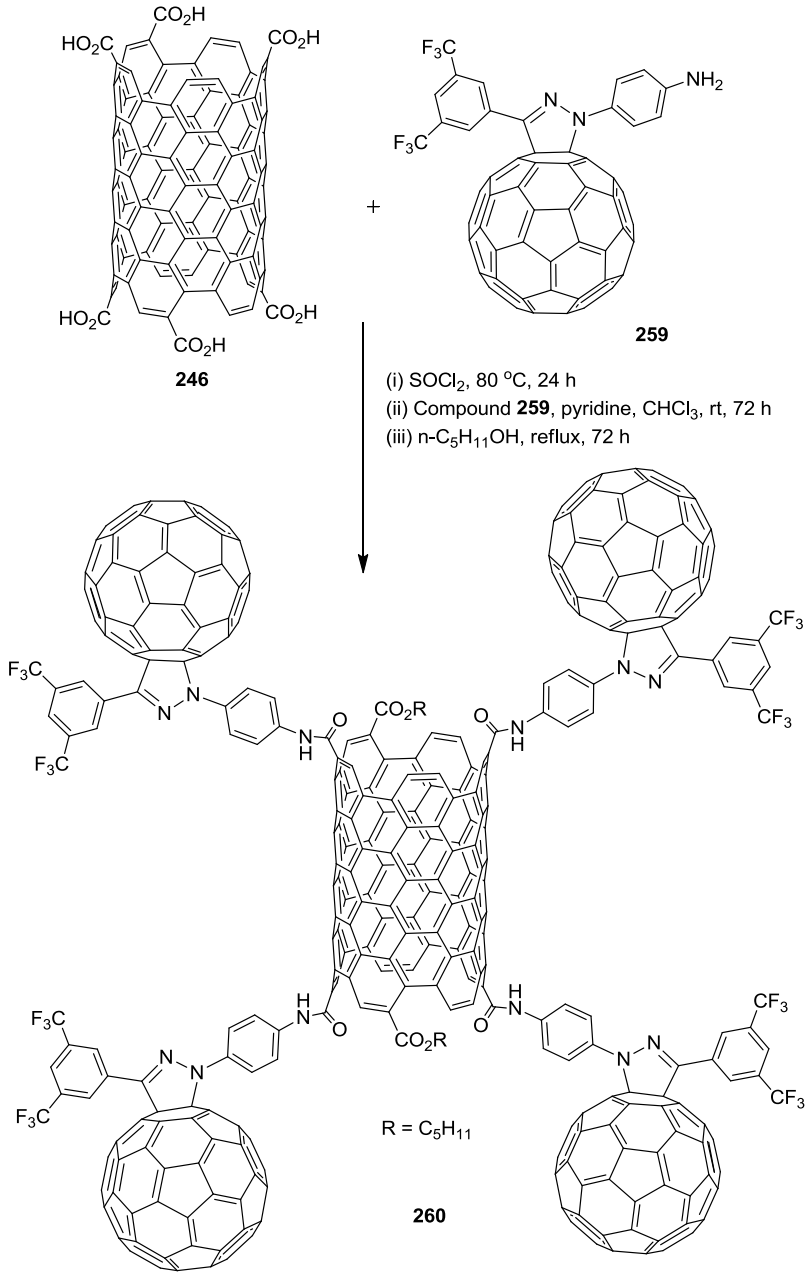

Scheme 3.4: Synthesis of C_{60}-SWNTs nanohybrid material **260**.

Although covalent functionalization is an effective way for dispersing nanotube bundles and creating a large number of nanomaterials; however, it has some drawbacks.

The chemical reactions happening on the surface of the nanotubes can cause structural damage to the tube, which leads to the undesirable disruption in the electronic and mechanical properties of the SWNTs. On the other hand, the noncovalent functionalization method has obvious advantages over the covalent method, as it does not require any chemical reactions to be performed on the surface of the nanotube. In the following section, the noncovalent functionalization of SWNTs will be presented in detail with some representative examples from the recent literature.

3.1.3 Noncovalent functionalization of SWNTs

Noncovalent functionalization of SWNTs has received considerable attention in the field of nanotube-based science and technology, not only because it provides a direct solution to the problems of insolubility and poor processability of as-produced SWNTs, but also because it enables easy ways for sorting specific types of SWNTs out of as-produced SWNT mixtures.[16,17] Usually, in this method, the SWNTs can be functionalized through surface binding of macromolecule-based dispersants such as surfactants,[9,18] polymers[17,19-23] and DNA,[24] and adhesion of small molecules[25-27] to improve the solubility in various solvents.

Jeffrey S. Moore and co-workers recently reported that the noncovalent functionalization of SWNTs using an oligo(*m*-phenylene ethynylene)s foldamers (m-PE 13 mers) as shown in Figure 3.3.[28] These oligomers do not show significant intramolecular π-stacking and adopt unfoldable confirmation in chlorinated solvents. When mixed with SWNTs, stable supramolecular complexes are formed in which

SWNTs are wrapped by the oligomers through π-π interactions. Interestingly, by the addition of polar solvents such as acetonitrile to the dispersed oligomer-SWNT complexes, the oligomers show a stronger tendency for self-folding as a result of increasing solvophobic effect, and the conformational change in the oligomers disrupts the intramolecular π-π interactions between the surface of the nanotube and the oligomers, resulting in the nanotubes being released from solution. The dissolved SWNTs were measured to be 700 mg/L in chloroform as solvent. The authors have concluded that these foldable oligomers can potentially be used for the purification of SWNTs.

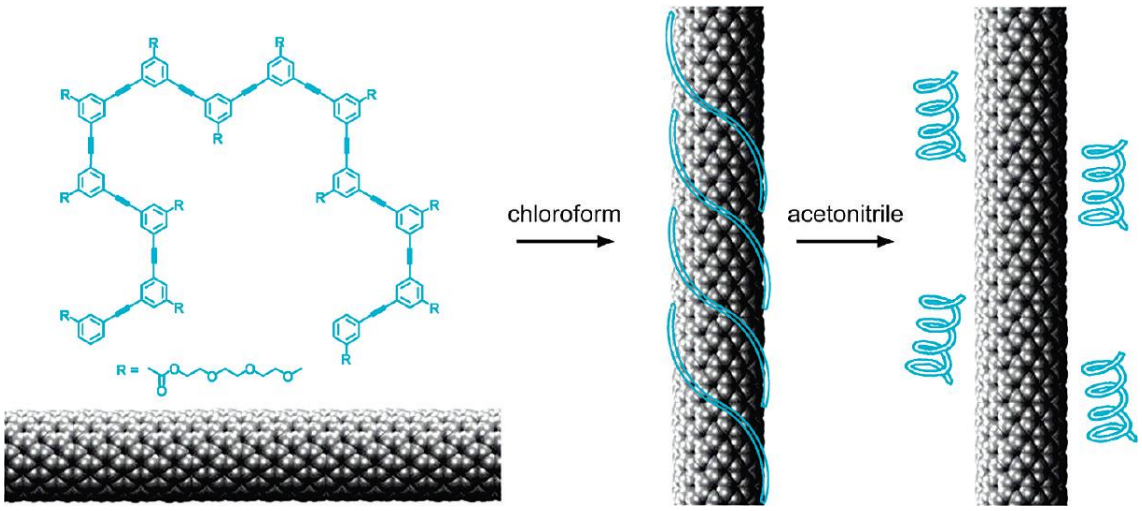

Figure 3.3: Solution process for dispersion and release of SWNTs by mPE-13mers (adopted from reference 28 with permission).

Bao and co-workers reported that the dithiafulvalene (DTF)/thiophene based copolymers such as poly(dithiafulvalene-fluorene-*co*-*m*-thiophene)s (pDTFF-*m*T) could selectively disperse semiconducting SWNTs in toluene through noncovalent wrapping.[29] The DTF groups are substituted on the polymer back bone to create large planar surfaces which facilitate the strong interaction with SWCNT walls as well as the possibility of interaction through charge transfer. It is noted that the presence of thiophene units in the polymer backbone is helpful in the selective dispersion of SWNTs. The results from UV-Vis-NIR and Raman spectroscopy indicated that small length polymers (pDTFF-1T) are more selective towards semiconducting SWNTs and higher length polymers (pDTFF-3T) are selective towards metallic SWNTs. Interestingly, the polymer that has only one thiophene in the repeat unit shows high degree of dispersion of SWNTs in comparison with other analogous polymers.

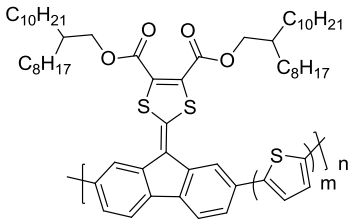

pDTFF-*m*T

m = 1, 2, 3

261

Figure 3.4: Chemical structure of pDTFF-*m*T **261** designed for the noncovalent functionalization of SWNTs.

In the Zhao group, TTFV-based conjugated polymers have been designed and synthesized to reversibly disperse and release SWNTs in organic solvents simply under the control of pH or redox stimuli (Figure 3.5).[30] The wrapping mode facilitates the interactions between TTFV-polymer **262** and SWNTs, leading to a strong dispersion of individual small diameter tubes, while the adhesion mode works better for large-diameter tubes to form supramolecular networks and produces TTFV-polymer/SWNTs sol-gels. The TTFV unit is known to undergo reversible protonation that is associated with switching of its conformation from *cis* to *trans*. This switching behavior of TTFV has been successfully utilized in controlling the TTFV-polymers to perform reversible SWNT dispersion and their release in organic solvents.

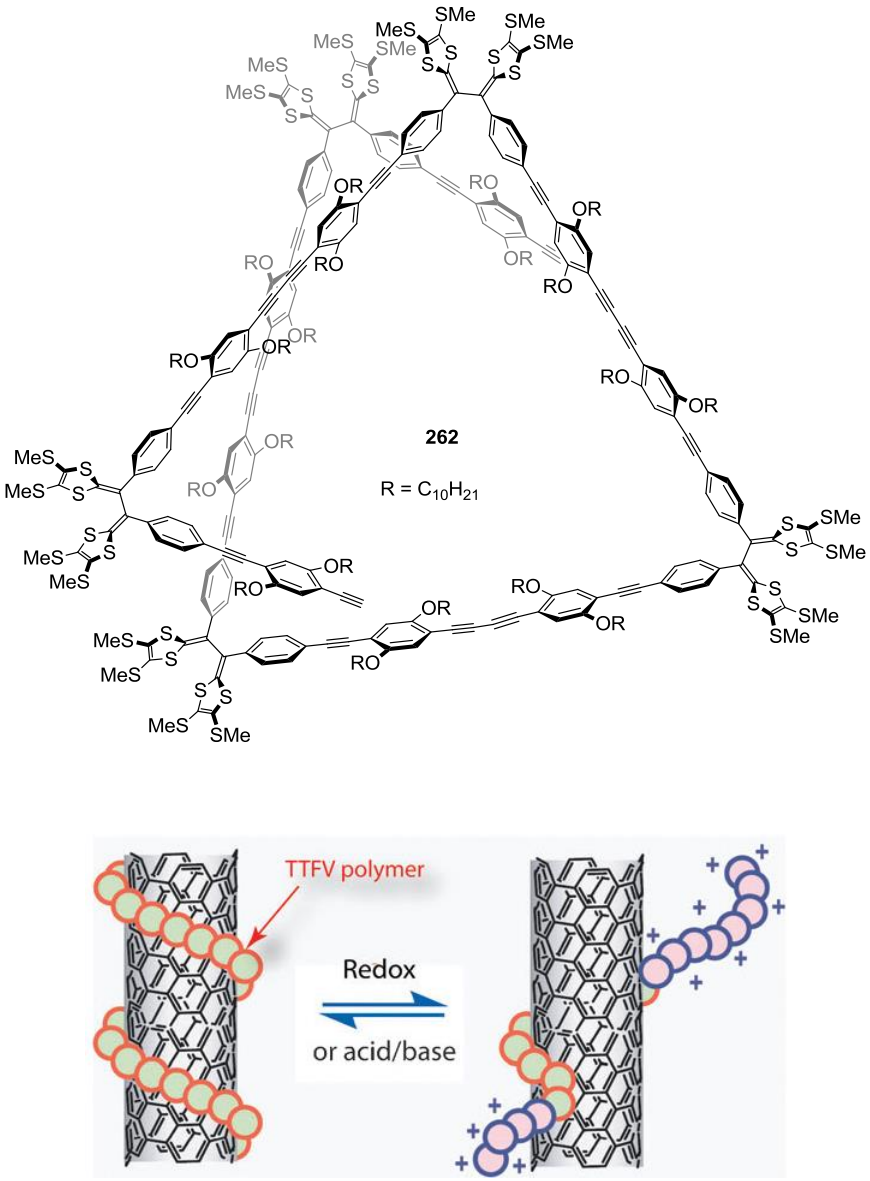

Figure 3.5: Chemical structure of TTFV-polymer **262** for SWNTs wrapping (top), and schematic representation showing the reversible wrapping and unwrapping of SWNT by a TTFV polymer (down) (adopted form reference 30 with permission).

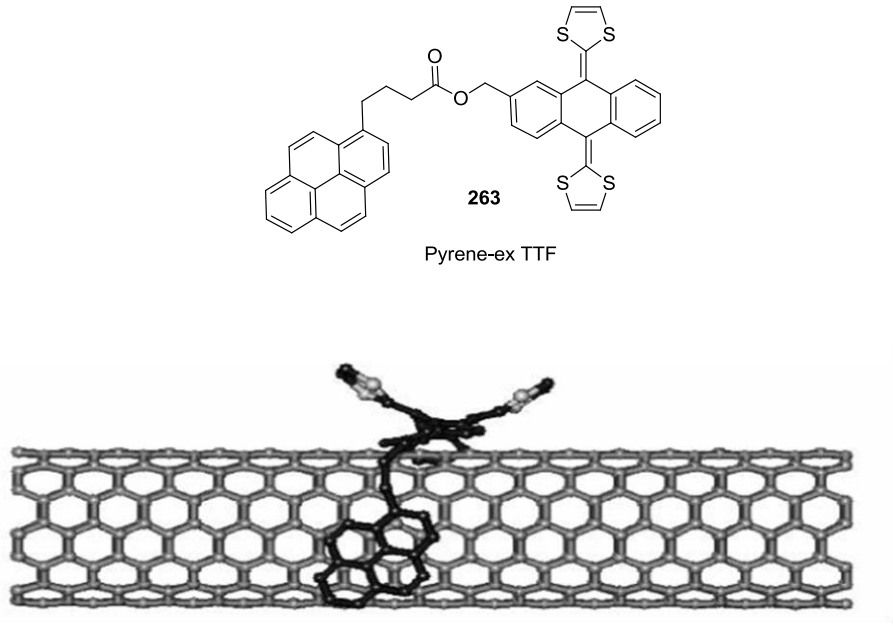

Figure 3.6: Chemical structure of pyrene-ex TTF **263** (top), and molecular modeling image of SWNT/pyrene-ex TTF complex (down) (adopted from reference 31 with permission).

The noncovalent functionalization of SWNTs by using small aromatic moieties such as anthracene, pyrene, and porphyrin derivatives has been studied in the literature. Martin and co-workers reported supramolecular interactions between SWNTs and π-extended TTFs such as "pyrene-ex-TTF".[31] The pyrene unit is essential to surface immobilization on SWNTs through π-π interactions. The electronic properties of the complex have been investigated because of the electron donor ability of ex-TTF and electron accepting properties of SWNTs.

Park and co-workers recently studied the use of naphthalene based azo dispersants for the selective extraction of semiconducting SWNTs from a mixture. The compound

264 shows unique double selectivity for SWNTs. The undecomposed form of compound **264** selectively disperses semiconducting SWCNTs, whereas the decomposed product of **264** which is a naphthyl-based radical species can selectively bond to metallic SWNTs. This result provides a simple method for the separation and purification of semiconducting SWNTs in high yield. With density gradient ultracentrifugation, they have obtained >98% semiconducting SWNTs in a single pass of purification.[32]

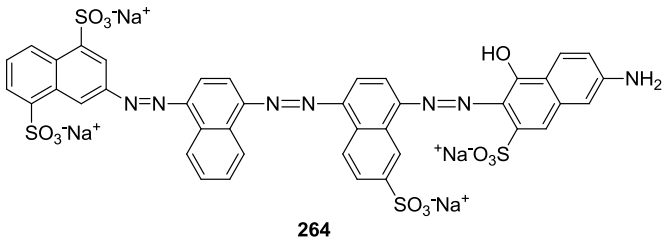

264

Figure 3.7: Chemical structure of naphthalene-based azo dispersant **264**.

3.1.4 Objectives of this chapter

As mentioned earlier, SWNTs have attracted much attention due to their exceptional mechanical, thermal, chemical, electrical, and electronic properties which may find in various devices. For device fabrication, high-purity metallic or semiconducting SWNTs are highly desired. However, all current reported methods produce a mixture of metallic and semiconducting SWNTs, and highly efficient purifications methods are required for the separation of these SWNTs. For this purpose, various chemical functionalization methods can be used, among which noncovalent functionalization presents a particularly intriguing approach not only because it provides a direct solution to the problems of insolubility and poor processability of as-produced

SWNTs, but also because it enables easy ways for sorting specific types of SWNTs out of as-produced SWNT mixtures.

Usually, macromolecule-based dispersants such as surfactants, polymers, and DNA are preferred for debundling and dispersion of SWNTs in various solvents, as they tend to form stable complexes with SWNTs with sufficient dispersant–SWNT interactions via van der Waals forces or π-stacking. The use of relatively small π-conjugated oligomers to disperse SWNTs, however, has not been extensively studied yet. In recent years, various DTF- and TTF-containing compounds have been found to show significant supramolecular interactions with SWNTs. These results thus inspired us to investigate the supramolecular interactions between the DTF–oligomers (**265**, **266**, **267**, and **268**) and the carbon nanomaterials such as SWNTs and fullerenes.

Most of the data in this chapter have been published in *J. Mater. Chem. C.* **2013**, *1*, 5116-5127 as a full article, in which I am the first author of the paper.

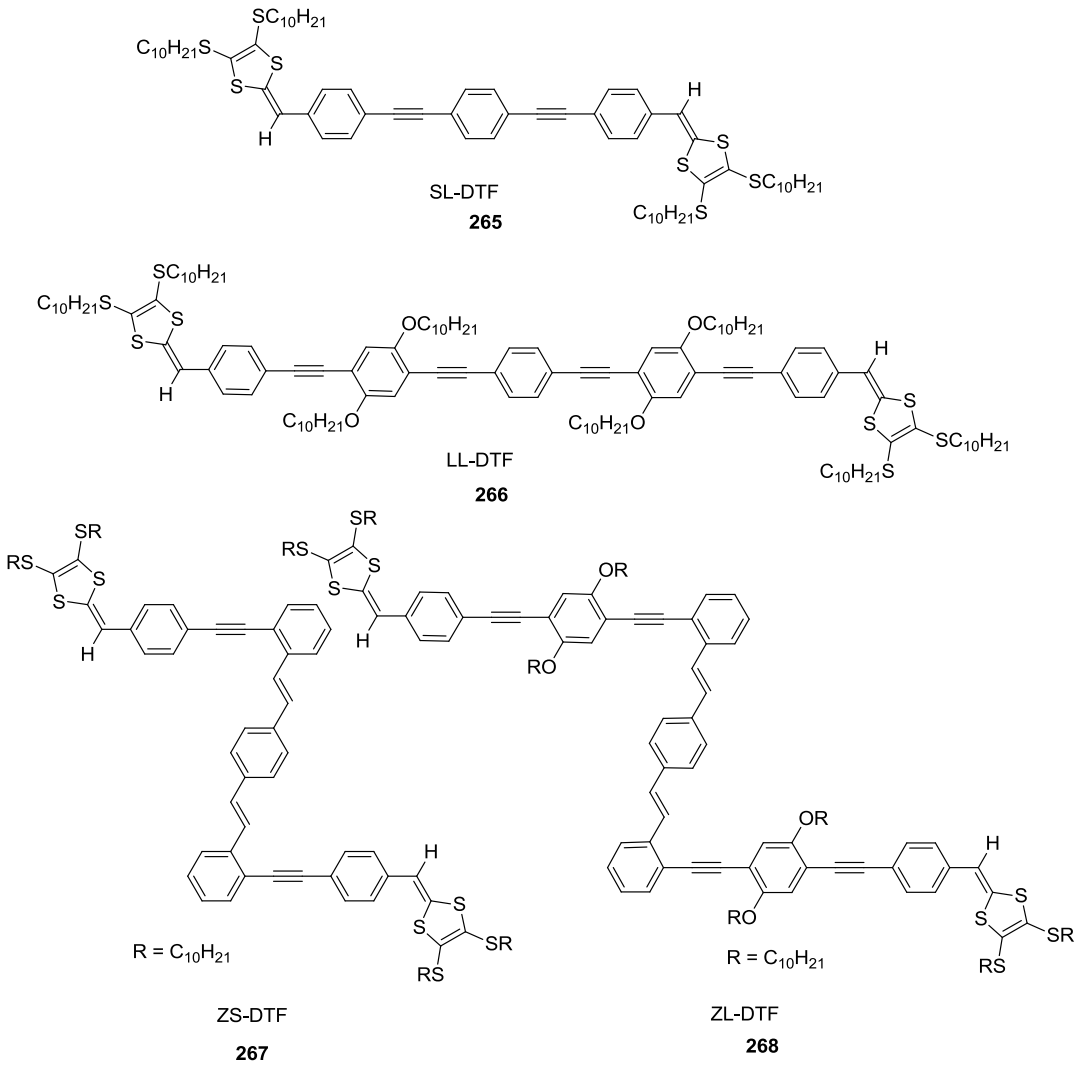

Figure 3.8: Chemical structures of DTF-oligomers designed for SWNT dispersion.

3.2 Results and Discussions

3.2.1 Synthesis of DTF substituted linear and Z-shaped OPE/OPV co-oligomers

The synthesis began with the preparation of a key intermediate *S*-decyl thione **270** and linear and Z-shaped π-conjugated aldehyde building blocks **273**, **276** and **278**, **279**. The following section describes the synthetic details of all the intermediates and final target compounds.

Synthesis of *S*-decyl thione

S-decyl thione **270** was prepared using known procedures. As shown in Scheme 3.5, the synthesis started with a radical reaction between Na and CS_2 using DMF as solvent. The resulting dithiolate was chelated with Zn^{2+} upon addition of $ZnCl_2$ and $NH_3.H_2O$, and precipitated out as a stable red colored salt **269** in the presence of tetraethylammonium bromide (TEAB). The overall yield of this sequence of reactions was 88%. Salt **269** was then dissociated into free dithiolate in refluxing acetone, and the resulting intermediate was subsequently alkylated with 1-decyl bromide to afford *S*-decyl thione **270** in 74% yield.

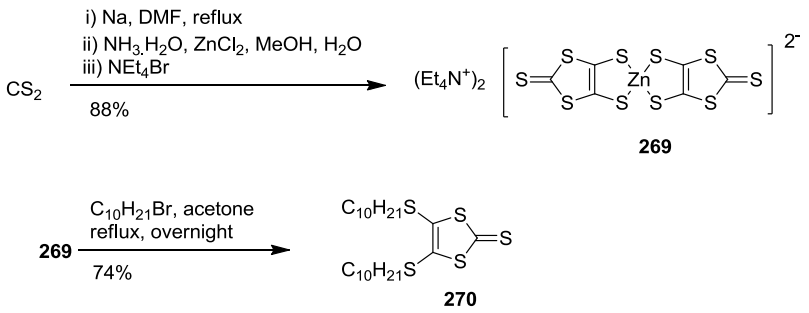

Scheme 3.5: Synthesis of *S*-decyl thione intermediate **270**.

3.2.2 Synthesis of linear and Z-shaped π-conjugated aldehydes

(a) Synthesis of short and long linear π-conjugated aldehydes

As shown in Scheme 3.6, the synthesis of short linear shaped π-conjugated (SL-CHO) **273** was started with a Sonagashira reaction performed on commercially available 4-bromobenzaldehyde with trimethylsilylacetylene (TMSA), and subsequent desilylation using K_2CO_3 resulted in compound **272**. Compound **272** was converted into SL-CHO **273** via the cross-coupling reaction with 1,4-diiodobenzene with a 78% yield (crude). Compound SL-CHO **273** showed very poor solubility in common organic solvents due to the lack of any solubilizing groups, and for this reason it was isolated merely in a crude form.

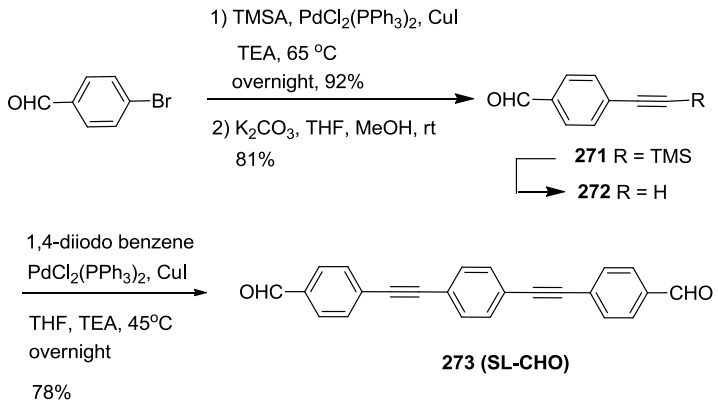

Scheme 3.6: Synthesis of short linear aldehyde (SL-CHO) **273**.

The synthesis of long linear π-conjugated (LL-CHO) **276** is outlined in Scheme 3.7. The first step was the cross-coupling reaction of compound **215** with compound **272**, followed by desilylation, yielding the phenyl acetylene building block **275.** Next, compound **275** was cross-coupled with 1,4-diiodobenzene under Sonagashira conditions to afford LL-CHO **276**.

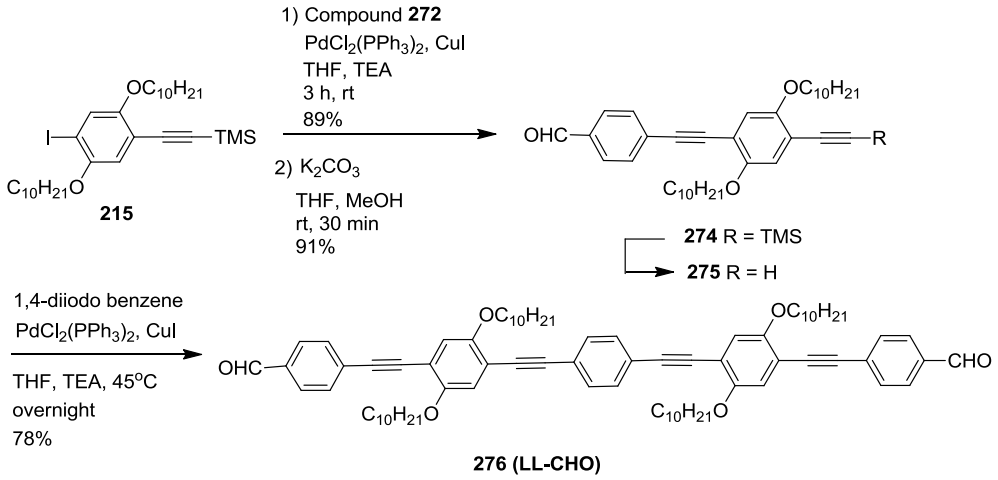

Scheme 3.7: Synthetic route for LL-CHO **276**.

(b) Synthesis of short and long Z-shaped π-conjugated aldehydes

To construct the short and long Z-shaped aldehydes, the essential diiodo building block **277** was first prepared as shown in Scheme 3.8. A Horner-Wittig reaction between 2-iodobenzaldehyde and 1,4-bis(diethylphosphonatomethyl)benzene **234** in the presence of NaH afforded compound **277** as a yellow solid. Treating **277** with compound **272** under Sonagashira conditions gave short Z-shaped aldehyde **278** in 65% yield as a yellow solid. Similarly, the reaction of compound **277** with the phenylacetylene building block **275** under Sonagashira conditions afforded the long Z-shaped aldehyde **279** in 72% yield.

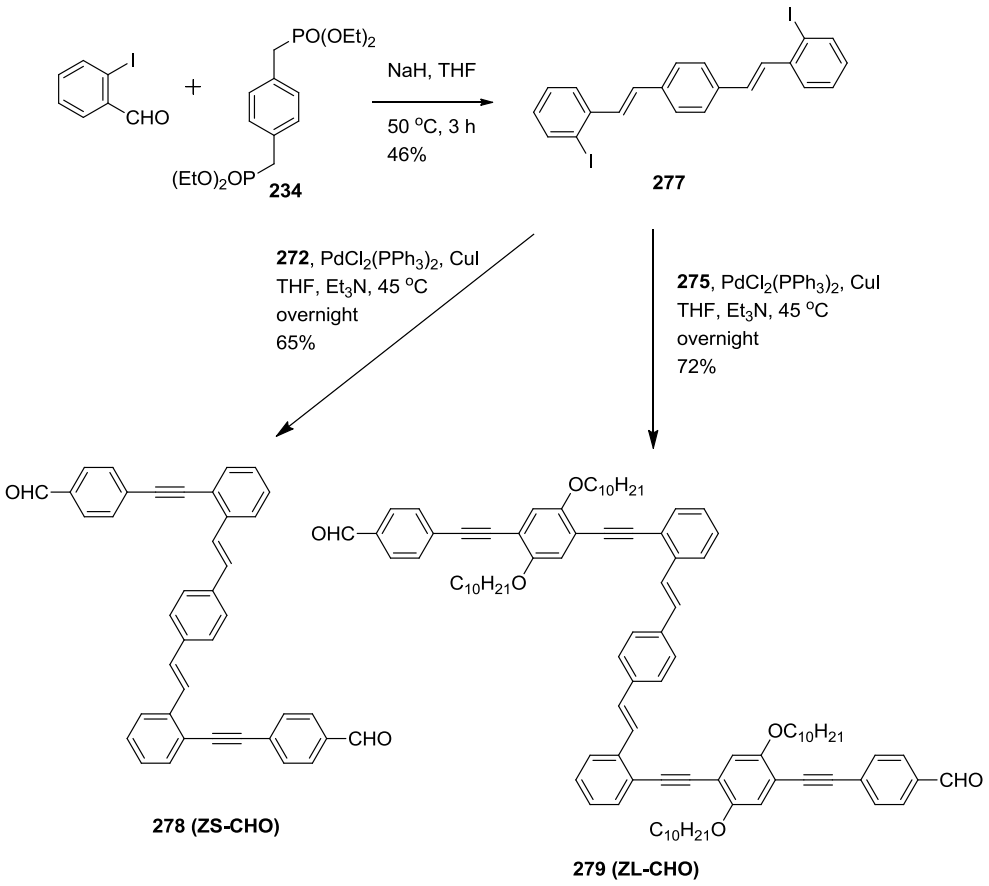

Scheme 3.8: Synthesis of both short and long Z-shaped OPE/OPV aldehyde precursors.

(c) Synthesis of linear OPE/OPV co-oligomers with DTF end groups

With compounds SL-CHO **273** and LL-CHO **276** in hand, the synthesis of linear DTF substituted co-oligomers was straightforward and it was achieved as outlined in Scheme 3.9. Despite the difficulty in attaining satisfactory purity**,** compound SL-CHO **273** was subjected to a $P(OMe)_3$-mediated olefination reaction with *S*-decyl thione **270**, giving DTF-endcapped phenylacetylene trimer **265** that showed much better solubility

and was readily purified by column chromatography. By a similar olefination reaction, the aldehyde groups of compound **276** were reacted with *S*-decyl thione **270** to yield DTF-endcapped phenylacetylene pentamer **266** in 76% yield .

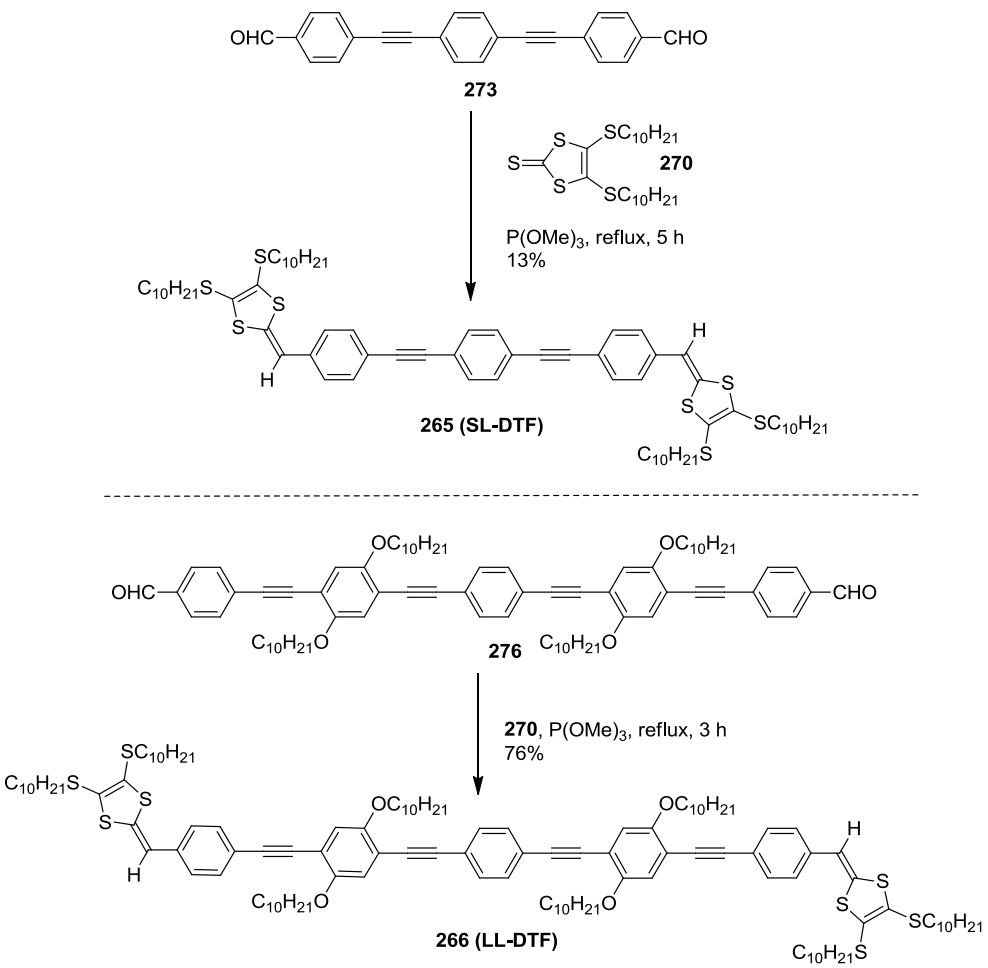

Scheme 3.9: Synthesis of DTF endcapped linear OPE/OPV trimer and pentamer.

For the synthesis of Z-shaped DTF substituted OPE/OPV oligomers, the aldehydes **278** and **279** were subjected to $P(OMe)_3$-mediated olefination reactions with *S*-decyl thione **270** to afford short Z-shaped and long Z-shaped DTF oligomers **267** and **268**

in 67% and 71% yields respectively (Scheme 3.10). The short Z-shaped DTF oligomer **267** was obtained as thick brown syrup and its long oligomer **268** as a yellow colored solid.

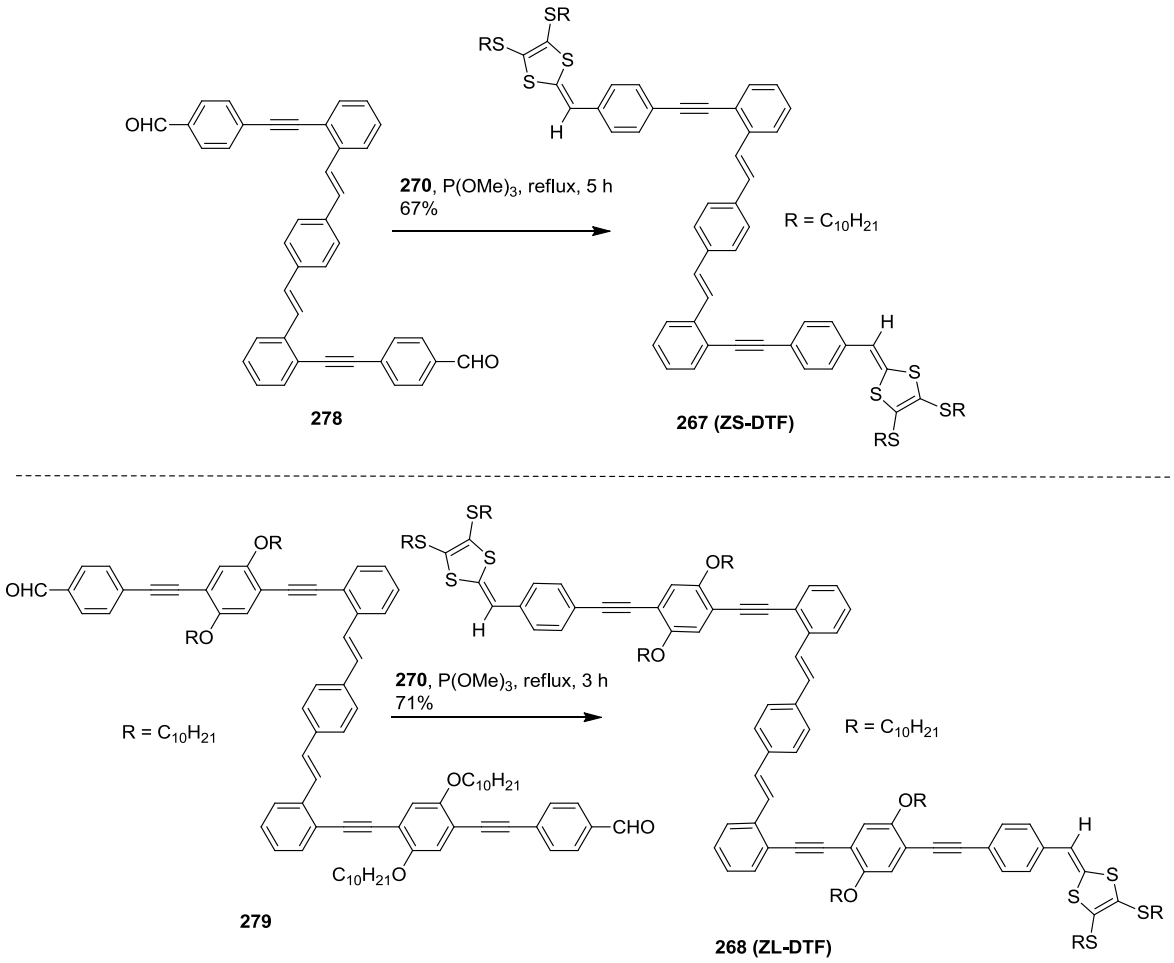

Scheme 3.10: Synthesis of DTF substituted short and long Z-shaped oligomers.

All the DTF functionalized OPE/OPV linear and Z-shaped oligomers and their corresponding OPE/OPV precursors have been characterized by IR, ^{1}H and ^{13}C NMR

spectroscopy and mass spectrometry, the results of which offer convincing proof of their molecular structures and purities.

3.2.2 UV-Vis absorption, emission, and electrochemical properties

(a) UV-Vis absorption properties

As shown in Figure 3.8a shows the UV-Vis absorption spectra of all DTF functionalized co-oligomers in comparison with their aldehyde-endcapped precursors, except the short linear aldehyde-OPE **273** due to its poor solubility, measured in chloroform at room temperature. It can be seen from Figure 3.8a that the maximum absorption wavelength of long linear DTF-OPE **266** (at 423 nm) is redshifted by only 12 nm relative to short linear DTF-OPE **265** (at 412 nm), as a consequence of increased conjugation of the oligomer π-framework. Comparison of the absorption spectra of long linear DFT-OPE **266** and its precursor aldehyde-OPE **276** (λ_{max} = 408 nm) reveals a redshift of λ_{max} by 15 nm, which is ascribed to the substitution effect of DTF endgroups on the electronic properties of the oligomer unit.

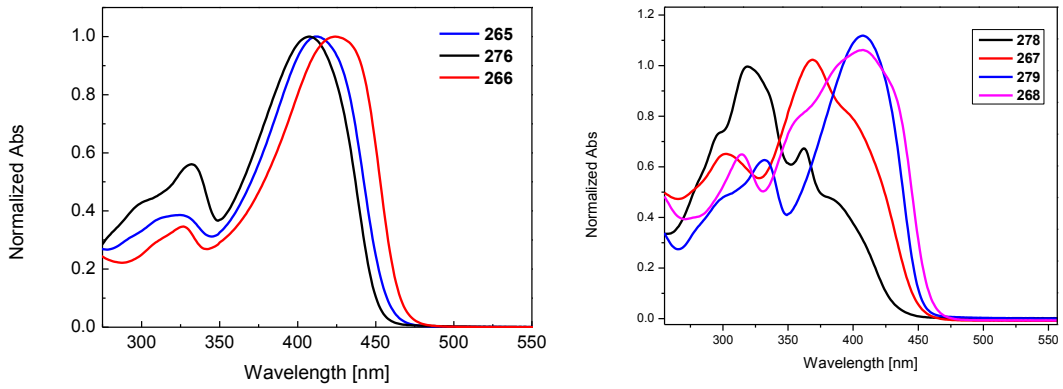

Figure 3.8a: Normalized UV-Vis absorption spectra of oligomers **265**, **276**, **266**, and **278**, **267**, **279**, and **268** measured in $CHCl_3$ at room temperature.

The spectrum of short *Z*-shaped DTF-OPE/OPV **267** shows a low-energy absorption band at 368 nm along with a shoulder at 402 nm. Its precursor aldehyde-OPE/OPV **278** exhibits a similar low-energy spectral profile, but the absorption band and shoulder are slightly blueshifted to 361 nm and 387 nm respectively. The spectrum of long *Z*-shaped DTF-OPE/OPV **268** shows a maximum absorption band at 408 nm, which is similar to that of its precursor aldehyde-OPE/OPV **279** (λ_{max} = 407 nm). The spectrum of **268** shows a distinctive absorption band at 388 nm and a shoulder at 432 nm in the low-energy region.

(b) Emission properties

The electronic emission properties of DTF-functionalized co-oligomers and related aldehyde-oligomer precursors were investigated by fluorescence spectroscopic

analysis. As shown in Figure 3.9, the aldehyde-endcapped oligomers appear to be highly fluorescent when compared to their DTF functionalized co-oligomers.

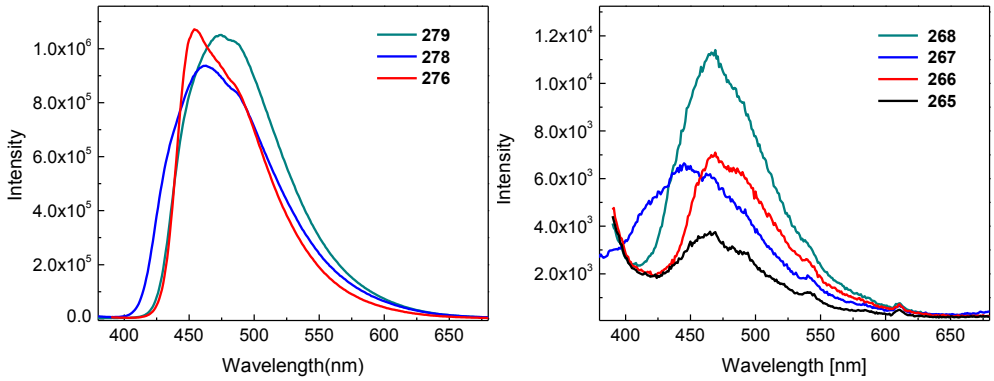

Figure 3.9: Fluorescence spectra of oligomers **276**, **278**, **279**, and **265-268** measured in $CHCl_3$ at room temperature.

From Table 3.1, it can be predicted that the emission of DTF-endcapped oligomers is substantially attenuated with quantum yields around *ca*. 1%. The suppressed emission is attributed to facile non-radiative decay mainly due to photoinduced electron transfer which takes place from the DTF donor to the oligomer fluorophores.

Table 3.1: Summary of photophysical data for DTF-oligomers and their aldehyde-oligomer precursors

Entry	Absorption λ /nm (ε / 10^4 cm^{-1} M^{-1})	Emission λ /nm	Quantum yield (Φ)
265	412 (6.72), 319 (2.56)	488, 466	0.012
276	407 (7.92), 331 (4.45), 299(3.42),	485, 454	0.591
266	423(11.2), 326 (3.82)	487, 468	0.013
278	387(2.51), 361(3.65), 318(5.38)	487, 462	0.406
267	296 (3.98), 246 (1.78)	444	0.010
279	402(s) (4.90), 368 (6.49), 301(4.14) 401(s) (6.21), 366(7.65), 327(5.98),	487, 474	0.676
268	308(6.41) 432(8.47), 406(10.5), 384(9.33), 357(7.52), 314(6.19), 245(5.04)	488, 466	0.013

(c) Electrochemical properties

The electrochemical redox properties of DTF-functionalized oligomers were investigated by cyclic voltammetry (CV). Figure 3.10 shows the cyclic voltammograms that were measured in the multi-cycle scan mode. For the first cycle of CV scans, the voltammogram of DTF-OPE **265** clearly shows an anodic peak at +0.82 V and a cathodic

peak at +0.54 V, which are assigned to the oxidation of DTF into $[DTF]^+$ and the reverse reduction.[33-35] Starting from the second cycle of CV scans, a new anodic peak at *ca*. +0.6 V emerges and its intensity grows steadily together with the cathodic peak at +0.54 V. The rise of this new peak is due to the continuous formation of $[TTFV]^{2+}$ as a result of oxidative dimerization of DTF (Scheme 3.11) on the surface of working electrode. The voltammogram of long linear DTF-OPE **266** shows a similar growth of $[TTFV]^{2+}$ peak upon multi-cycle scans; however, the $[DTF]^+$ peak appears to reduce more dramatically in intensity in comparison with **265**.

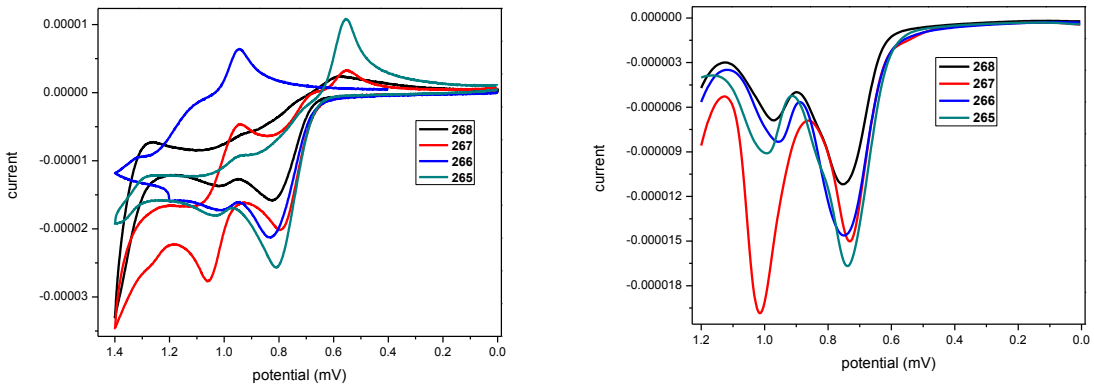

Figure 3.10: Cyclic voltammograms (CV) (left) and Differential pulse voltammogram (DP) (right) of **265** (1.33×10^{-3} M), **266** (0.98×10^{-3} M), **267** (1.45×10^{-3} M), and **268** (0.94×10^{-3} M). Experimental conditions (CV): Bu_4NBF_4 (0.1 M) as the supporting electrolyte, CH_2Cl_2 as the solvent, glassy carbon as the working electrode, Pt wire as the counter electrode, Ag/AgCl as the reference electrode, and the scan rate: 50 mV s^{-1}. Experimental conditions (DP): Bu_4NBF_4 (0.1 M) as the supporting electrolyte, CH_2Cl_2 as the solvent, glassy carbon as the working electrode, Pt wire as the counter electrode,

Ag/AgCl as the reference electrode, scan rate: 20 mV s^{-1}, pulse width: 20 mV, pulse period: 200 ms, pulse amplitude: 50 mV, and step: 4 mV.

Rationalization for the different CV patterns can be made as follows: when one of the DTF groups in **265** undergoes oxidative dimerization, the resulting $[TTFV]^{2+}$ dication imposes a significant electron-withdrawing effect on the other DTF group via the relatively short OPE π-spacer, which in turn lowers its reactivity toward dimerization.

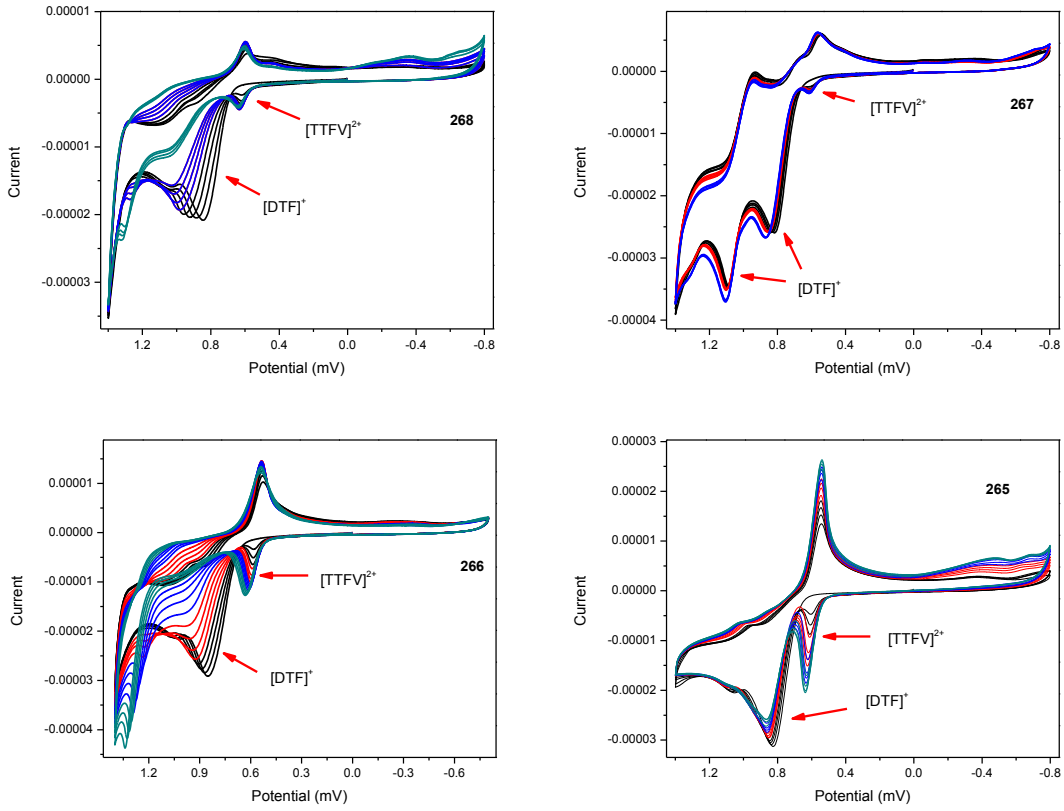

Figure 3.11: Cyclic voltammograms of DTF–oligomers measured in the multi-cycle scan mode. Experimental conditions: Bu_4NBF_4 (0.1 M) as the supporting electrolyte, CH_2Cl_2

as the solvent, glassy carbon as the working electrode, Ptwire as the counter electrode, Ag/AgCl as the reference electrode, and scan rate = 100 mV s^{-1}.

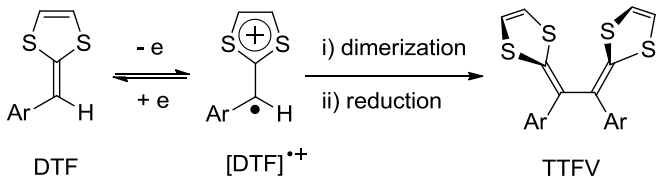

Scheme 3.11: Oxidative dimerization of DTF.

The electrochemical reactions on the working electrode therefore result in dimerization or a low-degree of oligomerization of **265**, after which a significant amount of DTF endgroups still remain unreacted. For DTF-OPE **266**, however, the relatively longer OPE bridge attenuates electronic communications between the two DTF endgroups. As a result, each of them undergoes oxidative dimerization independently, resulting in a quicker consumption of DTF units and relatively higher degrees of polymerization upon multiple CV scans (Figure 3.11). The voltammogram of long *Z*-shaped DTF-OPE/OPV **268** shows a similar electrochemical behaviour to that of the compound, long linear DTF-OPE **266**. Of particular note are the CV features of short Z-shaped DTF-oligomer **267**. In the first cycle of scan, two anodic peaks at +0.82 V and +1.09 V and two cathodic peaks at +0.56 V and +0.94 V can be seen. This result suggests that the two DTF groups in **267** have such a significant degree of electronic communications that they are oxidized in a stepwise rather than a simultaneous manner. With increasing cycles of CV scans, the $[TTFV]^{2+}$ peak at *ca*. +0.61 V becomes observed but with a rather weak current intensity. The voltammogram of **267** clearly shows that its

DTF endgroups are quite unreactive towards oxidative dimerization. Such a different electrochemical behaviour is tied to the strong electronic communications between the two DTF groups via the short Z-shaped OPE/OPV π-bridge of **267**. Overall, our comparative CV studies confirm that the π-spacers exert an important effect on the electrochemical properties and reactivities of DTF-endcapped oligomers

3.2.3 Interactions of DTF-endcapped oligomers with fullerenes

When a small amount of fullerene (C_{60} or C_{70}) was added into diluted solutions of the DTF- oligomers, a steadily increasing fluorescence was observed. At the first glance, this property was a bit puzzling, given the known fluorescence quenching effects arising from both DTF endgroups and fullerenes on oligomer fluorophores.

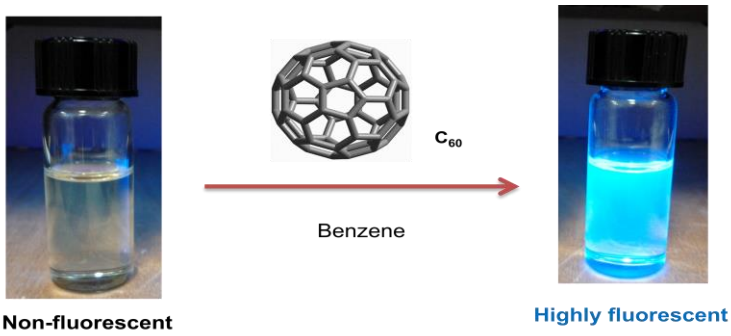

Figure 3.12: Photographic images of DTF-oligomer **268** before and after addition of C_{60} fullerene.

To shed light on this issue, ^{1}H NMR analysis was performed on a solution of oligomer **268** and C_{60} fullerene (3 eq) at various time intervals, which was not deliberately degassed. It was observed that the DTF units of oligomer **268** are gradually

converted into aldehyde groups, leading to compound **279** and thione as products (Figure 3.12). Fullerene C_{60} has a wide spectral absorption range and a low-lying triplet state. It is therefore reasonable to assume that upon exposing to ambient light, some kind of fullerene-sensitized reaction pathway leads to singlet oxygen ($^1O_2$) formation.[36,37] Singlet oxygen is known to react with electron-rich alkenes to form 1,2-dioxetane, which subsequently undergoes O-O bond cleavage to yield C=O products.[38-40] Scheme 3.12 outlines a proposed mechanism to account for the transformation of DTF to aldehyde promoted by singlet oxygen.

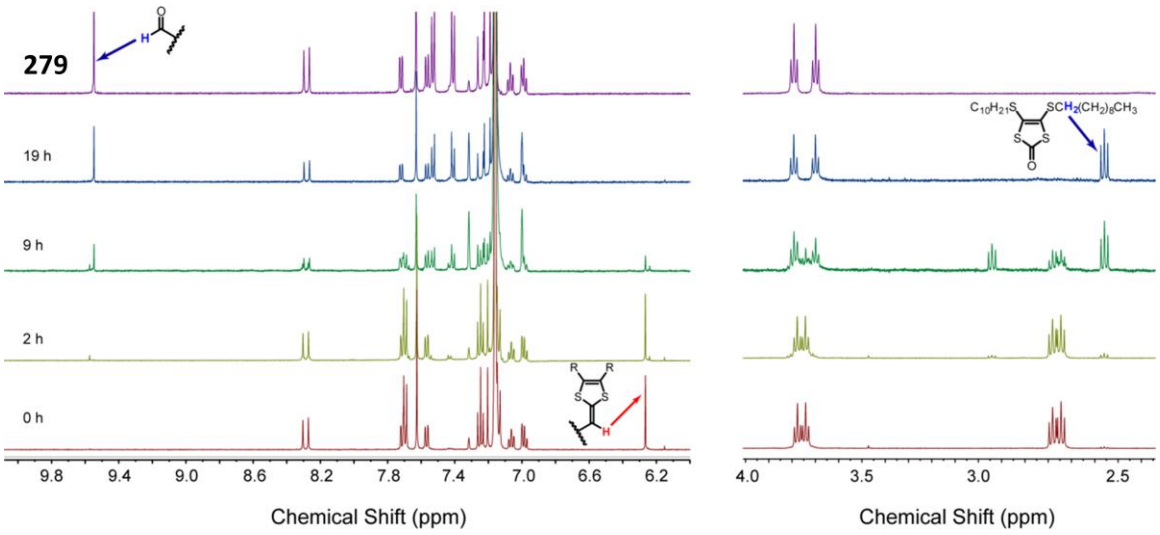

Figure 3.13: ^{1}H NMR spectra in the aromatic and aliphatic regions showing the gradual conversion of DTF–oligomer **268** to aldehyde–oligomer **279** in the presence of C_{60} fullerene at 298 K. Initial concentration of **268**: 8.9 x 10^{-4} M, concentration of C_{60}: 26.7 x 10^{-4} M, and solvent: C_6D_6.

Non-fluorescent DTF-oligomers undergoing this singlet oxygen promoted C=C cleavage reaction afford highly fluorescent aldehyde-oligomers, giving rise to the observed fluorescence enhancement. A value of 149 fold fluorescence enhancement was observed in the case of reaction with C_{60} fullerene, whereas the reaction with C_{70} results 162 fold fluorescence turn on with respect to the emission intensity of DTF-oligomer **268**.

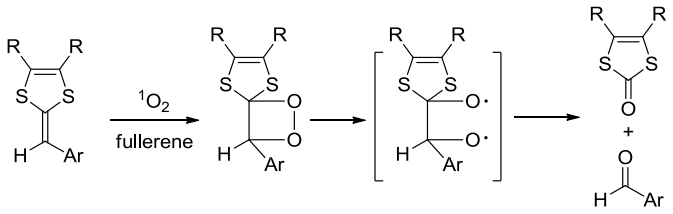

Scheme 3.12: Proposed mechanism for singlet oxygen-induced C = C bond cleavage of DTF.

To further probe the kinetic properties of the fullerene-sensitized C=C bond cleavage reactions, diluted solutions of **268** mixed with either C_{60} or C_{70} fullerene were examined by fluorescence spectroscopic analysis at varied times (Figure 3.14). From Figure 3.14A, the fluorescence enhancement ($F - F_0$) is observed to show a linear relationship with reaction time (τ) in the first 16 h. Assuming that ($F - F_0$) is proportional to the concentration of fluorescent product **279**, the correlation is in line with a zero-order kinetics. When C_{70} was used instead of C_{60} as the sensitizer, the correlation of ($F - F_0$) with τ appears to be in a good agreement with a first order kinetics.

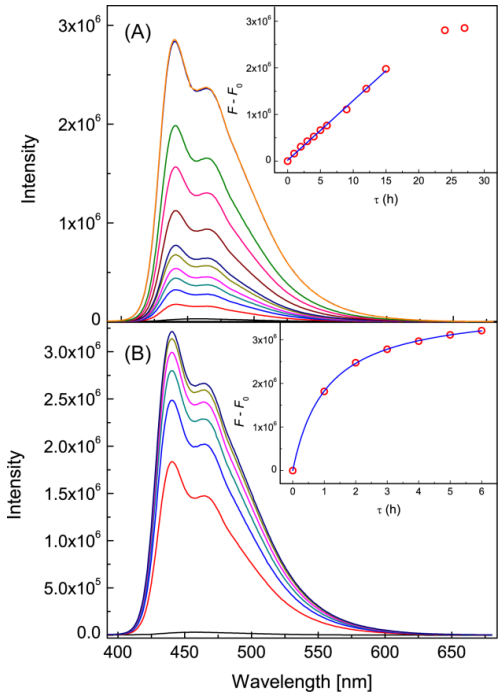

Figure 3.14: (A) Fluorescence spectra of **268** (1.8 x 10^{-6} M) with C_{60} in benzene at varied times. (B) Fluorescence spectra of **268** with C_{70} in benzene at varied times. Inset plots: fluorescence enhancement ($F - F_0$) as a function of time (τ). F_0 and F denote fluorescence intensities measured at initial and later stages at 440 nm.

A tentative rationalization of these different kinetic properties can be made based on the kinetic analysis described in Scheme 3.13. In the case where singlet oxygen generation is the rate determining step and the concentration of dissolved oxygen in solution is deemed as constant, a steady-state approximation can be assumed to give zero-order behavior for the observed reaction rate. On the contrary, if the C=C bond cleavage is the rate determining step, a rapid equilibrium approximation is valid, which leads to a

first-order kinetics for the overall reaction. The results of kinetics analysis suggest that C_{70} produces singlet oxygen at a much faster rate than C_{60}.

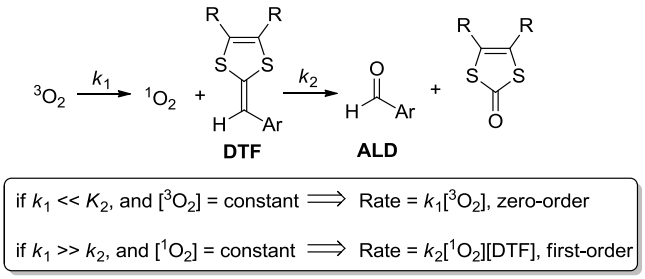

Scheme 3.13: Kinetics of singlet oxygen induced C=C bond cleavage of aryl-DTF.

The involvement of singlet oxygen as an oxidant in the fullerene-sensitized C=C bond cleavage is evidenced by the following experimental observations:

(i) The reaction rate was considerably slowed down when the reaction was carried out under argon. As can be seen from Figure 3.15, after the solution of **268** and C_{60} in benzene was deoxygenated by three cycles of free-pump-thaw and then placed under argon, the fluorescence spectral monitoring shows a much slower reaction rate in comparison with that observed in the presence of oxygen. This result suggests that oxygen in the air is the oxidant of the reaction.

(ii) The use of a classical singlet oxygen sensitizer, methylene blue, in place of C_{60}, also led to the same C=C bond cleavage reaction. As shown in Figure 3.16, after mixing with methylene blue under air for 48 h, the fluorescence intensity grew significantly, indicating the occurrence of C=C bond cleavage leading to a highly fluorescent aldehyde product **279**. The result suggests singlet oxygen is the active oxidant

to induce C=C bond cleavage in **268**; however, the reaction under this condition proceeded relatively at a slower rate than the case where C_{60} is used as the sensitizer, indicating that methylene blue is a poorer sensitizer than fullerenes.

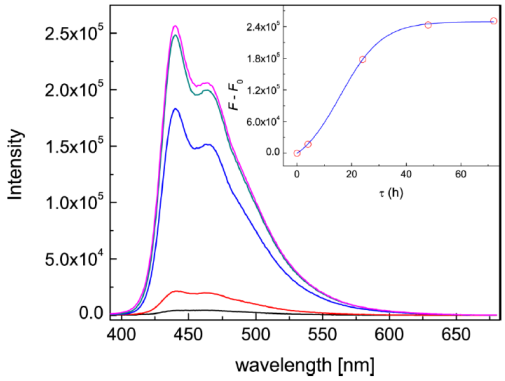

Figure 3.15: Fluorescence spectra of **268** (1.8×10^{-6} M) with C_{60} under argon in benzene at varied times. The solution was subjected to three cycles of free-pump-thaw under argon before fluorescence spectroscopic analysis. Inset plot: fluorescence enhancement ($F - F_0$) as a function of time (τ). F_0 and F denote fluorescence intensities measured at initial and later stages at 440 nm. Excitation wavelength = 370 nm.

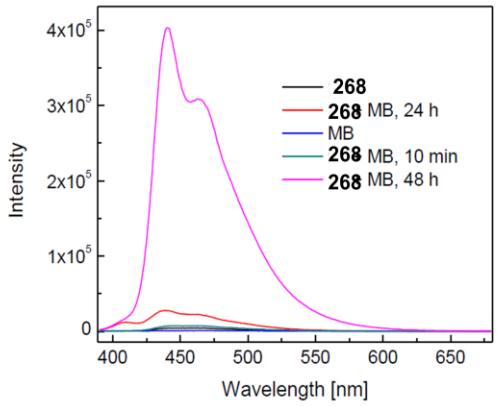

Figure 3.16: Fluorescence spectra of **268** (1.8×10^{-6} M) in benzene upon addition of methylene blue (MB) under air for varied times and the fluorescence spectrum of pure MB in benzene. Excitation wavelength = 370 nm.

(iii) Upon UV light irradiation under air, DTF-oligomer **268** underwent the same C=C bond cleavage reaction without the presence of C_{60}. As shown in Figure 3.17, the solution of **268** in benzene under air was subjected to UV light irradiation at 365 nm and monitored by fluorescence spectroscopy at varied times. The results show a steady increase in the fluorescence intensity similar to the case of Figure 3.14A but with a longer reaction time, indicating that 15 underwent oxidative cleavage reaction in the presence of singlet oxygen.

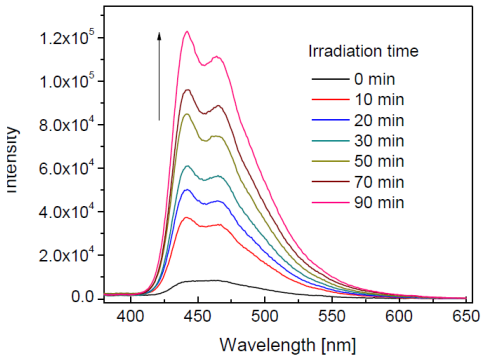

Figure 3.17: Fluorescence spectra of **268** (1.8 × 10-6 M) in benzene upon UV light irradiation (at 365 nm) under air for varied times. Excitation wavelength = 370 nm.

Finally, the reaction has also been attempted on a larger scale, where DTF-oligomer **268** was converted into **279** in a high yield of 89% (isolated) in the presence of C_{60} (3 molar equiv) at room temperature within 20 hours.

3.2.4 Interactions of DTF-oligomers with carbon nanotubes

(a) UV-Vis-NIR results of DTF-oligomers-SWNTs complexes

Two commercially available SWNTs were studied throughout this work, namely HiPCO and CoMoCAT nanotubes. With the DTF-oligomers in hand, dispersion experiments were then conducted with each type of carbon nanotube in a similar manner. In our experiments, first pristine SWNTs were added to the solutions of DTF-oligomers, the mixture was subjected to the ultrasonication for 60 min at rt, and then filtered through a cotton plug to remove undissolved material. The resulting solutions were centrifuged for 10 min and filtered through a cotton plug again to afford SWNTs suspension. If the

DTF-oligomers successfully dissociated the carbon nanotube bundles, a stable black solution would be observed after filtration.

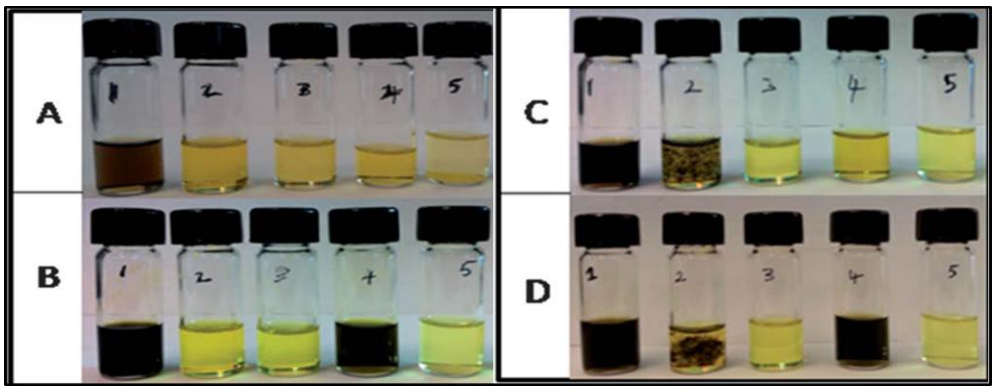

Figure 3.18: Photographic images of filtrates of DTF–oligomer solutions mixed with HiPCO SWNTs after sonication for 1 h. Rows: (A) oligomer **265**, (B) oligomer **266**, (C) oligomer **267**, and (D) oligomer **268**. Solvents tested (from left to right): chloroform, chlorobenzene, toluene, methylene chloride, and hexanes.

The photographic images in Figure 3.18 depict the outcomes of HiPCO SWNTs dispersed with DTF– oligomers, from which it is clearly seen that HiPCO SWNTs form stable black suspensions in the chloroform solutions of all four DTF–oligomers, where long oligomers **266** and **268** give much better dispersion results than short oligomers **265** and **267**. In methylene chloride, long oligomers **266** and **268** can also induce efficient dispersion of HiPCO SWNTs, but short oligomers **265** and **267** cannot. For other common organic solvents, including chlorobenzene, toluene, and hexanes, no effective dispersion of HiPCO SWNTs can be obtained using DTF–oligomers as dispersants. Although both short and long Z-shaped oligomers **267** and **268** were able to effect

dispersion of SWNTs in chlorobenzene immediately after sonication and filtration through a cotton plug, the suspensions were not stable enough and SWNTs precipitated out of the solution within a short period of time.

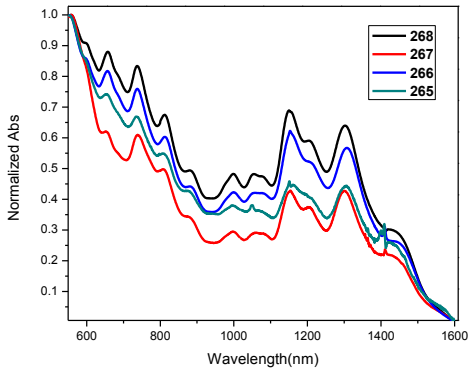

Figure 3.19: Normalized UV-Vis-NIR spectra of HiPCO SWNTs dispersed by DTF–oligomers in chloroform.

The HiPCo SWNTs suspensions in chloroform were then examined by UV-Vis-NIR absorption analysis. From Figure 3.19, it can be seen that the Vis-NIR absorption profiles of the SWNTs dispersed by the four oligomers are very similar to one another. There are two distinct sections in the spectrum of HiPCO SWNT solutions that can be attributed to metallic and semiconducting nanotubes. From the literature, it is known that the peaks which are seen in the range of 930–1500 nm are attributed to inter-band transitions of semiconducting SWNTs (S_{11}), while the peaks from 500–930 nm are due to metallic (M_{11}) and semiconducting (S_{22}) bands.[41,42] The results indicate that the SWNTs were well dispersed and debundled in the solution of DTF-oligomers.

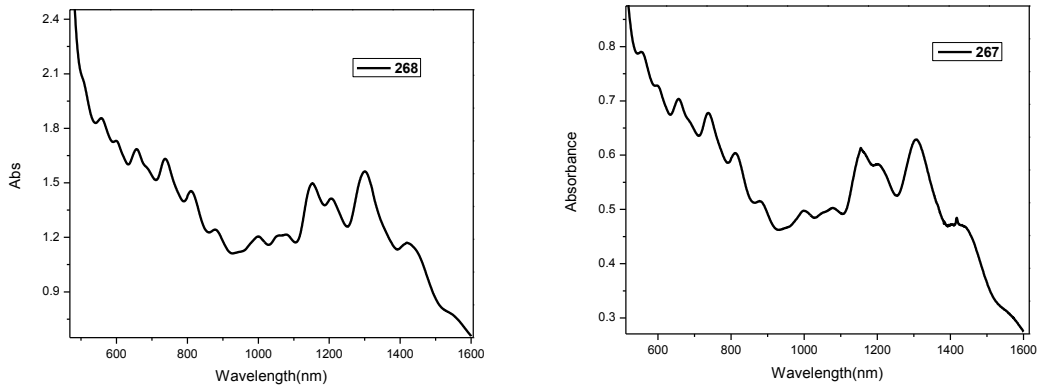

Figure 3.20: UV-Vis-NIR spectrum of HiPCO SWNTs dispersed with **268**, and **267** in CH_2Cl_2.

As mentioned earlier, only long DTF-oligomers could disperse SWNTs in DCM solvent. Similar characteristic bands have been observed with HiPCO SWNTs dispersed by long DTF oligomers in DCM solvent (Figure 3.20). In the spectrum of CoMoCAT SWNTs dispersed by long linear DTF-oligomer **266** in DCM solvent, a prominent peak at 999nm is observed, which is assigned to SWNTs with chiral index of (6,5) (Figure 3.21). In addition, peaks at 576 and 668 nm can be assigned to (6,5) and (7,6) SWNTs respectively.[43,44]

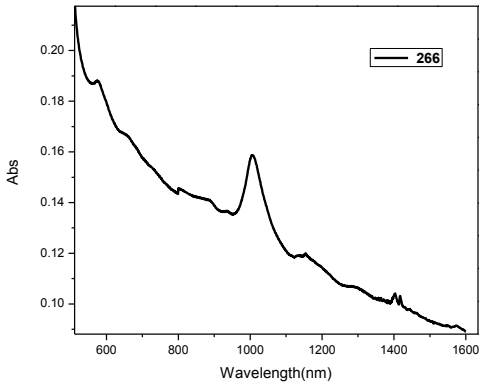

Figure 3.21: UV-Vis-NIR spectrum of CoMoCAT SWNTs dispersed with **266** in CH_2Cl_2.

(b) Raman spectroscopic results of DTF-oligomers SWNTs complexes

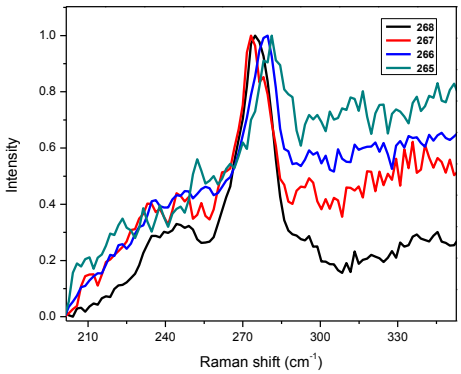

Figure 3.22: Raman spectra of HiPCO SWNTs dispersed by DTF oligomers in the RBM region (λ_{ex} 534 nm).

The dark solutions were evaporated to obtain SWNTs-oligomers complexes, which were then characterized by Raman spectroscopy. Figure 3.22 shows the Raman spectra in the radial breathing mode (RBM) region. Usually, Raman frequency in this

region is inversely proportional to the diameter of the nanotubes. The Raman frequency in the region of 265-280 nm can be ascribed to small diameter nanotubes, while the peaks at 190-220 nm are assigned to relatively large diameter nanotubes. It is concluded from the figure that the DTF-oligomers can selectively disperse the nanotubes of relatively smaller diameters in pristine HiPCO SWNTs.

(c) AFM results of CoMoCAT SWNTs-DTF oligomer complexes

The samples for AFM measurement were prepared by spin-coating of dilute SWNT-DTF oligomers suspensions on a freshly cleaved mica surface. The excess DTF-oligomers were rinsed off with chloroform followed by drying with nitrogen flow. Figure 3.23 depicts the AFM image of the supramolecular assemblies of HiPCO SWCNTs and DTF-oligomer **266** wherein oligomer agglomerates are clearly observed to stack around the sidewalls of debundled SWNTs. Such interactions are believed to be the major driving force for effective dispersion of SWNTs in the solution phase. Figures 3.24 and 3.25 are examples of results obtained for DTF-oligomers **268** and **267** with HiPCO SWCNTs. Both images show fairly consistent surface morphologies as obtained for DTF-oligomer **266**.

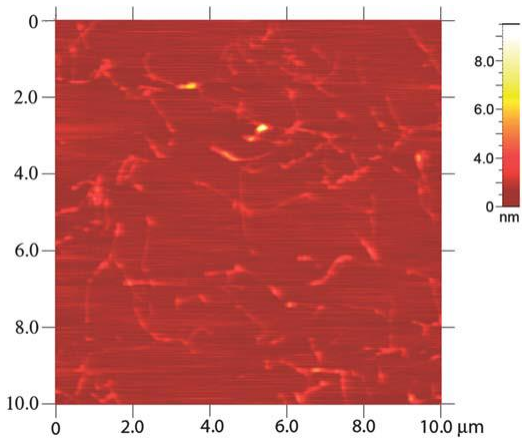

Figure 3.23: AFM image of supramolecular assemblies of HiPCO SWNTs and oligomer **266** spin-cast on a mica surface (tapping mode).

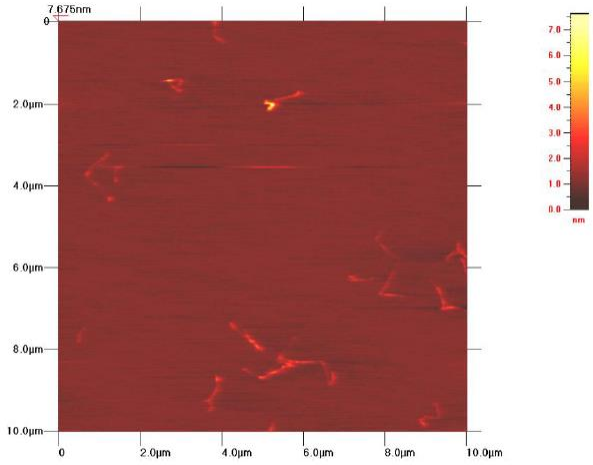

Figure 3.24: AFM image of supramolecular assemblies of HiPCO SWNTs and oligomer **268** spin-cast on a mica surface (tapping mode).

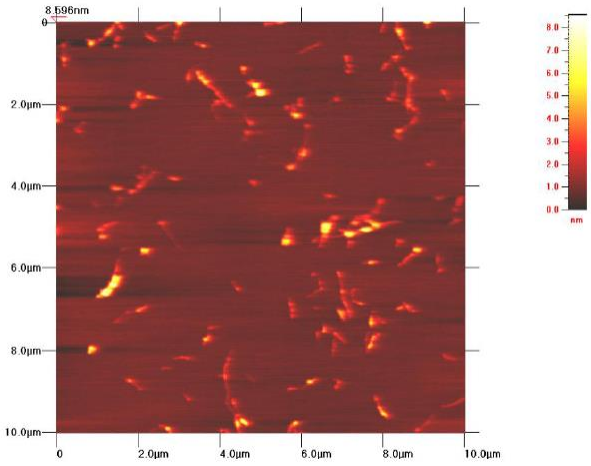

Figure 3.25: AFM image of supramolecular assemblies of HiPCO SWNTs and oligomer **267** spin-cast on a mica surface (tapping mode).

(d) Releasing of SWNTs from DTF oligomer-SWNTs complexes

The releasing of SWNTs was readily accomplished by a simple solvent mixing method. To a stable suspension of HiPCO SWNTs and DTF-oligomer **268** in chloroform (1 mL), an equal amount of hexane (1 mL) was added. Precipitation of SWNTs was immediately observed (Figure 3.26). The mixture was then filtered through a filter paper to separate the released SWNTs from DTF-oligomer solution.

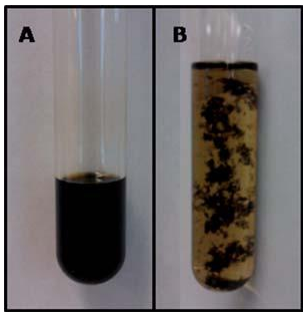

Figure 3.26: Photographic images of (A) HiPCO SWNT suspension with **268** in chloroform and (B) after addition of an equal amount of hexanes.

By this way, pristine SWNTs were conveniently recovered from the dispersion. The actual solubility of SWNTs in DTF-oligomer solutions was then determined. As listed in Table 3.2, the solubility of SWNTs in the solutions of long DTF-oligomers **268** and **266** is much greater than their short oligomers **267** and **265**, likely due to their longer π-conjugated lengths and more solubilizing decyl side chains.

Table 3.2: Solubility of HiPCO SWNTS in DTF–oligomer chloroform solutions

DTF-oligomer	Concentration of the oligomer (mM)	Solubility of SWNTs (mg mL^{-1})
265	2.34	0.01
266	1.58	0.20
267	2.00	0.05
268	1.39	0.29

The HiPCO SWNTs released from the suspension in the solution of DTF-oligomer **268** were examined by Raman spectroscopy. As shown in Figure 3.27, the spectrum of the released SWNTs shows only one significant peak at 272 cm^{-1} in the region of radial breathing mode (RBM). The spectral feature is quite similar to that of the HiPCO SWNTs dispersed in the chloroform solution of DTF-oligomer **268**. For pristine SWNTs, the Raman spectrum shows two significant peaks at 267 and 225 nm respectively. It is evidenced that DTF-oligomer **268** can selectively disperse the nanotubes of relatively smaller diameters in pristine HiPCO SWNTs.

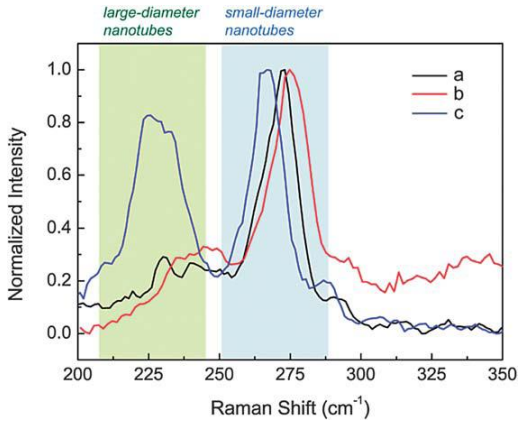

Figure 3.27: Normalized Raman spectra showing the RBM region of (a) HiPCO SWNTs released from the dispersion, (b) HiPCO SWNTs dispersed with **268**, and (c) pristine HiPCO SWNTs.

It has been observed that the released SWNTs are cleanly separated from oligomer dispersants, which is evidenced by Raman spectroscopic analysis. As shown in Figure 3.28, the spectrum of the released SWNTs does not show significant signals at ca. 2200 cm^{-1}, which is due to the C≡C stretching mode of oligomer **268**.

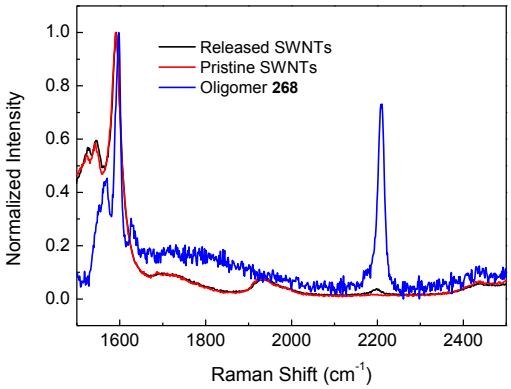

Figure 3.28: Normalized Raman spectra of the released SWNTs, pristine SWNTs, and pure oligomer **268** in the region of 1500 to 2500 cm-1.

The DTF group is a crucial and indispensable factor to SWNT dispersion. This point has been confirmed by a comparative study in which the aldehyde–oligomer precursors (**273**, **276**, **278**, and **279**) were tested for SWNT dispersion under the same conditions used by the DTF–oligomers. The results clearly showed that, without DTF groups, the π-oligomers could not induce any effective dispersion on SWNTs in common organic solvents.

3.2.3 Solvent effects on DTF-oligomers

It is believed that the solvent plays a major role in the supramolecular properties of these DTF-oligomers for the reversible dispersion of SWNTs. From the results disclosed, it is clear that the dispersion of HiPCO SWNTs with DTF–oligomers appears to be particularly effective in chloroform. However, the exact reason is unclear and awaits further investigation. Nevertheless, ^{1}H NMR analysis on DTF–oligomer **268**

discloses a dramatic degree of changes in the resonance frequencies of aromatic protons in different solvents (Figure 3.29). Of particular note is that one of the vinyl protons was found greatly downfield shifted from 7.84 ppm (in $CDCl_3$) to 8.29 ppm (in C_6D_6). This behavior is indicative of substantial changes in conformation and aggregation states in different solvent systems,[45] which is believed to cause the different dispersion outcomes in various solvents. Non-polar chlorinated solvents such as chloroform and methylene chloride happen to solubilize the supramolecular assemblies of DTF–oligomers and HiPCO SWNTs more effectively than other organic solvents.

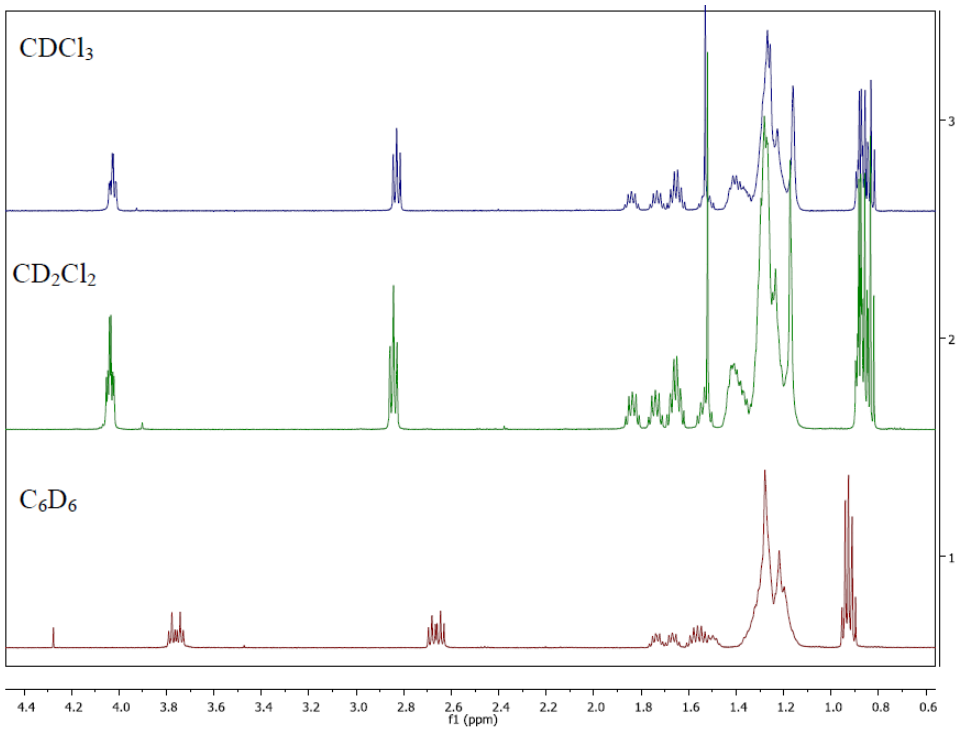

Figure 3.29: ^{1}H NMR (500 MHz) spectrum of **268** in different solvents (showing the aliphatic region).

3.3 Conclusions

The thesis work described in this Chapter focuses on a series of DTF-endcapped OPE/OPV hybrid conjugated oligomers **268**, **267**, **266**, and **265** in a linear and Z-shaped molecular structures. The electronic and electrochemical properties of the DTF groups have been found to vary with the properties of the π-oligomer. As a strong electron donor, the DTF group exerted a substantial quenching effect on the fluorescence emission of the π-oligomers. When the DTF-endcapped oligomers were mixed with fullerenes (C_{60} and C_{70}), the C=C bond of DTF undergoes a facile oxidative cleavage reaction under air and ambient light to form highly fluorescent aldehyde-endcapped oligomers as the product. A fullerene-sensitized photooxygenation mechanism has been proposed to rationalize this reaction, while C_{70} fullerene appeared to be a more efficient sensitizer than C_{60} in promoting this unique reaction. The consequence of this reaction is a substantial fluorescence turn-on response to fullerenes by these DTF–oligomers, suggesting potential use in fullerene sensing and recognition.

The DTF endgroups have imparted the π-oligomers with remarkable effectiveness at dispersing SWNTs in chloroform or methylene chloride. Moreover, the supramolecular interactions between DTF-oligomers and SWNTs have been demonstrated to be tube diameter-dependent. The dispersion outcomes are highly solvent-dependent and very easy to control. Based on this property, reversible dispersion and release of SWNTs in the solution phase were achieved, which are expected to find application in making SWNT-based semiconducting electronic devices. In conclusion, this chapter has

demonstrated that DTF is a fascinating substituent group which not only introduces rich redox and electronic properties, but also can bring about novel chemical reactivities, photophysical and supramolecular properties to organic functional materials.

3.4 Experimental

Chemicals were purchased from commercial suppliers and used directly without purification. HiPCO SWNTs were purchased from Carbon Nanotechnologies Inc. CoMoCAT SWNTs were purchased from Southwest Nanotechnologies Inc. All reactions were conducted in standard, dry glassware and under an inert atmosphere of nitrogen unless otherwise noted. Evaporation and concentration were carried out with a water-aspirator. Flash column chromatography was performed using 240-400 mesh silica gel, and thin-layer chromatography (TLC) was carried out with silica gel F254 covered on plastic sheets and visualized by UV light. Melting points (m.p.) were measured with SRS OptiMelt melting point apparatus and are uncorrected. 1H and 13C NMR spectra were measured on a BrukerAvance 500 MHz spectrometer and BrukerAvance III 300 MHz multinuclear spectrometer. Chemical shifts are reported in ppm downfield from the signal of the internal reference $SiMe_4$ for ^{1}H and ^{13}C NMR spectra. Coupling constants (*J*) are given in Hz. Infrared spectra (IR) were recorded on a Bruker tensor 27 spectrometer. UV-Vis-NIR absorption spectra were measured on a Cary 6000i spectrophotometer. Atomic force microscopy (AFM) images were taken with a Q-Scope AFM operated in tapping mode. Raman spectra were measured on a Horiba Jobin Yvon confocal Raman spectrometer operated at a laser wavelength of 532nm. Cyclic voltammetric (CV)

experiments were carried out in a standard three-electrode setup controlled by a BASi Epsilon workstation. MALDI-TOF MS analyses were performed on an Applied Biosystems Voyager instrument using dithranol as the matrix.

Bis(tetraethylammonium) bis(1,3-dithiole-4,5dithiolate)zincate (269)

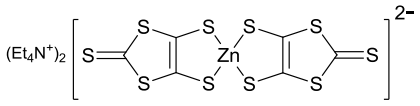

269

Na (8.56 g, 372 mmol) and CS_2 (47 mL, 779 mol) were mixed and then refluxed for 20 min under N_2 protection. Dried DMF (50 mL) was added dropwise over a period of 20 min. The mixture was refluxed for 2 h and then concentrated under vacuum at 30 °C. MeOH (60 mL) was added to the residue under cooling in an ice-water bath to quench unreacted Na. A solution of $ZnCl_2$ (13.3 g, 97.5 mmol) in 1:1 MeOH/NH_3-H_2O (100 mL) was then added carefully to the filtrate. To the resulting mixture, Et_4NBr (24.9 g, 118 mmol) in H_2O (80 mL) was then added. Then the mixture was left standing in the fume hood overnight. The resulting mixture was then subjected to suction filtration. The residue was sequentially washed with H_2O and Et_2O to yield **269** as a red-colored solid (29.8 g, 41.0 mmol, 88%). The salt was directly taken to the next step without further characterization.

4,5-Bis(decylthio)-1,3-dithiol-2thione (270)

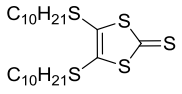

270

To a solution of **269** (10.1 g, 14.1 mmol) in acetone (100 mL) was added 1-decyl bromide (18.4 g, 83.2 mmol). The mixture was refluxed for overnight and filtered. The residue was washed with acetone. The filtrate was cooled under ice bath condition for 0.5 h. Precipitate was collected by suction filtration to afford **270** as a bright yellow solid (4.97 g, 10.4 mmol, 74%). ^{1}H NMR (500 MHz, CD_2Cl_2): δ 2.85 (t, *J* = 7.2 Hz, 4H), 1.69-1.63 (m, 4H), 1.42-1.27 (m, 28H), 0.88 (t, *J* = 6.1 Hz, 6H); The ^{1}H NMR data is consistent with those reported in the literature.[46]

4-(trimethylsilylethynyl)benzaldehyde (271)

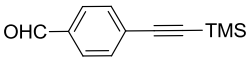

271

To an oven-dried round-bottom flask protected under N_2 were charged 4-bromobenzaldehyde (5.10 g, 27.5 mmol), trimethylsilylacetylene (22.8 mL, 15.8 g, 161 mmol), $PdCl_2(PPh_3)_2$ (94.1 mg, 0.134 mmol), CuI (52.8 mg, 0.277 mmol), and Et_3N (100 mL). The solution was degassed by N_2 bubbling at rt for 5 min, and then was heated to 65 ^{o}C under stirring and N_2 protection overnight. After the reaction was complete as checked by TLC analysis, the solvent was removed by rotary evaporation. The residue was diluted with EtOAc and was filtered through a $MgSO_4$ pad. The solution obtained was

sequentially washed with aq HCl (10%) and brine. The organic layer was dried over $MgSO_4$ and concentrated under vacuum to give crude product **271**, which was purified by flash silica column chromatography (5% EtOAc/Hexanes) to yield pure compound **271** (5.13 g, 25.3 mmol, 92%) as a off-white solid. ^{1}H NMR (500 MHz, $CDCl_3$); δ 10.01 (s, 1H), 7.82 (d, *J* = 8.8 Hz, 2H), 7.61 (d, *J* = 8.8 Hz, 2H), 0.28 (s, 9H). The ^{1}H NMR data is consistent with those reported in the literature.[47]

4-(ethynyl)benzaldehyde (272)

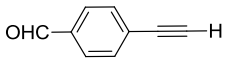

272

To a solution of compound **271** (1.0 g, 4.9 mmol) in MeOH/THF (1:1, 20 mL) was added K_2CO_3 (2.1 g, 15 mmol). The mixture was stirred at rt for 30 min, and then the reaction solvent was removed by rotary evaporation. The residue was diluted in CH_2Cl_2 and sequentially washed with aq HCl (10%) and brine. The organic layer was dried with $MgSO_4$ and concentrated under vacuum to afford the crude product of **272**, which was further washed with methanol and dried to yield pure compound **272** (0.52 g, 4.0 mmol, 81%) as a yellow solid. ^{1}H NMR (300 MHz, $CDCl_3$); δ 10.02 (s, 1H), 7.84 (d, *J* = 8.5 Hz, 2H), 7.64 (d, *J* = 8.3 Hz, 2H), 3.29 (s, 1H). The ^{1}H NMR data is consistent with those reported in the literature.[47]

4,4[1]-(1,4-Phenylenebis(ethyne-2,1-diyl))dibenzaldehyde (273)

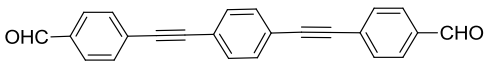

273

To an oven-dried round-bottom flask protected under N_2 were charged compound **272** (0.354 g, 2.72 mmol), 1,4-diiodobenzene (0.409 g, 1.23 mmol), $PdCl_2(PPh_3)_2$ (21.2 mg, 0.0299 mmol)), CuI (11.5 mg, 0.0603 mmol), and Et_3N (40 mL). The solution was degassed by N_2 bubbling at rt for 5 min, and then was heated to 45 ^oC under stirring and N_2 protection overnight. The obtained precipitate from the reaction was filtered and washed with CH_2Cl_2 and air dried to give compound **273** (0.365 g, 1.09 mmol, 78% crude) as off-white solid. m.p. 191-194 ^oC; IR (neat): 1696, 1595, 1417, 1204 cm^{-1}; Meaningful ^1H NMR and ^{13}C spectra of **273** could not be obtained due to poor solubility. HRMS (MALDI-TOF, +eV) *m/z* calcd for $C_{24}H_{14}O$, 334.0994; found 334.1039 $[M]^+$.

Synthesis of compound (274)

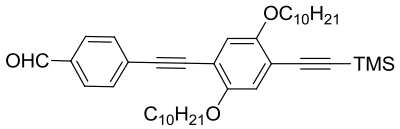

274

To an oven-dried round-bottom flask protected under N_2 were charged compound **215** (0.300 g, 2.30 mmol), compound **272** (1.41 g, 2.30 mmol), $PdCl_2(PPh_3)_2$ (40.1 mg, 0.0584 mmol), CuI (21.9 mg, 0.116 mmol), dry Et_3N (30 mL), and dry THF (20 mL). The solution was degassed by N_2 bubbling at rt for 5 min, and then was stirred at rt under N_2 protection overnight. After the reaction was complete as checked by TLC analysis, the

solvent was removed under vacuum. The residue was diluted with CH_2Cl_2 and was filtered through a $MgSO_4$ pad. The resulting solution was sequentially washed with water, dried over $MgSO_4$, and concentrated under vacuum to give crude product **274**, which was further purified by silica flash column chromatography (hexanes/CH_2Cl_2, 9:1) to yield pure compound **274** (1.26 g, 2.05 mmol, 89%) as a yellow solid. m.p. 45-46 ^oC; IR (neat): 2924, 2850, 2208, 1699, 1595, 1463, 1382 cm^{-1}; ^1H NMR (300 MHz, $CDCl_3$) δ 10.02 (s, 1H), 7.86 (d, *J* = 8.5 Hz, 2H), 7.66 (d, *J* = 8.2 Hz, 2H), 6.97 (d, *J* = 3.6 Hz, 2H), 3.99 (q, *J* = 6.3 Hz, 4H); 1.88-1.77 (m, 4H), 1.57-1.50 (m, 4H), 1.32-1.25 (m, 24), 0.90-0.84 (m, 6H) 0.27 (s, 9H); ^{13}C NMR (75 MHz, $CDCl_3$): δ 191.4, 154.2, 153.8, 135.4, 132.0, 129.8, 129.6, 117.2, 116.9, 114.7, 113.3, 93.9, 90.2, 69.59, 69.57, 31.9, 29.70, 29.65, 29.61, 29.49, 29.41, 29.39, 29.35, 26.12, 26.09, 22.7, 14.1; HRMS (MALDI-TOF, +eV) *m/z* calcd for $C_{40}H_{58}O_3Si$ 614.4155; found 614.4179 $[M]^+$.

Synthesis of compound (275)

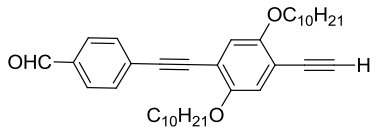

275

To a solution of compound **274** (1.19 g, 1.94 mmol) in MeOH/THF (20 mL, 1:1) was added K_2CO_3 (0.805 g, 5.83 mmol). The mixture was stirred at rt for 30 min and then diluted with CH_2Cl_2 (100 mL). The mixture was sequentially washed with brine and water. The organic layer was dried over $MgSO_4$ and concentrated under vacuum to afford the pure product of **275** (0.951 g, 1.76 mmol, 91%) as a yellow solid. m.p. 43-44 ^oC; IR

(neat): 3284, 2918, 2849, 2364, 1698, 1597, 1501, 1462, 1385 cm^{-1}; ^1H NMR (500 MHz, $CDCl_3$) δ 10.02 (s, 1H), 7.86 (d, *J* = 8.3 Hz, 2H), 7.67 (d, *J* = 8.3 Hz, 2H), 7.00 (d, *J* = 4.7 Hz, 2H), 4.01 (dt, *J* = 6.6, 2,9 Hz, 4H); 3.36 (s, 1H); 1.86-1.70 (m, 4H), 1.55-1.45 (m, 4H), 1.40-1.24 (m, 24H), 0.90-0.85 (m, 6H); ^{13}C NMR (75 MHz, $CDCl_3$): δ 191.4, 154.1, 153.7, 135.4, 132.0, 129.7, 129.6, 117.7, 116.9, 113.7, 113.5, 93.9, 89.9, 82.7, 79.9, 77.2, 69.7, 69.6, 31.91, 31.89, 29.7, 29.6, 29.4, 29.34, 29.29, 29.1, 26.1, 25.9, 22.7, 14.1; HRMS (MALDI-TOF, +eV) *m/z* calcd for $C_{37}H_{50}O_3$ 542.3760, found 542.3799 $[M]^+$.

Long linear aldehyde-OPE (276)

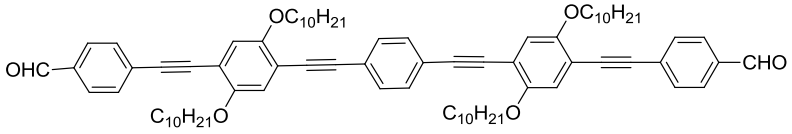

276

To an oven-dried round-bottom flask protected under N_2 were charged compound **274** (0.102 g, 0.309 mmol), 1,4-diiodobenzene (0.369 g, 0.679 mmol), $PdCl_2(PPh_3)_2$ (5.30 mg, 0.0075 mmol)), CuI (2.80 mg, 0.014 mmol), and Et_3N (50 mL). The solution was degassed by N_2 bubbling at rt for 5 min, and then was heated to 45 ^oC under stirring and N_2 protection overnight. After the reaction was completed as checked by TLC analysis, the solvent was removed by rotary evaporation. The residue was diluted with CH_2Cl_2 and was filtered through a $MgSO_4$ pad. The solvent was removed by vacuum evaporation and the residual was washed with hexanes to give pure compound **276** (0.275 g, 0.237 mmol, 78%) as a yellow solid. m.p. 123-124 ^oC; IR (neat): 2919, 2850, 1698, 1596, 1459, 1212, 943 cm^{-1}; ^1H NMR (300 MHz, $CDCl_3$): δ 10.02 (s, 2H), 7.87 (d, *J* =

8.4 Hz, 4H), 7.68 (d, *J* = 8.2 Hz, 4H), 7.51 (s, 4H), 7.03 (d, *J* = 0.9 Hz, 4H), 4.05 (t, *J* = 6.4 Hz, 8H), 1.91-1.82 (m, 8H), 1.60-1.50 (m, 8H), 1.41-1.25 (m, 48H), 0.89-0.85 (m, 12); ^{13}C NMR (75 MHz, $CDCl_3$): δ 191.3, 153.9, 153.7, 135.4, 132.0, 131.5, 129.8, 129.6, 123.3, 116.9, 116.8, 114.7, 113.3, 95.0, 94.0, 90.2, 87.9, 69.7, 69.6, 31.91, 31.90, 29.7, 29.6, 29.43, 29.36, 29.33, 26.1, 22.70, 22.68, 14.14, 14.12; HRMS (MALDI-TOF, +eV) *m/z* calcd for $C_{80}H_{102}O_6$ 1158.7676, found 1158.7665 $[M]^+$.

1,4-Bis((*E*)-2-iodostyryl)benzene (277)

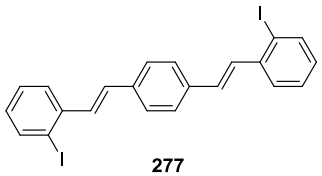

277

To an oven-dried flask protected under N_2 were charged tetraethyl 1,4-phenylene bis(methylene)diphosphonate (**234**) (1.03 g, 2.64 mmol), NaH (60%) (0.320 g, 7.92 mmol), and dry THF (50 mL). The solution gradually turned into dark yellow color at 50 °C. A solution of 2-iodobenzaldehyde (1.21 g, 5.21 mmol) in THF (20 mL) was added in small portions over a period of 10 min via a syringe. The reaction was kept under stirring at same temperature for another 3 h before workup. On completion as checked by TLC analysis, the reaction mixture was poured in to ice, and the obtained solid was extracted into CH_2Cl_2 and washed with water several times. The organic layer was dried over $MgSO_4$, concentrated under vacuum to afford compound **277** which was finally washed with methanol to give to the pure form (0.690 g, 1.29 mmol, 49%) as a yellow solid. m.p. 159-161 ^oC; IR (neat): 1460, 1424, 1007, 957, 814 cm^{-1}; ^{1}H NMR (500 MHz, $CDCl_3$): δ

7.89 (dd, *J* = 7.9, 1.1 Hz, 2H), δ 7.65 (dd, *J* = 7.8, 1.5 Hz, 2H) 7.57 (s, 4H), 7.37-7.34 (m, 4H), 7.00-6.95 (m, 4H); ^{13}C NMR (75 MHz, $CDCl_3$): δ 140.2, 139.7, 136.7, 132.6, 131.1, 129.0, 128.4, 127.2, 126.2, 100.6; HRMS (EI-TOF, +eV) *m/z* calcd for $C_{22}H_{16}I_2$,533.9341; found 533.9336 $[M]^+$.

Aldehyde OPV (278)

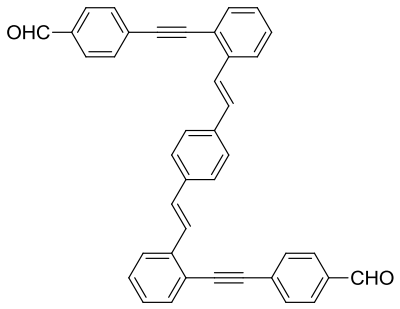

278

To an oven-dried round-bottom flask protected under N_2 were charged compound **277** (0.301 g, 0.561 mmol), compound **272** (0.183 g, 1.40 mmol), $PdCl_2(PPh_3)_2$ (9.80 mg, 0.0139 mmol)), CuI (5.30 mg, 0.027 mmol), and Et_3N (50 mL). The solution was degassed by N_2 bubbling at rt for 5 min, and then was heated to 45 ^oC under stirring and N_2 protection overnight. After the reaction was complete as checked by TLC analysis, the solvent was removed by rotary evaporation. The residue was diluted with CH_2Cl_2 and was filtered through a $MgSO_4$ pad. The solution obtained was sequentially washed with water, dried over $MgSO_4$, and concentrated under vacuum to give crude product **278**, which was further purified by silica flash column chromatography (hexanes/EtOAc, 95:15) to yield pure compound **278** (0.197 g, 0.366 mmol, 65%) as a yellow solid. m.p. 175-178 ^oC; IR (neat): 1695, 1598, 1389, 1293, 1206, 1158, 1013 cm^{-1}; ^{1}H NMR (500

MHz, $CDCl_3$): δ 10.04 (s, 2H), 7.91-7.87 (m, 4H), 7.76-7.70 (m, 8H), 7.59-7.58 (m, 4H), 7.40 (t, *J* = 7.4 Hz, 2H), 7.30-7.23 (m, 2H); Meaningful ^{13}C NMR spectrum of **12** could not be obtained due to its limited solubility. HRMS (MALDI-TOF, +eV) *m/z* calcd for $C_{40}H_{26}O_2$ 538.1933; found 538.1939 $[M]^+$.

Aldehyde-OPE/OPV (279)

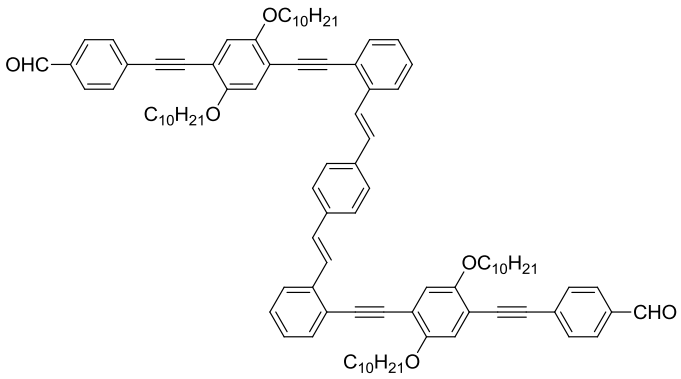

279

To an oven-dried round-bottom flask protected under N_2 were charged compound **277** (0.260 g, 0.490 mmol), compound **275** (0.661 g, 1.07 mmol), $PdCl_2(PPh_3)_2$ (6.80 mg, 0.0970 mmol)), CuI (3.60 mg, 0.0194 mmol), and Et_3N (100 mL). The solution was degassed by N_2 bubbling at rt for 5 min, and then was heated to 45 ^oC under stirring and N_2 protection overnight. After the reaction was complete as checked by TLC analysis, the solvent was removed by rotary evaporation. The residue was diluted with CH_2Cl_2 and was filtered through a $MgSO_4$ pad. The solution obtained was sequentially washed with water, dried over $MgSO_4$ and concentrated under vacuum to give crude product **279**, which was further purified by silica flash column chromatography (hexanes/EtOAc, 9:1) to yield pure compound **279** (0.480 g, 0.352 mmol, 72%) as a yellow solid. m.p. 153-155

^{o}C; IR (neat): 2919, 2851, 2204, 1704, 1598, 1420, 1340, 1213 cm^{-1}; ^{1}H NMR (500 MHz, $CDCl_3$): δ 10.00 (s, 2H), 7.84-7.81 (m, 8H), 7.74 (d, *J* = 7.9 Hz, 2H), 7.65 (d, *J* = 8.2 Hz, 4H), 7.58-7.56 (m, 4H), 7.35 (t, *J* = 7.7 Hz, 2H) 7.25-7.22 (m, 4H), 7.06 (s, 4H), 4.03 (t, *J* = 6.3 Hz, 8H), 1.87-1.81 (m, 4H), 1.76-1.71 (m, 4H), 1.56-1.46 (m, 8H), 1.41-1.31 (m, 12H), 1.27-1.16 (m, 36 H), 0.86-0.82 (m, 12H); ^{13}C NMR (75 MHz, $CDCl_3$) δ 191.3, 153.9, 153.6, 138.8, 137.1, 135.3, 132.7, 132.0, 129.8, 129.5, 128.6, 127.3, 127.2, 126.9, 124.7, 122.4, 117.2, 116.8, 115.2, 113.1, 93.98, 93.95, 91.1, 90.3, 77.2, 69.9, 69.6, 45.8, 31.89, 31.87, 29.7, 29.61, 29.59, 29.56, 29.5, 29.4, 29.2, 26.1, 25.9, 22.7, 14.1; HRMS (MALDI-TOF, +eV) *m/z* calcd for $C_{96}H_{114}O_6$ 1362.8615; found 1362.8542 $[M]^+$.

Short linear DTF-OPE (265)

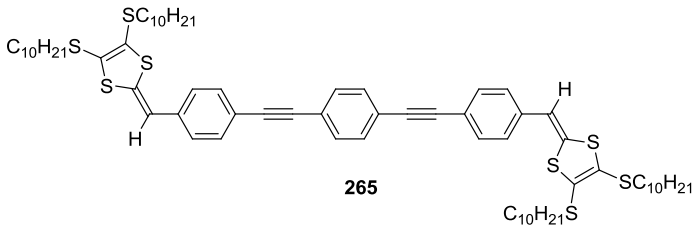

265

A solution of thione **270** (0.109 g, 0.396 mmol) and compound **273** (0.342 g, 0.172 mmol) in trimethylphosphite (20 mL) was stirred and heated to 130 ^{o}C for about 6 h under N_2 atmosphere. On completion, the excess trimethylphosphite was removed by vacuum distillation. The obtained crude product was purified by silica flash column chromatography (EtOAc/hexanes, 1:99) followed by recrystallization from acetone to yield pure compound **265** (0.0500 g, 0.0418 g mmol, 13%) as yellow solid. m.p. 103-104 ^{o}C; IR (neat) : 2916, 2846, 1571, 1414, 933 cm^{-1}; ^{1}H NMR (500 MHz, CD_2Cl_2): δ 7.52 (t,

J = 5.2 Hz, 8H), 7.22 (d, *J* = 8.4 Hz, 4H), 6.49 (s, 2H), 2.85 (td, *J* = 7.3, 2.6 Hz, 8H), 1.69-1.62 (m, 8H), 1.45-1.39 (m, 8H), 1.32-1.27 (m, 48H), 0.89-0.86 (m, 12H); ^{13}C NMR (75 MHz, CD_2Cl_2): δ 136.9, 134.9, 132.1, 131.9, 128.3, 126.9, 125.4, 123.5, 120.1, 113.6, 91.9, 89.9, 36.6, 36.5, 32.3, 30.3, 30.2, 29.97, 29.93, 29.7, 29.5, 28.92, 28.90, 23.0, 14.3 ; HRMS (MALDI-TOF, +eV) *m/z* calcd for $C_{70}H_{98}S_8$ 1194.5434, found 1194.5444 $[M]^+$.

Long linear DTF-OPE (266)

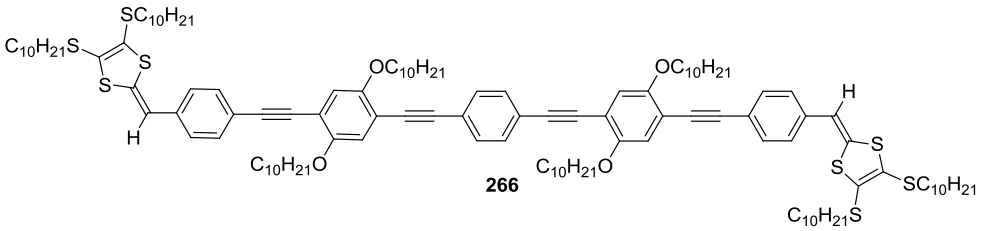

266

A solution of thione **270** (0.190 g, 0.396 mmol) and compound **276** (0.200 g, 0.172 mmol) in trimethylphosphite (15 mL) was stirred and heated to 130 ^{o}C for about 3 h under N_2 atmosphere. On completion, the excess trimethylphosphite was removed by vacuum distillation. The obtained crude product was purified by silica flash column chromatography (EtOAc/hexanes, 1:99) followed by recrystallization from acetone to yield pure compound **266** (0.264 g, 0.131 mmol, 76%) as yellow solid. m.p. 81-82 ^{o}C; IR (neat) : 2918, 2850, 1568, 1460, 1212, 1059 ; ^{1}H NMR (500 MHz, CD_2Cl_2): δ 7.52-7.50 (m, 8H), 7.22 (d, *J* = 8.6 Hz, 4H), 7.03 (s, 4H), 6.49 (s, 2H), 4.04 (td, *J* = 6.4, 1.9 Hz, 8H) 2.84 (td, *J* = 7.4, 1.8 Hz, 8H), 1.88-1.83 (m, 8H), 1.69-1.52 (m, 8H), 1.59-1.54 (m, 8H), 1.56-1.50 (m, 4 H), 1.45-1.37 (m, 16 H), 1.34-1.27 (m, 88H), 0.89-0.86 (m, 24H); ^{13}C NMR (75 MHz, $CDCl_3$): δ 154.1, 154.0, 136.7, 134.7, 132.0, 131.8, 128.4, 126.9, 125.4,

123.7, 120.5, 117.2, 117.1, 114.7, 113.9, 113.7, 95.6, 94.8, 88.5, 87.0, 70.0, 32.3, 36.6, 36.5, 32.3, 30.3, 30.2, 30.1, 30.0, 29.97, 29.94, 29.84, 29.77, 29.73, 29.55, 29.53, 28.93, 28.91, 26.5, 23.11, 23.09, 14.31, 14.28; HRMS (MALDI-TOF, +eV) *m/z* calcd for $C_{126}H_{186}O_4S_8$ 2019.2117, found 2019.2097 $[M]^+$.

Short Z-shaped DTF-OPV (267)

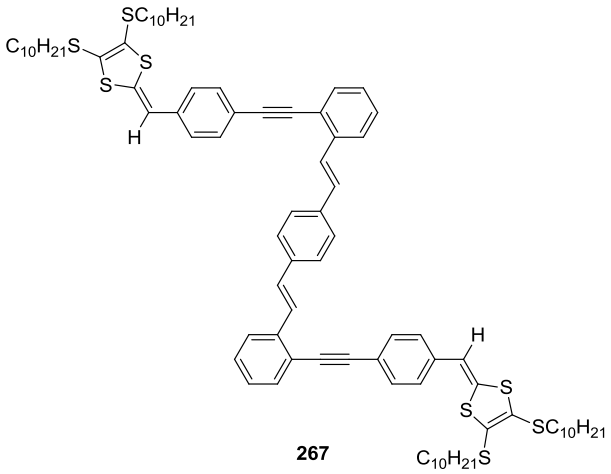

267

A solution of thione **270** (0.408 mg, 0.888 mmol) and compound **278** (0.208 g, 0.386 mmol) in trimethylphosphite (15 mL) was stirred and heated to 130 ^oC for about 3 h under N_2 atmosphere. On completion, the excess trimethylphosphite was removed by vacuum distillation. The obtained crude product was purified by silica flash column chromatography (EtOAc/hexanes, 1:99) to yield pure compound **267** (0.362 g, 0.258 mmol, 67%) as thick syrup. IR (neat) : 2919, 2849, 1671, 1599, 1458, 1259, 957; ^1H NMR (500 MHz, $CDCl_3$): δ 7.77 (d, *J* = 16.4 Hz, 2H), 7.73 (d, *J* = 7.7 Hz, 2H), 7.60 (s, 4H), 7.56 (d, *J* = 7.7 Hz, 4H), 7.34 (t, *J* = 7.5 Hz, 2H), 7.25-7.20 (m, 6H), 6.45 (s, 2H), 2.84-2.79 (m, 8H), 1.69-1.60 (m, 8H), 1.42-1.37 (m, 8H), 1.29-1.24 (m, 48H), 0.89-80

(m, 12H); ^{13}C NMR (75 MHz, $CDCl_3$): δ 138.9, 137.5, 136.9, 134.9, 132.9, 132.0, 130.1, 128.9, 128.3, 127.8, 127.5, 127.0, 125.4, 125.1, 122.7, 120.4, 113.6, 95.3, 88.9, 36.6, 36.5, 32.3, 30.3, 30.1, 29.9, 29.7, 29.6, 28.96, 28.91, 23.1, 18.9, 14.3; HRMS (MALDI-TOF, +eV) *m/z* calcd for $C_{86}H_{110}S_8$ 1398.6373, found 1398.6267 $[M]^+$.

Long Z-shaped DTF-OPE/OPV (268)

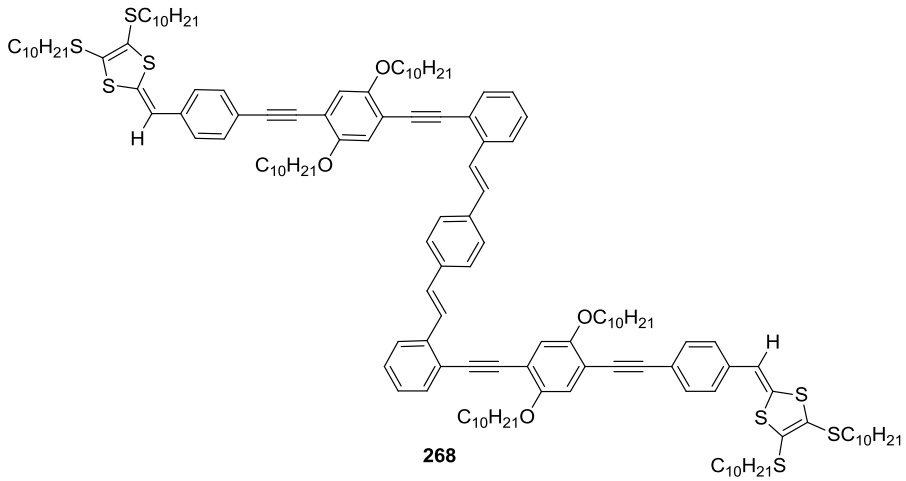

268

A solution of thione **270** (0.169 g, 0.354 mmol) and compound **279** (0.210 g, 0.153 mmol) in trimethylphosphite (15 mL) was stirred and heated to 130 ^{o}C for about 3 h under N_2 atmosphere. On completion, the excess trimethylphosphite was removed by vacuum distillation. The obtained crude product was purified by silica flash column chromatography (EtOAc/hexanes, 1:99) followed by recrystallization from acetone to yield pure compound **268** (0.240 g, 0.107 mmol, 71%) as yellow solid. m.p. 92-93 ^{o}C; IR (neat): 2918, 2948, 1601,1565, 1419, 1383, 1213, 1027 cm^{-1}; ^{1}H NMR (500 MHz, CD_2Cl_2): δ 7.85 (d, *J* = 16.4 Hz, 2H), 7.77 (d, *J* = 7.9 Hz, 2H), 7.61 (s, 4H), 7.57 (dd, *J* = 7.7, 1.0 Hz, 2H), 7.49 (d, *J* = 8.4 Hz, 4H), 7.37 (td, *J* = 7.5, 1.0 Hz, 2H), 7.29-7.25 (m,

4H), 7.18 (d, *J* = 8.4, 4H), 7.07 (d, *J* = 0.8 Hz, 4H), 6.46 (s, 2H) 4.04 (td, *J* = 6.7, 3.1 Hz, 8H) 2.84 (td, *J* = 6.6, 0.9 Hz, 8H), 1.86-1.81 (m, 4H), 1.77-1.71 (m, 4H), 1.69-1.62 (m, 8H), 1.56-1.50 (m, 4 H), 1.45-1.35 (m, 16 H), 1.34-1.17 (m, 92H), 0.90-0.82 (m, 24H); ^{13}C NMR (75 MHz, CD_2Cl_2): δ 154.0, 139.1, 137.5, 136.7, 134.6, 132.9, 132.0, 130.2, 129.0, 128.4, 127.7, 127.6, 127.2, 126.9, 125.3, 125.1, 122.8, 120.6, 117.2, 114.6, 114.3, 113.7, 95.6, 93.7, 91.8, 87.1, 70.2, 70.1, 36.6, 36.5, 32.32, 32.29, 30.3, 30.2, 30.1, 30.0, 29.98, 29.94, 29.89, 29.82, 29.79, 29.76, 29.74, 29.6, 29.56, 29.54, 28.94, 28.92, 26.6, 26.4, 23.12, 23.09, 14.32, 14.29; HRMS (MALDI-TOF, +eV) *m/z* calcd for $C_{142}H_{198}O_4S_8$ 2223.3056, found 2223.3082 $[M]^+$.

3.5 References

(1) Dumitrescu, I.; Unwin, P. R.; Macpherson, J. V. *Chem. Commun.* **2009**, 6886-6901.

(2) Avouris, P. *Acc. Chem. Res.* **2002**, *35*, 1026-1034.

(3) Collins, P. G.; Avouris, P. *Sci. Am.* **2000**, *283*, 62-69.

(4) Dai, H. J. *Acc. Chem. Res.* **2002**, *35*, 1035-1044.

(5) Kong, J.; Franklin, N. R.; Zhou, C.; Chapline, M. G.; Peng, S.; Cho, K.; Dai, H. *Science* **2000**, *287*, 622-625.

(6) Kong, J.; Chapline, M. G.; Dai, H. *Adv. Mater.* **2001**, *13*, 1384-1386.

(7) Choi, W. B.; Chung, D. S.; Kang, J. H.; Kim, H. Y.; Jin, Y. W.; Han, I. T.; Lee, Y. H.; Jung, J. E.; Lee, N. S.; Park, G. S.; Kim, J. M. *Appl. Phys. Lett.* **1999**, *75*, 3129-3131.

(8) Ajayan, P. M. *Chem. Rev.* **1999**, *99*, 1787-1799.

(9) Hirsch, A. *Angew. Chem., Int. Ed. Engl.* **2002**, *41*, 1853-1859.

(10) Tchoul, M. N.; Ford, W. T.; Lolli, G.; Resasco, D. E.; Arepalli, S. *Chem. Mater.* **2007**, *19*, 5765-5772.

(11) Liu, J.; Rinzler, A. G.; Dai, H.; Hafner, J. H.; Bradley, R. K.; Boul, P. J.; Lu, A.; Iverson, T.; Shelimov, K.; Huffman, C. B.; Rodriguez-Macias, F.; Shon, Y.-S.; Lee, T. R.; Colbert, D. T.; Smalley, R. E. *Science* **1998**, *280*, 1253-1256.

(12) Gromov, A.; Dittmer, S.; Svensson, J.; Nerushev, O. A.; Perez-Garcia, S. A.; Licea-Jimenez, L.; Rychwalski, R.; Campbell, E. E. B. *J. Mater. Chem.* **2005**, *15*, 3334-3339.

(13) Li, H.; Cheng, F.; Duft, A. M.; Adronov, A. *J. Am. Chem. Soc.* **2005**, *127*, 14518-14524.

(14) Palacin, T.; Khanh, H. L.; Jousselme, B.; Jegou, P.; Filoramo, A.; Ehli, C.; Guldi, D. M.; Campidelli, S. p. *J. Am. Chem. Soc.* **2009**, *131*, 15394-15402.

(15) Delgado, J. L.; de la Cruz, P.; Urbina, A.; López Navarrete, J. T.; Casado, J.; Langa, F. *Carbon* **2007**, *45*, 2250-2252.

(16) Karousis, N.; Tagmatarchis, N.; Tasis, D. *Chem. Rev.* **2010**, *110*, 5366-5397.

(17) Zhao, Y.-L.; Stoddart, J. F. *Acc. Chem. Res.* **2009**, *42*, 1161-1171.

(18) O'Connell, M. J.; Bachilo, S. M.; Huffman, C. B.; Moore, V. C.; Strano, M. S.; Haroz, E. H.; Rialon, K. L.; Boul, P. J.; Noon, W. H.; Kittrell, C.; Ma, J.; Hauge, R. H.; Weisman, R. B.; Smalley, R. E. *Science* **2002**, *297*, 593-596.

(19) Star, A.; Stoddart, J. F.; Steuerman, D.; Diehl, M.; Boukai, A.; Wong, E. W.; Yang, X.; Chung, S.-W.; Choi, H.; Heath, J. R. *Angew. Chem. Int. Ed.* **2001**, *40*, 1721-1725.

(20) Steuerman, D. W.; Star, A.; Narizzano, R.; Choi, H.; Ries, R. S.; Nicolini, C.; Stoddart, J. F.; Heath, J. R. *J. Phys. Chem. B* **2002**, *106*, 3124-3130.

(21) Star, A.; Liu, Y.; Grant, K.; Ridvan, L.; Stoddart, J. F.; Steuerman, D. W.; Diehl, M. R.; Boukai, A.; Heath, J. R. *Macromolecules* **2003**, *36*, 553-560.

(22) Nakayama-Ratchford, N.; Bangsaruntip, S.; Sun, X.; Welsher, K.; Dai, H. *J. Am. Chem. Soc.* **2007**, *129*, 2448-2449.

(23) Kang, Y. K.; Lee, O.-S.; Deria, P.; Kim, S. H.; Park, T.-H.; Bonnell, D. A.; Saven, J. G.; Therien, M. J. *Nano Lett.* **2009**, *9*, 1414-1418.

(24) Zheng, M.; Jagota, A.; Semke, E. D.; Diner, B. A.; McLean, R. S.; Lustig, S. R.; Richardson, R. E.; Tassi, N. G. *Nat. Mater.* **2003**, *2*, 338-342.

(25) Chen, R. J.; Zhang, Y.; Wang, D.; Dai, H. *J. Am. Chem. Soc.* **2001**, *123*, 3838-3839.

(26) Nakashima, N.; Tomonari, Y.; Murakami, H. *Chem. Lett.* **2002**, *31*, 638-639.

(27) Li, H.; Zhou, B.; Lin, Y.; Gu, L.; Wang, W.; Fernando, K. A. S.; Kumar, S.; Allard, L. F.; Sun, Y.-P. *J. Am. Chem. Soc.* **2004**, *126*, 1014-1015.

(28) Zhang, Z.; Che, Y.; Smaldone, R. A.; Xu, M.; Bunes, B. R.; Moore, J. S.; Zang, L. *J. Am. Chem. Soc.* **2010**, *132*, 14113-14117.

(29) Wang, H.; Mei, J.; Liu, P.; Schmidt, K.; Jiménez-Osés, G.; Osuna, S.; Fang, L.; Tassone, C. J.; Zoombelt, A. P.; Sokolov, A. N.; Houk, K. N.; Toney, M. F.; Bao, Z. *ACS Nano* **2013**, *7*, 2659-2668.

(30) Liang, S.; Chen, G.; Peddle, J.; Zhao, Y. *Chem. Commun.* **2012**, *48*, 3100-3102.

(31) Herranz, M. Á.; Ehli, C.; Campidelli, S.; Gutiérrez, M.; Hug, G. L.; Ohkubo, K.; Fukuzumi, S.; Prato, M.; Martín, N.; Guldi, D. M. *J. Am. Chem. Soc.* **2007**, *130*, 66-73.

(32) Sundramoorthy, A. K.; Mesgari, S.; Wang, J.; Kumar, R.; Sk, M. A.; Yeap, S. H.; Zhang, Q.; Sze, S. K.; Lim, K. H.; Chan-Park, M. B. *J. Am. Chem. Soc.* **2013**, *135*, 5569-5581.

(33) Lorcy, D.; Carlier, R.; Robert, A.; Tallec, A.; Le Magueres, P.; Ouahab, L. *J. Org. Chem.* **1995**, *60*, 2443-2447.

(34) Roncali, J. *J. Mater. Chem.* **1997**, *7*, 2307-2321.

(35) Chen, G.; Mahmud, I.; Dawe, L. N.; Zhao, Y. *Org. Lett.* **2010**, *12*, 704-707.

(36) Chronakis, N.; Vougioukalakis, G. C.; Orfanopoulos, M. *Org. Lett.* **2002**, *4*, 945-948.

(37) Tokuyama, H.; Nakamura, E. *J. Org. Chem.* **1994**, *59*, 1135-1138.

(38) Ciscato, L. F. M. L.; Weiss, D.; Beckert, R.; Bastos, E. L.; Bartoloni, F. H.; Baader, W. J. *New. J. Chem.* **2011**, *35*, 773-775.

(39) Hoffmann, N. *Chem. Rev.* **2008**, *108*, 1052-1103.

(40) Adam, W.; Baader, W. J. *Angew. Chem. Int. Ed.* **1984**, *23*, 166-167.

(41) Tanaka, T.; Jin, H.; Miyata, Y.; Fujii, S.; Suga, H.; Naitoh, Y.; Minari, T.; Miyadera, T.; Tsukagoshi, K.; Kataura, H. *Nano Lett.* **2009**, *9*, 1497-1500.

(42) Tu, X.; Manohar, S.; Jagota, A.; Zheng, M. *Nature* **2009**, *460*

(43) Feng, J.; Alam, S. M.; Yan, L. Y.; Li, C. M.; Judeh, Z.; Chen, Y.; Li, L.-J.; Lim, K. H.; Chan-Park, M. B. *J. Phys. Chem. C* **2011**, *115*, 5199-5206.

(44) Hennrich, F.; Krupke, R.; Lebedkin, S.; Arnold, K.; Fischer, R.; Resasco, D. E.; Kappes, M. M. *J. Phys. Chem. B* **2005**, *109*, 10567-10573.

(45) Fracaroli, A. M.; Granados, A. M.; de Rossi, R. H. *J. Org. Chem.* **2009**, *74*, 2114-2119.

(46) Moore, A. J.; Bryce, M. R. *Tetrahedron Lett.* **1992**, *33*, 1373-1376.

(47) Yang, X.; Li, Z.; Zhi, J.; Ma, J.; Hu, A. *Langmuir* **2010**, *26*, 11244-11248.

Chapter 4

TTFV Tweezers and Macrocycles: Fluorescent and Electrochemical Sensors for Fullerenes, Metal Ions, and Saccharides

4.1 Introduction

As introduced in Chapter 1, chemical sensing involves the use of receptors that provide detectable responses to specific interactions with analytes. The association between a sensor and an analyte could be achieved by non-covalent interactions through hydrogen bonding, metal coordination, hydrophobic interactions, π-π interactions, or electrostatic forces. Many useful chemosensors have been introduced in order to monitor biologically and environmentally important analytes. In particular, fluorescence-based chemical sensing has been studied extensively for the past several decades.[1-5] As mentioned in Chapter 2, a fluorescence sensor is a molecular system in which the photophysical properties change upon interaction with a chemical species in such a way that a detectable fluorescent signal is elicited. Over the past years, different techniques have been developed for fluorescence sensing of analytes based on various signaling mechanisms; for example, photoinduced electron (PET),[6] photoinduced charge transfer (PCT),[7] intramolecular charge transfer (ICT),[8] and so on. In particular, fluorescence turn-

on sensing is advantageous over turn-off sensing in several aspects, including good signal−to−noise ratio, high sensitivity, and reduced false signaling. Further research on the development of chemosensors is still needed to satisfy the demand of biological and environmental research. The following section will discuss the fluorescence and electrochemical sensing of few important analytes (metal ions, fullerenes, and saccharides) that is relevant to the thesis work reported in this chapter.

4.1.1 Chemical receptors for the detection of fullerenes

The search for synthetic receptors capable of forming stable complexes with fullerenes has been an active field of research in fullerene chemistry. With the increasing application of fullerene-containing materials in modern materials science and biological technology, how to detect and separate different types of fullerenes has captured considerable attention.[9-13] In this context, the use of various synthetic receptors to form guest-host inclusion complexes with fullerenes has been extensively studied.[14-16] From a practical viewpoint, three important features are desirable for an ideal fullerene receptor: (1) selectivity for specific types of fullerenes, (2) effective sensory function, and (3) controllable reversibility in interactions with fullerenes.

The selectivity issue has been widely sought after by design of aromatic-rich molecular and macromolecular systems pre-organized in such shapes as molecular tweezers, rings, helix, cups, and cages, based upon the notion of concave-convex complementarity (Figure 4.1).[14] The chemical sensing of fullerenes by rapid and non-invasive methods such as fluorescence spectroscopy, on the contrary, has been rarely

reported in the literature.[17,18] It is particularly worth noting that devising fluorescence turn-on sensing for fullerenes is a challenging task, given that fullerenes usually cause attenuation of emission when bound to various fluorescent systems.[19-21] Finally, reversibility of fullerene binding/release requires certain switching mechanism(s) to be included in fullerene receptors, as such a function is of great value for the effective separation of different types of fullerenes.[22,23]

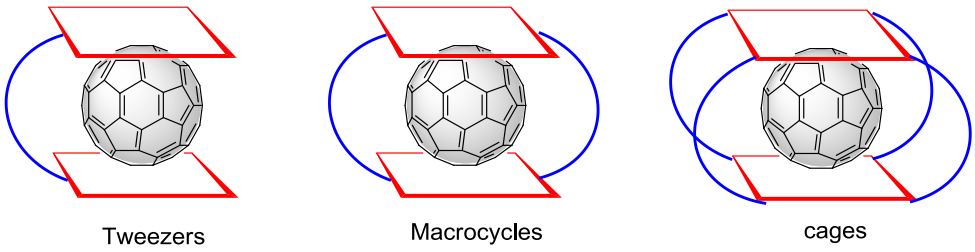

Figure 4.1: Shapes of synthetic receptors for the detection of fullerenes.

In 1992, Diederich and co-workers reported the first molecular receptor for C_{60} fullerene, where they used aza-crown ether with lipophilic alkyl chains as a receptor unit.[24] Two years later, Atwood and co-workers synthesized bowl-shaped calixarenes with hydrophobic cavities and studied their binding properties with C_{60} and C_{70} fullerenes.[10] These calixarene receptors were successfully utilized to separate C_{60} fullerene from the fullerene extract. Over the years, several synthetic receptors have been developed in the molecular recognition of fullerenes. Among them, porphyrins[22,25-30] and calixarenes[10,17,31-33] are well known and extensively studied receptors to interact favorably with fullerenes both in solution and in the solid state. In addition, large π-conjugated compounds such as corannulenes have been studied as receptors for

fullerenes.[34] As shown in Figure 4.2, Georgiou and co-workers recently reported the solid-state structure of a 1:1 complex made of C_{60} fullerene and corannulene.[35] As relevant to this chapter, a selection of synthetic receptors taking the shapes of molecular tweezers, macrocycles and cages are presented in the following section.

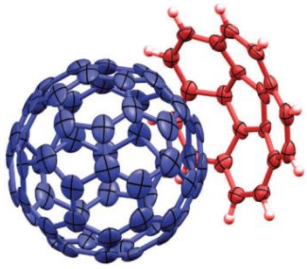

Figure 4.2: X-ray structure of C_{60} fullerene and corannulene complex (1:1).

In 2006, Martin and co-workers investigated the molecular properties of ex-TTFs **280** as a tweezer-like receptor for fullerenes.[36] In their design, the two exTTF units are separated by a spacer, an isopththalate diester. As evidenced by the Job plot, the binding behavior of tweezer **280** with C_{60} fullerene was found to be solvent dependant. In aromatic solvents such as chlorobenzene, the tweezer **280** formed a 1:1 complex with C_{60} fullerene, whereas in $CHCl_3/CS_2$ mixtures, the tweezer gave 2:1 and 2:2 complexes (Scheme 4.1).

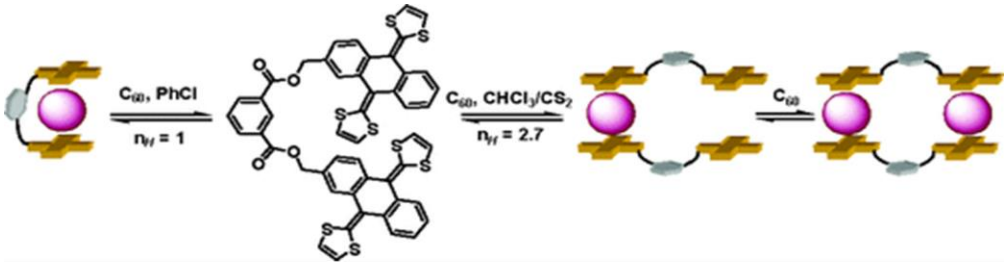

280

Scheme 4.1: Molecular tweezers **280** and its complexation of C_{60} fullerene.

The same group also synthesized a series of a bis-exTTFs based macrocycles **281** with different aromatic spacers (Figure 4.3) and investigated the binding properties with fullerenes.[37] It was observed that the UV-Vis spectral features of the macrocycle and C_{60} complex are very similar to those of tweezers **280**. Very large binding constants were obtained from the UV-Vis titration of macrocycle **281a** with C_{60}. They also probed the binding event by ^{13}C NMR spectroscopy, which confirmed the association of macrocycle **281a** with C_{60}.

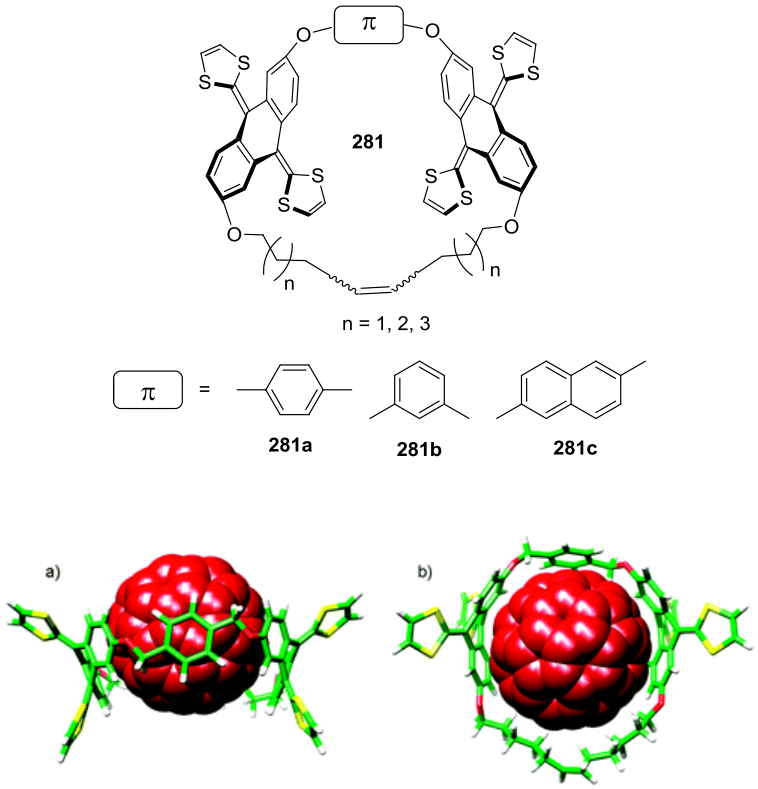

Figure 4.3: Molecular structures of macrocycle **281** (top), and the energy-minimized structure of macrocycle **281a** and C_{60} (bottom), a) side-view and b) top-view.

Recently, a porphyrin cyclic trimer **282** was synthesized and its binding affinities with C_{60} and C_{70} fullerenes were studied by Anderson and co-workers (Figure 4.4).[21] The binding constants of macrocycle **282** were determined to be 2×10^6 and 2×10^8 M^{-1} with C_{60} and C_{70} fullerenes respectively. It was demonstrated that the binding between macrocycle **282** and C_{60} or C_{70} fullerene was highly solvent dependent, where the highest binding constant was achieved in cyclohexane as solvent.

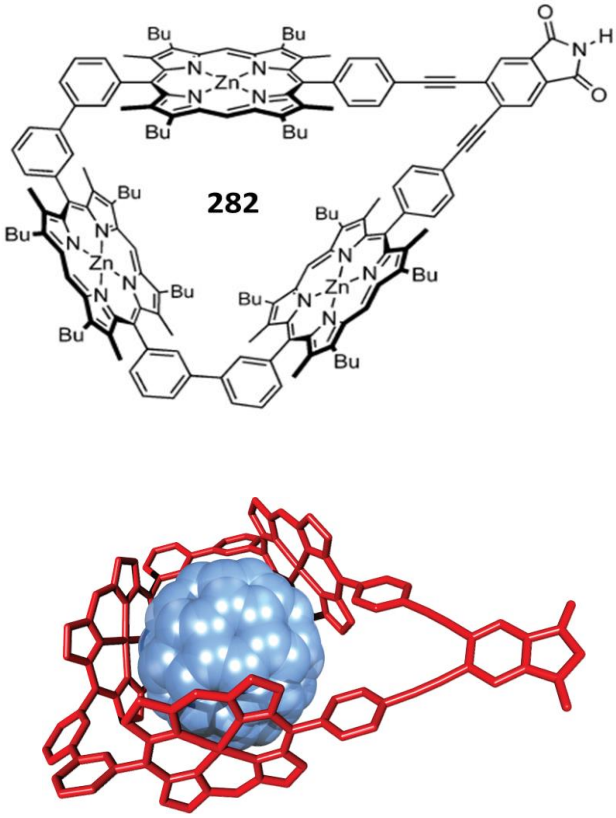

Figure 4.4: Molecular structure of macrocycle **282** and the calculated structure of its complex with C_{60}.

Very recently, as shown in Figure 4.5, Chiu and co-workers synthesized molecular cages **283a** and **283b** and demonstrated their potential use as selective receptors for C_{70} fullerene.[38] The data from ^{1}H NMR studies indicated that the receptor **283b** could not show any binding with both fullerenes (C_{60} and C_{70}) tested, as neither of the guests (C_{60} or C_{70}) could enter into the cavity of receptor **283b** by penetrating its smaller openings. However, molecular cage **283a** showed high binding affinity for C_{70}

even in the presence of C_{60} fullerene. Dissociation of the complex **283a**/C_{70} can be achieved by adding CH_2Cl_2 to the solution of complex **283a**/C_{70} in toluene.

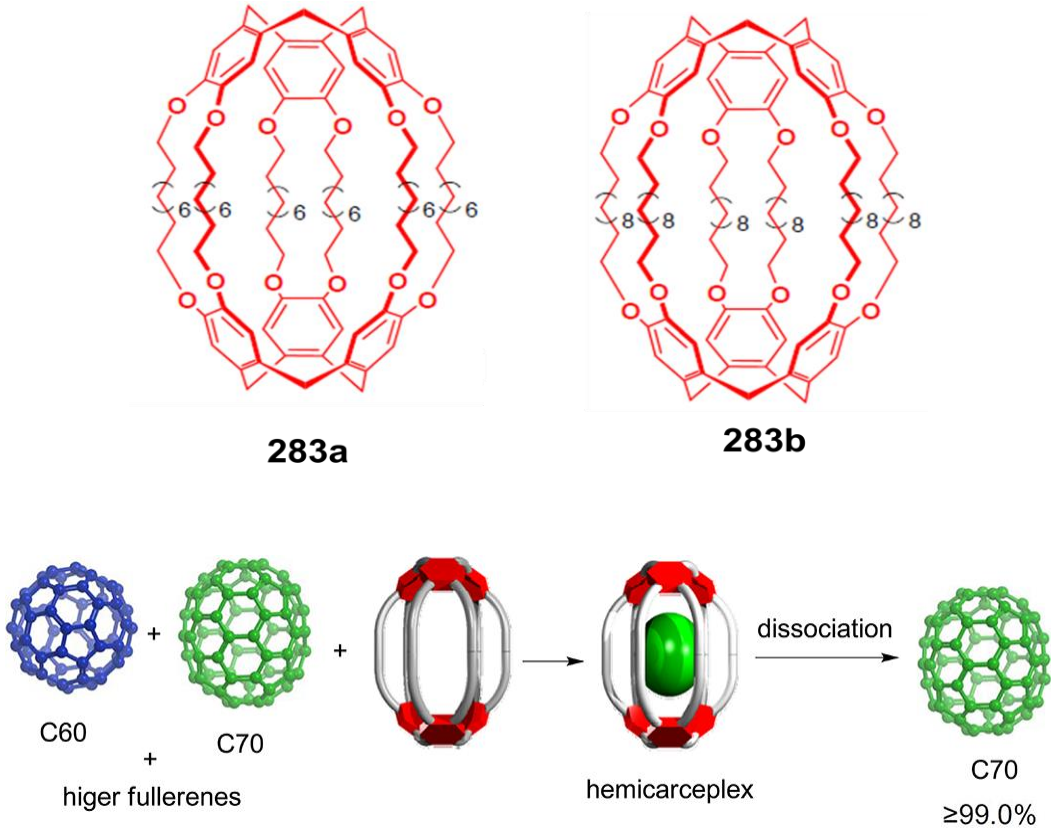

Figure 4.5: Molecular structures of cages **283a** and **283b** (top) and schematic representation showing the purification of C_{70} from mixture of C_{60} and C_{70} (bottom).

4.1.2 Chemosensors for the detection of metal ions

The detection of metal ions is of great interest with respect to environmental remediation, biological studies, and industrial applications.[39] In this area of research, numerous recent literature reports have been dedicated to the development of various chemosensors with fluorescent, colorimetric and electrochemical sensing functions to

selectively and sensitively detect metal ions.[8,40-47] In this regard, considerable effort has been given to fluorescent chemosensors. As relevant to this chapter, examples of several newly developed fluorescent chemical sensors are highlighted in the following section.

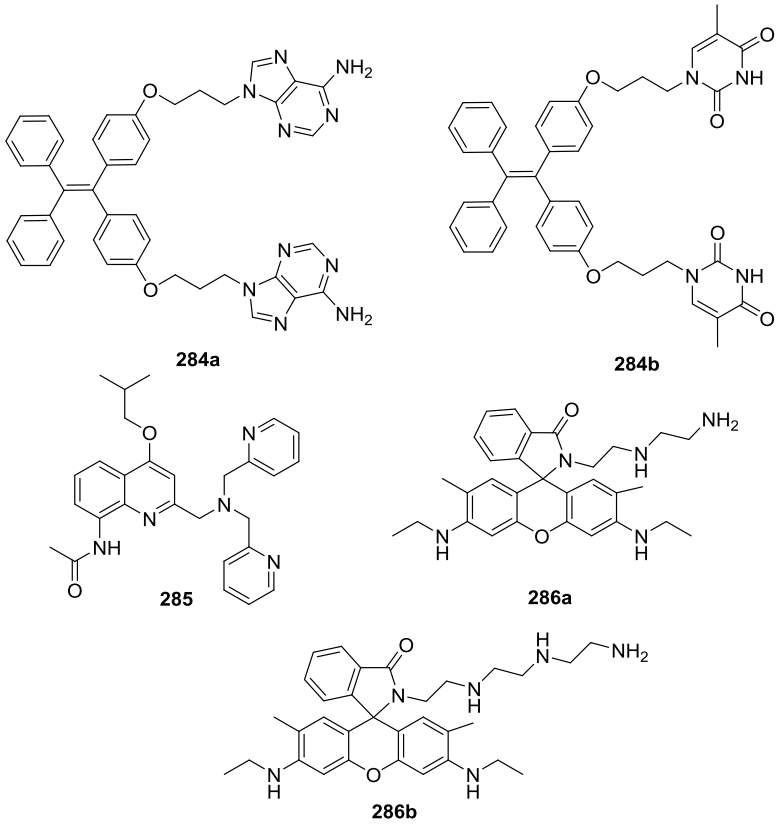

Figure 4.6: Representative examples of fluorescent chemical sensors for metal ions detection.

Zhang and co-workers designed fluorescent chemosensors **284a** and **284b**, in which tetraphenylethylene (TPE) compounds are linked to adenine and thymine moieties, respectively (Figure 4.6).[48] They have also investigated the sensing properties of TPE chemosensors **284a** and **284b** for transition metal cations. Among all the metal ions

tested, it was found that sensor **284a** was very selective to Ag^{+} ions, whereas the sensor **284b** showed selectivity towards Hg^{2+} ions. It was hypothesized that the sensors **284a** and **284b** gave weak fluorescence in solution, but they became more emissive after aggregation induced suitable metal ions. This selective fluorescence enhancement was ascribed to the so-called aggregation induced emission (AIE) mechanism.

Jiang and co-workers reported the behavior of an acetamidoquinoline based sensor **285** bearing di-2-picolylamine groups (DPA) as receptor units for metal ions (Figure 4.6).[49] Compound **285** displayed a strong fluorescence enhancement upon interaction with Zn^{2+} and Cd^{2+} metal ions. Moreover, the sensor **285** not only showed the selectivity to distinguish Cd^{2+} from Zn^{2+} by two different sensing mechanisms (PET for Cd^{2+} and ICT for Zn^{2+}). In 2007, two rodamine based fluorimetric chemosensors **286a** and **286b** were synthesized (Figure 4.6),[50] in which diethylenetriamine or triethylenetetriamine are attached as receptor units. These compounds exhibited sensing function toward Fe^{3+} and Cr^{3+} ions respectively. Interestingly, sensor **286a** formed a 1:1 (host:guest) complex with Fe^{3+} ion, whereas a 2:1 (host:guest) complex was observed in case of sensor **286b** bound to Cr^{3+} ion.

The applications of TTFV based compounds in chemical sensing of metal ions are rarely reported.[51,52] TTFV derivatives are very good electron donors,[53] and they show substituent-dependant conformational changes upon oxidation, making them attractive building blocks for the construction of electrochemical sensors. As shown in Scheme 4.2, in 2008, Lorcy and co-workers investigated the electrochemical behavior of TTFV

derivative **287**.[54] It was demonstrated that when sensor **287** was bound to Zn^{2+}ions, the conformational change during oxidation was restricted. According to CV experiments, the oxidation potential was shifted to the positive direction and coalescence of two single-electron oxidations into a two-electron oxidation was observed. It was proposed that a clip motion would occur, when the sensor reacted with $ZnCl_2$ to form **287** and a bivalent zincate complex (Scheme 4.2).

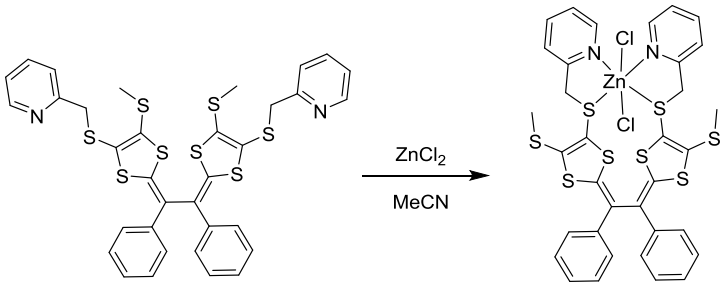

Scheme 4.2: Molecular clip function of sensor **287** with Zn^{2+} ion.

4.1.3 Electrochemical receptors for saccharides

Although a vast array of fluorescent synthetic receptors for saccharides detection have been reported in the literature, in recent years, however, the development of boronic acid-based electrochemical sensors to detect saccharides has been growing significantly as an alternative to the current commercially available enzymatic electrochemical sensors.[55] In this area of research, several electrophores such as ferrocene[56,57] and polyanilines[58,59] have been extensively studied as reporter units.

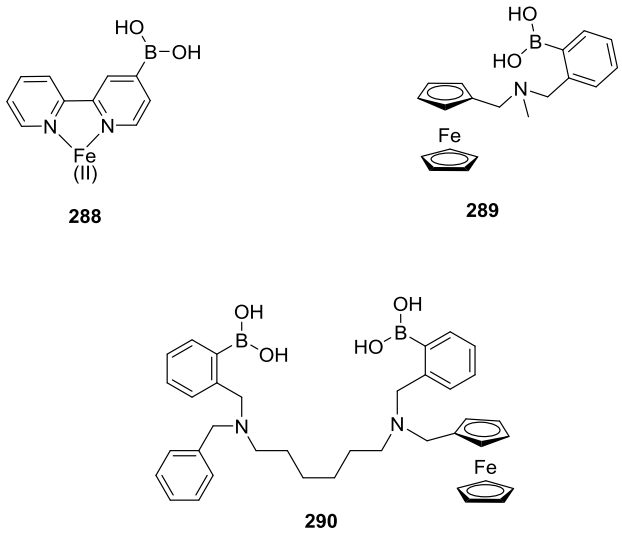

Figure 4.7: Electrochemical sensors **288-290** for saccharides detection.

For example, as shown in Figure 4.7, Fabre and co-workers[60] studied the electrochemical behavior of the boronic acid appended bipyridine iron (II) complex **288** with various mono-saccharides in aqueous buffer solution at pH 6.4. It was observed that upon addition of high concentrations of D-fructose, the oxidation peak in the DPV of complex **288** was shifted towards more positive values by 50 mV. In 2002, James and co-workers prepared mono- and bis-boronic acid electrochemical sensors **289** and **290** and compared their selectivity for different saccharides (Figure 4.7).[61] The electrochemical sensor **290** showed much better selectivity towards D-glucose than other saccharides tested. In particular, the stability constant of the bis-boronic acid sensor **290** with D-glucose was 40 times greater than with the mono-boronic sensor **289**. The results from the DPV spectrum showed that the oxidation peak of sensor **290** was shifted by nearly 100 mV to the positive potential when bound to D-glucose.

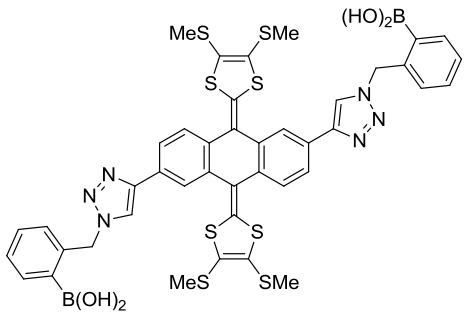

291

Figure 4.8: Boronic acid-appended exTTF-based electrochemical sensor **291**.

Despite their remarkable redox activities in organic electronic materials, the TTFs and exTTFs are very rarely utilized in the electrochemical sensing of saccharides. Our group previously investigated the electrochemical properties of sensor **291**, in which the π-extended tetrathiafulvalene (TTFAQ) unit acted as redox reporter (Figure 4.8).[62] Although sensor **291** gives satisfactory electrochemical responses to various saccharides owing to the excellent redox activity of TTFAQ, it still has some drawbacks. First, the extended anthraquinone unit in compound **291** renders it hydrophobic and limits its water solubility. Actually, a significant amount of DMSO needs to be used as co-solvent to reasonably solubilize **291** in H_2O. Second, sensor **291** only sensitively responds to saccharides under basic conditions (pH 8.75). For practical purposes, a saccharide sensor is desired to work under physiological conditions (*i.e.*, aqueous pH 6 – 8).

4.2Project design and objectives

As an excellent organic π-electron donor, the tetrathiafulvalene (TTF) and related analogues have attracted enormous attention in the development of functional organic electronic materials and devices.[63,64] Due to its unique structural and redox properties, the research involving TTF has been expanded to the preparation of a vast array of TTF analogues such as TTF conductors,[65] TTF macrocycles,[66,67,68] and TTF polymers and dendrimers.[69,70] A commonly used strategy for the preparation of new TTF derivatives can be achieved by expanding the backbone of TTF through diverse π-spacers placed between the dithiole rings, leading to the π-extended TTFs (exTTFs). Numerous examples of exTTFs have been reported in the literature.[71-73]

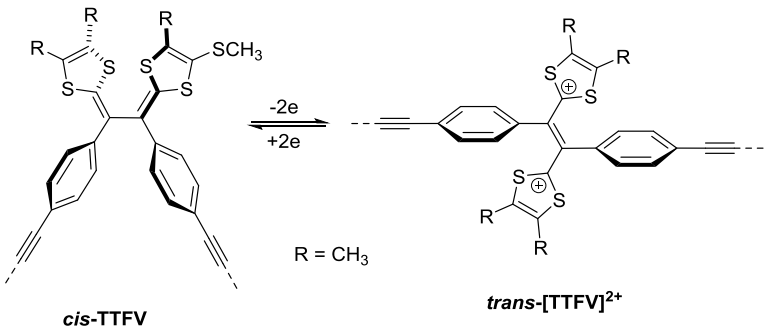

Figure 4.9: Structures of TTFV in the neutral and oxidized states.

Although tetrathiafulvalene (TTF) and its derivatives have been extensively studied as important organic electronic materials for many years, tetrathiafulvalene vinylogues (TTFVs) still remain a relatively underdeveloped branch in the family of TTF derivatives. In the past few years, however, tetrathiafulvalene vinylogue (TTFV) has

captured much attention as an appealing molecular building block owing to its versatile redox and structural switchability and tunability. As shown in Figure 4.9,[53] the phenyl-substituted TTFVs are well known to adopt pseudo-cisoid conformation due to the steric hindrance of the two phenyl substituents (Figure 4.13). Upon oxidation, the molecule can undergo simultaneous two-electron transfer, which leads to dramatic *cis*-to-*trans* structural change.

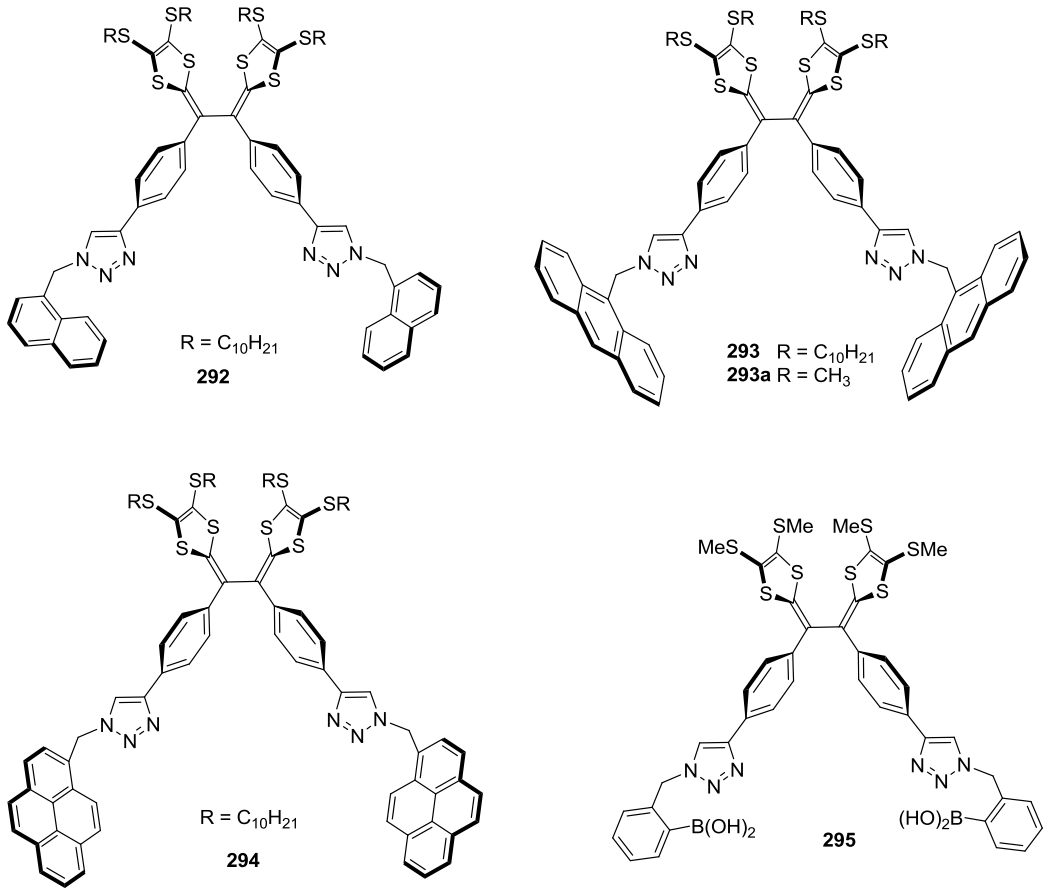

Figure 4.10: Molecular structures of TTFV-tweezers **292-295**.

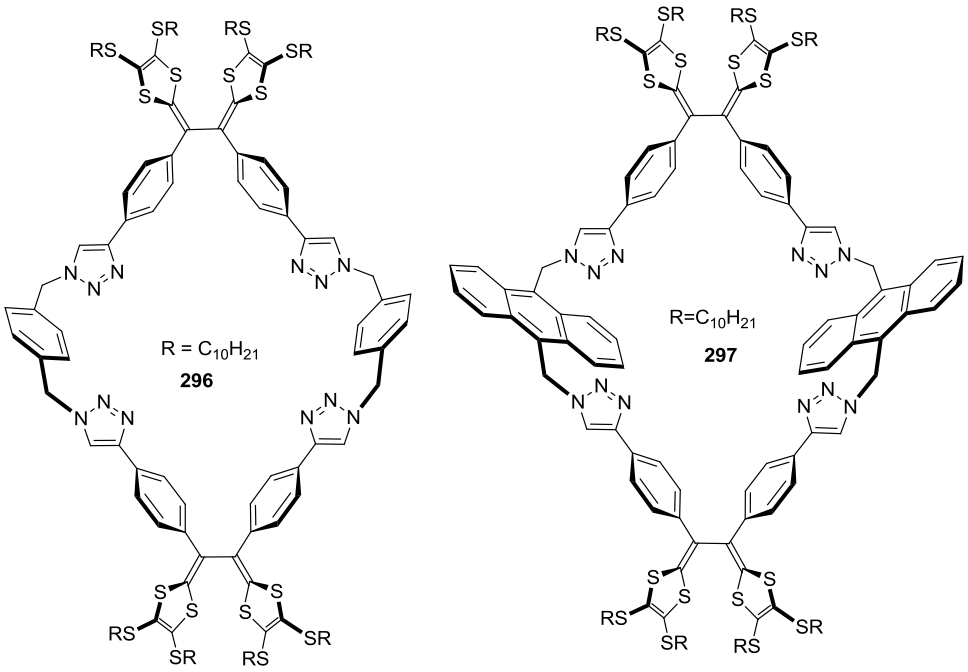

Figure 4.11: Molecular structures of TTFV-macrocycles **296** and **297**.

In addition to redox conditions, our recent studies have also demonstrated that diphenyl-TTFV can be reversibly protonated to switch its conformation from *cis*-to-*trans*.[74] These switching behaviors thus led us to the design of new types of redox and pH responsive TTFV-tweezers (**292**, **293**, **293a**, **294**, and **295**), and macrocycles (**296** and **297**) as receptors for different analytes including metal ions, anions, fullerenes, and saccharides (Figures 4.10 and 4.11).

Further, our theoretical investigations have also revealed that the electronic properties of diphenyl-TTFV derivatives are subject to the electronic nature of substituents. As an example, the molecular structure and electronic properties of dianthryl–TFV **293** were investigated by density functional theory (DFT) calculations at

the B3LYP/6-31G (d) level. In the optimized geometry of **293** (Figure 4.12), the TTFV unit shows a pseudo-cis conformation. The HOMO is distributed at the central TTFV core, while two degenerated LUMOs are solely located at the two anthryl groups. Such spatially separated FMO characters together with the low oxidation potential of TTFV suggest that photoinduced electron transfer (PET) quenching of the fluorophore would provide a mechanistic basis for sensing function.[75] Indeed, compound **293** was found to show very weak fluorescence ($\Phi = 0.009$) in THF.

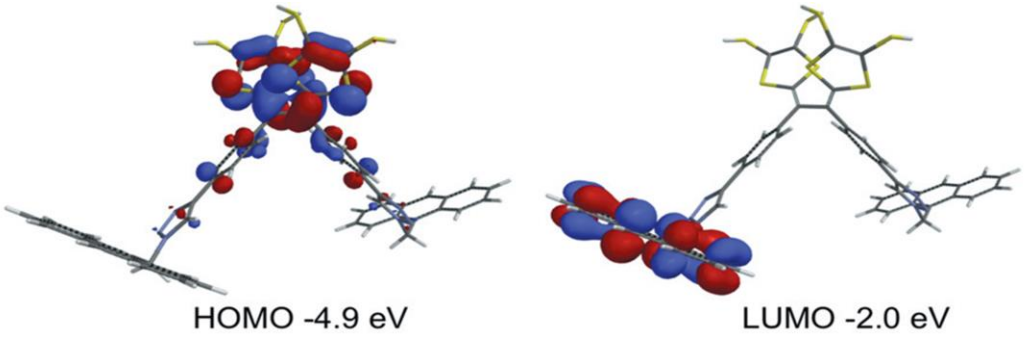

Figure 4.12: FMO properties of TTFV-anthracene tweezers **293** calculated at the B3LYP/6-31G (d) level of theory using Spartan'10.

Most of the data in this chapter have been published in the following research articles, in which I am the first author of the papers. As part of collaboration with Professor David W. Thompson, Chemistry Department, Memorial University, his PhD student Prateek Dongare conducted spectroscopic characterizations of TTFV-anthracene tweezers **293a** with various metal ions.

1) *Tetrahedron Lett.*,**2014**, *55*, 382-386 (saccharide sensing)

2) *Org. Lett.*,**2013**, *15*, 4532-4535 (fullerene receptors)

3) *Org. Biomol. Chem.*, **2012**, *10*, 2542-2544 (metal ion sensing)

4.3 Results and discussion

4.3.1 Synthesis of TTFV-tweezers (292-295) and macrocycles (296 and 297)

The synthesis began with the preparation of essential precursors such as acetylenic phenyl-TTFVs (**300** and **300a**) and azido compounds (**304**, **307**, **311**, **314**, and **315**). As described in Scheme 4.4, for the preparation of acetylenic phenyl-TTFVs (**300** and **300a**), the synthesis was undertaken via a $P(OMe)_3$-mediated olefination reaction between *S*-decylthione **270** and aldehyde precursor **271** to afford DTF precursor **298** as a thick reddish brown syrup in 72% yield.

DTF precursor **298** was then subjected to an iodine-promoted oxidative dimerization reaction, yielding cationic dimerized products which were subsequently treated with $Na_2S_2O_3$ to afford neutral acetylenic phenyl TTFV **299** in a good yield of 82%. The desilylation reaction on compound **299** in the presence of K_2CO_3 as base resulted in acetylenic phenyl-TTFV **300** as a thick syrup. A similar synthetic strategy was applied for the preparation of the methyl version of TTFV precursor **300a** by taking methyl substituted thione **270a** as the staring material (Scheme 4.4).

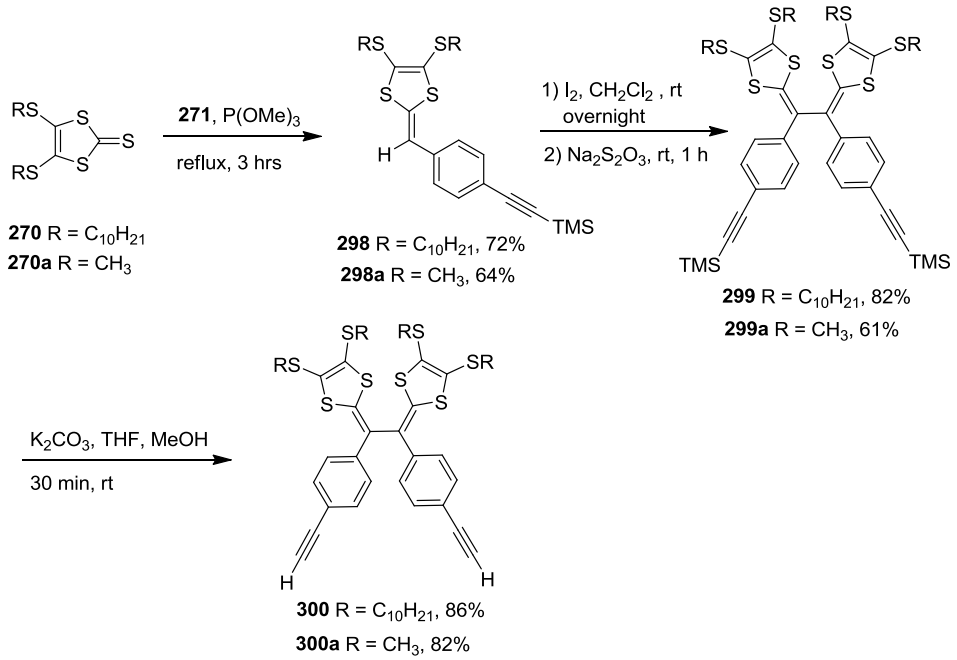

Scheme 4.4: Synthetic route for the preparation of acetylenic TTFV precursors **300** and **300a**.

The synthetic routes for the preparation of azido precursors are outlined in Scheme 4.5. 1-(Azidomethyl)naphthalene **304** was prepared by a series of reactions on 1-naphthaldehyde (**301**). First, 1-naphthaldehyde was reduced to the corresponding alcohol **302** with $NaBH_4$, and then the subsequent mesylation reaction with mesyl chloride led to chlorinated **303** instead of the expected mesylated product. An azidation reactions on **303** gave 1-(azidomethyl)naphthalene **304** as a liquid. In the same manner, 9-(azidomethyl)anthracene **307** was prepared as shown in Scheme 4.5. A commercially available compound **305** was subjected to a mesylation reaction with mesyl chloride as reported in the literature. This reaction gave 9-(chloromethyl)anthracene **306** exclusively

as a yellow solid, instead of the generally expected mesylated product. Further, 9-(chloromethyl)anthracene **306** was reacted with NaN_3 in DMF to afford 9-(azidomethyl)anthracene **307** as a yellow solid.

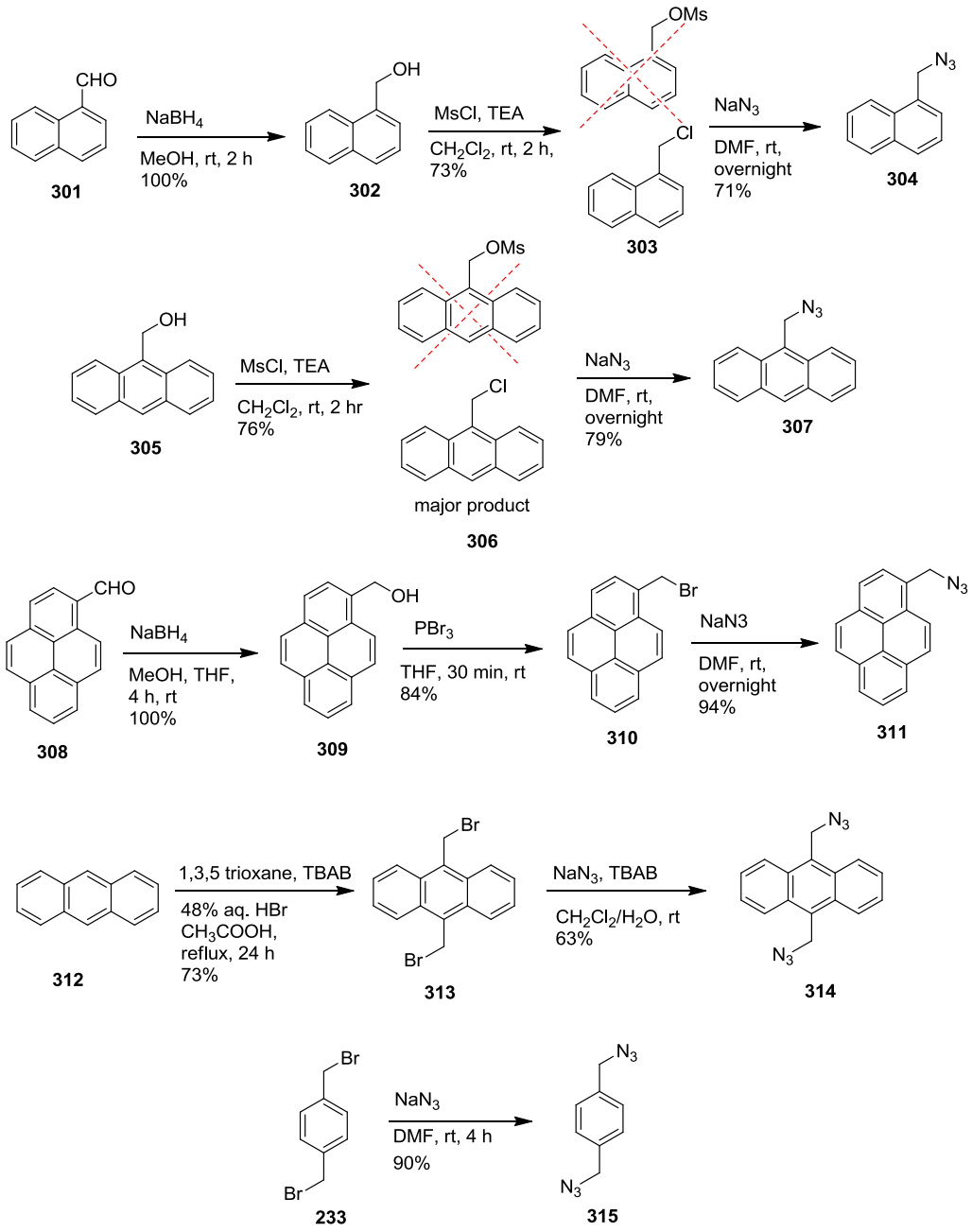

Scheme 4.5: Synthesis of mono and di azido precursors.

As demonstrated the synthesis of 2-(azidomethyl)pyrene **311** in Scheme 4.5, 2-pyrenealdehyde **308** was reduced to alcohol **309**, and brominated to afford 2-bromopyrene **310** as an unstable product. The brominated product was immediately converted to 2-(azidomethyl)pyrene **311** without any further purification and characterization. Similar type of reactions were performed to synthesize diazidoarenes as shown in Scheme 4.5. For instance, bis(azidomethyl)anthracene **314** was prepared by bromomethylation on anthracene and followed by an immediate azidation with NaN_3, since the brominated product **313** was obtained as a dark green solid and was too unstable to be stored for prolonged period of time. An azidation reaction on compound **233** led to the product **315** as a colorless liquid.

With all the precursors in hand, the synthesis was carried out further to prepare desired TTFV-tweezers and macrocycles as outlined in Scheme 4.6. The three mono-azido precursors **304**, **307**, and **311**were subjected to reaction with acetylenic TTFV precursor **300** via the well established click chemistry. In this work, a Cu-catalyzed alkyne-azide coupling reaction (CuAAC) was explored to generate corresponding TTFV tweezers **292**, **293** (and **293a**), and **294** in the yields between 83% and 91%. TTFV-naphthalene tweezer **292** was obtained as a thick syrup and the other two tweezers **293** and **294** were yellow solids.

In a similar manner, acetylenic TTFV precursor **300** was coupled with diazidoarene **315** and **314** via the CuAAC reaction, wherein the amounts of TTFV precursor **300** and respective diazido-arene were controlled at a 1:1 ratio. The click

reactions led to the formation of [2 + 2] macrocyclic adducts **296** and **297** in yields of 47% and 54% respectively (Scheme 4.6), which are quite efficient for a one-pot cyclization synthesis. The relatively high yields can be attributed to a "templating effect" imposed by the Cu(I) catalyst, for it is known that the triazole group resulting from the click reaction can coordinate to transition metal ions to form stable complexes.[40] It is proposed that such an effect enhances the preorganization of reactive intermediates to favor macrocyclization over other possible side-reactions.

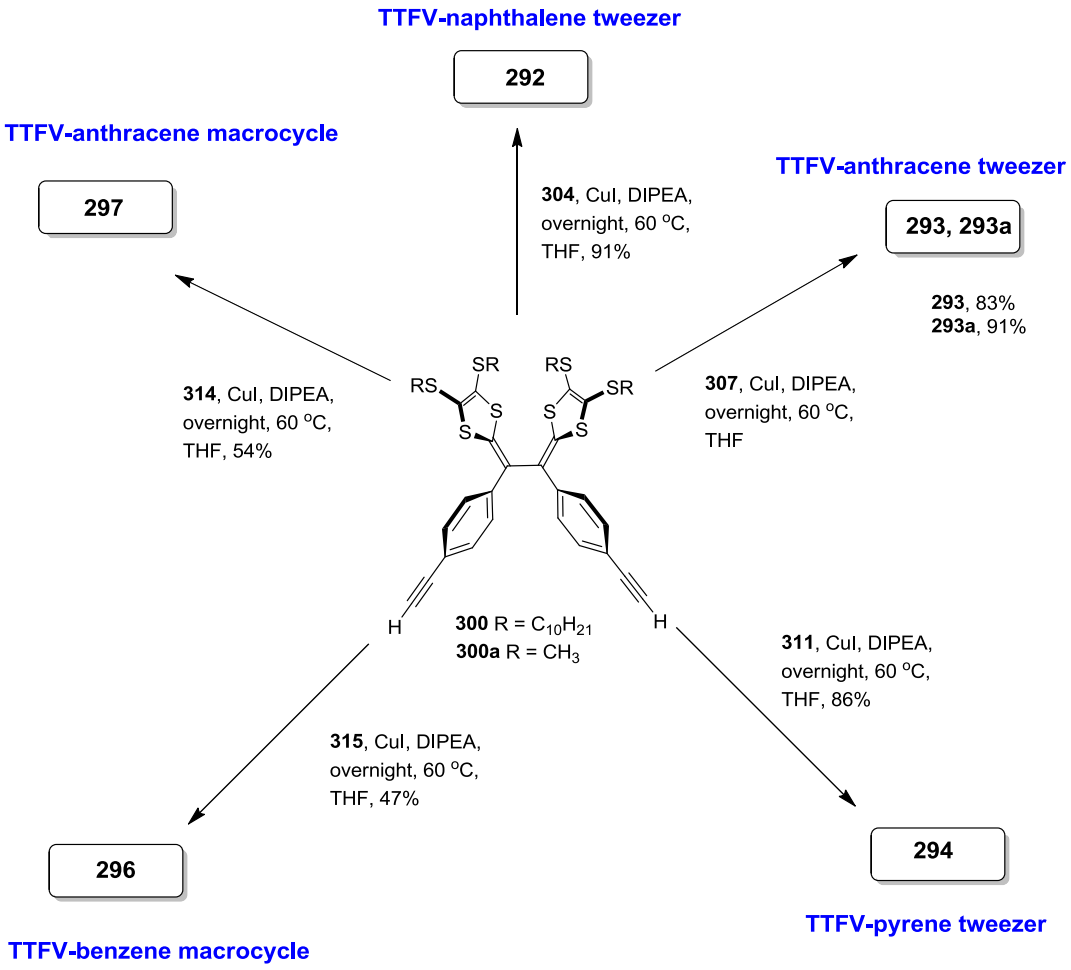

Scheme 4.6: Click strategy to construct TTFV tweezers and macrocycles.

Finally, the synthesis of boronic acid-appended TTFV tweezers **195** was carried out through the route described in Scheme 4.7. At first, acetylenic TTFV precursor **300a** was subjected to a CuAAC (click) reaction with azido-phenylboronate **210** to afford bis(phenylboronate)-TTFV tweezers **316** in a very good yield. Treatment of compound **316** with KHF_2 led to TTFV-trifluoroborate **317**, which was then hydrolyzed into phenylboronic acids with LiOH. The desired product **295** was obtained in 79% yield after acidic aqueous workup.

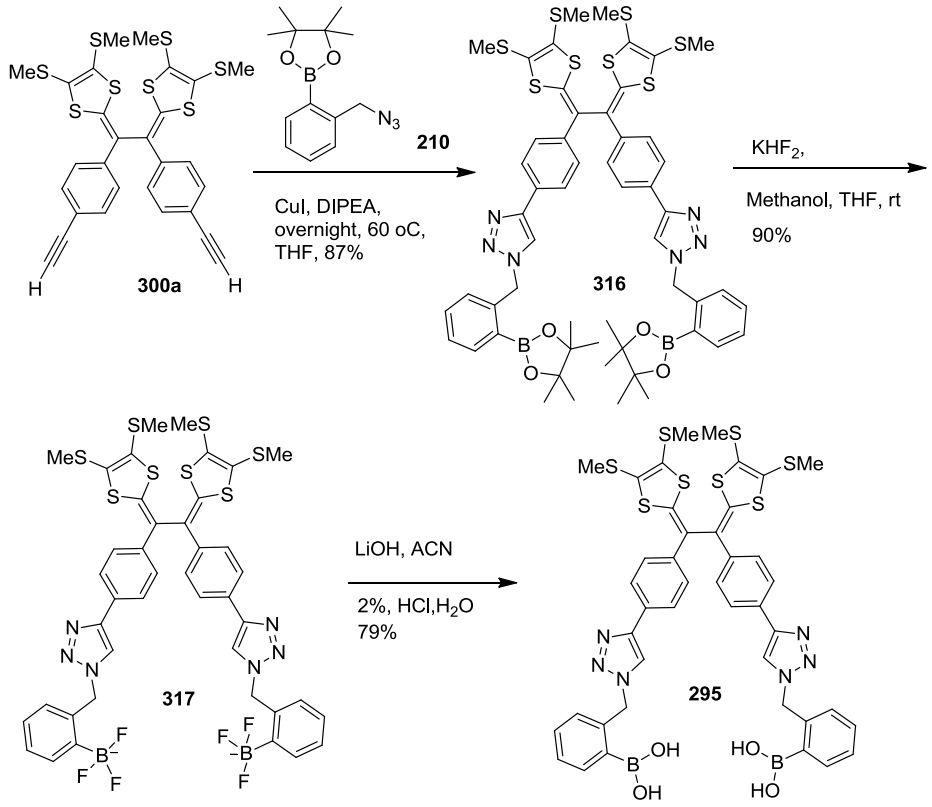

Scheme 4.7: Synthesis of boronic acid-appended molecular tweezers **295**.

4.3.2 X-ray structure analysis of TTFV precursor 299a and TTFV-anthracene tweezer 300a

Single crystals of TTFV precursor **299a** and TTFV tweezer **300a** were grown by slow evaporation of its solutions in $CHCl_3$/methanol (1:1) at low temperature (4 ^oC), and their detailed molecular and solid-state structures were characterized by single crystal X-ray crystallography. As predicted, the X-ray structures of **299a** and **293a** show tweezer-like non-planar and pseudo-cisoid conformations.

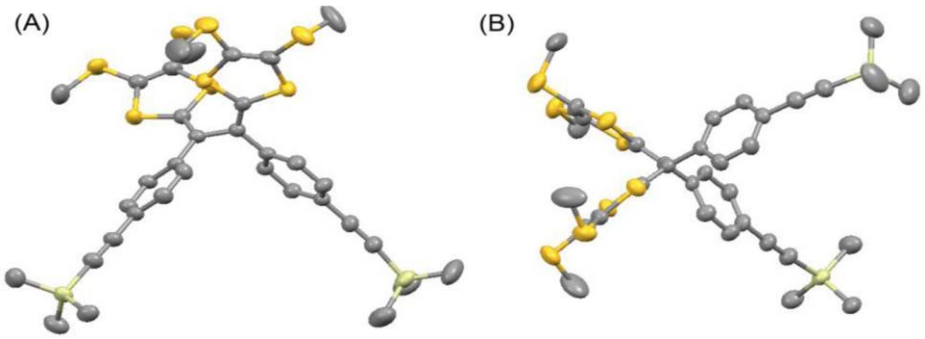

Figure 4.13: X-ray single-crystal structure of compound **299a**: (A) front view; (B) side view.

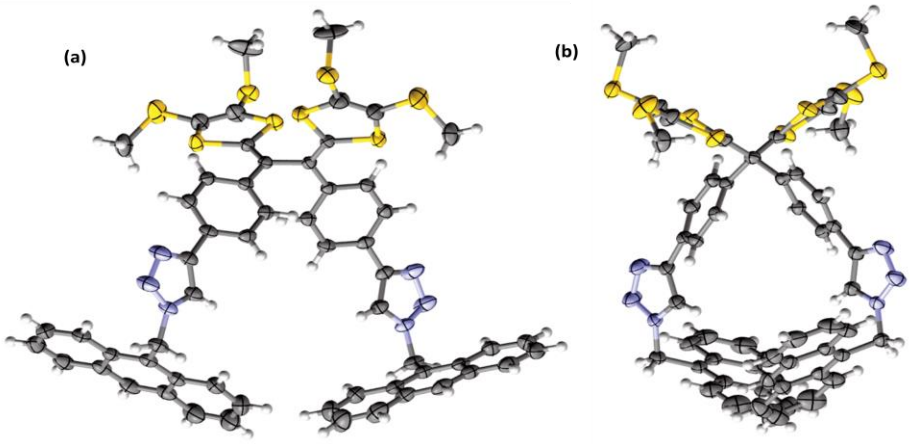

Figure 4.14: (a) ORTEP plot of **293a** (50% probability) and (b) side view.

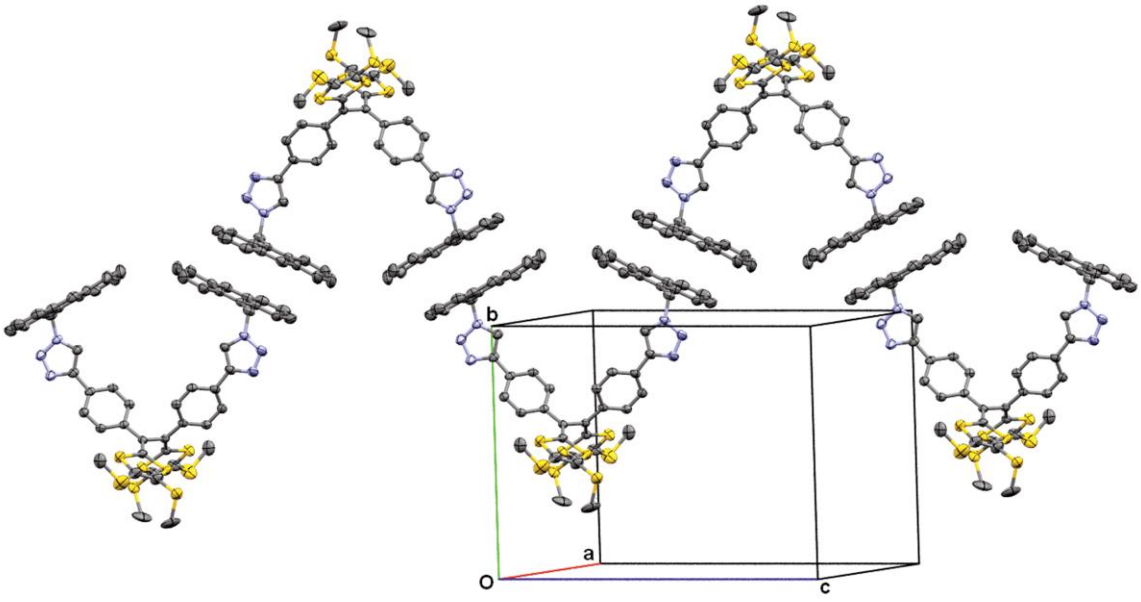

Figure 4.15: Solid-state packing of **293a** between anthracene units (50 % probability ellipsoid representation).

4.3.3 Electronic properties of TTFV-tweezers and macrocycles

The UV-Vis absorption spectra of TTFV tweezers and macrocycles were measured in chlorobenzene at room temperature and are shown in Figure 4.16. Figure 4.16A compares the absorption spectra of **292**, **293**, **293a**, **294**, **296**, and **297**. In the spectrum, TTFV tweezers **292** and TTFV macrocycle **296** show a broad absorption band at 370 nm in the low-energy region. In the spectrum of TTFV tweezers **293**, a notable absorption bands at **352** nm, **370** nm, and **391** nm are observed and can be assigned to the $S_0 \rightarrow S_1$ transition featuring three distinctive vibronic modes of anthracene. Irrespective of *S*-alkyl chain length, similar absorption spectrum was observed in the case of TTFV tweezers **293a**. However, the spectrum of TTFV–anthracene macrocycle**297** shows three absorption bands which are similar to TTFV tweezers **293** and are slightly red-shifted. The UV-Vis spectrum of TTFV tweezers **294**, two sharp absorption bands at 330 nm and 347 nm and a notable absorption shoulder at 375 nm along with a broad long-wavelength absorption tail extending to *ca.* 430 nm are observed.

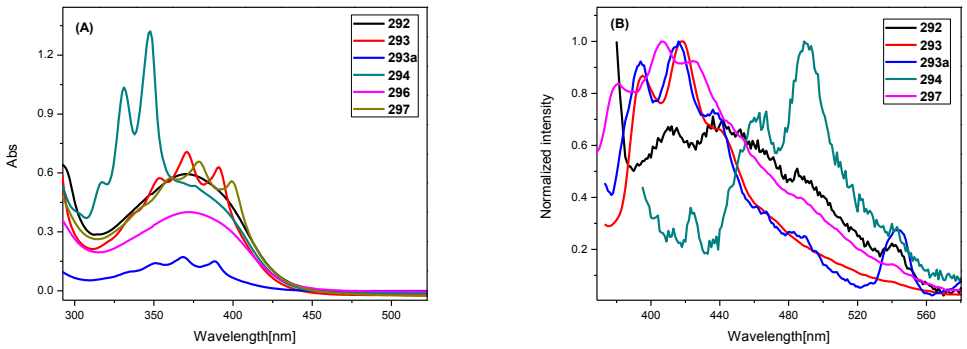

Figure 4.16: (A) UV-Vis absorption and (B) normalized fluorescence spectra of TTFV tweezers and macrocycles measured in chlorobenzene.

All TTFV tweezers and macrocycles are very weakly emissive upon photo-excitation. To gain insight into the properties of their first excited states, steady-state fluorescence spectroscopic measurements were carried out in chlorobenzene. Figure 4.16B shows the fluorescence spectra of TTFV tweezers and macrocycles except TTFV-benzene macrocycle **296,** and TTFV tweezers **295** as no meaningful spectrum was obtained due to the weak fluorophore benzene.

The emission spectra of TTFV-anthracene tweezers **293** shows an approximate mirror image relation with their absorption spectra (Figure 4.16A). Three emission bands are seen at 395 nm, 416 nm and 439 nm and are assigned to the $S_1 \rightarrow S_0$ transition featuring three distinctive vibronic modes. Similar emission profile was noticed for the remaining two TTFV-anthracene tweezers **293a** and TTFV-anthracene macrocycle **297**. The TTFV-naphthalene tweezers **292** shows very weak emission intensity with a featureless emission profile. Compared to the spectra of all TTFV tweezers and macrocycles, the emission bands in the spectrum of TTFV-pyrene tweezers **294** are red-shifted due to the bulky fluorophore. The emission bands appear at 450 nm and 490 nm.

4.3.4 Electrochemical redox properties of TTFV tweezers and macrocycles

The electrochemical redox properties of TTFV-hinged tweezers and macrocycles were investigated by cyclic voltammetric analysis. Figure 4.17shows the detailed cyclic voltammograms of these compounds. From Figure 4.17, it can be seen that TTFV-anthracene tweezers **293** gives a quasi-reversible redox couple at E_{pa}= +0.94 V and E_{pc}= +0.42 V, which are attributed to a simultaneous two-electron process. With E_{pa} at a less

positive potential of +0.81 V and E_{pc} at a same potential of +0.42 V, the peak separation of TTFV-anthracene macrocycle **297** is much smaller than TTFV-anthracene tweezers **293**. Regardless of the nature of fluorophores attached to the TTFV moiety, little or no changes in the oxidation potentials of TTFV moieties are observed in the spectra of all TTFV tweezers and macrocycles.

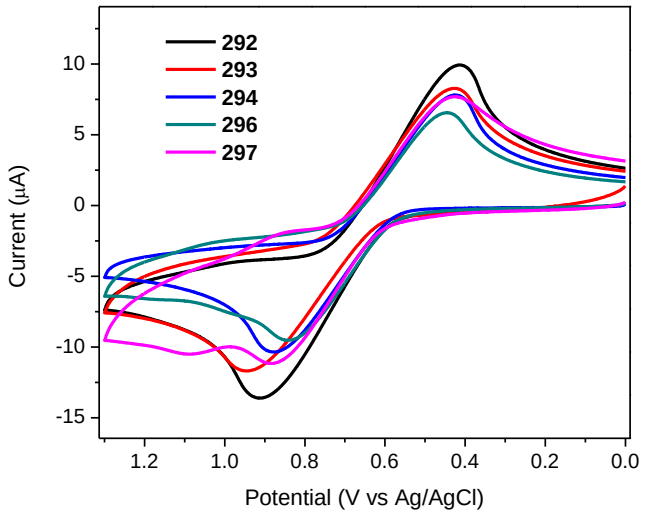

Figure 4.17: Cyclic voltammograms of **292** (2.01×10^{-3} M), **293** (1.47×10^{-3} M), **294** (1.68×10^{-3} M), **296** (1.14×10^{-3} M), and **297** (0.94×10^{-3} M). Experimental conditions: Bu_4NBF_4(0.1 M) as the supporting electrolyte, chlorobenzene as the solvent, glassy carbon as the working electrode, Pt wire as the counter electrode, satd. Ag/AgCl as the reference electrode, and scan rate at 50 mV s^{-1}.

4.3.5 Fluorescent sensing properties of TTFV-anthracene tweezers 293a with metal ions

To explore its sensing functions, TTFV-anthracene tweezers **293a** in THF at μM concentrations was subjected to UV-Vis and fluorescence titrations with a variety of metal ions and a strong Brønsted acid, TFA. As shown in Figure 4.18, of eight transition metal ions tested, Cu^{2+}, Fe^{2+}, and Cd^{2+} give rise to very significant fluorescence enhancement. Figure 4.18A illustrates the fluorescence spectral changes of **293a** in titration with Cu^{2+}. The titration results clearly show that with increasing addition of Cu^{2+}, three emission bands at 395, 416, and 440 nm and one shoulder band at *ca*. 470 nm emerge and grow steadily. At the endpoint of titration, the fluorescence intensity is increased by ca. 26-fold at 461 nm (detection limit: 0.26 μM). Besides Cu^{2+} ion, compound **293a** also shows a considerable degree of fluorescence enhancement in titration with Fe^{2+} and Cd^{2+} (Figure 4.18C and E).

The limits of detection are determined to be 0.48 μM and 0.86 μM respectively. For comparison purposes, the titration of **293a** with a strong protic acid, trifluoroacetic acid (TFA) was also performed. It is observed as in Figure 4.18 that at the sensitivity of **293a** towards the tested cations exhibits a decreasing trend as follows: Cu^{2+}> Fe^{2+}> Cd^{2+}> Ag^{+}> Mn^{2+}> Zn^{2+} ~ Hg^{2+}> Pb^{2+}> H^{+} (Figure 4.19).

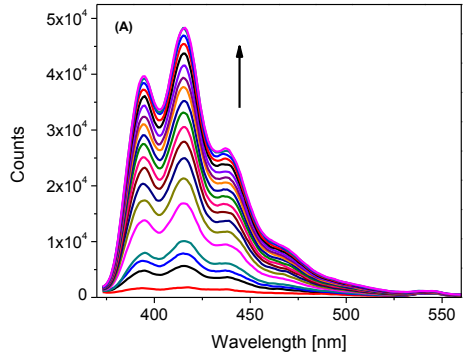
(A)
Counts
Wavelength [nm]

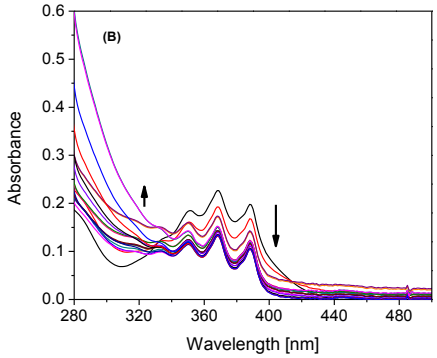
(B)
Absorbance
Wavelength [nm]

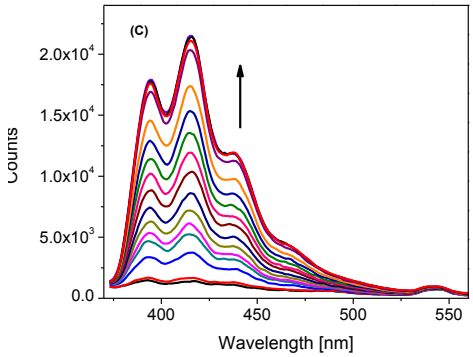
(C)
Counts
Wavelength [nm]

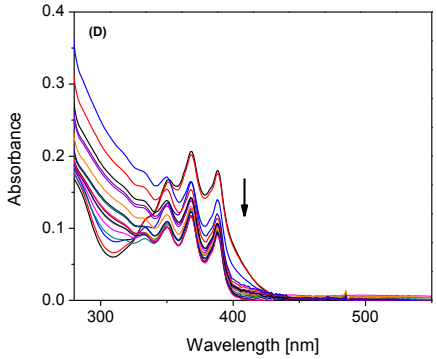
(D)
Absorbance
Wavelength [nm]

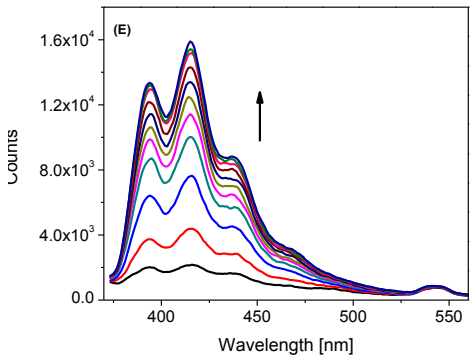
(E)
Counts
Wavelength [nm]

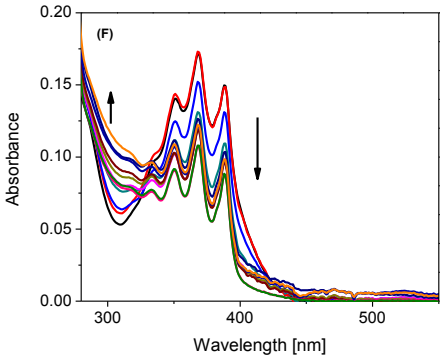
(F)
Absorbance
Wavelength [nm]

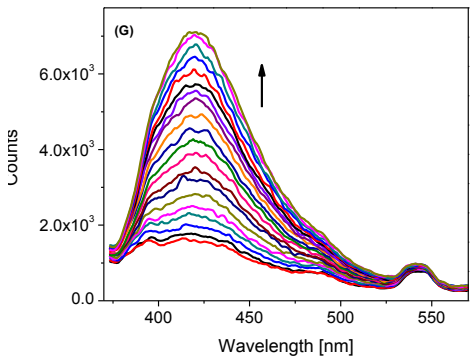
(G)
Counts
Wavelength [nm]

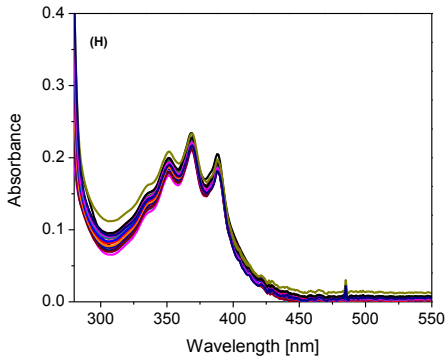
(H)
Absorbance
Wavelength [nm]

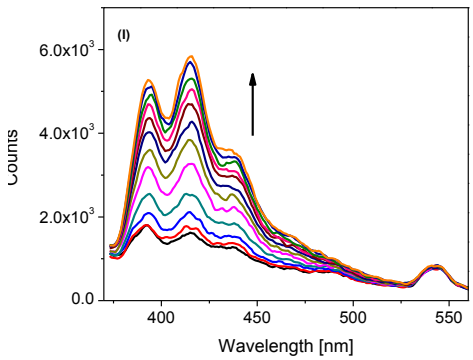
(I)
Counts
Wavelength [nm]

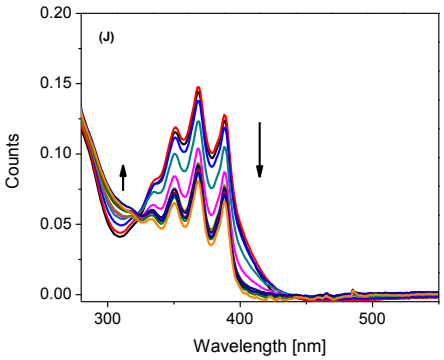
(J)
Counts
Wavelength [nm]

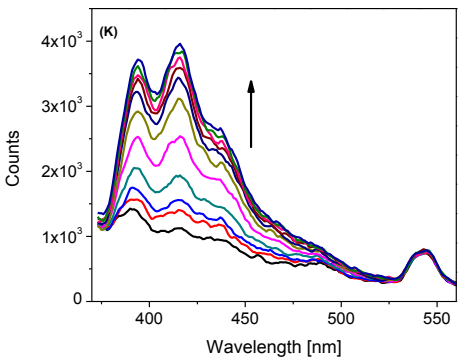
(K)
Counts
Wavelength [nm]

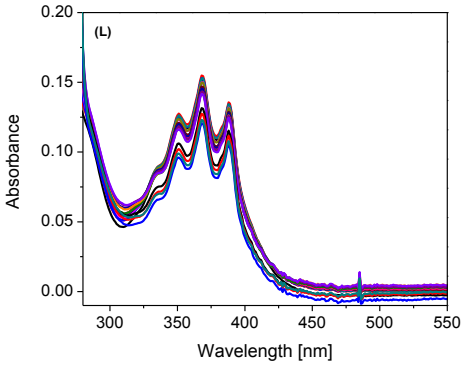
(L)
Absorbance
Wavelength [nm]

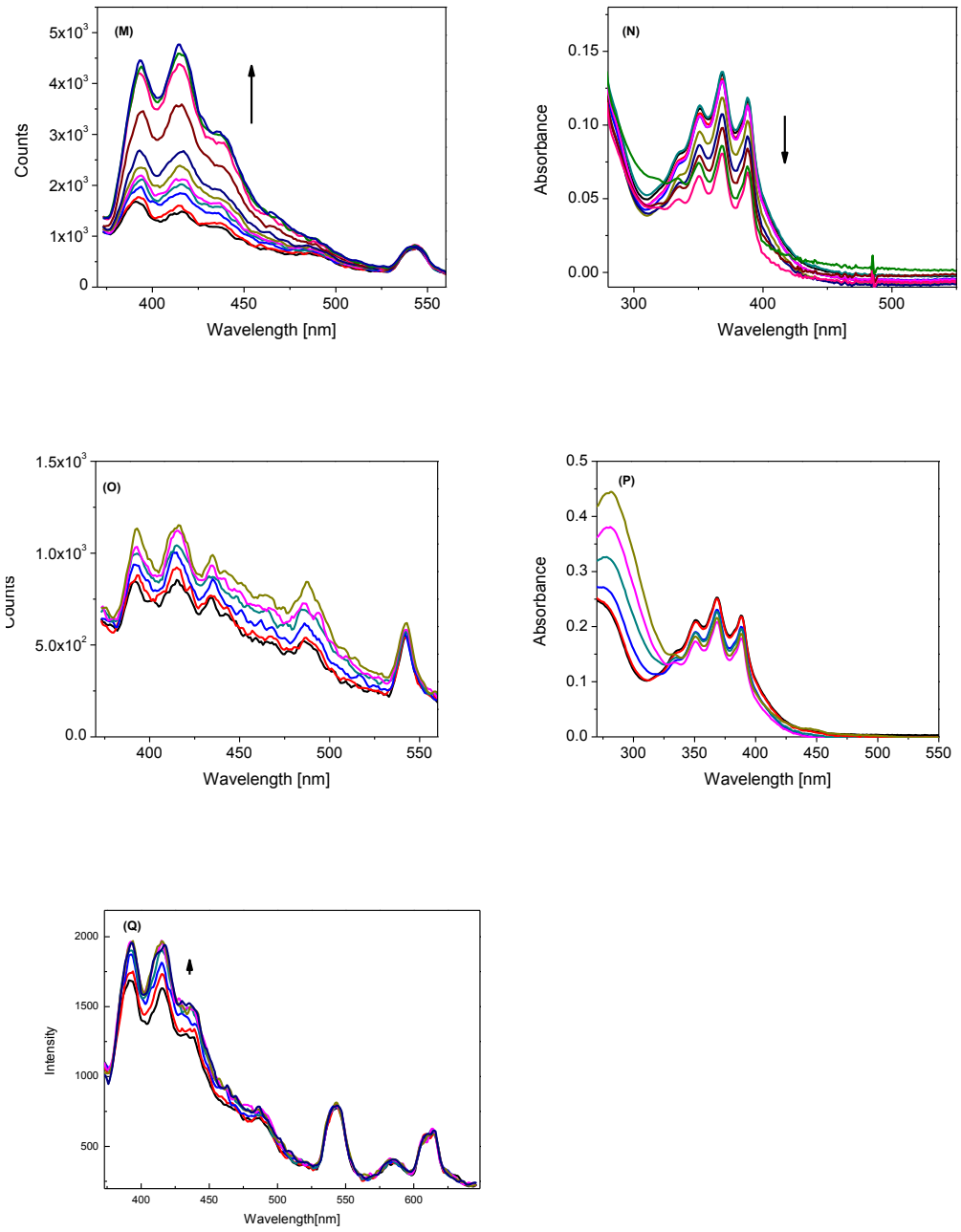

Figure 4.18:(A) Fluorescence spectra, (B) UV-Vis absorption of **293a** (5.55 μM) obtained as a function of increasing concentration of $Cu(OTf)_2$ (0 to 10.1 μM); (C) Fluorescence spectra, (D) UV-Vis absorption of **293a** (5.49μM) obtained as a function of

increasing concentration of $Fe(ClO_4)_2$ (0 to 39.8 μM); (E) Fluorescence spectra, (F) UV-Vis absorption of **293a** (5.52 μM) obtained as a function of increasing concentration of $Cd(ClO_4)_2$ (0 to 76.2 μM); (G) Fluorescence spectra, (H) UV-Vis absorption of **293a** (5.92 μM) obtained as a function of increasing concentration of AgOTf (0 to 13.2 μM); (I) Fluorescence spectra, (J) UV-Vis absorption of **293a** (5.51 μM) obtained as a function of increasing concentration of $Cd(ClO_4)_2$ (0 to 180 μM); (K) Fluorescence spectra, (L) UV-Vis absorption of **293a** (5.57 μM) obtained as a function of increasing concentration of $Zn(OTf)_2$ (0 to 356 μM); (M) Fluorescence spectra, (N) UV-Vis absorption of **293a** (5.09 μM) obtained as a function of increasing concentration of $Hg(ClO_4)_2$ (0 to 21.0 mM); (O) Fluorescence spectra, (P) UV-Vis absorption of **293a** (5.98 μM) obtained as a function of increasing concentration of $Pb(ClO_4)_2$ (0 to 1.0 M); (Q) Fluorescence spectra, of **293a** (5.00 μM) obtained as a function of increasing concentration of TFA (0 to 6.91 mM) in THF at 298 ± 3 K, λ_{ex} = 350 nm. No meaningful UV-Vis titration spectra of **293a** with TFA.

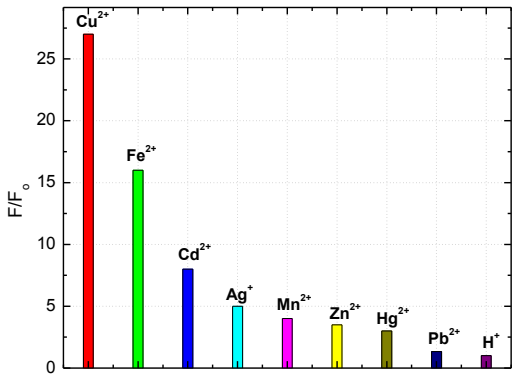

Figure 4.19: Fluorescence enhancement (λ = 415 nm) at the endpoint of titration. F_o and F refer to the fluorescence intensities at the initial and ending points of titration.

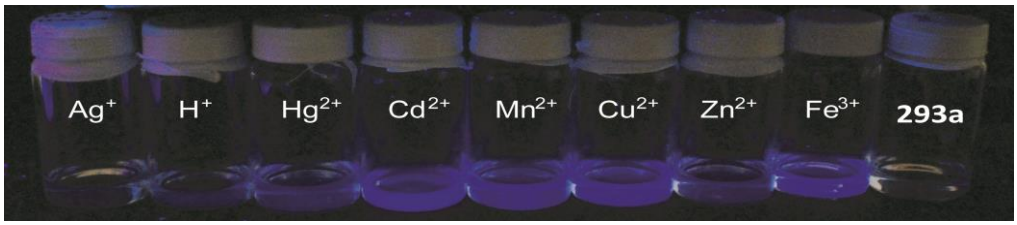

Figure 4.20: Photographic images showing visual detection of sensor **293a** with metal ions.

To further quantify the binding properties of TTFV-tweezers **293a** with various metal ions, the fluorescence titration data were subjected to SPECFIT global analyses, using the Levenberg-Marquardt nonlinear regression minimization procedure. The detailed binding stoichiometry and binding constants are listed in Table 4.1. The SPECFIT analyses indicate that sensor **293a** can bind with transition metal and proton ions to form both 1:1 and 1:2 complexes, while the binding constants vary substantially.

Table 4.1: Binding constants of **293a** with select transition metal ions and TFA and standard electrode potentials (E^o) of the cations

Cation	log ($\beta_{11}\times M^1$)	log ($\beta_{12}\times M^2$)	$E°$ (298K, V)
Cu^{2+}	7.12 ± 0.7	12.1 ± 0.8	+0.34 ($Cu^{2+} \rightarrow Cu^0$)
Cd^{2+}	5.22 ± 0.6	9.75 ± 0.6	-0.40 ($Cd^{2+} \rightarrow Cd^0$)
Zn^{2+}	4.78 ± 0.2	8.59 ± 0.3	-0.76 ($Zn^{2+} \rightarrow Zn^0$)
Fe^{2+}	4.62 ± 0.4	10.8 ± 0.2	-0.44 ($Fe^{2+} \rightarrow Fe^0$)
Mn^{2+}	4.58 ± 0.1	7.56 ± 0.1	-1.19 ($Mn^{2+} \rightarrow Mn^0$)
Ag^{+}	3.57 ± 0.1	6.67 ± 0.1	+0.80 ($Ag^{+} \rightarrow Ag^0$)
Hg^{2+}	2.72 ± 0.2	4.47 ± 0.2	+0.79 ($Hg^{2+} \rightarrow Hg^0$)
Pb^{2+}	1.72 ± 0.2	2.46 ± 0.3	-0.12 ($Pb^{2+} \rightarrow Pb^0$)
H^{+}	1.63 ± 0.5	2.95 ± 0.6	+0.00 ($H^{+} \rightarrow H_2$)

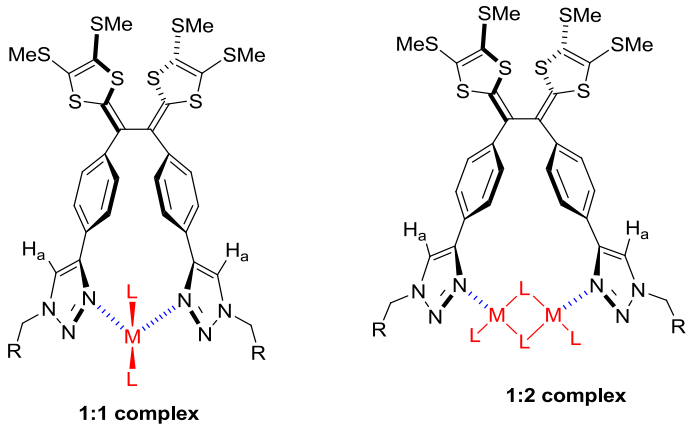

Figure 4.21: Proposed 1:1 and 1:2 binding modes of sensor **293a** with metal ions.

Plotting the binding constants (log β_{11} and log β_{12}) of these cations against standard electrode potentials of the metal ions ($E°$) turns out to be very informative. As shown in Figure 4.22, the cations fall in two distinct groups in terms of linear correlation between log β and $E°$. Group I consists of Cu^{2+}, Cd^{2+}, Zn^{2+}, Fe^{2+}, and Mn^{2+} ions, which afford considerably larger binding constants than those of Group II, which includes Ag^{+}, Hg^{2+}, H^{+}, and Pb^{2+} ions. These observations are in line with expectations based on hard-soft acid/base (HSAB) theory. The three metal ions (Cu^{2+}, Fe^{2+}, and Cd^{2+}) that cause sizeable fluorescence enhancement of sensor **293a** share two common features: (1) they belong to Group I, and (2) their relatively high E^{o} values facilitate charge transfer from TTFV to metal ions, which efficiently attenuates the PET process from TTFV to anthracene. Overall, the relationships revealed in Figure 4.22 are instructive for further design and fine-tuning of the selectivity and sensitivity of chemosensors with analogous molecular architectures.

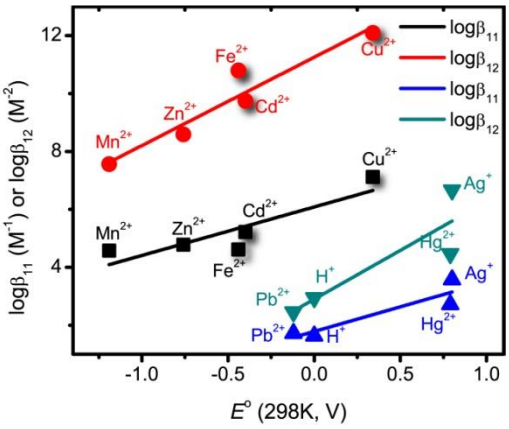

Figure 4.22: Linear correlations of binding constants (log β) and standard electrode potentials (*E*°) of transition metal and proton ions.

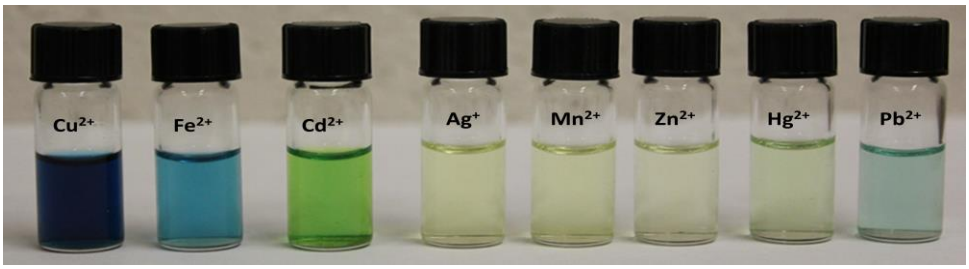

Figure 4.23: Photographic images of solutions of compound **293a** and various transition metal ions in acetonitrile.

It was also noted that when the solution of compound **293a** was prepared at mM or higher concentrations in THF, significant precipitation took place upon addition of various metal ions. It is rationalized that, at higher concentrations, metal-sulfur interactions become significant in addition to the metal-triazole interactions. As such, the resulting complexes would stay in the form of clusters or agglomerates, which lead to substantial fluorescence quenching. These complexes are soluble in polar organic

solvents such as acetonitrile, and the solutions of certain metal complexes (Cu^{2+}, Fe^{2+}, Cd^{2+}, and Pb^{2+}) in acetonitrile display visually distinct colors to enable straightforward colorimetric detection (Figure 4.23).

UV-Vis spectral analyses (Figure 4.24) clearly show that Cu^{2+}, Fe^{2+}, and Cd^{2+} ions when complexing with **293a** at relatively high concentrations give pronounced absorptions in the Vis-NIR region of the spectrum. Of particular note is the rise of a new band at *ca*. 500-800 nm, which is likely due to the formation of $[TTFV]^{+}$ and $[TTFV]^{2+}$ via TTFV-to-metal charge transfer.[53,76] In addition, a broad weak band ranging from ca. 800 to 1100 nm can be clearly seen in the Vis-NIR profiles of Cu^{2+} and Fe^{2+} complexes, which is tentatively assigned to $[TTFV]^{+}$. The UV-Vis data substantiate that at high concentrations the sulfur groups of **293a** can also act as ligands to interact with oxidative metal ions, such as Cu^{2+}, Fe^{2+}, and Cd^{2+}, to form colorful charge-transfer complexes.

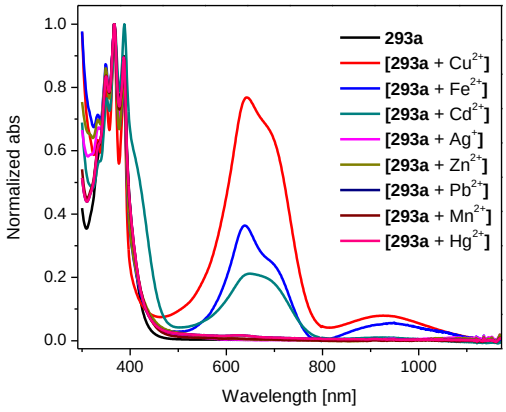

Figure 4.24: UV-Vis absorption spectra of compound **293a** with various transition metal ions measured in acetontrile at room temperature.

4.3.5.1 UV-Vis titration of TTFV precursor 299a with TFA and transition metal salts

To understand the electronic absorption features arising from the complexation between the TTFV moiety and H^+ or various transition metal ions, UV-Vis titration experiments were carried out by adding H^+, Cu^{2+}, Cd^{2+}, and Fe^{2+} respectively to the solution of TTFV **299a** in THF (Figures 4.25-4.28).

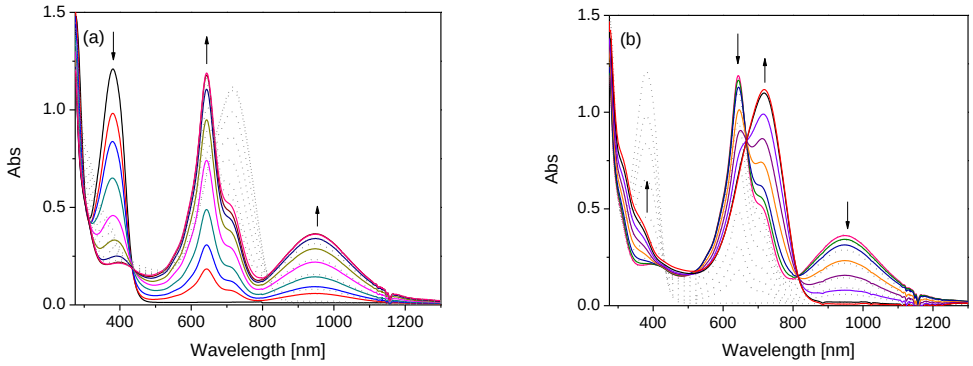

Figure 4.25: UV-Vis titration of TTFV **299a** (40 mM) with TFA in $CHCl_3$. (a) Addition of TFA from 0 to 16,000 molar equivalents. (b) Addition of TFA from 16,000 to 70,000 molar equivalents.

Note that in Figure 4.25A, the emerging bands at 643 nm and 950 nm are assigned to mono protonated species, $[TTFV+H]^+$. As the titration progresses, these two bands decrease and another absorption band grows at 719 nm, which is assigned to the deprotonated species, $[TTFV + 2H]^{2+}$.

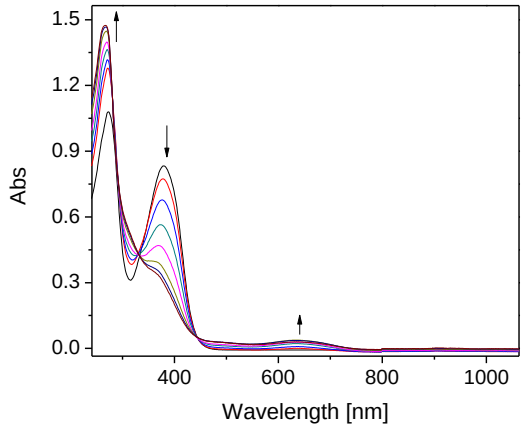

Figure 4.26: UV-Vis titration of TTFV **299a** (26 mM) with $Cu(OTf)_2$ in THF. Addition of $Cu(OTf)_2$ from 0 to 18.2 molar equivalents.

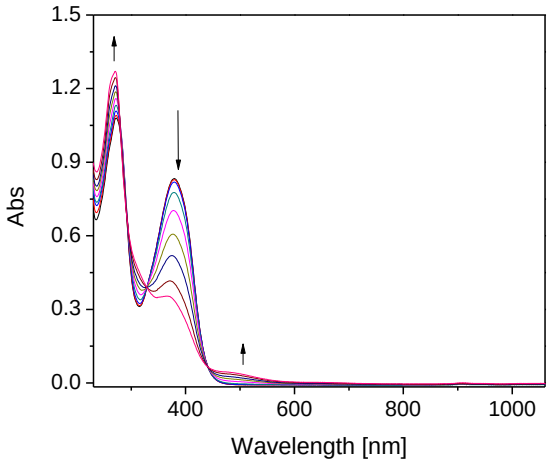

Figure 4.27: UV-Vis titration of TTFV **299a** (26 mM) with $Cd(ClO_4)_2$ in THF. Addition of $Cd(ClO_4)_2$ from 0 to 56.0 molar equivalents.

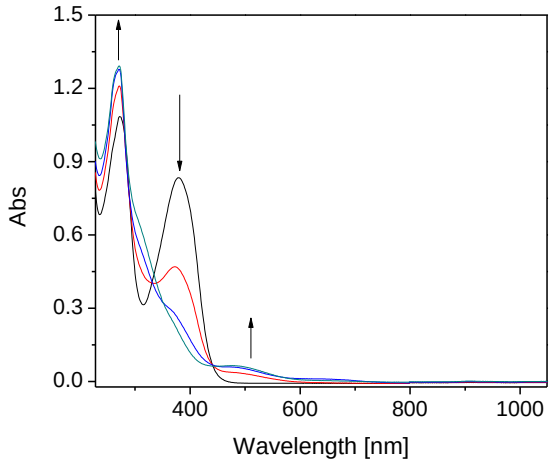

Figure 4.28: UV-Vis titration of TTFV **299a** (26 mM) with $Fe(ClO_4)_2$ in THF. Addition of $Fe(ClO_4)_2$ from 0 to 13.8 molar equivalents.

4.3.5.2 ^{1}H NMR studies on 293a

To shed more light on metal ion binding properties, ^{1}H NMR titration experiments were conducted between dianthryl-TTFV **293a** and select transition metal ions, Cu^{2+}, Cd^{2+}, and Ag^+ in THF-d_8. For the Cu^{2+} ion titration, pronounced line-broadening of all the NMR signals (Figure 4.29) and significant precipitation was observed. The results suggest strong interactions between Cu^{2+} and **293a** and a considerable degree of aggregation for the resulting complexes in THF-d_8. For the titration of Cd^{2+} and Ag^+ ions, the formation of precipitate was not as evident as in the Cu^{2+} titration. In general, the ^{1}H NMR spectral responses of **293a** to Cd^{2+} and Ag^+ ions are kind of similar.

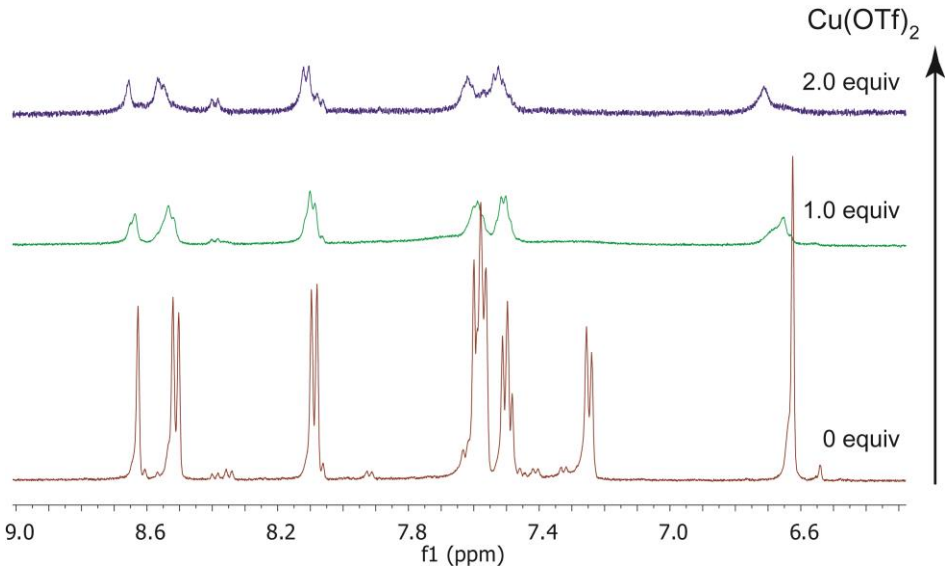

Figure 4.29: Partial ^{1}H NMR titration spectra of compound **293a** (7.4 mM) with $Cu(OTf)_2$ in THF-d_8 showing the aromatic region.

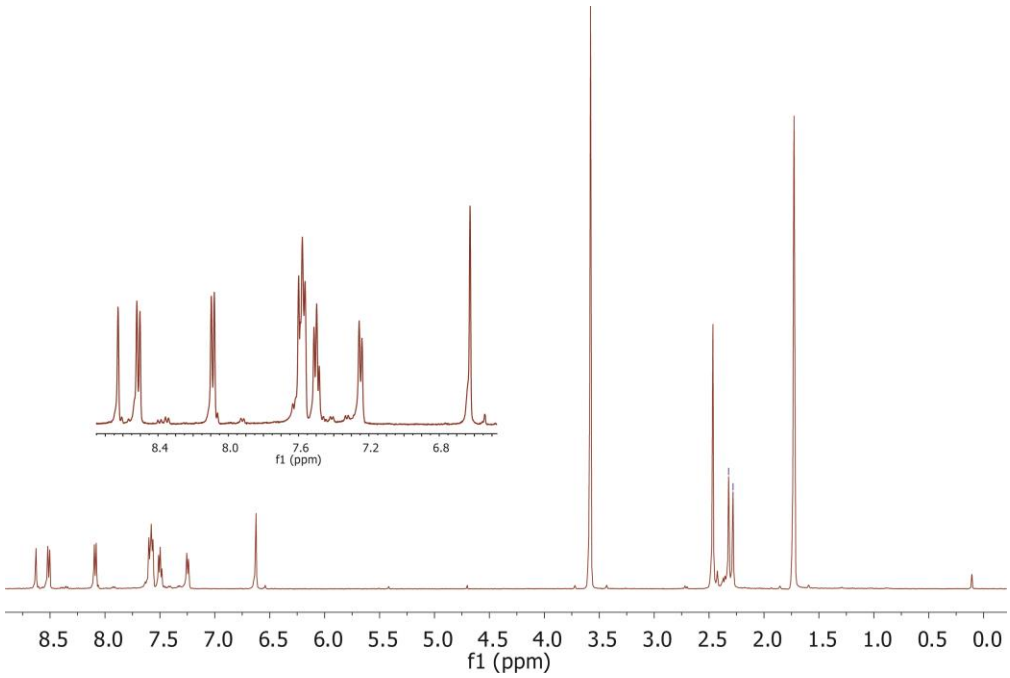

Figure 4.30: ^{1}H NMR (500 MHz, CD_3CN) spectrum of compound **293a** complexed with 2 mol equiv of $Cu(OTf)_2$.

Figure 4.31 illustrates the detailed ^{1}H NMR spectral variations in the aromatic region upon addition of Cd^{2+}ions. It can be clearly seen that most of the aromatic protons do not shift with increasing Cd^{2+} addition, except for the triazolyl proton (marked by * in the Figure 4.31) which shows a downfield shift from 7.60 to 7.73 ppm after *ca*. 7.0 molar equivalents of Cd^{2+} were added. It is also noted that the line-broadening of certain phenyl protons and the SMe protons appear to be far more pronounced than that of the other protons. This unusual phenomenon suggests that ligand exchange is rapid on the NMR time scale, when specific metals are bound to sensor **293a**.

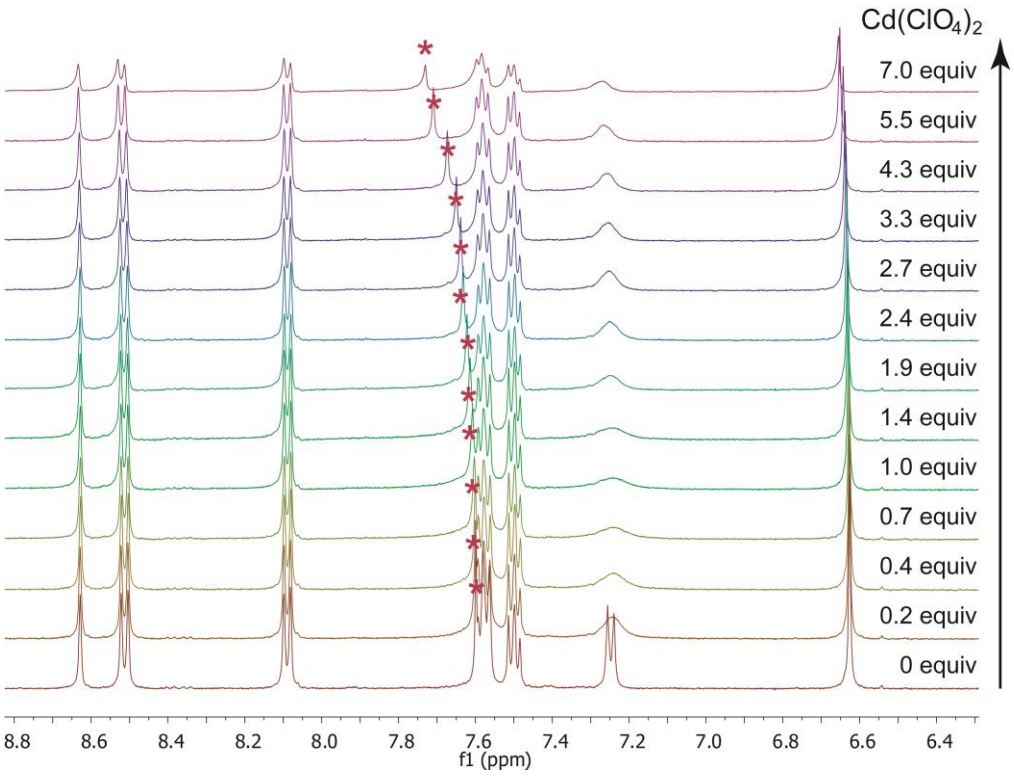

Figure 4.31: Partial ^{1}H NMR spectra of compound **293a** (7.4 mM) in titration with $Cd(ClO_4)_2$ in THF-d_8 showing the aromatic region. Signals labeled by * refers to the triazolyl proton.

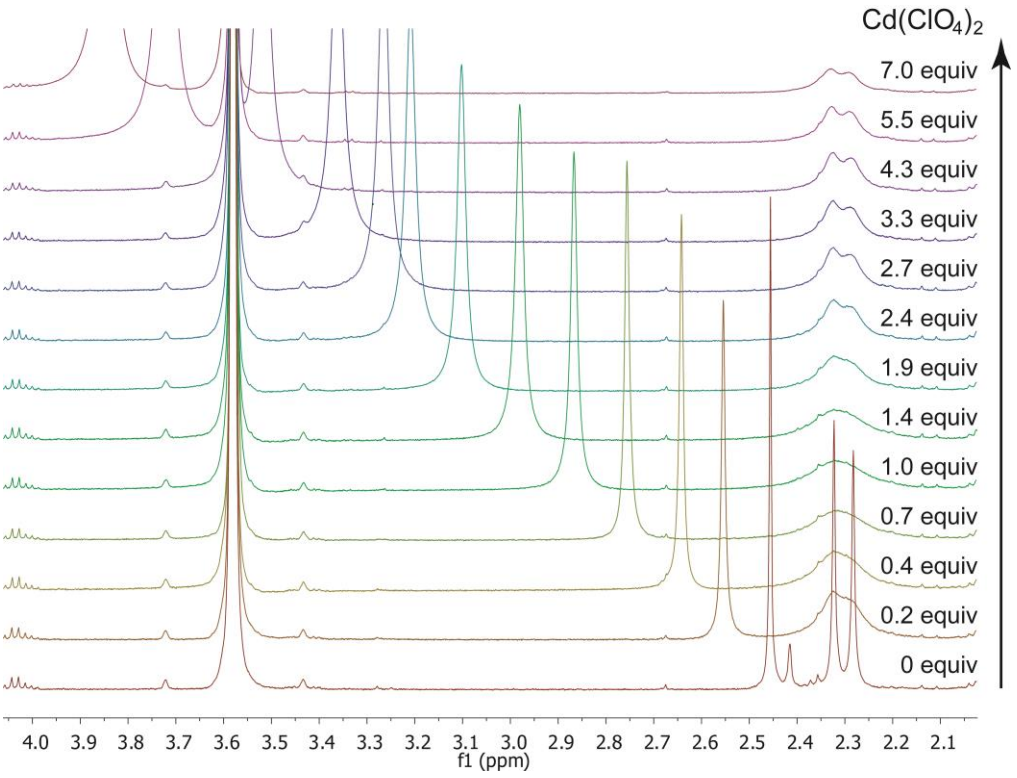

Figure 4.32: Partial ^{1}H NMR spectra of compound **293a** (7.4 mM) in titration with $Cd(ClO_4)_2$ in THF-d_8 showing the aliphatic region.

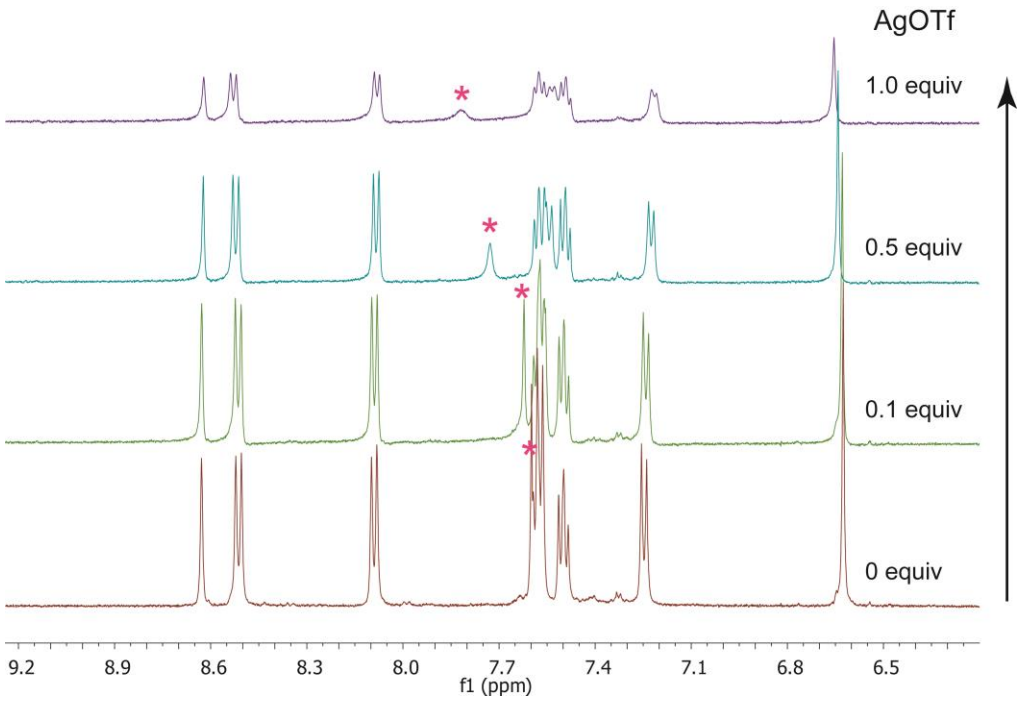

Figure 4.33: Partial ^{1}H NMR spectra of compound **293a** (7.4 mM) in titration with AgOTf in THF-d_8 showing the aromatic region. Signals labeled by * refers to the triazolyl proton.

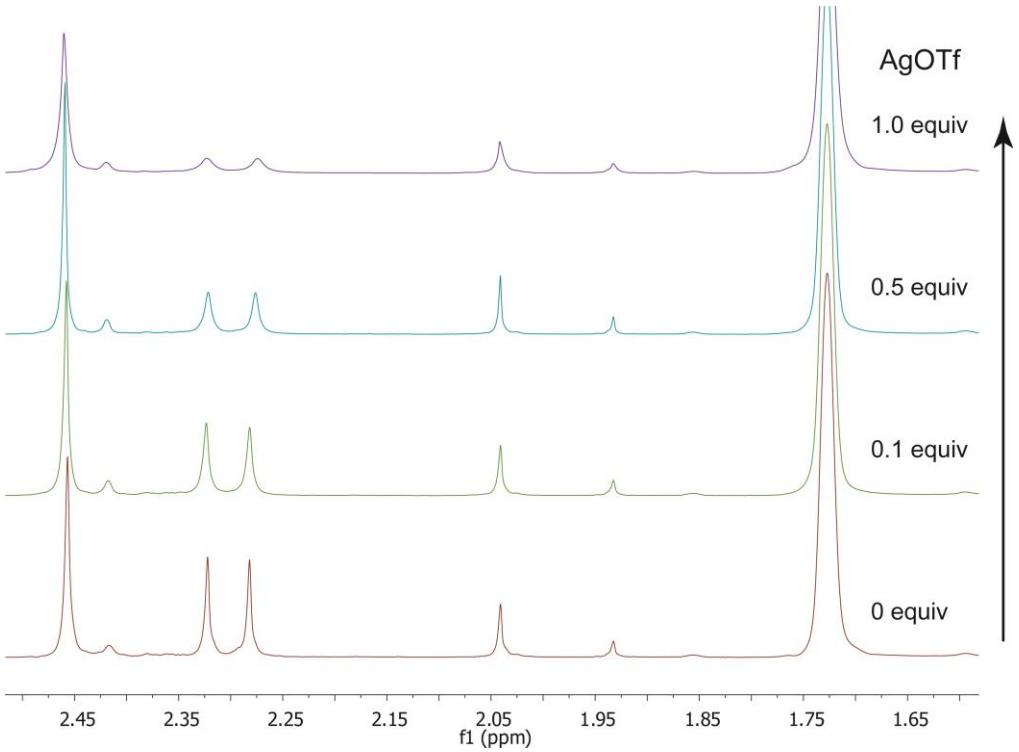

Figure 4.34: Partial ^{1}H NMR spectra of compound **293a** (7.4 mM) in titration with AgOTf in THF-d_8 showing the aliphatic region.

4.3.6 Binding properties of TTFV tweezers and macrocycles with fullerenes

The binding properties of TTFV tweezers **292**, **293**, **294** and macrocycles **296** and **297**with C_{60} and C_{70} fullerenes were investigated by UV-Vis and fluorescence titration experiments in chlorobenzene at room temperature. During the titration of TTFV – anthracene tweezers **293** with C_{60}, the low-energy absorption bands of **293** at 371 nm and 391 nm do not change, but the absorptions of pristine C_{60} at 335 nm and a weak tail beyond 450 nm are observed to grow steadily (Figure 4.35A). The emission intensity of **293** shows a very small degree of enhancement upon addition of C_{60} (Figure 4.35B). The titration results disclose that C_{60} binds rather weakly with tweezers **293**.

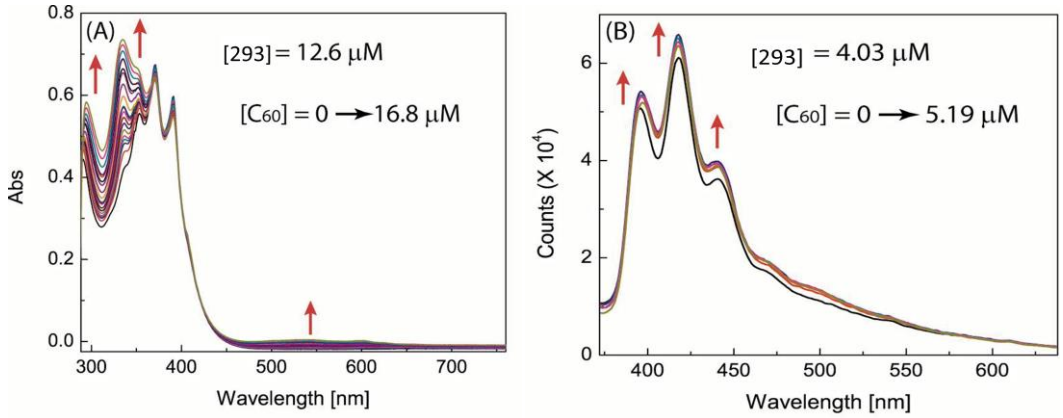

Figure 4.35: (A) UV-Vis spectral changes of **293** upon addition of C_{60} (B) Fluorescence spectral changes of **293** upon addition of C_{60} (λ_{ex}= 350 nm) in chlorobenzene.

The titration of **293** with C_{70}, however, shows markedly different outcomes. The UV-Vis spectral changes (Figure 4.36A) are complex and difficult to decipher, due to the overlap of the absorption bands of C_{70} with those of **293** in the range of *ca*. 350-450 nm.

The fluorescence bands of **293** show very significant enhancement in intensity during the titration of C_{70} without any shifts in emission wavelength. At the saturation point, the maximum emission peak at 418 nm is increased by 1.7 times (Figure 4.36B). Clearly, tweezers **293** can effectively bind with C_{70} in the solution phase.

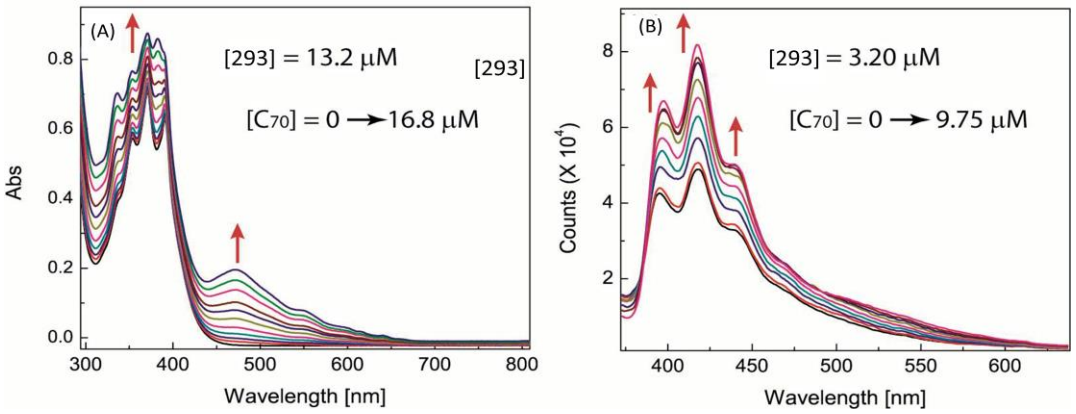

Figure 4.36: (A) UV-Vis spectral changes of **293** upon addition of C_{70} (B) Fluorescence spectral changes of **293** upon addition of C_{70} (λ_{ex}= 350 nm) in chlorobenzene.

For the titration of the TTFV-anthracene macrocycle **297** with C_{60}, the UV-Vis spectra show two distinct stages of changes. As shown in Figure 4.37A, during the addition of up to *ca*. 1 molar equivalent of C_{60} to the solution of **297**, a peak at 339 nm grows continuously, while other three absorption peaks at 360 nm, 368 nm, and 399 nm decrease in intensity slightly. An isosbestic point is observed at 357 nm in this process. During the addition of *ca*. 1 to 2 equivalents of C_{60} to **297**, the absorption bands decrease monotonously together with an increasing low-energy absorption tail from *ca*. 450 nm to 700 nm (Figure 4.37B). The UV-Vis titration data clearly indicate two distinct steps of complexation, likely due to the formation of 1:1 and 1:2 complexes between macrocycle

297 and C_{60}. Macrocycle **297** showed fluorescence turn-on responses to both C_{60} andC_{70} (Figure 4.37C and E).

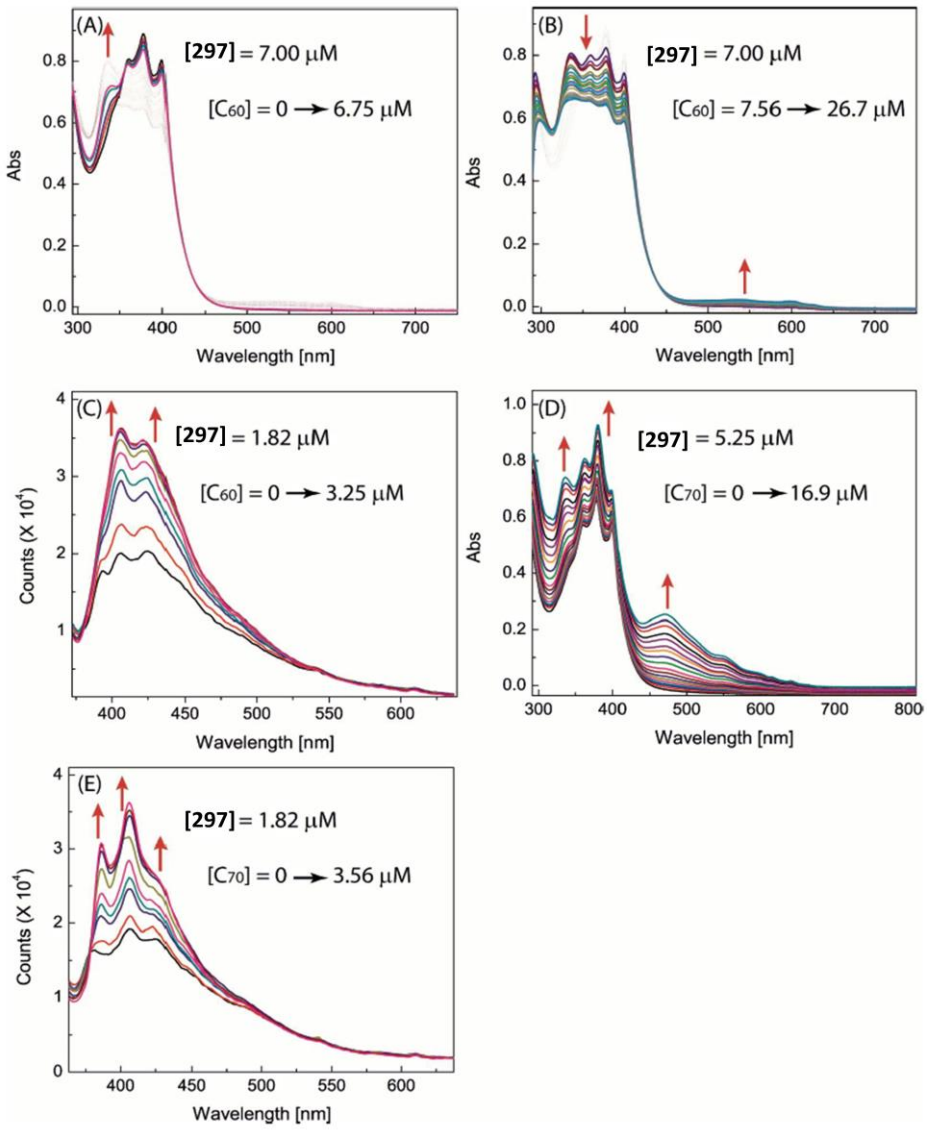

Figure 4.37: (A) UV-Vis spectral changes of **297** upon addition of up to ca. 1 equiv of C_{60}. (B) UV-Vis spectral changes of **297**upon addition of ca. 1-2 equiv of C_{60}. (C) Fluorescence spectral changes of **297** upon addition of C_{60} (λ_{ex}= 350 nm). (D) UV-Vis

spectral changes of **297** upon addition of C_{70}. (E) Fluorescence spectral changes of **297** upon addition of C_{70} (λ_{ex} = 340 nm) in chlorobenzene.

The TTFV-pyrene tweezer **294** showed prominent fluorescence turn-on responses to both C_{60} and C_{70} (Figure 4.38B to D) than other TTFV tweezers and macrocycles. In particular, **294** gave a 11.4-fold enhancement at the endpoint of a titration with C_{60} and a 4.4-fold enhancement with C_{70} fullerene. TTFV-naphthalene tweezers **292** and TTFV-benzene macrocycle **296** did not show any significant fluorescence and UV-Vis absorption changes upon titration of fullerenes (Figures 4.49 and 4.40), likely due to their arene units (*i.e.*, naphthalene and benzene) being very poor fluorophores.

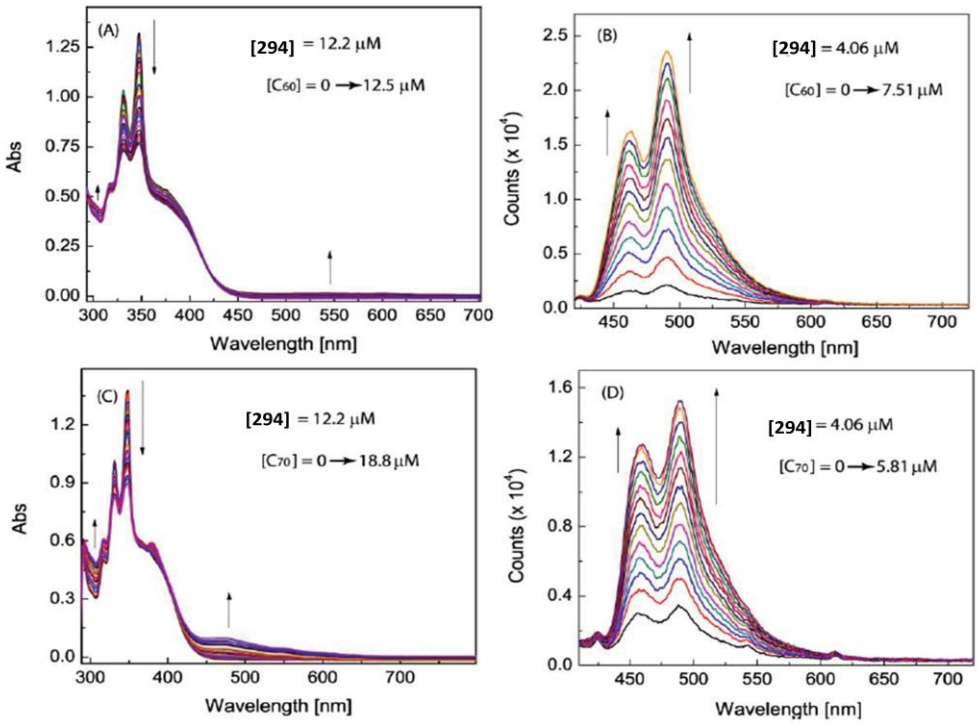

Figure 4.38: (A) UV-Vis spectral changes of **294** upon addition of C_{60} (B) Fluorescence spectral changes of **294** upon addition of C_{60} (λ_{ex}= 350 nm) (C) UV-Vis spectral changes of **294** upon addition of C_{70}(D) Fluorescence spectral changes of **294** upon addition of C_{70} (λ_{ex} = 350 nm) in chlorobenzene.

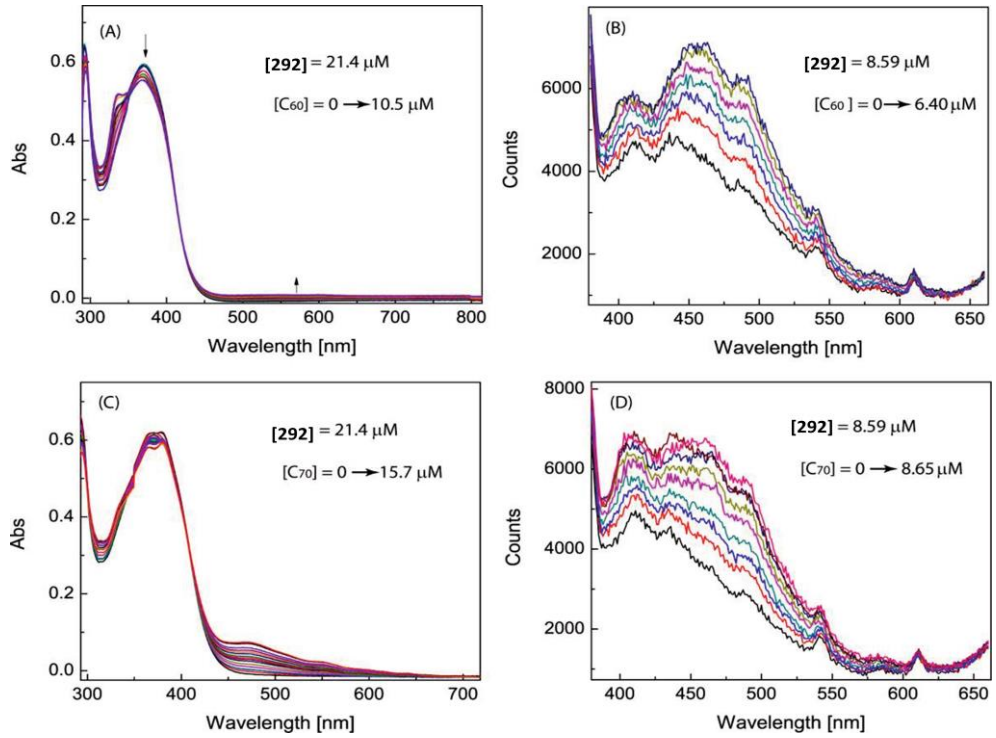

Figure 4.39: (A) UV-Vis spectral changes of **292** upon addition of C_{60} (B) Fluorescence spectral changes of **292** upon addition of C_{60} (λ_{ex}= 350 nm) (C) UV-Vis spectral changes of **292** upon addition of C_{70} (D) Fluorescence spectral changes of **292** upon addition of C_{70} (λ_{ex} = 350 nm) in chlorobenzene.

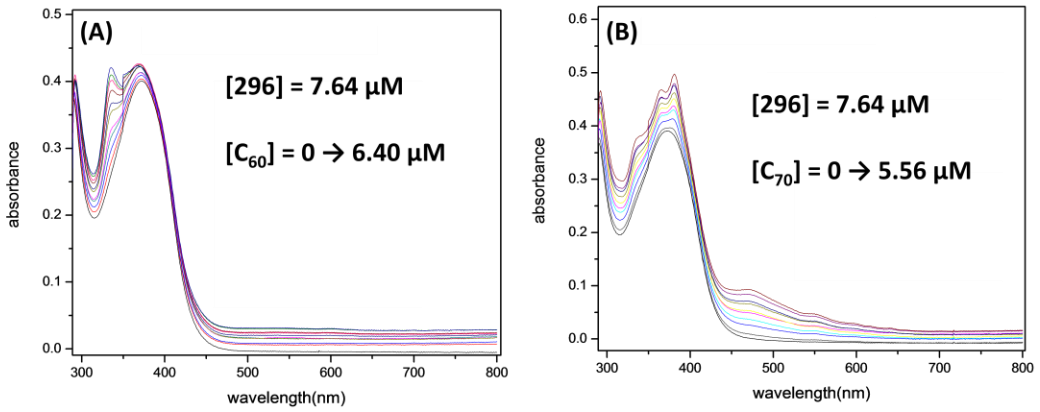

Figure 4.40: UV-Vis spectral changes of **292** upon addition of (A) C_{60} (B) C_{70} in chlorobenzene.

4.3.6.1 Photoinduced electron transfer (PET) mechanism

The origin of fluorescence turn-on with TTFV-tweezers and macrocycles can be explained by a photoinduced electron transfer (PET) mechanism. As mentioned in the previously, these TTFV tweezers (**293** and **294**) and macrocycle **297** show moderate to weak fluorescence, as a result of the quenching effect by the central electron-donating TTFV unit via a PET mechanism (Figure 4.41). Upon addition of C_{60} or C_{70} fullerene, the fluorescence turn-on properties are likely originated from the interactions of electron-accepting fullerenes with the electron-donating TTFV moiety in the excited state, which attenuates non-radiative decay pathways including the PET mechanism. The direct contact between C_{60} or C_{70} fullerene and the TTFV unit is believed to induce facile PET from TTFV to fullerenes, which gives rise to appreciable fluorescence enhancement in the titration experiments.

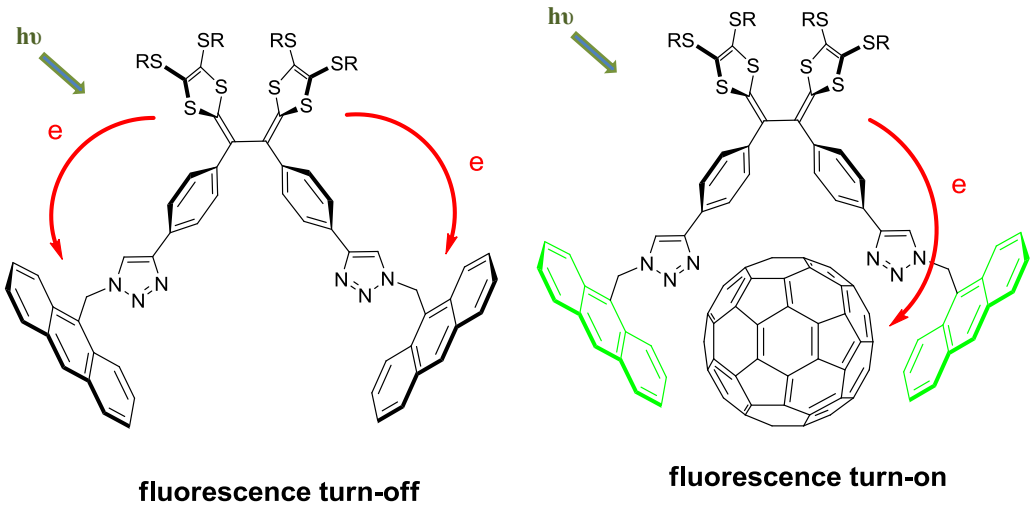

Figure 4.41: Proposed PET mechanism for fluorescence turn-on sensing of C_{60} fullerene.

4.3.6.2. Binding analysis and modeling studies

Subjecting the titration data to global spectral analysis using the *SPECFIT* software allows the determination of binding stoichiometry and binding constants (listed in Table 4.2). Meaningful spectral fitting could not be attained from the UV-Vis titration results due to the complex spectral overlap of various colorful species. The fluorescence data, however, allowed good spectral fitting to be achieved to quantitatively elucidate the binding properties. The data form binding analysis evidences that all tweezers show 1:1 complex and macrocycles give 1:2 complex in binding to fullerenes.

Table 4.2: Binding constants for TTFV tweezers and macrocycles with fullerenes obtained from global spectral analysis of the fluorescence spectral titration data

host	guest	complexation ratio (H/G)	$\log\beta_{11}$ (M^{-1})	$\log\beta_{12}$ (M^{-2})
293	C_{60}	---	---	---
293	C_{70}	1:1	4.90 ± 0.05	---
294	C_{60}	1:1	4.87 ± 0.04	---
294	C_{70}	1:1	4.72 ± 0.03	---
297	C_{60}	1:2	---	11.10 ± 0.06
297	C_{70}	1:2	---	10.11 ± 0.11

According to the binding constant analysis, tweezers **293** appears to be highly selective in binding with C_{70} over C_{60}. A Molecular modeling study has cast light on the origin of the very different binding affinities. Figure 4.42B shows the optimized structure for the 1:1 complex of **293** and C_{60}, where intimate π-π contacts take place only between C_{60} and the two anthracene units. The spherical shape of C_{60} does not allow the central TTFV moiety to be involved in the π-interactions with C_{60}. The lack of contact between C_{60} and TTFV donor thus accounts for the very weak binding as well as insignificant fluorescence changes in the titration results. The 1:1 complexation of **293** with C_{70}, on the contrary, shows a very close contact between one of the dithiole rings of the TTFV unit

and C_{70}, in addition to the C_{70} and anthracene interactions (Figure 4.42C). Apparently, the ellipsoidal shape of C_{70} makes it fit better in the π-cavity created by the dianthryl-TTFV framework of tweezers **293**, rendering it a highly selective receptor for C_{70} over C_{60}.

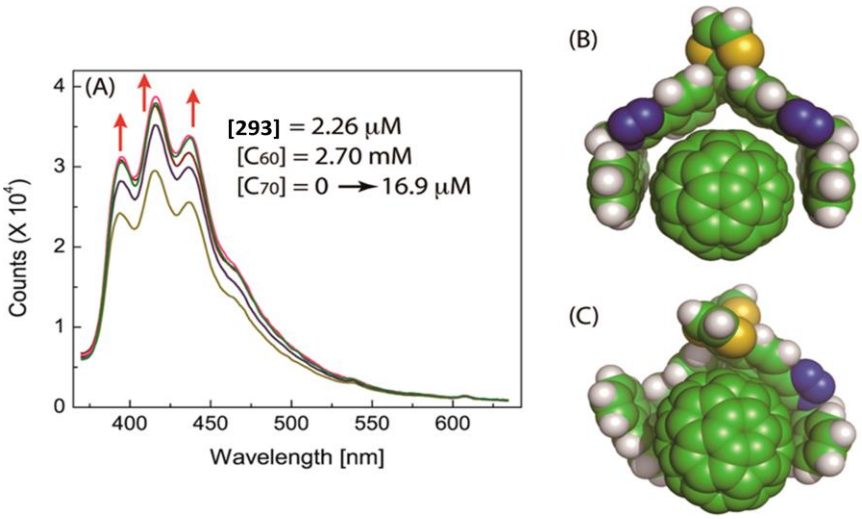

Figure 4.42: (A) Fluorescence spectral changes of **293** upon addition of C_{70} in the presence of a large excess of C_{60} (λ_{ex} = 350 nm). CPK models of optimized molecular structures for the complexes of (B) **293** with C_{60}, and (C) **293** with C_{70}.

To further test the performance of **293** as a selective C_{70} sensor, a fluorescence titration of a solution of **293** with C_{70} in the presence of a large excess of C_{60} (>1000 molar equivalents) was conducted and the results are shown in Figure 4.42A. To our satisfaction, significant the fluorescence turn-on sensing property for C_{70} is still retained under these conditions, attesting to the extraordinary efficacy of tweezers **293**in discriminating a trace amount of C_{70} in a large excess of C_{60}.

However, the interactions of macrocycle **297** with C_{60} or C_{70} follow the 1:2 binding ratio as disclosed by global spectral analysis (Table 4.2). The optimized structures of macrocycle **297** binding with C_{60} and C_{70} respectively in 1:1 and 1:2 ratios are shown in Figure 4.43C and D. Compared with tweezers **293**, the structure of macrocycle **297** is much more rigid and pre-organized in a cup-like shape. As a result, the binding of **297** with C_{60} and C_{70} invariably involves the π-interactions with the dithiole rings of the TTFVs. In contrast to dianthryl-TTFV **293**, the relatively larger π-surface of the dipyrenyl groups in **294** gives rise to more intimate π-π contact with C_{60} and C_{70} fullerenes (Figure 4.43A and B), resulting in strong binding strength but without particular selectivity.

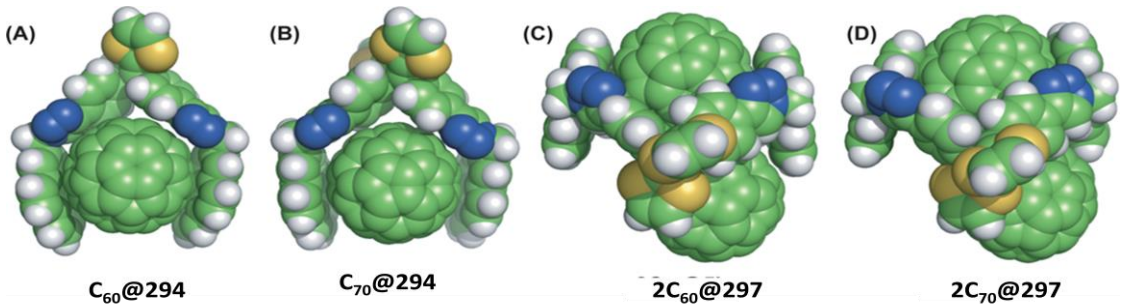

Figure 4.43: CPK models of optimized molecular structures for the complexes of (A) C_{60}@**294**, (B) C_{70}@**294**, (C) $2C_{60}$@**297**, and (D) $2C_{70}$@**297**.

4.3.6.3 Releasing experiments

Finally, the controllability over reversible interactions of fullerenes with TTFV-anthracene receptors was investigated. As mentioned, the TTFV moiety is known to undergo reversible protonation/deprotonation processes, which have been recently

applied by our group to achieve reversible wrapping and release of single-walled carbon nanotubes using a TTFV-phenylacetylene polymer.[74] To demonstrate this feature, UV-Vis titration of the complexes of macrocycle **297** and C_{60} with trifluoroacetic acid (TFA) was undertaken, where the signature absorption bands of C_{60} at 334 nm and TTFV cations at 646 nm were specifically monitored. Figure 4.44A shows the plot of the absorption intensity of 297 at 334 nm as a function of increasing [C_{60}]. The absorption changes here show a bell-shaped trend with a maximum appearing at the point where approximately one equivalent of C_{60} is added. The two distinct stages of absorbance changes can be ascribed to the stepwise formation of 1:1 and 1:2 complexes. Figure 4.44B shows the absorbance changes of **297**/C_{60} complexes at 334 nm as a function of increasing [TFA]. The plot gives an inverted bell-shaped trend with the minimum coinciding with the midpoint of titration. The titration of **297** with TFA exhibits only a decreasing trend for the absorbance at 334 nm (Figure 4.44C), while monitoring the absorbance at 646 nm reveals a continuous increase of TTFV cations (Figure 4.44D). The titration analysis here offers clear evidence for the dissociation of **297**/C_{60} complexes with increasing acidity in solution.

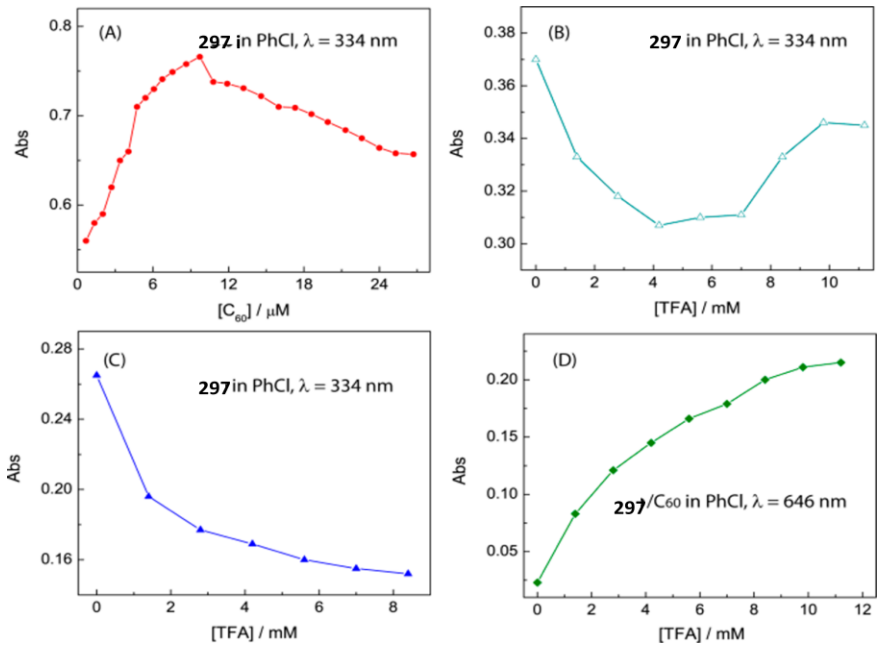

Figure 4.44: (A) Absorbance of **297** (7.0 μM) at 334 nm as a function of [C_{60}]. (B) Absorbance of **297** (6.1 μM) and C_{60} (30.3 μM) at334 nm as a function of [TFA]. (C) Absorbance of **297** (4.3 μM) at 334nm as a function of [TFA]. (D) Absorbance of **297** (6.1 μM) and C_{60} (30.3 μM) at 646 nm as a function of [TFA]. All titrations were done in chlorobenzene at rt.

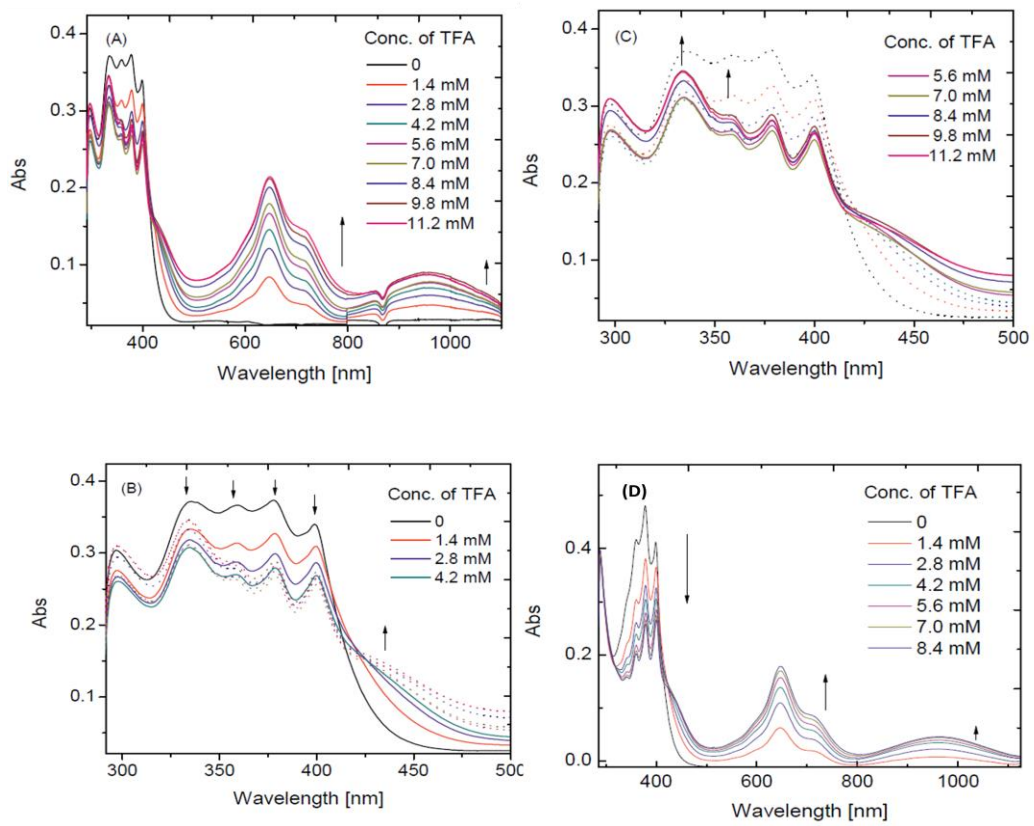

Figure 4.45: (A) UV-Vis spectral changes of macrocycle **297**(6.1 μM) and C_{60} (30.3 μM) in chlorobenzene as a function of [TFA] at room temperature. (B) Expansion of UV-Vis spectra showing the titration of TFA from 0 to 4.2 mM. (C) Expansion of UV-Vis spectra showing the titration of TFA from 5.6 to 11.2 mM. (D) UV-Vis spectral changes of macrocycle **297** (4.3 μM) in chlorobenzene as a function of [TFA] at room temperature.

4.3.7 Electrochemical properties of TTFV tweezers 295 with saccharides

The electrochemical saccharide sensing function of boronic acid-appended TTFV tweezers **295** was investigated by electrochemical titrations. In the experiments, the tweezers **295** was dissolved in a mixture of DMSO and aqueous phosphate buffer

solution, wherein the pH value was kept at 7.41. The prepared solution of **295** was then subjected to titrations with four different monosaccharides (i.e., fructose, ribose, galactose, and glucose) respectively. The titration processes were monitored by differential pulse voltammetry (DPV), and the results are shown in Figure 4.46.

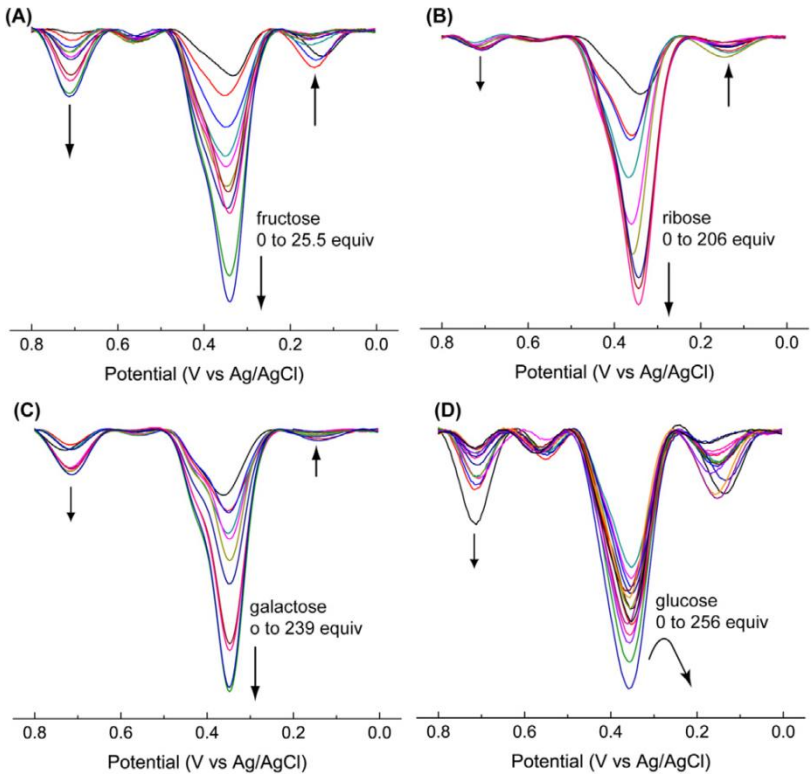

Figure 4.46: Differential pulse voltammetric (DPV) titrations of sensor **295** (2.06 mM) with (A) fructose, (B) ribose, (C) galactose, and (D) glucose. Experimental conditions: solvent: DMSO/phosphate buffer (1:2, v/v); working electrode: glassy carbon; counter electrode: Pt wire; reference electrode: Ag/AgCl, NaCl (3 M); scan rate: 20 mV/s; pulse width: 50 mV; pulse period: 200 ms; step: 4 mV. The baselines of the voltammograms were corrected.

As shown in Figure 4.46, the DPV profile of compound **295** in the DMSO/buffer solvent showed two noticeable oxidation peaks at *ca*.+0.34 and +0.14 V. Upon titration with fructose (Figure 4.46A), the peak at +0.34 increased steadily in intensity with increasing fructose concentration, whereas the change of the peak at +0.14 V showed a decreasing trend. In the meantime, a new oxidation peak at ca.+0.73 V began to grow with the progress of titration. For the most significant peak at +0.34 V, its oxidation potential was found to change in two stages. In the early stage of the titration, up to addition of 3 molar equiv of fructose, the peak shifted slightly to the positive direction, while in the later stage the potential shifted back to the negative direction and saturated after about 17 M equiv of fructose were added. The correlation of changes in peak current and peak potential with the concentration of fructose is presented in Figure 4.47A. From the trends showing there, it is reasonable to assume that the binding of fructose with sensor **295** undergo two distinct stages, most likely due to stepwise formation of 1:1 and 2:1 complexes given that compound **295** bears two phenylboronic acid groups for binding with saccharides.

The titration of sensor **295** with ribose showed a similar trend to that of fructose titration, but took much more titrant (more than 200 molar equiv) to reach saturation (Figure 4.46B). The results indicate that sensor **295** binds to fructose and ribose by the same mechanism; however, the binding strength of **295** with fructose is much stronger than with ribose.

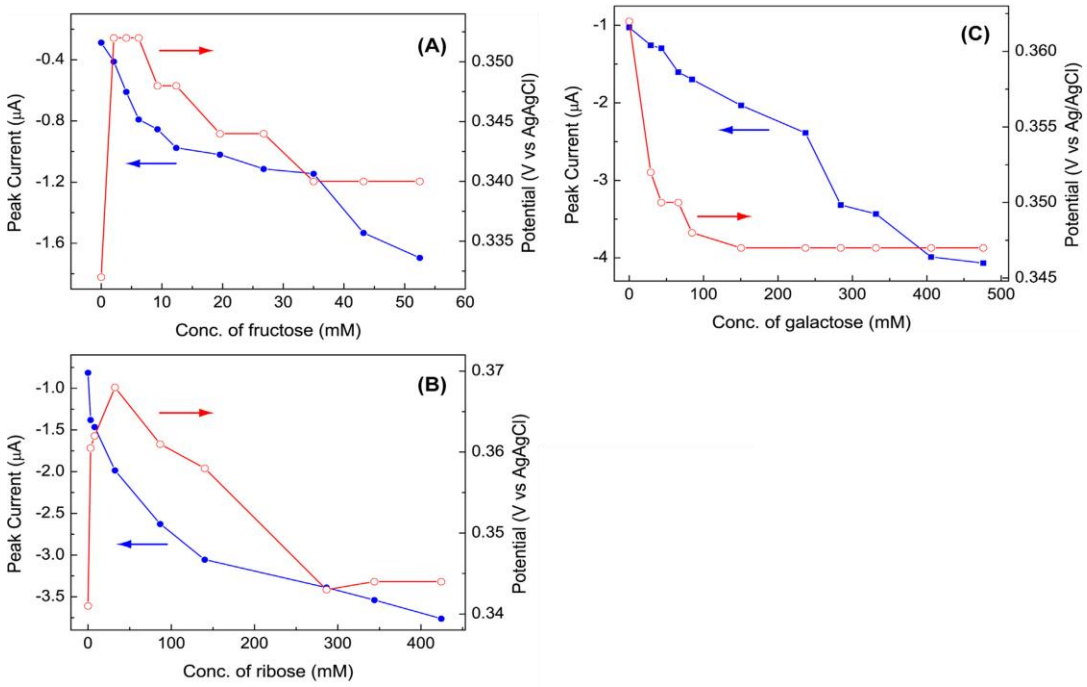

Figure 4.47: Correlations of current intensity (blue traces) and potential (red traces) for the peak at ca.+0.34 V in the DPV titrations of sensor **295** (2.06 mM) with concentration of saccharides.

The titration of sensor **295** with galactose also gave characteristic changes in its DPV profiles, wherein the peak current at ca.+0.34 V significantly increased in intensity with titration (Figure 4.46C). The change in peak potential however showed only a monotonous decreasing trend and became saturated when about 115 molar equiv of galactose were added. The correlation diagram in Figure 4.47 C suggests that the binding of galactose with sensor **295** occurs via a mechanism different from that for fructose and ribose binding. A reasonable rationalization is that compound **295** directly forms a 1:2 complex with galactose during the titration. The voltammetric responses of **295** in the

titration of glucose are shown in Figure 4.46D. Unlike the previous three saccharides, the changes in oxidation peak potential and current appear to be kind of random and lack a clear trend. An explanation for this voltammetric behavior can be made by assuming that sensor **295** does not bind significantly to glucose.

4.3.8 Electrochemical properties of TTFV tweezer 316 with fluoride ions

Apart from the saccharide sensing properties of **295**, we further investigated the electrochemical responses of TTFV-boronate **316** to the fluoride anion and other halides in an organic solvent, THF. The DPV profile of **316** showed an oxidation peak at +0.65 V(Figure 4.48A), which is consistent with the quasi-reversible redox wave pair (E_{pa} = +0.95 V, E_{pc} = +0.51 V) observed in its cyclic voltammetric(CV) diagram (Figure 4.48C). Upon addition of tetrabutylammonium fluoride (TBAF) from 0 to 1.0 M equiv, the oxidation peak in DPV was observed to decrease steadily in intensity and shifted in the negative voltage direction. In the CV profiles, the cathodic peak made a significant shift from +0.90 to +0.76 V, while the anodic peak remained nearly unchanged. The peak currents were observed to reduce considerably as the titration progressed.

When more than 1.0 molar equiv of TBAF was added to the solution of TTFV-boronate **316**, both the DPV and CV profiles showed very different patterns of changes compared with the results of titration with less than 1.0 equiv of TBAF. In the DPV, the oxidation peak at +0.76 V continuously decreased but without significant potential shift. In the meantime, two new peaks at +0.38 and +0.94 V emerged. In the CV data, the cathodic peak at +0.76 V diminished and two new cathodic peaks at +0.49 and +1.00 V

grew steadily. The anodic peak at +0.51 V gradually disappeared as the titration continued. Overall, in the process of titration of **316** with TBAF from1.2 to 2.0 equiv, the CV characteristics changed from a quasi-reversible to an irreversible pattern.

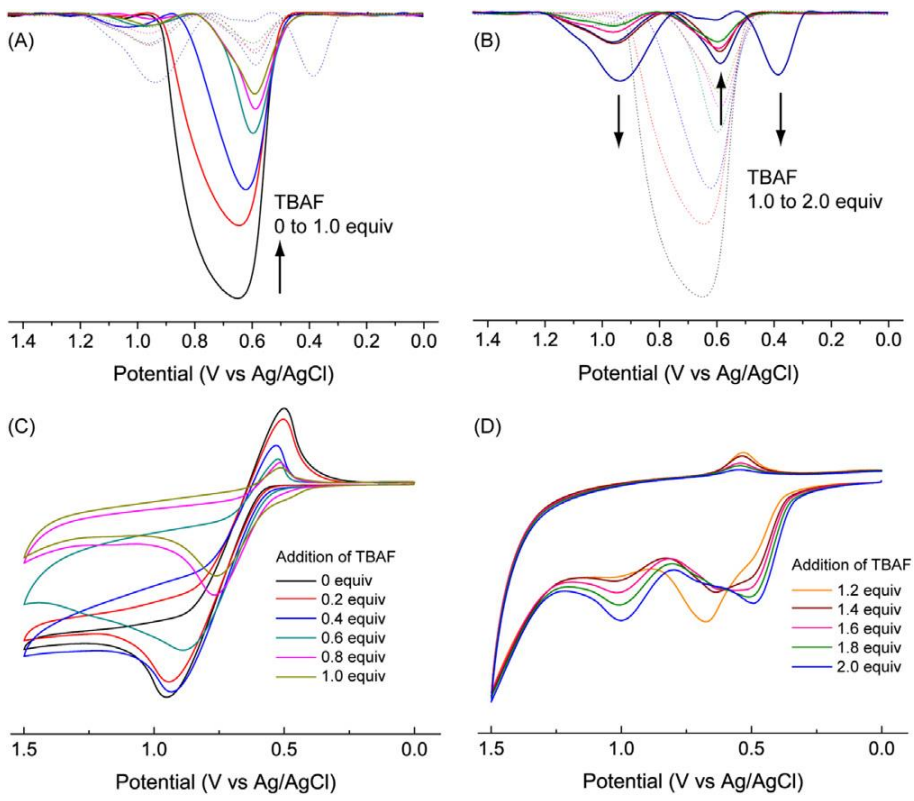

Figure 4.48: Differential pulse voltammetric (DPV) changes of TTFV-boronate **316** (2.35 mM) upon addition of TBAF (A) from 0 to 1.0 molar equiv, (B) from 1.2 to2.0 molar equiv. Experimental conditions: solvent: THF; electrolyte: Bu_4NBF_4(0.1 M); working electrode: glassy carbon; counter electrode: Pt wire; reference electrode: Ag/AgCl, NaCl (3 M); scan rate: 20 mV/s; pulse width: 50 mV; pulse period: 200 ms; step: 4 mV. The baselines of the voltammograms were corrected. Cyclic voltammetric

titration of **316** with TBAF (C) from 0 to 1.0 molar equivalent, (D) from 1.2 to 2.0 molar equiv. Scan rate: 50 mV/s.

The distinct two stages of changes in electrochemical properties observed in DPV and CV titrations suggest that the binding of TTFV-boronate **316** with the fluoride anion undergoes a mechanism in which 1:1 and 1:2 complexes are formed sequentially (Scheme 4.48). When the fluoride anion is added to one of the boronate groups, the resulting electron-rich fluoroborate anion would make the central TTFV moiety have a lowered oxidation potential, which is in agreement with the observations in the DPV and CV measurements. When the two boronate groups of **316** are both bound to the fluoride anion, the two anionic fluoroborate endgroups are therefore expected to engender significant electrostatic repulsive forces. If such is the case, the conformation of the TTFV moiety should be greatly changed, very likely to a shape more close to a *trans* conformation. Previous studies done by us and others have shown that TTFV in a trans conformation would exhibit a stepwise two electron release upon electrochemical oxidation,[77,78] which can reasonably explain the unique electrochemical behavior of the 1:2 complex of **316** and the fluoride ion. Electrochemical response of sensor **316** with other halide ions (Cl^-, Br^-, and I^-) is presented in the Appendix.

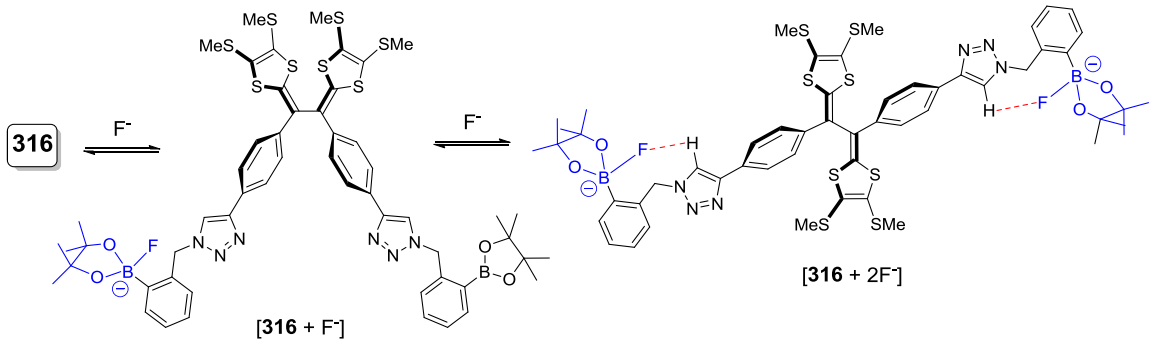

Scheme 4.8: Stepwise binding of compound **316** with the fluoride anion.

4.3.8.1 ^{1}H NMR studies on sensor 316

To further understand the binding properties of boronate **316** with the fluoride ion, ^{1}H NMR titration experiments were conducted. Figure 4.49 shows the changes of proton signals in the aromatic region with increasing titration of TBAF in CD_2Cl_2. As can be seen, when less than 2 molar equiv of the fluoride ion were added, the ^{1}HNMR signals of boronate **316** exhibited broadened line shapes as the titration carried on. In this stage, the binding of **316** with the fluoride ion should predominantly result in the formation a 1:1 complex, in which the fluoride ion possibly undergoes rapid exchange between the two boron binding sites.

When more than two equiv of the fluoride ion were added, the ^{1}H NMR signals gradually changed back to sharp and well-resolved features. In addition, the signal due to the two chemically equivalent triazolyl protons was observed to give a considerable downfield shift (labeled by asterisks in Figure 4.49). This observation can be rationalized by the hydrogen bonding interaction between the triazolyl protons and fluoride ions when

a stable 1:2 complex is formed as proposed in Scheme 4.8. Clearly, the triazole group plays an important role in assisting the binding of the fluoride ion with the boron center.

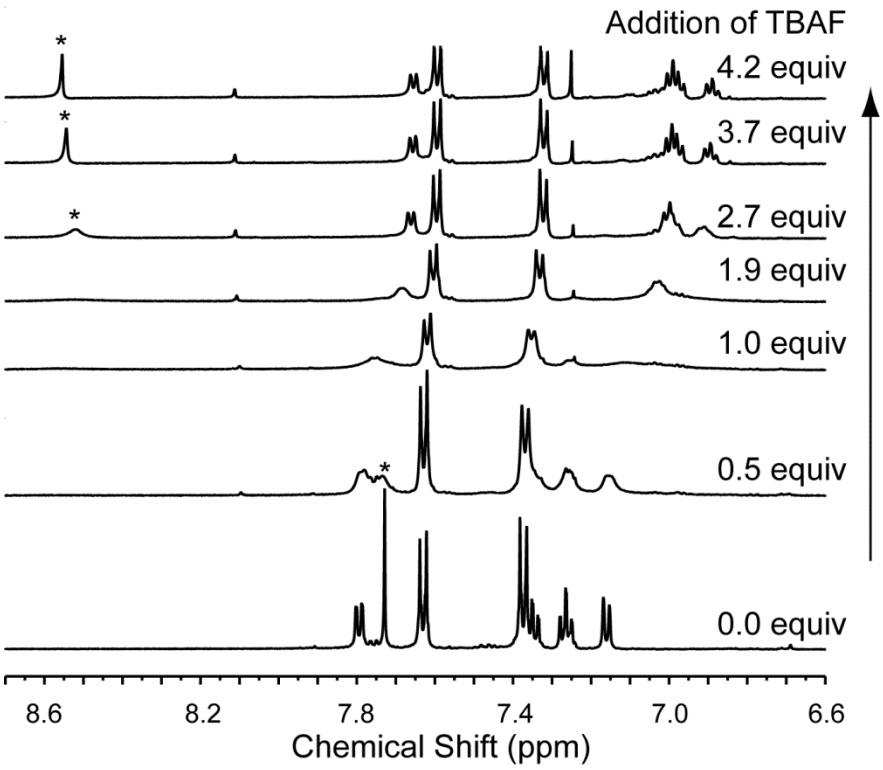

Figure 4.49: ^{1}H NMR (500 MHz) titration of boronate **316** (3.86 mM) with TBAF in CD_2Cl_2 at room temperature. Signals corresponding to the triazolyl protons are indicated by asterisks (*).

4.4 Conclusions

In this chapter, we have once again demonstrated the power of the click reaction to generate a series of TTFV based molecular tweezers and macrocycles. Electronic, spectroscopic and electrochemical properties of the all tweezers and macrocycles were investigated by cyclic voltammetry (CV), UV-Vis absorption and fluorescence spectroscopic characterizations. The dianthryl–TTFV **293a** exhibits fluorescence turn-on sensing function towards $Cu^{2+,}$ Fe^{2+}, and Cd^{2+}ions at μM concentrations in THF with excellent sensitivity, while at mM concentrations in acetonitrile it allows for colorimetric detection of these three metal ions. The investigation on metal-ion binding properties has shown that triazole linkers in compound **293a** serve as effective ligands (receptors) to coordinate with metal ions. To the best of our knowledge, compound **293a** is the first example of TTFV-based "click sensors", and we believe it can be a useful design motif for the development of fluorophore-based molecular sensory and optoelectronic devices.

We have also designed and synthesized a new class of supramolecular hosts for fullerenes with tweezer-like (**293**, and **294**) and macrocyclic architectures (**297**). The molecular tweezer **293** can selectively bind to C_{70} fullerene and give fluorescence turn-on sensing function toward C_{70} in the presence of excessive C_{60}, while the macrocycle exhibits a very large binding affinity for C_{60} and C_{70} fullerenes with 1:1 and 1:2 host/fullerene complexation ratios. Moreover, these receptors not only show unique fluorescence turn-on sensing properties for fullerenes, but have the capability of reversibly interacting with fullerenes under the simple control of acidity.

Finally, we have designed and synthesized a new type of tweezer-like TTFV derivatives carrying phenylboronate and phenylboronic acid endgroups using same synthetic strategy. The TTFV-boronic acid derivative **295** was found to show selective electrochemical responses to different saccharides, while the TTFV-boronate derivative **316** exhibited characteristic electrochemical responses to the fluoride anion. The findings indicate that more efficient electrochemical probes for saccharides and halide anions by fine-tuning analogous molecular structures.

4.5 Experimental

Chemicals were purchased from commercial suppliers and used directly without purification. All reactions were conducted in standard, dry glassware and under an inert atmosphere of nitrogen unless otherwise noted. Evaporation and concentration were carried out with a water-aspirator. Flash column chromatography was performed with 240-400 mesh silica gel, and thin-layer chromatography (TLC) was carried out with silica gel F254 covered on plastic sheets and visualized by UV light. Melting points (m.p.) were measured using an SRS OptiMelt melting point apparatus and are uncorrected. ^{1}H and ^{13}C NMR spectra were measured on a Bruker Avance 500 MHz spectrometer and a Bruker Avance III 300 MHz multinuclear spectrometer. Chemical shifts (δ) are reported in ppm downfield from the signal of the internal reference $SiMe_4$ for ^{1}H and ^{13}C NMR spectra. Coupling constants (*J*) are given in Hz. Infrared spectra (IR) were recorded on a Bruker tensor 27 spectrometer. Cyclic voltammetric (CV) experiments were carried out in a standard three-electrode setup controlled by a BASi Epsilon workstation. UV-Vis-NIR absorption spectra were measured on a Cary 6000i spectrophotometer. Emission spectra were measured on a Photon Technology International (PTI) Quantamaster 6000 spectrofluorometer equipped with a continuous xenon arc lamp as the excitation source. MALDI-TOF MS analyses were performed on an Applied Biosystems Voyager instrument using dithranol as the matrix.

Acetylenic DTF (298)

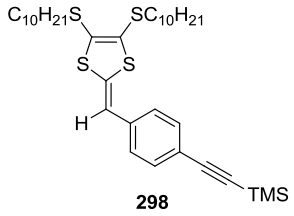

298

A solution of thione **270** (1.05g, 2.19 mmol) and 4-(trimethylsilylethynyl)benzaldehyde **271** (0.443g, 2.19 mmol) in trimethylphosphite (15 mL) was stirred and heated to 130^{o}C for about 3 h under a N_2 atmosphere. After the reaction was complete as checked by TLC analysis, the excess trimethylphosphite was removed by vacuum distillation. The resulting crude product was purified by silica flash column chromatography (EtOAc/hexanes, 1:9) to yield pure compound **298** (0.999 g, 1.57 mmol, 72%) as reddish brown syrup. IR (neat): 2957, 2923, 2852, 2155, 1567, 1542, 1464, 1249 cm^{-1}; ^{1}HNMR (500 MHz, CD_2Cl_2): δ 7.42 (d, *J* = 8.4 Hz, 2H), 7.16 (d, *J* = 8.3 Hz, 2H), 6.45 (s,1H), 2.83 (t, *J* = 7.3 Hz, 4H), 1.68-1.61 (m, 4H), 1.43-1.26 (m, 28H), 0.88 (t, *J* = 7.0 Hz, 6H), 0.24(s, 9H); ^{13}C NMR (75 MHz, CD_2Cl_2): δ 136.8, 134.7, 132.3, 128.3, 126.8, 125.3, 120.3, 113.6, 105.4, 95.0, 36.5, 36.4, 32.3, 30.2, 30.1, 30.0, 29.9, 29.7, 29.5, 28.90, 28.87, 23.1, 14.3; HRMS (MALDI-TOF, +eV) *m/z* calcd for $C_{35}H_{56}S_4Si$ 632.3034, found 632.3146 $[M]^+$.

TMS protected -DTF (298a)

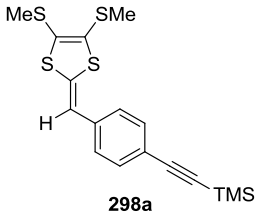

298a

Compound **270a** (2.51g, 11.0 mmol) was olefination reaction compound 271 (2.24 g, 11.0 mmol) in trimethyl phosphate (25 mL) for 3 h as described in the procedure for the synthesis of compound **298**. Silica flash column chromatography (EtOAc/hexane 1.5:8.5) afforded **298a** (2.70, 7.09 mmol, 64%) as yellow solid. ^{1}H NMR (500 MHz, CD_2Cl_2): δ 7.43 (d, *J* = 8.3 Hz, 2H), 7.12 (d, *J* = 8.3 Hz, 2H), 6.44 (s, 1H), 2.44 (s, 3H), 2.43 (s, 3H), 0.25 (s, 9H). The data are consistent with literature report.[79]

Neutral acetylenic phenyl TTFV precursor (299)

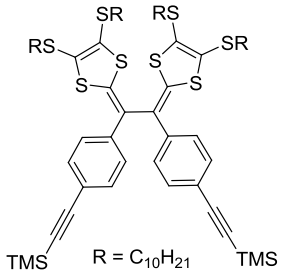

299

To a solution of compound **298** (0.700 g, 1.10 mmol) in CH_2Cl_2 (100 mL) were added iodine chips (0.813 g, 3.20 mmol). The resulting dark solution was stirred at rt overnight. A saturated aqueous solution of $Na_2S_2O_3$ (25 mL) was then added to the dark solution and stirred for another 3 h at rt. The resulting yellow organic layer was separated, washed with water, dried over $MgSO_4$, and concentrated under reduced

pressure. The resulting crude product was subjected to silica flash column chromatography for purification (EtOAc/hexanes, 1:9), giving pure compound **299** (0.569g, 0.450 mmol, 82%) as a reddish brown syrup. IR (neat): 2957, 2923, 2852, 2155, 1521, 1463, 1248 cm^{-1};^{1}H NMR (300 MHz, $CDCl_3$): δ 7.37 (d, *J* = 8.6 Hz, 4H), 7.30 (d, *J* = 8.6 Hz, 4H), 2.83-2.71 (m, 8H), 1.68-1.57 (m, 8H), 1.42-1.26 (m, 56H), 0.88 (t, *J* = 6.4 Hz, 12H), 0.23(s, 18H); ^{13}C NMR (75 MHz, $CDCl_3$): δ 138.2, 137.2, 132.2, 128.8, 126.3, 125.5, 123.5, 121.1, 105.2, 94.8, 36.2, 36.0, 31.95, 31.93, 29.7, 29.6, 29.38, 29.35, 29.21, 29.18, 28.6, 28.5, 22.73, 22.71, 14.2, 0.0; HRMS (MALDI-TOF, +eV) *m/z* calcd for $C_{70}H_{110}S_8Si_2$ 1262.5912, found 1262.6032 $[M]^+$.

Neutral acetylenic phenyl TTFV precursor (299a)

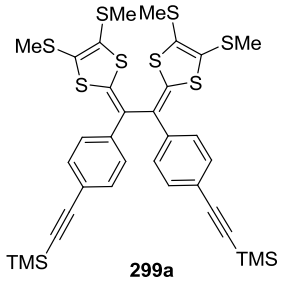

299a

Compound **298a** (1.2 g, 3.2 mmol) was subjected to oxidative dimerization reaction in presence of Iodine (2.4 g, 9.4 mmol) in CH_2Cl_2 for overnight as described in the procedure for the synthesis of compound **299**. Silica flash column chromatography (EtOAc/hexane 2:8) afforded **299a** (0.73 g, 1.9 mmol, 61%) as yellow solid. ^{1}HNMR (500 MHz, $CDCl_3$): δ 7.38 (d, *J* = 8.3 Hz, 4H), 7.30 (d, *J* = 8.3 Hz, 4H), 2.42 (s, 6H), 2.37 (s, 6H). The data are consistent with literature report.[79]

Acetylenic phenyl TTFV precursor (300)

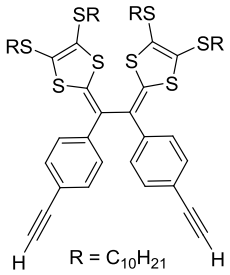

300

Compound **299** (0.500g, 0.395mmol) was dissolved in MeOH/THF (1:1, 30 mL), and to the mixture was added K_2CO_3 (0.327 g, 2.37 mmol). The reaction mixture was stirred for 2 h at rt. On completion, the solvent was removed under reduced pressure. The residue was dissolved in CH_2Cl_2, washed with water, dried over $MgSO_4$, and concentrated under reduced pressure to give crude **300**. The crude product was subjected to column chromatographic purification (EtOAc/hexanes, 3:7) to yield pure compound **300** (0.380g, 0.339 mmol, 86%) as a reddish brown syrup. IR (neat): 3303, 2956, 2922, 2850, 2107, 1552, 1484, 1463, 1115 cm^{-1}; ^1H NMR (500 MHz, CD_2Cl_2): δ 7.41 (d, *J* = 8.5 Hz, 4H), 7.34 (d, *J* = 8.5 Hz, 4H), 3.07 (s, 2H), 2.84-2.80 (m, 4H), 2.74 (t, *J* = 7.3 Hz, 4H), 1.66-1.55(m, 8H), 1.43-1.25 (m, 56H), 0.88 (t, *J* = 6.8 Hz, 12H); ^{13}C NMR (75 MHz, CD_2Cl_2): δ 139.3, 137.8, 132.7, 129.3, 126.7, 126.0, 123.5, 120.4, 83.8, 78.0, 36.6,36.4, 32.3,30.16, 30.14, 30.0, 29.96, 29.8, 29.7, 29.59, 29.56, 28.92, 28.89, 23.1, 14.3; HRMS (MALDI-TOF, +eV) *m/z* calcd for $C_{64}H_{94}S_8$ 1118.5121, found 1118.5137 $[M]^+$.

Acetylenic phenyl TTFV precursor (300a)

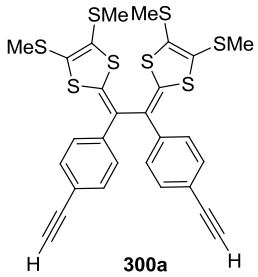

300a

Compound **299a** (0.62 g, 0.82 mmol) was desilylated in presence of K_2CO_3 (0.68 g, 4.9 mmol) in MeOH/THF (1:1, 30 mL), for overnight as described in the procedure for the synthesis of compound **300**. Silica flash column chromatography (EtOAc/hexane 3:7) afforded **300a** (0.41 g, 0.66 mmol, 82%) as yellow solid. m.p. 140.1-142.3 ^{o}C; IR (neat) 3276, 2916, 2096, 1595, 1471, 1309, 885, 833 cm^{-1}; ^{1}H NMR (500 MHz, $CDCl_3$): δ 7.43 (d, *J* = 8.4 Hz, 4H), 7.35 (d, *J* = 8.4 Hz, 4H), 3.08 (s, 2H), 2.43 (s, 6H), 2.39 (s, 6H); ^{13}C NMR (125 MHz, $CDCl_3$): δ 138.3, 137.2, 132.5, 128.6, 126.3, 125.2, 123.3, 120.1, 83.6, 77.8, 18.9, 18.8; HRMS (MALDI-TOF, +eV) *m/z* calcd for $C_{28}H_{22}S_8$ 613.9487, found 613.9497 $[M]^+$.

1-(Hydroxymethyl)naphthalene (302)

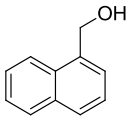

302

To a solution of 1-naphthaldehyde **301** (1.01 g, 6.41 mmol) in MeOH (20 mL) was slowly added $NaBH_4$ (0.721 g, 19.2 mmol) at 0 ^{o}C under N_2 atm. The reaction mixture was brought to rt and stirred for 2 h. Then the reaction was slowly quenched with

ice water at 0 ^{o}C. The solvent was reduced under vacuum to give crude product **302**, which was dissolved in DCM, washed with water and dried over $MgSO_4$, and concentrated under vacuum to give pure product **302** (1.02 g, 6.41, 100%) as an off-white solid. ^{1}H NMR (300 MHz, $CDCl_3$): δ 8.13 (d, *J* = 7.8 Hz, 1H), 7.90-7.87 (m, 1H), 7.82 (d, *J* = 8.1 Hz, 1H), 7.59-7.43 (m, 4H), 5.16 (s, 2H).

1-(Chloromethyl)naphthalene (303)

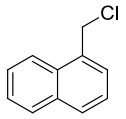

303

To a solution of 1-(hydroxymethyl)naphthalene **302** (0.816 g, 5.16 mmol) and TEA (2.4 mL, 16.7 mmol) in DCM (50 mL) was slowly added mesyl chloride (0.8 mL, 1.18 g, 10.3mmol) at rt under N_2 atm. The reaction mixture was stirred at rt for 2 h. On completion as checked by TLC analysis, the reaction mixture was diluted with DCM (50 mL) and washed with water, aq. NH_4Cl solution, and water. The organic layer was separated, dried over $MgSO_4$, and concentrated under vacuum to give pure product **303** (0.670 g, 3.79 mmol, 73%) as thick syrup. ^{1}H NMR (300 MHz, $CDCl_3$): δ 8.16 (d, *J* = 8.7 Hz, 1H), 7.89 (t, *J* = 9.0 Hz, 2H), 7.64-7.51(m, 3H), 7.46-7.41 (m, 1H), 5.07 (s, 2H). The data are consistent with literature report.[80]

1-(Azidomethyl)naphthalene (304)

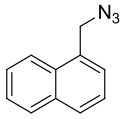

304

To a solution of compound **303** (0.603 g, 3.42 mmol) in dry DMF (5 ml) was added NaN_3 (0.495 g, 7.61 mmol) and stirred at rt for overnight. After the reaction was monitored by TLC, water was added and the compound was extracted into ether (100 mL). The organic layer was washed with cold water to remove traces of DMF and dried over $MgSO_4$ and removed under vacuum to afford pure compound **304** as liquid (0. 447 g, 2.43 mmol, 71%). ^{1}H NMR (300 MHz, $CDCl_3$): δ 8.04 (d, *J* = 8.3 Hz, 1H), 7.93-7.86 (m, 2H), 7.62-7.52 (m, 2H), 7.50-7.44 (m, 2H), 4.78 (s, 2H). The data are consistent with literature report.[81]

9-(Chloromethyl)anthracene (306)

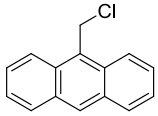

306

To a solution of 9-(hydroxymethyl)anthracene **305** (3.02 g, 14.5 mmol) and TEA (7.4 mL, 26.7 mmol) in DCM (150 mL) was slowly added mesyl chloride (2.2 mL, 3.16 g, 27. 5 mmol) at rt under N_2 atm. The reaction mixture was stirred at rt for 2 h. On completion as checked by TLC analysis, the reaction mixture was diluted with DCM (40 mL) and washed with water, aq. NH_4Cl solution, and water. The organic layer was separated, dried over $MgSO_4$, and concentrated under vacuum to give pure product **306**

(2.51 g, 11.1 mmol, 76%) as yellow solid. ^{1}H NMR (500 MHz, $CDCl_3$): δ 8.50 (s, 1H), 8.33 (d, *J* = 8.9 Hz, 2H), 8.05 (d, *J* = 8.1 Hz, 2H) 7.63 (t, *J* = 7.8 Hz, 2H), 7.51 (t, *J* = 7.7 Hz, 2H), 5.63 (s, 2H).

9-(Azidomethyl)anthracene (307)

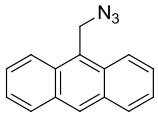

307

To a solution of compound **306** (1.51 g, 6.66 mmol) in dry DMF (10 mL) was added NaN_3 (0.860 g, 13.2 mmol) and stirred at rt for overnight. After the reaction was monitored by TLC, water was added and the compound was extracted into ether (150 mL). The organic layer was washed with cold water to remove traces of DMF and dried over $MgSO_4$ and removed under vacuum to afford pure compound **307** as yellow solid (1.22 g, 5.26 mmol, 79%). ^{1}H NMR (500 MHz, $CDCl_3$): δ 8.51 (s, 1H), 8.30 (d, *J* = 8.8 Hz, 2H), 8.06 (d, *J* = 8.4 Hz, 2H) 7.60 (t, *J* = 7.7 Hz, 2H), 7.52 (t, *J* = 8.0 Hz, 2H), 5.34 (s, 2H). The data are consistent with literature report.[82]

2-(Hydroxymethyl)pyrene (309)

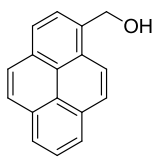

309

To a solution of 2-pyrenealdehyde **308** (1.04 g, 4.34mmol) in MeOH (10 ml) and THF (10 mL) was slowly added $NaBH_4$ (0.492 g, 13.0mmol) at 0 ^oC under N_2 atm. The reaction mixture was brought to rt and stirred for 2 h. Then the reaction was slowly quenched with ice water at 0 ^oC. The solvent was reduced under vacuum to give crude product **309**, which was dissolved in DCM, washed with water and dried over $MgSO_4$, and concentrated under vacuum to give pure product **309** (1.05, 4.34 mmol, 100%) as off-white solid. ^1H NMR (300 MHz, $CDCl_3$): δ 8.38 (d, *J* = 9.2 Hz, 1H), 8.22-8.14 (m, 4H), 8.06 (m, 4H), 5.41 (s, 2H). The data are consistent with literature report.

2-(Bromomethyl)pyrene (310)

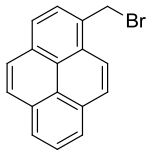

310

To a solution of 2-(hydroxymethylpyrene) **309** (0.51 g, 2.2 mmol) in THF(50 mL) was added phosphorous tribromide (0.2 mL, 0.59 g, 2.2 mmol) at rt and stirred for 1 h. The resulting mixture was filtered and the residue was washed with ether to yield the desired 2-(bromomethyl) pyrene **310** as a pale green solid (0.55 g, 1.8 mmol 84%). The product **309** was taken to the next reaction without further characterization.

2-(Azidomethyl)pyrene (311)

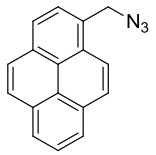

311

To a solution of 2-(azidomethyl)pyrene **310** (0.701 g, 2.37 mmol) in dry DMF (5 mL) was added NaN_3 (0.464 g, 7.13 mmol) and stirred at rt for overnight. After the reaction was monitored by TLC, water was added and the compound was extracted into ether (100 mL). The organic layer was washed with cold water to remove traces of DMF and dried over $MgSO_4$ and removed under vacuum to afford pure compound **311** as yellow solid (0. 578 g, 2.24 mmol, 94%). ^{1}H NMR (300 MHz, $CDCl_3$): δ 8.30-8.16 (m, 5H), 8.12-7.97 (m, 4H), 5.05 (s, 2H). The data are consistent with literature report.[83]

9,10-Bis(bromomethyl)anthracene (313)

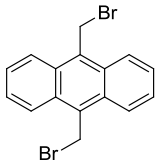

313

To a solution of anthracene **312** (5.0 g, 28mmol) in a mixture of 48% aqueous hydrobromic acid (100 mL) and glacial acetic acid (25 mL) was added 1,3,5-trioxane (5.0 g, 64 mmol) and tetrabutylammonium bromide (0.2 g, catalytic amount) were added. The mixture was stirred and refluxed for 24 h. After cooling, the green solid formed was filtered and washed with water and ethanol. The resulting crude product **313** was

recrystallized from toluene to give pure product **313** as a green solid (7.5 g, 20 mmol, 73%). No meaningful ^{1}H NMR obtained. The compound **313** was taken to the next step.

9,10-Bis(azidomethyl)anthracene (314)

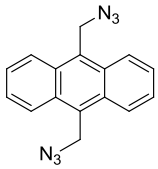

314

To a solution of 9,10-bis(bromomethyl)anthracene **313** (3.0 g, 8.2 mmol) in DCM (20 mL) and water (10 mL) was added NaN_3 (2.1 g, 32 mmol) and TBAB (0.26 g, 0.81 mmol) and stirred at rt for 3 h. On completion as checked by TLC analysis, the reaction mixture was diluted with DCM (100 mL) and washed with water. The organic layer was separated, dried over $MgSO_4$, and concentrated under vacuum to give pure product **314** as yellow solid (1.5 g, 5.2 mmol, 63%). ^{1}H NMR (300 MHz, $CDCl_3$): δ 8.41-8.35 (m, 4H), 7.68-7.62 (m, 4H), 5.37 (s, 4H). The data are consistent with literature report.[84]

1,4-bis(azidomethyl)benzene (315)

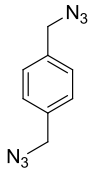

315

To a solution of 1,4-bis(bromomethyl)benzene **233** (0.920 g, 3.48 mmol) in dry DMF (10 mL) was added NaN_3 (0.682 g, 10.4 mmol) and stirred at rt for 3 h. After the reaction was monitored by TLC, water was added and the compound was extracted into ether (100 mL). The organic layer was washed with cold water to remove traces of DMF and dried over $MgSO_4$ and removed under vacuum to afford pure compound **315** as a colorless liquid (0. 591 g, 3.14 mmol, 90%). ^{1}H NMR (300 MHz, $CDCl_3$): δ 7.34 (s, 4H), 4.35 (s, 4H). The data are consistent with literature report.[85]

TTFV-boronate (316)

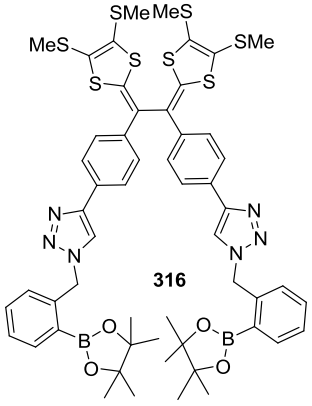

316

Compound **300a** (0.151 g, 0.245 mmol), azido-phenylboronate **315** (0.254 g, 0.982 mmol) and ^{i}Pr$_2$EtN (21 µL, 0.123 mmol) were dissolved in dry THF (10 mL). The solution was degassed by bubbling N_2 at rt for 5 min. CuI (23.3 mg, 0.123 mmol) was then added, and the reaction mixture was heated at 60 ^{o}C overnight. After the reaction mixture was complete as checked by TLC analysis, the solvent was removed under vacuum. The residue was diluted with CH_2Cl_2 and then filtered through a $MgSO_4$ pad. The filtrate was sequentially washed with brine and water. The organic layer was dried

over $MgSO_4$ and concentrated under vacuum to afford crude compound **316**, which was further purified by silica flash column chromatography (EtOAc/hexanes, 3:7) to yield pure compound **316** (0.242 g, 0.214 mmol, 87%) as a pale green solid. m.p. 122-125 ^{o}C; IR (neat): 2980, 1490, 1345, 1216, 1142, 1071, 963 cm^{-1}; ^{1}H NMR (500 MHz, $CDCl_3$): δ 7.91 (dd, *J* = 7.4, 1.2 Hz, 2H), 7.71-7.70 (m, 6H), 7.44-7.40 (m, 6H), 7.36-7.33 (m, 2H), 7.24 (d, *J* = 7.7 Hz, 2H), 5.88 (s, 4H), 2.42 (s, 6H), 2.37 (s, 6H), 1.36 (s, 24H); ^{13}C NMR (75 MHz, $CDCl_3$): δ 147.3, 140.9, 136.7, 136.6, 136.53, 136.50, 131.9, 129.2, 128.3, 127.9, 127.0, 125.8, 124.9, 124.2, 119.8, 84.2, 53.4, 24.9, 24.8, 18.9, 18.6; HRMS (MALDI-TOF, +eV) *m/z* calcd for $C_{54}H_{58}B_2N_6O_4S_8$ 1132.2471, found 1132.2486 $[M]^+$.

TTFV-trifluoroborate (317)

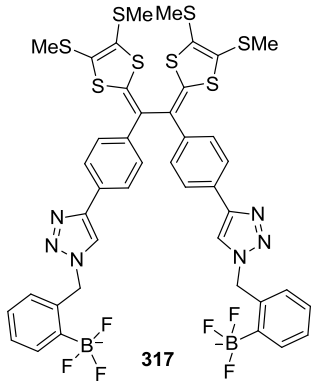

317

A solution of compound **316** (106 mg, 0.0935 mmol) in MeOH (5 mL) and THF (5 mL) was added to aqueous potassium hydrogen difluoride (1 mL, 3 M, 2.99 mmol) in a plastic beaker. The resulting pale green color slurry was stirred for 3 h at rt. After the reaction was complete as checked by TLC analysis, the solvent was concentrated under vacuum. The residue was then dissolved in acetone and the subjected to filtration. The filtrate was concentrated under vacuum to give crude product **317**, which was washed

with methanol to afford compound **317** (92.0 mg, 0.0842 mmol, 90%) as yellow solid. m.p. 205-209 ^{o}C; IR (neat): 2977, 1597, 1487, 1431, 1349, 1191, 958 cm^{-1}; ^{1}H NMR (500 MHz, DMSO-d_6): δ 8.34 (s, 2H), 7.80 (d, J = 8.5 Hz, 4H), 7.46-7.40 (m, 6H), 7.07-6.99 (m, 4H), 6.68 (d, J = 7.7 Hz, 2H), 5.69 (s, 4H), 2.44 (s, 6H), 2.37 (s, 6H); ^{13}C NMR (75 MHz, DMSO-d_6): δ 145.8, 138.3, 135.5, 135.3, 132.04, 132.00, 130.2, 129.6, 126.7, 126.3, 125.9, 125.8, 125.6, 124.8, 123.9, 121.6, 52.9, 24.9, 18.2, 18.20, 18.16.

TTFV-naphthalene tweezers (292)

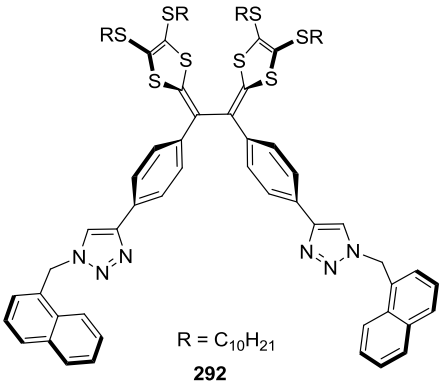

292

To a solution of compound **300** (0.300g, 0.267mmol), 1-(azidomethyl)naphthalene **304** (0.196 g, 1.07 mmol) and ^{i}Pr$_2$EtN (22.0 µL, 0.133 mmol) in dry THF (8 mL) was added CuI (25.5 mg, 0.133 mmol). The reaction mixture was degassed by bubbling N_2 at rt for 5 min before it was heated to 60 ^{o}C overnight. On completion, the solvent THF was removed under reduced pressure. The obtained residue was dissolved in CH_2Cl_2 and filtered through a $MgSO_4$ pad. The filtrate was sequentially washed with brine and water. The organic layer was dried over $MgSO_4$ and concentrated under vacuum to give crude **292**, which was further purified by silica flash column

chromatography (EtOAc/hexanes, 3:7) to yield pure compound **292** (0.362 g, 0.243 mmol, 91 %) as a thick syrup. IR (neat): 2920, 2850, 1525, 1495, 1457, 1349, 1265, 1043 cm^{-1}; ^{1}H NMR (500 MHz, $CDCl_3$): δ 7.98-7.95 (m, 2H), 7.92-7.88 (m, 4H), 7.63 (d, *J* = 8.5 Hz, 4H), 7.52-7.43 (m, 10H), 7.36 (d, *J* = 8.3 Hz, 4H), 6.01(s, 4H), 2.78 (t, *J* = 7.3 Hz, 4H), 2.73 (t, *J* = 7.3 Hz, 4H), 1.63-1.52 (m, 8H), 1.40-1.21 (m, 56H), 0.87 (t, *J* = 6.9 Hz, 12H);^{13}C NMR (75 MHz, $CDCl_3$): δ 147.7, 136.9, 136.8, 133.9, 131.2, 130.1, 129.8, 128.9, 128.7, 128.4, 127.7, 127.3, 126.9, 126.4, 125.8, 125.3, 123.9, 122.8, 119.3, 52.4, 36.1, 36.0, 31.90, 31.89, 29.63, 29.58, 29.54, 29.53, 29.34, 29.31, 29.2, 28.6, 28.5, 22.7, 14.1; HRMS (MALDI-TOF, +eV) *m/z* calcd for $C_{86}H_{112}N_6S_8$, 1484.6714, found 1484.6796 $[M]^+$.

TTFV-anthracene tweezers (293)

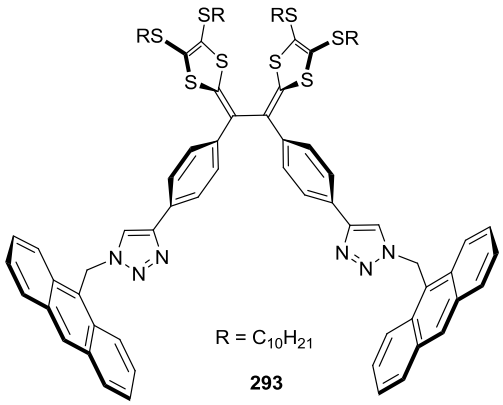

293

To a solution of compound **300** (0.150g, 0.133 mmol), 9-(azidomethyl)anthracene **307** (0.156g, 0.668 mmol) and $^{i}Pr_2EtN$ (11.0 µL, 0.070 mmol) in dry THF (8 mL) was added CuI(7.60 mg, 0.040 mmol). The reaction mixture was degassed by bubbling N_2 at rt for 5 min before it was heated to 60 ^{o}C overnight. On completion, the solvent THF was

removed under reduced pressure. The obtained residue was dissolved in CH_2Cl_2 and filtered through a $MgSO_4$ pad. The filtrate was sequentially washed with brine and water. The organic layer was dried over $MgSO_4$ and concentrated under vacuum to give crude **293**, which was further purified by silica flash column chromatography (EtOAc/hexanes, 3:7) to yield pure compound **293** (0.171 g, 0.107 mmol, 83%) as a pale yellow solid. m.p. 114-117 ^{o}C; IR (neat): 2920, 2849, 1527, 1492, 1449, 1337, 1258, 1213, 1037 cm^{-1}; ^{1}H NMR (500 MHz, $CDCl_3$): δ 8.58 (s, 2H), 8.30(d, *J* = 8.8 Hz, 4H), 8.08 (d, *J* = 8.4 Hz, 4H), 7.60-7.57(m, 4H), 7.54-7.48 (m, 10H), 7.24-7.23 (m, 2H), 7.19(s, 2H), 6.54(s, 4H), 2.73 (t, *J* = 7.3 Hz, 4H), 2.68 (t, *J* = 7.3 Hz, 4H), 1.59-1.48 (m, 8H), 1.35-1.18 (m, 56H), 0.88 (td, *J* = 6.7, 1.5 Hz, 12H); ^{13}C NMR (75 MHz, $CDCl_3$): δ 147.5, 136.8, 136.7, 131.5, 130.8, 129.9, 129.5, 128.6, 128.3, 127.7, 126.9, 125.7, 125.4, 125.3, 123.9, 123.7, 122.9, 119.0, 46.5, 36.0, 35.9, 29.6, 29.5, 29.32, 29.29, 29.1, 28.5, 28.4, 22.7, 14.1; HRMS (MALDI-TOF, +eV) *m/z* calcd for $C_{94}H_{116}N_6S_8$ 1584.7027, found 1584.6682 $[M]^+$.

TTFV-anthracene tweezer (293a)

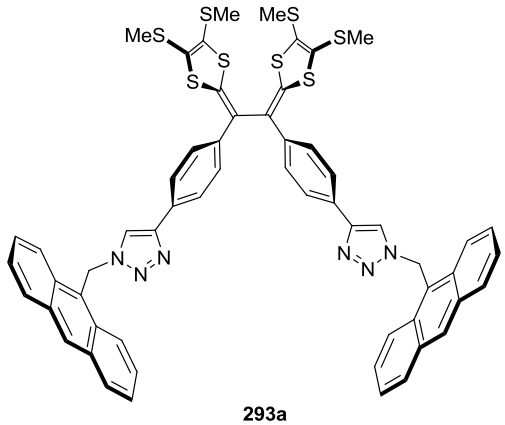

293a

Compound **300a** (50.0 mg, 0.081 mmol), 9-(azidomethyl)anthracene **307** (94.8 mg, 0.406 mmol) and $^{i}Pr_2EtN$ (0.007 mL, 0.040 mmol) were dissolved in dry THF (5 mL). The solution was degassed by bubbling N_2 at rt for 5 min. Then CuI (1.54 mg, 0.0081 mmol) was added, and the reaction mixture was heated at 60^{o}C for overnight. After the reaction mixture was completed as checked by TLC analysis, the solvent was removed under reduced pressure. The residue was diluted with CH_2Cl_2. The mixture was filtered through a $MgSO_4$ pad and the filtrate was sequentially washed with brine and water. The organic layer was dried over $MgSO_4$ and concentrated under vacuum to give crude **293a**, which was further purified by silica flash column chromatography (EtOAc/hexanes, 3:7) to yield pure compound **293a** (80.5 mg, 0.078 mmol, 91%) as a pale yellow solid. m.p. > 265 ^{o}C (decomp); IR (neat) : 2916, 2365, 1614, 1523, 1484, 1433, 1421, 1315, 1209, 1181, 1038, 966 cm^{-1}; ^{1}H NMR (500 MHz, $CDCl_3$): δ 8.59 (s, 2H), 8.32 (d, *J* = 8.9 Hz, 2H), 8.09 (d, *J* = 8.4 Hz, 2H), 7.61-7.49 (m, 14H), 7.25-7.20 (m, 2H), 6.55 (s, 2H), 2.34 (s, 2H), 2.29 (s, 2H); ^{13}C NMR (125 MHz, $CDCl_3$): δ 147.4, 136.6, 136.3, 131.4, 130.8, 129.9, 129.4, 128.7, 127.9, 127.7, 126.8, 125.7, 125.4, 124.9, 124.0, 123.7, 122.9, 119.0, 46.4, 18.7; HRMS (MALDI-TOF, +eV) *m/z* calcd for $C_{58}H_{44}N_6S_8$ 1080.1393, found 1080.1464 $[M]^{+}$.

TTFV-pyrene tweezers (294)

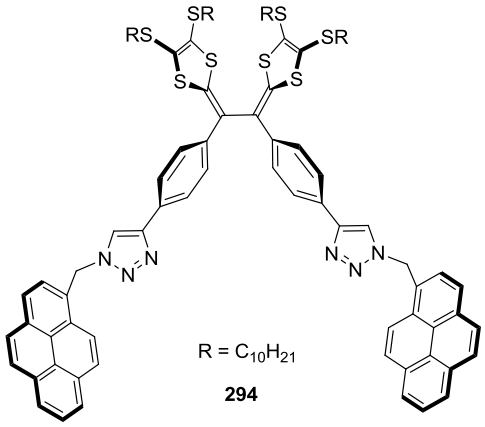

294

To a solution of compound **300** (0.150g, 0.133mmol), 2-(azidomethyl)pyrene **311** (0.803 g, 0.668 mmol) and $^{i}Pr_2EtN$ (11.0 µL, 0.0669 mmol) in dry THF (10 mL) was added CuI (12.7 mg, 0.0666 mmol). The reaction mixture was degassed by bubbling N_2 at rt for 5 min before it was heated to 60 ^{o}C overnight. On completion, the solvent THF was removed under reduced pressure. The obtained residue was dissolved in CH_2Cl_2 and filtered through a $MgSO_4$ pad. The filtrate was sequentially washed with brine and water. The organic layer was dried over $MgSO_4$ and concentrated under vacuum to give crude **294**, which was further purified by silica flash column chromatography (EtOAc/hexanes, 4:6) to yield pure compound **294** (0.189 g, 0.115 mmol, 86%) as a pale yellow solid. m.p. 88-89 ^{o}C; IR (neat): 2920, 2849, 1528, 1494, 1456, 1349, 1288, 1213, 1043 cm^{-1}; ^{1}H NMR (500 MHz, $CDCl_3$): δ 8.24-8.18 (m, 8H), 8.14-8.12 (m, 4H), 8.09-8.03 (m, 4 H), 7.96 (d, *J* = 7.9 Hz, 2H), 7.57 (d, *J* = 8.5 Hz, 4H), 7.39 (s, 2H), 7.29 (d, *J* = 8.7 Hz, 4H), 6.27 (s, 4H), 2.73 (t, *J* = 7.3 Hz, 4H), 2.68 (t, *J* = 7.3 Hz, 4H), 1.59-1.48 (m, 8H), 1.36-1.17 (m, 56H), 0.85 (td, *J* = 4.7, 1.9 Hz, 12H); ^{13}C NMR (75 MHz, $CDCl_3$): δ 147.7, 136.9, 136.8, 132.2, 131.2, 130.6, 129.3, 129.1, 128.7, 128.4, 128.3, 127.6, 127.2, 126.9,

126.8, 126.4, 125.9, 125.8, 125.7, 125.3, 125.1, 124.9, 124.5, 123.9, 121.9, 119.3, 52.5, 36.1, 35.9, 31.9, 29.6, 29.55, 29.51, 29.49, 29.31, 29.29, 29.1, 28.5, 28.4, 22.7, 14.1; HRMS (MALDI-TOF, +eV) *m/z* calcd for $C_{98}H_{116}N_6S_8$, 1632.7027, found 1632.7168 $[M]^+$.

Boronic acid-appended TTFV tweezers (295)

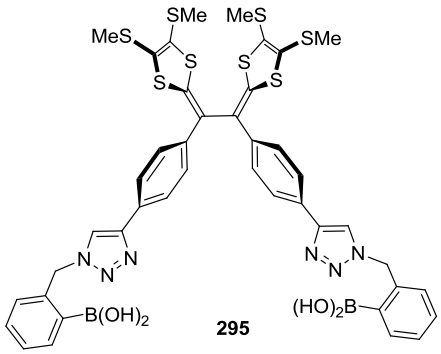

295

Compound **317** (56.0 mg, 0.0512 mmol) was dissolved in a mixture of acetonitrile (4 ml) and water (1 ml). This was added lithium hydroxide (9.80 mg, 0.125 mmol) and stirred at rt for overnight. The acetonitrile was concentrated under vacuum and crude solution was added 1.2 M HCl (until the solution reaches pH 6). The obtained precipitate was filtered and washed with water and methanol to afford pure product **295** (39.2 mg, 0.0404 mmol, 79%) as a pale green solid. m.p. 195-198 ^oC; IR (neat): 3382, 2957, 1600, 1528, 1489, 1451, 1346, 1057, 967 cm^{-1}; ^1H NMR (500 MHz, DMSO-d_6): δ 8.43 (s, 2H), 8.32 (s, 4H), 7.81 (d, *J* = 8.3 Hz, 4H), 7.64 (d, *J* = 7.6 Hz, 2H) 7.42 (d, *J* = 7.2 Hz, 4H),

7.36-7.28 (m, 4H), 7.03 (d, J = 7.6 Hz, 2H), 5.82 (s, 4H), 2.44 (s, 6H), 2.38 (s, 6H); ^{13}C NMR spectrum could not be obtained due to low solubility; HRMS (MALDI-TOF, +eV) *m/z* calcd for $C_{42}H_{38}B_2N_6O_4S_8$ 968.0906, found 968.0904 $[M]^+$.

TTFV-benzene macrocycle (296)

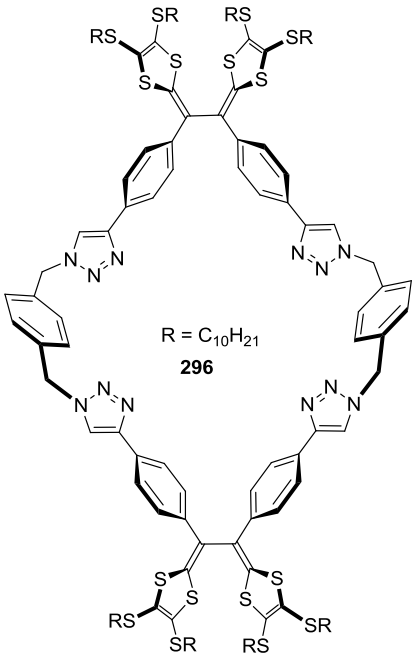

To a solution of compound **300** (0.109g, 0.0972mmol), 1,4-bis(azidomethyl)benzene **315** (0.0183 g, 0.0972 mmol) and $^{i}Pr_2EtN$ (8.0 µL, 0.0486 mmol) in dry THF (8 mL) was added CuI (9.20 mg, 0.0486 mmol). The reaction mixture

was degassed by bubbling N_2 at rt for 5 min before it was heated to 60 ^oC overnight. On completion, the solvent THF was removed under reduced pressure. The obtained residue was dissolved in CH_2Cl_2 and filtered through a $MgSO_4$ pad. The filtrate was sequentially washed with brine and water. The organic layer was dried over $MgSO_4$ and concentrated under vacuum to give crude **296**, which was further purified by silica flash column chromatography (EtOAc/hexanes, 2.5:7.5) to yield pure compound **296** (0.0603 g, 0.0230 mmol, 47%) as a pale green solid. m.p. 81-86 ^oC; IR (neat): 2921, 2850, 2096, 1526, 1493, 1454, 1348, 1258, 1217, 1041 cm^{-1}; ^1H NMR (500 MHz, $CDCl_3$): δ 7.72-7.61 (m, 12H), 7.44 (d, *J* = 8.0 Hz, 8H), 7.31-7.22 (m, 8H), 5.56-5.51 (m, 8H), 2.82-2.75 (m, 16H), 1.64-1.56 (m, 16H), 1.41-1.24 (m, 112H), 0.88-0.85 (m, 24H); ^{13}C NMR (75 MHz, $CDCl_3$): δ 147.9, 137.1, 136.1, 135.4, 134.8, 128.9, 128.5, 128.4, 127.0, 125.9, 125.3, 123.8, 119.4, 54.3, 53.8, 53.6, 36.2, 36.0, 34.9, 29.63, 29.56, 29.4, 29.3, 29.2, 28.6, 28.3, 22.7, 14.1; HRMS (MALDI-TOF, +eV) *m/z* calcd for $C_{114}H_{204}N_{12}S_{16,}$ 2613.1863, found 2613.1551 $[M]^+$.

TTFV-anthracene macrocycle (297)

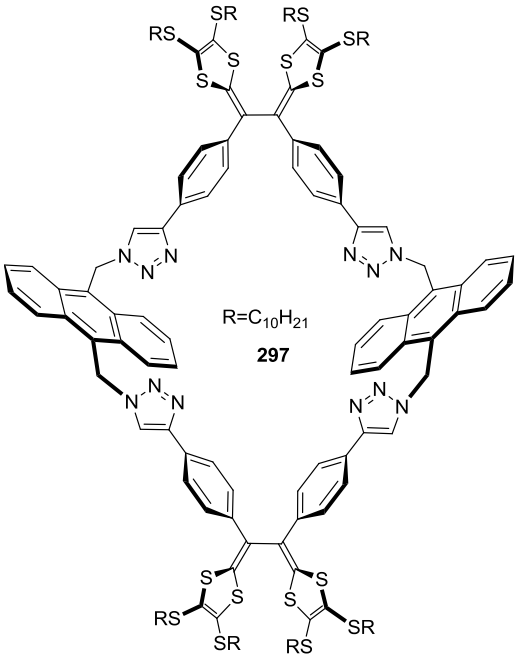

To a solution of compound **300** (0.103g, 0.092 mmol), 9,10-bis(azidomethyl)anthracene **314**(26.5 mg, 0.0920mmol) and $^{i}Pr_2EtN$ (7.50 µL, 0.046 mmol) in dry THF (6 mL) was added CuI (5.10mg, 0.040mmol). The reaction mixture was degassed by bubbling N_2 at rt for 5 min before it was heated to 60^{o}C overnight. On completion, the solvent THF was removed under reduced pressure. The obtained residue was dissolved in CH_2Cl_2 and filtered through a $MgSO_4$ pad. The filtrate was sequentially washed with brine and water. The organic layer was dried over $MgSO_4$ and concentrated under vacuum to give crude **297**, which was further purified by silica flash column chromatography (EtOAc/hexanes, 5:5) to yield pure compound **297** (69.6 mg, 0.024 mmol, 54%) as a pale green solid. m.p. 142-147 ^{o}C; IR (neat): 2922, 2850, 1528, 1462, 1447, 1224, 1209, 1040 cm^{-1}; ^{1}H NMR (500 MHz, CD_2Cl_2): δ 8.45-8.42 (m, 10H), 7.69-7.64 (m, 10H), 7.54-7.42 (m, 8H), 7.35-7.28 (m, 8H), 6.59 (s, 8H), 2.80-2.71 (m, 16H),

1.60-1.55 (m, 16H), 1.36-1.20 (m, 112H), 0.88-0.84 (m, 24H); ^{13}C NMR (75 MHz, CD_2Cl_2): δ 147.6, 137.1, 131.1, 131.0, 130.9, 129.8, 129.3, 128.5, 128.2, 127.8, 127.7, 127.4, 127.3, 127.1, 126.6, 125.9, 125.1, 124.7, 124.4, 119.7, 47.0, 46.9, 36.5, 32.3, 29.9, 29.7, 29.5, 28.9, 28.8, 23.1, 14.3; HRMS (MALDI-TOF, +eV) *m/z* calcd for $C_{160}H_{212}N_{12}S_{16}$ 2814.2523, found 2814.2557 $[M]^+$.

4.6 References

(1) Martínez-Máñez, R.; Sancenón, F. *Chem. Rev.* **2003**, *103*, 4419-4476.

(2) Zhang, X.; Yin, J.; Yoon, J. *Chem. Rev.* **2014**.

(3) Kathayat, R. S.; Finney, N. S. *J. Am. Chem. Soc.* **2013**, *135*, 12612-12614.

(4) Ravikumar, I. *Asian J. Exp. Sci.* **2008**, *22*, 103-111.

(5) Askim, J. R.; Mahmoudi, M.; Suslick, K. S. *Chem. Soc. Rev.* **2013**, *42*, 8649-8682.

(6) Gunnlaugsson, T.; Davis, A. P.; O'Brien, J. E.; Glynn, M. *Org. Lett.* **2002**, *4*, 2449-2452.

(7) Leray, I.; Lefevre, J.-P.; Delouis, J.-F.; Delaire, J.; Valeur, B. *Chem. Eur. J.* **2001**, *7*, 4590-4598.

(8) Xu, Z.; Xiao, Y.; Qian, X.; Cui, J.; Cui, D. *Org. Lett.* **2005**, *7*, 889-892.

(9) Wilson, M. A.; Pang, L. S. K.; Vassallo, A. M. *Nature* **1992**, *355*, 117.

(10) Atwood, J., L,; Kaoutsantonis, G., A,; Raston, C., L. *Nature* **1994**, *368*, 229-231.

(11) Scrivens, W. A.; Bedworth, P. V.; Tour, J. M. *J. Am. Chem. Soc.* **1992**, *114*, 7917-7919.

(12) Suzuki, T.; Nakashima, K.; Shinkai, S. *Chem. Lett.* **1994**, 699.

(13) Nagata, K.; Dejima, E.; Kikuchi, Y.; Hashiguchi, M. *Chem. Lett.* **2005**, *34*, 178.

(14) Perez, E. M.; Martı´n, N. *Pure Appl. Chem.* **2010**, *82*, 523-533.

(15) Perez, E. M.; Martin, N. *Chem. Soc. Rev.* **2008**, *37*, 1512-1519.

(16) Kawase, T.; Kurata, H. *Chem. Rev.* **2006**, *106*, 5250-5273.

(17) Haino, T.; Araki, H.; Fujiwara, Y.; Tanimoto, Y.; Fukazawa, Y. *Chem. Commun.* **2002**, 2148-2149.

(18) Zhang, G.; Zhang, D.; Zhou, Y.; Zhu, D. *J. Org. Chem.* **2006**, *71*, 3970-3972.

(19) Wang, M.-X.; Zhang, X.-H.; Zheng, Q.-Y. *Angew. Chem. Int. Ed.* **2004**, *43*, 838-842.

(20) Nielsen, K. A.; Cho, W.-S.; Sarova, G. H.; Petersen, B. M.; Bond, A. D.; Becher, J.; Jensen, F.; Guldi, D. M.; Sessler, J. L.; Jeppesen, J. O. *Angew. Chem. Int. Ed.* **2006**, *45*, 6848-6853.

(21) Gil-Ramírez, G. n.; Karlen, S. D.; Shundo, A.; Porfyrakis, K.; Ito, Y.; Briggs, G. A. D.; Morton, J. J. L.; Anderson, H. L. *Org. Lett.* **2010**, *12*, 3544-3547.

(22) Zhang, C.; Wang, Q.; Long, H.; Zhang, W. *J. Am. Chem. Soc.* **2011**, *133*, 20995-21001.

(23) Stefankiewicz, A. R.; Tamanini, E.; Pantoş, G. D.; Sanders, J. K. M. *Angew. Chem. Int. Ed.* **2011**, *50*, 5725-5728.

(24) Effing, J.; Jonas, U.; Jullien, L.; Plesnivy, T.; Ringsdorf, H.; Diederich, F.; Thilgen, C.; Weinstein, D. *Angew. Chem. Int. Ed.* **1992**, *31*, 1599-1602.

(25) Marois, J.-S.; Cantin, K.; Desmarais, A.; Morin, J.-F. *Org. Lett.* **2007**, *10*, 33-36.

(26) Shirakawa, M.; Fujita, N.; Shinkai, S. *J. Am. Chem. Soc.* **2003**, *125*, 9902-9903.

(27) Hosseini, A.; Taylor, S.; Accorsi, G.; Armaroli, N.; Reed, C. A.; Boyd, P. D. W. *J. Am. Chem. Soc.* **2006**, *128*, 15903-15913.

(28) Kubo, Y.; Sugasaki, A.; Ikeda, M.; Sugiyasu, K.; Sonoda, K.; Ikeda, A.; Takeuchi, M.; Shinkai, S. *Org. Lett.* **2002**, *4*, 925-928.

(29) Wu, Z.-Q.; Shao, X.-B.; Li, C.; Hou, J.-L.; Wang, K.; Jiang, X.-K.; Li, Z.-T. *J. Am. Chem. Soc.* **2005**, *127*, 17460-17468.

(30) Sun, D.; Tham, F. S.; Reed, C. A.; Chaker, L.; Burgess, M.; Boyd, P. D. W. *J. Am. Chem. Soc.* **2000**, *122*, 10704-10705.

(31) Suzuki, T.; Nakashima, K.; Shinkai, S. *Chem. Lett.* **1994**, *23*, 699-702.

(32) Haino, T.; Yanase, M.; Fukazawa, Y. *Angew. Chem. Int. Ed.* **1997**, *36*, 259-260.

(33) Iglesias-Sánchez, J. C.; Fragoso, A.; de Mendoza, J.; Prados, P. *Org. Lett.* **2006**, *8*, 2571-2574.

(34) Sygula, A.; Fronczek, F. R.; Sygula, R.; Rabideau, P. W.; Olmstead, M. M. *J. Am. Chem. Soc.* **2007**, *129*, 3842-3843.

(35) Dawe, L. N.; AlHujran, T. A.; Tran, H.-A.; Mercer, J. I.; Jackson, E. A.; Scott, L. T.; Georghiou, P. E. *Chem. Commun.* **2012**, *48*, 5563-5565.

(36) Pérez, E. M.; Sánchez, L.; Fernández, G.; Martín, N. *J. Am. Chem. Soc.* **2006**, *128*, 7172-7173.

(37) Canevet, D.; Gallego, M.; Isla, H.; de Juan, A.; Pérez, E. M.; Martín, N. *J. Am. Chem. Soc.* **2011**, *133*, 3184-3190.

(38) Li, M.-J.; Huang, C.-H.; Lai, C.-C.; Chiu, S.-H. *Org. Lett.* **2012**, *14*, 6146-6149.

(39) Czarnik, A. W.; Desvergne, J. P. *Chemosensors of Ion and Molecule Recognition, Kluwer Academic, Dordrecht.* **1997**.

(40) Lau, Y. H.; Rutledge, P. J.; Watkinson, M.; Todd, M. H. *Chem. Soc. Rev.* **2011**, *40*, 2848-2866.

(41) Lyskawa, J.; Le Derf, F.; Levillain, E.; Mazari, M.; Sallé, M.; Dubois, L.; Viel, P.; Bureau, C.; Palacin, S. *J. Am. Chem. Soc.* **2004**, *126*, 12194-12195.

(42) Zhao, Y.-P.; Wu, L.-Z.; Si, G.; Liu, Y.; Xue, H.; Zhang, L.-P.; Tung, C.-H. *J. Org. Chem.* **2007**, *72*, 3632-3639.

(43) Batista, R. M. F.; Oliveira, E.; Costa, S. P. G.; Lodeiro, C.; Raposo, M. M. M. *Org. Lett.* **2007**, *9*, 3201-3204.

(44) Kurishita, Y.; Kohira, T.; Ojida, A.; Hamachi, I. *J. Am. Chem. Soc.* **2010**, *132*, 13290-13299.

(45) Xue, L.; Liu, Q.; Jiang, H. *Org. Lett.* **2009**, *11*, 3454-3457.

(46) Kang, J.; Choi, M.; Kwon, J. Y.; Lee, E. Y.; Yoon, J. *J. Org. Chem.* **2002**, *67*, 4384-4386.

(47) Xue, H.; Tang, X.-J.; Wu, L.-Z.; Zhang, L.-P.; Tung, C.-H. *J. Org. Chem.* **2005**, *70*, 9727-9734.

(48) Liu, L.; Zhang, G.; Xiang, J.; Zhang, D.; Zhu, D. *Org. Lett.* **2008**, *10*, 4581-4584.

(49) Xue, L.; Liu, C.; Jiang, H. *Org. Lett.* **2009**, *11*, 1655-1658.

(50) Mao, J.; Wang, L.; Dou, W.; Tang, X.; Yan, Y.; Liu, W. *Org. Lett.* **2007**, *9*, 4567-4570.

(51) Guerro, M.; Carlier, R.; Boubekeur, K.; Lorcy, D.; Hapiot, P. *J. Am. Chem. Soc.* **2003**, *125*, 3159-3167.

(52) Massue, J.; Bellec, N.; Guerro, M.; Bergamini, J.-F.; Hapiot, P.; Lorcy, D. *J. Org. Chem.* **2007**, *72*, 4655-4662.

(53) Chen, G.; Mahmud, I.; Dawe, L. N.; Zhao, Y. *Org. Lett.* **2010**, *12*, 704-707.

(54) Guerro, M.; Pham, N. H.; Massue, J.; Bellec, N.; Lorcy, D. *Tetrahedron* **2008**, *64*, 5285-5290.

(55) Tucker, J. H. R.; Collinson, S. R. *Chem. Soc. Rev.* **2002**, *31*, 147-156.

(56) Ori, A.; Shinkai, S. *J. Chem. Soc., Chem. Commun.* **1995**, 1771-1772.

(57) Moore, A. N. J.; Wayner, D. D. M. *Can. J. Chem.* **1999**, *77*, 681-686.

(58) Shoji, E.; Freund, M. S. *J. Am. Chem. Soc.* **2002**, *124*, 12486-12493.

(59) Deore, B. A.; Braun, M. D.; Freund, M. S. *Macromol. Chem. Phys.* **2006**, *207*, 660-664.

(60) Nicolas, M.; Fabre, B.; Simonet, J. *Electrochim. Acta* **2001**, *46*, 1179-1190.

(61) Arimori, S.; Ushiroda, S.; Peter, L. M.; Jenkins, A. T. A.; James, T. D. *Chem. Commun.* **2002**, 2368-2369.

(62) Shao, M.; Zhao, Y. *Tetrahedron Lett.* **2010**, *51*, 2508-2511.

(63) Bendikov, M.; Wudl, F.; Perepichka, D. F. *Chem. Rev.* **2004**, *104*, 4891-4946.

(64) Canevet, D.; Salle, M.; Zhang, G.; Zhang, D.; Zhu, D. *Chem. Commun.* **2009**, 2245-2269.

(65) Williams, J. M.; Kini, A. M.; Wang, H. H.; Carlson, K. D.; Geiser, U.; Montgomery, L. K.; Pyrka, G. J.; Watkins, D. M.; Kommers, J. M. *Inorg. Chem.* **1990**, *29*, 3272-3274.

(66) Nielsen, K. A.; Jeppesen, J. O.; Levillain, E.; Thorup, N.; Becher, J. *Org. Lett.* **2002**, *4*, 4189-4192.

(67) Gontier, E.; Bellec, N.; Brignou, P.; Gohier, A.; Guerro, M.; Roisnel, T.; Lorcy, D. *Org. Lett.* **2010**, *12*, 2386-2389.

(68) Loosli, C.; Jia, C.; Liu, S.-X.; Haas, M.; Dias, M.; Levillain, E.; Neels, A.; Labat, G.; Hauser, A.; Decurtins, S. *J. Org. Chem.* **2005**, *70*, 4988-4992.

(69) Geng, Y.; Wang, X.-J.; Chen, B.; Xue, H.; Zhao, Y.-P.; Lee, S.; Tung, C.-H.; Wu, L.-Z. *Chem. Eur. J.* **2009**, *15*, 5124-5129.

(70) Bryce, M. R.; Devonport, W.; Moore, A. J. *Angew. Chem. Int. Ed.* **1994**, *33*, 1761-1763.

(71) Díaz, M. C.; Illescas, B. M.; Martín, N.; Viruela, R.; Viruela, P. M.; Ortí, E.; Brede, O.; Zilbermann, I.; Guldi, D. M. *Chem. Eur. J.* **2004**, *10*, 2067-2077.

(72) Chen, G.; Dawe, L.; Wang, L.; Zhao, Y. *Org. Lett.* **2009**, *11*, 2736-2739.

(73) Chen, G.; Wang, L.; Thompson, D. W.; Zhao, Y. *Org. Lett.* **2008**, *10*, 657-660.

(74) Liang, S.; Chen, G.; Peddle, J.; Zhao, Y. *Chem. Commun.* **2012**, *48*, 3100-3102.

(75) de Miguel, G.; Wielopolski, M.; Schuster, D. I.; Fazio, M. A.; Lee, O. P.; Haley, C. K.; Ortiz, A. L.; Echegoyen, L.; Clark, T.; Guldi, D. M. *J. Am. Chem. Soc.* **2011**, *133*, 13036-13054.

(76) Lorcy, D.; Carlier, R.; Robert, A.; Tallec, A.; Le Magueres, P.; Ouahab, L. *J. Org. Chem.* **1995**, *60*, 2443-2447.

(77) Bouzan, S.; Chen, G.; Mulla, K.; Dawe, L. N.; Zhao, Y. *Org. Biomol. Chem.* **2012**, *10*, 7673-7676.

(78) Yamashita, Y.; Tomura, M.; Badruz Zaman, M. *Chem. Commun.* **1998**, 1657-1658.

(79) Chen, G.; Mahmud, I.; Dawe, L. N.; Daniels, L. M.; Zhao, Y. *J. Org. Chem.* **2011**, *76*, 2701-2715.

(80) Shahnaz, M.; Kaura, S.; Shubhlata; Prasad, D. N.; Dev, D. *Int. J. Bioassays.* **2013**, *2*, 1317-1321.

(81) Suzuki, T.; Ota, Y.; Kasuya, Y.; Mutsuga, M.; Kawamura, Y.; Tsumoto, H.; Nakagawa, H.; Finn, M. G.; Miyata, N. *Angew. Chem. Int. Ed.* **2010**, *49*, 6817-6820.

(82) Chang, K.-C.; Su, I.-H.; Senthilvelan, A.; Chung, W.-S. *Org. Lett.* **2007**, *9*, 3363-3366.

(83) Park, S. Y.; Yoon, J. H.; Hong, C. S.; Souane, R.; Kim, J. S.; Matthews, S. E.; Vicens, J. *J. Org. Chem.* **2008**, *73*, 8212-8218.

(84) Grundberg, H. E.; Wendt, O. F.; Nilsson, U. J. *Tetrahedron Letters* **2004**, *45*, 6083-6085.

(85) Abu-Orabi, S. T.; Harmon, R. E. *J. Chem. Eng. Data.* **1986**, *31*, 379-380.

Chapter 5

Conclusions and Future Work

In conclusion, I shall begin with reflecting, at the methodological level, on the key steps that make most of my projects successfully implemented. One of underlying themes that run across the diversified research projects in this thesis is the development of efficient synthetic access to novel functional organic materials based on π-conjugated oligomers, DTF derivatives, and TTFV analogues, with the intention to contribute new synthetic tools and materials in the field of materials science. In this context, the power of click reaction has been judiciously utilized and the results demonstrated in the synthetic work have clearly testified to its wide-ranging applicability in modularly making complex functional structures. In parallel, the use of comparative approach in investigating the molecular and supramolecular properties has proven to be highly valuable in gaining understanding on how to control and fine-tune the performances of functional molecular materials or devices at the molecular level.

In the first project, a series of fluorescent saccharide sensors made up of π-conjugated oligomers functionalized with phenylboronic acids were synthesized in three different conjugated structures (linear, cruciform, and H-shaped). As synthetic methodologies, the combination of Sonogashira coupling and Horner-Wittig olefination reactions operated effectively in preparing these OPE/OPV co-oligomers. In terms of fluorescence sensing for saccharides, the markedly different fluorescence turn-on

responses displayed by cruciform **194** and other oligomers **195** and **196** indicate the importance of the fluorophore effect in controlling their molecular sensing performances. For the detailed fluorescence sensing mechanism(s), current experimental results correlate the fluorescence turn-on behavior to a de-aggregation effect induced by saccharide binding events in aqueous media. However, parameters governing the de-aggregation process still await further clarification. Investigations on the saccharide binding with H-shaped oligomers provided a reasonable explanation on the fluorescence sensing mechanism; that is, the fluorescence properties of the oligomer fluorophores are highly environment-sensitive. So far, with limited data from mechanistic studies, the "environment sensitivity" argument has not been convincingly confirmed yet, while other rationalizations such as the typically used photoinduced electron/energy transfer mechanism still remain plausible. Studies on the detailed photophysical mechanism(s) involved in the sensing processes should therefore be carried out through collaboration with Prof. David W. Thompson' group in the future work. Nonetheless, the results achieved from the current study have demonstrated that this new environment-sensitive fluorophore strategy intermarried with the powerful click chemistry would open a new avenue for the development of efficient and selective fluorescent sensors and modular sensor arrays for saccharides.

In the second project, DTF-functionalized conjugated oligomers were conveniently prepared by Horner-Wittig reaction as a key synthetic strategy. Our results have disclosed that fullerenes can act as efficient photo-sensitizer to induce an oxidative cleavage of the DTF double bonds in DTF-functionalized oligomers. The aldehyde-

oligomer products resulting from this unique photochemical process show substantially increased fluorescence quantum yields in comparison with the corresponding DTF-oligomers. Such properties may be useful for developing ultra-sensitive detection of fullerenes. Furthermore, the DTF-oligomers not only show the ability to bind with SWNTs in chloroform, but also can release SWNTs as controlled by solvent effects. The reversible supramolecular interactions with SWNTs thus point to a promising application in SWNT purification techniques. In the future work, not only fundamental understanding on the selective interactions between DTF-oligomers and SWNTs need to be established, but practical techniques to reversibly control the dispersion and release of SWNTs with easy and effective stimuli (e.g., solvent, pH, redox) must be pursued. These challenges can be best addressed through a rational molecular design approach based on well-understood structure-property relationships.

In the last project, the click reaction generated TTFV macrocycles and TTFV tweezers serve as efficient supramolecular hosts to bind with fullerenes, saccharides, anions, and certain transition metal ions. It is evident that the triazole group resulting from the click reaction acts as a non-innocent linker, assisting the binding events through π-stacking and hydrogen bonding. In the meantime, selectivity of binding with certain guest molecules, such as between C_{60} and C_{70} fullerenes, can be controllable by tailoring the polyaromatic groups in the TTFV molecular tweezers. For the first time, a highly selective fluorescence turn-on sensing for C_{70} fullerene has been achieved by the click synthesized TTFV-anthracene tweezers. Future work of immobilizing such tweezers on stationary phases, such as silica gels or polymer resins, is logically conceived so as to

develop efficient chromatographic separation techniques for various fullerenes. Furthermore, supramolecular self-assembly of the TTFV-based macrocycles and tweezers on various metal surfaces is envisioned to be a very intriguing and fruitful research direction with significant impact in the fields of solid-state optoelectronic and sensory devices.

Appendix

^{1}H NMR and ^{13}C NMR spectra of unpublished compounds

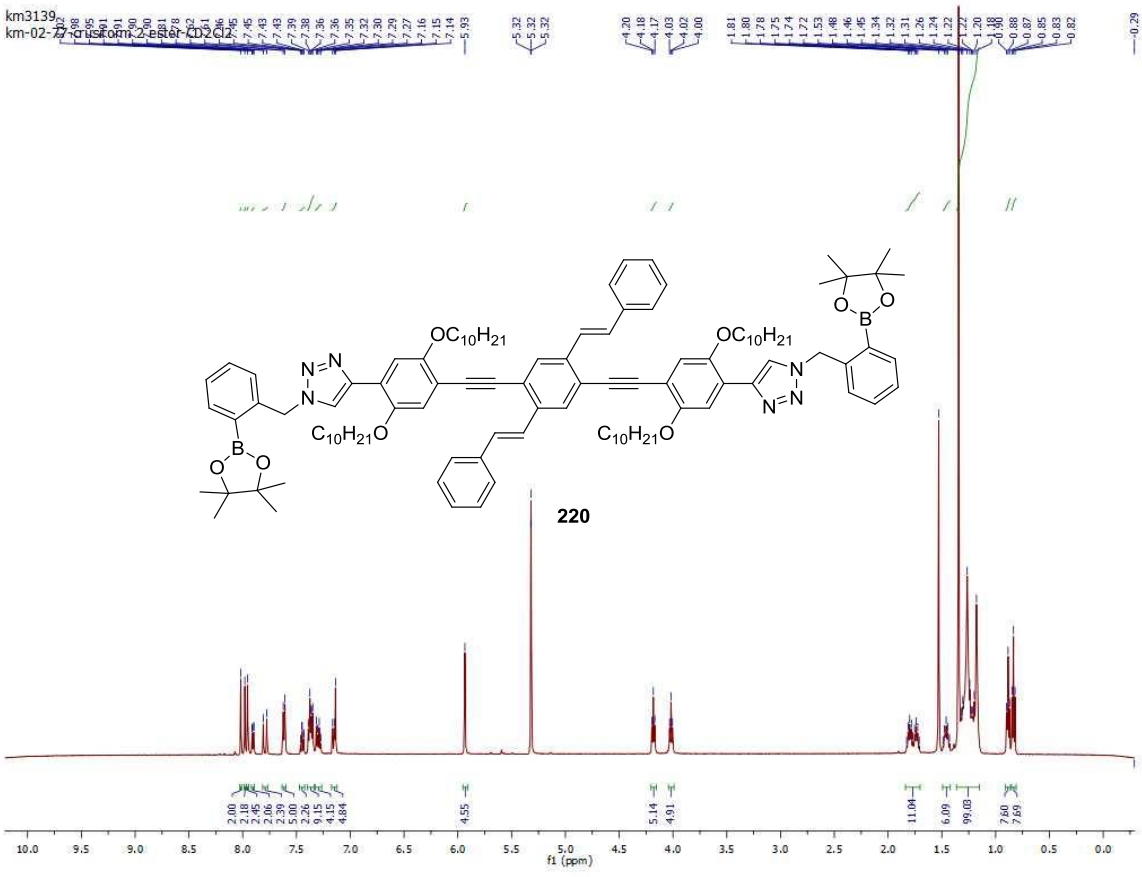

Figure S1: ^{1}H NMR (500 MHz, CD_2Cl_2) of compound **220**

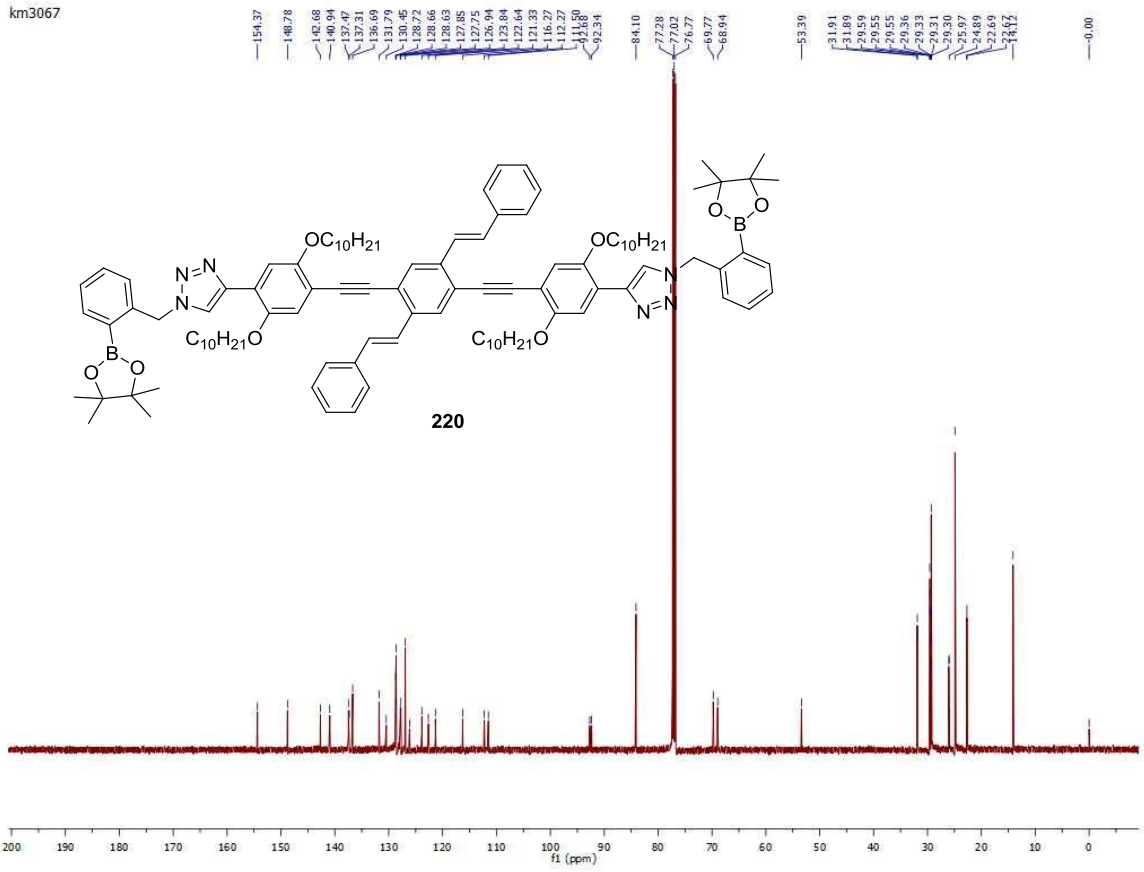

Figure S2: ^{13}C NMR (75 MHz, $CDCl_3$) of compound **220**

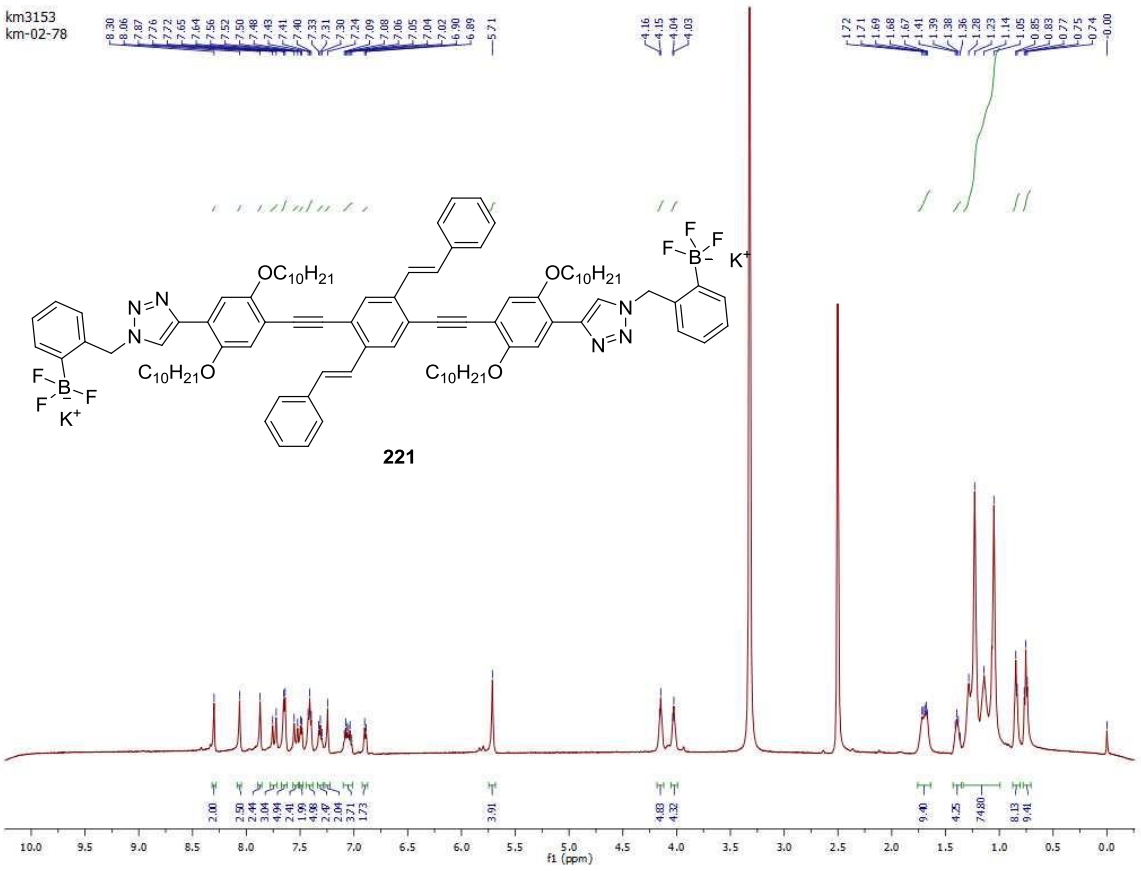

Figure S3: ^{1}H NMR (500 MHz, DMSO-d_6) of compound **221**

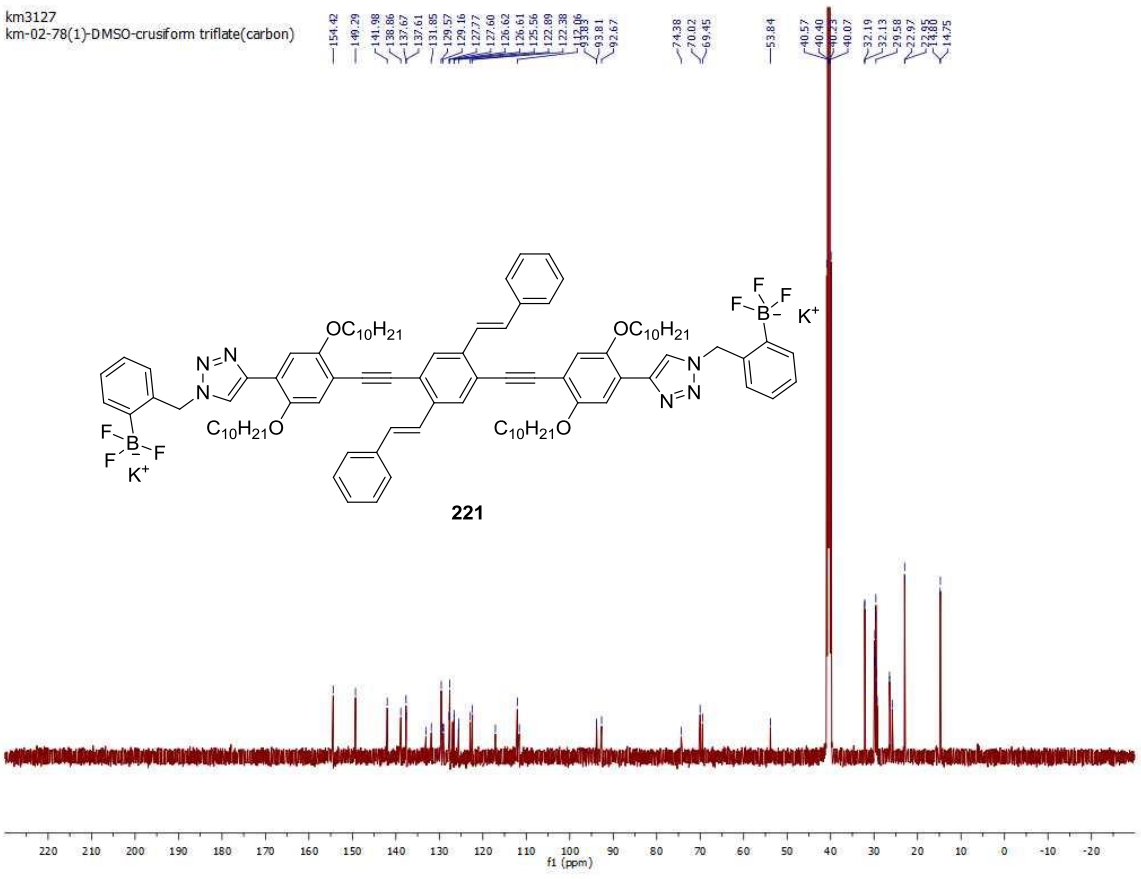

Figure S4: ^{13}C NMR (75 MHz, DMSO-d_6) of compound **221**

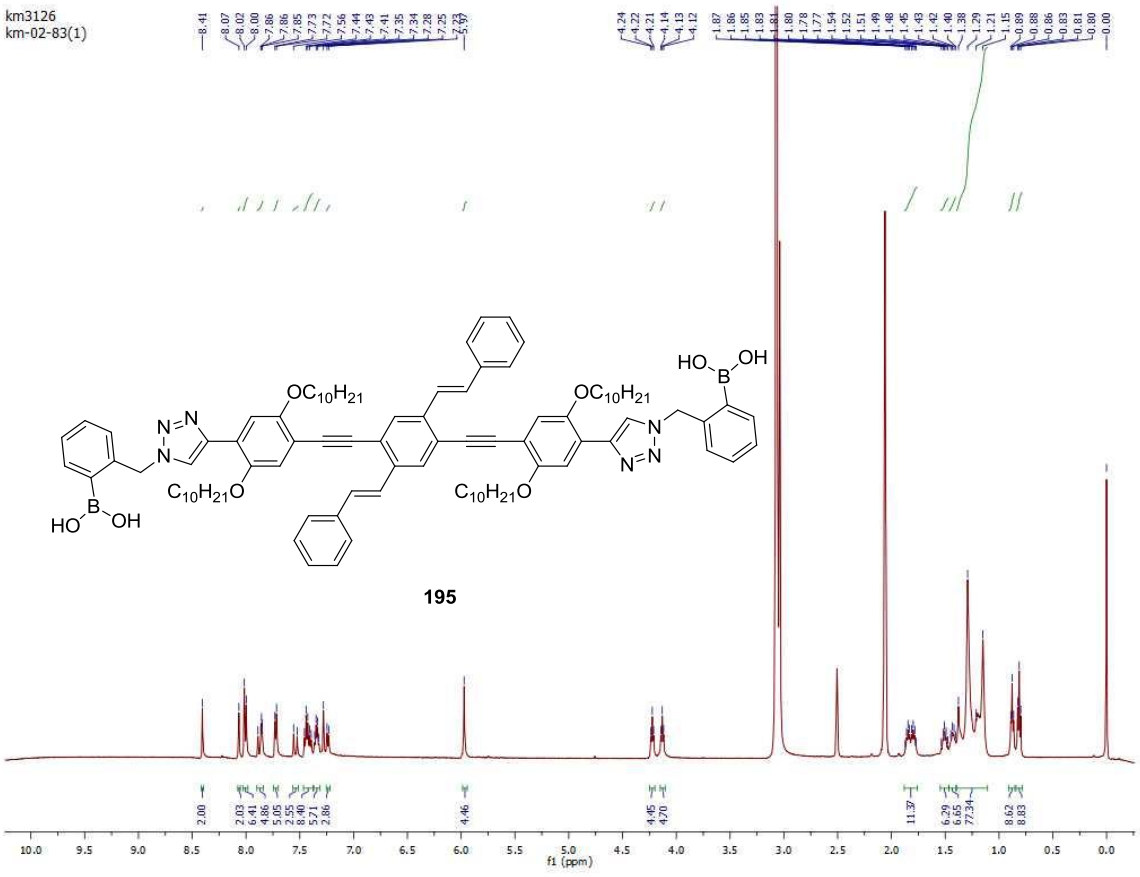

Figure S5: ^{1}H NMR (500 MHz, Acetone-d_6/DMSO-d_6) of compound **221**

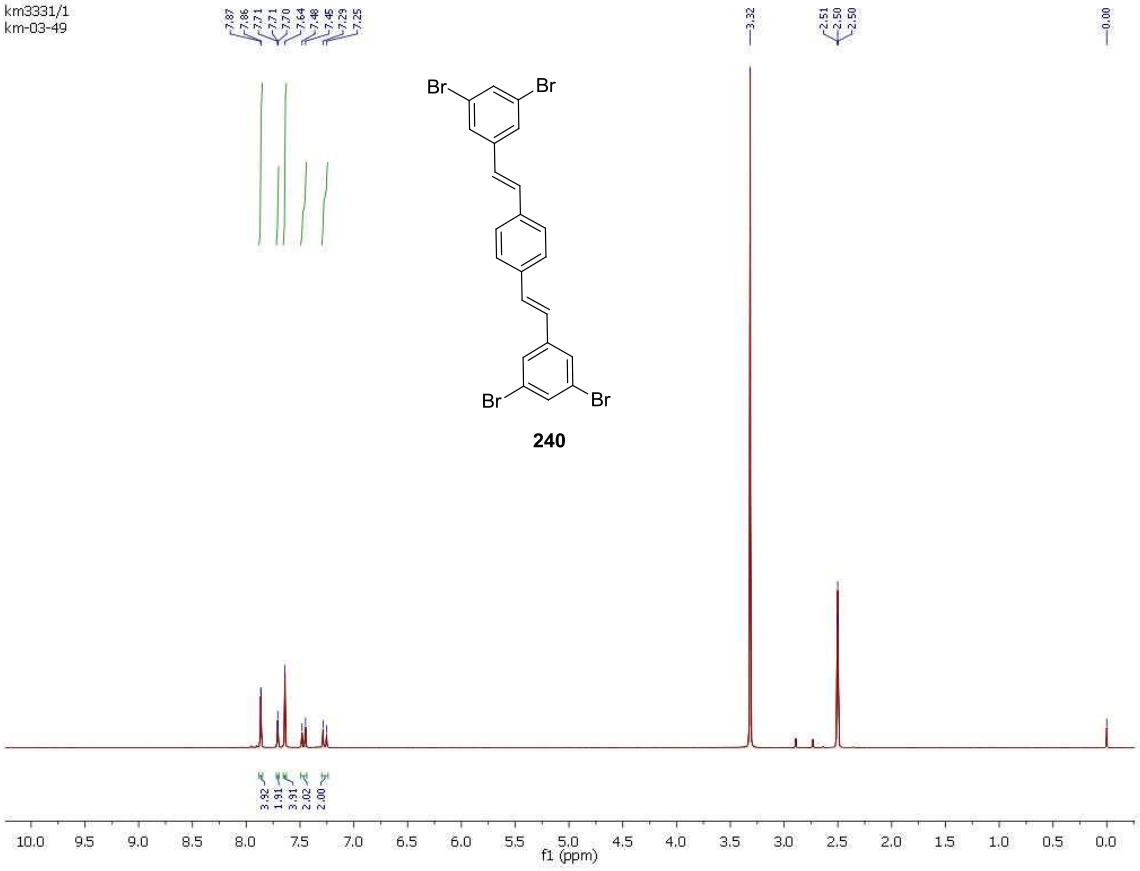

Figure S6: ^{1}H NMR (500 MHz, DMSO-d_6) of compound **240**

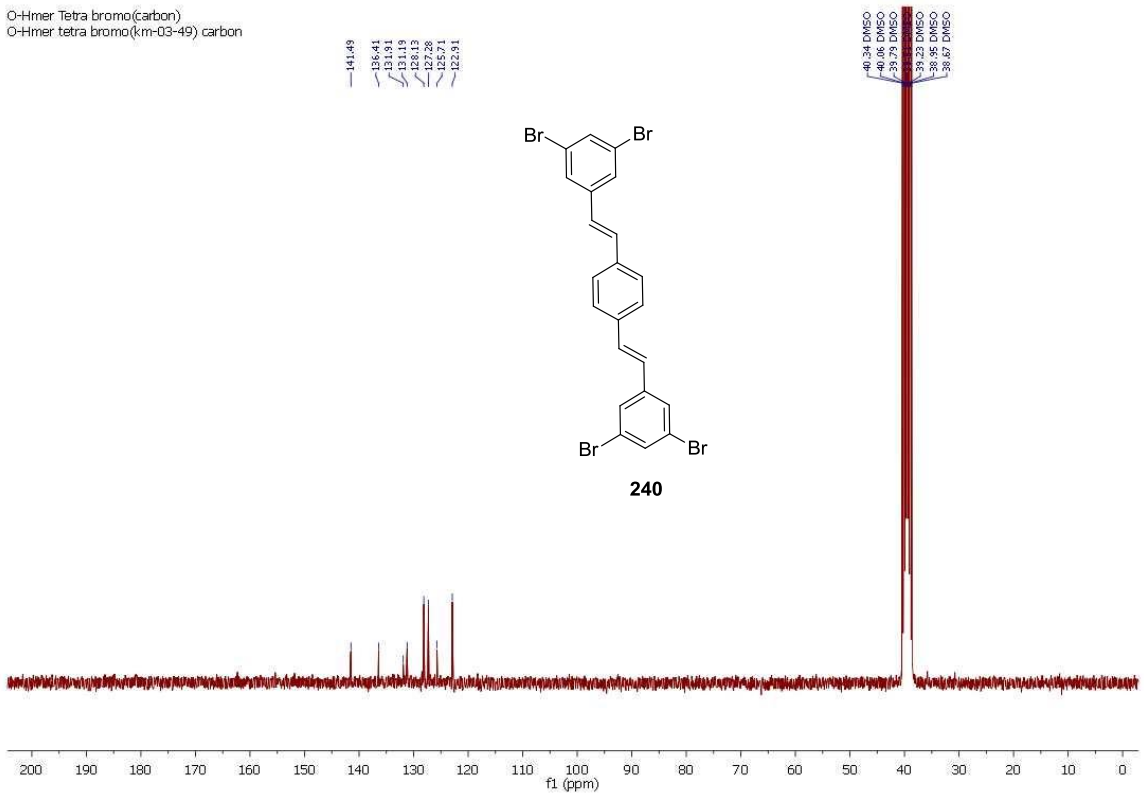

Figure S7: ^{13}C NMR (75 MHz, DMSO-d_6) of compound **240**

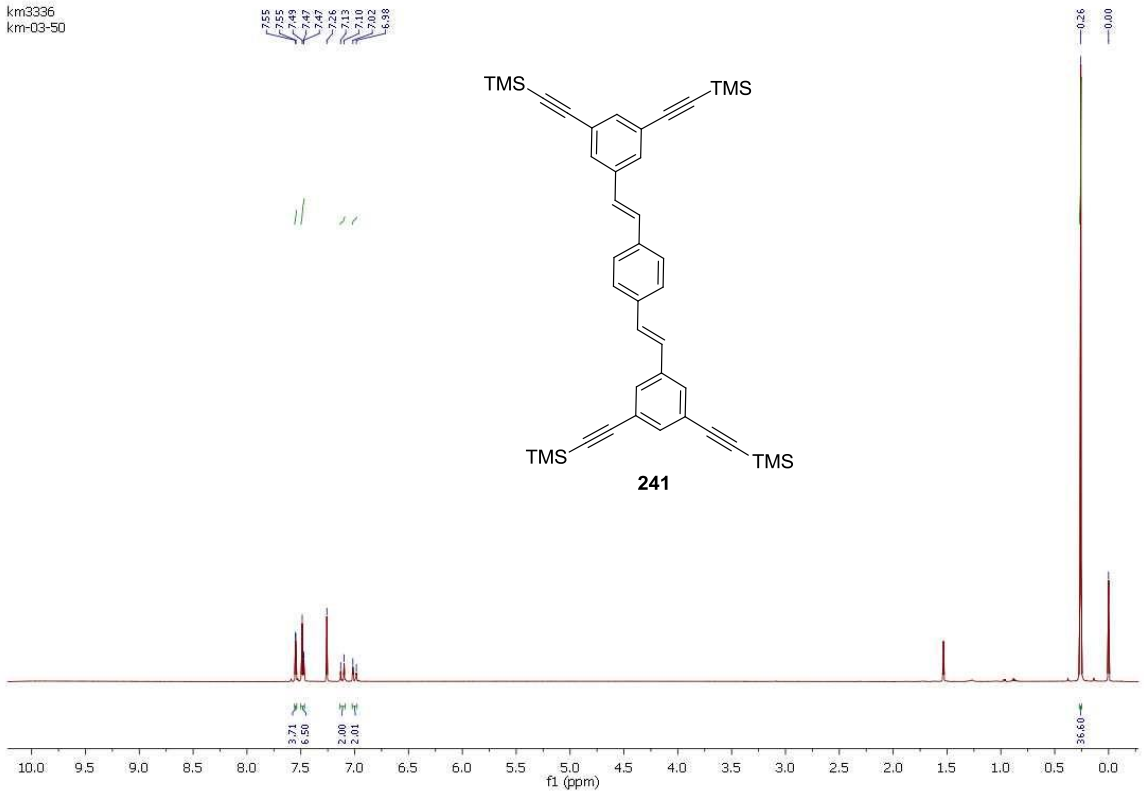

Figure S8: ^{1}H NMR (500 MHz, $CDCl_3$) of compound **241**

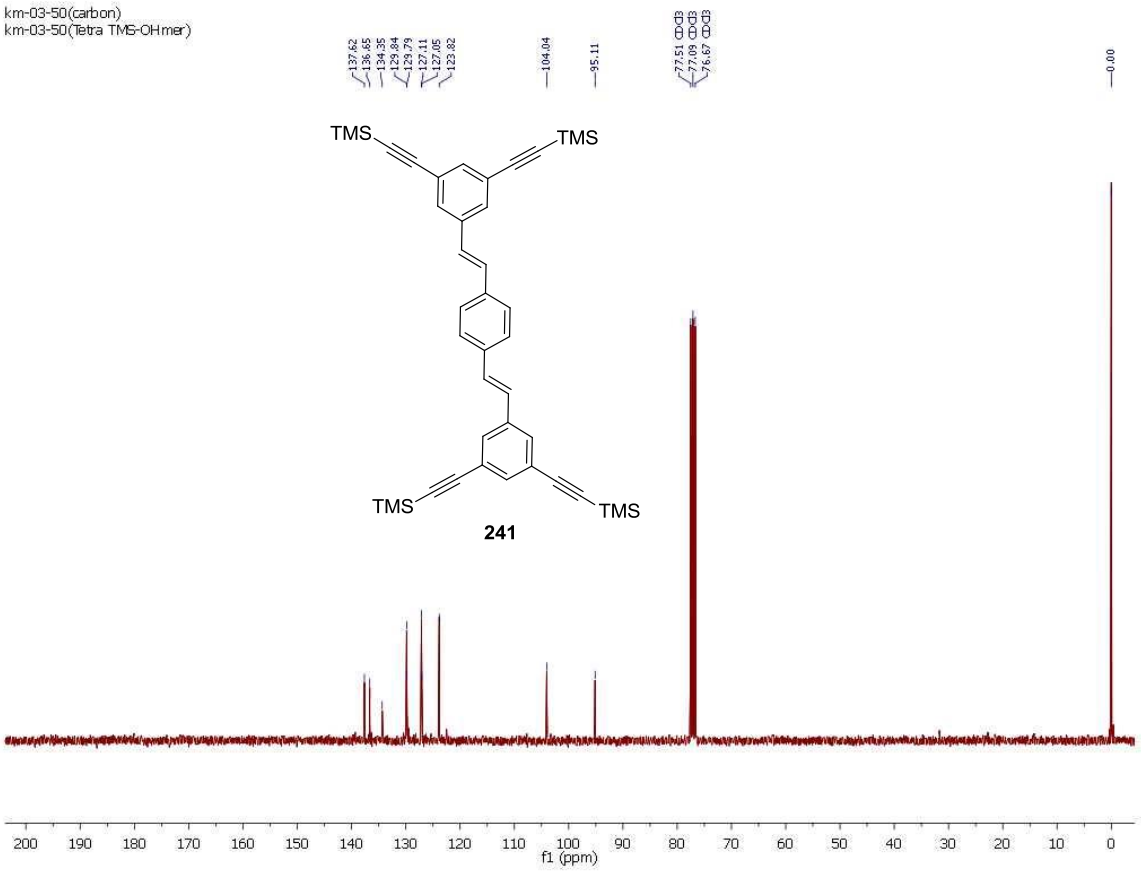

Figure S9: ^{13}C NMR (75 MHz, $CDCl_3$) of compound **241**

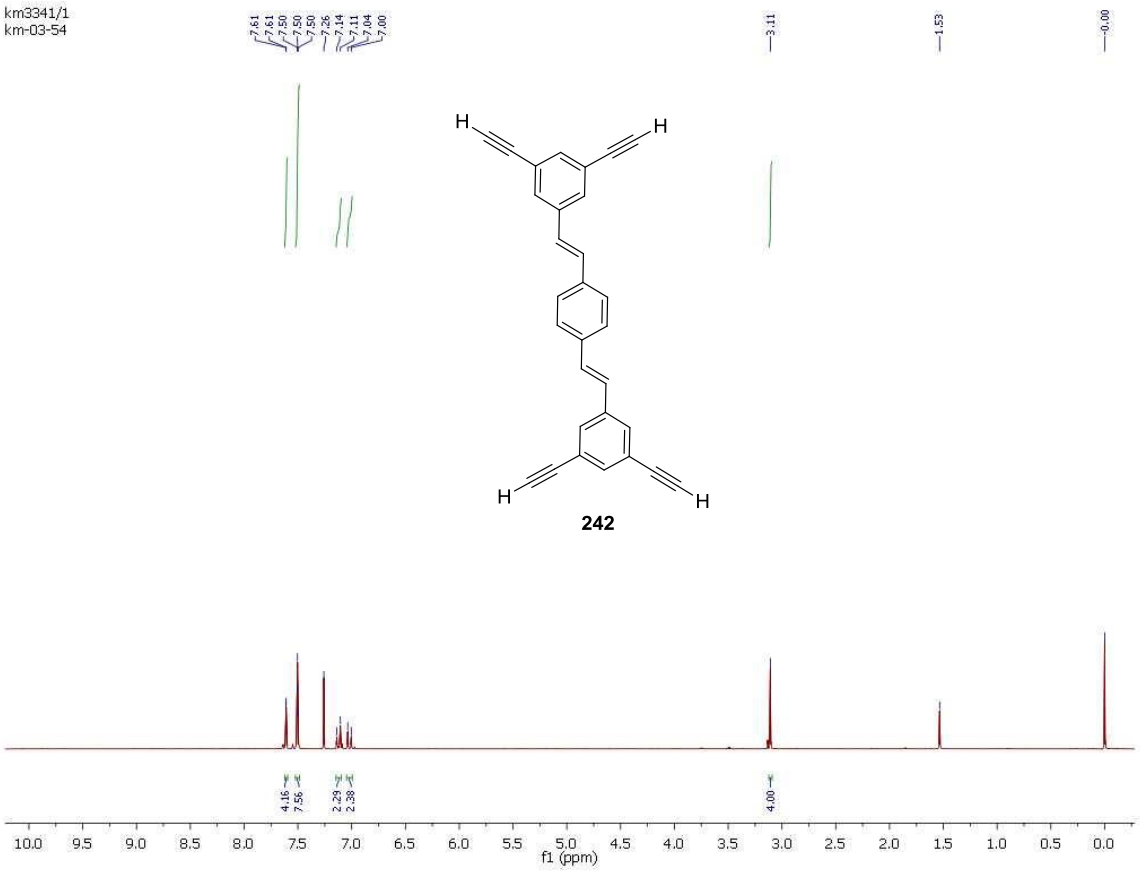

Figure S10: ^{1}H NMR (500 MHz, $CDCl_3$) of compound **242**

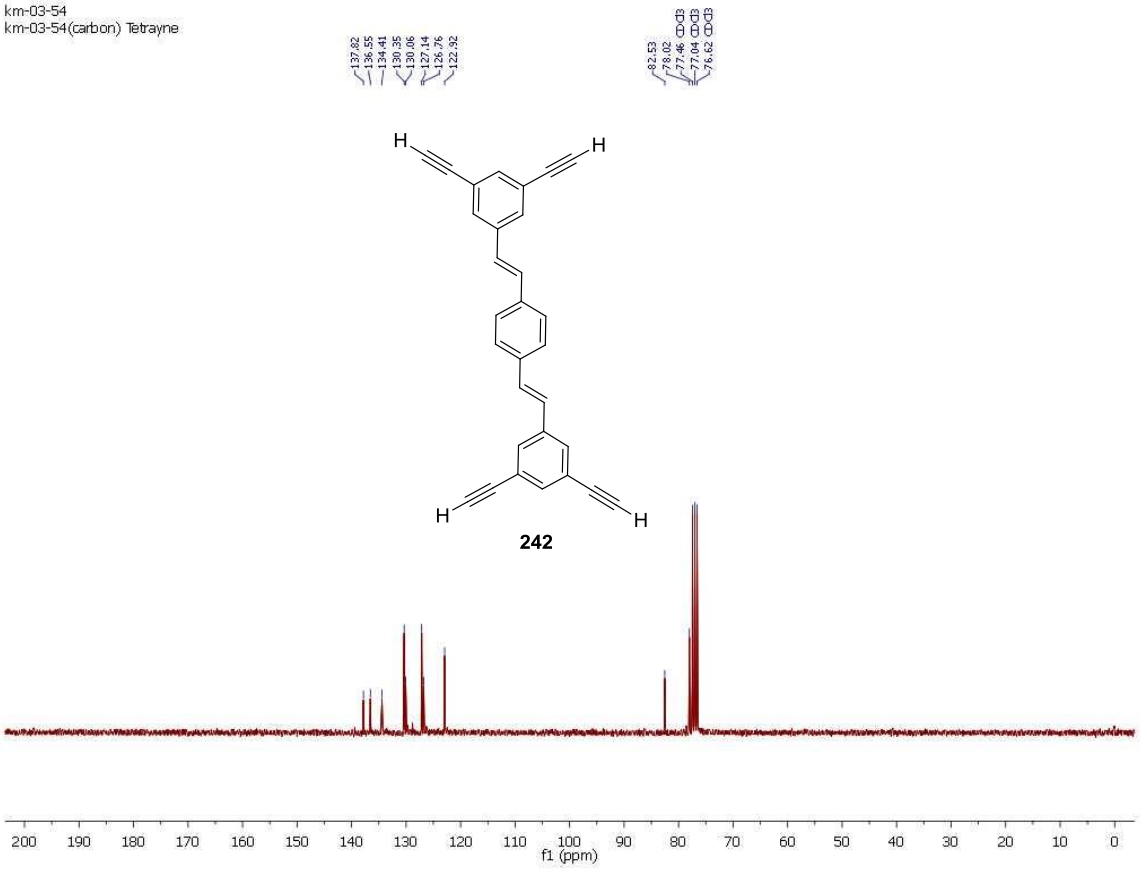

Figure S11: ^{13}C NMR (75 MHz, $CDCl_3$) of compound **242**

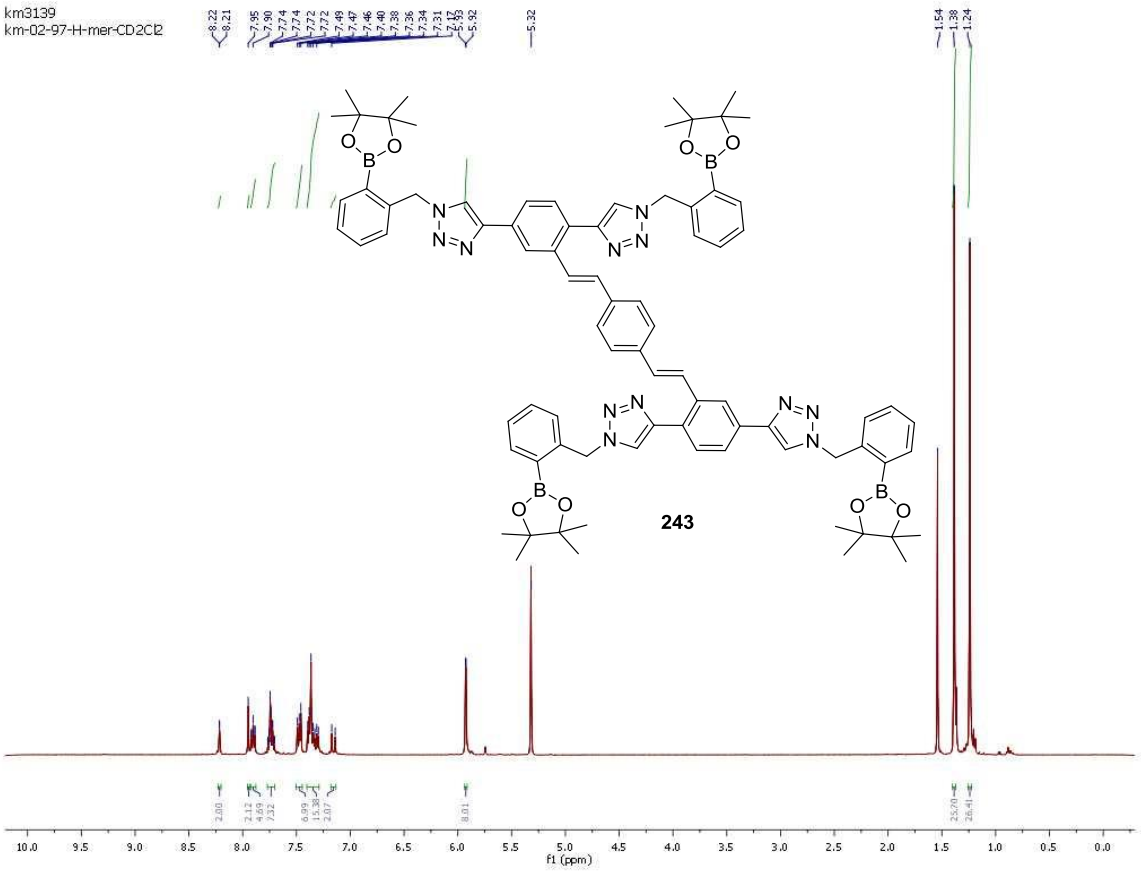

Figure S12: ^{1}H NMR (500 MHz, CD_2Cl_2) of compound **243**

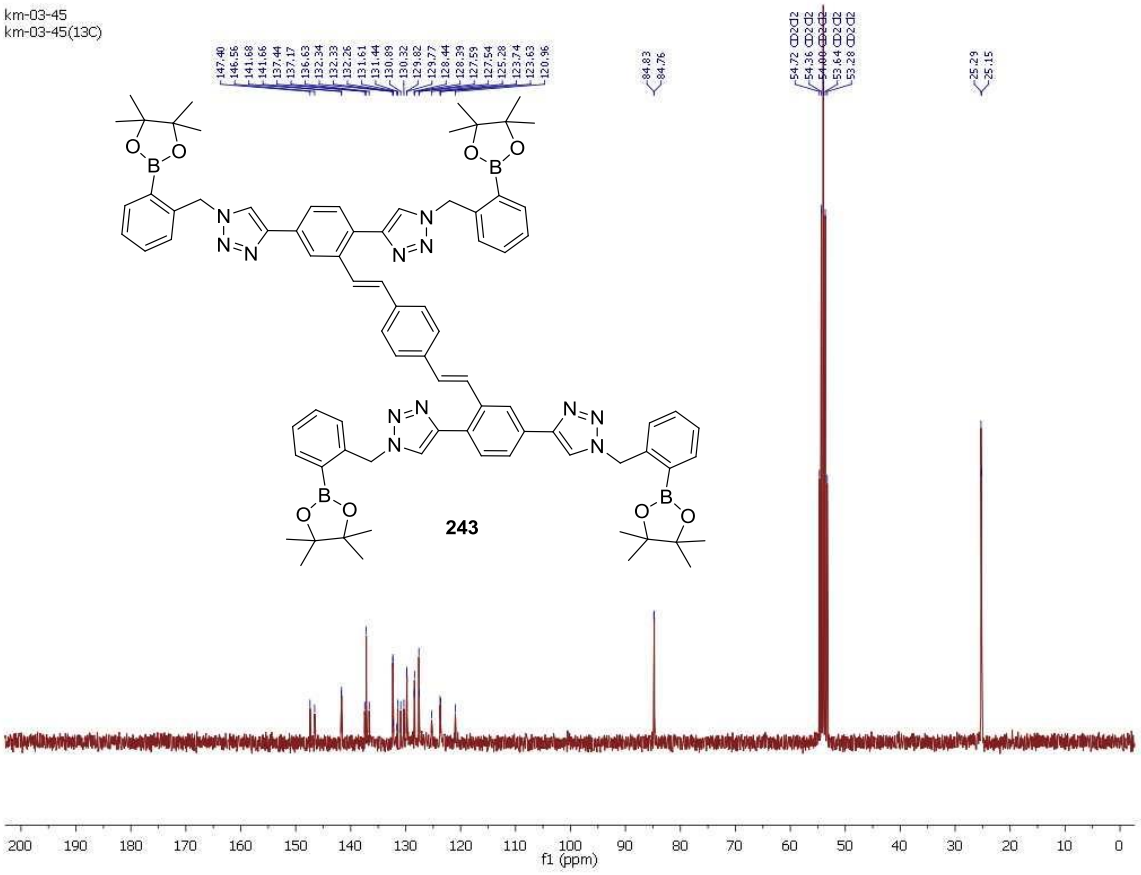

Figure S13: ^{13}C NMR (75 MHz, CD_2Cl_2) of compound **243**

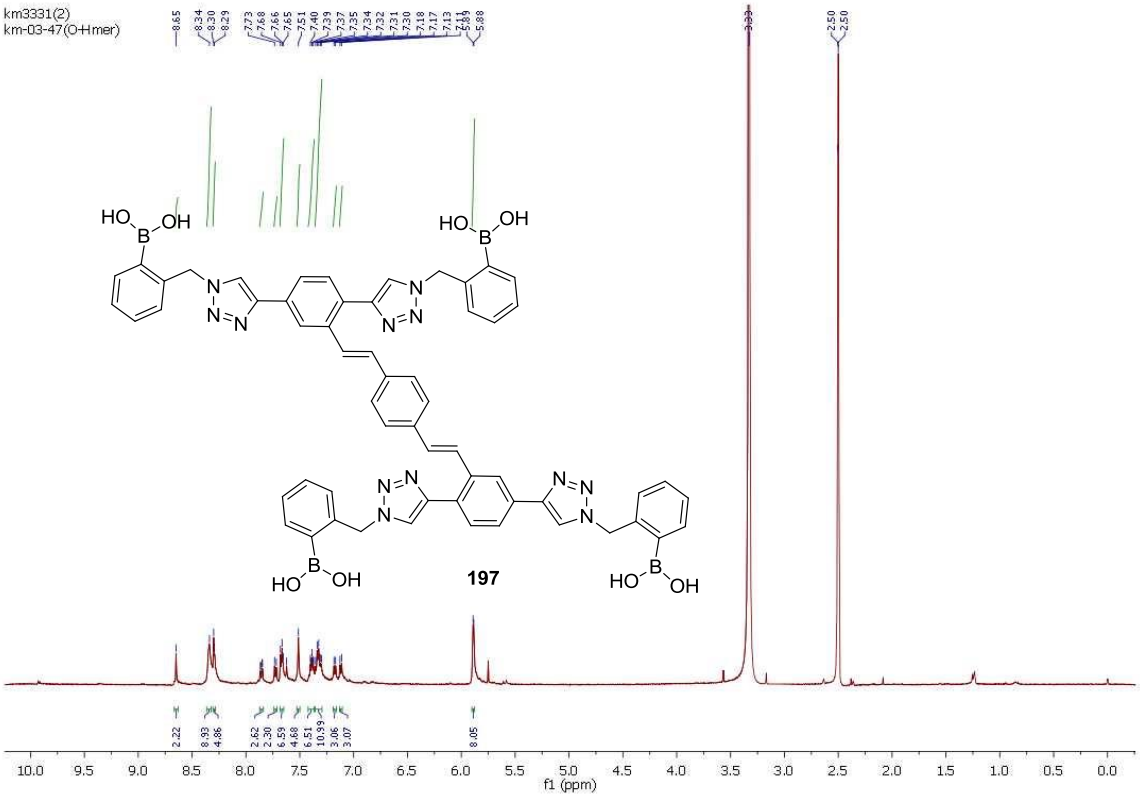

Figure S14: ^{1}H NMR (500 MHz, DMSO-d_6) of compound **197**

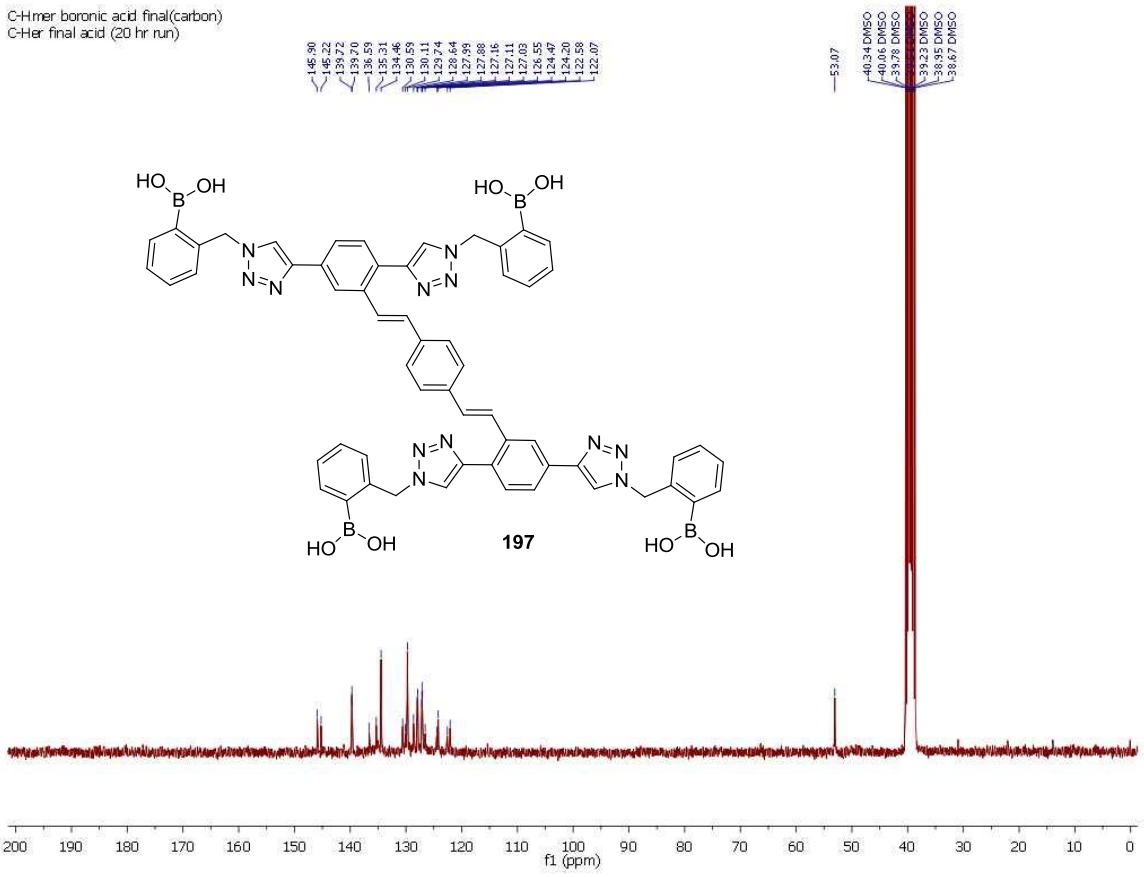

Figure S15: ^{13}C NMR (75 MHz, DMSO-d_6) of compound **197**

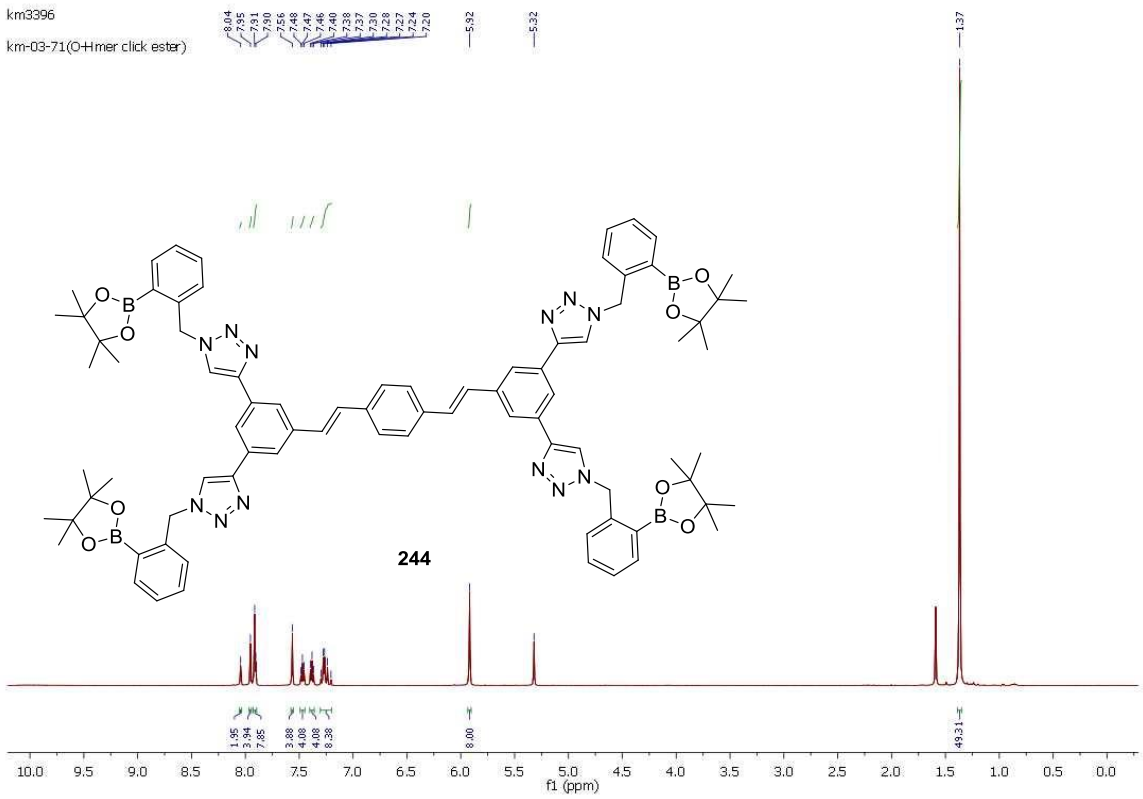

Figure S16: ^{1}H NMR (500 MHz, CD_2Cl_2) of compound **244**

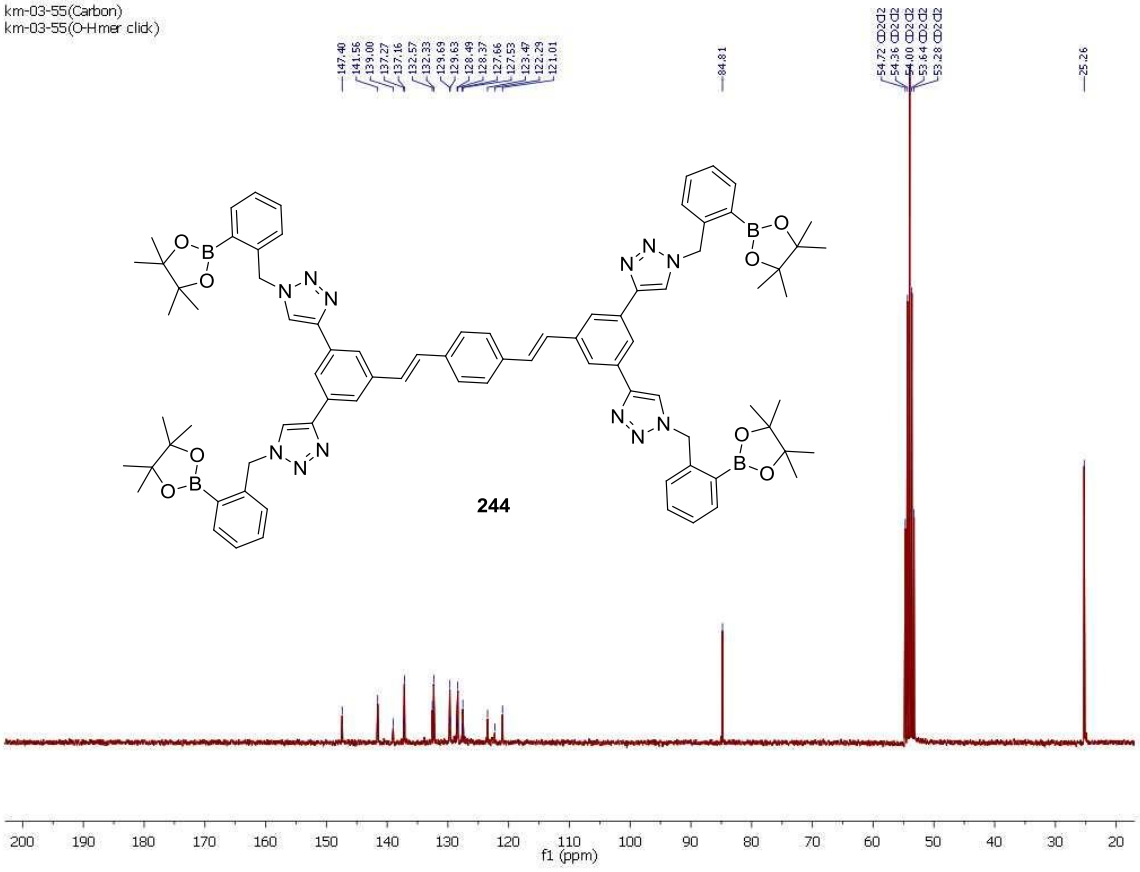

Figure S17: ^{13}C NMR (75 MHz, CD_2Cl_2) of compound **244**

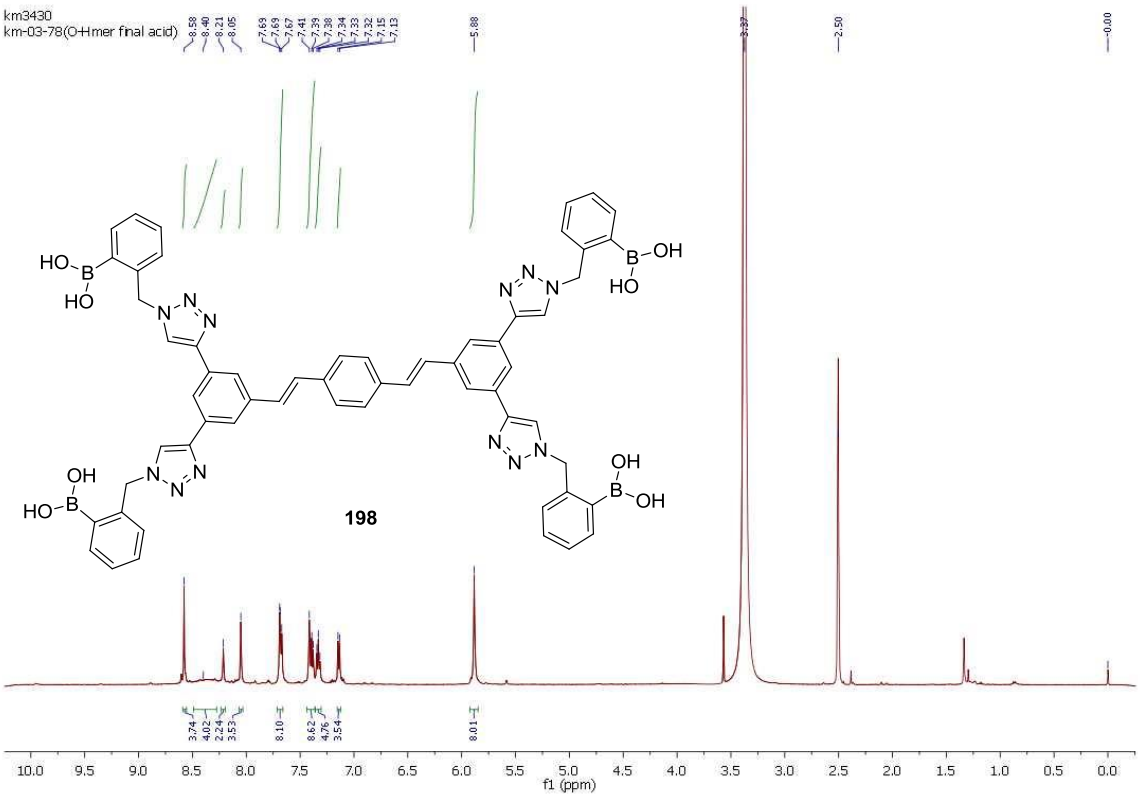

Figure S18: ^{1}H NMR (500 MHz, DMSO-d_6) of compound **198**

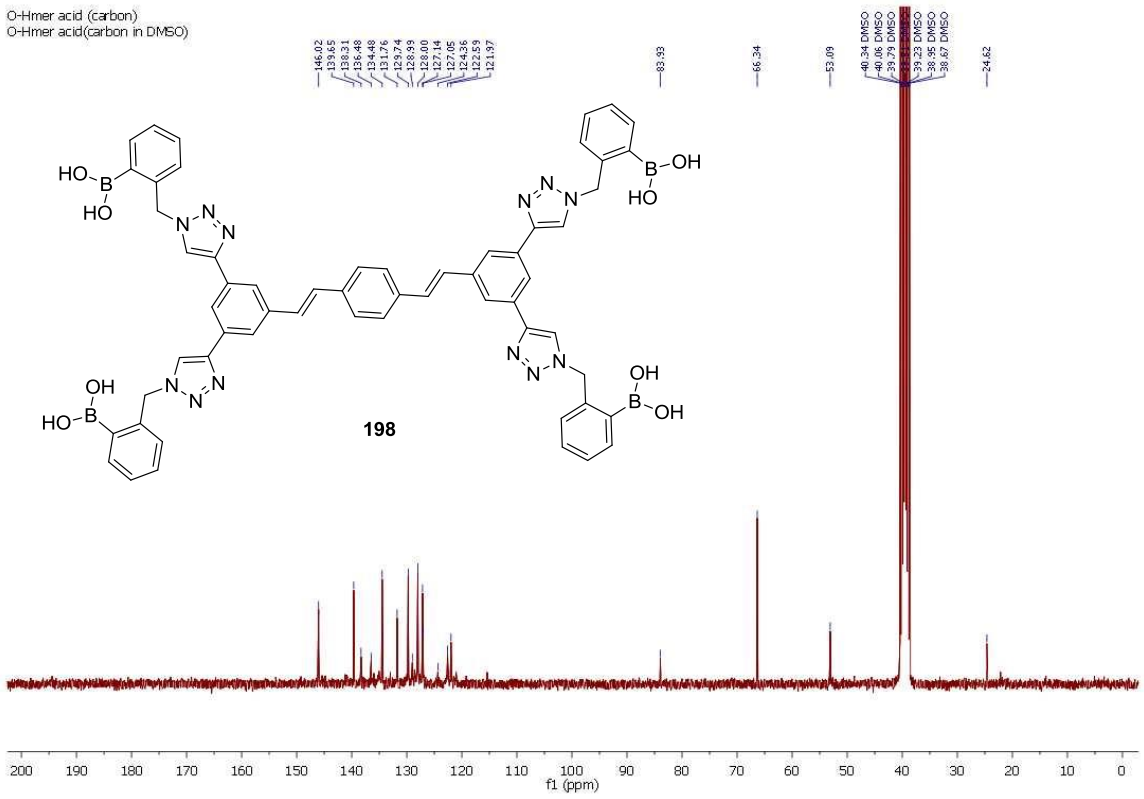

Figure S19: ^{13}C NMR (75 MHz, DMSO-d_6) of compound **198**

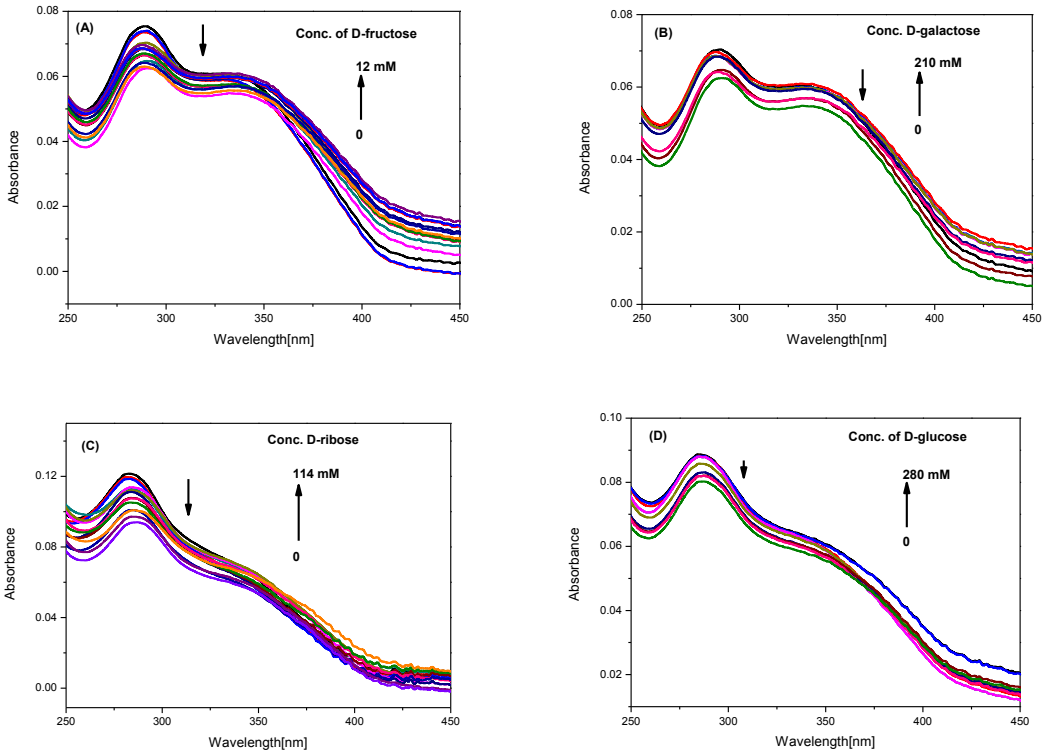

Figure S20: UV-Vis titration of **194** (11.8 µM) with D-fructose in an aqueous buffer solution (pH 7.41) at 298 ± 3 K (B) Fluorescence titration of **194** (13.8 µM) with D-galactose in an aqueous buffer solution (pH 7.41) at 298 ± 3 K (C) Fluorescence titration of **194** (13.8 µM) with D-ribose in an aqueous buffer solution (pH 7.41) at 298 ± 3 K (D) Fluorescence titration of **194** (12.0 µM) with D-glucose in an aqueous buffer solution (pH 7.41) at 298 ± 3 K.

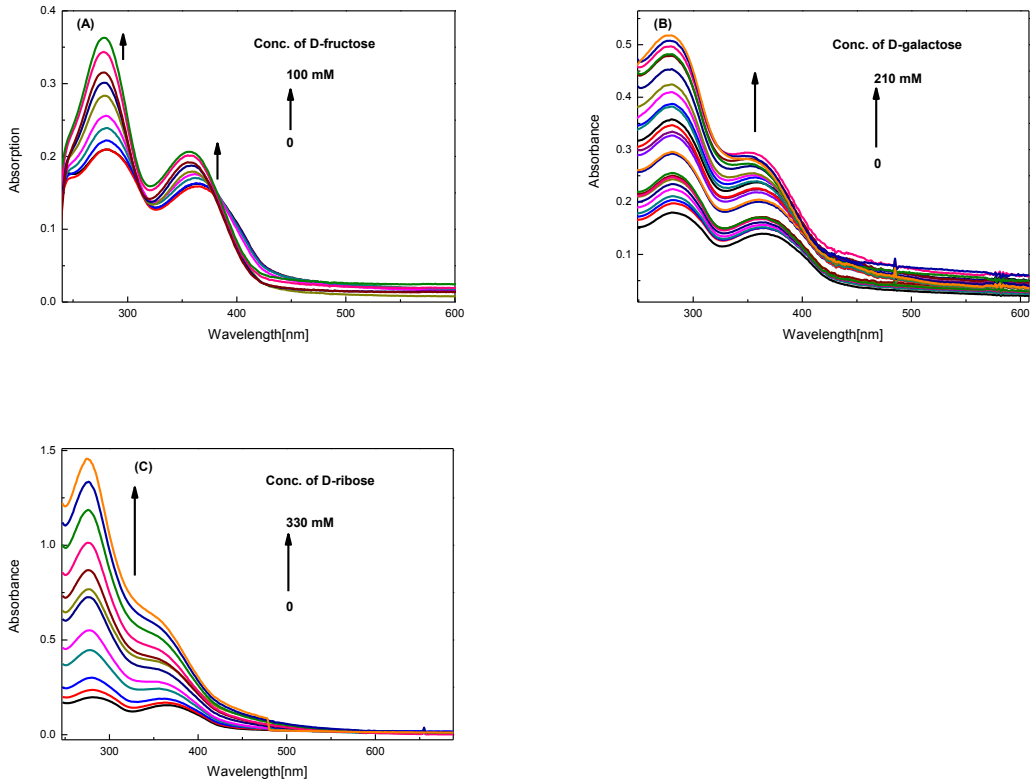

Figure S21: UV-Vis titration of H-mer **197** (7.67 µM) with (A) D-fructose, (B) D-galactose, (C) D-ribose in an aqueous phosphate buffer solution (pH 7.41) at 298 ± 3 K.

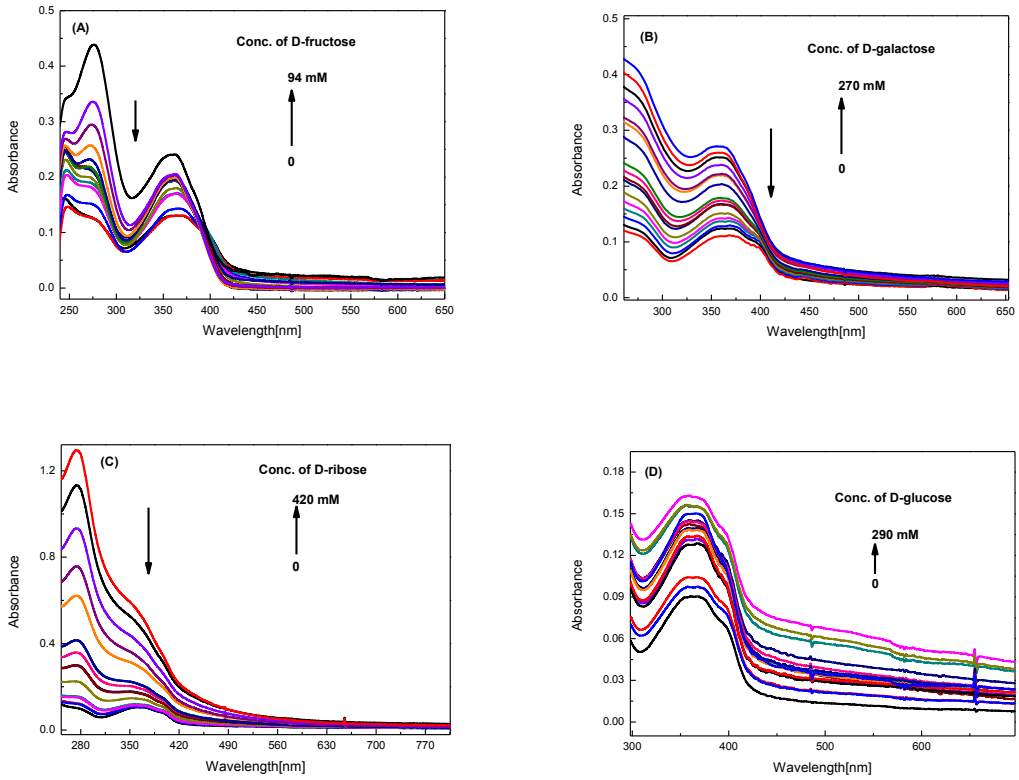

Figure S22: Fluorescence titration of H-mer **198** (7.36 µM) with (E) D-fructose, (F) D-galactose, (G) D-ribose, and (H) D-glucose in an aqueous phosphate buffer solution (pH 7.41) at 298 ± 3 K.

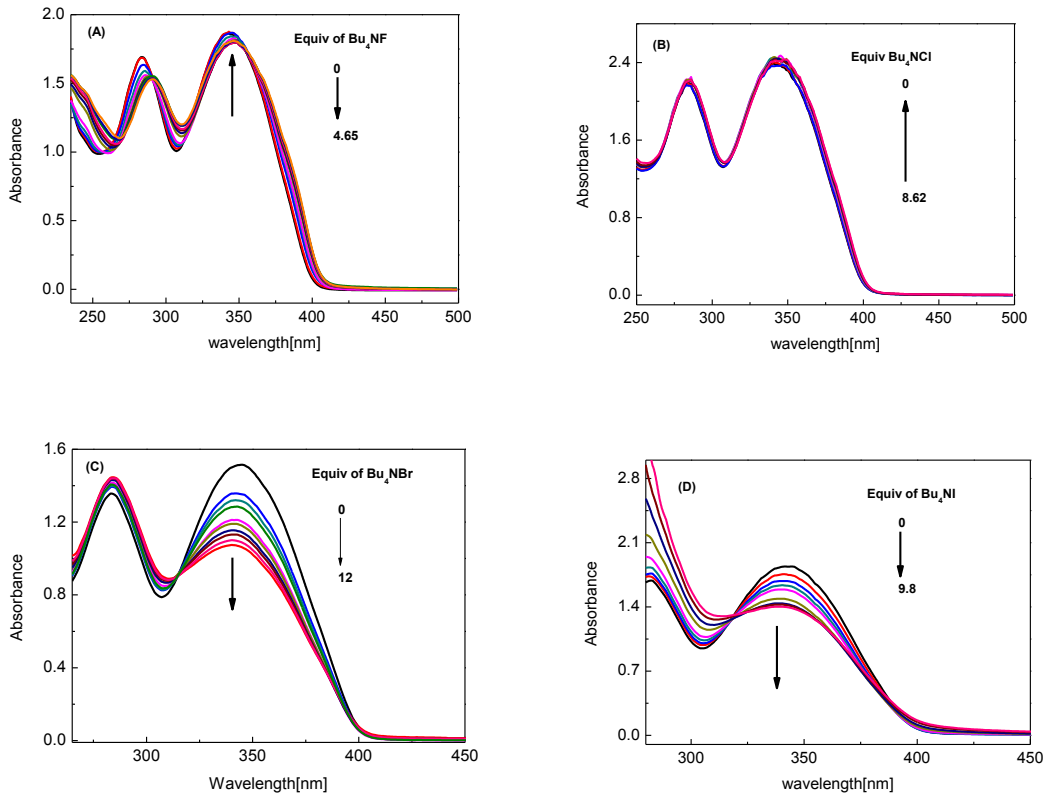

Figure S23: (A) UV-Vis titration of boronate-oligomer fluorophore **211** (39.5 µM) with *n*-Bu_4NF (B) UV-Vis titration of boronate-oligomer fluorophore **211** (36.0 µM) with *n*-Bu_4NCl (C) UV-Vis titration of boronate-oligomer fluorophore **211** (42.2 µM) with *n*-Bu_4NBr, and (D) UV-Vis titration of boronate-oligomer fluorophore **211** (38.6 µM) with *n*-Bu_4NI in THF at 298 K.

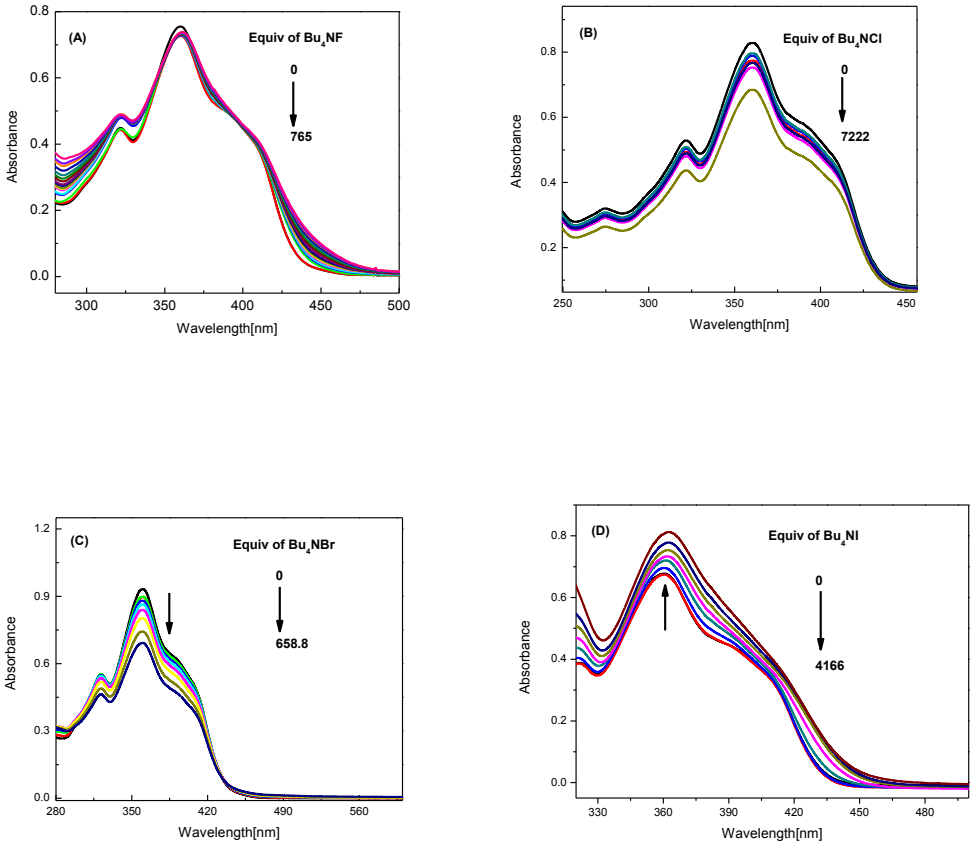

Figure S24 : UV-Vis titration of boronate-oligomer fluorophore **220** (10.0 µM) with (A) *n*-Bu_4NF (B) *n*-Bu_4NCl (C) *n*-Bu_4NBr, and (D) *n*-Bu_4NI in THF at 298 K.

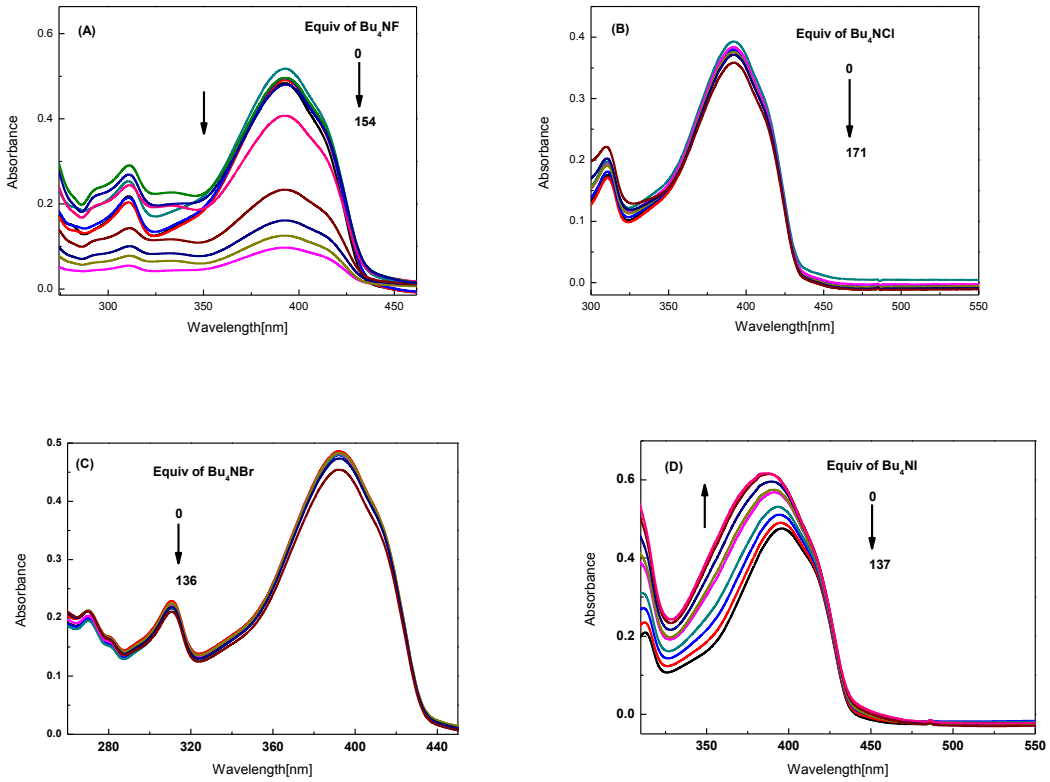

Figure S25: UV-Vis titration of boronate-oligomer fluorophore **226** (1.5 µM) with (A) *n*-Bu_4NF (B) *n*-Bu_4NCl (C) *n*-Bu_4NBr, and (D) *n*-Bu_4NI in THF at 298 K.

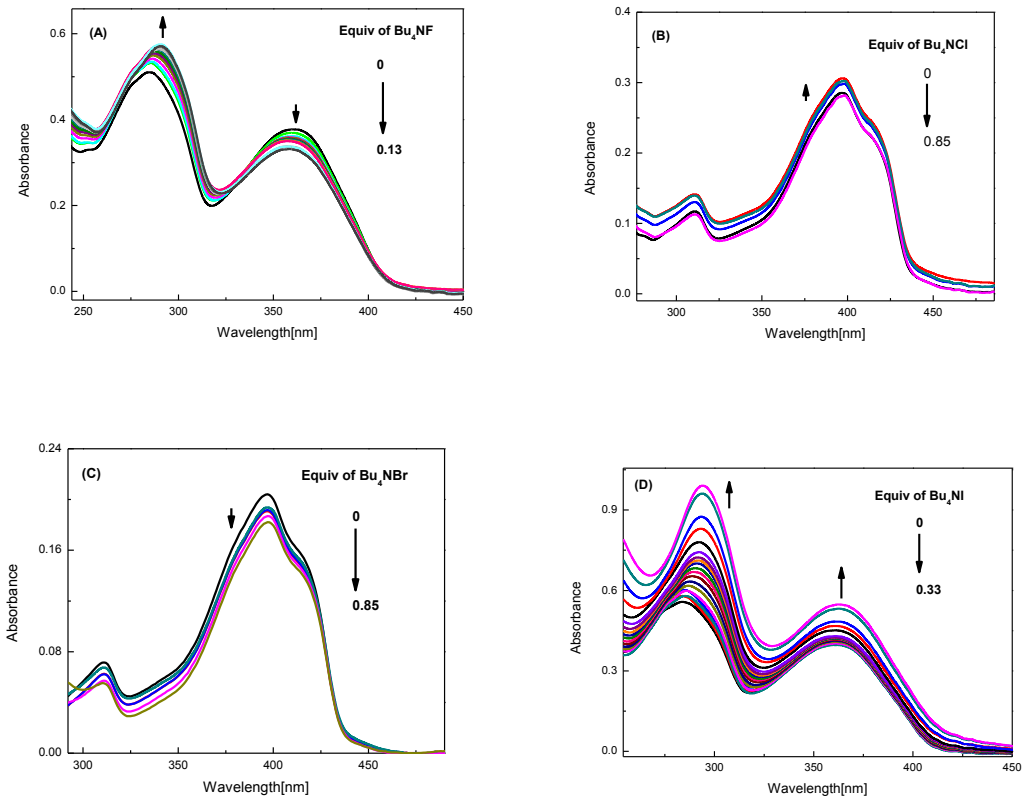

Figure S26: UV-Vis titration of boronate-oligomer fluorophore **243** (8.86 μM) with (A) *n*-Bu_4NF, (B) *n*-Bu_4NCl, (C) *n*-Bu_4NBr, and (D) *n*-Bu_4NI in THF at 298 K.

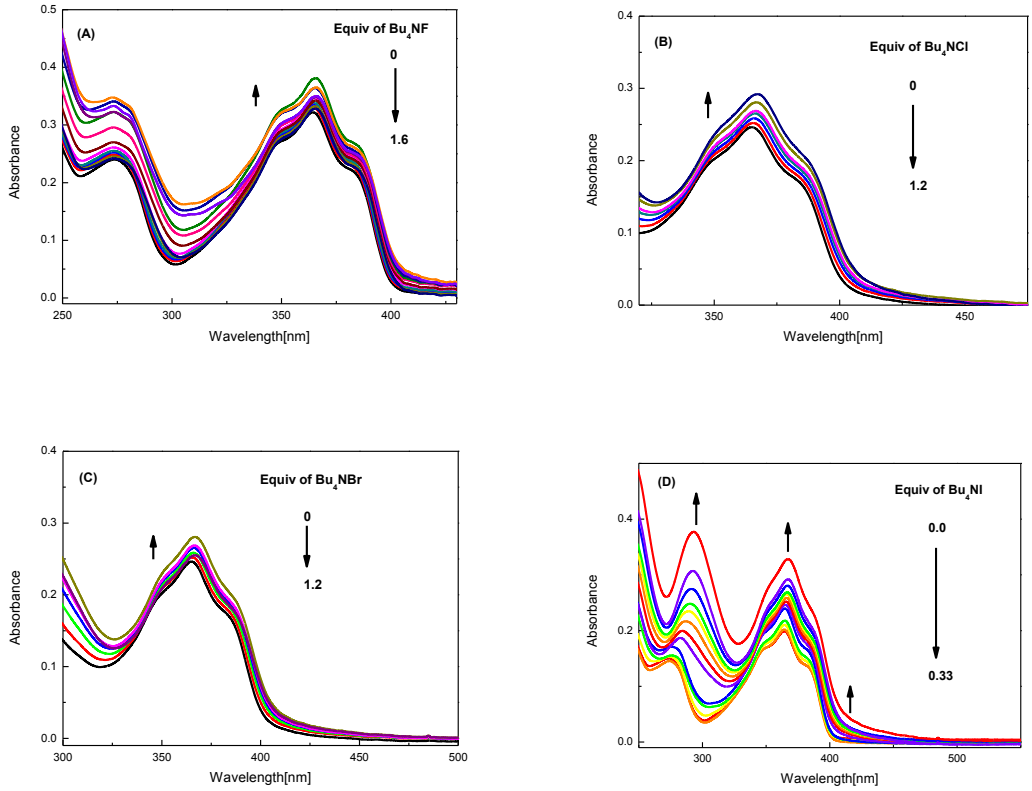

Figure S27: UV-Vis titration of boronate-oligomer fluorophore **244** (4.51 μM) with (A) *n*-Bu_4NF, (B) *n*-Bu_4NCl, (C) *n*-Bu_4NBr, and (D) *n*-Bu_4NI in THF at 298 K.

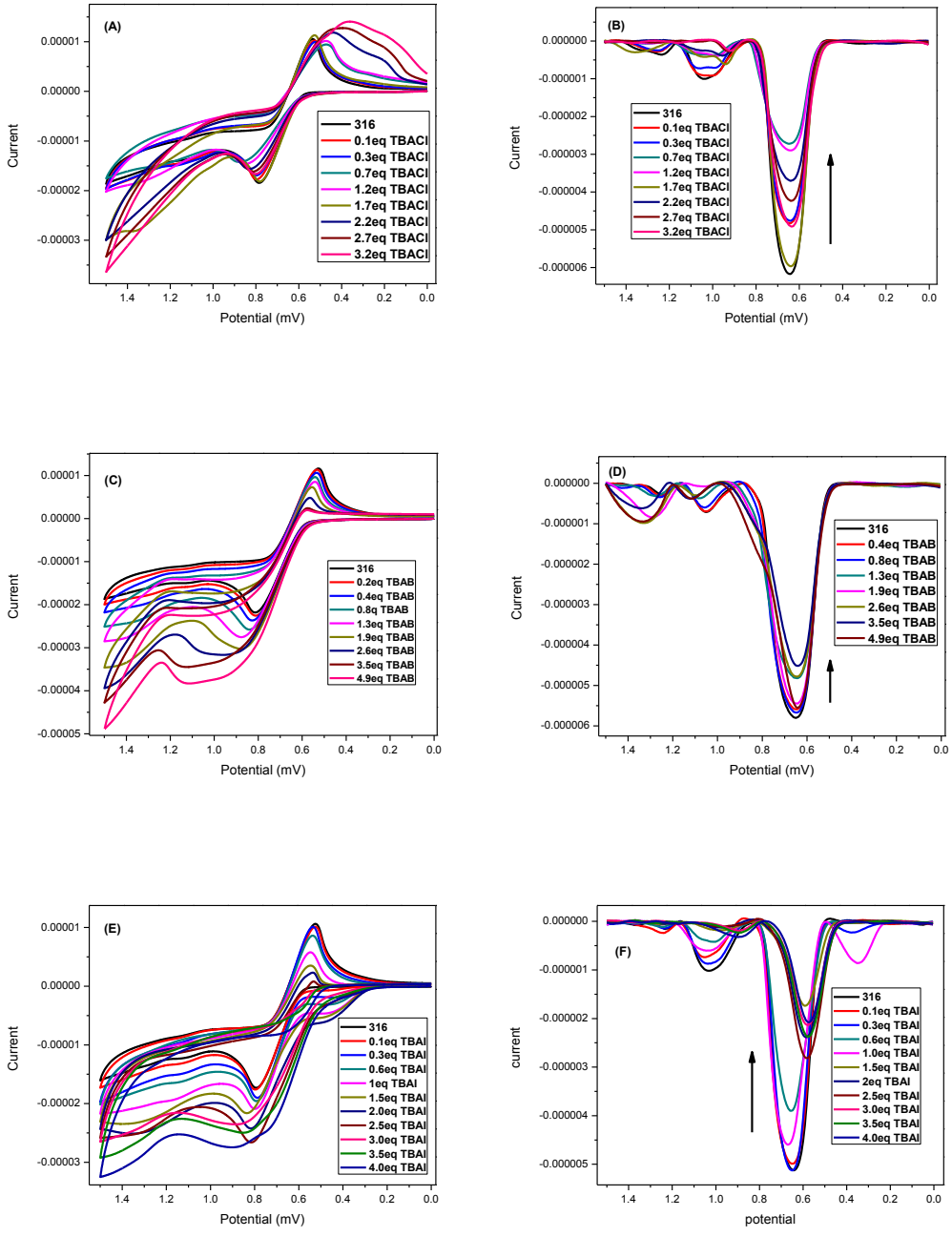

Figure S28: Cyclic voltammetric titration of **316** (2.35 mM) with (A) TBACl, (C) TBAB, and (E) TBAI. DPV changes of **316** (2.35 mM) upon addition of (B) TBACl, (D) TBAB, and (F) TBAI. Scan rate: 50 mV/s. Experimental conditions (DPV): solvent:

THF; electrolyte: Bu_4NBF_4 (0.1 M); working lectrode: glassy carbon; counter electrode: Pt wire; reference electrode: Ag/AgCl, NaCl (3 M); scan rate: 20 mV/s; pulse width: 50 mV; pulse period: 200 ms; step: 4 mV.